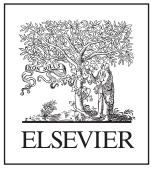
Light Alloys

Light Alloys

Metallurgy of the Light Metals

Fifth Edition

Ian Polmear
David StJohn
Jian-Feng Nie
Ma Qian





Butterworth-Heinemann
An imprint of Elsevier

Butterworth-Heinemann is an imprint of Elsevier
The Boulevard, Langford Lane, Kidlington, Oxford OX5 1GB, United Kingdom
50 Hampshire Street, 5th Floor, Cambridge, MA 02139, United States

Copyright © 2017 Ian Polmear, David StJohn, Jian-Feng Nie, Ma Qian. Published by Elsevier Ltd. All rights reserved.

No part of this publication may be reproduced or transmitted in any form or by any means, electronic or mechanical, including photocopying, recording, or any information storage and retrieval system, without permission in writing from the publisher. Details on how to seek permission, further information about the Publisher's permissions policies and our arrangements with organizations such as the Copyright Clearance Center and the Copyright Licensing Agency, can be found at our website: www.elsevier.com/permissions.

This book and the individual contributions contained in it are protected under copyright by the Publisher (other than as may be noted herein).

Notices
Knowledge and best practice in this field are constantly changing. As new research and experience broaden our understanding, changes in research methods, professional practices, or medical treatment may become necessary.

Practitioners and researchers must always rely on their own experience and knowledge in evaluating and using any information, methods, compounds, or experiments described herein. In using such information or methods they should be mindful of their own safety and the safety of others, including parties for whom they have a professional responsibility.

To the fullest extent of the law, neither the Publisher nor the authors, contributors, or editors, assume any liability for any injury and/or damage to persons or property as a matter of products liability, negligence or otherwise, or from any use or operation of any methods, products, instructions, or ideas contained in the material herein.

British Library Cataloguing-in-Publication Data
A catalogue record for this book is available from the British Library

Library of Congress Cataloging-in-Publication Data
A catalog record for this book is available from the Library of Congress

ISBN: 978-0-08-099431-4

For Information on all Butterworth-Heinemann publications
visit our website at https://www.elsevier.com/books-and-journals



Publisher: Matthew Deans
Acquisition Editor: Christina Gifford
Editorial Project Manager: Ana C Glaudia Garcia
Production Project Manager: Susan Li
Designer: Mark Rogers

Typeset by MPS Limited, Chennai, India

PREFACE TO THE FIRST EDITION

The fact that the light metals aluminium, magnesium and titanium have traditionally been associated with the aerospace industries has tended to obscure their growing importance as general engineering materials. For example, aluminium is now the second most widely used metal and production during the next two decades is predicted to expand at a rate greater than that for all other structural metals. Titanium, which has a unique combination of properties that have made its alloys vital for gas turbine engines, is now finding many applications in aircraft structures and in the chemical industry.

Light alloys have never been the subject of a single book. Moreover, although the general metallurgy of each class of light alloys has been covered in individual texts, the most recent published in English appeared some time ago—aluminium alloys in 1970, magnesium alloys in 1966 and titanium alloys in 1956. Many new developments have occurred in the intervening periods and important new applications are planned, particularly in transportation. Thus it is hoped that the appearance of this first text is timely.

In preparing the book I have sought to cover the essential features of the metallurgy of the light alloys. Extraction of each metal is considered briefly in Chapter one, after which the casting characteristics, alloying behaviour, heat treatment, properties, fabrication and major applications are discussed in more detail. I have briefly reviewed the physical metallurgy of aluminium alloys in Chapter two although the general principles also apply to the other metals. Particular attention has been devoted to microstructure/property relationships and the role of individual alloying elements, which provides the central theme. Special features of light alloys and their place in general engineering are highlighted although it will be appreciated that it has not been possible to pursue more than a few topics in depth.

The book has been written primarily for students of metallurgy and engineering although I believe it will also serve as a useful guide to both producers and users of light alloys. For this reason, books and articles for further reading are listed at the end of each chapter and are augmented by the references included with many of the figures and tables.

The book was commenced when I was on sabbatical leave at the Joint Department of Metallurgy at the University of Manchester Institute of Science and Technology and University of Manchester, so that thanks are due to Professor K. M. Entwistle and Professor E. Smith for the generous facilities placed at my disposal. I am also indebted for assistance given by the Aluminium Development Council of Australia and to many associates who have provided me with advice and information. In this regard, I wish particularly to mention the late Dr E. Emley, formerly of The British Aluminium Company Ltd; Dr C. Hammond, The University of Leeds; Dr M. Jacobs; TI Research Laboratories; Dr D. Driver, Rolls-Royce Ltd; Dr J. King and Mr W. Unsworth, Magnesium Elektron Ltd; Mr R. Duncan, IMI Titanium; Dr D. Stratford, University of Birmingham; Dr C. Bennett, Comalco Australia Ltd; and my colleague Dr B. Parker, Monash University. Acknowledgement is also made to publishers, societies and individuals who have provided figures and diagrams which they have permitted to be reproduced in their original or modified form.

Finally I must express my special gratitude to my secretary Miss P. O'Leary and to Mrs J. Colclough of the University of Manchester who typed the manuscript and many drafts, as well as to Julie Fraser and Robert Alexander of Monash University who carefully produced most of the photographs and diagrams.

IJP
Melbourne
1980

PREFACE TO THE SECOND EDITION

In this second edition, the overall format has been retained although some new sections have been included. For the most part, the revision takes the form of additional material that has arisen through the development of new compositions, processing methods, and applications of light alloys during the last 8 years.

Most changes have occurred with aluminium alloys which, because of their widespread use and ease of handling, are often used to model new processes. Faced with increasing competition from fiber-reinforced plastics, the aluminium industry has developed a new range of lightweight alloys containing lithium. These alloys are discussed in detail because they are expected to be important materials of construction for the next generation of passenger aircraft. More attention is given to the powder metallurgy route for fabricating components made from aluminium and titanium alloys. Treatment of this topic includes an account of techniques of rapid solidification processing which are enabling new ranges of alloys to be produced having properties that are not attainable by conventional ingot metallurgy. Metal–matrix composites based on aluminium are also finding commercial applications because of the unique properties they offer and similar magnesium alloys are being developed. New methods of processing range from methods such as squeeze casting through to advances in superplastic forming.

In preparing this new edition, I have again paid particular attention to microstructure/property relationships and to the special features of light alloys that lead to their widespread industrial use. In addition to an expanded text, the number of figures has been increased by some 40% and the lists of books and articles for further reading have been extended. Once more, the book is directed primarily at undergraduate and postgraduate students although I believe it will serve as a useful guide to producers and users of light alloys.

I am again indebted for assistance given by colleagues and associates who have provided me with information. Acknowledgment is also made to publishers, societies, and individuals who have provided photographs and diagrams which they have permitted to be produced in their original or modified form.

Finally I wish to express my gratitude to Mesdames J. Carrucan, C. Marich, and V. Palmer, who typed the manuscript, as well as to Julie Fraser, Alan Colenso, and Robert Alexander of Monash University who carefully produced most of the photographs and diagrams.

Melbourne, 1988

PREFACE TO THE THIRD EDITION

The central theme of the first two editions was microstructure/property relationships in which special attention was given to the roles of the various alloying elements present in light alloys. This general theme has been maintained in the third edition although some significant changes have been made to the format and content.

As before, much of this revision involves the inclusion of new material which, in this case, has arisen from developments during the seven years since the second edition was published. The most notable change in format has been to group together, into a new chapter, information on what have been called new materials and processing methods. Examples are metal matrix and other composites, structural intermetallic compounds, nanophase and amorphous alloys. Interest in these and other novel light alloys has increased considerably during the last decade because of the unceasing demands for improvements in the properties of engineering materials. Since light alloys have been at the forefront of many of these developments, the opportunity has been taken to review this area which has been the focus of so much recent research in materials science.

Another feature of the third edition is the greater attention given to applications of light alloys and their place in engineering. More case studies have been included, such as the use of light alloys in aircraft and motor cars. Economic factors associated with materials selection are also discussed in more detail. Moreover, since the light metals are often placed at a competitive disadvantage because of the high costs associated with their extraction from minerals, more attention has been given to these processes. This has led to a considerable increase in the size of the first chapter. Joining processes are described in more detail and, once again, service performance of light alloys is discussed with particular regard to mechanical behaviour and corrosion resistance.

As a result of these various changes, the text has been expanded and the number of figures has been increased by a further 20%. Lists of books and articles for further reading have been updated. While the book continues to be directed primarily at senior undergraduate and postgraduate students, I believe it will again serve as a useful guide to the producers and users of light alloys.

I am again indebted for assistance given by colleagues and associates who have provided me with information and helpful discussions. General acknowledgement is made to publishers, societies and individuals who have responded to requests for photographs and diagrams that have been reproduced in their original or modified form. Finally I wish to express my gratitude to my wife Margaret for her constant encouragement, to Carol Marich and Pam Hermansen who typed the manuscript and to Julie Fraser and Robert Alexander who once again carefully produced so many of the photographs and diagrams.

I. J. Polmear
Melbourne 1995

PREFACE TO THE FOURTH EDITION

Since the third edition of *Light Alloys* appeared in 1995, developments with new alloys and processes have continued at an escalating rate. Competition between different materials, metallic and nonmetallic, has increased as producers seek both to defend their traditional markets and to penetrate the markets of others. New compositions of aluminium, magnesium, and titanium alloy have been formulated, and increasing attention has been given to the development of novel and more economical processing methods. Because of their ease of handling, aluminium alloys in particular have been used as experimental models for many of the changes. Recently, potential automotive applications have led to a resurgence of interest in cast and wrought magnesium alloys.

The central theme of earlier editions was microstructure/property relationships, and particular attention was given to the roles of the various alloying elements present in light alloys. This general theme has been maintained in the fourth edition although further significant changes have been made to format and content. Special consideration has again been given to the physical metallurgy of aluminium alloys and many of the general principles also apply to magnesium and titanium alloys. The description of changes occurring during the processing of the major class of nonheat-treatable aluminium alloys has been extended. Although a century has now elapsed since the discovery of age hardening by Alfred Wilm, new observations are still being made as the latest experimental techniques reveal more details of the actual atomic processes involved. As examples, more information is now available about the role of solute and vacancy clusters during the early stages of aging, as well as other phenomena such as secondary hardening. Some success has been achieved with the modeling of precipitation processes. Precipitation hardening was hailed as the first nanotechnology and now it is possible to develop fine-scale microstructures in a much wider range of alloys through the use of novel processing methods.

Some new topics in this fourth edition are strip and slab casting, creep forming, joining technologies such as friction stir and laser welding, metallic foams, quasicrystals, and the production of nanophase materials. Economic factors associated with the production and selection of light metals and alloys

are considered in more detail and information on recycling has been included. Sections dealing with the commercial applications of light alloys and their general place in engineering have also been expanded. This applies particularly to transportation as aluminium alloys face increasing competition from fiber-reinforced polymers for aircraft structures, and where higher fuel costs make both aluminium and magnesium alloys more attractive for reducing the weight of motor vehicles.

Because of these and other developments, the text has been updated and expanded by about 20%. A further 50 figures and several new tables have been added. References to original sources of information are shown with most figures and tables but are not included in the general text. Relevant articles and books for further reading have been revised and are listed at the end of each chapter. As originally intended, the book is directed primarily at senior undergraduate and postgraduate students, but it is also believed it will to serve as a useful general guide to producers and users of light alloys.

I am again indebted for the assistance given by colleagues and associates who have provided me with information and advice. In this regard, special mention should be made of J. Griffiths, E. Grosjean, J. Jorstad, R. Lumley, J.-F. Nie, R.R. Sanders, H. Shercliff, J. Taylor, and the Australian Aluminium Council. General acknowledgment is again made to publishers, societies, and individuals who have responded to requests for photographs and diagrams. Facilities provided by the Department of Materials Engineering at Monash University have been much appreciated and, as with all other editions, many of the figures have been skillfully reproduced in their original or modified form by Julie Fraser. Finally I wish to express my gratitude to my wife Margaret for her constant support.

I. J. Polmear
Melbourne, 2005

PREFACE TO THE FIFTH EDITION

When the first edition of *Light Alloys* was published in England in 1981, the metallurgy of aluminium, magnesium, and titanium alloys had not been reviewed in a single book. Since then three more editions have been prepared, the fourth one having appeared in 2006. During the last decade, more light alloys have been developed, new processing methods have been adopted, and applications for these materials have expanded. To update these interesting developments, I have been delighted to welcome as co-authors three Australian colleagues with research interests in light alloys, namely Prof. David StJohn, University of Queensland, Prof. Jian-Feng Nie, Monash University, and Prof. Ma Qian, RMIT University. I thank them all for their valuable contributions to this fifth edition.

The central theme of the earlier editions has been microstructure/property relationships in which special attention was given to the specific roles of the various alloying elements present in aluminium, magnesium, and titanium alloys. This theme has been maintained in this fifth edition and various topics have been introduced or expanded. As an introduction to the three metals, Chapter 1 describes their characteristics, availability, methods of production, and global importance. The physical metallurgy of aluminium alloys is then reviewed and these general principles also apply to the alloys of the other two light metals. Examples are given to the remarkable ability of modern microscopic techniques to reveal the actual atomic events occurring during heat treatment processes such as precipitation hardening. A new chapter has been added to outline the theory and practice of casting processes used to make products from aluminium and magnesium alloys. Wrought aluminium alloys remains the largest chapter since approximately 70% of all aluminium is used for manufacturing these products. Chapters devoted to magnesium and titanium alloys have both been expanded by one-third and a section on additive manufacturing by 3D printing has been included in a final chapter that is concerned with novel materials and their processing methods.

Because of these various developments, the text for this fifth edition has been expanded by about 25% and more than 80 new or modified figures have been included. Tables have also been updated. Relevant articles and books for further reading are listed at the end of each chapter. As with earlier editions, the book is directed primarily at senior undergraduate and postgraduate students, although it will serve as a useful guide for producers and users of light alloys.

Melbourne, 2016

1

THE LIGHT METALS

1.1 GENERAL INTRODUCTION

The term "light metals" has traditionally been given to both aluminium and magnesium, because they are frequently used to reduce the weight of components and structures. On this basis, titanium also qualifies and beryllium should be included although it is little used and will only be mentioned briefly later. These four metals have relative densities ranging from 1.7 (magnesium) to 4.5 (titanium) which compare with 7.9 and 8.9 for the older structural metals, iron, and copper, and 22.6 for osmium, the heaviest of all metals. Ten other elements that are classified as metals are lighter than titanium but, with the exception of boron in the form of strong fibers embedded in a suitable matrix, none is used as a base material for structural purposes. The alkali metals lithium, potassium, sodium, rubidium, and cesium, and the alkaline earth metals calcium and strontium are too reactive, whereas yttrium and scandium are comparatively rare.

1.1.1 Characteristics of light metals and alloys

The property of lightness translates directly to material property enhancement for many products since by far the greatest weight reduction is achieved by a decrease in density (Fig. 1.1). This is an obvious reason why light metals have been associated with transportation, notably aerospace, which has provided great stimulus to the development of light alloys during the last century. Strength:weight ratios have also been a dominant consideration and the central positions of the light alloys based on aluminium, magnesium, and titanium with respect both to other engineering alloys and to all materials are represented in an Ashby diagram in Fig. 1.2. The advantages of decreased density become even more important in engineering design when parameters such as stiffness and resistance to buckling are involved. For example, the stiffness of a simple rectangular beam is directly proportional to the product of the elastic modulus

Light Alloys. DOI: http://dx.doi.org/10.1016/B978-0-08-099431-4.00001-4
Copyright © 2017 Ian Polmear, David StJohn, Jian-Feng Nie, Ma Qian.
Published by Elsevier Ltd. All rights reserved.

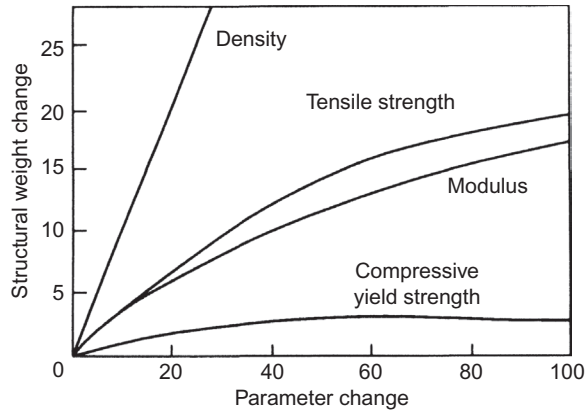


Figure 1.1 Effect of property improvement on structural weight. Courtesy from Lockheed Corporation.

and the cube of the thickness. The significance of this relationship is illustrated by the nomograph shown in Fig. 1.3 which allows the weights of similar beams of different metals and alloys to be estimated for equal values of stiffness. An iron (or steel) beam weighing 10 kg will have the same stiffness as beams of equal width and length weighing 7 kg in titanium, 4.9 kg in aluminium, 3.8 kg in magnesium, and only 2.2 kg in beryllium. The Mg–Li alloy is included because it is the lightest (relative density 1.35) structural alloy that is available commercially. Comparative stiffnesses for equal weights of a similar beam increase in the ratios 1:2.9:8.2:18.9 for steel, titanium, aluminium, and magnesium respectively.

Concern with aspects of weight saving should not obscure the fact that light metals possess other properties of considerable technological importance. Examples are the generally high corrosion resistance and high electrical and thermal conductivities of aluminium, the castability and machinability of magnesium, and extreme corrosion resistance of titanium. Comparisons of some physical properties are made in Table 1.1.

1.1.2 Beryllium

This element was discovered by Vauquelin in France in 1798 as the oxide in the mineral beryl (beryllium aluminium silicate) and in emerald. It was first isolated independently by Wöhler and Bussy in 1828 who reduced the chloride with potassium. Beryl has traditionally been a by-product of emerald mining and was until recently the major source of beryllium metal. Currently more beryllium is extracted from the closely associated mineral bertrandite (beryllium silicate hydroxide). Beryllium has some remarkable properties (Table 1.1). Its stiffness, as measured by specific elastic modulus, is nearly an order

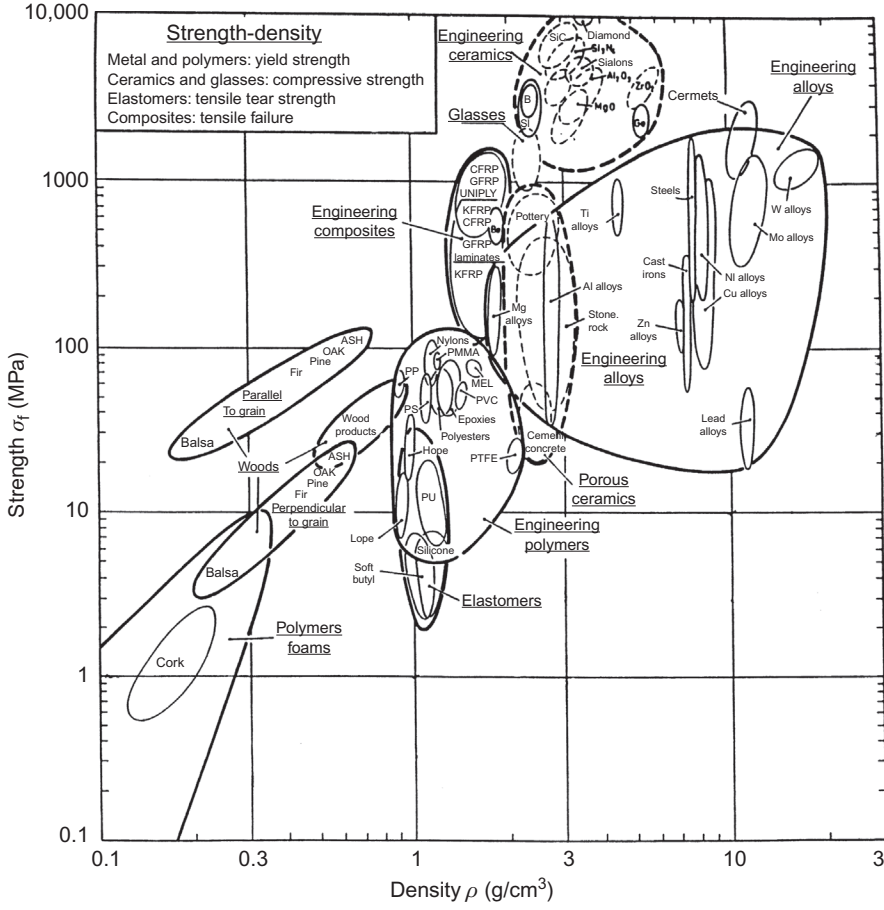


Figure 1.2 The strength:density ratios for light alloys and other engineering materials. Note that yield strength is used as the measure of strength for metals and polymers, compressive strength for ceramics, tear strength for elastomers, and tensile strength for composites. Courtesy from M. F. Ashby.

of magnitude greater than that for the other light metals, or for the commonly used heavier metals iron, copper, and nickel. This has led to its use in gyroscopes and in inertial guidance systems. It has a relatively high melting point, and its capture cross section (i.e., permeability) for neutrons is lower than for any other metal. These properties have stimulated much interest by the aerospace and nuclear industries. For example, a design study specifying beryllium as the major structural material for a supersonic transport aircraft has indicated possible weight savings of up to 50% for components for which it could be used. However, its structural uses have been confined largely to components for spacecraft and for applications such as satellite antenna booms.

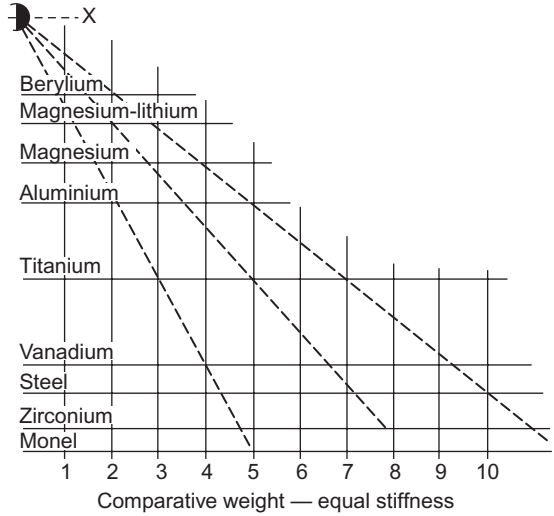


Figure 1.3 Nomograph allowing the comparative weights of different metals or alloys to be compared for equal levels of stiffness. These values can be obtained from the intercepts that lines drawn from point X make with lines representing the different metals or alloys. Courtesy from Brooks and Perkins Inc.

In nuclear engineering it has had potential for use as a fuel element can in power reactors. Another unique property of beryllium is its high specific heat which is approximately twice that of aluminium and magnesium, and four times that of titanium. This inherent capacity to absorb heat, when combined with its low density, led to the selection of beryllium as the basis for the reentry heat shield of the Mercury capsule used for the first manned spacecraft developed in the United States. In a more general application, it has served as a heat sink when inserted in the center of composite disk brakes used in the landing gear of a large military transport aircraft. Beryllium also shows outstanding optical reflectivity, particularly in the infrared, which has led to its combat use in target acquisition systems as well as in space telescopes.

Despite much research in several countries, wider use has not been made of beryllium because it is costly to mine and extract, it has an inherently low ductility at ambient temperatures, and the fact that the powdered oxide is extremely toxic to some people. The problem of low ductility arises because of the dimensions of the close-packed hexagonal crystal structure of beryllium. The *c*/*a* ratio of the unit cell is 1.567 which is the lowest and most removed of all metals from the ideal value of 1.633. One result of this is a high degree of anisotropy between mechanical properties in the a and c crystallographic directions. At room temperature, slip is limited and only possible on the basal plane, which also happens to be the plane along which cleavage occurs. Furthermore, there has also been little opportunity to improve properties by alloying because

Table 1.1 Some physical properties of pure metals

Property	Unit	Al	Mg	Ti	Be	Fe	Cu
Atomic number	–	13	12	22	4	26	29
Relative atomic mass (C= 12.000)	–	26.982	24.305	47.90	9.012	55.847	63.546
Crystal structure	–	fcc	cph	cph	cph	bcc	fcc
a	nm	0.4041	0.3203	0.2950	0.2286	0.2866	0.3615
c	nm	–	0.5199	0.4653	0.3583	–	–
Melting point	°C	660	650	1678	1289	1535	1083
Boiling point	°C	2520	1090	3289	2472	2862	2563
Relative density (*d*)	–	2.70	1.74	4.51	1.85	7.87	8.96
Elastic modulus (*E*)	GPa	70	45	120	295	211	130
Specific modulus (*E*/*d*)	–	26	26	26	160	27	14
Mean specific heat 0–100°C	$J\,kg^{-1}\,K^{-1}$	917	1038	528	2052	456	386
Thermal conductivity 20–100°C	$W\,m^{-1}\,K^{-1}$	238	156	26	194	78	397
Coefficient of thermal expansion 0–100°C	$10^{-6}\,K^{-1}$	23.5	26.0	8.9	12.0	12.1	17.0
Electrical resistivity at 20°C	μ ohm cm	2.67	4.2	54	3.3	10.1	1.69

From Lide, DR (Ed.): *Handbook of Chemistry & Physics*, 72nd Ed., CRC Press, Boca Raton, FL, USA, 1991–92; *Metals Handbook*, Volume 2, 10th Ed., ASM International, Metals Park, OH, USA, 1990.
Note: Conversion factors for S1 and Imperial units are given in the Appendix.

the small size of the beryllium atom severely restricts its solubility for other elements. One exception is the eutectic composition Be–38Al in which some useful ductility has been achieved. This alloy was developed by the Lockheed Aircraft Company in 1976 and became known as Lockalloy. Because beryllium and aluminium have little mutual solid solubility in each other, the alloy is essentially a composite material with a microstructure comprising stiff beryllium particles in a softer aluminium matrix. Lightweight (specific gravity 2.09) extrusions and sheet have found limited aerospace applications.

Beryllium is now prepared mainly by powder metallurgy methods. Metal extracted from the minerals beryl or bertrandite is vacuum melted and then either cast into small ingots, machined into chips and impact ground, or directly inert gas atomized to produce powders. The powders are usually consolidated by hot isostatic pressing and the resulting billets have properties that are more isotropic than are obtained with cast ingots. Tensile properties depend on the levels of retained BeO (usually 1–2%) and impurities (iron, aluminium, and silicon) and ductilities usually range from 3% to 5%. The billets can then be hot worked by forging, rolled to sheet, or extruded to produce bar or tube. Lockalloy (now also known as AlBeMet™ 162) is now also manufactured by inert gas atomization of molten prealloyed mixtures and the resulting powders are consolidated and hot worked as described earlier.

1.1.3 Relative abundance

The estimated crustal abundance of the major chemical elements is given in Table 1.2 which shows that the light metals aluminium, magnesium, and titanium are first, third, and fourth in order of occurrence of the structural metals.

Table 1.2 Crustal abundance of major chemical elements

Element	% by weight
Oxygen	45.2
Silicon	27.2
Aluminium	8.0
Iron	5.8
Calcium	5.06
Magnesium	2.77
Sodium	2.32
Potassium	1.68
Titanium	0.86
Hydrogen	0.14
Manganese	0.10
Phosphorus	0.10
Total	99.23

From Stanner, RJL: *Am. Sci.*, 64, 258, 1976.

It can also be seen that the traditional metals copper, lead, and zinc are each present in amounts <0.10%. Estimates are also available for the occurrence of metals in the ocean which, for example, is known to contain 0.13% magnesium. This is equivalent to 1.3 million tonnes per km^3 and approximately equals 1.4 times the annual world consumption of this metal in 2015. Overall, reserves of each of the light metals are adequate to cope with anticipated demands for some centuries to come. The extent to which they will be used would seem to be controlled mainly by their future costs relative to competing materials such as steel and plastics, as well as the availability of electrical energy that is needed for extraction from their minerals.

1.1.4 Trends in production and applications

Trends in the production of various metals and plastics are shown in Fig. 1.4 and it is clear that the light metals are very much materials of the 20th century. Between 1900 and 1950, the annual world production of aluminium increased

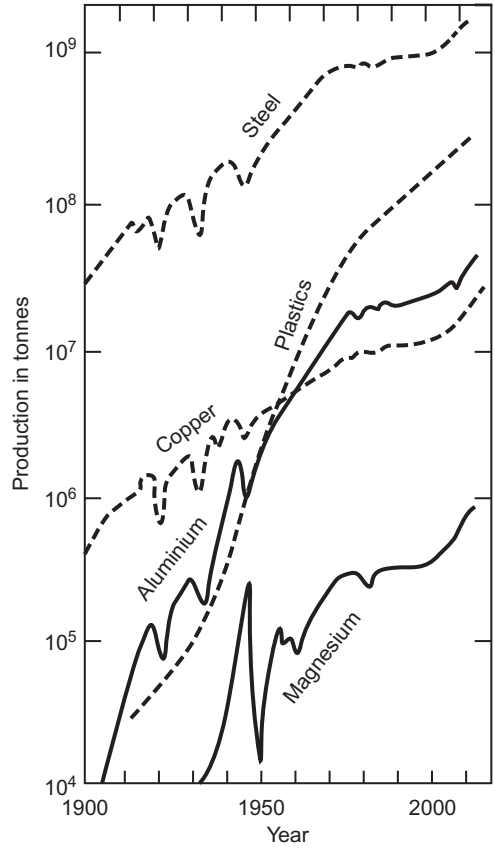


Figure 1.4 World production figures for various metals and plastics.

250 times from around 6000 tonnes to 1.5 million tonnes. A further eightfold increase took place during the next quarter century when aluminium surpassed copper as the second most used metal.

During this period the annual rate of increase in aluminium production averaged 9.2%. Since the late 1970s the demand for most basic materials has fluctuated and overall annual rate increases have been much less (Fig. 1.4). These trends reflect world economic cycles, the emergence of China and the Russian Federation as major trading nations, and the greater attention being given to metals recycling. World production of primary (new) aluminium grew by an annual average of around 4% during the two decades to 2000 when it was reported to have reached 24.66 million tonnes. Since then annual world production has more than doubled to an estimated 57.9 million tonnes in 2015 due mainly to a massive increase in output from China. During this period the production of secondary (recycled) aluminium has also increased and now accounts for about one-third of global consumption. For comparative purposes, however, it may be noted that steel still amounts to more than 90% of all metal used with 1.6 billion tonnes being produced in 2015. Moreover, it is interesting to record that the cumulative total of all the aluminium ever produced remains <1 year's current output of steel! It may also be noted that the production of commodity plastics and other polymeric materials, which have enjoyed spectacular growth since the 1950s, exceeded 310 million tonnes per annum in 2014.

Two political events have had a major impact on the production and pricing of the light metals in recent years. The first was the change from the former Soviet Union to the Commonwealth of Independent States (C.I.S.) in 1991 which was followed by the release of large quantities of metals for sale in Western nations, often at discounted prices. More significant has been the rapid transition of China over the last 30 years from a largely agrarian society to an increasingly industrialized economy. In 2015, China produced 57% of the world's primary (new) aluminium, whereas the outputs of traditional suppliers from North America and Europe have tended to decrease (Table 1.3). Further major expansion is expected in China where the per capita consumption of aluminium is still relatively low. China has also become by far the world's largest producer of magnesium and titanium.

Metal prices change from month to month and depend on factors that influence supply and demand. For example, the release of large quantities of aluminium by the C.I.S. that was mentioned earlier, combined with the effects of the world depression in the early 1990s, caused the price of aluminium to fall from an average of US$1675 per tonne in 1990 to under $US1100 in 1993. One consequence of this was the closure of some Western smelters, and cutbacks in others, even though smelters in the C.I.S. were then generally regarded as being less efficient. In recent years it has been China that has had the major influence on global prices which, in 2015, averaged close to $US1500 per tonne.

In most countries, aluminium is used in five major areas: transportation, building and construction, containers and packaging, electrical, and machinery

Table 1.3 World production of primary aluminium for the years 1995, 2005, and 2015

	1995	2005	2015
Africa	636	1753	1687
Asia (except China)	1656	3139	3001
China	NA	7806	31672
Europe Eastern (include Russian Fed.)	NA	4194	3829
Europe Western	5885	4352	3715
Gulf countries	–	–	5104
North America	5546	5382	4469
South America	2056	2391	1325
Oceania	1566	2252	1978

From International Aluminium Institute, London.
Thousands of tonnes.

and equipment (Fig. 1.5). Patterns vary widely from country to country depending on levels of industrialization and wealth. For the year 2013, the major users in the advanced economies were industries associated with transportation (35%), containers and packaging (20%), building and construction (16%), and machinery and equipment (10%). In the developing countries, the order was the building and construction (27%), transportation (20%), consumer durables (17%), and electrical (13%) industries. In 2013, China consumed 48% of the world's production of aluminium which compares with 16% in Europe and 12% in North America.

As shown in Fig. 1.4, global production of magnesium was relatively constant at about 250,000 tonnes per annum for the more than two decades from around 1970 until the late 1990s. During this period, some three-quarters of magnesium metal was consumed as alloying additions to aluminium (~55%), as a desulfurizing agent for steels (~15%), and to produce nodular cast iron (~6%). Less than 20% was actually used to produce magnesium alloys, mostly for die castings in the aerospace and general transport industries. During the next decade, the increase in the production of these die castings averaged 16% per annum and the amount of magnesium used for this purpose was estimated to have risen to about 150,000 tonnes by 2004. By 2015, the annual global output of magnesium had increased to approximately 900,000 tonnes of which one-third was now being used for magnesium alloy die castings. Less attention has been given to the development of wrought magnesium alloys because their hexagonal crystal structure renders them less amenable than aluminium to hot or cold working. However, recent research has led to some promising developments that are described in Chapter 6.

During the decade 1983–93, the price of magnesium was relatively constant and, on average, was around twice that of aluminium on the basis of weight.

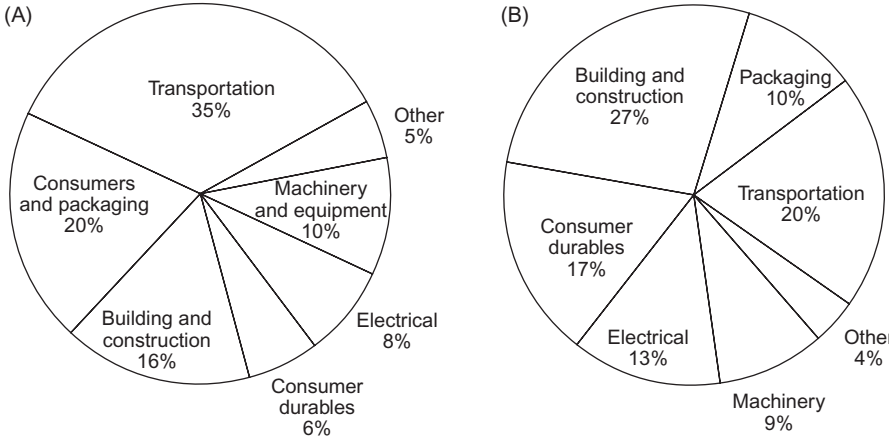


Figure 1.5 Outlets for the consumption of aluminium globally in (A) advanced economies and (B) emerging economies in 2013. Courtesy from Rusal and Aluminium Consumers.

However, volatility in the price of both metals since then has meant that the magnesium:aluminium price ratio has at times ranged from 2.5 to just below 1.5, the level at which magnesium becomes competitive on a volumetric basis. This was the situation in 2015 when the average price of magnesium was close to US$2000 per tonne.

Titanium was not produced in quantity until the late 1940s when its relatively low density and high melting point (1678°C) made it uniquely attractive as a potential replacement for aluminium for the skin and structure of high-speed aircraft subjected to aerodynamic heating. Liberal military funding was provided in the decade 1947–57 and one of the major metallurgical investigations of all time was made of titanium and its alloys. It is estimated that $400 million was spent in the United States during this period and one firm examined more than 3000 alloys. One disappointing result was that titanium alloys showed relatively poor creep properties bearing in mind their very high melting points. This factor, together with a sudden change in emphasis from manned aircraft to guided weapons, led to a slump in interest in titanium in 1957–58. Since then, selection of titanium alloys for engineering uses has been made on the more rational bases of cost-effectiveness and the uniqueness of certain properties. The high specific strength of titanium alloys when compared with other light alloys, steels, and nickel alloys is apparent in Fig. 1.6. The fact that this advantage is maintained to around 500°C has led to the universal acceptance of certain titanium alloys for critical gas turbine components. Titanium alloys have also found increasing use for critical structural components in aircraft including forged undercarriages, engine mountings, and high strength fasteners. Traditionally, aerospace applications have accounted for as much as

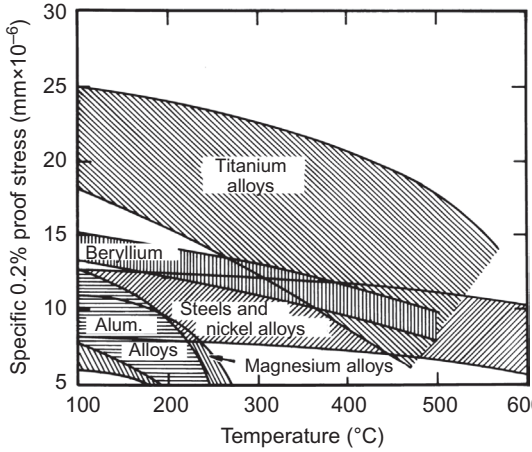


Figure 1.6 Relationship of specific 0.2% proof stress (ratio of proof stress to relative density) with temperature for light alloys, steels, and nickel alloys.

75% of titanium mill products, but this level has now fallen below 50%. Much of the remainder is finding increasing applications in the chemical industry where the high corrosion resistance of titanium is the key factor.

World production of titanium as sponge (see Section 1.4) peaked at around 180,000 tonnes in the mid-1980s when the Cold War had a dominant influence and had halved by the year 2002. At that time, worldwide production of titanium and titanium alloy mill products was 57,000 tonnes. It has been estimated that global production of titanium sponge had increased to about 280,000 tonnes in 2014 of which 114,000 (41%) was produced in China, 57,000 (20%) in Japan, and 46,500 (16.5%) in the C.I.S.

1.1.5 Recycling

Due to the realization that the supply of minerals is finite, much attention is now being paid to recycling as a means of saving metals, as well as reducing both the amount of energy and the output of greenhouse gases involved in their extraction. Based on known reserves, Fig. 1.7 shows one estimate of the dramatic effect that recycling rate may have on the remaining supply of several metals. With aluminium, for example, it has been predicted that a recycling rate of 50% would allow the reserves to last for about 320 years, whereas a rate of 80% would sustain these reserves for more than 800 years. In the United States, Japan, and much of Europe, some restrictions have been introduced that require materials used for consumer products to be recycled back into the same products. From 2006, for example, the European Union has required the fraction of metals recovered for reuse from old motor vehicles must be increased to at least 85% of the average vehicle weight.

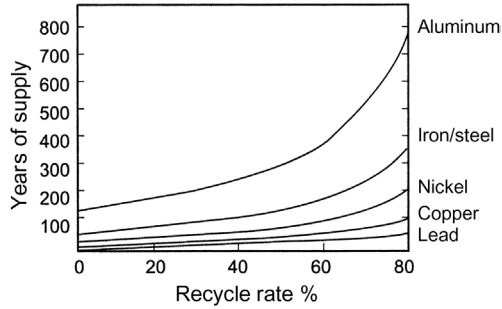


Figure 1.7 Estimated relationship between remaining years of supply of some metals and recycling rates based on known reserves of minerals. Courtesy from J. Rankin and T. Norgate, Commonwealth Scientific and Industrial Research Organization, Minerals Division, Melbourne.

The incentive for recycling light metals is particularly strong because their initial costs of production are relatively high. For aluminium, remelting of scrap requires only about 5% of the energy needed to extract the same weight of primary metal from its ore bauxite. Currently the ratio of secondary (scrap) to primary aluminium is around 30%, which is well below that recovered from steel or copper. However, as given in Table 1.4, the relatively long life span of some aluminium-containing products can limit the supply of used metal. In fact it has been estimated that around 70% of all the aluminium ever produced is still in circulation today.

The light alloys in general do present a special problem because they cannot be refined, i.e., alloying elements cannot be extracted or removed. Consequently, unless alloys for particular products are segregated and confined to a closed circuit, remelting tends to downgrade them. With aluminium alloys, the remelted general scrap is used mainly for foundry castings which, in turn, are limited in the amount they can absorb. Thus there is a need to accommodate more secondary aluminium alloys into cast billets that are used to produce wrought materials. In this regard, aluminium provides by far the highest value of any recyclable packaging material and, as an example, the efficient collection of all-aluminium alloy beverage cans to produce canstock is essential for the competitive success of this product (Section 4.6.5). Worldwide, four out of every five beverage cans are now made from aluminium alloys and the average recycling rate in 2015 is estimated to be 70%. In Switzerland and Sweden, it was 95% and in Finland and Germany, it is claimed to have reached 99%.

A schematic that seeks to represent the complex interactions involved in the production, use, and recycling of aluminium is shown in Fig. 1.8. The automotive industry is now the second largest provider of aluminium alloy scrap although sorting from other materials after discarded vehicles have been shredded into small pieces presents technical challenges. Currently flotation methods are commonly used. In the European Union, 95% of automotive parts and

Table 1.4 Global estimates of service lives and recycling rates for products made from aluminium

Major end markets	Average product life years	Average recycling rate per cent
Building and construction	25–50	80–85
Transportation—cars	10–15	90–95
Transportation—aerospace	15–25	90–95
Transportation—marine	15–40	40–90
Transportation—trucks, buses, rail	15–30	50–90
Engineering—machinery	10–30	30–90
Engineering—electrical	10–50	40–80
Packaging—cans	0.1–1.0	30–90
Packaging—foil	0.1–1.0	20–90

Courtesy from International Aluminium Institute, London.

building products made from aluminium alloys are recovered, together with 50% of rigid packaging. The aluminium industry in the United States has a vision of 100% recycling of aluminium alloys by the year 2020. Such an ambitious target will require major technological advances, notably the development of a low-cost process for metal purification so that the recycled scrap can become a source of primary aluminium.

In 2014, one-third of the world's output of magnesium was used as an alloying addition to aluminium and much of this is recycled along with these alloys. Otherwise, the recycling of magnesium alloy scrap is less advanced than for aluminium because of magnesium's high reactivity with oxygen and nitrogen, and problems with contamination by metals such as copper and nickel that adversely affect corrosion resistance. Clean and sorted magnesium alloy scrap arising from sprues, risers, and other discards from casting processes may be recycled within individual foundries. Other scrap is usually remelted under a refining flux that consists of a mixture of alkali and alkaline earth metal chlorides and fluorides. To maximize metal recovery, and reduce toxic gases, it is desirable to remove surface coatings such as paint, lacquer, and oil which add to the cost of recycling. Because of magnesium's high vapor pressure and relatively low boiling point (1090°C), distillation may offer a promising alternative solution to the problem of contamination from scrap. It may also provide the opportunity to produce pure magnesium metal from alloys which is much less feasible with aluminium or titanium (boiling points 2520°C and 3289°C, respectively).

More attention is now being directed to the recycling of titanium alloys because, on average, only 0.4 kg of each 1.3 kg of titanium metal produced as sponge ends up in the finished product. High-quality titanium alloy scrap can be

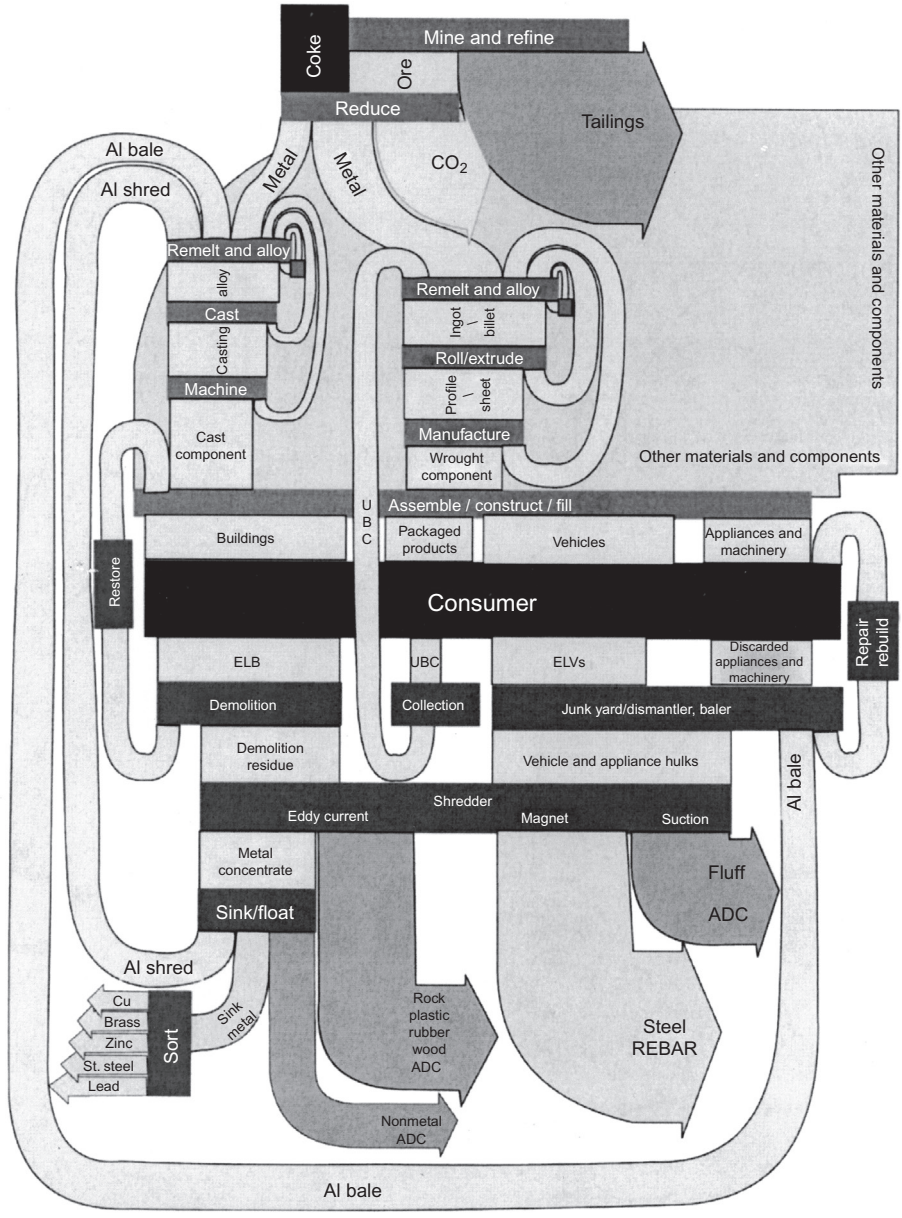


Figure 1.8 Schematic representation of the interactions in aluminium production, uses, and recycling. Courtesy from A. Gesing.

remelted within a closed circuit to make ingots or slabs. Other scrap, including sponge, can be used to produce ferrotitanium for adding to specialty steels. It has been reported that some 50,000 tonnes of scrap and sponge was recycled in 2014.

1.2 PRODUCTION OF ALUMINIUM

Although aluminium is now the second most used metal, it is a comparative newcomer among the common metals because of the difficulty in extracting it from its ores. Unlike iron, for example, it combines so strongly with oxygen that it cannot be reduced with carbon. An impure form of aluminium was first isolated in 1809 in England by Sir Humphry Davy which he produced from alum, its bisulfate salt. He called this new metal "aluminium," which is the name still used in the United States, whereas it is now known as "aluminium" in Europe and most other countries.

The first commercial preparation of aluminium occurred in France in 1855 when H. Sainte-Claire Deville reduced aluminium chloride with sodium. As is so often the case, the potential military applications of this new metal led to government support because Napoleon the Third foresaw its use in lightweight body armor. During the period 1855–59, the price of aluminium per kg fell from over US$500 to US$40, but all the Emperor is reported to have received were some decorative military helmets, an aluminium dinner set, and some aluminium toys for the children of the Imperial Court. The aluminium produced by Sainte-Claire Deville's process was <95% pure and it proved to be more expensive than gold at that time.

Independent discoveries in 1886 by Hall in the United States and Héroult in France led to the development of an economic method for the electrolytic extraction of relatively high-purity aluminium which remains the basis for production today. By 1888 the price had fallen to <US$4 per kg and in recent times it has varied between US$1 and US$2 per kg.

Aluminium is extracted from bauxite which was discovered by the French chemist P. Berthier, and named after the town of Les Baux in Provence, Southern France, where the ore was first mined. Bauxite is the end product of millions of years of surface weathering of aluminium silicates (e.g., feldspars) and clay minerals, usually in tropical locations. The principal aluminium-bearing minerals in bauxite exist as several forms of hydrated aluminium oxide, notably gibbsite ($Al_2O_3{\cdot}3H_2O$), which is also known as hydragillite or trihydrate, and boehmite ($Al_2O_3{\cdot}H_2O$) also known as monohydrate. The actual chemical composition varies with location and the geology of each deposit. Bauxite is usually mined simply by open cut methods and the largest known reserves exist in Guyana in West Africa (7400 million tonnes), Australia (6200 million tonnes), and Brazil (2600 million tonnes). Major world producers in 2014 were Australia (81 million tonnes) (34.6%), China (47 million tonnes) (20.1%), and Brazil (32.5 million tonnes) (14%).

Bauxite ore bodies typically contain 30–60% hydrated Al_2O_3 together with impurities comprising mainly iron oxides and silica. High-grade bauxites with

low silica contents are expected to be depleted in 20–30 years' time. When it becomes necessary to use grades with higher silica contents, the ore will first need to be processed to remove this impurity which will introduce a cost penalty. One method that has been developed in Russia is called thermochemical alkaline conditioning. This involves roasting the bauxite at high temperatures to convert the two most important silica-bearing minerals, kaolinite and quartz, into products that can be dissolved in caustic soda.

Immense amounts of aluminium are also present in clays, shales, and other minerals, and the amphoteric nature of aluminium provides the opportunity to use acidic as well as alkaline processes for its recovery. As one example, some attention has been given to acid extraction of alumina from kaolinite which is widely distributed as a clay mineral and is a major constituent of the ash in coal. The minerals, nepheline, $Na_3K(AlSiO_4)_4$, and alunite, $KAl_3(SO_4)_2(OH)_6$, are processed commercially in the C.I.S in plants located in regions remote from sources of bauxite. However, alumina obtained from these and other alternative sources is 1.5–2.5 times more costly than that produced from the Bayer process which is described in the following section.

1.2.1 Bayer process for alumina recovery

The Bayer process was developed and patented by Karl Josef Bayer in Austria in 1888 and essentially involves digesting crushed bauxite in strong sodium hydroxide solutions at temperatures up to 240°C. Most of the alumina is dissolved leaving an insoluble residue known as "red mud" which mainly comprises iron oxides and silica and is removed by filtration. The particular concentration of sodium hydroxide as well as the temperature and pressure of the operation are optimized according to the nature of the bauxite ore, notably the respective proportions of the different forms of alumina (α, β, or γ). This first stage of the Bayer process can be expressed by the equation:

$$Al_2O_3 \cdot xH_2O + 2NaOH \rightarrow 2NaAlO_2 + (x + 1)H_2O.$$

Subsequently, in the second stage, conditions are adjusted so that the reaction is reversed. This is referred to as the decomposition stage:

$$2NaAlO_2 + 2H_2O \rightarrow 2NaOH + Al_2O_3 \cdot 3H_2O.$$

The reverse reaction is achieved by cooling the liquor and seeding with crystals of the trihydrate, $Al_2O_3{\cdot}3H_2O$, to promote precipitation of this compound as fine particles rather than in a gelatinous form. Decomposition is commonly carried out at around 50°C in slowly stirred vessels and may require up to 30 h to complete. The trihydrate is removed and washed, with the sodium hydroxide liquor being recycled back to the digesters.

Alumina is then produced by calcining the trihydrate in rotary kilns or, more recently, fluidized beds. Calcination occurs in two stages with most of the water

of crystallization being removed in the temperature range 400–600°C. This produces alumina in the more chemically active γ-form which further heating to temperatures as high as 1200°C converts partly or completely to relatively inert α-alumina. Each form has different physical characteristics and individual aluminium smelters may specify differing mixtures of α- and γ-alumina. Typically the Bayer process produces smelter grade alumina in the range 99.3–99.7% Al_2O_3.

Over the decade 2005–15, the annual world production of alumina that was reported rose from 64.6 to 115.2 million tonnes. During this period, China's output increased by seven times from 8.5 to 59.0 million tonnes which is 51% of the total. Other major suppliers were Australia and Brazil. In 2015, the average world price for alumina was approximately US$250 per tonne.

1.2.2 Production of aluminium by the Hall–Héroult process

Alumina has a high melting point (2040°C) and is a poor conductor of electricity. The key to the successful production of aluminium lies in dissolving the oxide in molten cryolite (Na_3AlF_6) and a typical electrolyte contains 80–90% of this compound and 2–8% of alumina, together with additives such as AlF_3 and CaF_2. Cryolite was first obtained from relatively inaccessible sources in Greenland but is now made synthetically.

An electrolytic-reduction cell (known as a pot) consists essentially of baked carbon anodes that are consumed and require regular replacement, the molten cryolite–alumina electrolyte, a pool of liquid aluminium, a carbon-lined container to hold the metal and electrolyte, and a gas collection system to prevent fumes from the cell escaping into the atmosphere (Fig. 1.9). There are also alumina feeders that are activated intermittently under some form of automatic control. A typical modern cell is operated at around 950°C and takes up to 500 kA at an anode current density around 0.7 A cm^{-2}. The anode and cathode are separated by 4–5 cm and there is a voltage drop of 4–4.5 V across each cell. The cell is operated so that the carbon side linings are protected with a layer of frozen cryolite and the upper surface of the bath is covered with a crust of alumina. The molten aluminium is siphoned out regularly to be cast into ingots and alumina is replenished as required. The largest and most productive cells operate at a current efficiency of around 95% and have a daily output of about 4000 kg of aluminium. Typically, 150–300 cells are connected in series to make up a potline (Fig. 1.10).

The exact mechanism for the electrolytic reaction in a cell remains uncertain but it is probable that the current-carrying ions are Na^+, $AlF4^-$, AlF_6^{3-} and one or more ternary complex ions such as $AlOF_3^{2-}$. At the cathode it is considered that the fluroaluminate anions are discharged via a charge transfer at the cathode interface to produce aluminium metal and F^- ions while, at the anode, the oxofluroaluminate ions dissociate to liberate oxygen which forms CO_2. The overall reaction can be written simply as follows:

$$2Al_2O_3 + 3C \rightarrow 4Al + 3CO_2.$$

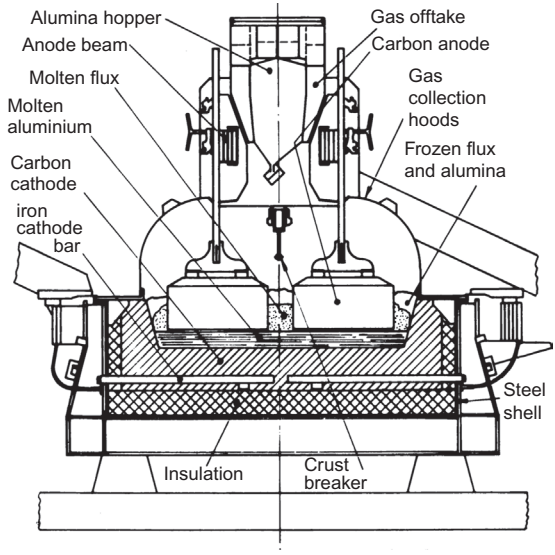


Figure 1.9 Hall–Héroult electrolytic cell for producing aluminium. Courtesy from Australian Aluminium Council.

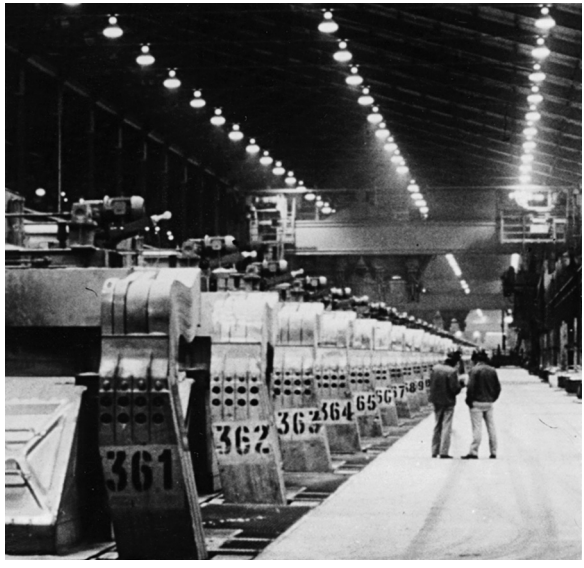


Figure 1.10 Potline of electrolytic cells for producing aluminium. Courtesy from Comalco Ltd.

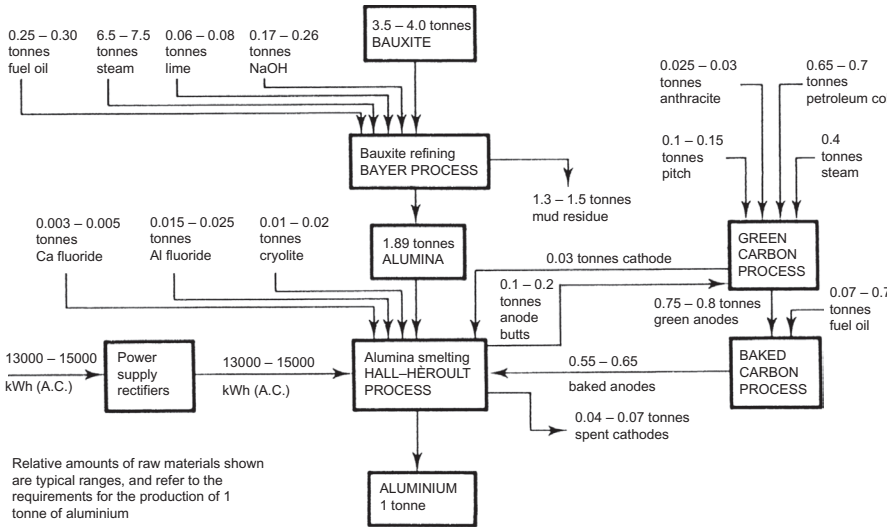


Figure 1.11 Flow diagram for integrated production of aluminium from bauxite. Courtesy from Australian Aluminium Council.

Fig. 1.11 shows a flow diagram for the raw materials needed to produce 1 tonne of aluminium. Commonly some 3.5–4 tonnes of bauxite are needed from which 2 tonnes of alumina are extracted that, in turn, yield 1 tonne of aluminium. Significant quantities of other materials, such as 0.4 tonne of carbon, are also consumed. However, the most critical factor is the consumption of electricity which, despite continual refinements to the process, modern smelters still require close to 13,000 kWh to extract each tonne of aluminium from alumina. This values compares with 28,000 kWh per tonne needed shortly after the Hall–Héroult process was first commercialized late in the 19th century, and the theoretical requirement which is about 6500 kWh. Traditionally, about 50% of this power has come from hydroelectricity.

Of the total voltage drop of 4.0–4.5 V across modern cells, only 1.2 V represents the decomposition potential or free energy of the reaction associated with the formation of molten aluminium at the cathode. The largest component of the voltage drop arises from the electrical resistance of the electrolyte in the space between the electrodes and this amounts to around 1.7 V, or 35–40% of the total. Efficiency can be increased if the anode–cathode distance is reduced and this aspect has been one focus of recent changes in cell design. A modification that shows promise is to coat the cathode with titanium diboride which has the property of being readily wetted by molten aluminium. This results in the formation of a thinner, more stable film of aluminium that can be drained away into a central sump if a sloped cathode is used (Fig. 1.12). Reductions in anode–cathode spacing from the normal 4–6 cm down to 1–2 cm have been

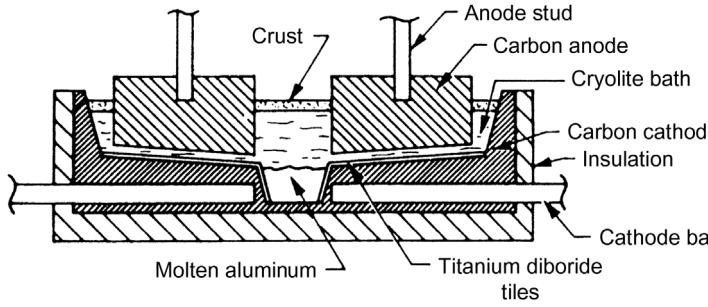


Figure 1.12 Modified cell design for electrolytic reduction of aluminium. Courtesy from Kaiser Aluminium & Chemical Corporation.

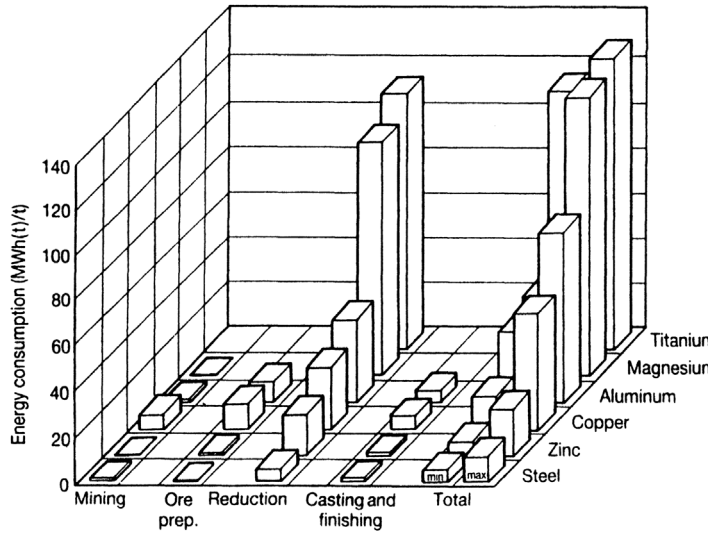


Figure 1.13 Total energy consumption in megawatt hours (thermal) for each stage in the production of the light metals and copper, zinc, and steel. From Yoshiki-Gravelsins, KS *et al.*: *J. Metals*, 45(5), 15, 1993.

claimed permitting a decrease of 1–1.5 V in cell voltage. Predictions on cell performance suggest that electrical energy consumption can be reduced to an average of 12,000 kWh per tonne of aluminium produced by the year 2020.

Fig. 1.13 summarizes one calculation of the total energy consumed during all stages in the production of the light metals, as well as that for copper, zinc, and steel. To produce 1 tonne of primary aluminium from bauxite in the ground has been estimated to require between 70,000 and 75,000 kWh (thermal), where the total energy required has been converted back to an equivalent amount of fossil fuel by assuming 1 kWh (electrical) = 3 kWh (thermal).

This reduces to 30,000 kWh (thermal) per tonne of aluminium, but is still much greater than the estimated 13,000–16,000 kWh (thermal) of energy required to produce 1 tonne of steel as finished product iron ore in the ground.

1.2.3 Alternative methods for producing aluminium

Because of the large disparity between the theoretical and actual requirements for electrical energy to produce each tonne of aluminium, it is to be expected that alternative methods of production would have been investigated. One example has been a chloride-based smelting process developed by Alcoa which commenced operation in the United States in 1976 with an initial capacity of 13,500 tonnes of aluminium per year and the potential to achieve a 30% cost saving. This process also used alumina as a starting material which was combined with chlorine in a reactor to produce $AlCl_3$. This chloride served as an electrolyte in a closed cell to produce aluminium and chlorine, the latter being recycled back into the reactor. The process had the advantage of being continuous but the provision of materials of construction that could resist attack by chlorine over long periods of time proved to be difficult. This factor, together with improvements in efficiencies in conventional electrolysis, led to the process being discontinued in 1985.

Several companies have investigated carbothermic methods for producing aluminium. One process involves mixing aluminium ore with coking coal to form briquettes, which are then reduced in stages in a type of blast furnace operating at temperatures ranging from 500°C to 2100°C. The molten metal product comprises aluminium combined with iron and silicon which is scrubbed and absorbed by a spray of molten lead at the bottom of the furnace. Since aluminium and lead are immiscible, the lighter aluminium rises to the surface where it can be skimmed off. Further purification of the aluminium is required. Although the overall cost savings have been predicted, no commercially viable process has so far eventuated.

1.3 PRODUCTION OF MAGNESIUM

One of the novel explanations for the disappearance of the dinosaurs is the Chinese theory that this was due to a magnesium deficiency which had an adverse effect on the strength of egg shells thereby preventing reproduction. Today it is recognized that human beings require a daily intake of 300–400 mg of magnesium which means that some 600,000 tonnes should be ingested annually throughout the world! Until recently, this was more than double the amount of magnesium metal actually produced each year.

In 1808, Sir Humphry Davy established that magnesium oxide was the oxide of a newly recognized element. Magnesium metal was first isolated in 1828 by the Frenchman Antoine-Alexander Bussy who fused $MgCl_2$ with metallic potassium. The first production of magnesium by the electrolytic

reduction of the chloride was accomplished by Michael Faraday in 1833. Commercial production commenced in Paris in the middle of the 19th century but had reached only some 10 tonnes per annum by the year 1890. Output increased to 3000 tonnes during the last year of the First World War, fell again afterward and then rose to around 300,000 tonnes per annum late in the Second World War. Global production varied during the next 50 years to reach 400,000 tonnes per annum by 2000. Since it then has risen more rapidly to approximately 900,000 tonnes by 2015 as mentioned earlier.

Magnesium compounds are found in abundance in solid mineral deposits in the earth's crust and in solution in the oceans and salt lakes. The most common surface minerals are the carbonates dolomite ($MgCO_3{\cdot}CaCO_3$) and magnesite ($MgCO_3$). The mineral brucite ($MgO{\cdot}H_2O$) is somewhat rarer, as are the chlorides of which carnallite ($MgO{\cdot}KCl{\cdot}6H_2O$) is one example. Concentrated aqueous solutions in the form of brine deposits occur at several places in the world including the Dead Sea in Israel and the Great Salt Lake in Utah, United States, where a total of close to 80,000 tonnes has been produced annually. Virtually unlimited reserves are present in the oceans which contain 0.13% magnesium and, until recently, seawater provided more than 80% of the world's supply of this metal which was extracted by the electrolytic reduction of molten $MgCl_2$. During the 1940s, the largest seawater plant was constructed in the United States at Freeport, Texas, and production peaked at 120,000 tonnes in the 1970s. Output then declined during the next two decades and the plant was closed in 1998 following severe storm damage. At present the extraction of magnesium from seawater has become uncompetitive for reasons that are explained later.

Two processes have been developed to produce magnesium by the direct reduction of dolomite by ferrosilicon at high temperatures. One is the Pidgeon process originating from Canada in 1941 in which this reaction is carried out in the solid state. Until recently it was only economic in rare conditions where there was a natural site advantage. The other is the Magnétherm process that was developed in France and which operates at much higher temperatures so that the reaction mixture is liquid. This process is also producing magnesium at prices that are currently uncompetitive with metal now produced in China by the Pidgeon process.

1.3.1 Electrolytic extraction of magnesium

Two types of electrolytic processes have been used to produce magnesium that differ in the degree of hydration of the $MgCl_2$ and in cell design. One was pioneered by IG Fabenindustrie in Germany in 1928 and was adopted later by the Norwegian company Norsk Hydro when it was a major European producer of this metal. Known as the IG process, it uses dry MgO derived from minerals in seawater which is briquetted with a reducing agent, e.g., powdered coal, and $MgCl_2$ solution. The briquettes are lightly calcined and then chlorinated at around 1100°C to produce anhydrous $MgCl_2$, which is fed directly

into the electrolytic cells operating at 740°C. Other chloride compounds such as NaCl and $CaCl_2$ are added to improve electrical conductivity and to change the viscosity and density of the electrolyte. Each cell uses graphite anodes that are slowly consumed and cast steel cathodes that are suspended opposite one another. Typically the cells operate at 5–7 V and currents may now exceed 200,000 A. Magnesium is deposited on the cathodes as droplets which rise to the surface of the electrolyte, whereas chlorine is liberated at the anodes and is recycled to produce the initial $MgCl_2$ cell feedstock.

The second electrolytic process for extracting magnesium from seawater was developed by the Dow Chemical Company for use at the Freeport plant mentioned earlier. Magnesium in $MgCl_2$ was precipitated as the hydroxide by the addition of lime and then dissolved in HCl. This solution was then concentrated and dried although the process stopped short of complete dehydration of the $MgCl_2$ which was then available as the cell electrolyte. In contrast, in the IG-Norsk Hydro process, the cells required external heat with the steel cell box serving as the cathode. These cells operated at 6–7 V and a current of 90,000 A.

The energy consumed per kg of magnesium produced was around 12.5 kWh for the Norsk Hydro cell and 17.5 kWh for the Dow cell. However, each process required the additional consumption of approximately 15 kWh of energy per kg for preparation of $MgCl_2$ cell feed.

Two new processes for extracting the basic feedstock anhydrous $MgCl_2$ in a high-purity form for use in electrolytic cells have been developed in Canada and Australia, although neither reached commercial production. In Canada, the Magnola process used tailings from asbestos mines to take advantage of magnesium silicate contained in serpentine ore. The tailings were leached in strong HCl by means of a novel procedure to produce a solution of $MgCl_2$ which was purified by adjusting the pH. Ion exchange techniques were then used to generate concentrated, high-purity brine that was dehydrated for use in an electrolytic cell. The Australian process was developed to exploit magnesite ($MgCO_3$) mined from a huge surface deposit in Queensland that is estimated to contain 260 million tonnes of high-grade ore. $MgCl_2$ was leached from the magnesite with HCl and glycol was added to the solution, after which water was removed by distillation. Magnesium chloride hexammoniate was then formed by sparging with ammonia. Final calcining produced a relatively low-cost, high-purity $MgCl_2$, and the solvent and ammonia were recycled. This process was successfully developed to pilot plant stage but has since been abandoned largely for economic reasons.

1.3.2 Thermic processes

Production of magnesium by direct thermal reduction of calcined dolomite with ferrosilicon proceeds according to the simplified equation:

$$2CaO \cdot MgO + Si \rightarrow 2Mg + (CaO)_2SiO_2.$$

In the Pidgeon process, briquettes of the reactants are prepared and loaded in amounts of around 150 kg each into a number of tubular steel retorts that are typically 250–300 mm in diameter and 3 m long. The retorts are then evacuated to a pressure of below 0.1 torr and externally heated to a temperature in the range 1150–1200°C, usually by burning coal. Magnesium forms as a vapor that condenses on removable water-cooled sleeves at the ends of the retorts that are located outside the furnace. Approximately 1.1 tonnes of ferrosilicon is consumed for each tonne of magnesium that is produced. Advantages of the Pidgeon process are the relatively low capital cost and the less stringent requirement that is placed on the purity of the raw materials. Major deficiencies are that it is a labor-intensive, batch process which usually only produces about 20 kg of magnesium from each retort, and requires a lengthy cycle time of around 8 h. The retorts must then be emptied, cleaned, and recharged in conditions that may be dusty and unpleasant. The Pidgeon process has been widely adopted in China where labor costs are low relative to Western nations, and there are readily available supplies of low-cost ferrosilicon and anthracite. Many hundreds of plants of varying sizes have been constructed which, in 2014, supplied about 80% of the world's magnesium.

The Magnétherm process employs an electric arc furnace operating at around 1550°C and with an internal pressure of 10–15 torr. Because the reaction takes place in the liquid phase, the time required for its completion is less than that needed for the Pidgeon process. The furnace may be charged continuously and discharged at regular intervals, and alumina or bauxite is added to the dolomite/ferrosilicon charge which keeps the reaction product, dicalcium silicate, molten so that it can be tapped as a slag. Magnesium is again produced as a vapor which is solidified in an external condenser. Batch sizes may be as high as 11,000 kg and plants have operated in France, Japan, the United States, and in the former Yugoslavia.

Alternative thermic techniques have been proposed, although none is currently operating commercially. One idea was to use a plasma arc furnace in which pelletized MgO and coke are fed into a premelted MgO, CaO, Al_2O_3 slag. The high energy density of the plasma, and the fact that high temperatures (e.g., 1500°C) are generated at the surface of the slag where the silicothermic reaction occurs, allows it to be sustained at normal atmospheric pressure. This advantage, combined with the efficient and near total silicon consumption, was claimed to enhance economic competitiveness of the thermic route to magnesium production. However, this development also occurred before use of the Pidgeon process was adopted and greatly expanded in China.

In 2014, one-third of the world's magnesium was consumed as an alloying element in aluminium and nearly another third was used to desulfurize steels (11%), refine titanium sponge (11%), or produce nodular cast irons (6%). As mentioned earlier, the residual one-third was mainly used to produce lightweight die castings for the automotive industry.

1.4 PRODUCTION OF TITANIUM

The existence of titanium was first recognized in 1791 by William McGregor, an English clergyman and amateur mineralogist, who detected the oxide of an unknown element in local ilmenite sand ($FeO{\cdot}TiO_2$). A similar observation was made in 1795 by a German chemist, Martin Klaproth, who examined the mineral rutile (TiO_2) and named the element titanium the Titans who, in Greek mythology, were the offspring of Mother Earth and Father Heaven. An impure sample of titanium was first isolated in 1825. Relatively pure but less ductile titanium was first produced in 1910 in the United States by Matthew A. Hunter, a chemist born in New Zealand, who reacted titanium tetrachloride ($TiCl_4$) with molten sodium under vacuum:

$$TiCl_4(g) + 4Na(l) \rightarrow 4NaCl(l) + Ti(s)\,\text{at}\,700 - 800^{\circ}C$$

The process is now known as the Hunter process and it can be used to produce very ductile titanium sponge today. However, metallic titanium of significant ductility or purity was not produced until 1925 when the Dutch scientists A. E. van Arkel and J. H. de Boer succeeded in dissociating titanium tetraiodide (TiI_4) on a hot tungsten filament (1400°C) in an evacuated glass bulb. The ultrapure titanium hairpins thus produced turned out to be very ductile and soft at room temperature. This represented a milestone in the history of titanium as it revealed that titanium was not inherently brittle. The brittleness of impure titanium arises from its high content of interstitial elements (see classification of commercial-purity titanium in Chapter 7), especially its oxygen level. Known as the *crystal bar process*, it is still used today for the production of ultrapure metals. In 1932, Wilhelm Kroll, in Luxembourg, invented the process of producing ductile titanium by reacting $TiCl_4$ with molten calcium. However, because calcium has a relatively high melting point (842°C) and was expensive at that time, he switched to using molten magnesium in 1937 and was able to produce 0.5 kg batches of titanium sponge by the following chemical reaction:

$$TiCl_4(g) + 2Mg(l) \rightarrow 2MgCl_2(l) + Ti(s)\,\text{at}\,800 - 900^{\circ}C$$

Kroll emigrated to the United States in 1940 where he stimulated the interest of the Bureau of Mines in his magnesium-reduction process. Based on the Bureau's concerted research, the DuPont Company built the world's first titanium plant and produced ~3 tonnes of sponge (>99% purity) in 1948. Subsequently, commercial production of the titanium sponge commenced in England (1951), Japan (1952), and the former Soviet Union countries (1954).

While the Kroll process was the dominant technology, the Hunter (sodium) process was also used for industrial production of titanium sponge in the United States, Japan, and United Kingdom. However, since about 1993, the

Honeywell's Salt Lake City Plant in the United States has been the only company which continues to produce sodium-reduced titanium sponge. The Kroll titanium sponge production process consists of four essential steps: (1) chlorination or production of titanium tetrachloride, (2) purification of titanium tetrachloride, (3) reduction with molten magnesium, and (4) vacuum distillation of the reaction products. These are described briefly later.

As given in Table 1.2, titanium is the ninth most abundant element in the earth's crust with its two prime sources being the minerals rutile (TiO_2) and ilmenite ($FeO{\cdot}TiO_2$). Rutile is found mainly in beach sands along the southwestern coasts of Australia, India, Mexico, and in estuaries in Sierra Leone, while ilmenite is available in a number of countries with particularly large deposits being found in China and Russia. $TiCl_4$ can be made from both rutile and ilmenite (after the removal of iron, known as rutile slag containing more than 95% TiO_2) by the following exothermic chlorination process:

$$TiO_2(\text{impure}) + 2C + 2Cl_2 \rightarrow TiCl_4 + 2CO + Q(\text{heat}) \text{ at } 1000 - 1100^{\circ}C$$

The impure rutile powder used in this reaction is usually controlled in the size range of 100–400 μm with no more than 10% of either the coarser (>400 μm) or finer (<100 μm) rutile particles. Calcined petroleum or asphalt coke is used as the carbonaceous agent. It should be noted that only about 5–8% of the $TiCl_4$ production is used for titanium production. The remainder is converted back into pure white pigment TiO_2 in paint through direct oxidation of $TiCl_4$ as the mineral rutile is impure.

$$TiCl_4 + O_2 \rightarrow TiO_2 + 2Cl_2$$

The $TiCl_4$ produced (≥98% purity) contains a variety of impurities including $SiCl_4$, $VOCl_3$, and $FeCl_3$, and is subsequently purified to more than 99.9% purity by a series of processes. Magnesium ingot materials with not less than 99.9% purity are melted and used to reduce the high-purity $TiCl_4$ in a high-purity argon atmosphere. The reaction product consists of about 39%Ti, 42%Mg, and 19%$MgCl_2$ (in vol.%). During subsequent vacuum distillation at 900–1000°C, the Mg (l) and $MgCl_2$ (l) entrapped in the titanium vaporize due to their high vapor pressures. The resulting titanium product is porous and is referred to as *titanium sponge*.

When pushed out of the vacuum distillation furnace, the titanium sponge product stands as a large cylindrical object (e.g., up to 12 tonnes) with quality varying from portion to portion. It is then cut into small pieces and classified into soft sponge (O ≤ 0.06%, Fe ≤ 0.04%, Cl ≤ 0.08%), mild sponge (O ≤ 0.10%, Fe ≤ 0.12%, Cl ≤ 0.12%), and hard sponge (O ≤ 0.25%, Fe ≤ 0.18%, Cl ≤ 0.12%), which are crushed to the size range from ~0.8 to ~25 mm. The last step is to pack the sponge particles into steel drums (100–250 kg capacity), filled with argon, for shipment or storage.

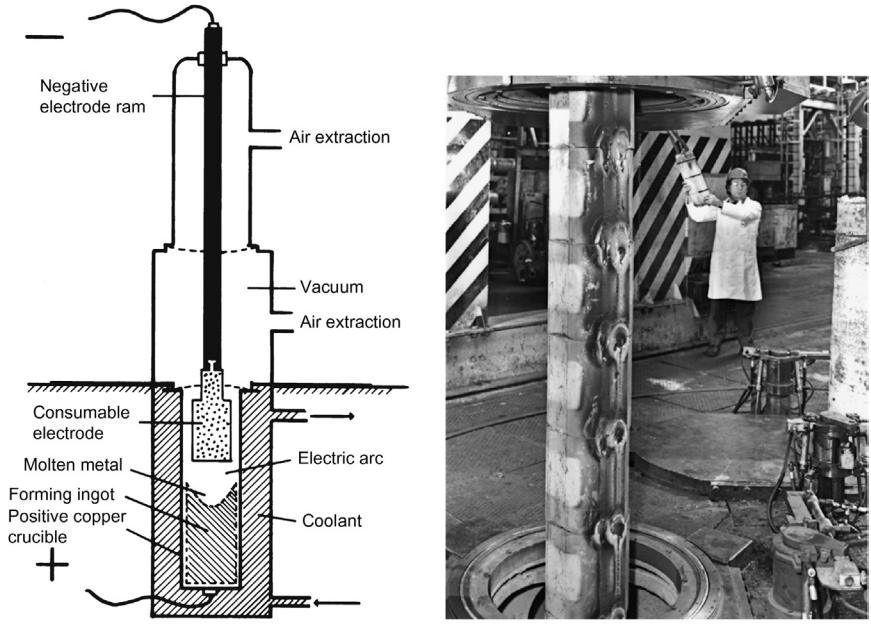


Figure 1.14 Schematic illustrations of (A) a consumable-electrode arc furnace for melting and refining titanium and (B) a consumable electrode made by welding together blocks of compacted titanium sponge. Courtesy from T.W. Farthing.

Commercially pure titanium ingots are made by arc melting titanium sponge or scrap, in a vacuum or inert environment. If alloys are required, the additional elements are also included. Since only two solid materials (yttrium oxide and molybdenum) are known to be relatively inert to molten titanium, identifying a suitable crucible material in which to melt titanium presents a difficult challenge. Consequently, novel melting methods had to be devised. The consumable-electrode vacuum arc remelting (VAR) process, introduced in the early 1950s, is one such invention, which is today still the most commonly used method for producing titanium and titanium alloy ingots (Fig. 1.14A). The consumable electrode in this process is made from compacts of titanium sponge and scrap (Fig. 1.14B), formed using a large press, which are then joined together by plasma arc welding. Internally water-cooled copper crucibles are normally used to solidify the melted sponge. However, a liquid sodium–potassium eutectic alloy may also serve this purpose because it does not react with molten titanium should the copper crucible be perforated by the electric arc, whereas water or steam can cause an explosion.

The melting begins by introducing a direct current arc between the consumable electrode and a starting slug of this material placed in the copper crucible.

As the consumable-electrode melts, the molten titanium or titanium alloy runs down into the crucible below and is cooled there to form the first melt ingot. The entire arrangement is encased in a vessel that can be evacuated and into which an inert gas such as argon is introduced (see Fig. 1.14A). The ingots are now commonly produced with diameters of 700–1200 mm and weight of 3–15 tonnes. To ensure homogeneity, double melting is often carried out by using the first melt ingots as new consumable electrodes, while more complex titanium alloys may require triple or even multimelting stages.

Electron beam cold hearth remelting (EBCHR) was introduced in the mid-1980s. It has the advantage of completely melting titanium sponge or scrap thereby eliminating the need to fabricate consumable electrodes. In addition, it can produce homogeneous round and square titanium ingots by single melting, where square ingots are desired for subsequent forging or slabbing. Another important attribute is that it can effectively remove both the high-density inclusions (e.g., containing tungsten, tantalum, or molybdenum) and low-density inclusions (e.g., titanium nitride), because the higher temperatures and longer residence times offer a greater opportunity for these inclusions to be dissolved or removed. In contrast, such inclusions can survive in the VAR process due to the lower melting temperature (~1800°C) available. Since titanium alloys are used for many critical applications such as the rotating parts in gas turbine engines, it is essential to eliminate all inclusions in ingots because they can serve as sites for the initiation of fatigue cracks in components machined from the forged blanks (e.g., forged compressor disks). In fact, it was the requirements for higher-quality titanium alloys for jet engine rotating components that promoted the application of the EBCHR technology in order to reduce the likelihood of high-density inclusions.

The plasma arc melting process has also been used to melt titanium and its alloys under an inert argon or helium almosphere. It has proved particularly well suited for fabricating titanium alloys containing alloying elements with greatly dissimilar melting points and vaporization pressures, where vaporization can be controlled by the positive pressure applied by an argon or helium gas atmosphere. This process can also effectively elimiate high-density inclusions and enable high-quality titanium alloys for demanding applications.

Overall, the Kroll process is energy-intensive, which consumes about 15–27 kWh per kg titanium sponge, equivalent to about 14 times the energy needed to produce steel ingots. Much effort has been made over the last two decades to develop alternative lower-cost titanium production methods, especially in the form of titanium powder. No significant commercial success has been made as yet. Growth in demand for titanium and the acceptance metal additive manufacturing technologies has stimulated renewed interest in improving or replacing the Kroll process with a more efficient process.

FURTHER READING

Ashby, MF: On the engineering properties of materials, *Acta Metall.*, 37, 1273, 1989.

Field, FR, III, Clark, JP and Ashby, MF: Market drivers and process development in the 21st century, *MRS Bulletin*, 716, 2001.

Bever, MB: *Encyclopedia of Materials Science and Engineering*, Pergamon Press, Oxford, England, 1986.

Altenpohl, DG: *Aluminium: Technology, Applications and Environment*, The Aluminium Association Inc., Washington, D.C., USA and TMS, Warrendale, PA, USA, 1998.

Marder, JM: Beryllium: alloying, thermomechanical processing, properties and applications, *Encyclopedia of Materials Science and Engineering*, Elsevier Ltd., Oxford, 2001,506.

Hogg, PJ: The role of materials in creating a sustainable economy, *Mater. Tech. Adv. Perform. Mater.*, 19, 70, 2004.

Davis, JR, (Ed.): Recycling technology *ASM Specialty Handbook on Aluminium Alloys*, ASM International, Materials Park, OH, USA, 47, 1993.

Gesing, A: Assuring the continued recycling of light metals in end-of-life vehicles: a global perspective, *JOM*, 56, 18, 2004.

West, EG: Aluminium—the first 100 years, *Metals and Materials*, 20, 124, 1986.

Kvante, H: Production of primary aluminium. In Lumley, R, (Ed.): *Fundamentals of Aluminium Metallurgy: Production, Processing and Applications*, Woodhead Publishing, Oxford, 2011, pp 49.

Welsh, BJ: Aluminium production paths in the new millennium, *JOM*, 51, 24, 1999.

Hunt, WH Jr.: The China factor: aluminium industry impact, *JOM*, 56, 21, 2004.

Clow, BB: History of primary magnesium since World War II. In Kaplan, HI, (Ed.): *Magnesium Technology 2002*, TMS, Warrendale, PA, USA, 2002, pp 3.

Emley, EF: *Principles of Magnesium Technology*, Pergamon Press, London, 1966.

Avedesian, MM and Baker, H: *ASM Specialty Handbook on Magnesium and Magnesium Alloys*, ASM International, Materials Park, OH, USA, 1999.

Okura, Y: Titanium sponge technology. In Blenkinsop, PA, (Ed.): *Titanium 95: Science and Technology, Proc. 8th World Conf. on Titanium*, The Institute of Metals, London, 1995, pp 1427.

Farthing, TW: The development of titanium alloys, *The Metallurgy of Light Alloys*, The Institute of Metallurgists, London, 1983, 9.

Lippert, TW: Titanium in U.S.A.. In Jaffee, RI and Promisel, NE, (Eds.): *The Science, Technology, and Application of Titanium*, Pergamon Press, Oxford, 1970, pp 5–9.

National Materials Advisory Board, *Titanium: Past, Present, and Future*, National Academy Press, Washington, D.C., USA, 1983.

Qian, M and Froes, FH: *Titanium Powder Metallurgy: Science, Technology and Applications*, Elsevier, 2015.

Kosemura, S, Fukusama, E, Ampo, S, Shiraki, T and Sannohe, T: *Technology Trend of Titanium Sponge and Ingot Production*, Nippon Steel Technical Report No. 85, January, 31–35, 2002.

Eylon, D and Seagle, SR: Titanium technology in the USA—an overview, *J. Mater. Sci. Technol.*, 17(4), 439, 2001.

Nagesh, ChRVS, Rao, ChS, Ballal, NB and Rao, PK: Mechanism of titanium sponge formation in the Kroll reduction reactor, *Metall. Mater. Trans. B*, 35, 65, 2004.

2

PHYSICAL METALLURGY OF ALUMINIUM ALLOYS

Although most metals will alloy with aluminium, comparatively few have sufficient solid solubility to serve as major alloying additions. Of the commonly used elements, only zinc, magnesium (both >10 at.%)[1], copper and silicon have significant solubilities (Table 2.1). However, several other elements with solubilities below 1 at% confer important improvements to alloy properties. Examples are some of the transition metals, e.g., chromium, manganese, and zirconium, which are used primarily to form compounds that control grain structure. With the exception of hydrogen, elemental gases have no detectable solubility in either liquid or solid aluminium. Apart from tin, which is sparingly soluble, maximum solid solubility in binary aluminium alloys occurs at eutectic and peritectic temperatures. Sections of typical eutectic and peritectic binary phase diagrams are shown in Figs. 2.1 and 2.2.

High-purity aluminium in the annealed condition has very low yield strength (7–11 MPa). When it is desired to use annealed material, strength may be increased only by solid solution hardening. For this to be achieved, the solute must:

1. have an appreciable solid solubility at the annealing temperature,
2. remain in solid solution after a slow cool,
3. not be removed by reacting with other elements to form insoluble phases.

Fig. 2.3 shows the increment in yield strength that occurs when selected solutes are added to high-purity aluminium. Some elements are shown in concentrations beyond their room temperature solubility but each alloy was processed to retain all the solute in solution. On an atomic basis, manganese and copper

[1]Unless stated otherwise, alloy compositions and additions are quoted in weight percentages.

Light Alloys. DOI: http://dx.doi.org/10.1016/B978-0-08-099431-4.00002-6
Copyright © 2017 Ian Polmear, David StJohn, Jian-Feng Nie, Ma Qian.
Published by Elsevier Ltd. All rights reserved.

Table 2.1 Solid solubility of elements in aluminium

Element	Temperature (°C)	Maximum solid solubility (wt.%)	Maximum solid solubility (at.%)
Cadmium	649	0.4	0.09
Cobalt	657	<0.02	<0.01
Copper	548	5.65	2.40
Chromium	661	0.77	0.40
Germanium	424	7.2	2.7
Iron	655	0.05	0.025
Lithium	600	4.2	16.3
Magnesium	450	17.4	18.5
Manganese	658	1.82	0.90
Nickel	640	0.04	0.02
Silicon	577	1.65	1.59
Silver	566	55.6	23.8
Tin	228	~0.06	~0.01
Titanium	665	~1.3	~0.74
Vanadium	661	~0.4	~0.21
Zinc	443	82.8	66.4
Zirconium	660.5	0.28	0.08

From Van Horn, KR (Ed.): *Aluminium*, Vol. 1, ASM, Cleveland, OH, USA, 1967; Mondolfo, LF: *Aluminium Alloys: Structure and Properties*, Butterworths, London, 1976.
Note:
(i) Maximum solid solubility occurs at eutectic temperatures for all elements except chromium, titanium, vanadium, zinc, and zirconium for which it occurs at peritectic temperatures.
(ii) Solid solubility at 20°C is estimated to be approximately 2 wt% for magnesium and zinc, 0.1–0.2 wt% for germanium, lithium, and silver, and below 0.1% for all other elements.

are the most effective strengtheners at 0.5% or less. However, manganese usually precipitates as the dispersoid Al_6Mn during ingot preheating (Section 4.1.4) and hot processing so that only 0.2–0.3% tends to remain in solution. Copper additions to the non-heat-treatable alloys are normally held to a maximum of 0.3% to avoid the possible formation of insoluble Al–Cu–Fe constituents. Magnesium is the most effective strengthener on a comparative weight basis because of its relatively high solid solubility, and annealed sheet and plate containing up to 6% of this element have yield strengths up to 175 MPa. It will also be noted that zinc, too, has a high solubility but causes little strengthening.

Aluminium alloys can be divided into two groups. One contains those alloys for which the mechanical properties are controlled by work hardening and annealing. Commercial-purity aluminium and alloys based on the Al–Mg and Al–Mn systems are the common examples. The second group comprises the

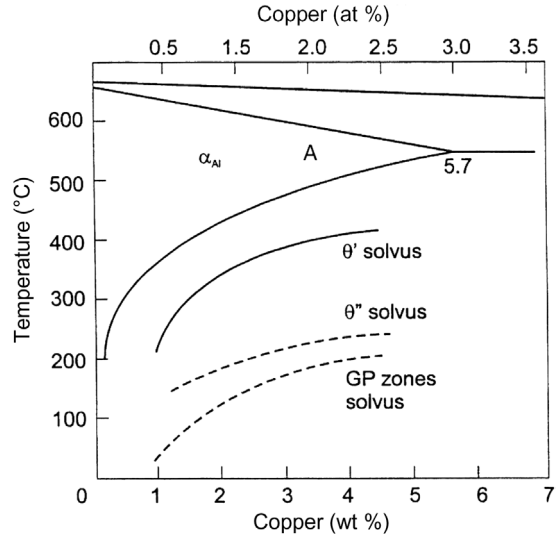


Figure 2.1 Aluminium-rich corner of the Al–Cu eutectic diagram. The positions of the solvus lines for GP zones and the other metastable precipitates are also shown. From Murray, JL: *Inter. Met. Rev.*, 30, 211, 1985.

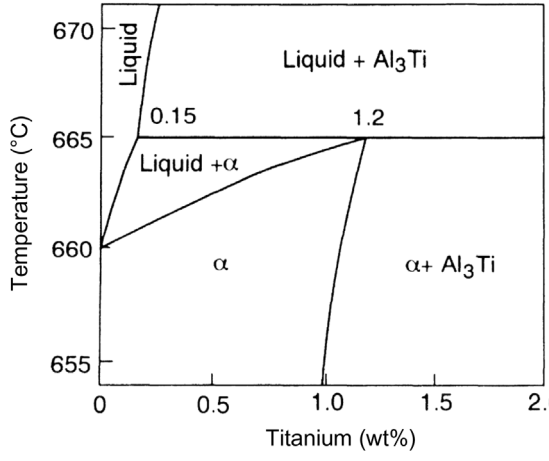


Figure 2.2 Section of Al–Ti peritectic phase diagram.

alloys such as Al–Cu–Mg, Al–Mg–Si, and Al–Zn–Mg–Cu that respond to age or precipitation hardening. In the next two sections, it is therefore desirable to present brief reviews of the essential principles associated with these processes before considering specific alloy systems. These remarks are also relevant to most magnesium and titanium alloys.

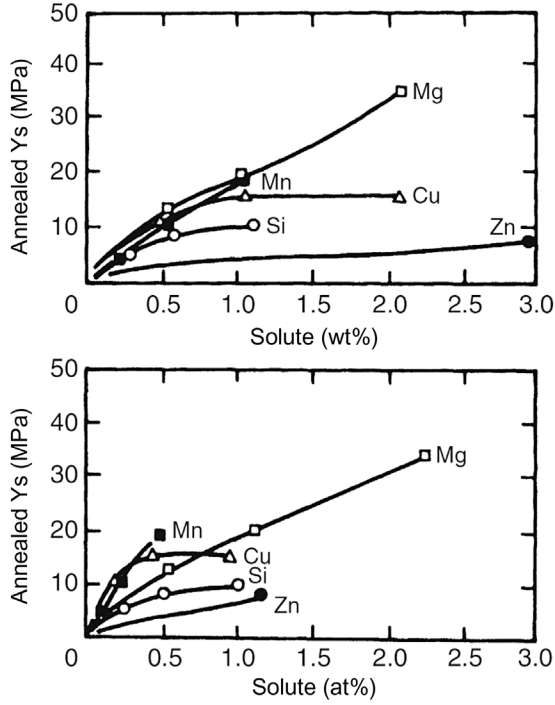


Figure 2.3 Solid solution strengthening of high-purity binary aluminium alloys. From Sanders, RE *et al.*: *Proc. of Inter. Conf. on Aluminium Alloys—Physical and Mechanical Properties*, Charlottesville, VA, USA, Engineering Materials Advisory Services, Warley, UK, 1941, 1986.

2.1 WORK HARDENING AND ANNEALING

During deformation of metals and alloys, the dislocation content increases when dislocation generation and multiplication occur faster than annihilation can take place by dynamic recovery. Dislocation tangles, cells, and subgrain walls are formed, grain shapes and internal structures change. All of these factors decrease mean free slip distance and give increased strength.

Fig. 2.4 is a schematic representation of the microstructure of a rolled aluminium alloy showing features that develop during deformation. Slip has occurred within the individual grains and grains have become elongated so that there is a large increase in total grain boundary area. A so-called deformation band or transition band (a) is shown within one grain which separates two internal regions that have developed two distinct orientations during the deformation process. Also there is a larger discontinuity known as a shear band (d) that tends to form in regions of high strain (true strain $\varepsilon > 1$). Such bands are

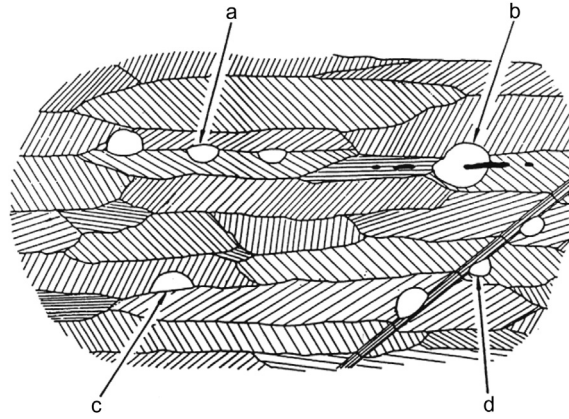


Figure 2.4 Schematic representation of the microstructure of a rolled alloy. Also shown are possible nucleation sites for recrystallized grains. Courtesy A. Oscarsson.

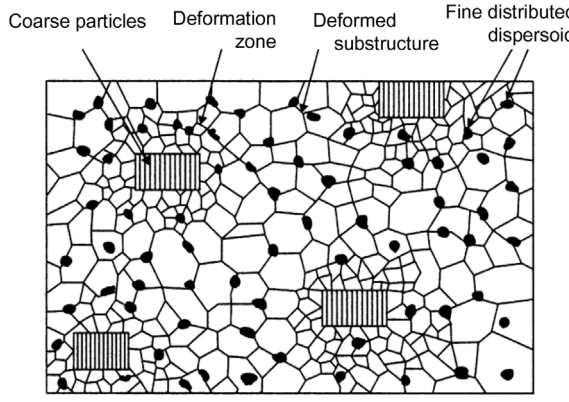


Figure 2.5 Schematic representation of the substructure of a cold-worked alloy containing coarse and fine intermetallic particles. From Nes, E: *Proc. 1st Riso Inter. Symp. on Metallurgy and Mater. Sci.*, Riso National Laboratory, Denmark, 36, 1980.

typically oriented at ~35° to the rolling plane and cut through existing grain structures. In sheet rolled to very high levels of strain, larger shear bands can develop that cross from one surface to another and provide paths along which failure may occur.

In multiphase aluminium alloys containing coarse intermetallic particles and finer dispersoids, deformation becomes more inhomogeneous. As shown schematically in Fig. 2.5, substructures may develop in intensely deformed zones around each of the coarse particles. The density of these deformed zones may become much higher in metal matrix composites that are reinforced with

large volume fractions of ceramic particulates (Section 8.1.3). The finer dispersoids may serve to pin grain boundaries during thermomechanical processing of aluminium alloys (Section 2.5). As will be discussed later, both types of particles influence recrystallization and grain growth during annealing or hot working (Section 2.1.6).

Before considering the characteristics of work-hardened aluminium alloys, it should be noted that elements in solid solution can influence deformation behavior in several ways. These include enhancing rates at which dislocations can multiply, decreasing the mobility of dislocations so that they serve as more effective barriers to metal flow, and reducing rates of recovery during thermomechanical processing. Copper is the most effective element in this regard but, as mentioned earlier, additions to non-heat-treatable aluminium alloys must normally be kept below 0.3%. Magnesium is less effective on an equi-atomic basis but has the greatest practical value because of its high solid solubility. As shown in Fig. 4.15, some heavily cold-worked alloys based on the Al–Mg system may develop yield strengths exceeding 400 MPa. Though having a high solid solubility, zinc has a negligible effect on the work hardening of aluminium alloys.

2.1.1 Strain-hardening characteristics

Strain hardening occurs during most working and forming operations and is the main method for strengthening aluminium and those alloys which do not respond to heat treatment. For heat-treatable alloys, strain hardening may supplement the strength developed by precipitation hardening.

Tensile properties are the most affected and Fig. 2.6 shows work-hardening curves for 1100 aluminium and the alloys 3003 (Al–Mn)[2] and 5052 (Al–Mg), the latter two being representative of the main classes of non-heat-treatable alloys. Cold working causes an initial rapid increase in yield strength, or proof stress, after which the increase is more gradual and roughly equals the change in tensile strength. These increases are obtained at the expense of ductility as measured by percentage elongation in a tensile test, and also reduced formability in operations such as bending and stretch forming. For this reason, strain-hardened tempers are not usually employed when high levels of ductility and formability are required. However, it should be noted that certain alloys, e.g., 3003, exhibit better drawing properties in the cold-worked rather than the annealed condition, and this is an important factor in making thin-walled beverage cans (Section 4.6.5).

The work-hardening characteristics of heat-treatable alloys, in both the annealed and T4 tempers,[3] are similar to those described earlier. Cold working prior to ageing some of these alloys may cause additional strengthening (T8 temper). In the fully hardened T6 temper, the increases in tensile properties by cold working after ageing are comparatively small, except at very high

[2]Alloy designations and compositions are given in Tables 4.2 and 4.4.
[3]Temper designations are described in the Section 4.2.

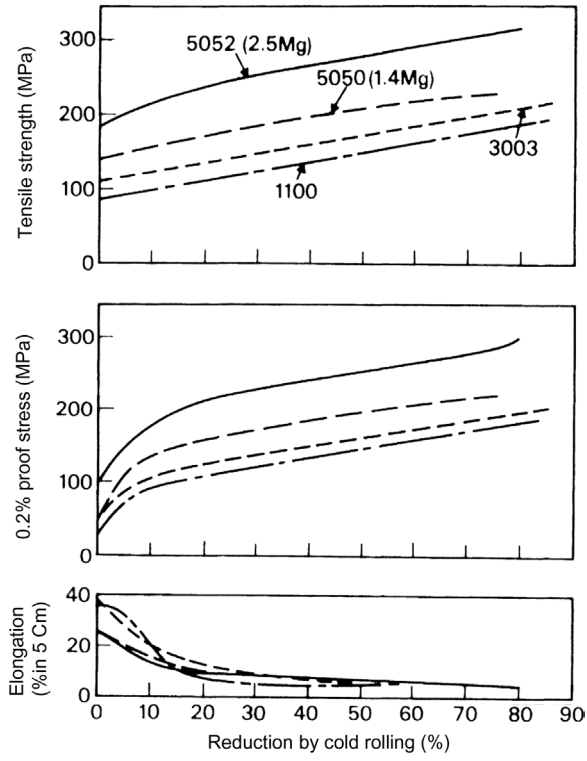


Figure 2.6 Work-hardening curves for the alloys 1100 (99Al), 3003 (Al–1.2Mn), 5050 (Al–1.4Mg), and 5052 (Al–2.5Mg). From Anderson, WA: *Aluminium*, Vol. 1, Van Horn, K (Ed.), ASM, Cleveland, OH, USA, 1967.

strains, and are often limited by the poor workability of alloys in this condition. The principal use of this practice is for some extruded and drawn products such as wire, rod, and tube which are cold drawn after heat treatment to increase strength and improve surface finish. This applies particularly to products made from Al–Mg–Si alloys.

Work-hardening curves for annealed, recrystallized aluminium alloys, when plotted as a function of true stress and true strain, can be described by:

$$\sigma = k\varepsilon^n$$

where σ is true stress, k is the stress at unit strain, ε is the true or logarithmic strain, which is defined as $\ln A_0/A_f$, where A_0 and A_f are the initial and final cross-sectional areas of a sample, respectively, and n is the work-hardening exponent. As the initial strengths of the alloys increase, k also increases, whereas for values of k in the stress range 175–450 MPa, n decreases from 0.25 to 0.17.

Rates of strain hardening can be calculated from the slopes of work-hardening curves. For non-heat-treatable alloys initially in the cold-worked or hot-worked condition, these rates are substantially below those of annealed material. For the cold-worked tempers, this difference is caused by the strain necessary to produce the temper and, if this initial strain equals ε_0, then the equation for strain hardening becomes:

$$\sigma = k(\varepsilon_0 + \varepsilon)^n$$

A similar situation exists for products initially in the hot-worked condition. The strain hardening resulting from hot working or forming is assumed to be equivalent to that achieved by a certain amount of cold work. From a knowledge of the tensile properties of the hot-worked product, the amount of equivalent cold work can be estimated by using the work-hardening curve for the annealed temper. By such procedures, it is usually possible to calculate work-hardening curves for hot-worked products that are in reasonable agreement with those for annealed products.

The work-hardening characteristics of aluminium alloys vary considerably with temperature. At cryogenic temperatures, strain hardening is greater than at room temperature, as shown in Fig. 2.7 which compares the work-hardening characteristics of the alloy 1100 at room temperature and −196°C. The gain in strength by working at −196°C can be as much as 40% although there is a significant reduction in ductility. At elevated temperatures, the work-hardening characteristics are influenced by both temperature and strain rate. Strain hardening decreases progressively as the working temperature is raised until a temperature is reached above which no effective hardening occurs due to dynamic recovery and recrystallization. This behavior is important in commercial hot-working processes and it is necessary to determine the strength–temperature–time–relationships when deforming different alloys in order to optimize these operations.

2.1.2 Substructure hardening

Aluminium has a high stacking fault energy (~170 mJ m^{-2}) and, during deformation, a cellular substructure is formed within the grains, rather than twins or stacking faults. This cellular substructure causes strengthening that can be defined by a Hall–Petch type equation having the form:

$$\sigma = \sigma_0 + k_1 d^{-m}$$

where σ is the yield strength, σ_0 is the frictional or Peierls stress, k_1 denotes the strength of the cell boundaries, and m is an exponent that varies from 1 to 0.5. The substructure produced by working at relatively low temperatures is usually referred to as cells. These cells differ in orientation by only ~1° and have walls

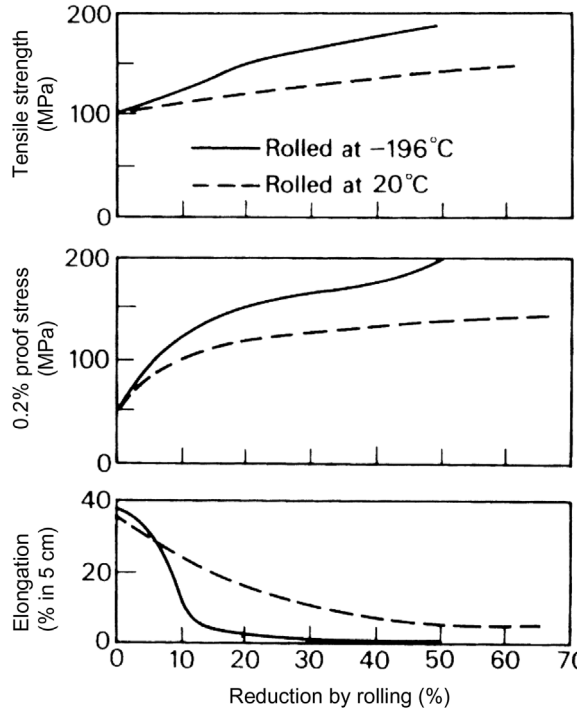


Figure 2.7 Work-hardening curves for 1100–O (99%Al, annealed) sheet at room temperature and −196°C. From Anderson, WA: *Aluminium*, Vol. 1, Van Horn, K (Ed.), ASM, Cleveland, OH, USA, 1967.

comprising tangled dislocations. On the other hand, deformation at higher temperatures produces "subgrains" bounded by narrow, well-defined walls, and for which the misorientation is greater. The value of m changes from 1 to 0.5 if the alloys undergo the process of recovery which causes the substructure to change from cells to subgrains. The formation of subgrains is favored if maximum substructure strengthening is desired.

2.1.3 Forming limit curves

The formability of sheet depends on both the work-hardening exponent n and the R-value which is a measure of the effect of metal thinning under axial strain. R is defined as the ratio of total width strain to total thickness strain. In simple terms, the significance of R is that, for values >1, a metal sheet characteristically resists thinning whereas there is a tendency for thinning to occur if $R < 1$. In deep drawing, for example, high R-values enable a deeper cup to be formed due to the greater resistance to thinning of the side walls. Determination of accurate values for n and R can prove difficult and the concept of the forming limit curve (FLC)

was developed as a convenient tool to analyze the inhomogeneous strains occurring in sheet components. These curves identify the boundary limits between no failure during forming on the one hand, and either failure by necking or actual fracture on the other. They are obtained experimentally by covering a sheet specimen with a grid and then measuring major and minor (90° orientation) strains that develop during a particular forming operation.

Examples of FLCs for a typical mild steel sheet, the naturally aged Al–Mg–Si–Cu alloy 6111, and for the Al–Mg–Mn alloy 5052 (in the annealed and cold-rolled conditions) are shown in Fig. 2.8. For strain conditions that lie below each of the respective curves, no failures are expected. For positive minor strains, the curve represents forming limits for stretching processes from uniaxial ($e_2 = 0$) to biaxial ($e_1 = e_2$) conditions. For negative minor strains, the curve represents forming limits for tension–compression strain conditions as found in the side walls of deep drawn components. As shown in the figure, steel sheet normally has forming characteristics that are superior to aluminium alloy sheet. This aspect is discussed further in Section 4.6.2. Also, it will be noted that alloy 5052 sheet displays a better capacity for forming in the annealed rather than the work-hardened condition, although the reverse is true for the canstock alloy 3004 (Section 4.6.5).

2.1.4 Textures

Deformation of aluminium and its alloys proceeds by crystallographic slip that normally occurs on the {111} planes in the <110> directions. Large amounts

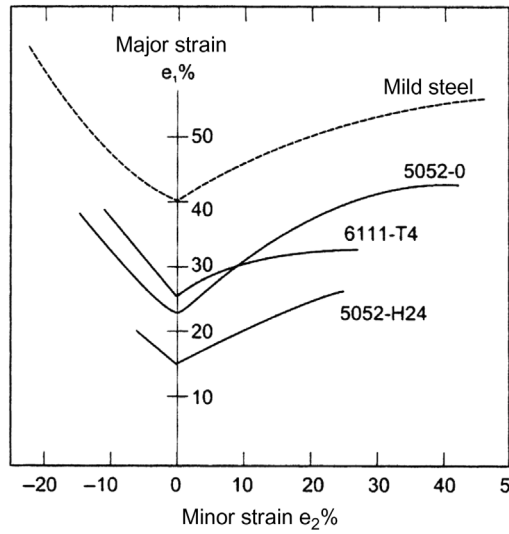


Figure 2.8 FLCs for a typical mild steel sheet and for the aluminium alloys 6111–T4 and 5052 in the annealed (O) and cold-rolled (H24) conditions. Courtesy Australian Aluminium Council.

of deformation at ambient temperatures lead to some strengthening through the development of textures, the nature of which depends in part on the mode of working. Aluminium wire, rod, and bar usually have a "fiber" texture in which the <110> direction is parallel to the axis of the product, with a random orientation of crystal directions perpendicular to the axis. In rolled sheet, the texture that is developed may be described as a tube of preferred orientations linking $(110)\langle\bar{1}12\rangle$, $(112)\langle11\bar{1}\rangle$, and $(123)\langle\bar{6}\bar{3}4\rangle$.

The standard method used for determining textures is X-ray pole figures in which a stereographic projection is produced that shows the distribution of a particular crystallographic direction in an assembly of grains in a specimen. More information about the fine details of textures can now be achieved from patterns obtained using the technique of electron backscattered diffraction. This technique involves the use of the scanning electron microscope in which the specimen is tilted to obtain the diffraction pattern. This technique has confirmed that nucleation of grains with a cube orientation texture is favored at transition bands (Fig. 2.4). This characteristic is critical in the annealing stage in the rolling of canstock (Section 4.6.5).

When cold-worked aluminium or its alloys are recrystallized by annealing, new grains form with orientations that differ from those present in the cold-worked condition. Preferred orientation is much reduced but seldom eliminated, and the annealing texture that remains has been extensively studied in rolled sheet. Some new grains form with a cube plane parallel to the surface and a cube edge aligned in the rolling direction, i.e., (100)[001] texture, and other strain-free grains developed in which the rolling texture is retained. The texture and final grain size in recrystallized products are determined by the amount of cold-work, annealing conditions (i.e., rate of heating, annealing temperature, and time), composition, and the size and distribution of intermetallic compounds which tend to restrict grain growth.

Textures developed by cold working cause directionality in certain mechanical properties. Texture hardening causes moderate increases in both yield and tensile strength in the direction of working, and it has been estimated that, with an ideal fiber texture, the strength in the fiber direction may be 20% higher than that for sheet with randomly oriented aggregates of grains. Forming characteristics of sheet may also be improved through an increase in the *R*-value for sheet which is the ratio of the strain in the width direction of a test piece to that in the thickness direction. A large *R*-value means there is a lack of deformation modes oriented to provide strain in the through-thickness direction. As a consequence, sheet will be more resistant to thinning during forming operations and this is desirable.

Preferred orientations in the plane of a sheet that are associated with textures may cause a problem known as earing. Earing describes the phenomenon of small undulations that may appear on the top of drawn cups (Fig. 2.9) and is wasteful of material because this uneven end of the cup must be trimmed off. Moreover, it may lead to production problems due to difficulties in ejecting products after a pressing operation. Four ears usually form because of

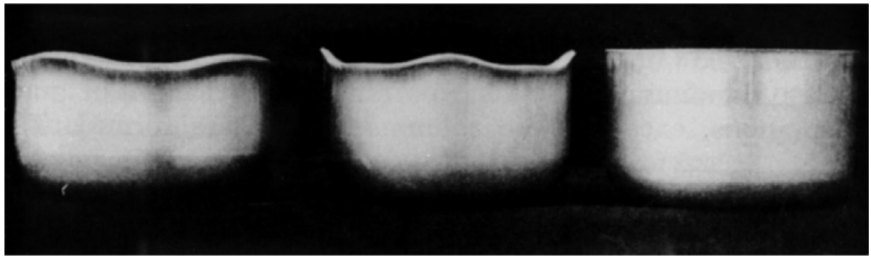


Figure 2.9 Deep drawn aluminium cups showing 45° earing, 0–90° earing, and no earing with respect to the rolling direction. From Anderson, WA: *Aluminium*, Vol. 1, Van Horn, K (Ed.), ASM, Cleveland, OH, USA, 1967.

nonuniform plastic deformation along the rim of deep drawn products. If the rolling texture is predominant, then ears will appear at 45° to the rolling direction of the sheet, whereas in the presence of the annealing (or cube) texture, they form in the direction of rolling and at right angles to it. If there is a desirable balance between the two textures, there will be either eight small ears or none at all. Earing may be minimized by careful control of rolling and annealing schedules, e.g., sheet is sometimes cross-rolled so that textures are less clearly defined. This matter is considered further when discussing the production of canstock in Section 4.6.5.

Crystallographic textures should not be confused with mechanical fibring that occurs because of changes in grain shape, banding of small grains, or the alignment of particles in worked alloys (Figs. 2.42 and 2.43). As mentioned in the Sections 2.5.1 and 2.5.2 these effects also contribute to the anisotropy of mechanical properties and they are often more important than crystallographic texture.

2.1.5 Secondary work-hardening effects

Aluminium products formed by stretching, bending, or drawing sometimes develop a roughened surface and this effect is known as "orange peeling." It is common to other materials and is caused by the presence of coarse grains at the surface.

A problem that occurs in a few aluminium alloys, but not in other nonferrous materials, is the formation of stretcher strain markings, or Lüders lines, during the forming or stretching of sheet. These markings occur in one of two forms and may give rise to differences in surface topography of sheet during drawing and stretch-forming operations. One type occurs in annealed or heat-treated solid solution alloys, notably Al–Mg, and is produced when yielding takes place in some parts of a sheet but not in others. It is similar in origin to the well-known Lüders lines that may form during the deformation of certain sheet steels. The second type is associated with the Portevin–LeChatelier

effect and it produces uneven or serrated yielding during a tensile test. Diagonal bands appear oriented approximately 50° to the tension axis, which move up or down during stretching and terminate at the grips. This type of marking is rarely observed in commercial forming operations but may appear when strain-hardened sheet or plate is stretched to produce flatness.

Stretcher strain markings are generally undesirable because they cause uneven and roughened surfaces. They can be avoided by forming with strain-hardened rather than annealed sheet, providing the material has adequate ductility. The formation of these markings can also be avoided or minimized by forming or working at temperatures above 150°C.

2.1.6 Annealing Behavior

Annealing at elevated temperatures allows partial or complete removal of the lattice distortions introduced by work hardening so that the pre-deformation properties can be progressively restored. Dislocation densities may be reduced from $\sim 10^{12}$ in the severely cold-worked condition to 10^{10} lines per cm^2 during recovery, and to between 10^7 and 10^8 lines per cm^2 after recrystallization. Strength properties decrease gradually during recovery and then more rapidly when recrystallization occurs, whereas there is an inverse increase in elongation. These changes are demonstrated in Fig. 2.10 for hard-rolled, commercial-purity aluminium sheet. Recrystallization does not commence until a definite temperature is reached which depends on alloy composition, annealing time, and the level of work hardening. The actual rate of recrystallization increases with increasing temperature; for hard-rolled, pure aluminium sheet, this process

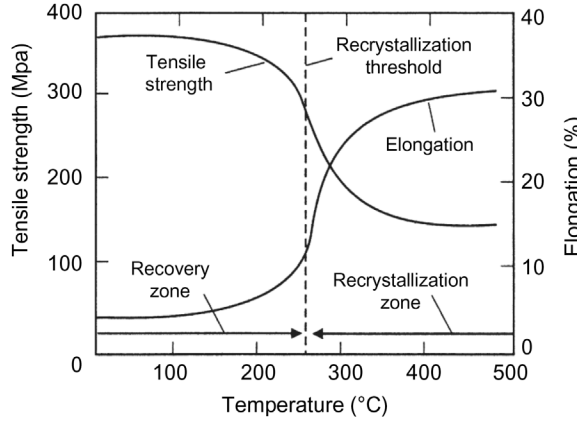


Figure 2.10 Tensile strength and elongation plotted against annealing temperature for hard-rolled, commercial-purity aluminium sheet. The annealing time at each temperature is 5 min. From Altenpohl, D, *Aluminium Viewed from Within*, 1st Ed., Aluminium-Verlag, Düsseldorf, Germany, 1982.

may take several hours to be complete at 280°C, a few minutes at 380°C, and only seconds at 500°C. Commercial aluminium alloys are normally annealed within the temperature range 300–420°C. Further slight softening will occur if recrystallization is followed by grain growth.

Recovery in aluminium and its alloys occurs when most dislocations are either annihilated or rearranged into walls leading to the formation of well-defined subgrain boundaries within the individual grains. Some of these changes may already have occurred by dynamic recovery during deformation, particularly hot working. The division between recovery and classical recrystallization in which new strain-free grains are formed may be difficult to define in deformed aluminium alloys. This is because new grains may, in fact, evolve by a process of extended recovery in which the growth and coalescence of the preexisting subgrains occurs until high angle grain boundaries are developed. Nevertheless, the appearance of the new grains is generally referred to as "recrystallization."

Four sites at which new grains may form have been identified in Fig. 2.4 as the (a) transition bands, (b) coarse intermetallic compounds, (c) previous grain boundaries, and (d) shear bands. Of these locations, the first two have proved to be the most important for deformed aluminium alloys and the final texture that evolves during annealing is largely the result of competition between these two processes. A transition band develops when neighboring volumes within a grain deform on different slip systems and rotate to adopt different orientations. Commonly they comprise a group of long, narrow cells or subgrains with a cumulative misorientation spreading from one side of the group to the other. Nucleation of grains with the cube orientation (100)[001] at transition bands is known to be favored when aluminium and its alloys are annealed after cold rolling, and also seems likely to occur after warm or hot rolling.

The other main mode of forming new grains during annealing of most aluminium alloys involves their nucleation at coarse intermetallic compounds having sizes generally greater than ~1 μm. This is known as particle stimulated nucleation, or PSN, for which two conditions must be fulfilled in order for new grains to grow. One is that the deformation zone around the particles (Fig. 2.5) must have sufficient stored energy to facilitate rapid formation of the recrystallized grains. This involves rapid subgrain migration. The other is that the new grain must be sufficiently large and stable to continue to grow out into the surrounding matrix which has a lower stored energy.

Continued heating after recrystallization may promote grain growth and the driving force for this further change is the reduction in energy that is stored in the form of grain boundaries. The amount of stored energy is much less than that involved in stimulating primary recrystallization and grain boundary migration normally occurs at a much slower rate. Grain growth may be divided into two types which are defined as normal and abnormal. Normal grain growth involves the gradual elimination of small grains and the microstructure changes in rather a uniform way. During abnormal grain growth, a few grains

grow excessively and consume the surrounding recrystallized grains so that the phenomenon is sometimes known as secondary recrystallization. As a result, a bimodal distribution of grain sizes develops. Where possible, coarse grain sizes are usually to be avoided except when there is a requirement for improved creep strength in an alloy. Tensile properties gradually decrease as grain growth occurs. Another problem is that coarse-grained products formed by bending, stretching, or drawing may develop roughened surfaces which is a phenomenon known as "orange peeling." This effect occurs because grains at a free surface are not constrained to deform like those in the interior and nonuniform deformation from grain to grain produces the orange peel appearance. Coarse surface grains that are shallow in depth result in less orange peeling than similar grains of greater thickness. Also hot-worked products are less prone to this defect than are cold-worked products.

The smaller dispersoid particles shown in Fig. 2.5 typically lie within the size range 0.05–0.5 μm and may serve to retard both recrystallization and grain growth by pinning the original grain boundaries in the deformed microstructure (Zener drag or pinning). They also delay recovery. As discussed in Section 2.5, and elsewhere, these dispersoids play several important roles in controlling the microstructure and properties of many aluminium alloys.

2.2 PRINCIPLES OF AGE HARDENING

It is now 100 years since the phenomenon of age or precipitation hardening was discovered by the German metallurgist, Alfred Wilm, who was working in Berlin where he was trying to develop a strong aluminium alloy to replace brass in ammunition. At that time, it was well known that steel could be hardened by quenching into water from a high temperature and Wilm was attempting to reproduce this behavior in aluminium alloys. To his frustration, most of the aluminium alloys in fact became softer the faster they were quenched. It then happened that hardness measurements being made on some quenched Al–Cu alloy specimens were interrupted at the end of a week and, the following Monday, he was astonished to find that the hardness had increased considerably. What was not realized until some years later was that this increase in hardness was caused by precipitation of a fine dispersion of nanometer-sized particles. Also, he did not know that he had discovered what has since been described as the first nanotechnology!

2.2.1 Decomposition of supersaturated solid solutions

The basic requirement for an alloy to be amenable to age hardening is a decrease in solid solubility of one or more of the alloying elements with decreasing temperature. Heat treatment normally involves the following stages:

1. Solution treatment at a relatively high temperature within the single-phase region, e.g., A in Fig. 2.1, to dissolve the alloying elements.

2. Rapid cooling or quenching, usually to room temperature, to obtain a supersaturated solid solution (SSSS) of these elements in aluminium.
3. Controlled decomposition of the SSSS to form a finely dispersed precipitate, usually by ageing for convenient times at one and sometimes two intermediate temperatures.

The complete decomposition of an SSSS is usually a complex process that may involve several stages. Typically, Guinier–Preston (GP) zones and an intermediate precipitate may be formed in addition to the equilibrium phase. In the Al–Cu system, which has been studied in much detail, four stages can be involved the crystal structures of which are depicted in Fig. 2.11. In addition, the technique of atom probe field ion microscopy (APFIM) has confirmed that small, disordered clusters of atoms (e.g., 20–50 in number) may precede the formation of GP zones in some alloys (see Fig. 2.20). These clusters may be retained on quenching or form as ageing commences. In some alloys, it seems that they may contribute to early stages of age hardening.

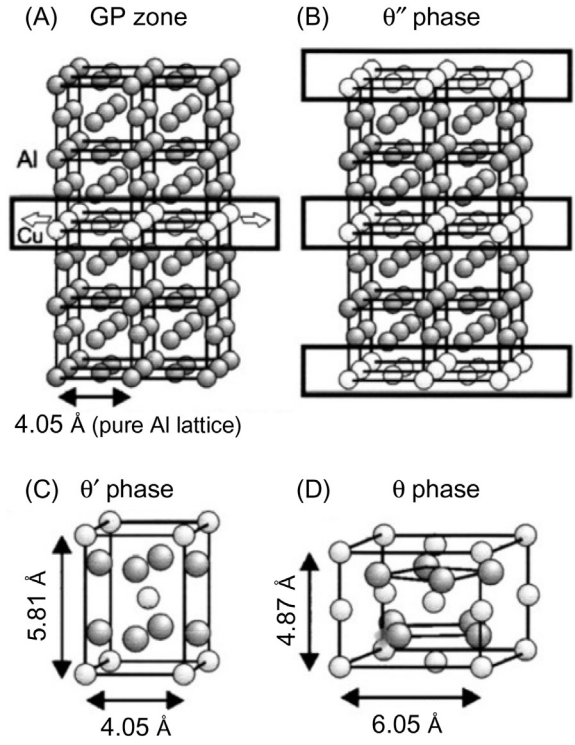


Figure 2.11 Models showing the crystal structures of (A) GP zones, (B) θ″, (C) θ′, and (D) θ (Al_2Cu) that may precipitate in aged binary Al–Cu alloys. Lighter balls represent copper atoms and darker balls represent aluminium atoms. Courtesy T. J. Bastow and S. Celotto.

GP zones are ordered, solute-rich groups of atoms that may be only one or two atom planes in thickness, e.g., Fig. 2.11A. They retain the structure of the matrix with which they are said to be coherent, although they can produce appreciable elastic strains in the surrounding matrix (Fig. 2.12). Diffusion associated with their formation involves the movement of atoms over relatively short distances and is assisted by vacant lattice sites that are also retained on quenching. GP zones are normally very finely dispersed and densities may be as high as 10^{17}–$10^{18}\,cm^{-3}$. Depending on the particular alloy system, the rate of nucleation and the actual structure may be greatly influenced by the presence of the excess vacant lattice sites.

The intermediate precipitate is normally much larger in size than a GP zone and is only partly coherent with the lattice planes of the matrix. It has been generally accepted to have a definite composition and crystal structure both of which differ only slightly from those of the equilibrium precipitate. However, studies using APFIM have revealed that the compositions may vary considerably. For example, the intermediate precipitate β′, that precedes the equilibrium phase β (Mg_2Si) in aged Al–Mg–Si alloys (Table 2.3), may have Mg:Si ratios closer to 1:1 rather than the expected 2:1. This suggests that aluminium atoms may substitute for some magnesium atoms in the structure of this phase.

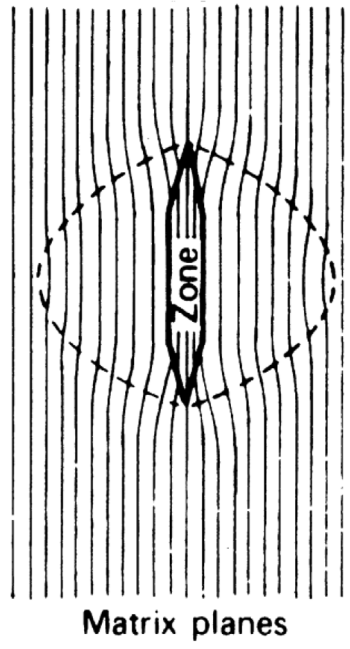


Figure 2.12 Representation of the distortion of matrix lattice planes near to the coherent GP zone. From Nicholson, RB *et al.*: *J. Inst. Metals*, 87, 429, 1958–59.

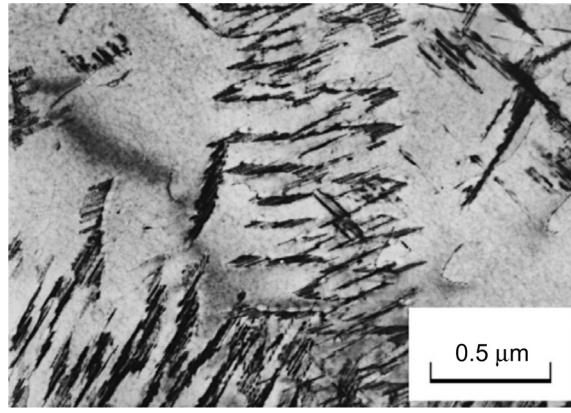


Figure 2.13 Transmission electron micrograph showing the rods of the S phase (Al_2CuMg) precipitated heterogeneously on dislocation lines. The alloy is Al–2.5Cu–1.5Mg, aged 7 h at 200°C. From Vietz, JT and Polmear, IJ: *J. Inst. Metals*, 94, 410, 1966.

In some alloys, the intermediate precipitate may be nucleated from, or at, the sites of stable GP zones. In others this phase nucleates heterogeneously at lattice defects such as dislocations (Fig. 2.13). Formation of the final equilibrium precipitate involves complete loss of coherency with the parent lattice. It forms only at relatively high ageing temperatures and, because it is coarsely dispersed, little hardening results.

Most aluminium alloys that respond to ageing will undergo some hardening at ambient temperatures. This is called "natural ageing" and may continue almost indefinitely, although the rate of change becomes extremely slow after months or years. Ageing at a sufficiently elevated temperature ("artificial ageing") is characterized by different behavior in which the hardness usually increases to a maximum and then decreases (e.g., Fig. 2.16). At one particular temperature, which varies with each alloy, the highest value of hardness will be recorded. Softening that occurs on prolonged artificial ageing is known as "overageing." In general, the maximum hardness achievable at a given temperature increases with a decrease in ageing temperature, for a given alloy composition. But this gain in hardness occurs at the expense of prolonged ageing time. In commercial heat treatment, an ageing treatment is usually selected that gives a desired response to hardening (strengthening) in a convenient period of time.

Apart from ageing temperature, another important parameter in determining age-hardening response is the concentration of major alloying elements in the alloy. Generally, the higher the alloying content, the greater the age-hardening response. It is for this reason that most commercial aluminium alloys contain sufficient amounts of alloying elements to achieve their useful strength. Maximum hardening in commercial alloys normally occurs when there is

present a critical dispersion of GP zones, or an intermediate precipitate, or a combination of both. In some alloys, more than one intermediate precipitate may be formed. For alloys in which the intermediate precipitate is difficult to nucleate, it is often desirable for them to be cold worked (e.g., by stretching 5%) after quenching and before ageing. Cold working increases the dislocation density and provides more sites at which heterogeneous nucleation of intermediate precipitates may occur during ageing. The increased nucleation rate and thus number density of the intermediate precipitate give a higher age-hardening response and greater strength. Occasionally, a more effective method for some alloy systems is to add a microalloying element that also stimulates nucleation of an intermediate precipitate in an alloy system, but examples of this phenomenon are comparatively rare. The roles of such microalloying elements in precipitation and their effects on age hardening are described in the Section 2.2.4.

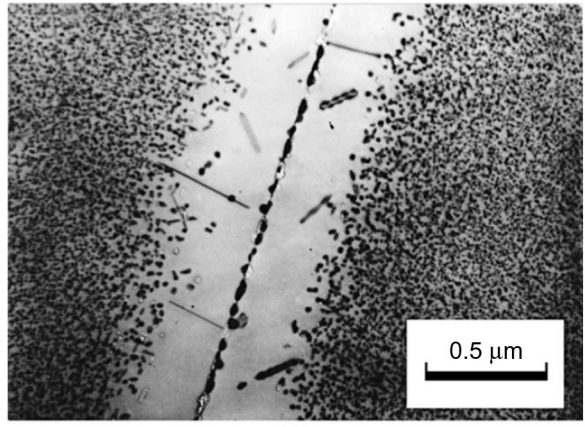
2.2.2 The GP zones solvus

An important concept is that of the GP zones solvus which may be shown as a metastable line in the equilibrium diagram (Fig. 2.1). It defines the upper temperature limit of stability of the GP zones for different compositions although its precise location can vary depending upon the concentration of excess vacancies. Solvus lines can also be determined for other metastable precipitates. There is strong experimental support for the model proposed by Lorimer and Nicholson whereby GP zones formed below the GP zones solvus temperature can act as nuclei for the next stage in the ageing process, usually the intermediate precipitate, providing they have reached a critical size d_{crit}. On the basis of this model, alloys have been classified into three types.

1. Alloys for which the quench-bath temperature and the ageing temperature are both above the GP zones solvus. Such alloys show little or no response to age hardening due to the difficulty of nucleating a finely dispersed precipitate. An example is the Al–Mg system in which quenching results in a very high level of supersaturation, but where hardening is absent in compositions containing < 5–6% magnesium.
2. Alloys in which both the quench-bath and ageing temperatures are below the GP zones solvus, e.g., some Al–Mg–Si alloys.
3. Alloys in which the GP zones solvus lies between the quench-bath temperature and the ageing temperature. This situation is applicable in most age hardenable aluminium alloys. Advantage may be taken of the nucleation of an intermediate precipitate from preexisting GP zones of sizes above d_{crit} using two-stage or duplex ageing treatments. These are now applied to some alloys to improve certain properties and this is discussed in more detail in Section 4.4.5. They are particularly relevant with respect to the problem of stress–corrosion cracking (SCC) in high-strength aluminium alloys.

2.2.3 Precipitate-free zones at grain boundaries

All alloys in which precipitation occurs have zones adjacent to grain boundaries which are depleted of precipitate and Fig. 2.14A shows comparatively wide zones in an aged, high-purity Al–Zn–Mg alloy. These precipitate-free zones (PFZs) are formed for two reasons. First, there is a narrow (~50 nm) region either side of a grain boundary which is depleted of solute due to the ready diffusion of solute atoms into the boundary where relatively large particles of precipitate are subsequently formed. Second, the remainder of a PFZ arises because of a depletion of vacancies to levels below that needed to assist with nucleation of precipitates at the particular ageing temperature.



(A)



(B)

Figure 2.14 (A) Wide PFZs in the alloy Al–4Zn–3Mg, aged 24 h at 150°C. (B) Effect of 0.3% silver on PFZ width and precipitate distribution in Al–4Zn–3Mg, aged 24 h at 150°C. From Polmear, IJ: *J. Australian Inst. Met.*, 17, 1, 1972.

The equilibrium concentration of vacancies decreases exponentially with temperature; it is relatively high at the solution treatment temperature and much lower at the ageing temperature. When an alloy is rapidly quenched from high temperature, there is no time for vacancies to diffuse to establish a new equilibrium concentration, and therefore the high vacancy concentration is retained. The distribution of vacancies near a grain boundary can take forms that are shown schematically in Fig. 2.15 and that a critical concentration C_v is needed before nucleation of the precipitate can occur at the ageing temperature. The width of the PFZ can be altered by heat treatment conditions; the zones are narrower for higher solution treatment temperatures and faster quenching rates, both of which increase the excess vacancy content (Fig. 2.15) and for lower ageing temperatures. This latter effect has been attributed to a higher driving force for precipitation which means that smaller nuclei will be stable, thereby reducing the critical vacancy concentration required for nucleation to occur (Fig. 2.15). However, the vacancy-depleted part of a PFZ may be absent in some alloys aged at temperatures below the GP zones solvus as GP zones can form homogeneously without the need of vacancies.

2.2.4 Microalloying effects

In common with other nucleation and growth processes, some precipitation reactions may be greatly influenced by the presence of minor amounts or traces of certain elements. These changes can arise for a number of reasons including:

1. Preferential interaction with vacancies which reduces the rate of nucleation of GP zones.

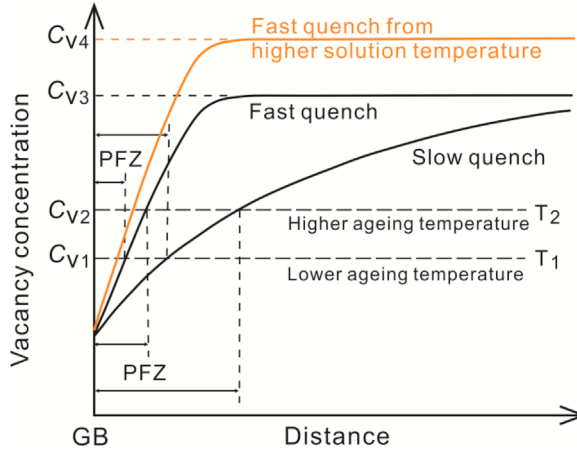


Figure 2.15 Representation of profiles of vacancy concentration adjacent to a grain boundary in quenched alloys. From Nie, JF: *Physical Metallurgy*, 5th Ed., Laughlin, D and Hono, K (Ed.), Elsevier, 2014.

2. Raising the GP zones solvus which alters the temperature ranges over which phases are stable.
3. Stimulating nucleation of an existing precipitate by reducing the interfacial energy between precipitate and matrix.
4. Stimulating nucleation of an existing precipitate by reducing the shear strain energy between precipitate and matrix.
5. Promoting formation of a different precipitate.
6. Providing heterogeneous sites at which existing or new precipitates may nucleate. These sites may be clusters of atoms or actual small particles.
7. Increasing supersaturation so that the precipitation process is stimulated.

An early example of a microalloying effect was the role of minor additions of cadmium, indium, or tin in changing the response of binary Al–Cu alloys to age hardening. These elements reduce room temperature (natural) ageing because they react preferentially with vacancies and thereby retard GP zone formation (mechanism 1). On the other hand, both the rate and extent of hardening at elevated temperatures (artificial ageing) are enhanced (Fig. 2.16) because these trace elements promote precipitation of a finer and more uniform dispersion of the semicoherent phase θ′ (Al_2Cu) in preference to coherent θ″ (Table 2.3). It was first proposed that these elements are absorbed at the θ′/matrix interfaces, thereby lowering the interfacial energy required to nucleate θ′ (mechanism 3). Subsequent studies by conventional transmission electron microscopy and three-dimensional atom probe indicated that θ′ is associated with small tin particles around 2–5 nm in diameter, Fig. 2.17A and B. Since tin particles precipitate first during the early stage of ageing, these observations appear to suggest that heterogeneous nucleation of θ′ has occurred at the sites of the pre-existing tin particles (mechanism 6). However, high-resolution transmission electron microscopy images obtained from such tin particles, arrowed in Fig. 2.17C, indicate that they have a different orientation relationship from those preexisting tin particles, implying that they form at a later stage of ageing, probably in association with the formation of θ′. More recent experimental observations using atomic-resolution Z-contrast scanning transmission electron microscopy have revealed that tin atoms segregate at the end facets of θ′ precipitate plates to reduce the shear strain energy involved in θ′ nucleation (mechanism 4). These latest observations indicate that the tin particles formed in the early stages of ageing are not heterogeneous nucleation sites for θ′, and that the tin particle that is in contact with a θ′ plate forms as the consequence of segregation of Sn atoms to the end facet of the θ′ nucleus.

The potent effect of traces of tin in stimulating nucleation of θ′ can also be demonstrated by observing changes in thermal energy that occur during heating in a differential scanning calorimeter. Fig. 2.18 compares the changes in the apparent specific heat during heating of the as-quenched alloys Al–4Cu and Al–4Cu–0.05Sn, and the areas cde and c′d′e′ between the mixture line (which

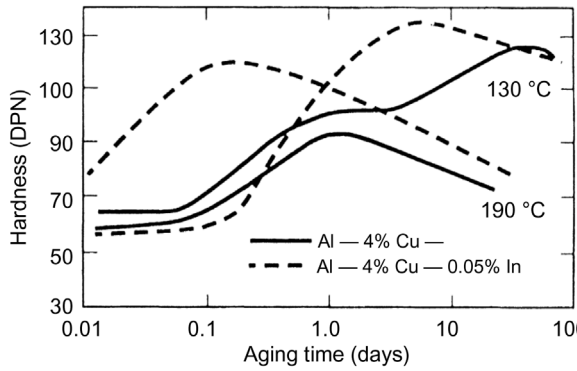


Figure 2.16 Hardness–time curves for Al–4Cu and Al–4Cu–0.05In aged at 130°C and 190°C. After Hardy, HK: *J. Inst. Metals*, 78, 169, 1950–51.

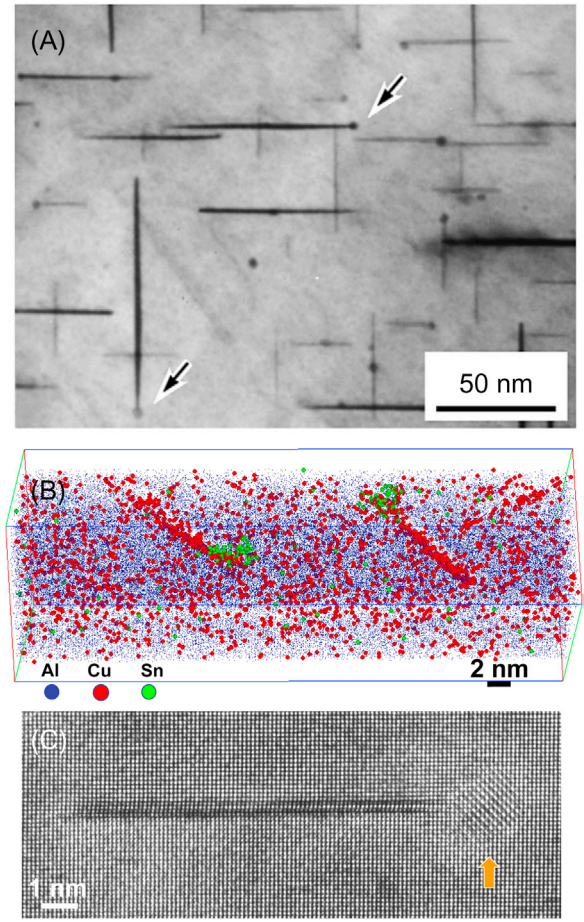


Figure 2.17 (A) Transmission electron micrograph, (B) three-dimensional atom probe map, and (C) high-resolution transmission electron micrograph showing θ′ precipitates associated with small particles of tin. Courtesy S. P. Ringer, K. Hono and T. Sakurai for (A), K. Hono for (B), and L. Bourgeois for (C).

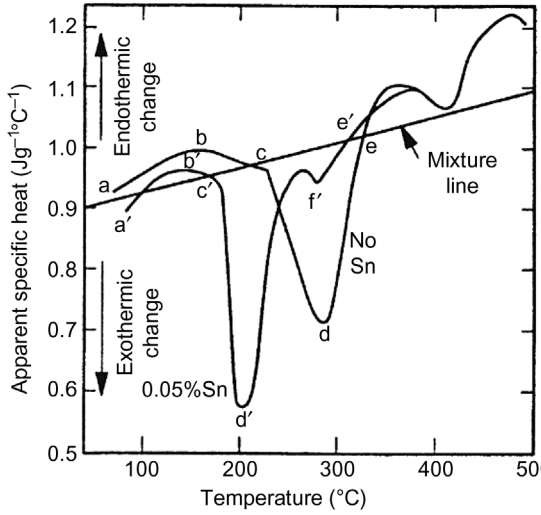


Figure 2.18 Apparent specific heat–temperature curves showing thermal energy changes occurring during heating of as-quenched alloys Al–4Cu and Al–4Cu–0.05Sn at 2°C a minute. From Polmear, IJ and Hardy, HK: *J. Inst. Metals*, 83, 393, 1954–55.

assumes no phase changes) and the curves represent the respective heat evolutions associated with precipitation of θ′. Each value is approximately $17\,J\,g^{-1}$ indicating that tin has not modified the volume fraction of θ′ that has precipitated. What has changed is the rate of precipitation of θ′ when tin is present. This effect is apparent in the Sn-containing alloy in three ways—by the steep slope c′d′, the lower minimum value of the apparent specific heat, and the fact that it occurs at a lower temperature (200°C) compared with 285°C for Al–4Cu. This behavior is characteristic of the way other microalloying additions affect precipitation in several aluminium alloys.

Another example of a microalloying effect is the role of small amounts of silver in modifying precipitation and promoting greater hardening in aluminium alloys that contain magnesium. Each system behaves differently. With Al–Zn–Mg alloys aged at elevated temperatures (e.g., Fig. 2.14B), silver stimulates the existing ageing process and this effect is attributed to an increase in the temperature range over which GP zones are stable (mechanism 2). In binary Al–Mg alloys, silver may induce precipitation in alloys in which normally it is absent (mechanism 6). For example, trace additions of Ag, in the range of 0.4–0.5 wt%, to Al–Mg alloys lead to the formation of an icosahedral quasicrystalline phase that has a much finer distribution after ageing. The resultant Al–Mg–Ag alloys have an accelerated age-hardening response and the maximum strength achievable at the same ageing temperature. Moreover, although binary Al–Mg alloys only age harden if the magnesium content exceeds 5%, Al–Mg–Ag alloys with only 0.5% magnesium will show some response.

Table 2.2 Details of precipitates formed by the addition of 0.4% (0.1 at.%) Ag to aged ternary Al–Cu–Mg alloys

Cu:Mg ratio	Precipitate	Crystal structure	
High: e.g., Al–4Cu–0.3Mg	Ω	Orthorhombic	$a = 0.496$ nm $b = 0.859$ nm $c = 0.848$ nm
Medium: e.g., Al–2.5Cu–1.5Mg	X′	c.p. hexagonal	$a = 0.496$ nm $c = 1.375$ nm
Low: e.g., Al–1.5Cu–4.0Mg	Z	Cubic	$a = 1.999$ nm

From Chopra, HD *et al.*: *Phil. Mag. Lett.*, 71, 319, 1995, and 73, 351, 1996.

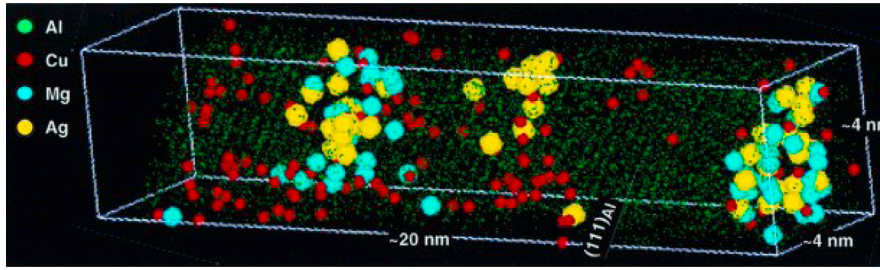


Figure 2.19 Three-dimensional elemental mapping of clusters in the alloy Al–4Cu–0.3Mg–0.4Ag aged 5 s at 180°C. The silver and magnesium atoms are represented by large yellow and blue balls. The copper atoms are shown as small red balls and the aluminium atoms are shown as green dots. From Murayama, M and Hono, K: *Scripta Mater.*, 38, 1315, 1998.

Of particular interest is the Al–Cu–Mg system in which 0.1 at.% silver promotes formation of three new and quite different precipitates depending on the Cu:Mg ratio (Table 2.2). APFIM has revealed that the effects of silver arise because clusters of silver and magnesium form within seconds after artificial ageing has commenced. Fig. 2.19 shows the appearance of these clusters that have formed after the alloy Al–4Cu–0.3 Mg–0.4 Ag has been aged for only 5 s at 180°C. These clusters have a loosely defined shape at the beginning, but gradually evolve into nanoscale platelets during continued ageing. Copper atoms then quickly diffuse to the clusters leading to nucleation of the precipitate Ω Al_2Cu (Fig. 4.16) that grows along the $\{111\}_\alpha$ planes. As will be described in the Section 4.4.1, Ω is relatively stable at elevated temperatures due to the segregation of silver and magnesium atoms at its broad surfaces, and its presence promotes good creep resistance in aluminium alloys. There is less understanding of the effects of silver in precipitation in Al–Cu–Mg–Ag alloys hardened by the X′ or Z phases, and little is known of the properties of these alloys. The experimental observations have indicated that the addition of 0.5 wt% Ag to the alloy Al–1.5Cu–4Mg promotes a finer distribution of Z phase at the expense of

S phase and hence a greater age-hardening response. Ag causes a greater density of vacancies to be retained by quenching. It also increases the stability of the Z phase. While clusters of solute (Cu, Mg, Ag) and vacancies form after very short ageing times, pre-precipitates such as GP zones does not appear to form preceded the formation of the Z phase.

Minor additions (e.g., 0.2 wt%) of scandium to aluminium alloys are also attracting interest despite the very high cost of extracting this metal from minerals containing rare earth elements, with which it is usually associated. Scandium combines with aluminium to form fine dispersions of coherent Al_3Sc particles that precipitate independently from any other phases that may be present in an alloy. Al_3Sc precipitates at relatively high temperatures (e.g., 350°C), is resistant to coarsening, and in addition to causing dispersion strengthening, inhibits recystallization in wrought products at temperatures as high as 600°C. Al_3Sc is an equilibrium phase with a cubic Ll_2 crystal structure and is isomorphous with a metastable form of the compound Al_3Zr that also inhibits recrystallization. When added together with zirconium, scandium combines to form particles of the stable compound $Al_3(Sc_x,Zr_y)$ that precipitate more rapidly and are more homogeneously dispersed than Al_3Zr. The $Al_3(Sc_x,Zr_y)$ precipitate has a core–shell structure, with the core being mostly Sc-rich, whereas the external shell is Zr-rich. This is because scandium has much faster diffusivity than zirconium in the aluminium solid solution and the absence of zirconium and scandium diffusion inside the precipitate. The core–shell structure of the $Al_3(Sc_x,Zr_y)$ precipitate provides a much higher resistance to Ostwald ripening.

Because extensive studies have already been made of the effects of major additions on the response of aluminium and other alloys to age hardening, it is to be expected that the role of microalloying elements will continue to receive attention. As indicated earlier, these minor elements can have important practical effects in changing ageing kinetics, microstructures, and properties, some of which are discussed further when considering individual alloy systems.

2.2.5 Hardening mechanisms

Although early attempts to explain the hardening mechanisms in age-hardened alloys were limited by a lack of experimental data, two important concepts were postulated. One was that hardening, or the increased resistance of an alloy to deformation, was the result of interference to slip by particles precipitating on crystallographic planes. The other was that maximum hardening was associated with a critical particle size. Modern concepts of precipitation hardening are essentially the consideration of these two ideas in relation to dislocation theory, since the strength of an age-hardened alloy is controlled by the interaction of moving dislocations with precipitates.

Obstacles to the motion of dislocations in age-hardened alloys are the internal strains around precipitates, notably GP zones, and the actual precipitates themselves. With respect to the former, it can be shown that maximum

impedance to the dislocation motion, i.e., maximum hardening, is to be expected when the spacing between particles is equal to the limiting radius of curvature of moving dislocation lines, i.e., ~50 atomic spacings or 10 nm. At this stage the dominant precipitate in most alloys is coherent GP zones, and high-resolution transmission electron microscopy has revealed that these zones are, in fact, sheared by moving dislocations. Thus individual GP zones per se have only a small effect in impeding glide dislocations and the large increase in yield strength these zones may cause arises from their high volume fraction.

Shearing of the zones increases the number of solute–solvent bonds across the slip planes in the manner depicted in Fig. 2.20 so that the process of clustering tends to be reversed. Additional work must be done by the applied stress in order for this to occur, the magnitude of which is controlled by factors such as relative atomic sizes of the atoms concerned and the difference in stacking-fault energy between matrix and precipitate. This so-called chemical hardening makes an additional contribution to the overall strengthening of the alloy.

Once GP zones are cut, dislocations continue to pass through the particles on the active slip planes and work hardening is comparatively small. Deformation tends to become localized on only a few active slip planes so that some intense bands develop which allows dislocations to pile up at grain boundaries in the manner shown schematically in Fig. 2.21A. As will be discussed in the Sections 2.5 and 4.4.6, the development of this type of microstructure may be deleterious with respect to mechanical properties such as ductility, toughness, fatigue, and stress corrosion.

If precipitate particles are intrinsically strong and are large and widely spaced, they can be readily bypassed by moving dislocations which bow out

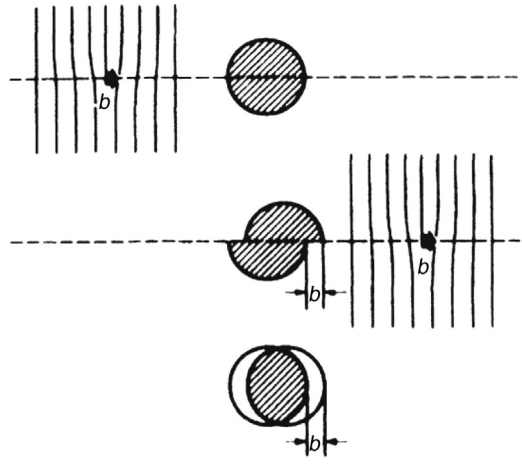


Figure 2.20 Representation of the cutting of a fine particle, e.g., GP zone, by a moving dislocation. From Conserva, M *et al.*: *Alumino E. Nuova Metallurgia*, 39, 515, 1970.

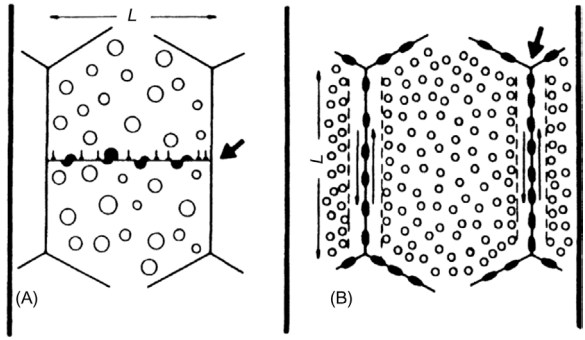


Figure 2.21 (A) Shearing of fine precipitates leading to planar slip and dislocation pile-ups at grain boundaries. (B) Stress concentration at grain boundary triple points due to presence of PFZs. From Lütjering, G and Gysler, A: *Aluminium Transformation, Technology and Applications*, ASM, Cleveland, OH, USA, 171, 1980.

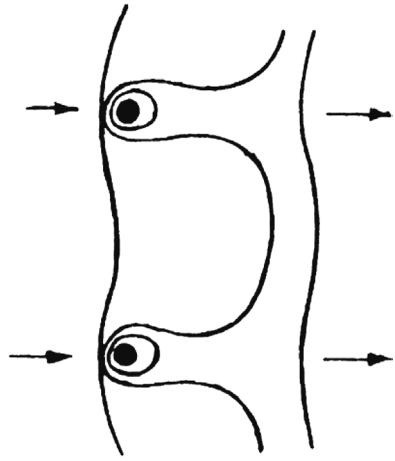


Figure 2.22 Representation of a dislocation bypassing widely spaced particles.

between them and rejoin by a mechanism first proposed by Orowan (Fig. 2.22). Loops of dislocations are left around the particles. The yield strength of the alloy is low but the rate of work hardening is high, and plastic deformation tends to be spread more uniformly throughout the grains. This is the situation with overaged alloys and the typical age-hardening curve in which strength increases then decreases with ageing time has been associated with a transition from shearing (curve A) to bypassing (curve B) of precipitates, as shown schematically in Fig. 2.23. In theory, the intersection point at P represents the maximum strength that can be developed in the alloy.

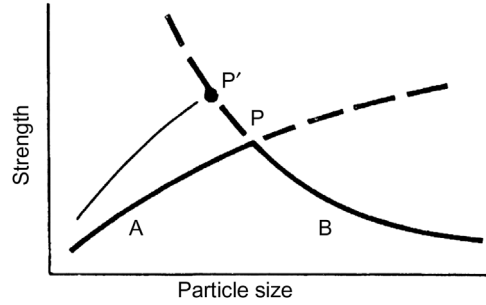


Figure 2.23 Representation of relationship between strength and particle size for a typical age-hardening alloy: (A) particles sheared by dislocations and (B) particles not sheared (i.e., bypassed) by dislocations. From Nicholson RB: *Strengthening Methods in Crystals*, Kelly, A and Nicholson, RB (Eds.), Elsevier, Amsterdam, p. 535, 1971.

Accompanying the formation of the intermediate precipitate is the development of wider, PFZs adjacent to grain boundaries as shown in Fig. 2.14A. These zones are relatively weak with respect to the age-hardened matrix and may deform preferentially leading to high stress concentrations at triple points (Fig. 2.21B) which, in turn, may cause premature cracking (Section 2.5).

The most interesting situation arises if precipitates are present which can resist shearing by dislocations and yet be too closely spaced to allow bypassing by dislocations. In such a case, the motion of dislocation lines would only be possible if sections can pass over or under individual particles by a process such as cross-slip. High levels of both strengthening and work hardening would then be expected. Normally such precipitates are too widely spaced for this to occur. However, some success has been achieved through the following strategies in stimulating formation of dispersions of precipitates that resist cutting by dislocations:

1. Duplex ageing treatments first below and then above the GP zones solvus temperature which enable finer dispersions of intermediate precipitates to be formed in some alloys (e.g., Section 4.4.5).
2. Co-precipitation of two phases, one which forms as finely dispersed zones or particles that contribute mainly to raising yield strength and the other as larger particles that resist shearing by dislocations so that plastic deformation is distributed more uniformly (e.g., Fig. 2.52B).
3. Co-precipitation of two or more intermediate phases, each of which forms on different crystallographic planes so that dislocation mobility is again reduced (e.g., Section 4.4.6).
4. Nucleation of uniform dispersions of intermediate precipitates by the addition of specific trace elements (e.g., Fig. 4.17).

An increase in the volume fraction of precipitate particles raises both curves A and B in Fig. 2.23 resulting in higher strength. Similarly, a decrease in the

particle size of precipitates that are still capable of resisting shearing by dislocations will also raise the peak strength by moving P to P′. The critical size, d_c, of particles capable of resisting shearing varies with different precipitate phases and depends on precipitate crystal structure, morphology, and distribution. For example, the T_1 phase (Al_2CuLi) that forms on the $\{111\}_\alpha$ planes in certain artificially aged, lithium-containing alloys has a smaller value of d_c than the phase θ′ (Al_2Cu) that forms on the $\{100\}_\alpha$ planes (Table 2.3).

Table 2.3 Probable precipitation processes in aluminium alloys of commercial interest

Alloy	Precipitates	Remarks
Al–Cu	GP zones as thin plates on $\{100\}_\alpha$	Usually single layers of copper atoms on $\{100\}_\alpha$.
	θ″ (formerly GP zones [2])	Coherent, probably two layers of copper atoms separated by three layers of aluminium atoms. May be nucleated at GP zones (Fig. 2.11).
	θ′ tetragonal Al_2Cu $a = 0.404\,nm$ $c = 0.580\,nm$	Semi-coherent plates nucleated at dislocations. Form on $\{100\}_\alpha$.
	θ body-centered tetragonal Al_2Cu $a = 0.607\,nm$ $c = 0.487\,nm$	Incoherent equilibrium phase. May nucleate at surface of θ′.
Al–Mg (>5%)	Spherical GP zones	GP zones solvus below room temperature if <5%Mg and close to room temperature in compositions between 5% and 10% Mg.
	β′ hexagonal $a = 1.002\,nm$ $c = 1.636\,nm$	Probably semi-coherent. Nucleated on dislocations. $(0001)_\beta//(001)_\alpha$; $[01\bar{1}0]_\beta//[110]_\alpha$.
	β face-centered cubic Mg_5Al_8 (formerly Mg_2Al_3) $a = 2.824\,nm$	Incoherent, equilibrium phase. Forms as plates or laths in grain boundaries and at a surface of β′ particles in matrix. $(111)_\beta//(001)_\alpha$; $[1\bar{1}0]_\beta//[010]_\alpha$.
Al–Si	Silicon diamond cubic $a = 0.542\,nm$	Silicon forms directly from SSSS.
Al–Cu–Mg	Disordered clusters of Cu and Mg atoms	Form rapidly in most compositions and promote hardening. May be an early stage of GP (Cu, Mg) zones.
	GP (Cu,Mg) zones as rods along $<100>_\alpha$ (also known as GPB zones)	May form from clusters. Stable to relatively high temperatures.

(*Continued*)

Table 2.3 Probable precipitation processes in aluminium alloys of commercial interest (Continued)

Alloy	Precipitates	Remarks
	S′ orthorhombic Al_2CuMg $a = 0.404\,nm$ $b = 0.925\,nm$ $c = 0.718\,nm$	Semi-coherent and nucleated at dislocations (Fig. 2.13). Forms as laths on $\{210\}_\alpha$ along $<001>_\alpha$. Very similar to equilibrium S.
	S orthorhombic Al_2CuMg $a = 0.400\,nm$ $b = 0.923\,nm$ $c = 0.714\,nm$	Incoherent equilibrium phase, probably transforms from S′. Note that precipitates from the Al–Cu system can also form in compositions with high Cu:Mg ratios.
Al–Mg–Si	Clusters and co-clusters of Mg and Si atoms GP zones	Form rapidly but cause little hardening (Fig. 2.32). GP zones solvus occurs at temperatures that are normally higher than the ageing temperatures. Zones seem spherical but structure not well defined.
	β″ monoclinic $a = 1.534\,nm$ $b = 0.405\,nm$ $c = 0.683\,nm$ $\beta = 106°$	Coherent needles, lie along $\langle 100\rangle_\alpha$. $(010)_{\beta''}//(001)_\alpha$; $[001]_{\beta''}//[310]_\alpha$. Lattice dimensions of monoclinic cell are changed in alloys with high Si contents. Main strengthening precipitate. Forms from GP zones. Composition close to MgSi.
	β′ hexagonal $a = 0.705\,nm$ $c = 0.405\,nm$	Semi-coherent rods, lie along $\langle 100\rangle_\alpha$. $(001)_\beta//(100)_\alpha$; $[100]_\beta//[011]_\alpha$. Composition close to $Mg_{1.7}Si$.
	β′ hexagonal $a = 1.04\,nm$ $c = 0.405\,nm$	Semi-coherent laths, lie along $\langle 100\rangle_\alpha$. $(0001)_{\beta'}//(001)_\alpha$; $(10\bar{1}0)_{\beta'}//[510]_\alpha$. Forms together with β′; favored by high Si:Mg ratios. Two other (orthorhombic and hexagonal) precipitates have been detected. Composition close to MgSi.
	β face-centered cubic Mg_2Si $a = 0.639\,nm$	Platelets on $\{100\}_\alpha$. May transform directly from β′. $(001)_\beta//(001)_\alpha$; $[110]_\beta//[100]_\alpha$.
Al–Zn–Mg	GP zones; two types	GP [1] Spherical, 1–1.5 nm, ordered. GP [2] thin Zn disks, 1–2 atom layers thick, form on $\{111\}_\alpha$. Partly ordered.

(*Continued*)

Table 2.3 Probable precipitation processes in aluminium alloys of commercial interest (Continued)

Alloy	Precipitates	Remarks
	η′ (or M′) hexagonal $a = 0.496\,nm$ $c = 1.405\,nm$	May form from GP zones in alloys with Zn:Mg > 3:1. $(0001)_{\eta'}//(111)_{\alpha}$; $[11\bar{2}0]_{\eta'}//[11\bar{2}]_{\alpha}$. Semi-coherent. Disk shaped. $a//<11\bar{2}>_{\alpha}$, $c//<111>_{\alpha}$. Composition close to MgZn (e.g., Fig. 2.14).
	η (or M) hexagonal $MgZn_2$ $a = 0.521\,nm$ $c = 0.860\,nm$	Forms at or from η′, may have one of nine orientation relationships with matrix. Most common are: $(10\bar{1}0)_{\eta}//(001)_{\alpha}$; $(0001)_{\eta}//(110)_{\alpha}$ and $(0001)_{\eta}//(1\bar{1}1)_{\alpha}$; $(10\bar{1}0)_{\eta}//(110)_{\alpha}$.
	T′ hexagonal, probably $Mg_{32}(Al, Zn)_{49}$ $a = 1.388\,nm$ $c = 2.752\,nm$	Semi-coherent. May form instead of η in alloys with high Mg:Zn ratios. $(0001)_{T'}//(111)_{\alpha}$; $(10\bar{1}1)_{T'}//(11\bar{2})_{\alpha}$.
	T cubic $Mg_{32}(Al, Zn)_{49}$ $a = 1.416\,nm$	May form from η if ageing temperature >190°C, or from *T*′ in alloy with high Mg:Zn ratios. $(100)_{T}//(111)_{\alpha}$; $[001]_{T}//[11\bar{2}]_{\alpha}$.
Al–Li–Mg	δ′ cubic Al_3Li $a = 0.404$ to $0.401\,nm$	Metastable coherent precipitate with ordered $Cu_3Au(L1_2)$ type superlattice (Fig. 4.35). Low misfit.
	Al_2LiMg cubic $a = 1.99\,nm$	Forms as coarse rods with <110> growth directions in alloys with ≥ 2%Mg. $(110)_{p}//(\bar{1}10)_{\alpha}$; $[1\bar{1}0]_{p}//[111]_{\alpha}$.
Al–Li–Cu	δ′ cubic Al_3Li δ cubic AlLi $a = 0.637\,nm$	As for Al–Li and Al–Li–Mg alloys. Nucleates heterogeneousy, mainly in grain boundaries. $(011)_{\delta}//(\bar{1}11)_{\alpha}$;$(0\bar{1}1)_{\delta}//(1\bar{1}2)_{\alpha}$.
	T_1 hexagonal Al_2LiCu $a = 0.497\,nm$ $c = 0.934\,nm$	Thin hexagonal-shaped plates with $\{111\}_{\alpha}$ habit plane. $(0001)_{T_1}//\{111\}_{\alpha}$; $<10\bar{1}0>_{T_1}//<\bar{1}10>_{\alpha}$ (Figs. 2.27 and 4.39).
	θ″, θ′	Phases present in binary Al–Cu alloys may also form at low Li:Cu ratios.

Modeling concepts are now permitting further refinements to be made in the understanding of the microstructural design of high-strength aluminium alloys. While it is agreed that the desired microstructure to obtain high strength combined with a high resistance to fracture is one that consists of a small volume fraction of very fine, hard particles, it is also recognized that a common feature in high-strength aluminium alloys is the presence of shear-resistant, plate-shaped precipitates that form on the $\{100\}_\alpha$ or $\{111\}_\alpha$ matrix planes, or rod-shaped precipitates that form in the $<100>_\alpha$ directions. Less attention has been paid to a quantitative analysis of the effects of particle shape and orientation because of a lack of appropriate versions of the Orowan equation that relate the critical resolved shear stress due to dispersion hardening to precipitate characteristics.

The version of the Orowan equation currently accepted for spherical particles is:

$$\Delta\tau = \frac{Gb}{2\pi\sqrt{1-\nu}} \cdot \frac{1}{\lambda} \cdot \ln\frac{\pi d}{4b}$$

where $\Delta\tau$ is increment in critical resolved shear stress due to dispersion strengthening, ν is Poisson's ratio, G is shear modulus, b is Burgers vector of gliding dislocations, λ is effective interparticle spacing, and d is diameter of precipitate particles. Within this equation, it is λ that varies with shape, orientation, and distribution of the particles, and derivation of appropriate versions of the Orowan equation require the calculation of λ for different particle arrays. If it is assumed that $\{100\}_\alpha$ precipitate plates are circular disks of diameter d and thickness t distributed at the center of each surface of a cubic volume of the matrix (Fig. 2.24A), then the intersection of these plates with the $\{111\}_\alpha$ slip plane in the matrix will have a triangular distribution on this slip plane (Fig. 2.24B).

Calculations show that the effective planar interparticle spacing for the $\{100\}_\alpha$ plates is given by $\lambda = 0.931(0.306\pi dt/f)^{1/2} - \pi d/8 - 1.061d$, where f is volume fraction of particles. Similar calculations for $\{111\}_\alpha$ precipitate plates show $\lambda = 0.931(0.265\pi dt/f)^{1/2} - \pi d/8 - 0.919t$, and for $<100>_\alpha$ rods $\lambda = 1.075d(0.433\pi/f)^{1/2} - (1.732d)^{1/2}$. Substitution of these expressions for λ in the Orowan equation shown earlier enables the critical resolved shear stresses to be determined for model alloys containing these three different types of precipitates. This analysis shows, quantitatively, that plate-shaped precipitates are more effective barriers to gliding dislocations than either rods or spherical precipitates. Furthermore, the increment of strengthening produced by $\{111\}_\alpha$ plates is invariably larger than that produced by $\{100\}_\alpha$ plates and, for both orientations, this increment becomes progressively larger as the aspect ratio (length to thickness) increases, Fig. 2.24C.

Fig. 2.25 shows a comparison of phase field simulations of dislocation gliding in a forest of particles that have same number density, volume fraction, and distribution of precipitates. The dislocation bows when it approaches the

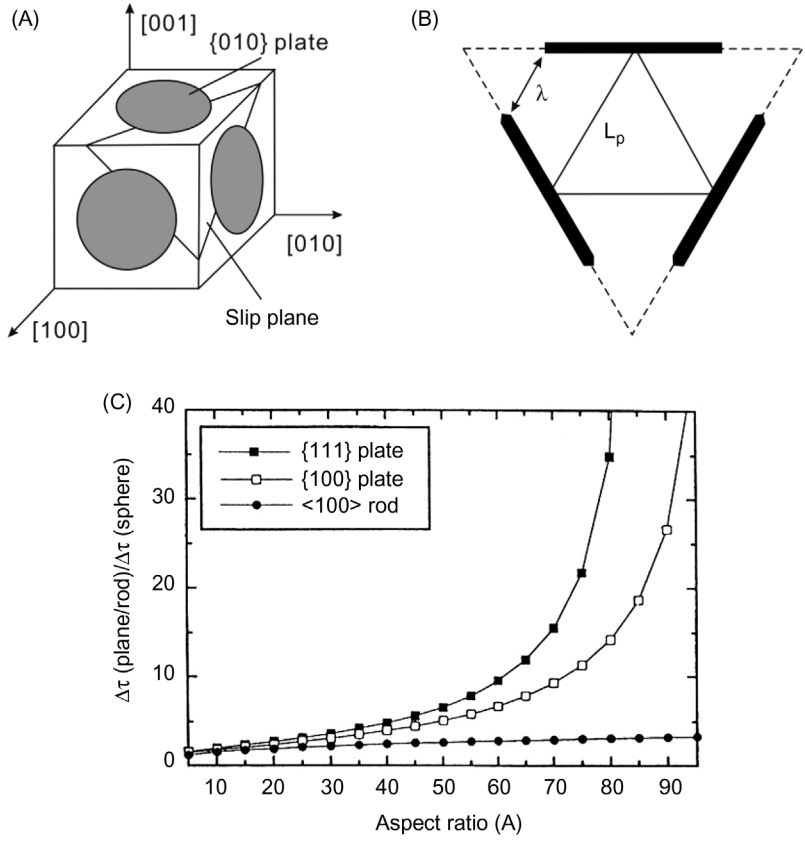


Figure 2.24 (A) Circular $\{100\}_\alpha$ precipitate plates in a cubic volume of the aluminium matrix and (B) projection of intersected $\{100\}_\alpha$ precipitate plates on a $\{111\}_\alpha$ plane of the matrix. (C) Variation in ratio of critical resolved shear stress $\Delta\tau$ (plate, rod)/$\Delta\tau$ (sphere) with aspect ratio for Orowan strengthening attributable to $\{111\}_\alpha$ and $\{100\}_\alpha$ precipitate plates and $<100>_\alpha$ precipitate rods. Volume fraction of precipitates is 0.05.

precipitates and bypasses the particles if the applied shear stress is sufficiently large. While a shear stress of 55 MPa is required for the dislocation to glide through the entire forest of spherical particles, a 50% higher stress is needed for the plate-shaped particles.

Above a critical value of aspect ratio, plates on either set of planes form what is essentially a closed network that entraps gliding dislocations. In such situation, it is inevitable that precipitate shearing occurs. The contribution of shearable precipitates to the critical resolved shear stress is:

$$\Delta\tau = \left(\frac{2}{b\sqrt{\Gamma}}\right)\left(\frac{1}{L_p}\right)\left(\frac{F}{2}\right)^{3/2}$$

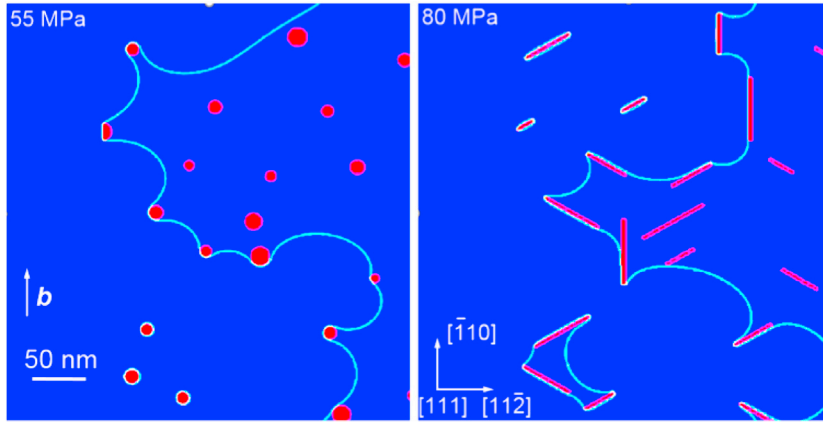


Figure 2.25 Effects of precipitate shape on critical resolved shear stress required for a dislocation to glide through precipitate forest. The number density and volume fraction of precipitates are identical in (A) and (B). Courtesy H. Liu.

where Γ is the dislocation line tension in the matrix phase, L_p is the mean planar center-to-center interprecipitate spacing, and force F is a measure of the resistance of the precipitates to dislocation shearing. For $\{111\}_\alpha$ precipitate plates, the dihedral angle between their habit plane and the $\{111\}_\alpha$ slip plane is 70.53°. Assuming the slip plane is $(1\bar{1}1)_\alpha$, shearing of a $(111)_\alpha$ precipitate plate occurs in $[10\bar{1}]_\alpha$, $[110]_\alpha$, or $[011]_\alpha$ directions on the $(1\bar{1}1)_\alpha$ slip plane (Fig. 2.26A). When a $(111)_\alpha$ plate is sheared in the $[110]_\alpha$ direction, the energy of the created particle/matrix interface is approximately $2\gamma_i d_p b \sin 60°$, and the precipitate strength is: $F = \dfrac{2d_p b\gamma_i \sin 60°}{t_p} = \dfrac{1.282db\gamma_i}{t}$, where γ_i is the specific interfacial energy of the newly created particle/matrix interface, d_p and t_p are the mean planar radius and planar thickness of the precipitate plate, respectively. Combining this expression and that for L_p, the interfacial strengthening increment in aluminium alloys containing $\{111\}_\alpha$ precipitate plates is given as $\Delta\tau_i = \dfrac{1.211d\gamma^{3/2}}{t^2}\left(\dfrac{bf}{\Gamma}\right)^{1/2}$. For $\{100\}_\alpha$ precipitate plates, the dihedral angle between their habit plane and the $\{111\}_\alpha$ slip plane is 54.74°. To shear the $\{100\}_\alpha$ plates with an additional particle/matrix interface area of $2d_p b \sin 60°$, the required shear force $F = \dfrac{2d_p b\gamma_i \sin 60°}{t_p} = \dfrac{1.110db\gamma_i}{t}$. Combining this equation and that for L_p, the interfacial strengthening increment in critical resolved shear stress is given as $\Delta\tau_i = \dfrac{0.908d\gamma^{3/2}}{t^2}\left(\dfrac{bf}{\Gamma}\right)^{1/2}$. For a given value

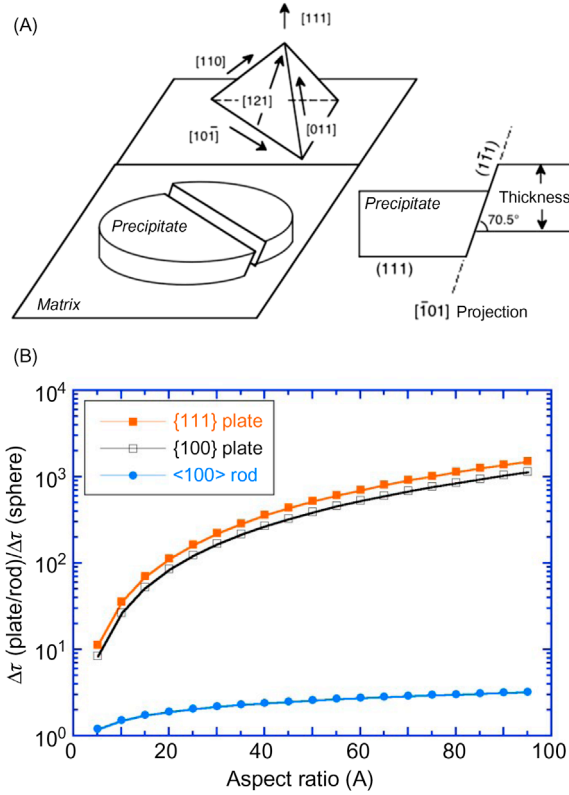


Figure 2.26 (A) Schematic diagrams showing shearing of a circular precipitate plate and projection of a sheared precipitate plate. (B) Variation of ratio $\Delta\tau$(plate/rod)/$\Delta\tau$(sphere) with aspect ratio for $\{111\}_\alpha$ and $\{100\}_\alpha$ plates and $<100>_\alpha$ precipitate rods, calculated assuming interfacial strengthening of sheared particles.

of dislocation line tension, the variations in the ratio $\Delta\tau_i$(plate)/$\Delta\tau_i$(sphere) with plate aspect ratio for various orientations of plates are also shown in Fig. 2.26B. Unlike the results for spherical or rod particles, it is evident that the contribution due to interfacial strengthening may become significant when particles take, in particular, a plate shape. For identical volume fractions and number densities of precipitates per unit volume, the yield stress increments produced by $\{111\}_\alpha$ and $\{100\}_\alpha$ precipitate plates are orders of magnitude larger than those produced by $<100>_\alpha$ precipitate rods and by spherical particles. The increments in CRSS produced by $\{111\}_\alpha$ and $\{100\}_\alpha$ plates increase substantially with an increase in plate aspect ratio and are up to three orders of magnitude larger than that produced by spheres, when the plate aspect ratio is in the range of 5:1 to 95:1.

Traditionally, attempts to improving alloy strength involve efforts to increase nucleation rate and hence number density of precipitates. Modeling

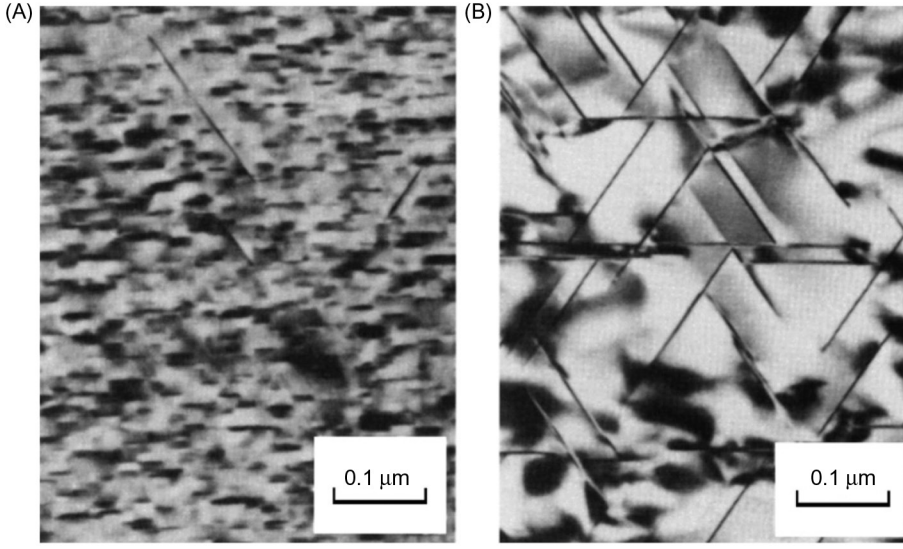


Figure 2.27 Electron micrographs of the alloy Al–5.3Cu–1.3Li–0.4Mg–0.4Ag–0.16Zr: (A) quenched and aged 8 h at 160°C showing finely dispersed, coherent θ″ particles and occasional plates of the T_1 phase. Hardness 146 DPN; (B) quenched, cold worked 6% and aged 8 h 160°C showing a much coarser but uniform dispersion of semi-coherent T_1 plates. Hardness 200 DPN. Electron beam is parallel to $<110>_\alpha$. (B) Courtesy S. P. Ringer.

results from both shear resistant and shearable precipitates indicate that an alternative approach to strengthening is to modify precipitate shape and orientation. Any further enhancement in strength may be achieved if precipitate plates of large aspect ratio could be formed in the alloy, probably via the addition of microalloying elements.

The influences of precipitate orientation and shape are in accord with the observed behavior of high-strength aluminium alloys. One example of high-strength alloys hardened by precipitates that form on the $\{111\}_\alpha$ planes is those based on the Al–Zn–Mg–Cu system (Table 2.3). Some of these commercial alloys develop yield strengths exceeding 600 MPa which are significantly higher than the yield strengths possible with alloys based on the Al–Cu system in which the precipitates form on the $\{100\}_\alpha$ planes. Another example of a precipitate which forms on the $\{111\}_\alpha$ planes is the T_1 phase (Al_2CuLi) that was mentioned earlier. This phase has a particularly high aspect ratio and its ability to promote greater hardening than a much higher density of zones of the finer, shearable phase θ″ formed on the $\{100\}_\alpha$ planes is illustrated in an Al–Cu–Li–Mg–Ag–Zr alloy in Fig. 2.27. In this regard, it may be noted that yield stresses exceeding 700 MPa have been recorded for this alloy which are close to the theoretical upper limit for aluminium (~900 MPa).

2.3 AGEING PROCESSES

2.3.1 Precipitation sequences

As mentioned earlier, several aluminium alloys display a marked response to age hardening. By suitable alloying and heat treatment, it is possible to increase the yield stress of high-purity aluminium by as much as 50 times. Details of the precipitates that may be present in alloy systems having commercial significance are given in Table 2.3. The actual precipitate or precipitates that form in a particular alloy during ageing depends mainly on the ageing temperature. For example, for GP zones to form, ageing must be carried out below the relevant GP zones solvus temperature as mentioned in the Section 2.2.2. If intermediate precipitates are formed, they may nucleate from pre-existing GP zones, at the sites of these zones, or independently depending on the alloy concerned. At some ageing temperatures, both GP zones and an intermediate precipitate may be present together. Cold work prior to ageing increases the density of dislocations which may provide sites for the heterogeneous nucleation of specific precipitates.

A partial phase diagram for the Al–Cu system was shown in Fig. 2.1. Al–Mg–Si alloys can be represented as a pseudo-binary Al–Mg_2Si system (Fig. 2.28) and sections of the ternary phase diagrams for the important Al–Cu–Mg and Al–Zn–Mg systems are shown in Figs. 2.29 and 2.30. Most commercial alloys based on these systems have additional alloying elements present that modify the respective ternary diagrams and, in Fig. 2.31, an example is shown

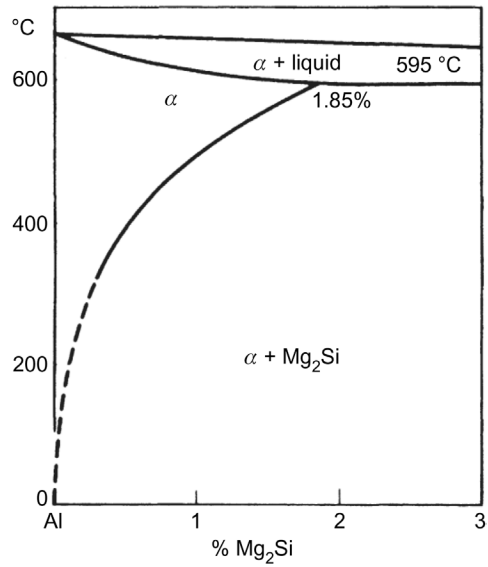


Figure 2.28 Pseudo-binary phase diagram for Al–Mg_2Si.

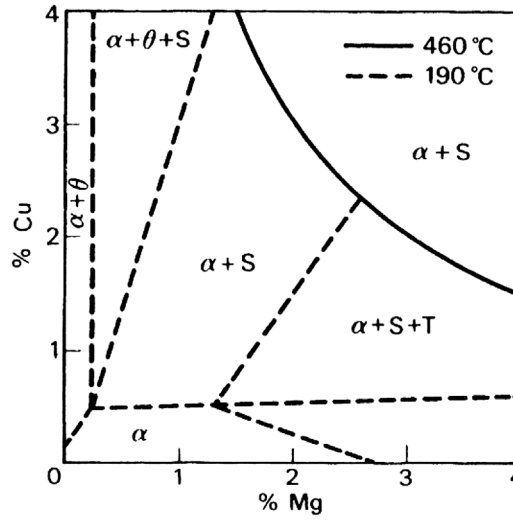


Figure 2.29 Section of ternary Al–Cu–Mg phase diagram at 460°C and 190°C (estimated). $\theta = Al_2Cu$, $S = Al_2CuMg$, $T = Al_6CuMg_4$.

for the section at 460°C for Al–Zn–Mg alloys containing 1.5% copper. Since this is close to the usual solution treatment temperature for alloys of this type, it should be noted that some quaternary compositions will not be single phase prior to quenching.

2.3.2 Clustering phenomena

Although the random clustering of solute atoms prior to precipitation in quenched and aged aluminium alloys was detected by small angle X-ray diffraction many years ago, the effects of this phenomenon on subsequent ageing processes have been little understood. Now there is evidence that clustering events may promote formation of existing precipitates in an alloy, stimulate nucleation of new precipitates as was discussed in the Section 2.2.4, and contribute to the actual age hardening of certain alloys.

In the Al–Mg–Si system in which ageing processes are particularly complex, atom probe studies have shown that the formation of GP zones may be preceded initially by the appearance of individual clusters of magnesium and silicon atoms, followed by the formation of co-clusters of these elements. This behavior is demonstrated in Fig. 2.32 which shows atom probe concentration profiles after ageing the alloy Al–1Mg–0.6Si for (A) 0.5 h and (B) 8 h at 70°C. These profiles are developed by collecting, counting, and identifying ions as they are evaporated from the tip of an alloy specimen in a field ion microscope. The clusters will, for example, form during a delay at ambient temperature after quenching and before artificial ageing. As described in the Section 4.4.3, their

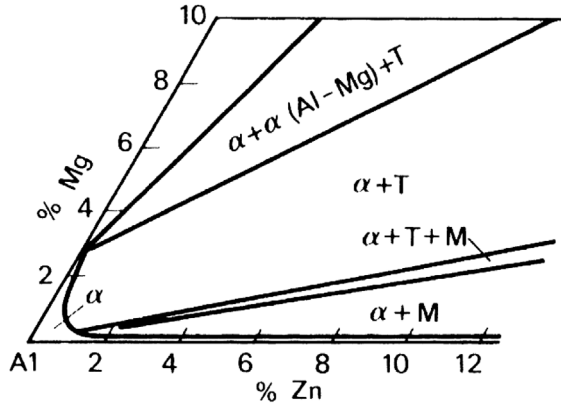


Figure 2.30 Section of ternary Al–Zn–Mg phase diagrams at 200°C. M = $MgZn_2$, T = $Al_{32}(Mg,Zn)_{49}$.

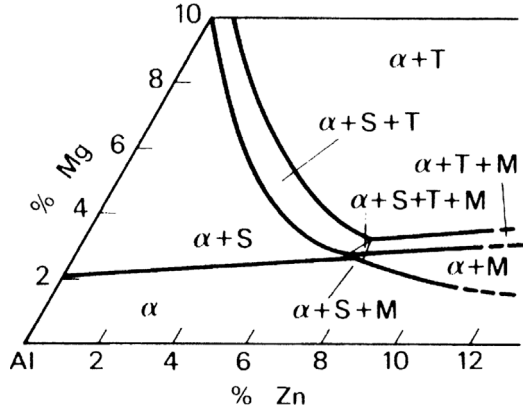


Figure 2.31 Section of Al–Zn–Mg–Cu phase diagram (1.5% Cu) at 460°C. S = Al_2CuMg, T = Al_6CuMg_4 + $Al_{32}(Mg,Zn)_{49}$, M = $MgZn_2$ + AlCuMg.

presence may alter the dispersion of precipitates that form on subsequent ageing such that the response to hardening is reduced.

It is well known that age hardening in most alloys based on the Al–Cu–Mg system occurs in two distinct stages over a wide temperature range (~100°C to 240°C). The first stage, which may account for 60–70% of the total hardening response, is characteristically and uniquely rapid, and may be completed within 60 s. This behavior is then followed by what, for some compositions, can be a prolonged period (e.g., 100 h) during which the hardness shows little or no change, and after which there is a second rise to a peak value, Fig. 2.33. Initially, this early hardening phenomenon was attributed to the rapid formation of GP(Cu,Mg) zones

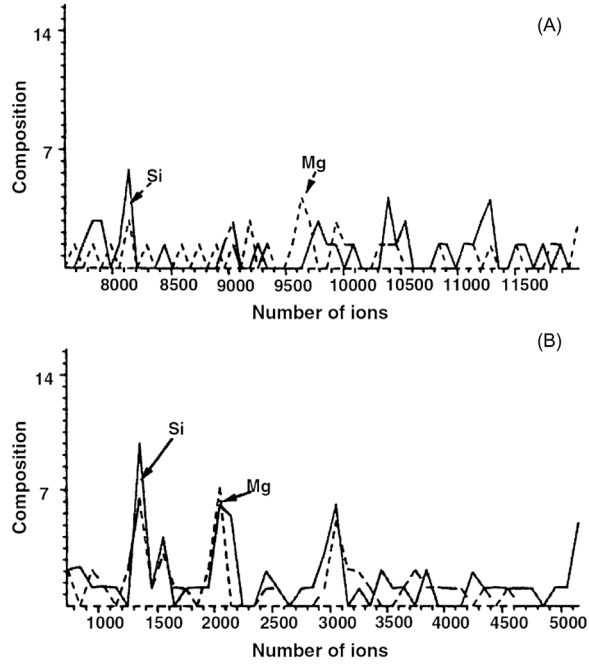


Figure 2.32 Atom probe profiles showing evidence of clustering of magnesium and silicon atoms in the alloy 6061 (Al–1Mg–0.6Si) quenched and aged (A) 0.5 h and (B) 8 h at 70°C. From Edwards, GA *et al.*: *Applied Surf. Sci.*, 76/77, 219, 1994.

(also known as GPB zones). However, later studies using high-resolution electron microscopy and electron diffraction did not detect evidence of these zones until alloys were aged for times that placed them further along the hardness plateau. Observations made from one-dimensional APFIM revealed the presence of a high density (e.g., $10^{19}\,cm^{-3}$) of small, disordered clusters of atoms immediately after rapid early hardening is completed, and the phenomenon was termed "cluster hardening" to distinguish it from normal precipitation reactions. However, subsequent work made by three-dimensional atom probe revealed little or no evidence of Cu–Mg co-clusters in the aluminium matrix. Recently, single pairs of copper and magnesium atoms were proposed to form in Al–Cu–Mg alloys based on thermodynamic calculations, but these pairs are yet to be confirmed experimentally. The formation of solute pairs or clusters might be responsible for the rapid hardening phenomenon in Fig. 2.33, also the mechanism by which they can cause hardening remains uncertain. One possibility is that rapid solute/dislocation interactions occur in which the relatively small copper atoms and large magnesium atoms immobilize edge dislocations by segregating preferentially to the respective compression and tension regions. Another suggestion is that hardening may arise because of differences in elastic moduli between aluminium and the Cu–Mg clusters.

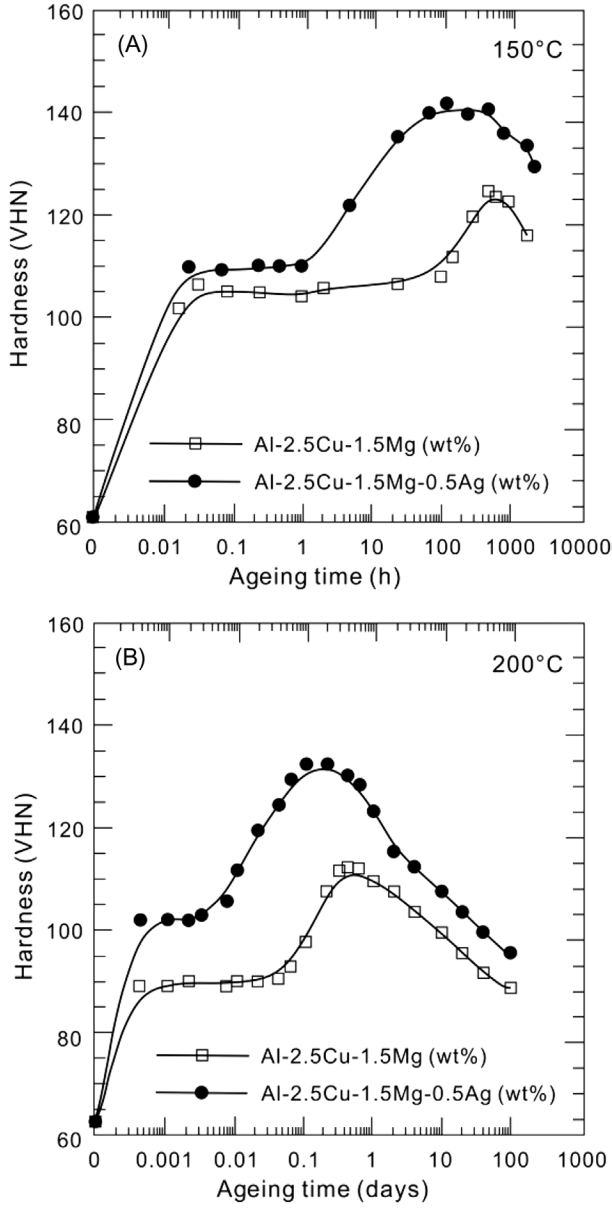


Figure 2.33 Rapid hardening phenomenon in Al–2.5Cu–1.5Mg and Al–2.5Cu–1.5Mg–0.5Ag alloys during isothermal ageing at (A) 150°C and (B) 200°C. From Vietz, JT and Polmear, IJ: *J. Inst. Met.*, 94, 410, 1966.

2.3.3 GPB zones in Al–Cu–Mg alloys

GPB zones have been observed towards the end of the hardness plateau shown in Fig. 2.33. It is at this stage that further ageing causes a second increase in hardness which reaches a maximum value when a critical distribution of the GPB zones has formed. The structure of these zones remains uncertain but a recent study using atomic-resolution Z-contrast scanning transmission electron microscopy has revealed that at least two distinctly different structures may form (Fig. 2.34): one structure is comprised of an agglomeration of structural units with a translational periodicity along a single $<001>_{\alpha}$ direction, while the other structure has a core having a hexagonal structure and a shell comprising structural units (Fig. 2.34).

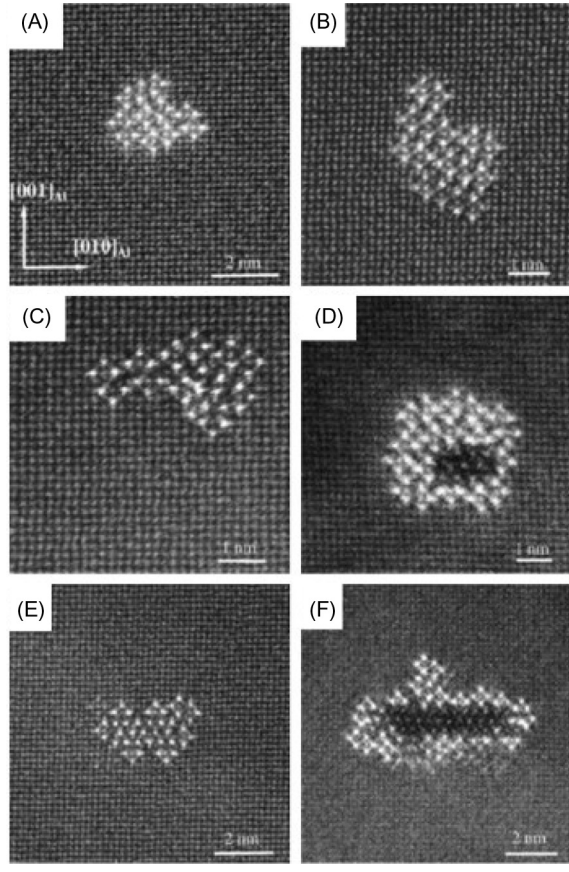


Figure 2.34 Cross sections of GPB zones in Al–Cu–Mg alloys. From Kovarik, L *et al.*: *Acta Mater.*, 56, 4804, 2008.

2.3.4 Intermediate precipitates

The intermediate precipitates are often the key strengthening phases in commercial aluminium alloys. For some of these precipitates, there is now strong evidence to show that microalloying elements segregate to the interface between the precipitates and the aluminium matrix, see for example Fig. 4.17. The interfacial solute segregation phenomenon is even found in θ′ precipitate plates in simpler binary Al–Cu alloys. A recent study using atomic-resolution Z-contrast scanning transmission electron microcopy has revealed the presence of excessive Cu atoms in the θ′/matrix coherent interface during early stages of the θ′ precipitation (Fig. 2.35A) which is distinctly different from that previously assumed for the θ′/matrix interface. This single layer of copper atoms is similar or identical to GP zones, and its presence in the interface appears to be critical in the early stages of thickening of θ′. In the late growth stage, the θ′/matrix interface becomes less enriched in copper. Apart from the copper segregation in the broad surface of θ′ plates, the end facet of θ′, or the semicoherent interface, is found to have a complex but well-defined structure (θ″) that enables the progression from aluminium structure to θ′, Fig. 2.35B. This structure allows interface to migrate through a series of individual atomic movements.

Solute segregation in precipitate/matrix interfaces is also found to occur in Al–Mg–Si–Cu alloys (Fig. 2.36) and in Al–Sc–Mg alloys where magnesium segregates in the Al_3Sc/matrix interface. This is similar to the co-segregation

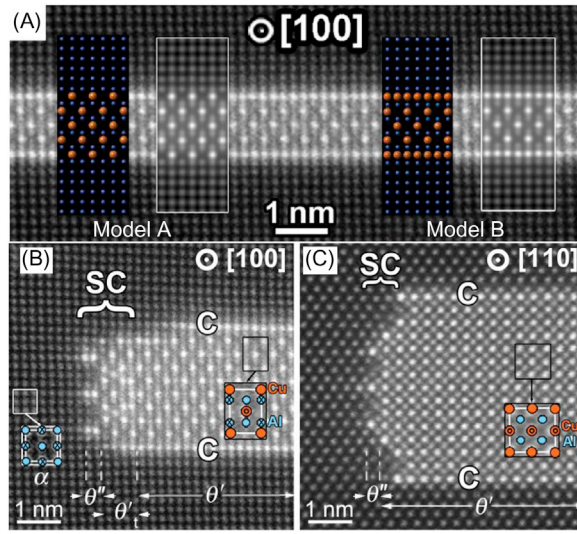


Figure 2.35 HAADF-STEM images showing (A) segregation of Cu atoms in the broad face of θ′ precipitates, and (B, C) θ′ precipitate end facet exhibiting a thin layer of θ″. From Bourgeois, L *et al.*: *Acta Mater.*, 59, 7043, 2011 and *Phys. Rev. Lett.*, 111, 046102, 2013.

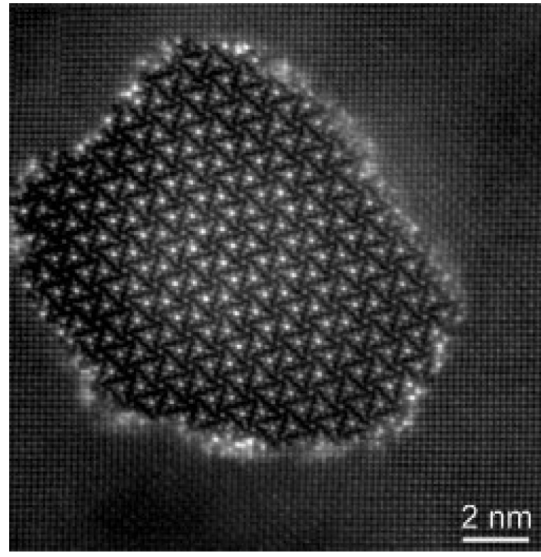


Figure 2.36 Segregation of copper (white contrast) in *Q*/matrix interface in an Al–Mg–Si–Cu alloy. From Fiawoo, M *et al.*: *Scripta Mater.*, 88, 53, 2012.

of silver and magnesium in interfaces associated with Ω and T_1 (Figs. 4.16 and 4.39). Different explanations have been proposed to account for the solute segregation, but the most commonly accepted one is interfacial energy minimization.

It has generally been accepted that most intermediate precipitates which form in aged aluminium alloys have compositions and crystal structures that differ only slightly from those of the respective equilibrium precipitates. In fact, for Al–Cu–Mg alloys in which the equilibrium precipitate is S(Al_2CuMg), the intermediate precipitate S′ differs so little in its crystallographic dimensions that it is sometimes ignored. However, studies of some alloys using one-dimensional and three-dimensional APFIM have revealed some unexpected compositional variations between other intermediate and equilibrium precipitates.

One example is the Al–Mg–Si system in which the compositions of the intermediate precipitates β″ and β′ were assumed to be the same as the equilibrium precipitate β (Mg_2Si) (Table 2.3). Because of this, the compositions of some commercial alloys have been designed deliberately to have a balanced (2:1) atomic ratio of magnesium and silicon in order to maximize precipitation of β″ and β′ during ageing. Now there is strong experimental evidence that the actual Mg:Si ratios of these intermediate precipitates are close to 1:1. As mentioned in Section 4.4.3, this has opened up the prospect of producing a new range of Al–Mg–Si alloys in which the magnesium content has been reduced to improve their hot working characteristics. Al–Zn–Mg–(Cu) alloys are others in

which atom probe studies have shown that the Mg:Zn ratio for the intermediate precipitate η' differs substantially from that of the equilibrium precipitate η ($MgZn_2$). In this case, the Mg:Zn ratio appears to lie in the range 1:1 to 1:1.15 rather than the expected 1:2. This suggests that the composition of η' is linked more to the preexisting GP zones than to the equilibrium precipitate η and supports the suggestion that η' can nucleate directly from these zones. These new observations about the compositions of some intermediate precipitates means that a substantial number of atom positions in their unit cells must still be occupied by aluminium atoms rather than the respective solute atoms.

2.3.5 Secondary precipitation

For many years there was an implicit acceptance that, once an alloy had been aged at an elevated temperature, its mechanical properties remained stable on exposure for an indefinite time at a significantly lower temperature. However, it was found that highly saturated Al–Zn alloys aged at 180°C will continue to age and undergo what has been termed "secondary precipitation" if cooled and then held at ambient temperature. Similar behavior has also been observed in highly saturated lithium-containing aluminium alloys aged first at 170°C and then exposed at temperatures in the range 60–130°C. In this case, there is a progressive increase in hardness and mechanical strength accompanied by an unacceptable decrease in ductility and toughness that is attributed to secondary precipitation of the finely dispersed δ' throughout the matrix. More recently, observations on a wide range of aluminium alloys have shown that secondary precipitation is, in fact, a more general phenomenon. This conclusion is supported by results obtained using the technique of positron annihilation spectroscopy which have indicated that vacancies may be retained and remain mobile at ambient temperatures after aged aluminium alloys are cooled from a higher ageing temperature.

Positron annihilation spectroscopy is proving to be a powerful tool for studying the role of lattice defects, such as vacancies, in the decomposition kinetics of aged alloys. This technique involves measurement of the lifetimes of positrons emitted from a radioactive source before there are annihilated by interacting with electrons in the alloy. The annihilation process may be thought of as a chemical reaction that has a rate which is directly proportional to the local electron density. Vacant lattice sites can be detected because they are open volume defects and offer temporary "shelter" to incident positrons, thereby slowing their annihilation rate. As an example, Fig. 2.37 shows the evolution of positron lifetimes during ageing the alloy Al–4Cu–0.3Mg at 20°C after first being solution treated, quenched, and aged for various times at 180°C. The increases in positron lifetimes, which are comparatively large for alloys initially aged for short times (30 and 120 s) at 180°C, but still significant for longer times of 1 and 10 h, are all taken to indicate that retained vacancies (and solute atoms) are mobile at 20°C thereby allowing further ageing to occur.

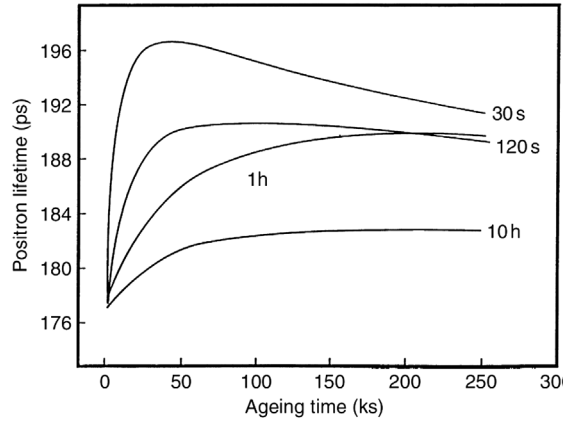


Figure 2.37 Positron lifetimes during secondary ageing Al–4Cu–0.3Mg at 20°C after solution treatment at 520°C, quenching at 0°C and first ageing 30 s, 120 s, 1 h, or 10 h at 180°C. From Somoza, A *et al.*: *Phys. Rev. B*, 61, 14454, 2000.

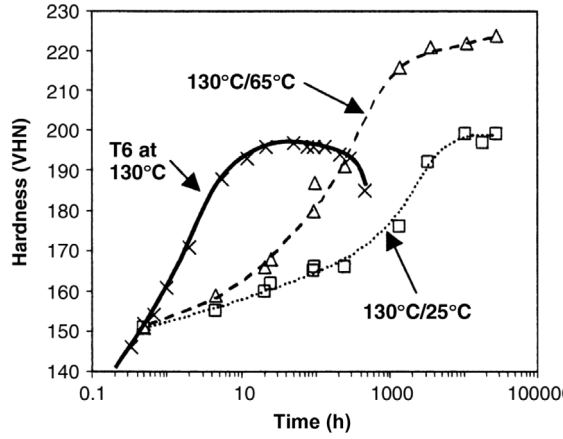


Figure 2.38 Hardness–time curves for the Al–Zn–Mg–Cu alloy 7075 aged at 130°C (solid line), and underaged 0.5 h at 130°C, quenched to 25°C, and held either at this temperature or at 65°C. From Lumley, RN *et al.*: *Mater. Sci. Tech.*, 22, 1025, 2005.

Detailed studies of secondary precipitation in a wide range of aluminium alloys have revealed that the levels of residual or "free" solute atoms that remain in solid solution until the alloys are in the overaged condition is higher than has generally been accepted. However, as expected from Fig. 2.37, the response to secondary precipitation at the lower ageing temperature is greater if an alloy is first artificially aged for a short time (i.e., underaged). The behavior is illustrated in Fig. 2.38 for the Al–Zn–Mg–Cu alloy 7075 which normally

reaches a peak hardness of 195 DPN if aged at 130°C for 24 h (T6 temper). If this alloy is first underaged for 0.5 h at 130°C and quenched to 25°C, the hardness is 150 DPN. During prolonged secondary ageing at this lower temperature, the hardness gradually increases and it becomes equal to the T6 value. Alternately, if 7075 is held at the slightly higher temperature of 65°C after quenching from 130°C, the hardness increases faster and reaches the higher value of 225 DPN after 10,000 h.

During secondary ageing at the lower temperature, GP zone formation usually occurs. If, after a dwell period, ageing at the initial elevated temperature is resumed, then the microstructure at peak hardness is refined so that a greater overall response to hardening can be achieved than is possible using a single-stage artificial ageing treatment. This effect is shown for the alloy Al–4%Cu in Fig. 2.39 in which the multistage ageing schedule is given the designation

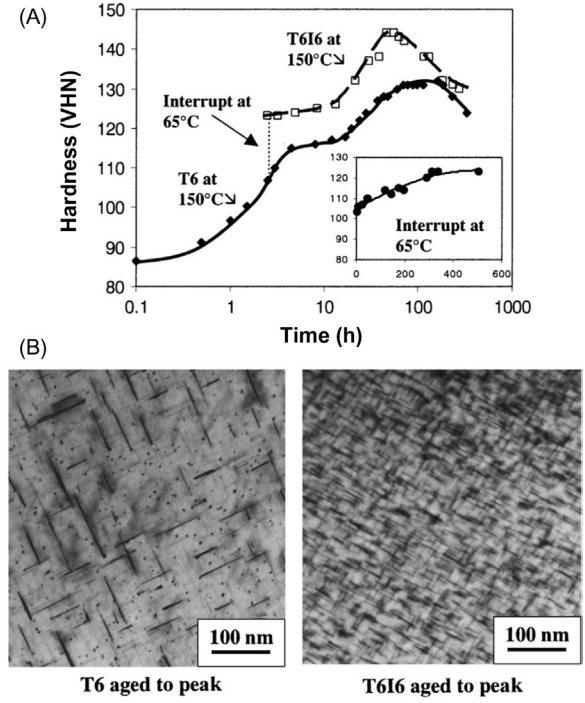


Figure 2.39 (A) Differences in the hardness curves for Al–4%Cu artificially aged at 150°C, with and without an interrupted period of secondary ageing at 65°C. The inset plot shows the hardness change during this dwell period at 65°C. (B) Transmission electron micrographs in the $[001]_{\alpha}$ direction showing dispersions of the θ' precipitate plates and minor amounts of the θ'' phase in these two aged conditions. T6 temper, 100 h at 150°C; T6I6 temper, 3 h at 150°C, quench, 500 h at 65°C, and 50 h at 150°C. From Lumley, RN *et al.*: *Mater. Sci. Tech.*, 19, 1453, 2003.

"T6I6," where "I" means that artificial ageing at an elevated temperature has been interrupted. As given in Table 4.7, experimental interrupted ageing cycles have been developed that enable simultaneous increases to be achieved in tensile and fracture toughness properties of a wide range of aluminium alloys.

2.4 CORROSION

2.4.1 Surface oxide film

Aluminium is an active metal which will oxidize readily under the influence of the high free energy of the reaction whenever the necessary conditions for oxidation prevail. Nevertheless, aluminium and its alloys are relatively stable in most environments due to the rapid formation of a natural oxide film of alumina on the surface that inhibits the bulk reaction predicted from thermodynamic data. Moreover, if the surface of aluminium is scratched sufficiently to remove the oxide film, a new film quickly reforms in most environments. As a general rule, the protective film is stable in aqueous solutions of the pH range 4.5–8.5, whereas it is soluble in strong acids or alkalis, leading to rapid attack of the aluminium. Exceptions are concentrated nitric acid, glacial acetic acid, and ammonium hydroxide.

The oxide film formed on freshly rolled aluminium exposed to air is very thin and has been measured as 2.5 nm. It may continue to grow at a decreasing rate for several years to reach a thickness of some tens of nanometers. The rate of film growth becomes more rapid at higher temperatures and higher relative humidities, so in water it is many times that occurring in dry air. In aqueous solutions, it has been suggested that the initial corrosion product is aluminium hydroxide, which changes with time to become a hydrated aluminium oxide. The main difference between this film and that formed in air is that it is less adherent and so is far less protective.

Much thicker surface oxide films that give enhanced corrosion resistance to aluminium and its alloys can be produced by various chemical and electrochemical treatments. The natural film can be thickened some 500 times, to say 1–2 μm, by immersion of components in certain hot acid or alkaline solutions. Although the films produced are mainly Al_2O_3, they also contain chemicals such as chromates that are collected from the bath to render them more corrosion resistant. A number of proprietary solutions are available and the films they produce are known generally as conversion coatings. Even thicker, e.g., 10–20 μm, surface films are produced by the more commonly used treatment known as anodizing. In this case the component is made the anode in an electrolyte, such as an aqueous solution containing 15% sulfuric acid, which produces a porous Al_2O_3 film that is subsequently sealed, i.e., rendered nonporous, by boiling in water. Both conversion and anodic coatings can be dyed to give attractive colors and the latter process is widely applied to architectural products.

It should be noted that chromate conversion coatings are widely used in corrosion protection schemes for aluminium alloys in aircraft structures and other applications. However, it has been recognized recently that chromates may present a health hazard which has led to an interest in other, nontoxic, coating processes. Promising results have been reported for cerium-rich coatings which can be applied by several methods. A durable cerium oxide/hydroxide film replaces natural Al_2O_3 and protection is afforded by partial or complete suppression of the reduction of oxygen at cathodic sites which normally occurs during electrolytic corrosion.

Chemicals known as inhibitors may be added to potentially corrosive liquid environments for the purpose of minimizing or preventing corrosion of aluminium and its alloys. Inhibitors may be classified as being anodic, cathodic, or mixed depending on whether they mainly affect the anodic, cathodic, or both anodic and cathodic corrosion processes. Anodic inhibitors stifle the anodic reaction, usually by depositing on the surface sparingly soluble substances as a direct anodic product. There is often no change in the surface appearance. Chromates are commonly used for this purpose and are generally effective. However, they can cause problems if present in insufficient amounts because they may decrease the surface area under attack without decreasing appreciably the amount of metal dissolution. Such a situation may lead to intensified local attack, e.g., by pitting. Cathodic inhibitors are safer in this respect. They serve to stifle the cathodic reaction either by restricting access to oxygen or by "poisoning" local spots favorable for cathodic hydrogen evolution. They form a visible film on the aluminium and are usually less efficient than anodic inhibitors as they do not completely prevent attack. Examples are phosphates, silicates, and soluble oils. The choice and concentration of an inhibitor depends on several factors such as the compositions of the alloy and the liquid environment to which it is to be exposed, the temperature, and the rate of movement of the liquid. An inhibitor that offers protection in one environment may increase it in another.

2.4.2 Contact with dissimilar metals

The electrode potential of aluminium with respect to other metals becomes particularly important when considering galvanic effects arising from dissimilar metal contact. Comparisons must be made by taking measurements in the same solution and Table 2.4 provides the electrode potentials with respect to the 0.1 M calomel electrode ($Hg–HgCl_2$, 0.1 M KCl) for various metals and alloys immersed in an aqueous solution of 1 M NaCl and 0.1 M H_2O_2. The value for aluminium is −0.85 V whereas aluminium alloys range from −0.69 to −0.99 V. Magnesium which has an electrode potential of −1.73 V is more active than aluminium whereas mild steel is cathodic having a value of −0.58 V.

Table 2.4 Electrode potentials of various metals and alloys with respect to the 0.1 M calomel electrode in aqueous solutions of 53 g l^{-1} NaCl and 3 g l^{-1} H_2O_2 at 25°C

Metal or alloy		Potential (V)
Magnesium		−1.73
Zinc	aluminium alloys[a]	−1.10
Alclad 6061, Alclad 7075		−0.99
5456, 5083		−0.87
Aluminium (99.95%), 5052, 5086		−0.85
3004, 1060, 5050		−0.84
1100, 3003, 6063, 6061, Alclad 2024		−0.83
2014–T4		−0.69
Cadmium		−0.82
Mild steel		−0.58
Lead		−0.55
Tin		−0.49
Copper		−0.20
Stainless steel (3xx series)		−0.09
Nickel		−0.07
Chromium		−0.49 to +0.18

From *Metals Handbook*, Vol. 1, ASM, Cleveland, OH, USA, 1961.
[a]Compositions corresponding to the numbers are given in Tables 4.2 and 4.4.

Table 2.4 suggests that sacrificial attack of aluminium and its alloys will occur when they are in contact with most other metals in a corrosive environment. However, it should be noted that electrode potentials serve only as a guide to the possibility of galvanic corrosion. The actual magnitude of the galvanic corrosion current is determined not only by the difference in electrode potentials between the particular dissimilar metals but also by the total electrical resistance, or polarization, of the galvanic circuit. Polarization itself is influenced by the nature of the metal/liquid interface and more particularly by the oxides formed on metal surfaces. For example, contact between aluminium and stainless steels usually results in less electrolytic attack than might be expected from the relatively large difference in the electrode potentials, whereas contact with copper causes severe galvanic corrosion of aluminium even though this difference is less.

Galvanic corrosion of aluminium and its alloys may be minimized in several ways. If contact with other metals cannot be avoided, these should be chosen so that they have electrode potentials close to aluminium; alternatively it may be

possible to locate a dissimilar metal joint away from the corrosive environment. If not then complete electrical isolation of aluminium and the other metal must be arranged by using nonconducting washers, sleeves, or gaskets. When paint is used for protection, it should be applied to the cathodic metal and not the aluminium. This practice is required because pinholes that may form in a paint film on aluminium can lead to pitting attack because of the large cathode to anode area ratio. In a closed loop system, such as used for cooling automobile engines, a mixed anodic and cathodic inhibitors should be added to the cooling water.

2.4.3 Influence of alloying elements and impurities

Alloying elements may be present as solid solutions with aluminium, or as microconstituents comprising the element itself, e.g., silicon, a compound between one or more elements and aluminium (e.g., Al_2CuMg) or as a compound between one or more elements (e.g., Mg_2Si). Any or all of the above conditions may exist in a commercial alloy. Table 2.5 provides values of the electrode potentials of some aluminium solid solutions and micro-constituents.

In general, a solid solution is the most corrosion-resistant form in which an alloy may exist. Magnesium dissolved in aluminium renders it more anodic although dilute Al–Mg alloys retain a relatively high resistance to corrosion, particularly to seawater and alkaline solutions. Chromium, silicon, and zinc

Table 2.5 Electrode potentials of aluminium solid solutions and microconstituents with respect to the 0.1 M calomel electrode in aqueous solutions of 53 g l^{-1} NaCl and 3 g l^{-1} H_2O_2 at 25°C.

Solid solution or microconstituent	Potential (V)
Mg_5Al_8	−1.24
Al−Zn−Mg solid solution (4% $MgZn_2$)	−1.07
$MgZn_2$	−1.05
Al_2CuMg	−1.00
Al−5% Mg solid solution	−0.88
$MnAl_6$	−0.85
Aluminium (99.95%)	−0.85
Al−Mg−Si solid solution (1% Mg_2Si)	−0.83
Al−1% Si solid solution	−0.81
Al−2% Cu SSSS	−0.75
Al−4% Cu SSSS	−0.69
$FeAl_3$	−0.56
$CuAl_2$	−0.53
$NiAl_3$	−0.52
Si	−0.26

From *Metals Handbook*, Vol. 1, ASM, Cleveland, OH, USA, 1961.

in solid solution in aluminium have only minor effects on corrosion resistance although zinc does cause a significant increase in the electrode potential. As a result, Al–Zn alloys are used as clad coatings for certain aluminium alloys (see Section 4.1.5) and as galvanic anodes for the cathodic protection of steel structures in seawater. Copper reduces the corrosion resistance of aluminium more than any other alloying element and this arises mainly because of its presence in micro-constituents. However, it should be noted that when added in small amounts (0.05–0.2%), corrosion of aluminium and its alloys tends to become more general and pitting attack is reduced. Thus, although under corrosive conditions, the overall weight loss is greater, perforation by pitting is retarded.

Microconstituents are usually the source of most problems with electrochemical corrosion as they lead to nonuniform attack at specific areas of the alloy surface. Pitting and intergranular corrosion are examples of localized attack (Fig. 2.40), and an extreme example of this is that components with a marked directionality of grain structure show exfoliation (layer) corrosion (Fig. 2.41). In exfoliation corrosion, delamination of surface grains or layers occurs under forces exerted by the voluminous corrosion products.



Figure 2.40 Microsection of surface pits in a high-strength aluminium alloy. Note that intergranular SCC are propagating from the base of these pits (× 100).

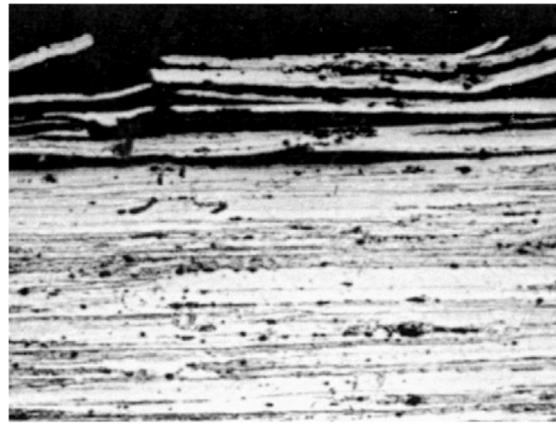


Figure 2.41 Microsection showing exfoliation (layer) corrosion of an aluminium alloy plate (× 100).

Iron and silicon occur as impurities and form compounds most of which are cathodic with respect to aluminium. For example, the compound Al_3Fe provides points at which the surface oxide film is weak, thereby promoting electrochemical attack. The rate of general corrosion of high-purity aluminium is much less than that of the commercial-purity grades which is attributed to the smaller size and number of these cathodic constituents throughout the grains. However, it should be noted that this may be a disadvantage in some environments as attack of high-purity aluminium may be concentrated in grain boundaries. Nickel and titanium also form cathodic phases although nickel is present in very few alloys. Titanium, which forms Al_3Ti, is commonly added to refine grain size (Sections 4.1.3 and 3.3) but the amount is too small to have a significant effect on corrosion resistance. Manganese and aluminium form Al_6Mn, which has almost the same electrode potential as aluminium, and this compound is capable of dissolving iron which reduces the detrimental effect of this element. Magnesium in excess of that in solid solution in binary aluminium alloys tends to form the strongly anodic phase Mg_5Al_8 which precipitates in grain boundaries and promotes intercrystalline attack. However, magnesium and silicon, when together in the atomic ratio 2:1, form the phase Mg_2Si which has a similar electrode potential to aluminium.

Where a basic alloy is vulnerable to corrosive attack, it is possible to provide surface protection for wrought products such as sheet, plate, and, to a lesser extent, tube and wire by means of metallurgically bonded thin layers of pure aluminium or an aluminium alloy. Such alloys are commonly those based on the Al–Cu–Mg and Al–Zn–Mg–Cu systems and products are said to be alclad (Fig. 4.8). In a corrosive environment, the cladding will anodic with respect to the core and provide sustained electrochemical protection at abraded areas and exposed edges.

2.4.4 Crevice corrosion

If an electrolyte penetrates a crevice formed between two aluminium surfaces in contact, or between an aluminium surface and a nonmetallic material such as a gasket or washer, localized corrosion may occur by etching or pitting. The oxygen content of the liquid in the crevice is consumed by the reaction at the aluminium surfaces and corrosion will be inhibited if replenishment of oxygen by diffusion into the crevice is slow. However, if oxygen remains plentiful at the mouth of the crevice, a localized electrolytic cell will be created in which the oxygen-depleted region becomes the anode. Furthermore, once crevice attack has been initiated, this anodic area becomes acidic and the larger external cathodic area becomes alkaline. These changes further enhance local cell action and more corrosion occurs in the crevice, particularly in a submerged situation.

A common example of crevice corrosion occurs when water is present in the restricted space between layers of aluminium sheets or foil in close contact in stacks or coils. This may take place by condensation during storage if the metal temperature falls below the dew point, or by the ingress of rain when being transported. Irregular stain patches may form which impair the surface appearance. In severe cases, the corrosion product may cement two surfaces together and make separation difficult.

A special form of crevice corrosion may occur on an aluminium surface that is covered by an organic coating. It takes the form of tracks of thread-like filaments and has the name filiform corrosion. The tracks proceed from one or more places where the coating is breached for some reason and the corrosion products raise bulges in the surface. The amount of aluminium consumed is small and filiform corrosion only assumes practical importance if the metal is of thin cross section. Filiform corrosion occurs only in the atmosphere and relative humidity is the key factor. It has been observed on lacquered aluminium surfaces in aircraft exposed to marine or high-humidity environments and may be controlled by anodizing, chemical conversion coatings or by using chromate-containing primers prior to painting.

2.4.5 Cavitation corrosion

Protective films on the surfaces of aluminium and its alloys may be removed by mechanical actions of many sorts such as turbulent effects arising from moving fluid. Electrolytic reactions may then occur which can proceed without inhibition. If voids (gas bubbles) form in the turbulent liquid because the pressure falls below the vapor pressure, then cavitation corrosion may take place. Collapse of these voids at the metal surface allows the sudden release the latent heat of vaporization, which may dislodge a protective film during service and even alter the state of work hardening of the metal at the surface. Cavitation corrosion therefore combines electrochemical action with mechanical damage, the relative proportion of each being controlled by the severity of the turbulence and the aggressiveness of the environment.

Weight loss in standard tests on aluminium alloys has been found to decrease as strength (and hardness) increases. However, compared with other nonferrous metals and alloys, aluminium and its alloys do not perform well under cavitation conditions. For example, common wrought aluminium alloys, that are considered to be relatively resistant to corrosion, have been found to suffer weight losses 100–200 times greater than the copper alloy, aluminium bronze, under cavitation conditions in fresh water.

2.4.6 Waterline corrosion

This form of corrosion can affect semisubmerged structures, such as ships, whereby the zone very close to the air/water boundary can suffer differential corrosion that is sometimes severe. With aluminium alloys, waterline corrosion may arise because of a difference in the chloride level between the seawater at the air/water parting line and that contained in the meniscus formed by capillary action in which the chlorides become concentrated by evaporation. This effect is weak in water that is in motion because the meniscus is constantly being renewed. Although aluminium alloys used for the hulls of ships and other semisubmerged structures are not very sensitive to waterline corrosion, this region should be painted to avoid the risk of attack. If the water is stagnant, painting is essential.

2.4.7 Metallurgical and thermal treatments

Treatments that are carried out to change the shape and achieve a desired level of mechanical properties in aluminium alloys may also modify corrosion resistance, largely through their effects on both the quantity and the distribution of microconstituents. In this regard, the complex changes associated with ageing or tempering treatments are on a fine scale and these are considered in Chapter 4. Both mechanical and thermal treatments can introduce residual stresses into components which may contribute to the phenomenon of stress-corrosion cracking and this is discussed in Section 2.5.4.

If one portion of an alloy surface receives a thermal treatment different from the remainder of the alloy, differences in potential between these regions can result. Welding processes provide an extreme example of such an effect and differences of up to 0.1 V may exist between the weld bead, heat-affected zones, and the remainder of the parent alloy.

Most wrought products do not undergo bulk recrystallization during subsequent heat treatment so that the elongated grain structure resulting from mechanical working is retained. Three principal directions are recognized: longitudinal, transverse (or long transverse), and short transverse, and these are represented in Fig. 2.42. This directionality of grain structure is significant in components when corrosion processes involve intercrystalline attack

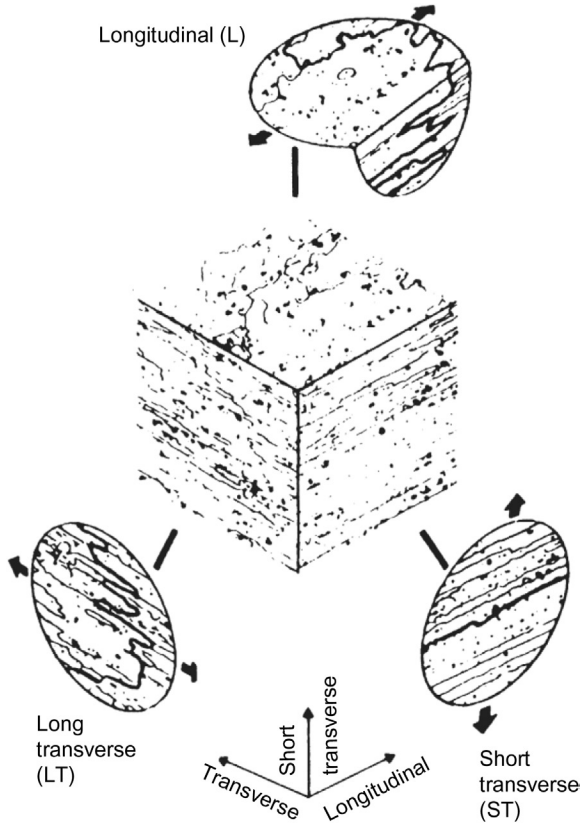


Figure 2.42 The three principal directions with respect to the grain structure in a wrought aluminium alloy. Note the appearance of cracks that may form when stressing in these three directions. From Speidel, MO and Hyatt, MV: *Advances in Corrosion Science and Technology*, Plenum Press, New York, NY, USA, 1972.

as has been illustrated by exfoliation corrosion. It is particularly important in regard to SCC, which is discussed in Section 2.5.4.

In certain products such as extrusions and die forgings, working is non-uniform and a mixture of unrecrystallized and recrystallized grain structures may form between which potential differences may exist. Large, recrystallized grains normally occur at the surface (see Fig. 4.7) and these are usually slightly cathodic with respect to the underlying, unrecrystallized grains. Preferential attack may occur if the relatively more anodic internal grains are partly exposed as may occur by machining.

2.5 MECHANICAL BEHAVIOUR

The principal microstructural features that control the mechanical properties of aluminium alloys are as follows:

1. Coarse intermetallic compounds (often called constituent particles) that form interdendritically by eutectic decomposition during ingot solidification. One group comprises virtually insoluble compounds that usually contain the impurity elements iron or silicon and examples are Al_6(Fe,Mn), Al_3Fe, α-Al(Fe,Mn,Si), and Al_7Cu_2Fe. The second group, which are known as the soluble constituents, consists of equilibrium intermetallic compounds of the major alloying elements. Typical examples are Al_2Cu, Al_2CuMg, and Mg_2Si. Both types of particles form as lacy networks surrounding the cast grains and one purpose of the process referred to as preheating or ingot homogenization (Section 4.1.5) is to dissolve the soluble constituents. During subsequent fabrication of the cast ingots, the largest of the remaining particles usually fracture, which reduces their sizes to the range 0.5–10 μm and causes them to become aligned as stringers in the direction of working or metal flow (Fig. 2.43).
   Constituent particles serve no useful function in high-strength wrought alloys and they are tolerated in most commercial compositions because their removal would necessitate a significant cost increase. They do, however, serve a useful purpose in certain alloys such as those used for canstock (Section 4.6.5).
2. Smaller submicron particles, or dispersoids (typically 0.05–0.5 μm) that form during homogenization of the ingots by solid-state precipitation of compounds containing elements which have modest solubility and which diffuse slowly in solid aluminium. Once formed, these particles resist either dissolution or coarsening. The compounds usually contain one of the transition metals and examples are $Al_{20}Mn_3Cu_2$, $Al_{12}Mg_2Cr$, and Al_3Zr. They serve to retard recrystallization and grain growth during processing and heat treatment of the alloys concerned. Moreover, they may also exert an important influence on certain mechanical properties through their effects both on the response of some alloys to ageing treatments and on dislocation substructures formed as a result of plastic deformation.
3. Fine precipitates (up to 0.1 μm) which form during age hardening and normally have by far the largest effect on strengthening of alloys that respond to such treatments.
4. Grain size and shape. The most significant microstructural feature that differentiates wrought products such as sheet from plate, forgings, and extrusions is the degree of recrystallization. Aluminium dynamically recovers during hot deformation producing a network of subgrains and this characteristic is attributed to its relatively high stacking-fault energy. However, thick sections, which experience less deformation, usually do not undergo bulk recrystallization during processing so that an elongated grain structure is retained (Fig. 2.42).

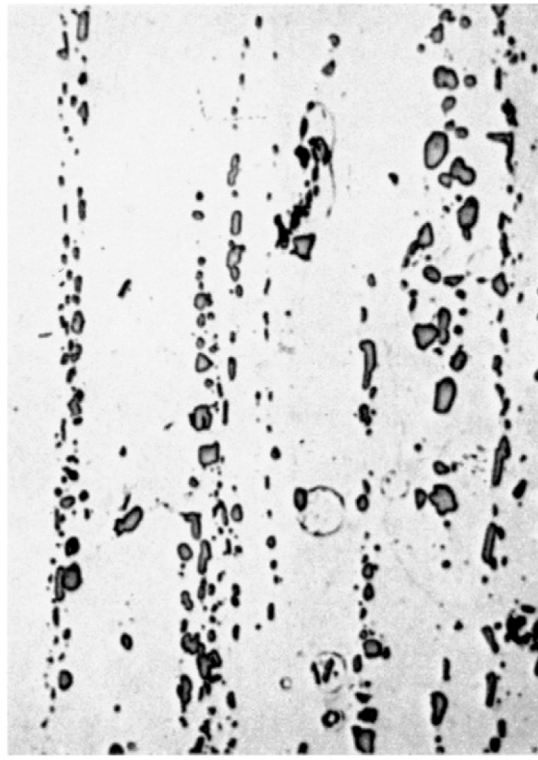


Figure 2.43 Aligned stringers of coarse intermetallic compounds in a rolled aluminium alloy (× 250).

5. Dislocation substructure, notably that caused by cold working of those alloys which do not respond to age hardening, and that developed due to service stresses.
6. Crystallographic textures that form as a result of working and annealing, particularly in rolled products. They have a marked effect on formability (Section 2.1.4) and lead to anisotropic mechanical properties.

Each of these features may be influenced by the various stages involved in the solidification and processing of wrought and cast alloys and these are discussed in detail in Chapters 4 and 5. Here it is relevant to consider how these features influence mechanical behavior.

2.5.1 Tensile properties

Aluminium alloys may be divided into two groups depending upon whether or not they respond to precipitation hardening. The tensile properties of commercial wrought and cast compositions are considered in Chapters 4 and 5. Here it is the finely dispersed precipitates that have the dominant effect in inhibiting

dislocation motion, thereby raising yield and tensile strengths. For the other group, the dislocation substructure produced by cold working in the case of wrought alloys and the grain size of cast alloys are of prime importance.

Coarse intermetallic compounds have relatively little effect on yield or tensile strength but they can cause a marked loss of ductility in both the cast and wrought products. The particles may crack at small plastic strains forming internal voids which, under the action of further plastic strain, may coalesce leading to premature fracture.

As mentioned earlier, the fabrication of wrought products may cause highly directional grain structures. Moreover, the coarse intermetallic compounds and smaller dispersoids also become aligned to form stringers in the direction of metal flow (Fig. 2.43). These microstructural features are known as mechanical fibring and, together with crystallographic texturing (Section 2.1.4), they cause anisotropy in tensile and other properties. Accordingly, measurements are often made in the three principal directions as shown in Fig. 2.42. Tensile properties, notably ductility, are greatest in the longitudinal direction and least in the short transverse direction in which stressing is normal to the stringers of intermetallics, e.g., Table 2.6.

2.5.2 Toughness

Early work on the higher-strength aluminium alloys was directed primarily at maximizing tensile properties in materials for aircraft construction. More recently, the emphasis in alloy development has shifted away from tensile strength as an overriding consideration and more attention is being given to the behavior of alloys under the variety of conditions encountered in service. Tensile strength controls resistance to failure by mechanical overload but, in the

Table 2.6 Variation in tensile properties with direction in 76 mm thick aluminium alloy plates

Alloy direction	0.2% proof stress (MPa)	Tensile strength (MPa)	Elongation (%)
Al–Zn–Mg–Cu (7075)			
Longitudinal (L)	523	570	15.5
Long transverse (LT)	482	552	12.0
Short transverse (ST)	445	527	7.5
ST/L ratio	0.85	0.93	0.48
Al–Cu–Mg (2014)			
Longitudinal (L)	441	477	14.0
Long transverse (LT)	423	471	10.5
Long transverse (ST)	404	449	4.0
ST/L ratio	0.91	0.94	0.29

From Forsyth, PJE and Stubbington, A: *Metals Technology*, 2, 158, 1975.

presence of cracks and other flaws, it is the toughness (and more particularly the fracture toughness) of the alloy that becomes the most important parameter.

In common with other metallic materials, the toughness of aluminium alloys decreases as the general level of strength is raised by alloying and heat treatment. Minimum fracture toughness requirements become more stringent and, in the high-strength alloys, it is necessary to place a ceiling on the level of yield strength that can be safely employed by the designer.

Crack extension in commercial aluminium alloys proceeds by the ductile, fibrous mode involving the growth, and coalescence of voids nucleated by cracking or by decohesion at the interface between second phase particles and the matrix (Fig. 2.44). Consequently, the important metallurgical factors are:

1. The distribution of the particles that crack.
2. The resistance of the particles and their interfaces with the matrix to cleavage and decohesion.
3. The local strain concentrations which accelerate coalescence of the voids.
4. The grain size when coalescence involves grain boundaries.

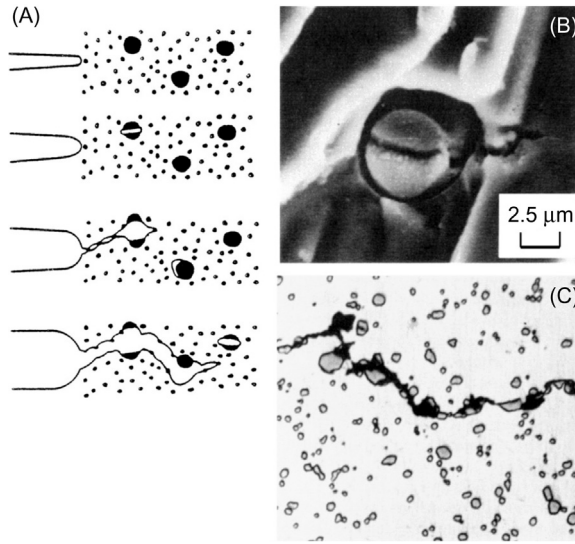


Figure 2.44 Crack extension by coalescence of microvoids nucleated at particles and dispersoids: (A) schematic showing nucleation of voids due to particle cleavage followed by progressive linkage of advancing crack to these voids. (B) Cleavage of an Al_7Cu_2Fe intermetallic particle with associated void nucleation and crack extension into the adjacent ductile matrix in a high-strength aluminium alloy. Scanning electron micrograph × 2800. (C) Crack path in an aluminium casting alloy which has been influenced by the presence of coarse, brittle silicon particles. Optical micrograph × 700. (A) Courtesy R. J. H. Wanhill, (B) courtesy R. Gürbüz, and (C) courtesy R. W. Coade.

The major step in the development of aluminium alloys with greatly improved fracture toughness has come from the control of the levels of the impurity elements iron and silicon. This effect is shown in Fig. 2.45 for alloys based on the Al–Cu–Mg system and it can be seen that plane strain fracture toughness values may be doubled by maintaining the combined levels of these elements below 0.5% as compared with similar alloys in which this value exceeds 1.0%. As a consequence of this, a range of high-toughness versions of older alloy compositions is now in commercial use in which the levels of impurities have been reduced (see Table 4.4).

The role of the submicron dispersoids with respect to toughness is more complex as they have both good and bad effects. To the extent that they suppress recrystallization and limit grain growth they are beneficial. The effect of these factors on a range of high-strength sheet alloys based on the Al–Zn–Mg–Cu system is shown in Fig. 2.46. Fine, unrecrystallized grains favor a high-energy absorbing, transcrystalline mode of fracture. On the other hand, such particles also nucleate microvoids by decohesion at the interface with the matrix which may lead to the formation of sheets of voids between the larger voids that are associated with the coarse intermetallic compounds. In this regard, the effects do vary with different transition metals and there is evidence to suggest that alloys containing zirconium to control grain shape are

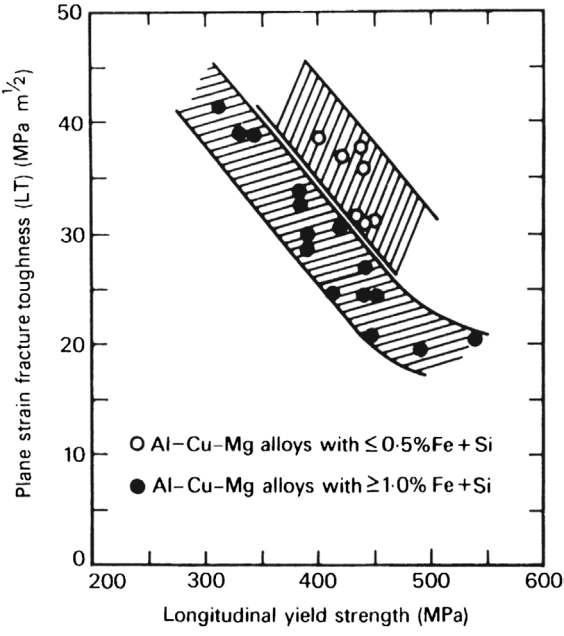


Figure 2.45 Plane strain fracture toughness of commercial Al–Cu–Mg sheet alloys with differing levels of iron and silicon. From Speidel, MO: *Proc. of 6th Inter. Conf. on Light Metals*, Leoben, Austria, Aluminium-Verlag, Düsseldorf, 1975.

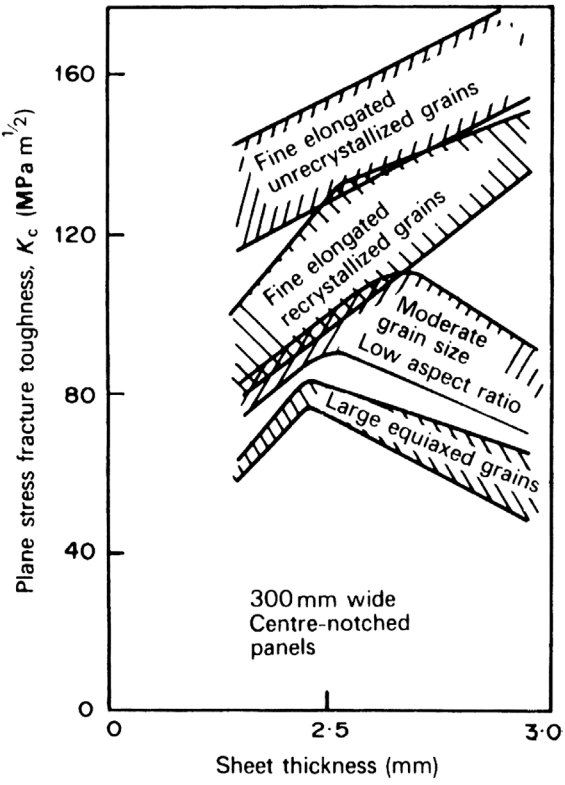


Figure 2.46 Effect of recrystallization and grain size and shape of various alloys based on the Al–Zn–Mg–Cu system. From Thompson, DS: *Metall. Trans*., 6A, 671, 1975.

more resistant to fracture than those to which chromium or manganese has been added to this purpose. This is attributed to the fact that zirconium forms relatively small particles of the compound Al_3Zr, which are around 20 nm in diameter.

The fine precipitates developed by age hardening are also thought to have at least two effects with regard to the toughness of aluminium alloys. To the extent that they reduce deformation, toughness is enhanced and it has been observed that, for equal dispersions of particles, an alloy with a higher yield stress has greater toughness. At the same time, these fine particles tend to cause localization of slip during plastic deformation, particularly under plane strain conditions, leading to development of pockets of slip or so-called super-bands ahead of an advancing crack. Strain is concentrated within these bands and may cause premature cracking at the sites of intermetallic compounds ahead of an advancing crack. This effect is usually greatest for alloys aged to peak hardness and the overall result is a net loss of toughness at the highest strength levels.

The fact that toughness does not follow a simple inverse relationship to the strength of age-hardened aluminium alloys is shown by comparing alloys in the under- and overaged conditions. Toughness is greatest in the underaged condition and decreases as ageing proceeds to peak strength. In some alloys, this condition corresponds to a minimum value of toughness and some improvement may occur on over-ageing which is associated with a reduction in yield strength (e.g., Al–Zn–Mg–Cu alloys: Section 4.4.5). However, where overageing leads to the formation of large precipitate particles in grain boundaries, or wide PFZs then toughness can continue to decrease because each of these features promotes more intergranular fracture. Lithium-containing alloys tend to behave in this way (Section 4.4.6).

2.5.3 Fatigue

It is well known that, contrary to steels, the increases that have been achieved in the tensile strength of most nonferrous alloys have not been accompanied by proportionate improvements in fatigue properties. This feature is illustrated in Fig. 2.47 which shows relationships between fatigue endurance limit (5×10^8 cycles) and tensile strength for different alloys. It should also be noted that the so-called fatigue ratios are lowest for age-hardened aluminium alloys and, as a general rule, the more an alloy is dependent upon precipitation hardening for its tensile strength, the lower its ratio becomes.

Detailed studies of the processes of fatigue in metals and alloys have shown that the initiation of cracks normally occurs at the surface. It is here that strain becomes localized due to the presence of preexisting stress concentrations such as mechanical notches or corrosion pits, coarse (persistent) slip bands in which

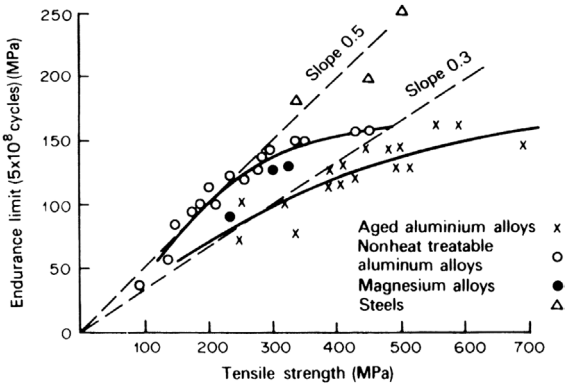


Figure 2.47 Fatigue ratios (endurance limit:tensile strength) for aluminium alloys and other materials. From Varley, PC: *The Technology of Aluminium and its Alloys*, Newnes-Butterworths, London, 1970.

minute extrusions and intrusions may form, or at relatively soft zones such as the precipitate-free regions adjacent to grain boundaries.

The disappointing fatigue properties of age-hardened aluminium alloys are also attributed to an additional factor which is the metastable nature of the metallurgical structure under conditions of cyclic stressing. Localization of strain is particularly harmful because the precipitate may be removed from certain slip bands which causes softening there and leads to a further concentration of stress so that the whole process of cracking is accelerated. This effect is shown in an exaggerated manner in a recrystallized, high-purity alloy in Fig. 2.48. It has been proposed that removal of the precipitate occurs either by over-ageing or re-solution, the latter now being considered to apply in most cases. One suggestion is that the particles in the slip bands are cut by moving dislocations, and re-solution occurs when they become smaller than the critical size for thermodynamic stability.

The fatigue behavior of age-hardened aluminium alloys should therefore be improved if fatigue deformation could be dispersed more uniformly. Factors which prevent the formation of coarse slip bands should assist in this regard. Thus it is to be expected that commercial-purity alloys should perform better than equivalent high-purity compositions because the presence of inclusions and intermetallic compounds would tend to disperse slip. This effect is demonstrated for the Al–Zn–Mg–Cu alloy 7075 in Fig. 2.49A which shows fatigue (*S*/*N*) curves for commercial-purity and high-purity compositions. Tests were carried out on smooth specimens prepared from the alloys which had been aged under similar conditions to produce fine, shearable precipitates. It will be noted that the fatigue performance of the commercial-purity alloys is superior because crack initiation is delayed due to the fact that slip is more uniformly

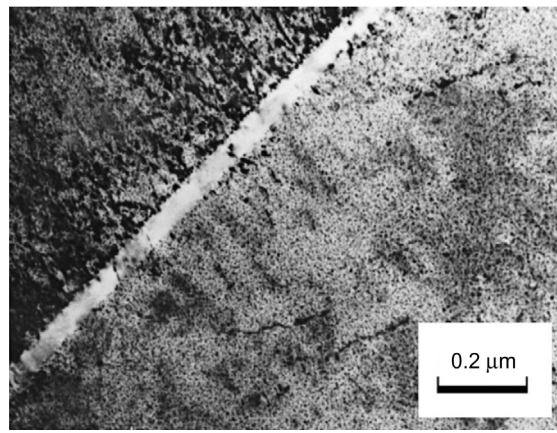


Figure 2.48 Transmission electron micrograph showing precipitate depletion in a persistent slip band formed by fatigue stressing a high-purity Al–Zn–Mg alloy. Courtesy A. Stubbington, copyright HMSO.

dispersed by dispersoid particles such as $Al_{12}Mg_2Cr$. These particles are absent in the high-purity alloy. However, the fatigue performance characteristics are reversed if tests are carried out on precracked specimens (Fig. 2.49B). In this condition, the rate of fatigue crack growth is faster in the commercial-purity alloy because voids nucleate more readily at dispersed particles which are within the plastic zone of the advancing crack (Fig. 2.44).

Thermomechanical processing whereby plastic deformation before, or during, the ageing treatment increases the dislocation density, has also been found to improve the fatigue performance of certain alloys although this effect arises in part from an increase in tensile properties caused by such a treatment (Fig. 2.50). It should be noted, however, that the promising results mentioned earlier were obtained for smooth specimens. The improved fatigue behavior has not been sustained for severely notched conditions and it seems that the resultant stress concentrations override the more subtle microstructural effects that have been described.

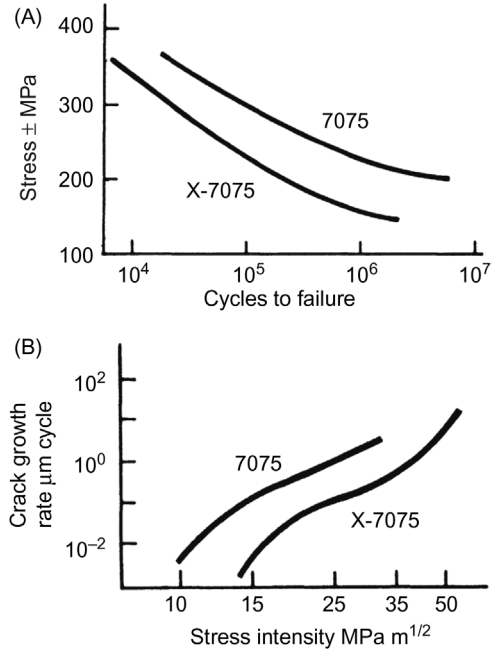


Figure 2.49 (A) Fatigue (*S/N*) curves for Al–Zn–Mg–Cu alloys 7075 and X7075. X7075 is a high-purity version of the commercial alloy 7075. (B) Fatigue crack growth rate curves for alloys 7075 and X7075. (A) From Lütjering, G: *Micromechanisms in Particle-Hardened Alloys*, Martin, JW, Cambridge University Press, 142, 1980). (B) From Albrecht, J *et al.*: *Proc. 4th Inter. Conf. on Strength of Metals and Alloys, J. de Physique, Paris*, 463, 1976.

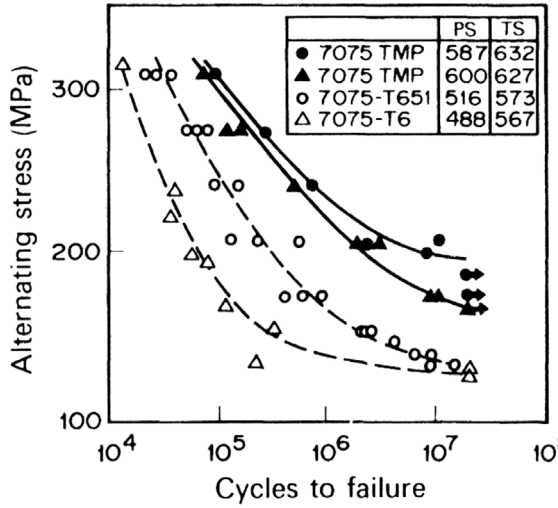


Figure 2.50 Effect of thermomechanical processing (TMP) on the unnotched fatigue properties of the commercial Al–Zn–Mg–Cu alloy 7075. PS, proof stress (MPa) and TS, tensile strength (MPa). From Ostermann, FG: *Metall. Trans*., 2A, 2897, 1971.

Alloys which are aged at higher temperatures, and thus form relatively more stable precipitates, might also be expected to show better fatigue properties and this trend is observed. For example, the fatigue performance of the alloys based on the Al–Cu–Mg system is generally better than that of Al–Zn–Mg–Cu alloys, although this effect is again greatly reduced for notched conditions.

The fact that the microstructure can have a greater influence upon the fatigue properties of aluminium alloys than the level of tensile properties has been demonstrated for an Al–Mg alloy containing a small addition of silver. It is well known that binary Al–Mg alloys such as Al–5Mg, in which the magnesium is present in solid solution, display a relatively high level of fatigue strength. The same applies for an Al–5Mg–0.5Ag alloy in the as-quenched condition and Fig. 2.51 shows that the endurance limit after 10^8 cycles is ± 87 MPa which approximately equals the 0.2% proof stress. This result is attributed to the interaction of magnesium atoms with dislocations which reduces their mobility and minimizes formation of coarse slip bands during fatigue. The silver-containing alloy responds to age hardening at elevated temperatures due to the formation of a finely dispersed precipitate, and the 0.2% proof stress may be raised to 200 MPa after ageing for 1 day at 175°C. However, the endurance limit for 10^8 cycles is actually decreased to ± 48 MPa due to the localization of strain in a limited number of coarse slip bands (Fig. 2.52A).

Continued ageing of the alloy at 175°C causes only slight softening (0.2% proof stress 175 MPa after 70 days) although large particles of a second precipitate are formed (Fig. 2.52B) which have the effect of dispersing dislocations

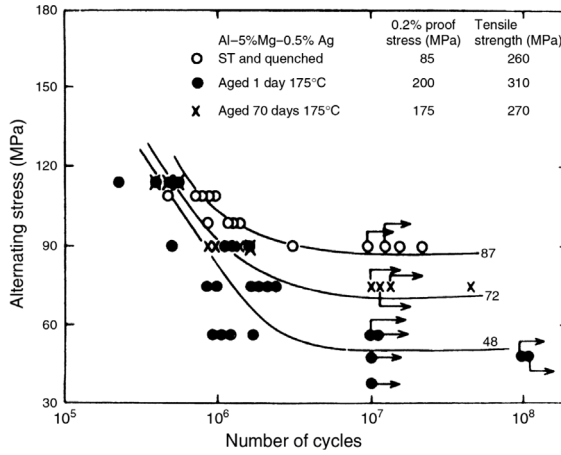


Figure 2.51 Fatigue (*S*/*N*) curves for the alloy Al–5Mg–0.5Ag in different conditions. From Boyapati, K and Polmear, IJ: *Fatigue Eng. Mater. Struct.*, 2, 23, 1979.

generated by cyclic stressing. As a result, fatigue properties are improved and the endurance limit for 10^8 cycles is raised to ±72 MPa (Fig. 2.51). These particles serve the same role as the submicron particles in the commercial alloy 7075 (Fig. 2.49) but they have formed by a precipitation process. This again demonstrates the desirability of having a duplex precipitate structure, fine particles to give a high level of tensile properties, and coarse particles to improve fatigue strength.

Studies of extrusions made from a more complex alloy Al–5.6Cu–0.45Mg–0.45Ag–0.3Mn–0.18Zr have also shown that the fatigue resistance following under-ageing for 2 h at 185°C is superior to that for the fully age-hardened condition (10 h at 185°C) despite the fact that the underaged alloy has lower tensile properties. This behavior is evident if a comparison is made of the respective cyclic stress/number of cycles to failure (*S*/*N*) curves obtained at room temperature that are shown in Fig. 2.53. These figures reveal that the scatter of individual test results for the fully hardened condition is greater which is undesirable. Furthermore, the curves of best fit have different slopes because the underaged alloy exhibits progressively longer lives as the cyclic stress levels are reduced. For example, these results show that, for a cyclic stress of 175 MPa, the underaged alloy has a lifetime to failure some 10 times that of the fully age-hardened alloy. Alternatively, for equal failure time after 10^7 cycles, the underaged alloy can sustain a stress that was 18% larger.

Two explanations have been proposed to account for this behavior, both of which depend on dynamic precipitation of residual solute in the matrix occurring during fatigue testing of the underaged alloy. One proposes that precipitation of the retained solute helps immobilize dislocations generated in the fatigue process that may otherwise assist the initiation of cracks. The other

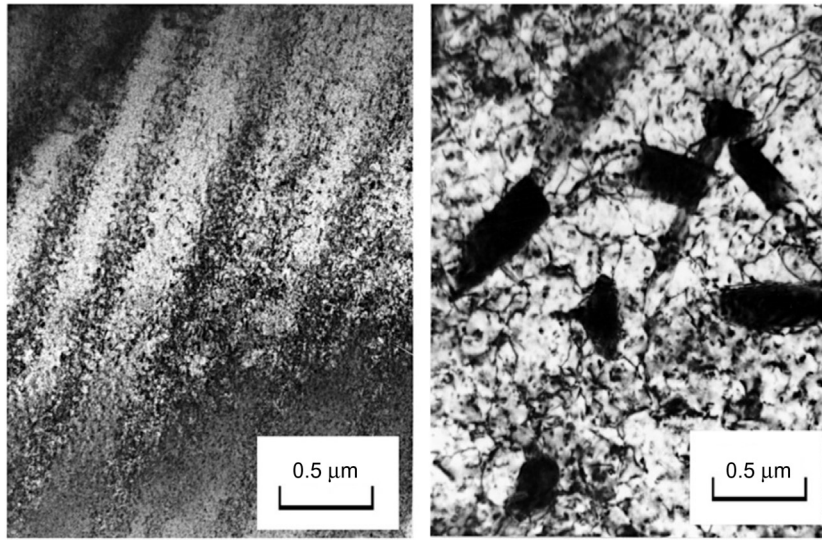


Figure 2.52 (A) Coarse slip bands containing a high density of dislocations. Alloy Al–5Mg–0.5Ag aged 1 day at 175°C and tested at a stress of ±75 MPa for 1.4×10^6 cycles; (B) large particles of a second precipitate, that have formed in the alloy aged 70 days at 175°C, which have dispersed dislocations generated by fatigue stressing for 10^7 cycles at a stress of ±75 MPa.

suggestion is that localized dynamic precipitation may actually facilitate closure of developing cracks.

2.5.4 Stress–corrosion cracking

SCC may be defined as a phenomenon which results in brittle failure in alloys, normally considered ductile, when they are exposed to the simultaneous action of surface tensile stress and a corrosive environment, neither of which when operating separately could cause major damage. It involves time-dependent interactions between the microstructure of a susceptible alloy, mechanical deformation, and local environmental conditions. A threshold stress is needed for crack initiation and growth, the level of which is normally well below that required to cause yielding. Specific corrosive environments can be quite mild, e.g., water vapor, although in the case of aluminium alloys it is common for halide ions to be present. The relative importance of each of the two factors, stress and corrosion (i.e., electrochemistry), varies with different alloy systems. For aluminium alloys, there is general agreement that electrochemical factors predominate and it has been on this basis that new compositions and tempers have been developed which provide improved resistance to SCC (e.g., Section 4.4.5).

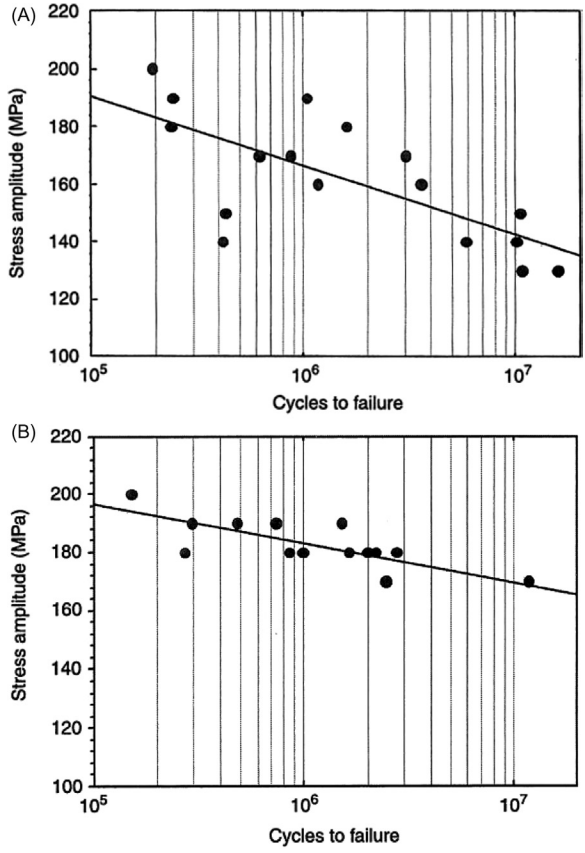


Figure 2.53 Stress–number of cycles (S–N) data for the Al–Cu–Mg–Ag–Mn–Zr alloy tested after (A) fully age hardening (10 h at 185°C) and (B) underageing (2 h at 185°C). From Lumley, RN *et al.*: *Mater. Sci. Forum*, 29, 256, 2005.

Only aluminium alloys that contain appreciable amounts of solute elements, notably copper, magnesium, silicon, zinc, and lithium, may be susceptible to SCC. In practical terms, the commonly used commercial alloys in which SCC may occur are those based on the systems Al–Cu–Mg (2xxx series), Al–Mg (5xxx) containing more than 3% magnesium, and Al–Zn–Mg and Al–Zn–Mg–Cu (7xxx). SCC has only been observed on rare occasions in Al–Mg–Si alloys (6xxx) and is absent in commercial-purity aluminium (1xxx), Al–Mn and Al–Mn–Mg (3xxx) alloys, and in Al–Mg alloys containing <3% magnesium. When cracking does occur, it is characteristically intergranular (e.g., Fig. 2.40) and involves the presence of an active anodic constituent in the grain boundaries. Alloys are usually most susceptible in the recrystallized condition and it is for

this reason that compositions, working procedures, and heat treatment temperatures for wrought alloys are normally adjusted to prevent recrystallization. It should be noted, however, that the resistance of a particular wrought alloy to SCC will now vary depending upon the direction of stressing with respect to the elongated grain structure. Maximum susceptibility occurs if stressing is normal to the grain direction, i.e., in the short transverse direction of components, because the crack path along grain boundaries is so clearly defined (Fig. 2.42).

Residual stresses are introduced into aluminium alloy products when they are solution treated and quenched. The quenching operation places surface regions of a component into compression and the center into tension. If the compressive surface stresses are not disturbed during subsequent fabrication procedures, then a component will actually have an enhanced resistance to SCC because a sustained tensile stress is required to initiate and propagate this type of cracking. On the other hand, if the central regions are exposed (e.g., by machining away sections in a component that has not been stress relieved), then the internal residual tensile tresses will be additive to any tensile stresses imposed in service, thereby increasing the probability of SCC. As mentioned in Section 4.1.5, it is for this reason that aluminium alloy products of constant cross section (rolled plate and extrusions) are usually given a mechanical stretch of 1–3% after quenching which greatly reduces the levels of residual stress.

Some uncertainty remains concerning the precise mechanisms responsible for SCC in susceptible aluminium alloys exposed to particular environments, and two basic theories have been invoked to explain how cracks advance along grain boundaries. One proposes anodic dissolution and the other hydrogen embrittlement.

In precipitation-hardened aluminium alloys aged at elevated temperatures, resistance to SCC varies with ageing condition and has generally been considered to be inversely related to strength in the manner shown in Fig. 2.54. However, there is now evidence that the reverse may be true with some alloys based on the Al–Zn–Mg–Cu system which is discussed in Section 4.4.5. Resistance to cracking also tends to increase as the ageing temperature is raised. Much attention has therefore been given to devising new ageing tempers and thermomechanical practices whereby high strength can be combined with an acceptable resistance to SCC.

Considerable effort has been directed toward understanding the mechanism of SCC in aluminium alloys and significance has been attached to the following microstructural features.

1. PFZs adjacent to grain boundaries (Fig. 2.14A and B).
   In a corrosive medium, it is considered that either these zones or the grain boundaries will be anodic with respect to the grain centers. Moreover, strain is likely to be concentrated in the zones because they are relatively soft.
2. Nature of the matrix precipitate.

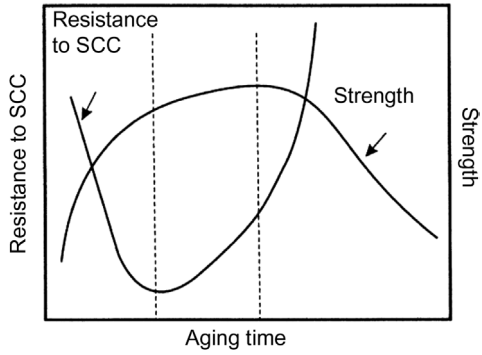


Figure 2.54 General relationship between resistance to SCC and strength during the ageing of aluminium alloys at elevated temperatures.

Maximum susceptibility to cracking occurs in alloys when GP zones are present. In this condition, deformation tends to be concentrated in discrete slip bands similar in appearance to those shown in Fig. 2.52A. It is considered that stress is generated where these bands impinge upon grain boundaries which can contribute to intercrystalline cracking under stress–corrosion conditions (Fig. 2.21A).

3. Dispersion of precipitate particles in grain boundaries.
   In some aged aluminium alloys, it has been shown that SCC occurs more rapidly when particles in grain boundaries are closely spaced.
4. Solute concentrations in the region of grain boundaries.
   Differences in solute levels that arise during ageing are thought to modify local electrochemical potentials. Moreover, it has been observed that a higher magnesium content develops in these regions. This results in an adjacent oxide layer with an increased MgO content which, in turn, is a less effective barrier against environmental influences.
5. Hydrogen embrittlement that may occur due to the rapid diffusion of atomic hydrogen along grain boundaries.
6. Chemisorption of atom species at the surface of cracks which may lower the cohesive strength of the interatomic bonds in the region ahead of an advancing crack.

Recent experimental work has shown that SCC at grain boundaries occurs in a brittle and discontinuous manner and there is clear evidence that hydrogen diffuses there, even in the absence of stress (e.g., Fig. 2.55). It thus seems that the presence of hydrogen does play a vital part in SCC due to one or both of mechanisms (5) and (6). However, the overall process of SCC is complex and it seems probable that one or more of the other microstructural factors are also involved. The relative importance of each of these factors may depend upon the particular combination of alloy and environment.

A useful measure of the relative susceptibility of alloys to SCC can be obtained by using precracked specimens that are subjected to sustained tensile

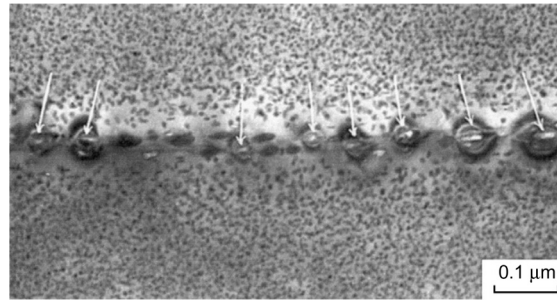


Figure 2.55 Transmission electron micrograph showing hydrogen bubble development at precipitate particles in a grain boundary of a thin foil of an artificially aged Al–Zn–Mg alloy exposed to laboratory air for 3 months. From Scamans, GM: *J. Mater. Sci.*, 13, 27, 1978.

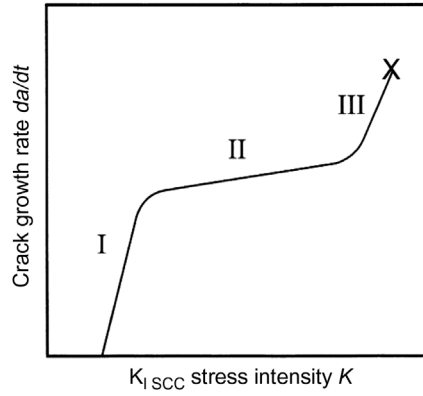


Figure 2.56 Typical relationship between rate of crack growth and stress intensity during SCC of a precracked specimen of a susceptible alloy loaded in tension and exposed to a corrosive environment.

loading in an appropriate corrosive environment. The rate of crack growth (d*a*/d*t*) is monitored as a function of the instantaneous value of stress intensity (*K*) and plots of the data take the form shown in Fig. 2.56. Three distinct regimes of crack growth are evident. In region I, d*a*/d*t* is strongly dependent on *K* whereas, in region II, d*a*/d*t* is virtually independent of the prevailing value of *K*. It is within this region that environmental factors predominate and, in some alloys, a steady state or plateau velocity is recorded (see also Figs. 4.21 and 4.32). In region III, d*a*/d*t* again becomes strongly dependent of until final overload failure occurs. At very low values of *K*, d*a*/d*t* becomes vanishingly small and the value (often referred to as K_{ISCC}) is considered to be the threshold level below which SCC does not occur in the particular environment.

2.5.5 Corrosion fatigue

Under conditions of simultaneous corrosion and cyclic stressing (corrosion fatigue), the reduction in strength is greater than the additive effects if each is considered either separately or alternately. Although it is often possible to provide adequate protection for metallic parts which are stressed under static conditions, most surface films (including naturally protective oxides) can be more easily broken or disrupted under cyclic loading. Corrosion fatigue is accentuated by the rapid movement of the corroding medium over the surface, since protecting layers that might form will be washed away. Localized attack of the aluminium surface, such as by pitting corrosion, will also provide stress concentrators that may greatly reduce fatigue life. Contrary to failures by SCC in aluminium alloys, which are invariably intercrystalline, corrosion fatigue cracks are characteristically transcrystalline in their mode of propagation.

In general, the reduction in a fatigue strength of a material in a particular corrosive medium will be related to the corrosion resistance of the material in that medium. Under conditions of corrosion fatigue, all types of aluminium alloys exhibit about the same percentage reduction in strength when compared with their fatigue strength in air. For example, under freshwater conditions the fatigue strength at 10^8 cycles is ~60% of that in air, and in NaCl solutions it is normally between 25% and 35% of that in air. Another general observation is that the corrosion fatigue strength of a particular aluminium alloy appears to be virtually independent of its metallurgical condition.

2.5.6 Creep

Creep fracture, even in pure metals, normally occurs by the initiation of cracks in grain boundaries. The susceptibility of this region to cracking in age-hardened aluminium alloys is enhanced because the grains are harder and less willing to accommodate deformation than the relatively softer PFZs adjacent to the boundaries (Figs. 2.14A and 2.21B). Moreover, the strength of the grain boundaries may be modified by the presence there of precipitate particles.

Precipitation-hardened alloys are normally aged at one or two temperatures which allow peak properties to be realized in a relatively short time. Continued exposure to these temperatures normally leads to rapid over-ageing and softening and it follows that service temperatures must be well below the final ageing temperature if a loss of strength due to over-ageing is to be minimized. For example, the alloy selected for the structure and skin of the supersonic Concorde aircraft, which was normally required to operate in service at 100–110°C, is aged at around 190°C.

Creep resistance in aluminium alloys is promoted by the presence of submicron intermetallic compounds such as Al_9FeNi or other fine particles that are stable at the required service temperatures (normally below 200°C). Fine, stable particles or fibers can be introduced by a variety of novel processing methods

and the products that result can show much improved creep resistance when compared with conventional age-hardened alloys. These new materials are discussed in Chapter 8.

Recent work has also shown that aged aluminium alloys may show superior creep resistance if they are tested in the underaged rather than fully hardened condition (T6 temper, Section 4.2.2). As demonstrated in Fig. 2.57A with an experimental Al–Cu–Mg–Ag alloy tested at 150°C and a stress of 300 MPa, this beneficial effect of underageing is manifest in significantly reduced rates of secondary creep. In this case, the creep rate has been reduced to one-third of the value for same alloy tested in the fully hardened T6 condition. With the commercial Al–Cu–Mg–Mn alloy 2024 (Table 4.4), underageing has nearly doubled the time to failure from 260 h for the T6 condition to 480 h (Fig. 2.57B). It is also interesting to note these results were obtained despite the fact that, in the

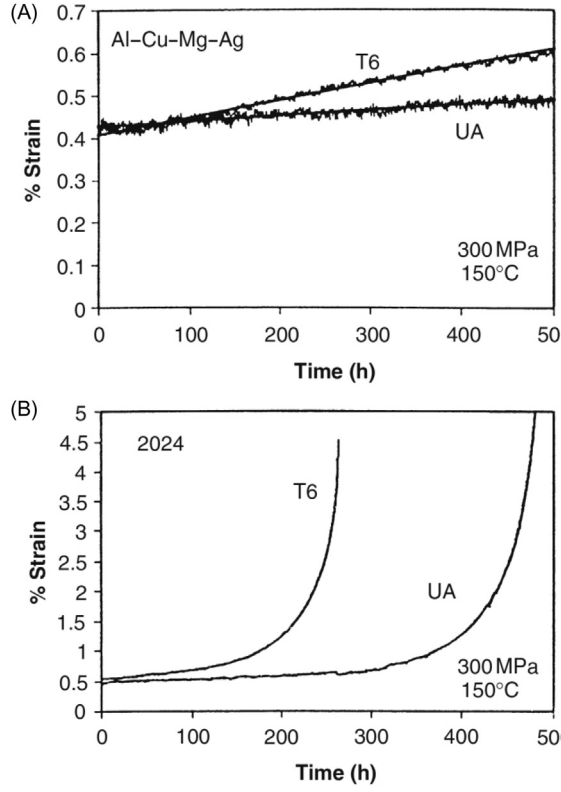


Figure 2.57 Creep curves for (A) an experimental Al–Cu–Mg–Ag alloy and (B) the commercial alloy 2024, both tested in the underaged and fully hardened (T6) conditions at 150°C and a stress of 300 MPa. After Lumley, RN *et al.*: *Acta Mater.*, 50, 3597, 2002.

underaged condition, both alloys had levels of yield stress significantly lower than the T6 values.

Microstructural studies have suggested that the enhanced resistance of aluminium alloys to creep in the underaged condition is a consequence of the presence of "free" solute in solid solution that is not yet committed to the precipitation process. This free solute is available to retard the motion of dislocations during creep deformation through the formation of solute atmospheres, or by facilitating dynamic precipitation within the matrix.

FURTHER READING

Lumley, RN, (Ed.): *Fundamentals of aluminium metallurgy: production, processing and applications*, Woodhead Publishing Limited, Cambridge, UK, 2011.

Murakami, Y: Aluminium-based alloys *Materials Science and Technology: A Comprehensive Treatment*, Vol. 8, Matucha, KH, Ed., VCH, Weinheim, Germany, 1996.

Humphreys, FJ and Hatherly, M: *Recrystallization and Related Annealing Phenomena*, Pergamon, Elsevier Science, Oxford, UK, 1996.

Vasudevan, AK and Doherty, RD, (Eds.): *Treatise on Materials Science and Technology, Vol. 31: Aluminium Alloys—Contemporary Research and Applications*, Academic Press, New York, NY, USA, 1989.

Polmear, IJ: Aluminium alloys: a century of age hardening *Proc. 9th Inter. Conf. on Aluminium Alloys, Mater. Forum* 1, IMEA, 2004.

Ardell, AJ: Precipitation hardening, *Metall. Trans. A*, 16A, 2131, 1985.

Lorimer, GW: *Precipitation Processes in Solids*, Russell, KC and Aaronson, HI (Eds.) Chap. 3, Met. Soc. AIME, New York, NY, USA 1978.

Martin, JW: *Precipitation Hardening*, 2nd Ed., Butterworth-Heinemann, Oxford, 1998.

Lloyd, DJ: Precipitation hardening, *Proc. 7th Inter. Conf. on Strength of Metals*, McQueen, HJ, Ed., Pergamon Press, Toronto, 3, 1745, 1985.

Nie, JF and Muddle, BC: Microstructural design of high-strength aluminium alloys, *J. Phase Equilibria*, 19, 543, 1998.

Shercliff, HR and Ashby, MF: A process model for age hardening of aluminium alloys, *Acta Mater.*, 38, 1789 and 1803, 1990.

Bratland, DH, Grong, O, Shercliff, H, Myhr, OR and Tjotta, S: Modelling of precipitation reactions in industrial processing, *Acta Mater.*, 45, 1, 1997.

Martin, JW: *Micromechanisms in Particle-Hardened Alloys*, CUP, Cambridge, UK, 1980.

Polmear, IJ and Ringer, SP: Evolution and control of microstructure in aged aluminium alloys, *J. Japan Inst. Light Metals*, 50, 633, 2000.

Polmear, IJ: Control of precipitation processes and properties in aged aluminium alloys by microalloying, *Mater. Forum*, 23, 117, 1999.

Ringer, SP and Hono, K: Microstructural evolution and age hardening in aluminium alloys: atom probe field ion microscopy and transmission electron microscopy studies, *Mater. Characterization*, 44, 101, 2000.

Hornbogen, E and Starke, EA:Jr, Theory assisted design of high strength low alloy aluminium, *Acta Metall. Mater.*, 41, 1, 1993.

Nie, JF: Physical metallurgy of light alloys. In Laughlin, DE and Hono, K, (Eds.): *Physical Metallurgy* (5th Ed.), Elsevier, 2014.

Dupasquier, A, Kögel, G and Somoza, A: Studies of light alloys by positron annihilation techniques, *Acta Mater.*, 52, 4707, 2004.

Hollingsworth, EH and Hunsicker, HY: Corrosion of aluminium and aluminium alloys, *Metals Handbook*, 10th Ed. ASM, Metals Park, OH, USA, 1987.

Cramer, SD and Corvino, BS, Jr (Eds.): *Metals Handbook Volume 13A, Corrosion: Fundamentals, Testing and Protection*, ASM International, Metals Park, OH, USA, 2003.

Staley, JT: Metallurgical aspects affecting strength of heat-treated products used in the aerospace industry *Proc. 3rd Inter. Conf. on Aluminium Alloys*, Vol. 3, Arnberg, L, Ed., NTH/SINTEF, Trondheim, Norway, 1992.

Kaufman, JG: *Fracture Resistance of Aluminium Alloys*, ASM International, Materials Park, OH, USA, 2001.

Kobayashi, T: *Strength and Toughness of Materials*, Springer-Verlag, Tokyo, 2004.

Sanders, TH and Staley, JT: Fatigue and fracture research on high-strength aluminium alloys, *Fatigue and Microstructure*, ASM, Cleveland, OH, USA, 1979.

Holroyd, NJH and Scamans, GM: Stress corrosion cracking in Al–Zn–Mg–Cu aluminium alloys in saline environments, *Metall. Mater. Trans. A*, 44A, 1230, 2014.

Knight, SP, Pohl, K, Holroyd, NJH, Birbilis, N, Rometsch, PA, Muddle, BC, Goswami, R and Lynch, SP: Some effects of alloy composition on stress corrosion cracking in Al–Zn–Mg–Cu alloys, *Corrosion Sci.*, 98, 50, 2015.

3

CASTING OF LIGHT ALLOYS

3.1 INTRODUCTION

The casting of metals is an art as well as a science. To be able to repeatably produce sound castings, each new casting configuration needs a combination of appropriate casting design software and the accumulated experience of knowledgeable foundry staff. This is because casting is a complicated combination of factors and parameters many of which cannot be independently varied. These include the complexity of the component to be cast, the mold materials, melt preheat and pouring temperatures, melt handling, runner and gating design, feeding capacity of the risers, alloy chemistry and shrinkage properties, melt treatment such as degassing and the addition of refiners and modifiers, and the quality and quantity of added recycled alloy. The process of solidification and development of the semisolid microstructure also impacts on the alloy's fluidity and the pathways for accessing the feed liquid and, therefore, on the formation of casting defects such as porosity and hot tearing.

Over the last two decades, the capability and accuracy of casting design packages for computer modeling and simulation of solidification processes has improved significantly. Applied initially to predicting heat transfer and freezing patterns, these software packages are now being used to model most aspects of the casting process, including the computer-aided design of molds, evolution of microstructures, and the estimation of thermal stresses generated during solidification. Software packages are also available to assist with gating and feeder design, and to describe fluid flow during mold filling. It is therefore possible to assess the performance of a casting process relative to the geometry of an engineered cast component before the first melt is poured. During this period, the direct observation of the actual solidification process has also become possible using techniques such as synchrotron X-ray tomography and 2D radiography that are providing new insights into the actual nucleation and growth of phases as the microstructure is developed. Nevertheless, unexpected outbreaks

Light Alloys. DOI: http://dx.doi.org/10.1016/B978-0-08-099431-4.00003-8
Copyright © 2017 Ian Polmear, David StJohn, Jian-Feng Nie, Ma Qian.
Published by Elsevier Ltd. All rights reserved.

of defects can still occur. Such occurrences are often blamed on the supplier of the alloy ingots being melted, or to small changes in casting parameters arising from deviations in process control, even though they may be within acceptable limits.

Both aluminium and magnesium alloys can be cast into components by a large range of technologies, the most common of which are sand casting, permanent mold (gravity die) casting, and cold- and hot-chamber pressure die casting. In 2014, about 16 million tonnes of aluminium were converted into cast products compared with 190,000 tonnes of magnesium. Only a small quantity of titanium is cast into components due to the high melting point and reactivity of titanium alloys. Control of the atmosphere or vacuum requires very expensive melting and casting equipment.

This chapter begins with a description of the solidification process from the molten state to the final as-cast solidified microstructure in the context of our current understanding of the factors affecting nucleation and growth of the phases that form during solidification. Next, factors that contribute to the ability of an alloy and casting process to produce sound products (referred to as castability) are considered followed by descriptions of the range of casting methods available for manufacturing cast light metal components. Details of the commercial aluminium casting alloys are presented in Chapter 5, Cast Aluminium Alloys, and commercial magnesium alloys are presented in Chapter 6, Magnesium Alloys. As the amount of titanium castings produced is so small, this chapter will focus on the casting of aluminium and magnesium alloys.

3.2 SOLIDIFICATION OF LIGHT ALLOYS

Most commercial light alloys are hypoeutectics (i.e., those alloys of composition less than the eutectic composition) with microstructures consisting of primary phase grains of aluminium (Fig. 3.1) or magnesium (Fig. 3.2) containing alloying elements in solid solution, which are surrounded by a eutectic phase. Ternary and quaternary eutectics may also form depending on the number of elements in the alloy. The morphology of the primary phase can vary from globular to rosette-like or dendritic grains depending on the composition, grain size, and casting conditions. Grain morphology also controls the distribution of the eutectic regions. As a better combination of strength and toughness is usually obtained by refining the microstructure, the grain size of the primary phase can be reduced by increasing the cooling rate or by adding a grain-refining master alloy. In Al–Si casting alloys, reducing the grain size has less effect on yield strength than refining the secondary dendrite arm spacing with which there is a Hall–Petch relationship. However, a reduced grain size usually improves castability and promotes a finer distribution of intermetallic particles and porosity which improves toughness and ductility. Finer grain size also has the advantage of reducing homogenization times when heat treating large wrought alloy billets.

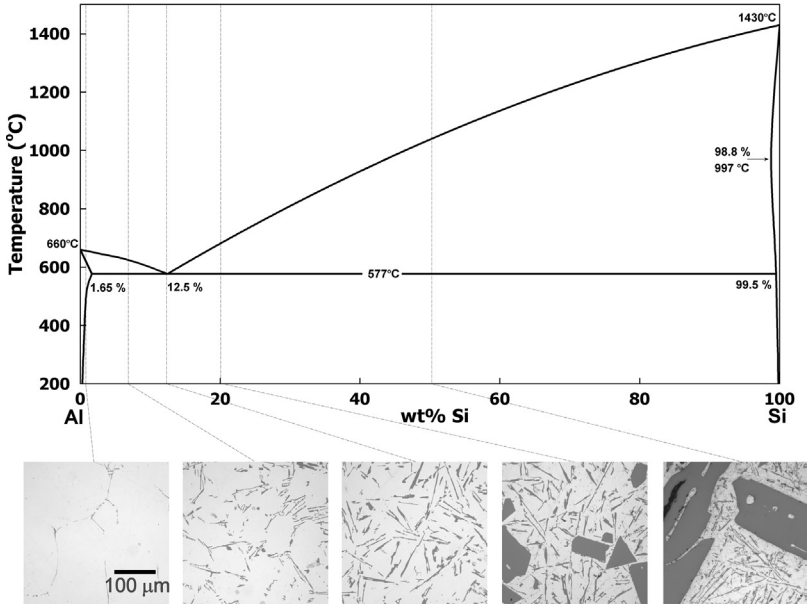


Figure 3.1 The aluminium–silicon phase diagram with associated microstructures showing the change in Si morphology for hypoeutectic (<12.5%), eutectic, and hypereutectic (>12.5%) silicon compositions. Courtesy S. McDonald, The University of Queensland.

A series of phase transformations occur during the solidification of a casting from the liquid state. In simple binary alloys such as Al–Si or Mg–Al (Figs. 3.1 and 3.2), the primary α-phase nucleates first and, as the temperature falls, the α-phase will grow until the eutectic temperature is reached at which point the eutectic nucleates consuming the remaining liquid. In ternary alloys such as the Al–Si–Cu alloys, a ternary eutectic will also form before solidification is complete. As practical casting conditions are nonequilibrium, the solidus line may be suppressed extending the two-phase region to lower alloy contents. This is particularly important in Mg–Al alloys (Fig. 3.2A) where the two-phase region is extended to about 2 wt% Al down from an equilibrium solubility limit of 12.7 wt% Al. The commercial 3, 6, and 9 wt% Al alloys fall within this nonequilibrium range of compositions. Fig. 3.2B shows representative high-pressure die cast microstructures of AM60 and AZ91. The white areas are β-$Mg_{17}Al_{12}$ and the lighter gray areas adjacent to the β-$Mg_{17}Al_{12}$ are high Al content ("eutectic") α-Mg. The dark gray areas surrounded by the eutectic α-Mg are primary α-Mg dendrites.

Before discussing solidification in more detail, there are concepts that are critical to understanding the development of microstructure. The most important are thermal undercooling and the concept of constitutional undercooling (also referred to as constitutional supercooling) which play important roles in nucleation and grain formation of both the primary and eutectic phases.

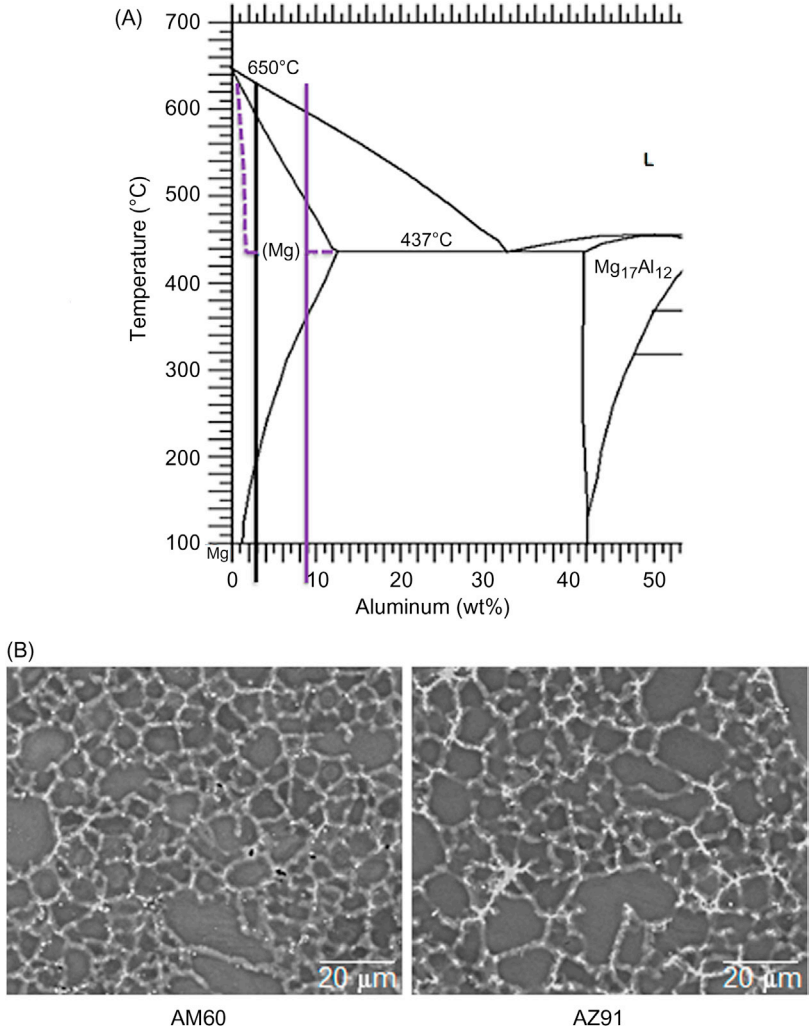


Figure 3.2 (A) The magnesium-rich end of the Mg–Al phase diagram with a dashed line indicating the suppression of the solidus line during nonequilibrium cooling. The vertical lines represent the range of commercial Mg–Al alloys (AZ31, AZ61, and AZ91). (B) Micrographs of pressure die cast AM60 and AZ91. From Zhu, SM *et al.*: *Metall. Mater. Trans. A*, 46, 3543, 2015.

Thermal undercooling promotes nucleation particularly near the mold wall of the casting where the cooling rate is higher. In this instance the thermally undercooled region near the mold wall will trigger nucleation of grains known as chill crystals or wall crystals, as illustrated in Fig. 3.3. The relative importance of thermal and constitutional undercooling on nucleation is described later.

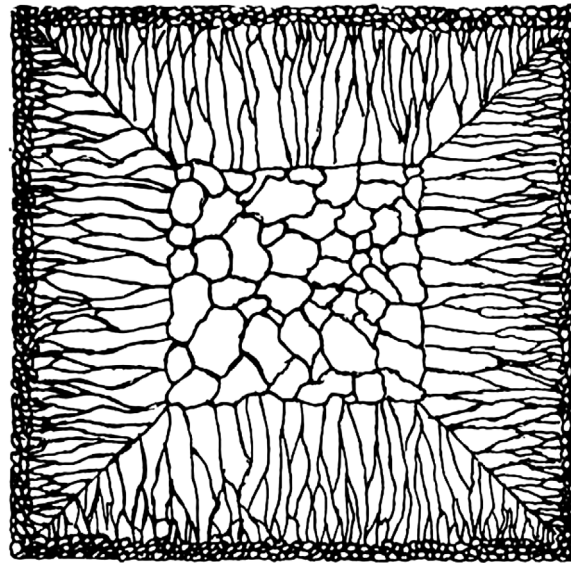


Figure 3.3 Schematic cast grain structure illustrating the transition from columnar to equiaxed grains. The finer grain structure adjacent to the mold walls is formed by chill crystals generated by the higher cooling rate at and/or near the mold walls. From Flemings, MC: *Solidification Processing*, McGraw-Hill, New York, NY, USA, 1974.

Fig. 3.4 is a representation of the development of constitutional undercooling in front of a growing equiaxed grain where the solute is rejected producing a concentration gradient within the diffusion field surrounding the grain (Fig. 3.4A). This concentration gradient can be converted to the gradient of the equilibrium liquidus temperature T_E as shown in Fig. 3.4B. Also, shown in Fig. 3.4B is the actual temperature, T_A. In the case of equiaxed solidification, the actual temperature gradient at the solid–liquid interface is slightly negative as latent heat is released through the liquid (Fig. 3.4C). The difference between T_E and T_A is the amount of constitutional undercooling generated by the grain's growth at that point in time. If there is a positive temperature gradient typical of directional solidification (Fig. 3.4B), then the amount of constitutional undercooling will decrease ahead of the interface eventually becoming zero when T_A is greater than T_E. For equiaxed solidification, constitutional undercooling is the dominant driving force for nucleation and, because nucleation is occurring within a constitutionally undercooled zone, the new grains are protected from remelting. Note that the maximum value of constitutional undercooling (Fig. 3.4C) is not at the solid–liquid interface but at the end of the solute diffusion field which is indicated by the vertical marker on the x-axis of Fig. 3.4.

Another important concept is the growth restriction factor designated by Q. Q is calculated from phase diagram parameters by $Q = C_o m_l(k-1)$, where C_o is the alloy composition, m_l is the slope of the liquidus line, and k is the partition

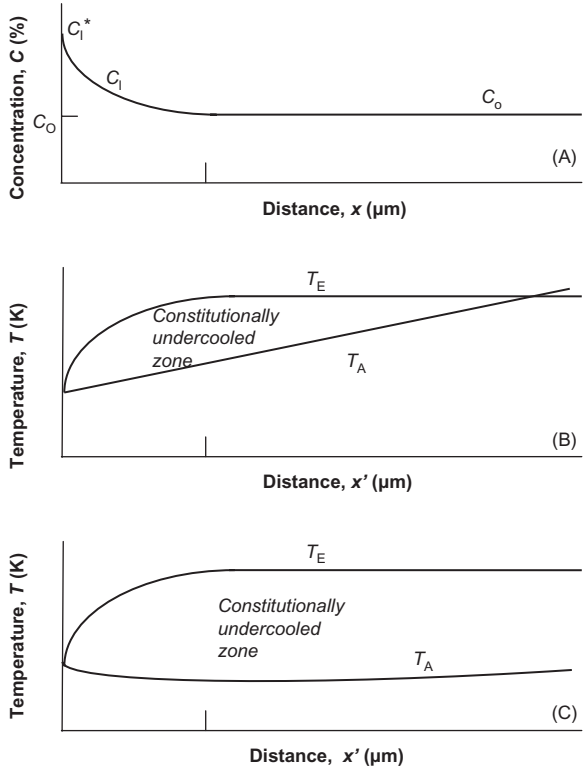


Figure 3.4 (A) A representation of the solute diffusion field in front of the growing solid–liquid interface. (B) The values of composition along the diffusion field in (A) converted to values of their equilibrium liquidus temperature. The constitutionally undercooled zone is the region between T_E and the actual temperature, T_A, due to heat extraction by the mold wall, and is typical of directional solidification. (C) As for (B) except in this case T_A is typical of equiaxed solidification where the gradient is negative at the solid–liquid interface due to heat flow from the hotter grains into the melt and then becoming positive due to heat flow out of the bulk melt into the colder mold walls.

coefficient equal to C_s(solidus composition)/C_l(liquidus composition). The term "growth restriction" is used to describe the decrease in the rate of interface growth as the composition of an alloy, and thus Q, increases and also when the type of solute is a more strongly segregating element (i.e., a higher Q value). It was determined that Q also represents the rate at which constitutional undercooling develops. This has important consequences for interface stability and nucleation. The higher the value of Q, the sooner the solid–liquid interface will break down from a planar to a dendritic morphology, and the sooner the amount of constitutional undercooling reaches the nucleation undercooling of a particle in the melt such that another nucleation event will occur.

3.2.1 Grain formation

Nucleation of the primary phase Nucleation on heterogeneous sites, such as impurity or oxide particles and inoculant particles provided by master alloys, is most relevant to commercial casting. At present it is generally accepted that the potency of a particle is related to the degree of lattice matching or the solid–liquid interfacial surface energy between the substrate and the newly formed phase, and particle size where a larger size requires less undercooling to trigger nucleation and thus is a particle with a higher potency. The proportion of large particles that become active nucleants depends on the size distribution of the particles. For example, in the case of AlTiB master alloys added to aluminium alloys, only a small proportion (<2%) of particles are sufficiently potent to trigger nucleation. While the scientific understanding of the development of grain morphology and eutectic solidification are well described by theory, and can be simulated by numerical models, nucleation remains an area of considerable research and debate. New analytical techniques that allow investigation at the atomic level, along with new modeling approaches, are revealing new insights into atomic ordering at the substrate interface and it is expected that, over the next decade, new theories of nucleation will be developed. These developments will not be covered in this book and the following will discuss nucleation in the context of casting processes. Grain refinement will be discussed separately later in this chapter.

Depending on the casting conditions, nucleation in an alloy melt may initially occur on or near the walls of the mold triggered by thermal undercooling due to the melt being cooler than in the bulk of the melt, or may occur uniformly throughout the melt. The process of nucleation is affected by the casting conditions in several ways:

1. When the temperature gradient into the melt is strongly positive such as in directional solidification, the first "chill" crystals to form near the walls evolve into aligned columnar grains as shown in Fig. 3.3. In this case, the columnar grains continue to grow toward the center of the casting with no further nucleation occurring.
2. As the temperature gradient across the casting decreases due to thermal equilibration of the melt and heating of the mold, a columnar to equiaxed transition may occur as illustrated in Fig. 3.3, because constitutional undercooling becomes the dominant driving force for nucleation.
3. The aim of grain refinement or processes that lower the temperature gradient in the melt, as illustrated in Fig. 3.4C, is to promote equiaxed solidification and eliminate columnar growth altogether. Once equiaxed grains form, the temperature gradient from the solid–liquid interface of each grain into the liquid becomes slightly negative. This results in an increase in the amount of constitutional undercooling, thus, enhancing the likelihood of further nucleation and the survival of grains as they are transported into the melt.

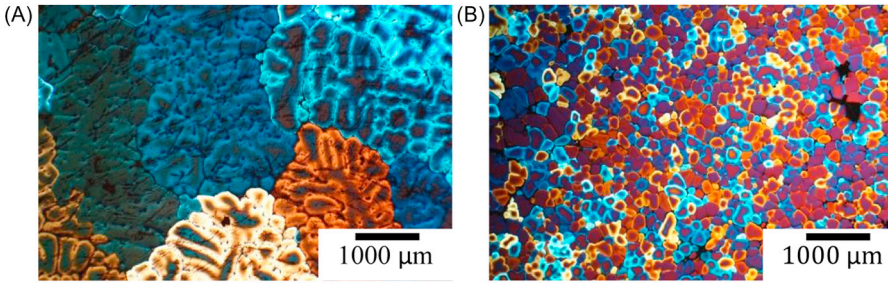


Figure 3.5 The microstructure of anodized samples from the central part of the Al–2Cu alloy ingot samples: (A) without ultrasonic treatment and (B) with ultrasonic treatment. Courtesy G. Wang, The University of Queensland.

4. An alternative mechanism occurs when the temperature gradient remains positive and solidification begins while the melt is turbulent due to, for example, pouring of melt into the die cavity. In this case, the grains nucleated on or near the mold walls are remelted by the hot metal being poured on top. Toward the end of filling the die, the wall crystals formed near the top of the walls of the casting survive and are carried into the bulk of the melt by convection. The macrostructure formed in this case is similar to case (2) above.

When nucleation readily occurs, the distance between grains becomes very small limiting the amount of grain growth. All grains begin with near spherical growth morphology and then the growth interface quickly transitions to globular (or cellular) and finally to a dendritic morphology as the grain continues to grow. If growth is interrupted by neighboring grains, the final as-cast morphology can be globular rather than dendritic which would be obtained when the growth distance is large. Fig. 3.5 shows that the macrostructure of an ingot of Al–2 wt% Cu alloy has large dendritic grains when solidified in a normal casting environment. However, if ultrasonic treatment is applied, many more nucleation events occur resulting in a near spherical morphology. (These morphological changes can also occur for eutectic cells/grains that form during eutectic solidification, especially for alloys containing ternary elements.)

Nucleation of grains occurs on particles naturally present in the base alloy (e.g., impurity intermetallic particles, oxide films) or on deliberately added inoculant particles via the addition of master alloys. Recent synchrotron studies on Al–Si and Al–Cu alloys have shown that nucleation in grain refined alloys occurs in waves of nucleation events as the alloy cools with a low, positive temperature gradient across the melt, and each wave forms an approximately linear array of new grains (Fig. 3.6). Once these arrays of grains form, no further nucleation occurs between the initially nucleated grains. This implies that the grains are nucleating near a specific temperature (i.e., the nucleation temperature of the largest refiner particles) when the amount of constitutional undercooling reaches the nucleation undercooling. The distance between the arrays

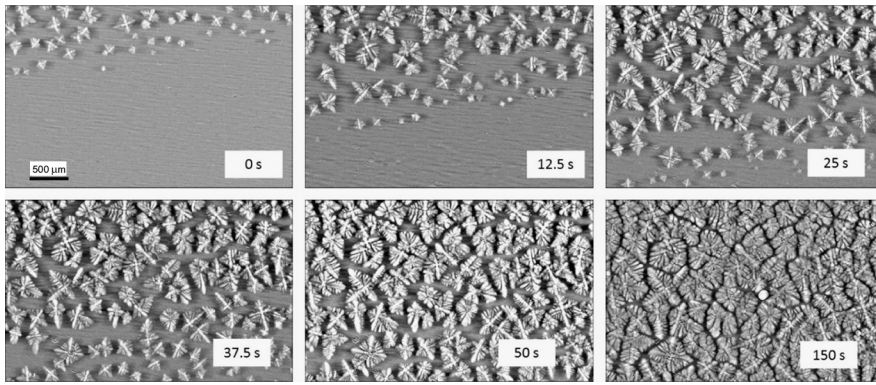


Figure 3.6 A sequence of images from real-time synchrotron X-ray observation of the solidification of an Al–15 wt% Cu alloy. From Prasad, A *et al. Mater. Sci. Eng.* 84, 012014, 2015.

of grains is affected by the formation of a nucleation-free zone (NFZ) by the diffusion field in front of the growing grains within the arrays (Section 3.3.1).

These new primary grains grow to be of spherical or globular morphology when the grain size is small (e.g., $<100\,\mu m$) or dendritic for larger grain sizes until they impinge on each other. Fig. 3.6 shows typical dendritic images of an Al–15 wt%Cu alloy.

Grain growth and morphology For a directionally solidified alloy, the growth morphology of the solid–liquid interface can be changed from a planar growth front to a dendritic morphology by independently manipulating the rate of growth of the interface, V, and the temperature gradient, G, as illustrated by Fig. 3.7. These morphological transitions are also affected by the cooling rate $\dot{T}\,(=GV)$, where higher cooling rates produce finer microstructures. The transitions represented in Fig. 3.7 are affected by the alloy composition. For example, an alloy with a low solute content subjected to a steeper temperature gradient will promote a planar interface while the opposite promotes a dendritic morphology eventually allowing nucleation of equiaxed grains ahead of the growing interface. As the alloy content increases, the concentration gradient in the melt ahead of the solid–liquid interface becomes steeper promoting earlier formation of perturbations on the initially planar interface. These perturbations become stable generating cellular growth and at higher compositions, and lower temperature gradients, secondary and tertiary perturbations can occur on the primary and secondary arms, respectively, producing highly dendritic grain morphologies.

In the case of equiaxed solidification of grains, G and V cannot be controlled in the same way as for directional solidification. G is not constant over time from the start of solidification nor throughout the casting, and depends on the location in the melt as well as the complexity of heat extraction pathways.

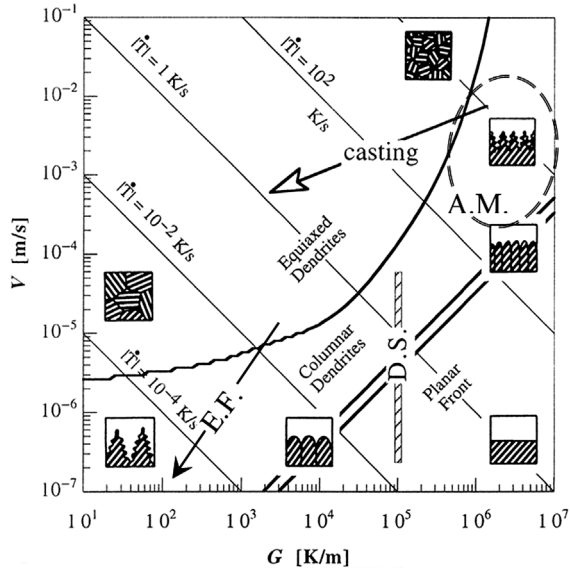


Figure 3.7 Schematic illustrating the change in grain morphology for a particular alloy composition due to changes in the interface growth velocity, *V*, and temperature gradient, *G*. The figure also shows the effect of cooling rate $\dot{T}$ (=*GV*) on the morphology which becomes finer at higher cooling rates. The base figure is from Kurz, W and Fisher, DJ: *Fundamentals of Solidification*. Trans Tech Publications, 1998, modified by the addition of data for the A.M. region derived from Collins, PC *et al.*: *Annu. Rev. Mater. Res.*, 46, 63, 2016 and Marshall, GJ *et al.*: *JOM*, 68(3), 778, 2016, and the data for region E. F. is from a recent study, courtesy of G. Wang, The University of Queensland.

The latter affects the local cooling rate which can vary significantly from place to place depending on the complexity of casting design. Therefore, *G* and/or *V* will also vary. Near the walls of the mold, *G* can be initially high and as the mold heats up *G* decreases. To complicate matters, the local temperature gradient at the grain–liquid interface will be slightly negative (Fig. 3.4C). However, the general relationships shown in Fig. 3.7 can provide a guide to the likely changes in the morphology of equiaxed grains at the location of interest during solidification of an alloy. Alloy composition also affects morphological changes. For example, for low alloy compositions, a decrease in *G* and/or an increase in *V* may change the grain morphology from spherical to globular/rosette (i.e., the equiaxed forms of planar and cellular solidification fronts, respectively, shown in Fig. 3.7) and then to dendritic. As the alloy compositions increase, the morphology will transition from globular to rosette to dendritic more rapidly.

The final morphology of a grain is also affected by the growth of the surrounding grains. If the growing grains are close together growth may be impeded before there is a transition from, for example, globular to dendritic.

This occurs because solute accumulates between the grains reducing V to very low levels which in turn promotes spherical or globular interfacial growth as predicted by Fig. 3.7. Thus, very fine grain structures can be almost spherical or globular while larger grain sizes of the same alloy will be fully dendritic. A simple example where a change in G during solidification causes a columnar to equiaxed transition is illustrated in Fig. 3.3 and by the "casting" arrow in Fig. 3.7, where the temperature gradient becomes lower with distance from the mold wall eventually promoting nucleation of equiaxed grains ahead of the columnar grains' interface.

The four areas marked in Fig. 3.7 are related to different solidification processes as follows:

- The region D.S. represents the range of directional solidification conditions for producing a perfect homogenous crystal at the bottom of the region to single crystals with an internal dendritically cored structure at the top of the region.
- The direction of the "casting" arrow marked on the figure indicates the reduction in the cooling rate, and G and V, during solidification of the melt in a die cavity as the mold becomes hotter, which leads to a transition from a columnar to equiaxed grain structure as illustrated in Fig. 3.3.
- The area marked A.M. is for the conditions present during additive manufacturing. During additive manufacturing, both G and V are very high resulting in columnar dendrites.
- The arrow denoted as E.F. is for solidification when external fields such as ultrasonic and oscillating magnetic fields are applied. When external fields are applied to the melt, strong convection induced by acoustic streaming generates a very low value of G throughout the melt. In addition, the large number of grains swept into the melt after nucleation (Fig. 3.5 and see Section 3.6.3) causes V to become much slower due to solute accumulation between the grains thus producing near spherical or globular grains. The E.F. arrow is an estimate derived from thermal modeling and recent measurements undertaken during ultrasonic treatment of an Al–2 wt% Cu alloy. Although the direction of the arrow indicates a change from equiaxed to columnar growth, once the equiaxed morphology is established, it remains to the end of the casting process because each grain is surrounded by many other equiaxed grains. As mentioned earlier, Fig. 3.7 has limited applicability to equiaxed solidification because the local temperature gradient at the interface is negative, a condition which is not taken into account by the figure. The calculated temperature gradients used here are the long range positive gradients due to heat being extracted by the mold walls. Thus, caution should be used when applying Fig. 3.7 to equiaxed solidification.

As the grains approach the point where they impinge on each other, the viscosity of the semisolid mush increases until mechanical interlocking of dendrites causes the movement of grains to cease. When the dendrites impinge

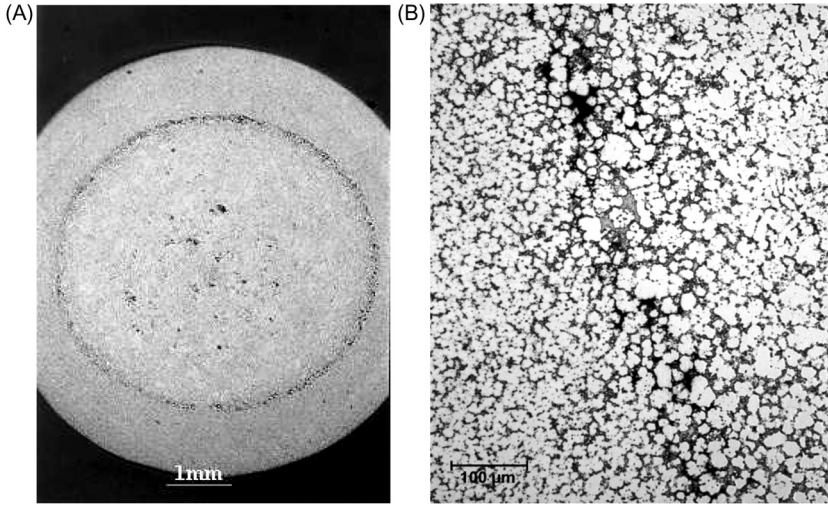


Figure 3.8 (A) A defect band containing segregation of eutectic and porosity in a circular section of a high-pressure die cast AM60. The flow direction is into the page. Note the very fine grain size on the outside of the defect band compared with the coarser microstructure inside. Higher magnification in (B) with the region outside the band on the left-hand side of the micrograph. From Dahle, AK *et al.*: *J. Light Metals*, 1 (1), 61, 2001.

on each other, a dendritic network is formed that exhibits a measureable shear strength which is dependent on the degree of mechanical interlocking between the grains. However, at this stage of solidification, the network of grains does not have any strength when placed under a tensile load. Magnesium high-pressure die castings (HPDC) can exhibit shear bands parallel to the flow direction of the molten metal during die filling (Fig. 3.8). These bands can be filled with porosity or tears. These shear bands are not necessarily a problem and may even improve fluidity, but the formation of cracks and interlinked porosity can lead to poor pressure tightness and reduced mechanical performance.

After grain impingement, the rate of dendritic growth decreases as the dendrite arms continue to thicken due to solidification and coarsening because of the driving force to reduce the surface area of the solid–liquid interface while the temperature drops to the eutectic temperature. During this stage, bridging across the dendrite tips of adjacent grains can occur. These bridges may tear under the tensile load caused by shrinkage. The eutectic then solidifies and, if feed liquid is insufficient, shrinkage can manifest as porosity or, when the dendritic network is under a tensile stress, hot tearing between the grains.

3.2.2 Eutectic solidification

Eutectic solidification begins when the melt temperature decreases to the eutectic temperature. For Al–Si alloys, a eutectic of α-Al and Si is formed at 577°C (Fig. 3.1) and for Mg–Al alloys a eutectic of α-Mg and $Mg_{17}Al_{12}$

is formed at 437°C (Fig. 3.2A). Because the primary phase is one of the two eutectic phases, the eutectic would be expected to nucleate on the surface of the primary phase as the barrier to nucleation should be low. However, this is not always the case as nucleation may depend on the barrier to nucleation of the other eutectic phase. Al–Si alloys are an example of this situation where formation of the eutectic first requires nucleation of silicon. In commercial purity alloys, the nucleation of silicon occurs independently of the α-phase—liquid interface on aluminium phosphide (AlP) particles. Once silicon forms, the two phases grow together with a morphology that is dependent on the relative volume fraction of the phases and whether one or more phases are faceted. Silicon grows as faceted flakes as shown in Fig. 3.1, which reduces the ductility of the alloy. To overcome this problem, a modifying agent (e.g., strontium) is added that converts the flakes to a fibrous morphology. Section 5.2.1 discusses the use of modifiers to refine the eutectic silicon microstructure of these alloys in order to improve their mechanical properties. These properties are also affected by the volume fraction of eutectic. Since the brittle silicon is contained within the eutectic, a higher volume fraction of eutectic tends to make the eutectic regions continuous leading to a decrease in fracture toughness of the material. The nucleation of silicon independently of the primary α-Al phase results in the formation of eutectic grains (also known as eutectic cells) in much the same way that the primary α-Al grains are nucleated. Once formed these eutectic grains grow through the interdendritic spaces of the α-Al grains until solidification is complete.

The magnesium–aluminium eutectic is a divorced or semi-divorced eutectic because $Mg_{17}Al_{12}$ forms a layer on the edge of the α-Mg dendrite arms rather than as part of a two-phase structure with α-Mg (Fig. 3.2B). Adjacent to this layer is an aluminium-rich region that may decompose during further cooling via discontinuous precipitation of $Mg_{17}Al_{12}$ forming a lamellar-like morphology with the aluminium-rich magnesium. Grain refinement of magnesium–aluminium alloys is usually the result of rapid cooling during high pressure die casting (HPDC), where the fine grain size allows the $Mg_{17}Al_{12}$ layer to be more or less continuous. Although a continuous $Mg_{17}Al_{12}$ layer improves corrosion resistance, it can reduce ductility.

3.3 GRAIN REFINEMENT

3.3.1 Factors influencing grain refinement

Grain refinement of the primary phase is a very important process for improving the properties and castability of aluminium and magnesium alloys. Recent studies have clearly shown that both potent particles and solute with a strong segregating ability (i.e., high Q value) are needed to promote effective nucleation. Each new nucleation event requires some growth of the previous grain to generate enough constitutional undercooling to trigger nucleation on the next most potent particle present ahead of the solid–liquid interface. On cooling, the

most potent of these particles nucleate the primary phase grains producing a finer grain size. This interdependence between solute and particle potency has been described by the Interdependence model where it was shown that there are three lengths that together establish the as-cast grain size (Fig. 3.9). They are the length x_{cs} the previous grain must grow to generate sufficient constitutional undercooling to trigger the next nucleation event, the length x'_{dl}, of the diffusion field, from the solid–liquid interface to the location where this critical amount of constitutional undercooling is established (Fig. 3.4), and the length x_{Sd} from this point to where a suitably potent particle is present. Fig. 3.9 illustrates how these three lengths change with the inverse of alloy composition converted to its growth restriction factor Q. It can be noted from Fig. 3.9 that as Q increases the first two lengths, x_{cs} and x'_{dl}, decrease resulting in a reduced grain size.

As mentioned earlier, a higher Q value generates constitutional undercooling faster causing nucleation to occur sooner resulting in a finer grain size. Table 3.1 lists the values of $m_l(k-1)$ for the alloying elements added to aluminium, magnesium, and titanium. The calculation of Q for complex alloys can often be undertaken by adding together the Q values for each alloying element. However, for some complex alloys, where there is interaction between the alloying elements, it is necessary to use thermodynamic software to calculate Q.

The first two lengths, x_{cs} and x'_{dl}, represent a nucleation-free zone (NFZ) surrounding each grain (Fig. 3.9), which is the sum of the distance a grain must grow to trigger the next nucleation event plus the length of the diffusion field around each growing grain where the amount of constitutional undercooling increases with distance ahead of the grain–liquid interface. Thus, close to the interface, the amount of constitutional undercooling is much lower than in the bulk liquid meaning that nucleation is most likely to occur away from the

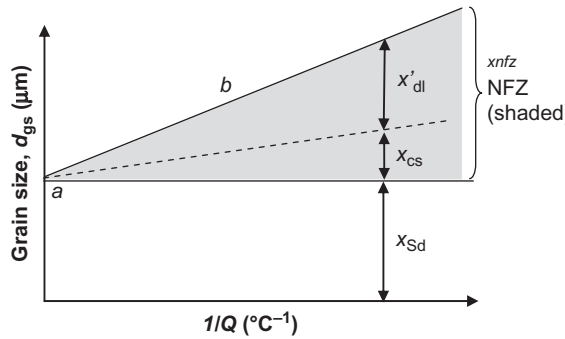


Figure 3.9 A simple representation illustrating that for each value of Q the grain size is the result of three components: x_{Sd} is the average distance between activated particles assuming a constant inoculant particle density, and b is equal to the gradient of x_{cs} plus x'_{dl} over a unit of $1/Q$. The shaded area is the NFZ and represents the minimum grain size that can be achieved for each value of Q. From Easton, M *et al.*: *Curr. Opin. Solid State Mater. Sci.*, 20, 13, 2016.

Table 3.1 The values of $m_l(k-1)$ for the alloying elements added to aluminium, magnesium, and titanium for calculating the value of Q (i.e. $C_o m_l(k-1)$)

Al alloys	$m_l(k-1)$	Mg alloys	$m_l(k-1)$	Ti alloys	$m_l(k-1)$
Ti	**~220**	Fe	52.56	Be	72
Zr	6.8	**Zr**	**38.29**	**B**	**66**
Si	5.9	Ca	11.94	Si	21.7
Cr	3.5	Si	9.25	Ni	14.3
Ni	3.3	Zn	5.31	O	10.2
Mg	3.0	Cu	5.28	Co	8.8
Fe	2.9	Al	4.32	Y	7.9
Cu	2.8	Sr	3.51	Sc	6.7
Mn	0.1	Ce	2.74	Cu	6.5
		Y	1.70	Al	~0
		Mn	0.15	V	~0

The elements in bold have very high values of Q and are known to be excellent grain refiners.

growing interface rather than near it. The size of NFZ can make a significant contribution to the final grain size as illustrated in Fig. 3.9.

Although the Interdependence model was developed for near equilibrium casting conditions, the linear relationship between grain size and the inverse of Q is often observed for casting processes involving dynamic conditions such as HPDC or when external fields such as ultrasonic treatments are applied during solidification.

3.3.2 Grain refinement by refinement methods and inoculation with master alloys

For aluminium alloys, grain refinement is well established with commercially available Al–Ti–B and, to a lesser extent, Al–Ti–C master alloys. These master alloys add TiB_2 or TiC particles and titanium solute into the melt. Additions of master alloy as low as 0.005 %Ti will result in grain refinement. The most common additions for aluminium alloys are Al5Ti1B and Al3Ti1B. In the Al–Ti–B master alloy, 2.2% of the titanium is combined with boron in the very stable TiB_2 particles. The remaining titanium is present as Al_3Ti intermetallic particles and in solid solution in the aluminium matrix up to 0.15%Ti. On addition to the melt, the Al_3Ti particles quickly dissolve providing titanium in solution. The higher amount of titanium in solution provided by Al5Ti1B is suitable for lean alloys (e.g., many wrought alloys) as the high Q values provided by titanium promote good refinement. Al3Ti1B is sometimes used in casting alloys as these alloys are already rich in growth restricting elements such as silicon.

Currently there is no reliable, safe, and cost-effective refiner for Mg–Al alloys which limits their use in sand and low-pressure die casting processes. Consequently, most magnesium alloys are cast by HPDC which produces a

very fine grain size without the need for refiner addition. For Mg–Zn alloys, zirconium is an excellent refiner for alloys that do not contain aluminium or manganese, because the zirconium dissolves providing high Q values and the zirconium particles that remain undissolved are potent nucleants for magnesium.

There are no commercial grain refiners available for titanium alloys. The common Ti6Al4V alloy has the distinction of having no growth restriction because both aluminium and vanadium have Q values of approximately 0 (Table 3.1). This combined with the fact that many elements and intermetallic compounds are soluble in liquid titanium, it has been difficult to identify stable intermetallic particles having good nucleation potencies. Significant grain size reduction is possible by adding solutes such as boron or silicon which have reasonably high Q values.

Aluminium alloys The Al–Ti–B master alloys are the most commonly used master alloys for achieving a fine grain size in commercial aluminium alloy castings. The reasons for their superior refining performance have been the subject of research for the last 80 years. Analyzing refinement across the broad spectrum of alloys was confusing as the performance of the refiner was better for direct chill (DC) cast wrought alloys (see Chapter 4, Wrought Aluminium Alloys) than for alloys suitable for foundry casting. As a result, a number of theories were developed such as the duplex, peritectic hulk, hypernucleation, and phase diagram related theories some of which seemed valid for wrought alloys but not valid for foundry alloys. These theories were created to satisfy two assumptions. One was that TiB_2 particles are relatively poor nucleants for aluminium and the other postulated that the peritectic reaction

$$\text{Liquid Al} + Al_3Ti \rightarrow \alpha\text{-Al} \tag{3.1}$$

is critical for improving the potency of TiB_2. Both these assumptions are still subjects of debate.

The first assumption is correct but only in relative terms. TiB_2 is a reasonably good nucleant of aluminium but not as good as Al_3Ti. This assumption arose from the fact that adding TiB_2 particles to pure aluminium did not produce fine equiaxed grains while master alloy addition did result in refinement. It is now known that in order to produce equiaxed grains, we need alloy additions that segregate during solidification (i.e., they have a reasonable value of Q). When Al_3Ti is added along with TiB_2 in a master alloy, the Al_3Ti dissolves generating very high values of Q. Therefore, a direct comparison between the two particles is not possible. Because Al_3Ti is not an equilibrium phase below 0.15 wt% Ti, a number of theories postulated that Al_3Ti must form a metastable layer on the surface of TiB_2 for it to become a potent nucleant. Recent research suggests that rather than metastable Al_3Ti forming directly on the

surface of TiB_2 particles when the amount of Ti is less than 0.15%Ti, the liquid atomic layers adjacent to surface of TiB_2 crystals develop a structure with a higher density of titanium atoms that promotes the nucleation and formation of α-aluminium.

Regarding the second assumption, peritectic solidification does not need the peritectic reaction (Eq. (3.1)) to occur. Rather α-Al simply nucleates on the TiB_2 particles (or the pre-peritectic Al_3Ti) and grows as the temperature decreases like any other solid solution alloy. Further, the calculation of Q based on a value of $m_l(1-k)$ of about 220 clearly shows why titanium solute provides exceptional refinement.

Some solutes interfere with (poison) the ability of TiB_2 to facilitate grain refinement. Zirconium is one example and it is considered that atomic substitution occurs on the surface of TiB_2 becoming $(Ti_{1-x},Zr_x)B_2$ which changes its lattice parameters reducing the nucleation potency of the particles. Silicon, which is present in large quantities in several casting alloys, may also lead to coarser grain sizes if added to alloys refined by AlTiB master alloy. Two suggestions have been proposed to explain this behavior. One is that higher silicon contents produce narrower dendrite arms that grow faster leading to larger grains. The other proposal is that the TiB_2 particles may become covered by $TiSi_2$ thereby rendering them incapable of nucleating α-Al grains. However, silicon poisoning still occurs when there is no titanium present and when other intermetallic and oxide particles are used instead of TiB_2 particles. Thus, neither theory is a satisfactory explanation for the cause of silicon poisoning, and the actual cause still needs to be established.

Magnesium alloys Grain refinement is also very important for magnesium alloys where it improves most mechanical properties, and for many alloys, also improves creep and corrosion resistance. Quite different refining practices are needed depending upon the presence or absence of zirconium.

The group of alloys based mainly on the Mg–Al system tends to have large and variable grain size unless cast by HPDC. The first method devised to control grain size was to superheat the melt to a temperature of 850°C and above for periods of about 30 min, after which the melt was quickly cooled to the normal casting temperature and poured. A comparatively fine grain size was achieved with fair success. The probable explanation is that foreign nuclei with suitable crystal structures such as Al_4C_3 precipitate on cooling to the casting temperature and act as nuclei for the magnesium grains during subsequent solidification. The superheating effect is only significant in Mg–Al alloys and presents problems because crucible and furnace lives are reduced and power requirements are increased.

An alternative technique was developed in Germany in which a small quantity of anhydrous $FeCl_3$ was added to the melt (Elfinal process) and grain refinement was attributed to nucleation by iron-containing compounds. This

method also had its disadvantages because the deliquescent nature of $FeCl_3$ made it hazardous, and the presence of as little as 0.005% iron could decrease the corrosion resistance of the alloys. The addition of manganese was made to counter this latter problem but effectively prevented grain refinement by $FeCl_3$.

The method in current use for alloys containing aluminium as a major alloying element is to add volatile carbon-containing compounds to the melt and hexachlorethane (0.025–0.1% by weight) is commonly used in the form of small briquettes which are held at the bottom of the melt while they dissociate into carbon and chlorine. Grain refinement has been attributed to inoculation of the melt with particles of Al_4C_3, Al_2MgC_2, $AlN{\cdot}Al_4C_3$ or magnesium oxide ($MgAl_2O_4$). However, rod-like substances rich in aluminium, carbon, and oxygen have now been detected inside the α-Mg grains which appear to serve as nucleation centers. In this regard, it has also been noted that the compound Al_2OC has lattice dimensions $a = 0.317\,\text{nm}$ and $c = 0.5078\,\text{nm}$ that are similar to magnesium ($a = 0.320\,\text{nm}$ and $c = 0.520\,\text{nm}$) and the same hexagonal crystal structure. Release of chlorine causes some degassing of the melt which is a further advantage of the method.

The ability of zirconium to provide excellent grain refinement (Fig. 3.10) of most other magnesium alloys can also be attributed to two factors related to the dissolved zirconium and the undissolved zirconium particles. The undissolved particles are the α-allotrope (stable below 862°C) which has a hexagonal crystal structure and lattice dimensions ($a = 0.323\,\text{nm}$, $c = 0.514\,\text{nm}$) close to those of magnesium. The zirconium solute provides a high level of growth restriction (high Q value, Table 3.1) which also promotes nucleation. These two factors imply that zirconium can nucleate magnesium during solidification and microprobe analysis has revealed the presence of zirconium-rich cores in the centers of magnesium grains due to the segregation of zirconium at the zirconium particle interface. The cores have formed as a consequence of peritectic solidification after nucleation on the zirconium particles as shown in the Mg–Zr phase diagram (Fig. 3.11). Both zirconium particles and zirconium solute make a significant contribution to the degree of grain refinement achieved.

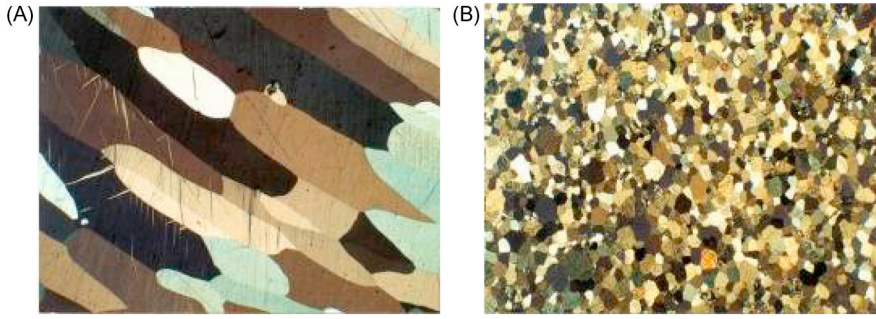


Figure 3.10 Microstructures of (A) pure magnesium and (B) magnesium with 1 wt% zirconium (× 50 for each photo).

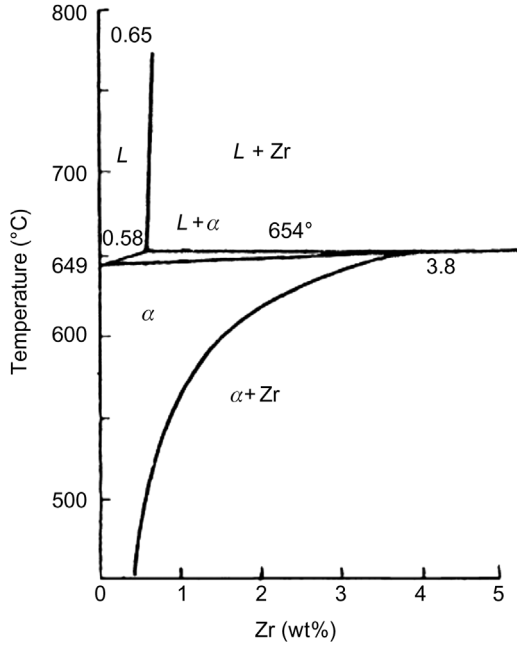


Figure 3.11 Section of the Mg–Zr phase diagram.

Undissolved zirconium particles tend to settle to the bottom of a crucible and, the longer the time elapsed after alloying with zirconium, the coarser will be the grain size of castings that happen to be poured from the top of a melt. If feasible, it is desirable to stir a melt before pouring. Because of the settling problem, it is also desirable to pour zirconium-containing alloy castings directly from the crucible in which they are melted. If transfer to another crucible is necessary, the alloy should be replenished with zirconium. Since the settling rate of the zirconium particles is dictated mainly by their size, attention is being directed to producing master alloys containing finer dispersions of particles. One possibility is to deform these master alloys, e.g., by rolling, in order to fragment the particles into smaller sizes.

Another potential problem is that zirconium will react preferentially with any iron present in the melt to form an iron–zirconium intermetallic compound. The resultant very low iron content in the melt will then provide a driving force for the rapid uptake of iron from the crucible, which is usually made of mild steel, if the temperature exceeds about 730°C. Practical solutions are to maintain a considerable excess of zirconium which increases costs, or to keep the melt temperature as low as possible and delay introducing the Mg–Zr master alloy until just before casting.

3.4 CASTABILITY

In general terms, an alloy can be described as being castable if it consistently and reliably produces castings that have sound microstructures and are

dimensionally accurate for a wide range of products, processes, and plants. The property of castability of an alloy is the sum of several factors of which the most notable are fluidity, mold-filling ability, volume shrinkage, susceptibility to hot tearing, porosity-forming characteristics, and surface quality. These factors are discussed below. Some depend strongly on chemical composition although mold design and process conditions are frequently more important. For example, aluminium foundries occasionally experience intermittent outbreaks of high reject rates because of porosity and shrinkage defects even though the chemical composition of an alloy appears to meet the required specification. In some instances, the batch of aluminium appears to be the culprit and it should be noted that several sources are used by foundries including:

- Primary metal supplied from a smelter as ingots that are provided in grades usually ranging from 99.5% to 99.85% aluminium, or as prealloyed ingots.
- Secondary metal ingots prepared by melting mixtures of recycled aluminium alloy products adjusted in composition to meet particular specifications.
- Molten metal delivered directly from a smelter or secondary producer to the foundry.
- In-house scrap returns.

The use of primary aluminium minimizes remelting and therefore reduces the formation of surface dross which is a mixture of aluminium metal, aluminium oxide, and other melt reaction products. Secondary metal can be cheaper, and certainly environmentally beneficial, to purchase because remelting of aluminium scrap consumes only about 5% of the energy needed to extract aluminium from its ore. However, impurity levels are inevitably higher and there is also a danger that undesirable elements may accumulate. An example is the buildup of iron from recycled scrap in Al–Si casting alloys that can lead to the formation of large intermetallic particles beyond a critical amount of iron resulting in the formation of damaging porosity. The additional remelting associated with the use of secondary metal also increases both the loss of aluminium to dross and the opportunity for the entrainment of oxide. Because of this, many foundries are adopting the practices of degassing and filtering melts prior to casting. Both magnesium and titanium have a strong propensity to oxidation and the melts need to be protected by a cover gas or vacuum respectively.

3.4.1 Fluidity

The fluidity of an alloy is commonly measured by pouring into a sand-molded spiral and alloys are compared by measuring the respective “running lengths” of travel before solidification occurs. Composition influences fluidity due to the effects of alloying elements on viscosity, surface tension, freezing range, and mode of solidification. Fluidity is reduced as the purity of aluminium

decreases and alloying elements are added. This is due mainly to a widening of the freezing range, the formation of intermetallic compounds, and to changes in the solidification pattern from a planar front to a mushy mode. This situation reverses close to a eutectic composition when fluidity is usually at a maximum.

Another aspect of fluidity is the ability to feed the interdendritic spaces remaining once the mold has been filled, but solidification is incomplete. As these spaces between the dendrites continue to narrow, melt viscosity and surface tension become more important and the pressure head needed to maintain flow increases. Volumetric shrinkage assists in this regard as normally there is an overall contraction during the change from liquid to solid.

3.4.2 Volumetric shrinkage

Total volumetric shrinkage during solidification also depends on alloy composition since each phase present has its own density characteristics. Shrinkage amounts to 6% for pure aluminium to as little as 1–2% for hypereutectic Al–Si alloys. Most alloying elements cause less change. Shrinkage is about 4% for magnesium alloys and varies from 3.5% for pure titanium to 5.5% for titanium alloys. Shrinkage may be evident as an overall contraction, as localized effects at surfaces, and at internal defects such as large isolated voids, interconnected porosity, or microporosity. The actual type that may occur in a casting depends on alloy composition, mold design, cooling rate, and mode of solidification. In pressure die castings, shrinkage will also occur if metal in the gate freezes before feeding of the casting has been completed.

3.4.3 Porosity

Most casting processes result in some internal porosity in a casting. This problem is usually most apparent in pressure die castings because of the speed of the operation, turbulent metal flow, and the opportunity to entrap gases. As mentioned earlier, it is because of the presence of porosity that aluminium die castings cannot normally be solution treated since this leads to surface blistering. In general, porosity in castings must be controlled and minimized so as to avoid detrimental effects on mechanical properties, pressure tightness, and surface appearance, particularly if machining is necessary. By attention to mold design and control of casting conditions, every effort is made to concentrate porosity in risers, or to redistribute it uniformly throughout a casting as less harmful micropores. Porosity arises primarily from shrinkage, the formation of internal oxide films, and from the entrapment of gases (air, steam, dissolved hydrogen, or products derived from the burning of organic lubricants). Porosity is usually worst in pressure die castings because of the highly turbulent metal flow and rapid solidification rates, although the entrapment of gases can be overcome by evacuating the mold prior to the entry of the molten metal. With regard to alloy composition,

porosity formation is closely related to the extent of the freezing range. Long ranges tend to result in the formation of dispersed, interdendritic, or intergranular micropores, whereas short freezing ranges may promote the formation of more localized regions of macro-shrinkage or larger intergranular pores. Porosity is also increased by the presence of intermetallic compounds with morphologies that may impede interdendritic feeding during casting. Examples are needles of the Al_5FeSi and $Al_{15}(MnFe)_3Si_2$ compounds which have the appearance of Chinese script.

3.4.4 Hot tearing

Hot tearing (or hot shortness) arises when the tensile stresses generated within a solidifying casting exceed the fracture stress of the partially solidified metal. The result is usually evident as surface tearing and cracking which tend to occur at the sites of local hot spots where the casting is physically restrained. Generally, alloys are more susceptible if they have wide solidification ranges and low volumes of eutectics that can fill and repair hot tears. The change in susceptibility for a range of alloys is often referred to as a lambda curve because susceptibility initially increases from the pure metal as the alloy composition increases and then decreases after a critical composition is reached. This trend in susceptibility can also apply to ternary alloys. Fig. 3.12 presents a contour map of the hot tearing susceptibility factor for a range of ternary Al–Si–Mg alloys where a contour with a high value (and lighter color) of the susceptibility factor is very susceptible to hot tearing. The change in the hot

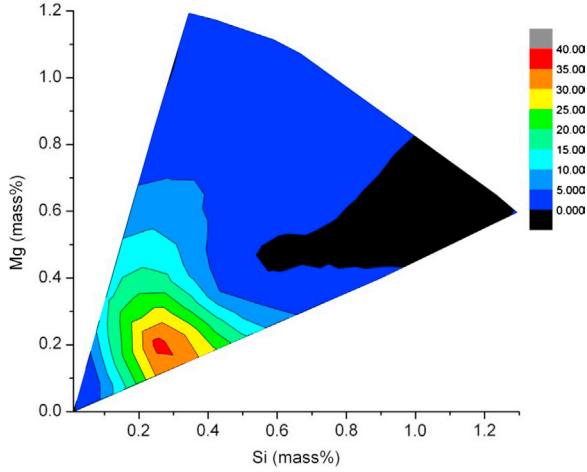


Figure 3.12 The measured hot tear crack width plotted as a contour map against the Si and Mg contents for a range of ternary Al–Si–Mg alloys. Larger value contours of a lighter color mean a higher susceptibility to hot tearing while lower value contours of darker colors mean there is a low likelihood of hot tearing. From Easton, MA *et al.*: *Metall. Mater. Trans. A*, 43, 3227, 2012.

tearing factor with alloy composition corresponds to a lambda curve and the maximum susceptibility occurs at about 0.15% Mg and 0.1% Si. Alloys based on the Al–Cu and Al–Mg system are most prone to hot tearing at similarly low Cu or Mg contents, whereas those based on Al–Si show the highest resistance to hot tearing.

A method of eliminating hot tearing of noncritical components is to promote porosity formation. In the distant past, potatoes were thrown into a melt to generate porosity during solidification. Another method is to generate more oxide films during pouring. The porosity reduces the need for feed liquid thus preventing hot tearing. On the other hand, where porosity needs to be eliminated, a study of gravity die cast aluminium automotive wheels showed that increasing the amount of Al–Ti–B master alloy led to large porosity and/or hot tears at the spoke–rim junction of the wheels. By gradually decreasing the amount of master alloy addition, the large localized porosity and hot tears gradually decreased being replaced by smaller internal porosity. The reason for this response is that the highly fined grains would flow into the melt and clog the mushy zone channel between fully solidified alloy against the spoke cavity walls placing considerable negative pressure on the hot spot at the spoke–rim junction which was cut off from the feed liquid, resulting in porosity and hot tears. The reduction in refiner meant fewer floating grains and a freer channel for liquid to flow into and feed the spoke–rim junction.

3.5 CASTING PROCESSES

3.5.1 Introduction

The first manufacturing step for most metallic products is a casting process. There are a variety of casting processes described in this section, many of which are used to cast aluminium and magnesium alloys. A typical aluminium producer will DC cast extrusion and rolling billets and remelt ingots on site to take advantage of producing product directly from the molten metal thereby removing a solidification and energy consuming remelting step. Magnesium producers will have ingot casting machines for producing foundry alloys nearby as most magnesium metal is then cast into shaped components via HPDC. Extrusions, sheet, and foil begin their manufacturing journey when the newly extracted molten metal is alloyed and then DC cast into billet or slab which is then extruded or rolled into semifabricated products. The alloys may also be cast by twin-roll or strip casting to reduce the need for many rolling passes to achieve thin sheet or foil. DC and ingot casting are described in more detail in Chapter 4.

Shape casting of components manufactured at foundries are produced from prealloyed remelt ingots which are cast by ingot casting machines. Sometimes molten-recycled aluminium is directly transported to foundries from recycling plants. The recycled melt is then blended with remelted casthouse ingots to

reduce the risk of casting defects. In general, alloys are classed as "primary" if prepared from new metal and "secondary" if recycled materials are used. Secondary alloys usually contain more undesirable impurity elements that complicate their metallurgy and often lead to properties inferior to those of the equivalent primary alloys.

The most commonly used casting processes are sand casting, permanent mold (gravity die) casting, and cold-chamber and hot-chamber pressure die casting. Sand molds are fed with molten metal by gravity except for low pressure and Cosworth precision casting processes where the melt is pumped upward into the mold cavity. The metal molds used in permanent mold casting are fed either by gravity or by using low-pressure air or other gas to force the metal up the sprue and into the mold. The following sections describe the casting processes commonly used in the commercial manufacture of aluminium and magnesium. Also covered are new casting processes that are used either for special applications or are under development and show promise for future adoption.

3.5.2 Melting

Aluminium alloys Aluminium and its alloys can be readily melted in air up to 750°C because of the protection of the tenacious surface oxide film and are therefore suitable for a wide range of casting processes. However, care needs to be taken in handling, pouring, and stirring the melt as new oxide films readily form whenever the protective oxide layer is broken. These films lead to the formation of dross which also traps aluminium and reaction products between the films producing waste material that is difficult to process and if left in the melt reduce the mechanical properties of the cast components. Graphite or refractory crucibles are suitable for melting aluminium but iron crucibles need to be coated with refractory materials to prevent dissolution of the iron into the melt.

Magnesium alloys It is usual for magnesium to be melted in mild steel crucibles for both the alloying and refining or cleaning stages before producing cast or wrought components. Unlike aluminium and its alloys, the presence of an oxide film on molten magnesium does not protect the metal from further oxidation. On the contrary, it accelerates this process. Melting is complete at or below 650°C and the rate of oxidation of the molten metal surface increases rapidly with rise in temperature such that, above 850°C, a freshly exposed surface spontaneously bursts into flame. Consequently, suitable fluxes or inert atmospheres must be used when handling molten magnesium and its alloys.

For many years, thinly fluid salt fluxes were used to protect molten magnesium which were mixtures of chlorides such as $MgCl_2$ with KCl or NaCl. In Britain, it was usual to thicken this flux with a mixture of CaF_2, MgF_2, and MgO

which formed a coherent, viscous cake that continued to exclude air and could be readily drawn aside when pouring. However, the presence of the chlorides often led to problems with corrosion when the cast alloys were used in service.

In the 1970s, it became usual to replace the salt fluxes with cover gases comprising either a single gas (e.g., SO_2 or argon), or a mixture of an active gas diluted with CO_2, N_2, or air. Sulfur hexafluoride (SF_6) was widely accepted as the active gas because it is nontoxic, odorless, colorless, and effective at low concentrations. Replacing the fluxes and SO_2 also improved occupational health and safety, and increased equipment life because corrosion was reduced. SF_6 is, however, relatively expensive, and is now realized to be a particularly potent greenhouse gas with a so-called global warming potential (GWP) of 22,000 to 23,000 on a 100-year time horizon. Efforts are therefore being made to find other active gases containing fluorine and one alternative is the organic compound HFC 134a (1,1,1,2-tetrafluoroethane) that is readily available worldwide because of its use as a refrigerant gas. It is also less expensive than SF_6. HFC 134a has a GWP of only 1600, and an estimated atmospheric lifetime of 13.6 years compared with 3200 years for SF_6. Moreover, less is consumed on a daily basis so that the overall potential to reduce greenhouse gas emissions is predicted to be 97%.

Most alloying elements are now added in the form of master alloys or hardeners. Zirconium has presented special problems as early attempts to use either zirconium metal or a Mg–Zr hardener were ineffective. Success was achieved eventually by means of mixtures of reducible zirconium halides, e.g., ones containing fluorozirconate, K_2ZrF_6, together with large amounts of $BaCl_2$ to increase the density of the salt reaction products. These salt mixtures were supplied under license to foundries. Subsequently it was found possible to prepare hardener alloys from the weighted salt mixtures and these proprietary hardeners made in this way were used for adding zirconium to magnesium alloy melts. Prior to the use of $BaCl_2$, severe problems were encountered with persistent flux inclusions which arose through entrainment of salt reaction products in the melt and could not be removed by presolidification or any flux-refining step.

Since the late 1960s, Mg–Zr master alloy hardeners have been the preferred method for introducing zirconium as a grain refiner and these master alloys usually contain between 10% and 60% of zirconium in weight percentage depending on the supplier. Since the approximate maximum solubility of zirconium in molten magnesium is only 0.6% (Fig. 3.11), almost all the zirconium present in the hardener is undissolved. Because of this, the Mg–Zr master alloys have microstructures comprising zirconium or zirconium-rich particles often embedded as clusters in an Mg–0.6Zr matrix. The major difference between the different master alloys lies in the size of the particles and how they are distributed in the matrix.

As with aluminium, hydrogen is the only gas that dissolves in molten magnesium although it is less of a problem in this case because of its comparatively

high solid solubility (average of ~30 ml $100\,g^{-1}$). The main source of hydrogen is from water vapor in damp fluxes or corroded scrap/ingot, so pickup can be minimized by taking adequate precautions with these materials. A low hydrogen content reduces the tendency to gas porosity which is common in Mg–Al and Mg–Al–Zn alloys and these materials should be degassed with chlorine. The optimum temperature for degassing is 725–750°C. If the melt is below 713°C, then solid $MgCl_2$ will form which gives little protection from burning, while at temperatures much above 750°C, magnesium losses through reaction with chlorine become excessive. Gas porosity is not normally a problem with zirconium-containing alloys since zirconium will itself remove hydrogen as ZrH_2 and it is generally unnecessary to degas these alloys. However, it should be noted that such a treatment does improve the tensile properties of certain Mg–Zn–Zr alloys, presumably by minimizing the loss of zirconium as the insoluble ZrH_2. In such a case, the degassing operation is completed before zirconium is added.

3.5.3 High-pressure die casting

Large tonnages of pressure die castings are produced in both aluminium and magnesium alloys because the process is well established with high productivity. Approximately half of all aluminium alloy castings and about 80% of all magnesium alloy castings made worldwide are manufactured in this way and used in the automotive industry and for a wide range of other consumer goods. The castings produced are often housings and other components for nonload-bearing applications that do not require a high degree of structural integrity throughout.

A disadvantage with HPDCs is that they may contain relatively high levels of porosity. This restricts opportunities for using heat treatment to improve their properties because exposure to high temperatures may cause the pores to swell and form surface blisters (e.g., Fig. 4.10). For comparison, sand castings and low-pressure permanent mold castings generally contain less porosity and are used to produce components having more complicated shapes. They can then be heat treated if the alloys respond to age hardening. With permanent mold casting, turbulence can be minimized by introducing the molten metal into the bottom of the mold cavity, under a controlled pressure, thereby allowing unidirectional filling of the mold. This method has features in common with the Cosworth process for producing high-quality aluminium castings (Fig. 3.22).

Aluminium alloys In HPDC, molten aluminium is forced into a steel die through a narrow orifice (or gate) at high speeds ranging from 20 to $100\,m\,s^{-1}$ (Fig. 3.13). This is achieved by means of a piston and cylinder (or hot sleeve) where the piston is driven by a hydraulic ram capable of exerting a pressure of up to 100 MPa on the metal. The aim is to continue feeding the casting as it solidifies

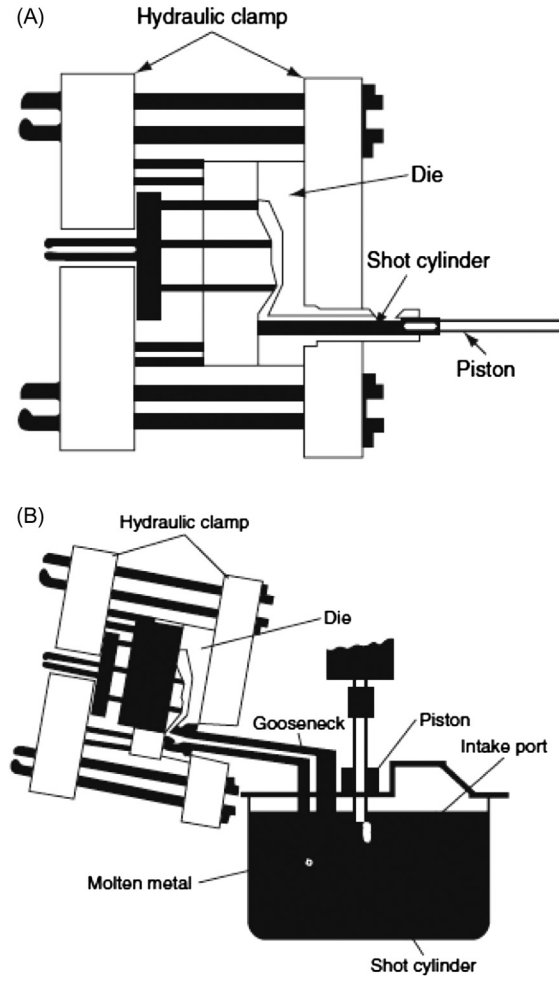


Figure 3.13 (A) Cold-chamber and (B) hot-chamber pressure die casting machines. Courtesy H. Westengen.

rapidly in the die. The following sections address two issues with alloy selection for die casting of aluminium alloys: die soldering and heat treatment.

Die soldering A particular problem with the pressure die casting of aluminium alloys is the tendency for the casting to stick (solder) to ferrous dies during solidification because of the high affinity iron and molten aluminium have for each other. Rapid interatomic diffusion can occur when they come into contact

resulting in the formation of a series of intermetallic compounds at the die surface. Die soldering may prevent automatic ejection of a casting which then has to be removed manually. This can cause delays and serious cost penalties, particularly if die surfaces are damaged and require repair.

Soldering is influenced by several factors:

1. *Die casting alloy composition.* Iron has the greatest beneficial effect and increasing amounts up to saturation level progressively alleviate soldering. For the widely used Al–Si casting alloys, the critical level of iron that is required can be estimated by the empirical relationship:

$$Fe_{crit} \approx 0.075\,[Si\%] - 0.05$$

2. Manganese and small amounts of titanium are also beneficial, whereas the presence of nickel has been found to be detrimental. Magnesium, silicon, and strontium have no significant effect.
3. *Die steel composition.* The plain carbon steel H–13 (Fe–0.35C–0.35Mn) is commonly used. More highly alloyed compositions can better resist attack by molten aluminium but are often not used because of the cost of these steels.
4. *Melt injection temperature.* This should be as low as possible and an upper limit of around 670°C before the molten metal enters the shot sleeve has been found to be critical to minimizing sticking to some die steels.
5. *Use of die surface coatings.* Such coatings can serve as diffusion barriers to the iron–aluminium reaction and thereby retard soldering. A number of coatings are used by the die casting industry and boron-based ceramics have proved particularly effective. Boron nitride deposited by physical vapor deposition (Section 8.7) also provides a barrier providing it is compatible with the steel substrate. An alternative method is to aluminize the surface by immersing the die in molten aluminium at 760–800°C after which it is removed, held for 12–24 h at 300°C to form a controlled layer of iron aluminide, and then the surface is highly polished.

Heat treatment Two features of conventionally produced HPDCs are the extreme turbulence experienced by the molten alloy as it is forced at high speed into a die, and the very rapid rate at which it solidifies. Because of this, the resulting castings usually contain internal pores in which gases such as air, hydrogen, and vapors that are formed by the decomposition of organic die wall lubricants become entrapped. Porosity may also result from metal shrinkage that occurs during solidification. Whereas it is normal to accept some level of porosity in HPDCs, the presence of internal gas-filled pores makes it undesirable to expose them to high temperatures. This follows because the pores expand and may cause both unacceptable surface blistering on components and dimensional instability due to swelling.

As given in Table 5.2, several aluminium alloys used for producing HPDCs are based on the systems Al–Si–Cu and Al–Si–Mg, both of which are amenable to strengthening by age hardening. However, this opportunity has not been exploited because conventional practice has required the alloys to be solution treated for several hours at temperatures around 520°C prior to quenching and ageing. Recently, however, it has been recognized that most of the solute elements copper, magnesium, and to some extent, silicon, dissolve in the α-aluminium grains during the early part of the solution treatment cycle. Because of this, it has been demonstrated that reducing both the solution treatment temperatures and times has enabled commercial HPDCs made from the above classes of alloys to undergo significant age hardening without causing blistering or swelling.

One example of a modified ageing schedule is to solution treat these HPDC alloys at 480°C for 0.25 h, quench into cold water and age to peak strength at 175°C (T6 temper). Fig. 3.14 shows results for HPDC aluminium

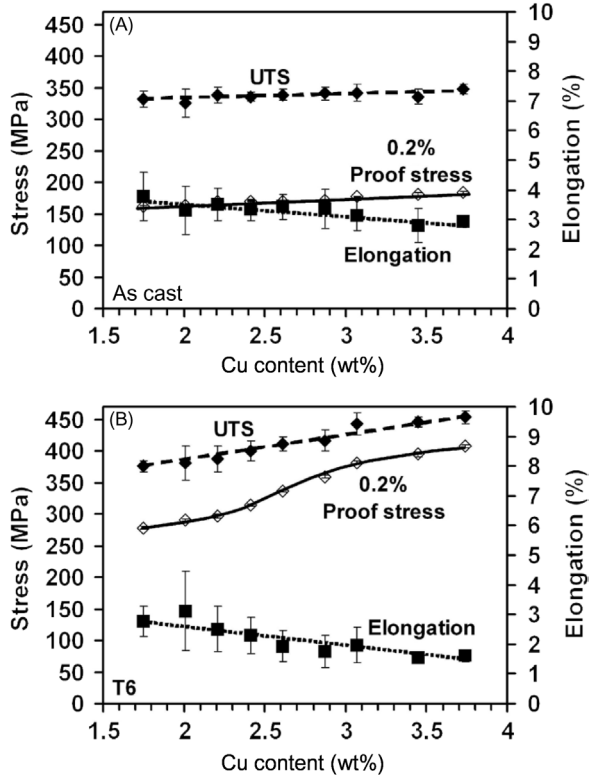


Figure 3.14 Effects of increasing levels of copper on the tensile properties of an HPDC alloy with nominal composition Al–10. 5Si–0.8Fe–0.75Zn–0.22Mg–0.18Mn in the (A) as-cast and (B) T6 age hardened conditions. From Lumley, RN: *Fundamentals of Aluminium Metallurgy*, p. 283, Woodhead Publishing Ltd., Oxford, 2011.

alloys containing 10%Si and 0.7%Mg with Cu levels ranging from 1.7% to 3.7%. Comparisons between the tensile properties in the normal as-cast condition, and after applying this modified age hardening heat treatment, have shown that the 0.2% proof stress can be more than doubled if these HPDC alloys contain more than 2.7% copper. With the absence of surface blistering and swelling, there is the prospect of achieving significant weight savings by redesigning HPDC components to take account of their much higher mechanical strength.

Magnesium alloys Most magnesium alloy components are now produced by HPDC (Fig. 3.13). Cold-chamber machines are used for the largest castings and molten shot weights of 10 kg or more can now be injected in less than 100 ms at pressures that may be as high as 150 MPa. Hot-chamber machines are used for most applications and are more competitive for smaller casting sizes due to the shorter cycle times that are obtainable. Magnesium alloys offer particular advantages for both these processes, namely:

1. Most molten alloys show high fluidity which allows casting of intricate and thin-walled parts, (e.g., 2 mm, Fig. 3.15). Magnesium may be used for castings with thinner walls (1–1.5 mm) than is possible with aluminium (2–2.5 mm) or plastics (2–3 mm).
2. Magnesium has a latent heat of fusion per unit volume that is two-thirds lower than that of aluminium. This means that magnesium castings cool more quickly and die wear is reduced.
3. High gate pressures can be achieved at moderate pressures because of the low density of magnesium.

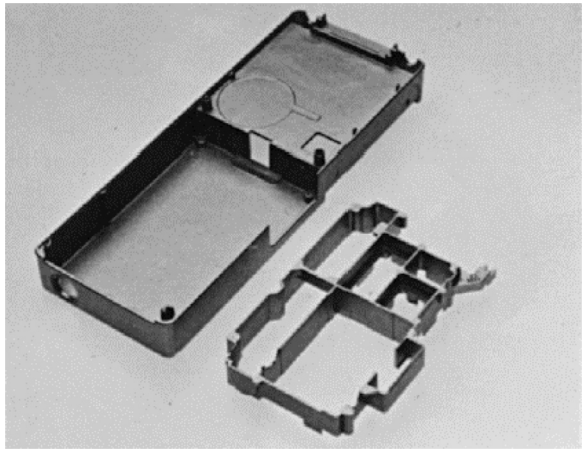


Figure 3.15 Thin-walled magnesium alloy case and chassis for a hand-portable cellular telephone. Courtesy Magnesium Services Ltd, Slough, UK.

4. Iron from the dies has very low solubility in magnesium alloys, which is beneficial because it reduces any tendency to die soldering.

3.5.4 Semi-solid processing

As metals and alloys freeze, the primary dendrites normally grow and intermesh with each other so that, as soon as a relatively small fraction (e.g., 20%) of the melt has frozen, viscosity increases sharply and flow practically ceases. If, however, the dendrites are broken up by vigorously agitating the melt during solidification, reasonable fluidity persists until the solid content reaches as much as 60%. Each fragment of dendrite becomes a separate crystal and very fine grain sizes can be achieved without recourse to the use of grain refiners (Fig. 3.16). Moreover, the semi-solid slurry has thixotropic characteristics, in that viscosity decreases on stirring, and this has interesting implications for casting processes.

In early laboratory studies of semisolid processing, a slurry was produced by agitating an alloy in a narrow, annular region between the furnace wall and a central cylindrical stirrer. A temperature difference was maintained so that the alloy within this region was in the two-phase semi-liquid state, while above it was fully molten. The slurry was then transferred and cast in a pressure die casting machine. The process was known as rheocasting. Slugs of the slurry could also be removed and forged in a die (thixoforging).

Commercialization of the slurry production process presented two major problems. One was the design of a furnace-stirrer system that would provide adequate quantities of slurry. The other was rapid chemical attack and

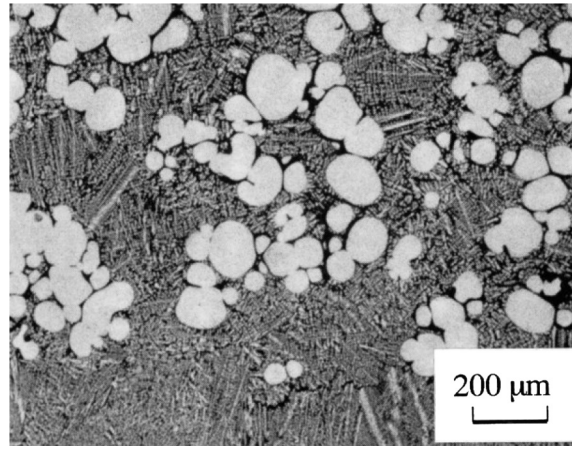


Figure 3.16 Microstructure of the alloy Al–6.5Si sheared at a rate of 180 s^{-1} showing rounded α-Al dendrite fragments of the primary α-Al phase in a matrix of finely dispersed eutectic. From Ho, Y *et al.*: *Nature and Properties of Semi-Solid Materials*, Sekhar, JA and Dantzig, J (Eds.), TMS, Warrnedale, PA, USA, p. 3, 1991.

erosion of materials used for the stirrer. These limitations were overcome with the development of the thixomolding process which was begun by Merton Flemings and his students at MIT and then further developed by the Dow Chemical Company. The technology (Fig. 3.17) is now marketed by Thixomat Pty Ltd, and applied to magnesium alloys predominantly AZ60 and AZ91D. In 2016, there are more than 480 machines worldwide in 13 countries, which range in clamp tonnages from 100 to 1600 tons enabling very large magnesium components such as large screen TV surrounds, to be cast in one piece.

Magnesium alloys are amenable to thixotropic casting which offers the opportunity to produce high-quality fine-grained products more cheaply than by high-pressure die casting. The mechanical properties of thixomolded parts compare well with those obtained with standard HPDC.

Thixomolding is a one-step process which combines plastic injection molding technology with metal pressure die casting (Fig. 3.17). Feedstock in the form of solid alloy pellets is heated to the semisolid temperature (~20°C below the liquidus temperature) to achieve 5–15% solid fraction and then sheared by a high torque screw drive) into a thixotropic state in a screw feeder before passing directly into the die casting machine. Very thin sections down to 0.7 mm thickness can be cast. An example of a thin-walled casting produced by thixomolding is shown in Fig. 3.18. An advantage of this process is that oxidation of the molten alloy is easily prevented by maintaining an inert atmosphere in the relatively small entry chamber (Fig. 3.17). Other advantages include reduced microporosity, prolonged die lives because heating and cooling cycles are less extreme, and there is no need for a furnace to melt the magnesium alloys prior to casting.

It has been demonstrated that thixoforming of rechipped sprues, gates, runners, and scrapped parts results in mechanical properties comparable to virgin

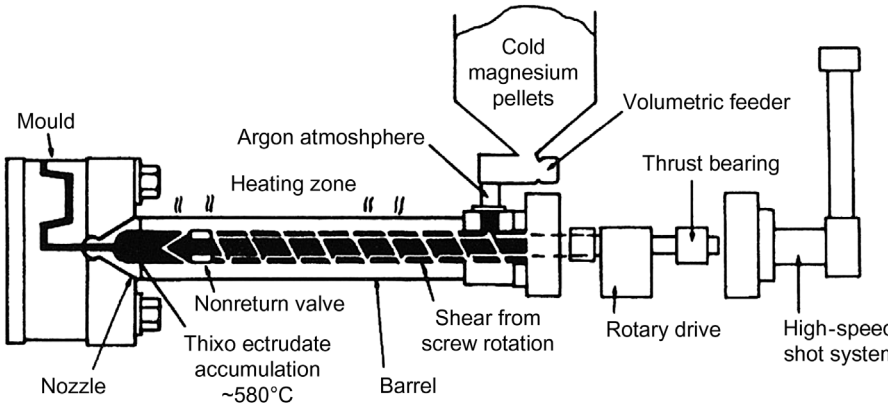


Figure 3.17 Schematic of a thixomold machine for producing die cast magnesium alloy components. Courtesy Thixomet Inc.

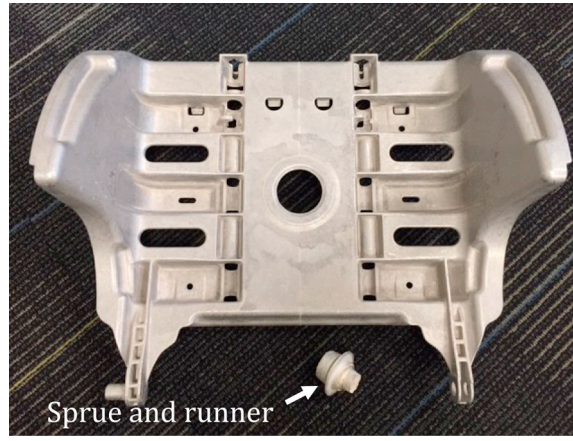


Figure 3.18 Child's safety auto seat manufactured by Molded Magnesium Products, 1.4 kg part thixomolded with a hot long nozzle enabling miniature sprue and runner and 95% metal yield, 430 mm × 380 mm × 178 mm, 2–5 mm section thickness. Courtesy Ray Decker, Thixomat, Inc/nanoMAG LLC.

Table 3.2 Comparison of thixomolded AZ91D from recycled scrap to that from virgin chips

% Recycled scrap	YS (MPa)	UTS (MPa)	Elongation (%)
100	167	254	6.1
50	167	263	6.5
10	162	256	7.0
0 (virgin)	145–169	230–299	6–8

Courtesy Ray Decker, Thixomat, Inc/nanoMAG LLC.
YS, yield strength, UTS, ultimate tensile strength.

granules (Table 3.2). Also, high-quality melt-recycled magnesium alloy chips are now available in commercial quantities.

Semi-solid processing offers the following advantages:

1. Significantly lower capital investment and operating costs when compared with conventional casting methods. The whole process can be contained within one machine so that the need for melting and holding furnaces as well as melt treatment are all avoided. Foundry cleanliness is easy to maintain and energy requirements are less because complete melting is not required, cycle times are reduced, and scrap is minimized.
2. Shrinkage and cracking within the mold are reduced because the alloy is already partly solidified when cast.
3. Lower operating and pouring temperatures lead to an increase in the life of metal dies.

4. Composite materials can be readily produced by adding fibers or other solid particulates into the feedstock (compocasting).

The uptake of rheocasting and thixocasting has been limited but examples of automotive components in current production are master brake cylinders, and pistons and compressors for air conditioners where high structural integrity and pressure tightness is required. Thixomolding has been more successful commercially especially for magnesium alloys. It is ideal for the casting of thin components such as mobile phone and laptop computer casings and automotive components (e.g., Fig. 3.18).

3.5.5 Squeeze casting

This process involves working or compressing the liquid metal in a hydraulic press during solidification which effectively compensates for the natural contraction that occurs as the liquid changes to solid. Pressures around 200 MPa are used which is several orders of magnitude greater than the melt pressures experienced in conventional foundry practice. As a consequence, the flow of the melt into incipient shrinkage pores is facilitated and entrapped gases tend to remain in solution. The high pressure also promotes intimate contact between casting and mold walls or tooling which assists heat extraction thereby leading to refinement of the microstructure. Squeeze casting has also been used to prepare higher-quality castings from existing alloys and to produce castings in alloys that could not be successfully cast by conventional processes.

Squeeze casting may be carried out in what are known as direct and indirect machines. In direct squeeze casting, metered amounts of molten metal are poured into a die similar to that used in permanent mold casting and then pressure is applied to the solidifying metal via the second, moving half of the die. For the indirect method, molten metal is first poured into a shot sleeve and then injected vertically into the die by a piston which sustains the pressure during solidification. In both cases, a high casting yield is obtained because runners and feeding systems are not required so that virtually all the molten metal enters the die cavity. Casting mass may vary from 200 g to 35 kg depending upon the capacity of the machine.

Squeeze casting has been used for half a century in Russia and is now being exploited in other countries, notably Japan. For example, the Toyota Motor Company in Japan introduced squeeze-cast aluminium alloy wheels into their product line for passenger cars in 1979. An indication of the potential of this technique is evident from Table 3.3, in which a comparison of the properties of the alloy 357 (Al–7Si–0.5Mg) prepared by sand, gravity die, and squeeze casting shows the latter clearly to be superior. Here the properties in each case are influenced mainly by the different levels of porosity, with improvements in ductility being particularly notable. GKN have developed their squeeze-forming process for the manufacture of aluminium wheels for demanding defense applications. The squeeze-formed wheels are 35% lighter than standard cast wheels and offer increased endurance four times that of a typical traditionally forged steel armoured fighting vehicle wheel.

Table 3.3 Mechanical properties of 357 aluminium alloy produced by different casting processes

Process	0.2% Proof stress (MPa)	Tensile strength (MPa)	Elongation (%)
Sand cast	200	226	1.6
Chill cast	248	313	6.9
Squeeze cast	283	347	9.3
Cosworth	242	312	9.8

From Lavington, MH: *Metals Mater.*, 2, 713, 1986.

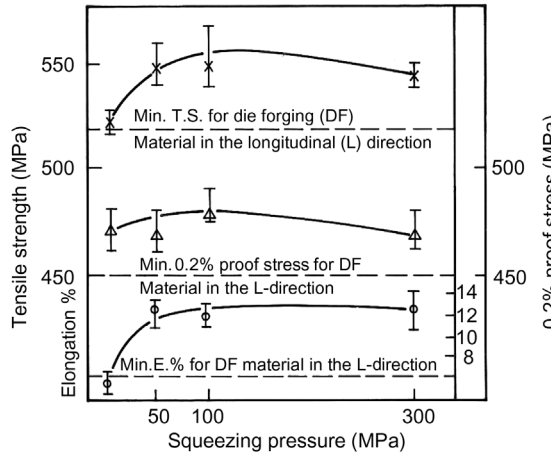


Figure 3.19 Tensile properties of squeeze-cast alloy 7010 as a function of squeeze-casting pressure. From Chadwick, GA: *Metals Mater.*, 2, 693, 1986.

Another advantage is that it is possible to squeeze cast some complex, high-strength alloys that are normally produced only as wrought products. For example, the Al–Zn–Mg–Cu aircraft alloy, 7010, has been successfully squeeze cast and, after a T6 ageing treatment, the minimum required properties for the wrought (die forged) condition are easily met (Fig. 3.19). A feature of the squeeze-cast material is that the casting has isotropic properties, whereas wrought products always suffer from directionality effects (see Fig. 2.42). What is also interesting is that the *S–N* curves obtained in fatigue tests on squeeze cast 7010 lie within the scatter band for wrought materials, whereas castings normally have much poorer performance (Fig. 3.20).

Properties may be further enhanced by incorporating fibers or particulates into squeeze-cast alloys, thereby producing the metal matrix composites that are discussed in the Section 8.1.3. In this regard, squeeze casting is superior to other low-pressure techniques for infiltrating liquid metal into a mesh or pad of fibers which has been a major limitation in the past. An advantage of such composites is that the fibers can be confined to strategic locations in castings where there is a need for increased strengthening or wear resistance. One recent example is the fiber reinforcement of regions of aluminium alloy pistons for cars that are now manufactured commercially.

3.5.6 Gravity and low-pressure casting processes

Gravity and permanent molds are usually machined or cast from steel or iron, that are fed either by gravity or by using low-pressure air or other gas to force the metal up the sprue and into the mold. Sand cores may be added to make hollow castings or cooling/air channels. Gravity casting is often used for short runs in castings for aftermarket or replacement components or special one-off components. For large campaigns of hundreds of castings, low-pressure die casting (Fig. 3.21) is used where consistent properties are required for

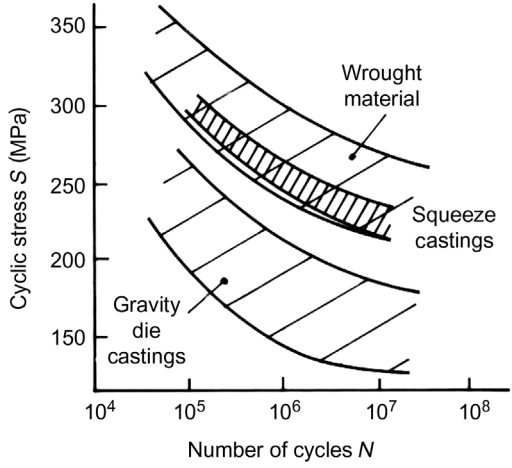


Figure 3.20 Fatigue (*S–N*) curves for alloy 7010 in wrought, gravity die cast, and squeeze-cast conditions. From Chadwick, GA: *Metals Mater.*, 2, 693, 1986.

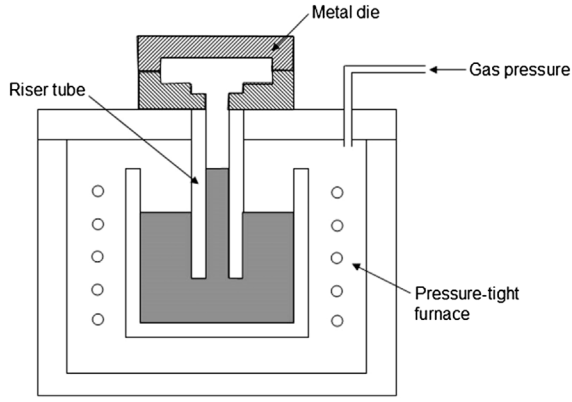


Figure 3.21 Schematic of low-pressure die casting machine. From *Fundamentals of Aluminium Metallurgy: Production, Processing and Applications*, p. 150, Lumley, R (Ed.), Woodhead Publishing Limited, Oxford, 2011.

load-bearing applications such as aluminium wheels. Low-pressure die casting allows controlled flow of the molten metal with low turbulence to enter the mold from a holding furnace underneath the mold. Although productivity is significantly lower than HPDC, the quality of the castings is far superior. The metal dies need to be monitored for wear and attached dross to ensure a good surface finish is achieved. Casting design is also crucial to ensure solidification occurs toward the hottest part of the casting so that all parts of the casting are fed to account for shrinkage. The holding furnace below the mold needs attention to ensure the melt is free from dross and does not accumulate too much grain refiner such as TiB_2 particles which tend to sink in the relatively quiescent environment.

3.5.7 Sand and precision sand casting processes

Sand casting Sand casting is one of the oldest casting methods and the subject is so large that only a brief description will be given here. Many ferrous and aluminium alloys are cast in sand molds. The process has been developed with various degrees of automation, but the traditional practice is still used for short runs and prototyping.

A mold pattern consisting of the die cavity, pouring basin, sprue, sprue well, runner and gates, and risers for feeding is often made of wood and designed so that sand can be readily packed around the pattern. The sand is usually processed with binders to give it strength and plasticity. Once the sand is sufficiently strong, the patterns are removed and the sand molds are put together for casting. Once the melt has been poured into the mold and the casting has solidified, the sand is removed and recycled to various degrees depending on how much sand is damaged/fractured by the high temperatures near the surface layers of the mold cavity.

Magnesium engine blocks have been made for some high-performance vehicles. However, due to the reactivity of magnesium, many precautions are needed which make the process unsuitable for most applications other than for highly complex casting designs and low numbers. Magnesium alloys can be successfully sand cast providing some general principles are followed which are dictated by the particular physical properties and chemical reactivity of magnesium.

1. Suitable inhibitors must be added to the molding sand in order to avoid reaction between molten magnesium and moisture which would liberate hydrogen. For green sand or sand gassed with carbon dioxide to aid bonding, sulfur is used, whereas for synthetic sands compounds such as KBF_4 and $KSiF_6$ are also added. Boric acid is also used for some sands, both as a molding aid and as a possible inhibitor through its tendency to coat the sand grains.
2. Metal flow should be as smooth as possible to minimize oxidation.

3. Because of the low density of magnesium, there is a relatively small pressure head in risers and sprues to assist the filling of molds. Sand molds need to be permeable and must be well vented to allow the expulsion of air.
4. Magnesium has a relatively low volumetric heat capacity which necessitates provision of generous risers to maintain a reservoir of hotter metal. Because of this need to make special provision by way of risers and other feeding devices, the volume ratio of poured metal to actual castings may average as much as 4:1 for magnesium alloys.

A variation on mold pattern manufacture was to use polystyrene which volatilizes when in contact with the melt. This process is referred to as lost foam or evaporative casting. This method enables the pattern to remain in situ during casting but a downside has been the turbulence caused by the conversion of the foam into gas. Recent advances have led to 3D printing of the pattern which is a major advantage for the manufacture of complex mold patterns and is a cost-effective method of undertaking prototype casting trials.

For complex castings such as an engine block with thin cooling channels, sand cores are made and placed within the mold cavity at appropriate locations. Due to their delicate nature, they need to be strong enough for placement and to resist metal flow. For mass production, this process is too labor intensive and better control and automation are needed to produce complex castings of high integrity. Two such methods which are used commercially are the Cosworth process and the improved low-pressure casting (ILP) process.

Cosworth process Conventional methods for casting aluminium and its alloys all involve turbulent transfer which has the undesirable effect of dispersing fine particles, oxide films, and other inclusions through the melt. Such particles and films are known to act as nuclei for the formation of microporosity in solidified castings.

The Cosworth process allows quiescent transfer of metal from the stage of melting of the ingots to the final filling of the mold (Fig. 3.22). The melting/

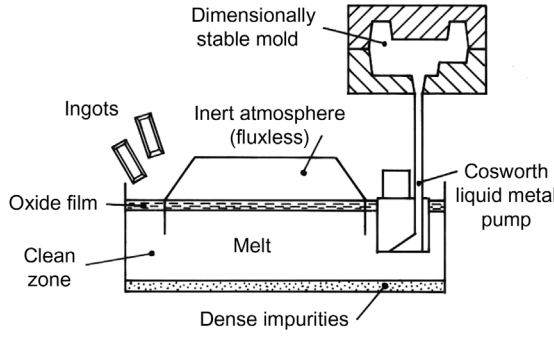


Figure 3.22 Diagrammatic representation of a casting unit using the Cosworth process. From Lavington, MH: *Metals Mater.*, 7, 213, 1986.

holding furnace has sufficient capacity to ensure that the dwell time for the alloy between melting and casting is long enough to allow oxide particles or inclusions to separate by floating or sinking. No fluxes or chemicals are used and a protective atmosphere is employed to minimize the risk of gas absorption and oxide formation. A unique feature of the process is that the mold is located above the furnace and gently filled with molten metal from below by a programmable electromagnetic pump which, itself, has no moving parts. The mold is permeable to allow air to escape from the cavity. The mold is then rolled over under an applied positive pressure immediately after filling. This practice further improves the quality of castings and allows higher production rates to be achieved. Taken overall, the generation and entrapment of oxide particles is minimized. Porosity is much reduced and this is reflected in improved tensile properties and ductility when compared with conventionally produced sand castings (Table 3.3). Fatigue properties at both room and elevated temperatures are also superior and scatter in the test results is much reduced.

Another feature of the Cosworth process is the use of reclaimable zircon sand rather than conventional silica for making molds and cores. This avoids the volume change associated with the phase transition from α to β quartz that occurs in silica at temperatures close to those used for melting aluminium alloys. The stability of both molds and cores is thus much improved which allows close dimensional tolerances of castings to be obtained and repeated. For example, within one mold piece, it is possible to apply tolerances of ±0.15 mm up to sizes of 100 and ±0.25 mm up to 800 mm. This feature, when combined with the greatly reduced porosity, allows thin-walled, pressure-tight castings to be produced. These have proved particularly beneficial in the manufacture of complex cylinder heads and other engine components for high-performance motor cars (e.g., Fig. 3.23). Size ranges of castings have so far been within the range 0.5–55 kg and integrated production lines have been established.

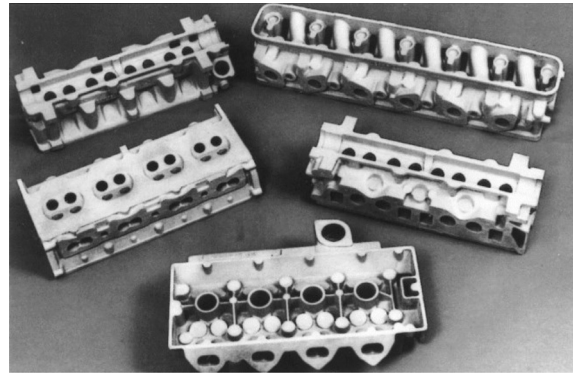


Figure 3.23 Cylinder head castings produced by the Cosworth process. Courtesy Cosworth Research and Development Ltd.

ILP Process Another precision casting method that utilizes the transfer of molten metal vertically up a riser tube into the bottom of the mold cavity is the ILP process developed in Australia. Degassed and filtered metal is delivered to the casting furnace, which uses a pressurized atmosphere of nitrogen to enable quiescent, computer-controlled filling of the mold. Once filled, the mold is sealed and immediately removed so that solidification occurs remote from the casting section. This allows another preassembled mold to be positioned on the station which facilitates high productivity, and cycle times of around 60 s become possible.

As shown in Fig. 3.24, a special feature of the ILP process is the use of a combination of thermal (metal) cores and resin-bonded silica sand for the mold which promotes rapid unidirectional solidification in those regions of the casting where optimal properties are required. Furthermore, the mold can be inverted to facilitate this controlled solidification, which may provide dendrite arm spacings less than 20 μm adjacent to the metal cores, and less than 0.5% microshrinkage overall.

The ILP process has been adapted to allow robotic handling of the molds so that movements are precisely repeatable. The benefits of the Cosworth and ILP processes have been further developed by Nemak into their low-pressure precision sand process for the mass production of cylinder heads and blocks for engines of some models of automobiles that are manufactured for the European and North American markets.

3.6 NEW CASTING PROCESSES

3.6.1 T-Mag

The T-Mag process was developed by CSIRO (the Commonwealth Scientific and Industrial Research Organisation in Australia) to enable permanent mold

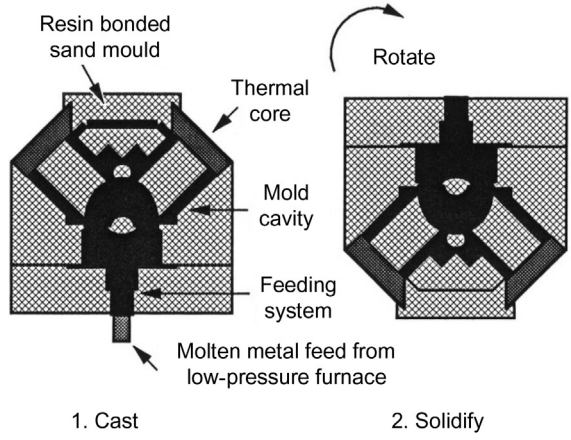


Figure 3.24 Diagrammatic representation of the ILP process. Courtesy Comalco Aluminium Ltd.

casting of magnesium alloys. The process, Fig. 3.25A, is contained within a protective atmosphere and the melt is gently poured to fill the die cavity from the bottom to reduce turbulence and oxide formation. The die cavity and melt transfer tube are rotated during filling so that the transfer tube is at the top of the casting to enhance feeding. Once solidification reaches the gate, the machine rotates back, the casting is ejected when sufficiently strong, and the cycle begins again. As the system is enclosed, cover gas consumption is minimized.

Benefits of the T-Mag process are lighter and stronger components allowing further weight reduction compared to traditional casting processes. An example component is shown in Fig. 3.25B.

3.6.2 Ablation casting

Ablation casting is a relatively new sand casting process where the sand is eroded away by powerful water jets which allows for a rapid increase in cooling rate while solidification occurs. The sand binder is water soluble and the process can be applied to large or small and thick or thin section castings. It has mainly been applied to aluminium alloys but should be suitable for other alloys such as magnesium with good process control. Ablation casting has been tested on magnesium alloy automotive control arm prototypes with some success. Honda applied the process to cast aluminium "large ultra-rigid nodes" for application in the crush zone of a car body. The nodes connect aluminium extrusions which are welded together as part of the spaceframe. This approach achieved the required energy absorption properties where conventional castings would have been too brittle.

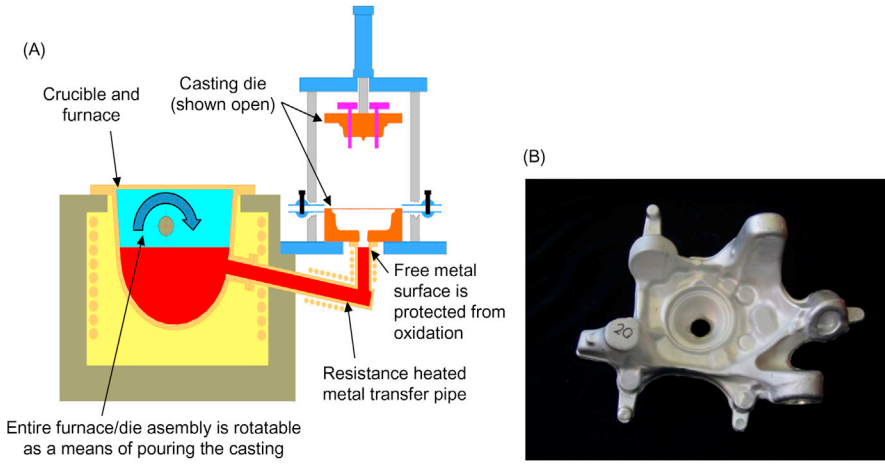


Figure 3.25 (A) Schematic of the T-Mag process and (B) as-cast passenger vehicle front suspension mount made by the T-Mag process. (A) From Wang, L *et al.*: *Metal Casting Design and Purchasing*, July/August, p. 30, 2011. (B) Courtesy G. de Looze, CSIRO and S. Groat, T-Mag Pty Ltd.

3.6.3 Application of external fields

The application of external fields to molten melt above the liquidus temperature or during cooling through the nucleation stage of solidification has attracted considerable attention over recent decades as a means to produce a very fine as-cast grain size (<100 μm) and as a means to produce nanocomposite materials. Several methods have been developed and three examples are presented that represent mechanical, ultrasonic, and magnetic fields.

Melt conditioning Melt conditioning is a process developed at Brunel University, London, where the melt is intensively sheared before entering the casting (Fig. 3.26). High shear is generated by a rotor/stator type mechanism, which comprises a stationary stator and a high-speed rotor capable of rotating at speeds of up to 10,000 rpm generating a shear rate of up to $10^5\,s^{-1}$. The process appears to shear and possibly wet oxide films or agglomerates and the resulting finer particles are well dispersed throughout the melt. The particles then act as nucleant particles for the formation of the primary phase of aluminium and magnesium alloys. The additional nucleation produces a highly refined microstructure. Recycled AZ91 magnesium alloy was treated by CSIRO using the melt conditioning device shown in Fig. 3.26 resulting in substantial grain refinement and a significant improvement in strength and elongation. Therefore, the high shear device can be used for physical grain refinement by dispersing naturally occurring oxides; for efficient degassing of aluminium melts from dissolved hydrogen; for the preparation of metal matrix composites; and also for preparation of semisolid slurries.

The melt conditioning technology has been applied to conventional casting processes such as ingot casting, sand casting, low- and high-pressure die

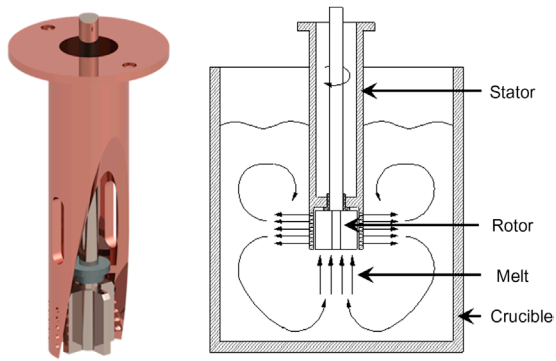
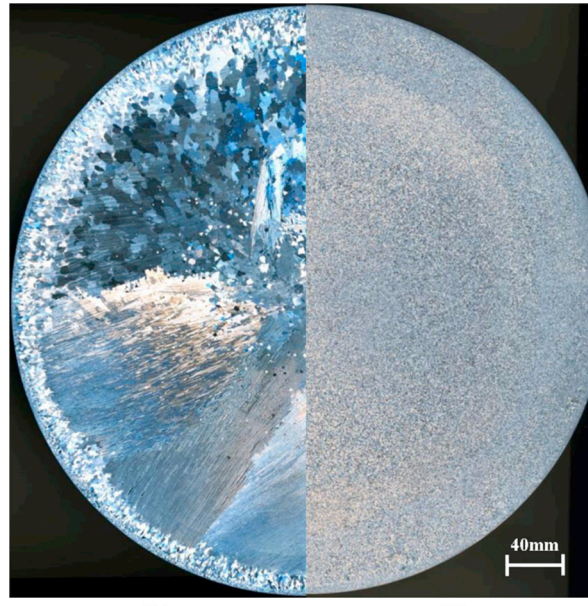


Figure 3.26 The newly developed rotor/stator type high shear device for conditioning of Al and Mg alloys melts by application of intensive melt shearing. Courtesy J. Patel and Z. Fan, BCAST, Brunel University, London.

casting, twin-roll casting, and DC casting, obtaining good refinement without the need for chemical grain refiner addition. Fig. 3.27 shows the dramatic reduction in grain size of a DC cast aluminium alloy billet when melt conditioning is applied.

Ultrasound and magnetic fields Although ultrasonic treatment is not new, there has been significant activity over the last decade in developing approaches to reduce the grain size well below that produced by conventional casting methods, even when grain-refining master alloys are added. As well as stimulating grain refinement, these processes show promise for manufacturing metal matrix nanocomposite materials. Fig. 3.28A is a simulation mesh of an ingot with an ultrasonic sonotrode submerged into the top of the melt. Underneath the sonotrode, a dark region is marked indicating the cavitation region.

Ultrasonic treatment has been studied for many years with limited industrial take-up. Most research has been undertaken on ultrasonic treatment of aluminium and magnesium alloys where ultrasonication above the cavitation threshold has proved to be an effective structural-refining method for metallic alloys. For example, high-intensity ultrasonication can increase the grain density



(A) (B)

Figure 3.27 Macrostructure of the cross section of an A6063 Al-alloy billet without the addition of chemical grain refiner, 205 mm diameter and 2 m length (A) DC cast and (B) melt conditioned and DC cast. From Patel, JB *et al.*: *Mater. Sci. Forum*, 794–796, 149, 2014.

enormously from about 15 grains mm^{-3} (grain size: ~500 μm) for Al–Mg–Zr alloys to ~3×10^4 grains mm^{-3} (grain size: ~40 μm).

Two basic mechanisms of grain formation have been proposed: cavitation-enhanced heterogeneous nucleation and dendrite fragmentation. Direct and indirect evidence produced to date shows that fragmentation occurs when the treatment is applied to the semisolid mixture but it may not make a significant contribution to the density of successful nucleation events thus favoring cavitation-enhanced nucleation.

Fig. 3.28B is a simulation of convection generated by acoustic streaming which is produced by the high-frequency vibrations of the sonotrode. Recent research has highlighted the importance of acoustic streaming. This process enables fast thermal equilibration throughout the melt. The very low-temperature gradient means that nearly all of the melt is undercooled to the same amount at the same rate. The newly formed grains of low solid fraction within the semisolid state thus remain stable and are transported throughout the melt by the vigorous convection resulting in a fine and uniform as-cast grain size.

Similarly, research on the application of pulsed currents to aluminium alloys showed that the nuclei are formed at the top of the casting and, due to thermal

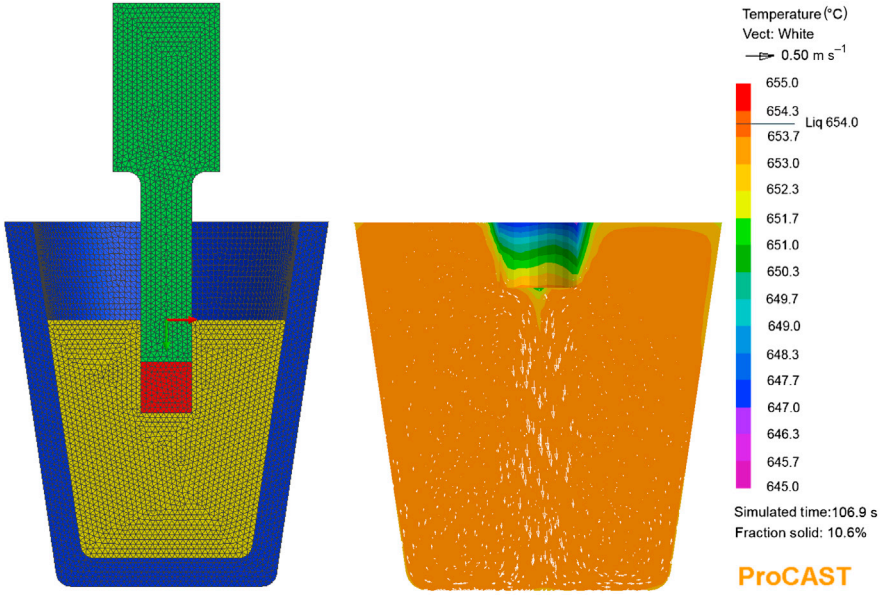


Figure 3.28 ProCAST simulation: (A) a meshed experimental arrangement for ultrasonic treatment of alloys and (B) a simulation of the flow pattern within the melt due to vigorous convection generated by acoustic streaming from the vibrating tip of the sonotrode. Courtesy G. Wang, The University of Queensland.

currents and gravity, the nuclei are distributed throughout the casting. The nuclei are formed when the pulses are applied during nucleation and not during the growth phase. Recent work on pulsed magnetic oscillation (illustrated in Fig. 3.29) of a pure aluminium melt applied from above to just below the melting point was able to generate equiaxed grains throughout most of the cast ingot. In order to be able to do this, the whole melt must be slightly undercooled and the cooling rate must be slow enough to allow time for growth and transport of grains throughout the melt. With good control, this can be achieved due to the action of acoustic streaming causing rapid convection and therefore rapid heat transfer generating a very low-temperature gradient.

A theoretical analysis has indicated that cavitation-enhanced nucleation on existing nucleants is driven by increased undercooling due to the pressure pulse from the collapse of cavities. In addition to affecting the nucleation rate, cavitation may enhance wetting of inoculants, deagglomeration of particle clusters, and mass transport in the melt.

Recently it has been shown that solute plays a major role in controlling the as-cast grain size when ultrasonic treatment is applied and this is illustrated in Fig. 3.30. It was shown that significant ultrasonic grain refinement occurs only in the presence of adequate solute and that the effectiveness of ultrasonic treatment increases with increasing solute content. For instance, under identical ultrasonication and solidification conditions, the resulting grain density in a 70-mm diameter pure Mg (99.98%) ingot reached only about 60 grains mm^{-3}, compared with about 5600 grains mm^{-3} in binary Mg–9Al and about 5700 grains mm^{-3} in commercial AZ91 (Mg–9Al–1Zn). The role of solute has since been verified on Al alloys and Mg–Al alloys.

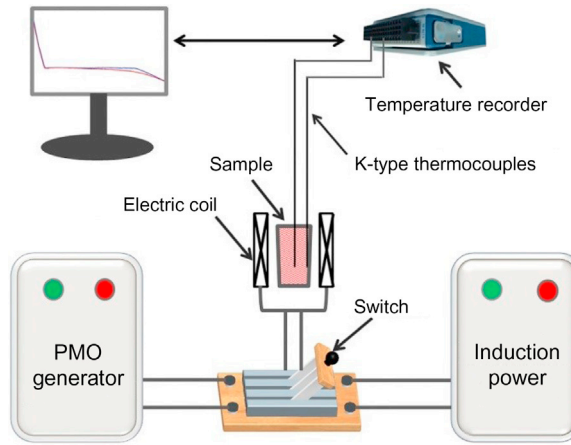


Figure 3.29 Schematic diagram of the pulsed magnetic oscillation (PMO) experimental apparatus. From Liang, D *et al.*: *Mater. Lett.*, 130, 48, 2014.

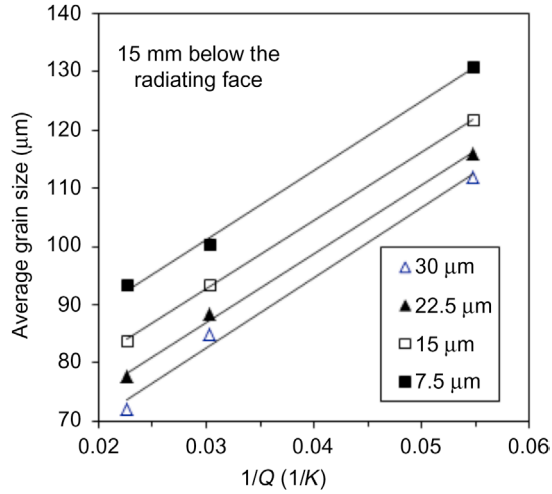


Figure 3.30 Grain size vs 1/*Q* (the inverse of the *Q* values for the range of Mg–Al alloy compositions corresponding to AZ31, AZ61, and AZ91), subjected to ultrasonic amplitudes between 7 and 30 μm. From Ma, Q and Ramirez, A: *J. Appl. Phys.*, 105, 013538, 2009.

3.6.4 Twin-roll casting of magnesium

Ingots for producing wrought products have mainly been cast in permanent metal molds. However, due to a demand for magnesium alloy sheet and extrusions, more attention is being given to semicontinuous DC methods which are broadly similar to those described for aluminium alloys (Section 4.1.1). Following extensive pilot scale trials, a vertical DC caster for magnesium alloys has been constructed in Austria that is capable of producing extrusion billets with a maximum weight of 4000 kg. Smaller, horizontal DC casters have also been developed.

For the conventional production of magnesium alloy sheet, cast ingots are usually produced with dimensions up to 0.3 m × 1 m × 2 m. These ingots are homogenized (e.g., at 480°C) for several hours, scalped, and hot rolled in stages in a reversing hot mill to a thickness of 5–6 mm. The sheet is then annealed (e.g., at 340°C) before each subsequent rolling pass which reduces the thickness by only between 5% and 20% because of the hexagonal crystal structure of the alloys. This latter part of the rolling process is costly and time consuming so that the current usage of magnesium alloy sheet worldwide is limited. This makes the prospect of strip casting an attractive alternative if sheet can be cast to near final thickness and given a final finish roll. Casting of magnesium sheet does, however, present some additional problems apart from the tendency of the molten metal to oxidize with the danger of catching fire. These problems arise because magnesium alloys freeze faster than aluminium alloys and generally have longer freezing ranges which makes as-cast sheet more prone to

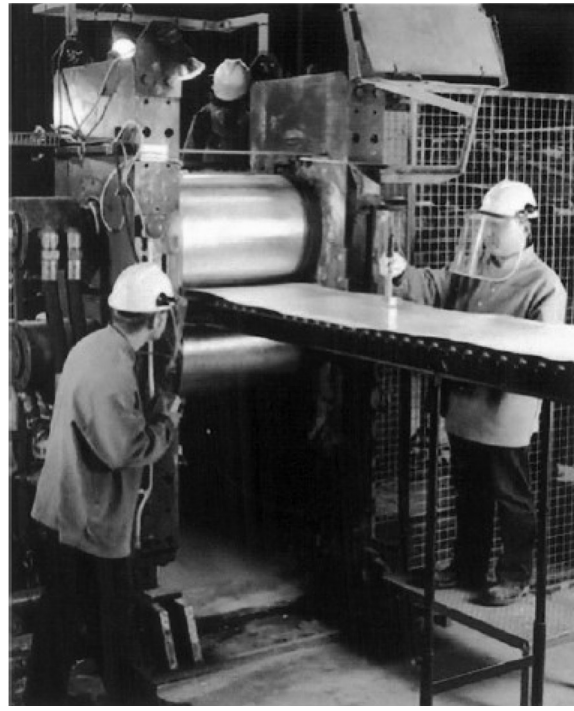


Figure 3.31 Pilot plant for twin-roll casting of magnesium alloys. Courtesy D. Liang, CSIRO Manufacturing, Melbourne.

surface defects and internal segregation. Nevertheless, some success has been achieved through the adaption of twin-roll casting practices developed for strip casting aluminium alloys. As an example, Fig. 3.31 shows a pilot plant that can directly cast a range of magnesium alloys as sheet up to 600 mm wide which has a thickness of 2.5 mm that can be further reduced down to 0.5 mm using a conventional finishing mill.

3.7 JOINING

Most aluminium casting alloys can be arc welded in a protective atmosphere of an inert gas, e.g., argon, provided they are given the correct edge preparation. Ratings of weldability are included in Table 5.3. In addition, some surface defects and service failures in sand and permanent mold castings may be repaired by welding. Filler metals are selected which are appropriate to the compositions of alloy castings with 4043 (Al–5Si) and 5356 (Al–5Mg–0.1Mn–0.1Cr) being commonly used. Special care must be taken when repair welding cast components such as automotive wheels that have previously been heat treated. Unless an appropriate reheat treatment schedule is available, this

process should be avoided. With respect to joining of castings by brazing, similar conditions apply to those discussed for wrought aluminium alloys in Section 4.5.2.

FURTHER READING

Kelton, KF and Greer, AL: *Nucleation in Condensed Matter: Applications in Materials and Biology*, Elsevier, Amsterdam, ISBN: 978-0-08-042147-6, 2010.

StJohn, DH, Prasad, A, Easton, MA and Qian, M: The contribution of constitutional supercooling to nucleation and grain formation, *Metall. Mater. Trans A.*, 46, 4868, 2015.

Flemings, MC: *Solidification Processing*, McGraw-Hill, New York, NY, USA, 1974.

Kurz, W and Fisher, DJ: *Fundamentals of Solidification*, Trans Tech Publications, Switzerland, 1986.

StJohn, DH, Easton, MA, Qian, M and Taylor, JA: Grain refinement of magnesium alloys: a review of recent research, theoretical developments and their application, *Metall. Mater. Trans. A*, 44(7), 2935, 2013.

Campbell, J: *Complete Casting Handbook: Metal Casting Processes, Techniques and Design*, Elsevier Ltd, 2011.

Dantzig, JA and Rappaz, M: *Solidification*, EPFL Press, Switzerland, 2009.

Lumley, R, (Ed.): *Fundamentals of Aluminium Metallurgy: Production, Processing and Applications*, Woodhead Publishing Limited, Oxford, 2011.

Grandfield, J, Eskin, D and Bainbridge, I: *Direct-Chill Casting of Light Alloys: Science and Technology*, John Wiley & Sons, Hoboken, NJ, USA, 2013.

Charles, JA Greenwood, GW, and Smith, GC, (Eds.): *Future Developments of Metals and Ceramics*, Institute of Materials, London, 179, 1992.

Taylor, JA: Metal-related castability effects in aluminium foundry alloys, *Cast Metals*, 8, 225, 1995.

Pehlke, RD: Computer simulation of solidification processes—the evolution of a technology, *Metall. Mater. Trans. A*, 33A, 2251, 2002.

Makhlouf, M and Guthy, HV: The aluminium–silicon eutectic reaction: mechanisms and crystallography, *J. Light Metals*, 1, 199, 2001.

Shankar, S and Apelian, D: Mechanism and preventative measures for die-soldering during Al casting in a ferrous mould, *JOM*, 58(8), 47, 2002.

Couper, MJ, Neeson, AE and Griffiths, JR: Casting defects and the fatigue behaviour of an aluminium casting alloy, *Fatigue Fract. Eng. Mater. Struct.*, 13, 213, 1990.

Lavington, MH: The Cosworth process—a new concept in aluminium alloy casting production, *Metals Mater*, 2, 213, 1986.

Kirkwood, DH: Semisolid processing, *Inter. Mater. Rev.*, 39, 173, 1993.

Sekhar, JA and Dantzig, J, (Eds.): *Nature and Properties of Semi-Solid Materials*, TMS, Warrendale, PA, USA, 1991.

Qian, M and Ramirez, A: An approach to assessing ultrasonic attenuation in molten magnesium alloys, *J. Appl. Phys.*, 105, 013538, 2009.

Bosworth, J: Repair welding of aluminium castings, *Mod. Cast.*, 74, No. 4, p. 19(3), 32, 1984.

4

WROUGHT ALUMINIUM ALLOYS

As a general average, 75–80% of aluminium is used for wrought products, e.g., rolled plate (>6 mm thickness), sheet (0.15–6 mm), foil (<0.200 mm), extrusions, tube, rod, bar, and wire. These are produced from cast ingots, the structures of which are greatly changed by the various working operations and thermal treatments. Each class of alloys behaves differently, with composition and structure dictating the working characteristics and subsequent properties that are developed. Relationships between the various wrought alloy systems are summarized concisely in Fig. 4.1. Before considering each system individually, it is desirable to examine how wrought alloys are produced and processed.

4.1 PRODUCTION OF WROUGHT ALLOYS

4.1.1 Melting and casting

Ingots are prepared for subsequent mechanical working by first melting virgin aluminium, scrap, and the alloying additions, usually in the form of a concentrated hardener or master alloy, in a suitable furnace. A fuel-fired reverberatory type is most commonly used. As mentioned in Chapter 3, the main essentials in promoting ingot quality are a thorough mixing of the constituents together with effective fluxing, degassing, and filtering of the melt before casting in order to remove dross, oxides, gases, and other non-metallic impurities. Hydrogen is the only gas with measurable solubility in aluminium, the respective equilibrium solubilities in the liquid and solid states at the melting temperature and a pressure of one atmosphere being 0.68 and 0.036 cm^3 per 100 g of metal—a difference of 19 times. Atomic size factors require that hydrogen enters solution in the atomic form and the gas is derived from the surface reaction of aluminium with water vapor:

$$2Al + 3H_2O \rightarrow Al_2O_3 + 3H_2$$

Light Alloys. DOI: http://dx.doi.org/10.1016/B978-0-08-099431-4.00004-X
Copyright © 2017 Ian Polmear, David StJohn, Jian-Feng Nie, Ma Qian.
Published by Elsevier Ltd. All rights reserved.

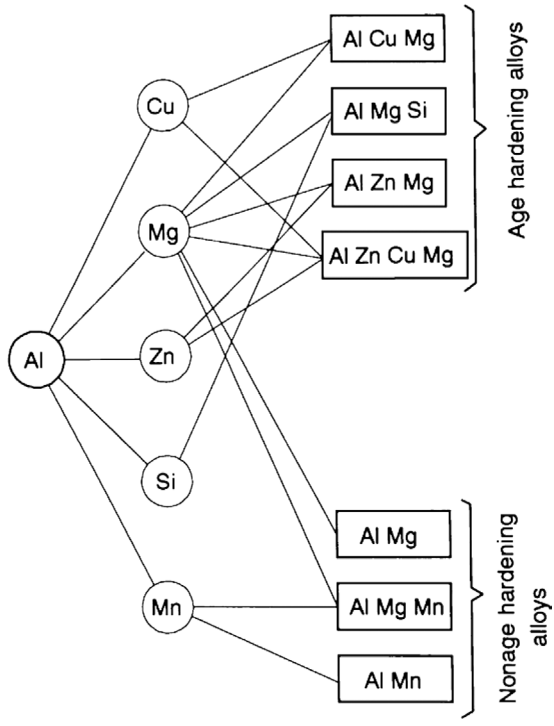


Figure 4.1 Representation of alloying relationships of the principal wrought aluminium alloys. Courtesy D. G. Altenpohl.

The standard free energy change for this reaction is very high (equilibrium constant = 8×10^{40} at 725°C) so that, for practical purposes, all traces of water vapor contacting the metal are converted to hydrogen. The main sources of water vapor are the furnace atmosphere in contact with the molten metal, hydrated surface contaminants, and residual moisture in launders and molds.

During solidification, excess hydrogen is rejected from solution and it recombines as molecular gas that may be entrapped in the solid structure leading to porosity, notably in interdendritic regions. In order to obtain an ingot that is free from gas porosity, it has been found necessary to reduce the hydrogen content of the molten metal to less than 0.15 cm^3 per 100 g. Although hydrogen can escape from molten aluminium by evaporation from the surface, the process is slow and it is common practice to purge by bubbling an insoluble gas through the melt in the reverberatory furnace prior to pouring. Partial pressure requirements cause hydrogen to diffuse to these bubbles and be carried out of the metal. According to circumstances, either nitrogen, argon, chlorine, mixtures of these gases, or a solid chlorinated hydrocarbon can be used. Chlorine is normally present because it serves the important additional function of increasing the surface tension between inclusions and the melt so that they tend to rise to the top and can be skimmed off. However, the use of chlorine does present

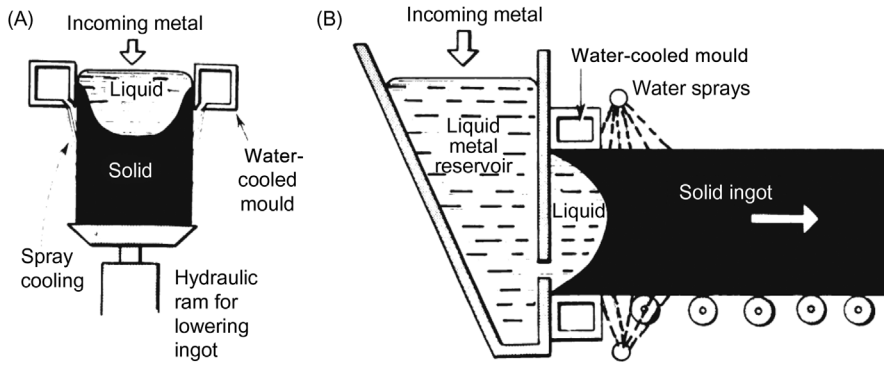


Figure 4.2 DC casting processes: (A) vertical and (B) horizontal.

environmental problems and an example of an alternative method is the continuous, fumeless, in-line degassing process developed by the former British Aluminium Company. In this process, the molten aluminium from the melting furnace enters a vessel through a liquid flux cover (KCl + NaCl eutectic with small amounts of CaF_2). It is then degassed with nitrogen under conditions which do not increase the inclusion content and passes through a bed of balls of Al_2O_3 that become coated with flux and serve to reduce further the content of non-metallic inclusions in the aluminium. This process eliminates the capital and operating costs of fume treatment, as well as the need to hold the aluminium in a furnace while degassing is carried out. Loss of metal as dross is also reduced. Other degassing regimes have been developed, including an Alcoa process that involves injecting a finely dispersed mixture of argon/chlorine bubbles into the molten metal by means of a spinning nozzle. Chlorine contents can be kept at a low level (1–10%) which reduces emissions while maintaining ingot quality. Removal of oxide skins and other undesirable particulate matter is also achieved by filtering the molten metal through a glass cloth on a porous ceramic foam block prior to casting.

The production of a uniform ingot structure is desirable and this is promoted by direct-chill (DC), semi-continuous methods. Most commonly, ingots are cast by the vertical process in which the molten alloy is poured into one, or more fixed, water-cooled molds having retractable bases (Fig. 4.2A). The process of solidification is accomplished in two stages: formation of solid metal around the chilled mold wall and solidification of the remainder of the billet cross section through the removal of heat by submold, spray cooling. Ingots may be rectangular in section for rolling (Fig. 4.3) and weigh as much as 15 tonnes. Round ingots for extrusion are now being DC cast with diameters exceeding 2 m. Several may be produced at once. Similar sections of generally smaller dimensions may be cast in a horizontal (Ugine) arrangement also shown in Fig. 4.2B, although control of microstructure, notably grain size, is more difficult in this process. Maximum section thicknesses are around 650 mm and cooling rates usually lie in the range 1–5°C s^{-1}.

Because fine grain size is so desirable, it is usual to add small amounts of master alloys of Al–Ti, Al–Ti–C, or Al–Ti–B to the melt before casting to promote further refinement. Al–Ti–B is the most widely used alloy with Ti:B ratios varying from 3:1 to 50:1, although Al–5Ti–1B is now the favored composition. These grain refiners used to be introduced to the melt in the form of tablets made from titanium and boron salts. Now they are prepared as small ingots that are added to the melt in the furnace, or as rods which are fed automatically into the launder and dissolved by the molten metal as it passes from the furnace to the casting station. This latter method is preferred because less time is available for the effects of the grain refiner to fade before the ingots have solidified. Despite the commercial importance of this practice, the actual mechanisms of grain refinement by these inoculants have remained uncertain and current theories have been discussed in Chapter 2.

A problem with these DC casting processes is that the surfaces of the ingots tend to be rippled in contour (Fig. 4.3) due to stick-slip contact as they move past the sides of the mold when solidification first occurs. Surface tears and microstructural inhomogeneities such as inverse segregation also tend to occur



Figure 4.3 DC cast ingots for subsequent rolling into plate, sheet, or foil. Courtesy Australian Aluminium Council.

in the surface regions which may cause edge cracking during rolling. For these reasons, it is necessary to machine or scalp the surfaces of DC ingots prior to rolling or extrusion which adds cost to the overall operation.

For vertically cast DC ingots, improved surface quality may be obtained by reducing the rate of heat flow from the solidifying billet to the mold through the use of a narrow stream of high-pressure air directed along the metal/mold interface. Scalping may be avoided altogether by using a novel method of casting in an electromagnetic field that was first invented in the Soviet Union. Further developments have occurred in the United States and elsewhere. In this process, the molten metal is contained and shaped by an internally water-cooled inductor which repels the liquid metal and prevents contact with the sides of the mold. Metal solidification occurs only on the aluminium bottom block or table (Fig. 4.2A). Subsequent solidification is rapid and is achieved by the direct application of water from the coolant jacket on to the ingot shell in the normal way. A very smooth ingot surface is achievable together with a finer and more uniform microstructure. Direct rolling to produce difficult products such as canstock (Section 4.6.5) is possible without scalping which offers economic advantages that outweigh the higher capital investment and energy costs associated with electromagnetic casting.

4.1.2 Continuous casting with moving molds

The concept of the moving mold has revolutionized the casting of some lower-strength aluminium alloys as it is now possible to produce continuous shapes in sizes close to the requirements of the final wrought products. This reduces the investment in the heavy equipment required for subsequent mechanical working. Basic methods for casting bar and sheet are shown in Fig. 4.4 and each offers considerable economic advantage over earlier practices involving

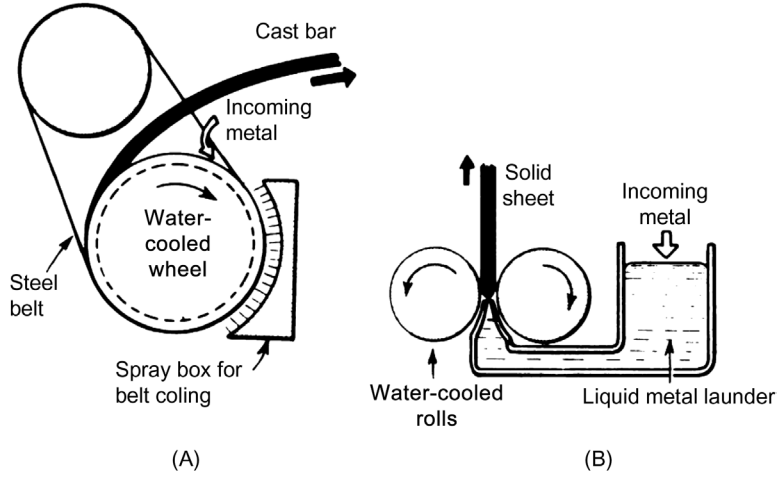


Figure 4.4 Processes for continuously casting bar and sheet in moving molds: (A) Properzi process and (B) Hunter process.

extrusion or rolling of large ingots to small section sizes. Developments with aluminium alloys are now being adapted for the continuous casting of other metals.

The application of continuous casting is expanding, particularly with the production of thin slab and sheet. Two thin slab casting processes are in commercial operation. One involves a block caster, first developed by the former Alusuisse in Switzerland, in which two sets of externally cooled cast iron, steel or copper blocks, rotate continuously in opposite directions on caterpillar tracks, to form the mold cavity into which the molten metal is introduced through an insulated nozzle. The other system has a similar configuration except that flexible steel belts are used (Hazelett process; Fig. 4.5). Molten metal is introduced into the caster via a holding tundish and through a wide ceramic nozzle placed accurately between the moving belts so that turbulence in minimized. The rotating belts are held in tension to form the top and bottom surfaces, and proprietary coatings may be applied continuously to provide specific characteristics to the mold/metal interface. At the same time, gas mixtures are injected to minimize oxidation and the belts are water cooled to enhance heat transfer from the solidifying strip or slab. Side chains made from small rectangular steel blocks, that move with the belts, are spaced to control the width. The strip or slab may range in thickness from around 12 to 75 mm, and up to a maximum designed width of 2.3 m. The mold section is around 2 m long and cooling rates for a 19 mm slab vary for 11–40°C s^{-1} at the surface, to 4°C s^{-1} in the center.

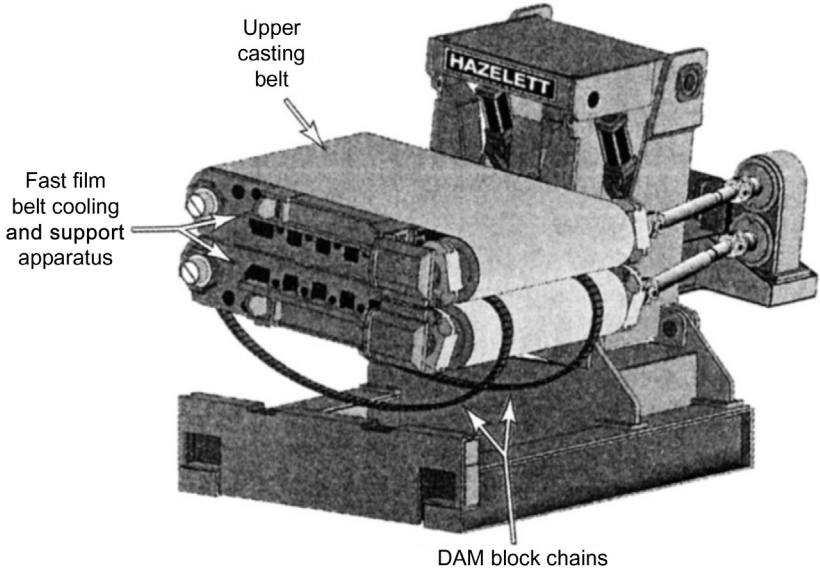


Figure 4.5 Schematic diagram showing a Hazelett twin belt continuous caster. From Hazelett, DN and Szczypiorski, WS: *Aluminium*, 79, 11, 2003.

Production rates are generally in the range 21–24.5 tonnes per meter of width per hour. As a contrast, twin roll casting of sheet occurs at much faster cooling rates that may be in the range 10^2–10^3 °C s^{-1}. In this case, sheet thicknesses are commonly 3–10 mm so that the minimal final rolling is required.

Rate of solidification has an important impact on the quality of an ingot, slab, or sheet. Faster rates are generally desirable as they lead to finer dendrite arm spacings, which, in turn, reduces microsegregation to the interdendritic regions. Dendrite cell sizes typically vary from 30 to 70 μm for vertical DC cast ingots to 5–10 μm for twin roll cast sheet. Faster casting rates also reduce the sizes of intermetallic compounds and promote finer and more uniform grain sizes. Another consequence of the faster solidification rates associated with continuous casting processes is that higher concentrations (supersaturations) of solute elements may be retained in solid solution. This applies particularly to the slowly diffusing transition metal elements, such as iron, and mechanical properties may differ from those of DC cast products even though the compositions are similar. In some situations a different alloy, or one with a lower solute content, can be substituted when a product is prepared by continuous casting.

4.1.3 Homogenization of DC ingots

Before DC ingots are fabricated into semi-finished forms, it is necessary to homogenize at a temperature commonly in the range of 450–600°C. This treatment has the following objectives:

1. Reduction of the effects of microsegregation.
2. Removal of non-equilibrium, low melting point eutectics that may cause cracking during subsequent working.
3. Controlled precipitation of excess concentrations of elements that are dissolved during solidification.

Homogenization mainly involves diffusion of alloying elements from grain boundaries and other solute-rich regions to grain centers. The time required depends upon diffusion distances, i.e., grain size (or dendrite arm spacing) and the rates of diffusion of the alloying elements. In this regard, the mean distance x which a particular atom may travel in time t is given by $x = (Dt)^{1/2}$, where D is the diffusion coefficient. D is strongly temperature dependent and values for different elements may vary by several orders of magnitude. Examples for some elements dissolved in aluminium at 500°C are Mn 5×10^{-13} $cm^2 s^{-1}$, Cu 5×10^{-10} $cm^2 s^{-1}$, Mg and Si 1×10^{-9} $cm^2 s^{-1}$. Obviously, the larger the dendrite cell size in an ingot, the greater the diffusion distances involved. For example, if x is doubled in the above expression, time t must be quadrupled. On the other hand, raising temperatures increases diffusion rates. As a rough guide, increasing the homogenization temperature by 50°C reduces the furnace time to approximately one-third of that needed at the lower temperature. In practice, homogenization times usually vary from 6 to 24 h depending upon casting conditions and the ingot alloy system.

Homogenization is particularly important for the higher-strength alloys as it serves to precipitate and redistribute submicron intermetallic compounds such as Al_6Mn, $Al_{12}Mg_2Cr$, and Al_3Zr. Transition metals may supersaturate in aluminium during the cooling of DC cast ingots and, more particularly, continuously cast slab or strip. It is necessary to promote their precipitation as uniformly dispersed compounds in order to control grain structure during subsequent fabrication and heat treatment. Moreover, it is now realized that they may exert a marked influence on various mechanical properties through their effects on the dislocation substructures formed by deformation and on the subsequent response to ageing treatments.

Regulation of these various functions requires a careful choice of conditions for homogenizing ingots of different alloys. When precipitation of these compounds is involved, both time and temperature are significant and the rate of heating to the homogenization temperature is of crucial importance. Relatively slow rates, e.g., $75°C\,h^{-1}$, are necessary to promote nucleation and growth of fine and uniform dispersions of the compounds. It has been found that the compounds are actually nucleated heterogeneously at the surfaces of precipitate particles which form and grow to relatively large sizes during the slow heating cycle. Once formed, the submicron compounds remain stable at the homogenization temperature, whereas the precipitates are redissolved. This effect is illustrated for an Al–Zn–Mg alloy in Fig. 4.6. In this case, the precipitate

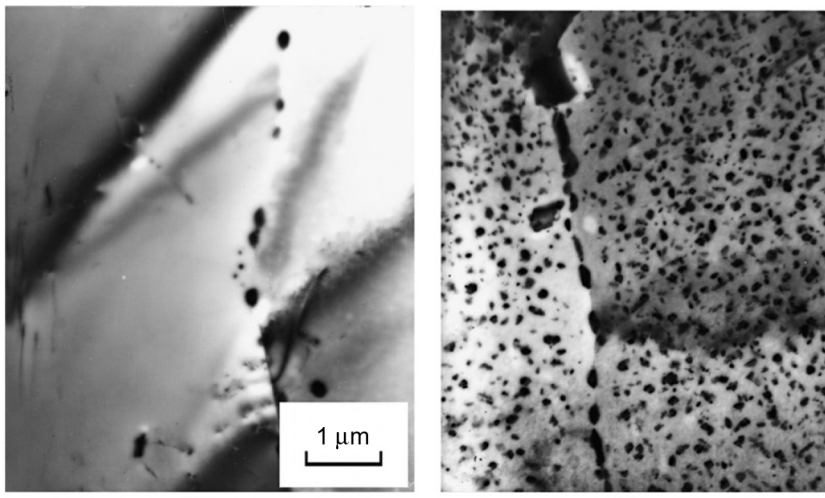


Figure 4.6 Transmission electron micrographs showing formation of submicron particles of Al_6Mn in an Al–Zn–Mg alloy containing 0.3Mn. The ingots were homogenized at 500°C for 24 h following: (A) a fast heating rate ($500°C\,h^{-1}$) and (B) a slow heating rate ($50°C\,h^{-1}$). From Thomas, AT: *Proc. of 6th Inter. Conf. on Light Metals*, Leoben, Austria, Aluminium-Verlag, Düsseldorf, 1975.

η ($MgZn_2$) has provided an interface for the subsequent heterogeneous nucleation of Al_6Mn in the ingot that was heated at the slower rate. Control of rates of cooling from the homogenization temperature may also be necessary and sometimes a second isothermal treatment is used to promote precipitation of the submicron particles.

Homogenization treatments are also important because they may change the dispersion and nature of large, primary intermetallic compounds that form in the interdendrite regions during casting. One example which is important in producing alloys for canstock (Section 4.6.5) is the reaction of dissolved silicon with the compound $Al_6(Fe,Mn)$ converting it to the harder phase α-$Al_{12}(Fe,Mn)_3Si$.

4.1.4 Fabrication of DC ingots

The next stage in the production of wrought alloys is the conversion of the ingot into semi-fabricated forms. Most alloys are first hot-worked to break down the cast structure with the aim of achieving uniformity of grain size as well as constituent size and distribution. Casting pores are also closed and usually welded up. Processing by cold working may follow, particularly for sheet, although it may be necessary to interrupt processing to give intermediate annealing treatments. Annealing usually involves heating the alloy to a temperature of 345–415°C and holding for times ranging from a few minutes up to 3 h, depending upon alloy composition and section size. Cold working is also important as the means of strengthening by work hardening those alloys that do not respond to age-hardening heat treatments.

To produce sheet or plate, modern hot mills usually commence with a reversing roughing mill in which the rectangular DC cast ingot, 200–600 mm thick, is rolled down with heavy reductions to a slab gauge of 15–35 mm. Hot rolling may then continue in a series of mills arranged in tandem resulting in a final thickness of 2.5–8 mm, after which the product is coiled. Grains become elongated in the rolling direction and, depending on the composition of the alloy, the temperature and the reduction made each pass, recovery, and partial recrystallization will occur during the hot rolling operation. With plate, the degree of working is initially uneven throughout the thickness, decreasing from surface to center. Uniformity of work can be improved by increasing the reduction for each pass or by preforging or pressing the cast ingot before rolling. The problem of differential working throughout a section also applies with forgings and several techniques are used to control grain flow. In addition, it is necessary to exercise particular control of reheating cycles for alloys containing elements that assist in inhibiting recrystallization, so that coarse grains do not form in critically strained regions.

Extrusion is second to rolling for making semi-fabricated products from aluminium and its alloys. Essentially, the process involves holding a round, preheated ingot in a container in a hydraulic press and forcing the ingot through

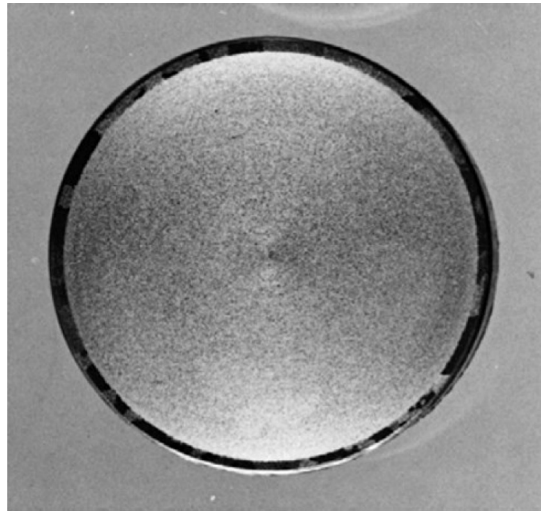


Figure 4.7 Section through an extruded bar etched to show coarse recrystallized grains around the periphery (× 1.5). Courtesy of A.T. Thomas.

a steel die opening to form elongated shapes or tubes with constant cross sections. Examples of extruded profiles are shown later in Fig. 4.22. Most sections are extruded straight, although increasing use is being made of curved profiles that are produced by placing one or more guiding devices at the front of the exit side of the die. As with rolled products, a major objective with extrusions is to avoid forming coarse, recrystallized grains which tend to form around the periphery of sections that are heavily worked as the alloy flows through and past the edges of the die (Fig. 4.7). This effect predominates at the back end of an extruded length because of the nature of flow during extrusion, and is detrimental for several reasons, notably that the longitudinal tensile strength can be reduced by 10–15%. However, the heavy deformation associated with the process of extrusion is beneficial in producing a highly refined microstructure elsewhere in an extruded section.

Most aluminium alloys are also amenable to forging by hammering or pressing, usually at high temperature (e.g., 450°C), which is the next most common way of forming wrought products. There are two main types of forging machines: a hammer or drop hammer that strikes the alloy with rapid blows and a press that squeezes metal slowly into the desired shape. Tooling comprises two types: open dies for forging between open tools and more costly closed dies which surround and shape the product.

With sheet alloys used for some building materials and for high-strength aircraft panels, it is usual to roll-clad the surfaces with high-purity aluminium or an Al–1Zn alloy as a protection against atmospheric corrosion. This is arranged

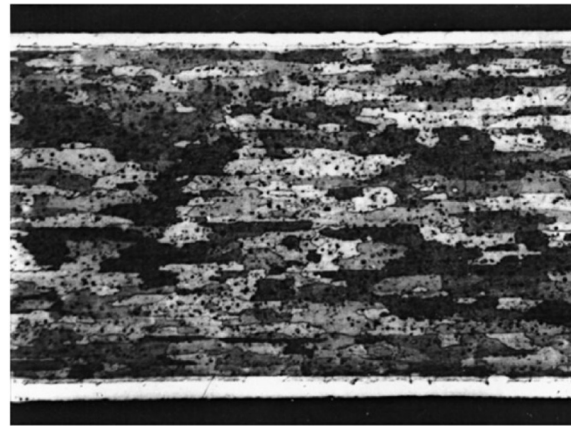


Figure 4.8 Section of a high-strength alloy sheet roll-clad with pure aluminium (× 50). Courtesy D.W. Glanvill.

by attaching the cladding plates to each side of the freshly scalped ingot at the first rolling pass, taking care that the mating surfaces are clean. Good bonding is achieved and each clad surface is normally 5% of the total thickness of the composite sheet (Fig. 4.8). The cladding layer is selected to be at least 100 mV more anodic than the core. Normally 1xxx alloys are chosen to protect 2xxx alloy cores, and 7072 (Al–1Zn) for 3xxx, 5xxx, 6xxx, or 7xxx cores.

4.1.5 Thermal treatment

The function of thermal treatment is to develop a desired balance of mechanical properties required for consistent service performance. It will be clear from the above considerations that such consistency presupposes attainment of a satisfactory uniformity of microstructure in the preceding stages of production of the wrought material. Also, annealing treatments, if required, are normally carried out within the temperature range 350–420°C. Attention must now be given to the processes of solution treatment, quenching and ageing, which are the three stages in strengthening alloys by precipitation (age) hardening.

Solution treatment Since the main purpose of this treatment is to obtain complete solution of most of the alloying elements, it should ideally be carried out at a temperature within the single-phase, equilibrium solid solution range for the alloy concerned (α_{Al} in Fig. 2.1). However, it is essential that alloys are not heated above the solidus temperature which will cause overheating, i.e., liquation (melting) of compounds and grain boundary regions with a subsequent adverse effect on ductility and other mechanical properties. Special problems are sometimes encountered with alloys based on the Al–Cu–Mg system in

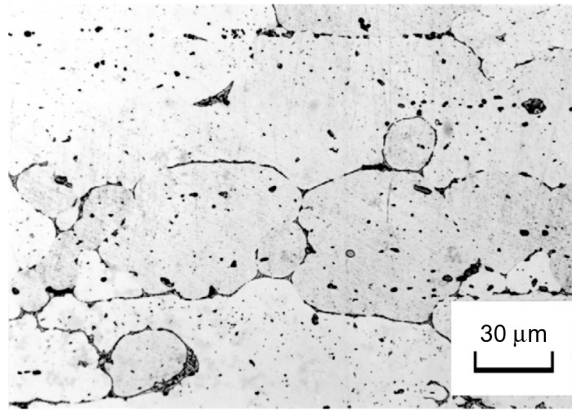


Figure 4.9 Liquation along grain boundaries caused by overheating of an Al–Cu–Mg alloy during solution treatment.

which adequate solution of the alloying elements is possible only if solution treatment is carried out within a few degrees of the solidus, and special care must be taken with control of the furnace temperature. An example of liquation along grain boundaries in an Al–Cu–Mg alloy is shown in Fig. 4.9.

Further precautions are necessary in solution treatment of hot-worked products, again to prevent the growth of coarse, recrystallized grains. Unnecessarily high temperatures and excessively long solution treatment times are to be avoided, particularly with extrusions or with forgings produced from extruded stock. Differential working that is common in such products is the reason why they are so sensitive to grain growth in localized regions.

The consequences of the introduction of hydrogen into molten aluminium through the surface reaction with water vapor were mentioned in the "Melting and casting" section. Such a reaction may also occur with solid aluminium during solution treatment leading to the adsorption of hydrogen atoms. These atoms can recombine at internal cavities to form pockets of molecular gas. Localized gas pressures can develop which, bearing in mind the relatively high plasticity of the metal at the solution treatment temperatures, may lead in turn to the irreversible formation of surface blisters (Fig. 4.10). Sources of the internal cavities at which blisters may form are unhealed porosity from the original ingot, intermetallic compounds that have cracked during fabrication and, possibly, clusters of vacant lattice sites that may have formed when precipitates or compounds are dissolved. In these cases, the presence of blisters, while spoiling surface appearance, may have little effect upon mechanical properties of the components. However, blistering is often associated with overheating because the hydrogen can readily collect at liquated regions and this is a more serious problem requiring rejection of the affected material.

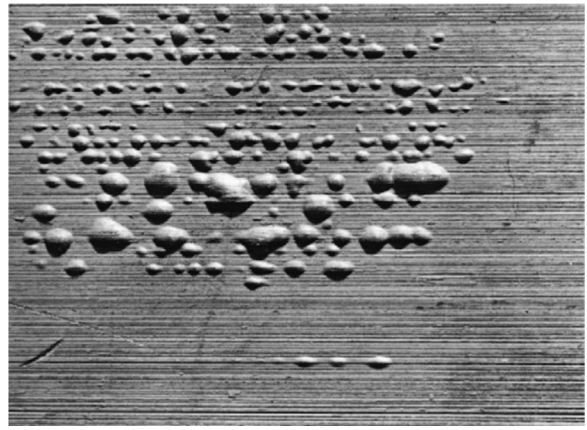


Figure 4.10 Blisters on the surface of an aluminium alloy component solution treated in a humid atmosphere (× 3). Courtesy A.T. Thomas.

As it is difficult to eliminate internal cavities in wrought products, it is imperative that the water vapor content of furnace atmospheres be minimized. Where this is not possible, the introduction of a fluoride salt into the furnace during the heat treatment of critical components can be beneficial by reducing the surface reaction with water vapor.

Finally, reference should be made to the solution treatment of roll-clad sheet. Here it is necessary to avoid dissolved solute atoms, e.g., copper, diffusing from the alloy core through the high-purity aluminium, or Al–Zn cladding, thereby reducing its effect in providing protection against corrosion. Such a risk is particularly serious in thinner gauges of sheet. Strict control of temperature and time is necessary and such times should be kept to a minimum consistent with achieving full solution of the alloying elements in the core. The rate of heating to the solution treatment temperature is also important and it is customary to use a mixed nitrate salt bath for clad material because this rate is much faster than that found in air furnaces.

Quenching After solution treatment, aluminium alloy components must be cooled or quenched, usually to room temperature, which is a straightforward operation in principle since the aim is simply to achieve a maximum supersaturation of alloying elements in preparation for subsequent ageing. Cold-water quenching is very effective for this and is frequently necessary in order to obtain adequate cooling rates in thicker sections. However, rapid quenching distorts thinner products such as sheet and introduces internal (residual) stresses into thicker products which are normally compressive at the surface and tensile in the core.

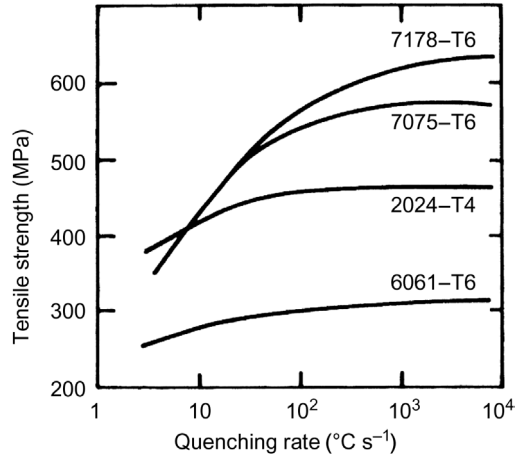


Figure 4.11 Tensile strengths of various commercial alloys as a function of quenching rate in the critical temperature range 400–290°C. Alloy compositions are given in Table 4.4. From Van Horn, KR (Ed.): *Aluminium*, Vol. 1, Chapter 5, ASM, Cleveland, OH, USA, 1967.

Residual stresses may cause dimensional instability, particularly when components have an irregular shape or when subsequent machining operations expose the underlying tensile stresses. What is also serious is that the level of residual stresses may approach the yield stress in some high-strength alloys which, when superimposed, upon normal assembly and service stresses, can cause premature failure. For products of regular section such as sheet, plate, and extrusions, the level of residual quenching stresses can be much reduced by stretching after quenching although this technique has limited use with sheet because it may cause an unacceptable reduction in thickness or gauge. In such cases, roller levelling or flattening in a press may be a more satisfactory operation. The ageing treatment also allows some relaxation of stresses, and reductions of between 20% and 40% have been measured.

Quenching stresses will be reduced if slower rates of cooling are used and this alternative is particularly important in the case of forgings. Some alloys may be quenched with hot or boiling water, water sprayed, or even air-cooled after solution treatment, and still show an acceptable response to subsequent age hardening. The extent to which slower quenching rates can be tolerated is controlled by what is known as the quench sensitivity of the alloy concerned. During slow cooling, there is a tendency of some of the solute elements to precipitate out as coarse particles which reduces the level of supersaturation and hence lowers the subsequent response of the alloys to age hardening. As is demonstrated in Fig. 4.11, this effect is more pronounced in highly concentrated alloys. It is also aggravated by the presence of submicron intermetallic compounds which provide interfaces for the heterogeneous nucleation of large precipitates (Fig. 4.12) during cooling. This behavior is in fact the reverse of that occurring during the heating cycle when homogenizing ingots (Fig. 4.6).

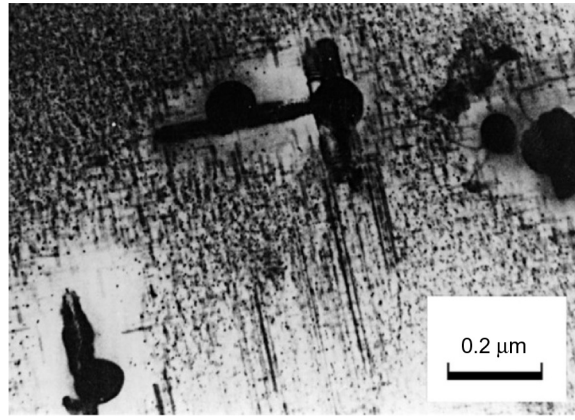


Figure 4.12 Heterogeneous nucleation of large needles of Mg_2Si phase on manganese-bearing intermetallic compounds in a slowly quenched and aged Al–Mg–Si alloy. This has caused denudation of the fine precipitate in surrounding regions of the matrix. From Harding, AR: *Aluminium Transformation Technology and Applications*, Pampillo, CA *et al.* (Eds.), ASM, Cleveland, OH, USA, 211, 1980.

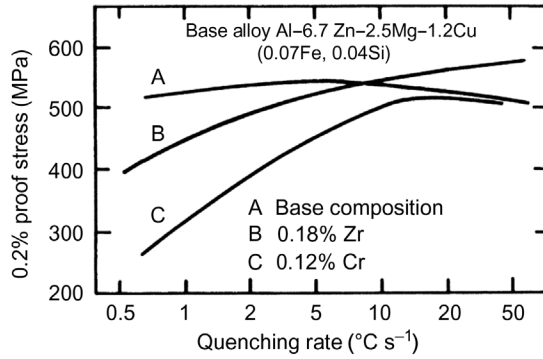


Figure 4.13 The effect of minor additions of chromium and zirconium on the quench sensitivity of an alloy similar to 7075 (Table 4.4). Quench rates are shown in the critical temperature range 400–290°C. From Spangler, GE *et al.*: *Aluminium Transformation Technology and Applications in 1981*, Pampillo, CA *et al.* (Eds.), ASM, Cleveland, OH, USA, 1982.

Of the dispersoids commonly present, the chromium-containing phase ($Al_{12}Mg_2Cr$) causes the greatest increase in quench sensitivity, whereas the zirconium-containing phase (Al_3Zr) has a much less deleterious effect in this regard (Fig. 4.13). The manganese-containing compound Al_6Mn has an effect intermediate between these two.

Microstructural changes may also occur in the region of grain boundaries which are a consequence of slow quenching. In particular, segregation to the grain boundaries of solute elements, such as copper, may cause reduced toughness and higher susceptibility to intergranular corrosion in service.

The critical temperature range over which alloys display maximum quench sensitivity is 290–400°C and specialized techniques have been devised which allow rapid cooling through this range but still permit a reduction in residual stresses. One method which has been used for certain high-strength Al–Zn–Mg–Cu alloys is to quench into a fused salt bath at 180°C and hold for a time before cooling to room temperature. A second technique involves the use of proprietary organic liquids having an inverse solubility/temperature relationship. Whereas immersion of a hot body in boiling water generates a tenacious blanket of steam around the body, thereby reducing the cooling rate in the critical temperature range, the organic liquids are formulated to have the reverse effect. Initially the cooling rate is reduced by localized precipitation of a solute in the quenching medium after which it increases through the critical temperature range as the precipitate redissolves. The overall cooling rate is comparatively uniform and a desirable combination of stress relief and high level of mechanical properties has been reported.

Ageing Age hardening is the final stage in the development of properties in the heat-treatable aluminium alloys. Metallurgical changes that occur during ageing have been discussed in Chapter 2. Some alloys undergo ageing at room temperature (natural ageing) but most require heating for a time interval at one or more elevated temperatures (artificial ageing) which are usually in the range 100–190°C. Ageing temperatures and times are generally less critical than those in the solution treatment operation and depend upon the particular alloys concerned. Where single stage ageing is involved, a temperature is selected for which the ageing time to develop high-strength properties is of a convenient duration, e.g., 8 h corresponding to a working day or 16 h for an overnight treatment. Usually the only other stipulation is to ensure that the ageing time is sufficient to allow for the charge to reach the required temperature.

Multiple ageing treatments are sometimes given to certain alloys which have desirable effects on properties such as the stress–corrosion resistance. Such treatments may involve several days at room temperature followed by one or two periods at elevated temperatures. If alloys are slowly quenched after solution treatment, room temperature incubation may be critical because the lower supersaturation of vacancies alters precipitation kinetics. Sufficient time is required for the formation and growth of Guinier–Preston (GP) zones, particularly if these zones are to transform to another precipitate on subsequent elevated temperature ageing (Section 4.2.2). Similar considerations apply with respect to the rate of heating to the ageing temperature.

A recent development has been the recognition that alloys may undergo secondary precipitation and further hardening at relatively low temperatures after first being artificially aged at a higher temperature (see Section 2.3.4). Response to these effects depends on alloy composition, the duration of artificial ageing, and the cooling rate to the lower temperature. Alloy properties may therefore continue to change with time, particularly if an alloy is first underaged at an elevated temperature.

Furthermore, if an alloy in this underaged condition, is then quenched, and artificial ageing is resumed after a dwell period at a lower temperature, then the overall level of age hardening may exceed what may be achieved following a standard, single stage (T6) temper. The effects of these interrupted ageing treatments on the tensile and fracture toughness properties of selected alloys are described in Section 4.4.2.

Thermomechanical processing Some alloys show an enhanced response to hardening if they are cold worked after quenching and prior to ageing and such treatments have been used for many years (T8 temper, see Section 4.2.2). Practices that combine plastic deformation with heat treatment are known generally as thermomechanical processing or thermomechanical treatments (TMT). There are two types which have been applied to some high-strength aluminium alloys.

1. Intermediate TMT (ITMT), in which the processing, usually during rolling, is controlled so as to result in recrystallized but very fine grain structure prior to solution treatment. One example of such a treatment is shown in Fig. 4.63.
2. Final TMT (FTMT), in which deformation is applied after solution treatment and may involve cold or warm working before, during, or after ageing. The purpose is to increase the dislocation density and to stabilize this configuration by precipitates that are nucleated along the lines. A schematic representation of one type of FTMT is shown in Fig. 4.31. The combination of precipitation and substructure hardening may enhance the strength and toughness of some alloys, and its effect on unnotched fatigue properties of Al–Zn–Mg–Cu alloys was illustrated in Fig. 2.50.

4.2 DESIGNATION OF ALLOYS AND TEMPERS

4.2.1 Nomenclature of alloys

The selection of aluminium alloys for use in engineering has often been difficult because specification and alloy designations have differed from country to country. Moreover, in some countries, the system used has been simply to number alloys in the historical sequence of their development rather than in a more logical arrangement. For these reasons, the introduction of an International Alloy Designation System (IADS) for wrought products in 1970 and its gradual acceptance by most countries has been welcomed. The system is based on the classification used for many years by the Aluminium Association of the United States and it is used when describing alloys in this book.

The IADS gives each wrought alloy a four digit number of which the first digit is assigned on the basis of the major alloying element(s) (Fig. 4.14). Hence there are the 1xxx series alloys which are unalloyed aluminium (with 99% aluminium minimum), the 2xxx series with copper as the major alloying element, 3xxx series with manganese, 4xxx series with silicon, 5xxx series with magnesium, 6xxx with magnesium and silicon, and 7xxx series with zinc (and

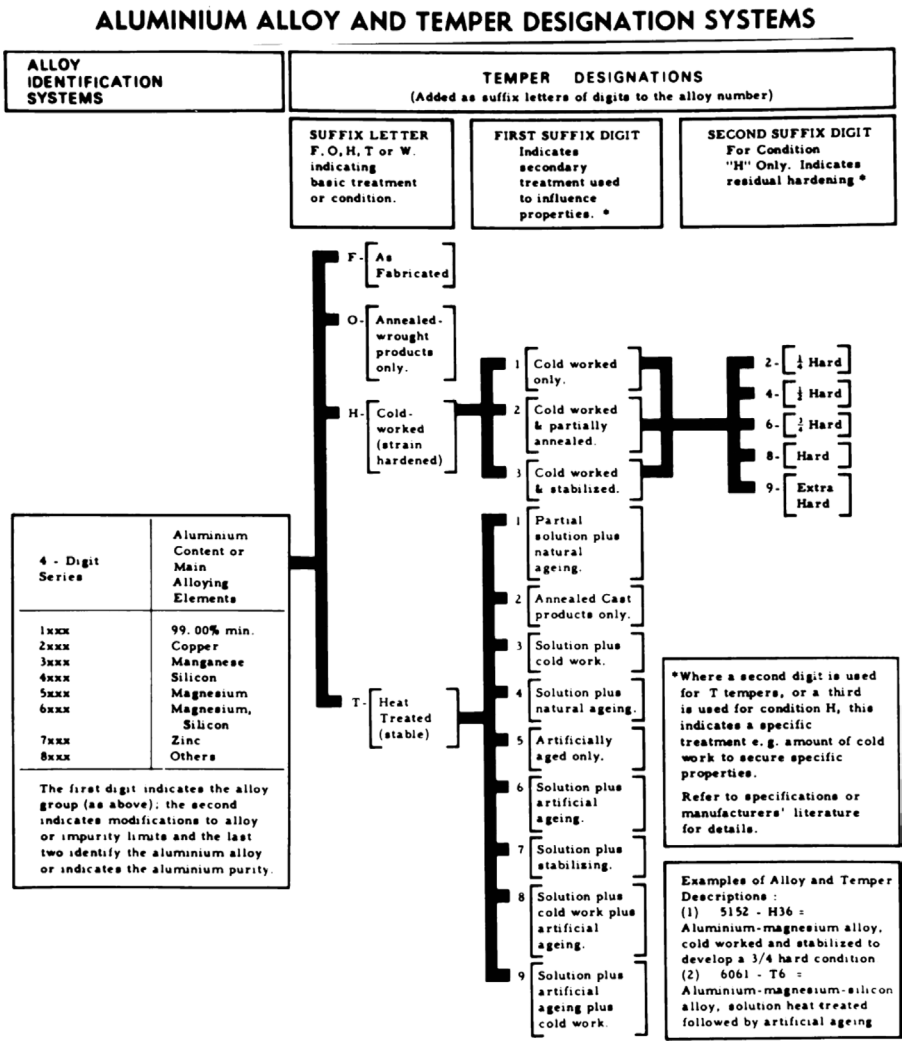


Figure 4.14 Aluminium alloy and temper designation systems. Courtesy Institute of Metals and Materials, Australia.

magnesium) as the major alloying elements. The 8xxx series is used for compositions not covered by the above designations and several different alloys are mentioned in some other sections of this chapter. It should also be noted that wrought Al–Si alloys of the 4xxx series are used mainly for welding and brazing electrodes and brazing sheet rather than for structural purposes.

The third and fourth digits are significant in the 1xxx series but not in other alloys. In the 1xxx series, the minimum purity of the aluminium is denoted by these digits, e.g., 1145 has a minimum purity of 99.45%; 1200 has a minimum purity of 99.00%. In all other series, the third and fourth digits have little

meaning and serve only to identify the different aluminium alloys in the series. Hence 3003, 3004, and 3005 are distinctly different Al–Mn alloys just as 5082 and 5083 denote two types of Al–Mg alloys (Table 4.2). The second digit indicates purity or alloy modifications. If the second digit is zero, it indicates the original alloy; integers 1–9, which are assigned consecutively, indicate alloy modifications. A close relationship usually exists between the alloys, e.g., 5352 is closely related to 5052 and 5252 (Table 4.2); just as 7075 and 7475 differ only slightly in composition (Table 4.4). A prefix X is used to denote that an alloy is at an experimental stage of its development.

In Britain, it has been traditional to use three principal types of specifications to which aluminium and its alloys have been supplied:

1. BS (British Standard) specifications for general engineering use.
2. BS Specifications for aeronautical use (designated as the L series).
3. DTD (Directorate of Technical Development) specifications issued by the Ministry of Technology for specialized aeronautical applications (which is now obsolete).

In addition there are several supplementary engineering specifications which cover other specialized alloys or those with limited use, while electrical applications are covered by a further six specifications.

The general engineering series is specified BS 1470–75, the six standards covering the different forms: plate, sheet, and strip (BS 1470); drawn tube (BS 1471); forging stock and forgings (BS 1472); rivet, bolt, and screw stock (BS 1473); bars, extruded round tube, and sections (BS 1474); and wire (BS 1475). Every composition is denoted by a number which always indicates the same chemical composition irrespective of form or condition. Pure aluminium (99.99% minimum content) is numbered 1 and the other grades by suffix 1A, 1B, and 1C. The alloys follow from 2 onward with numerous omissions corresponding to obsolete alloys or numbers not now used. Non-heat-treatable (NHT) alloys are prefixed with the letter N and the heat-treatable alloys with H. The various grades of aluminium (series 1) which are not heat-treatable do not, however, carry the N prefix. Other letters and figures indicate the form and condition of the material.

4.2.2 Temper or heat treatment nomenclatures

In order to specify the mechanical properties of an alloy and the way these properties were achieved, a system of temper nomenclature has also been adopted as part of the IADS. This takes the form of letters and digits that are added as suffixes to the alloy number. The system deals separately with the NHT, strain-hardening alloys on the one hand and heat-treatable alloys on the other. The essential features of the system are outlined in Fig. 4.14 although recourse to detailed specifications or manufacturer's literature is recommended, particularly when several digits are included in the temper designation.

Alloys supplied in the as-fabricated or annealed conditions are designated with the suffixes F and O, respectively. Strain hardening is a natural consequence of most

working and forming operations on aluminium alloys. For the various grades of aluminium (1xxx series) and the NHT Al–Mn (3xxx) and Al–Mg (5xxx) alloys, this form of hardening augments the strengthening that arises from solid solution and dispersion hardening. Strain hardened alloys are designated with the letter H. The first suffix digit indicates the secondary treatment: 1 is cold worked only; 2 is cold-worked and partially annealed; 3 is cold worked and stabilized. The second digit represents hardening and the severely cold worked or fully hard condition is designated H18. This corresponds to the tensile strength achieved by a 75% reduction in the original cross-sectional area following a full anneal (O temper). The H12 temper represents a tensile strength quarter way between that of the O temper and the H18 temper (i.e., quarter hard), while the H14 and H16 tempers are half and three-quarters of H18 respectively. Standards do not specify the actual cold reductions required for the H12, H14, and H16 conditions, and each individual mill determines its own cold rolling practices to fulfill these temper requirements. A combination of strain-hardening and partial annealing is used to produce the H2 series of tempers. In these the products are cold worked more than is required to achieve the desired mechanical properties and then reduced in strength by partial annealing. The H3 tempers apply only to Al–Mg alloys which have a tendency to soften with time at room temperature after strain hardening. This may be avoided by heating for a short time at an elevated temperature (120–175°C) to ensure completion of the softening process. Such treatment provides stable mechanical properties and improves working characteristics. It should also be noted that an H4 temper has been introduced which applies to products that are strain hardened and then subjected to some partial annealing during a subsequent paint baking or lacquering operation.

A series of H temper designations having three digits has been assigned to wrought products as follows:

- H111 applies to products which are strain hardened less than the amount required for a controlled H11 temper.
- H112 applies to products which are strain hardened less than the amount incidental to the shaping process. No special control is exerted over the amount of strain hardening or thermal treatment, but there are mechanical property limits and mechanical property testing is specified.
- H121 applies to products which are strain hardened less than the amount required for a controlled H12 temper.
- H311 applies to products which are strain hardened less than the amount required for a controlled H31 temper.
- H321 applies to products which are strain hardened less than the amount required for a controlled H32 temper.

In addition, temper designations H323 and H343 have been assigned to wrought products containing more than 4% magnesium and apply to products that are specially fabricated to have acceptable resistance to stress–corrosion cracking (SCC).

A different system of nomenclature applies for heat-treatable alloys. Tempers other than 0 are denoted by the letter T followed by one or more

digits. The more common designations are: T4 which indicates that the alloy has been solution treated, quenched, and naturally aged; T5 in which the alloy has been rapidly cooled following processing at an elevated temperature, e.g., by extrusion, and then artificially aged; and T6 which denotes solution treatment, quenching, and artificial ageing. For the T8 condition in which products are cold worked between quenching and artificial ageing to improve strength, the amount of cold work is indicated by a second digit, e.g., T85 means 5% cold work. It should also be noted that the letter W may be used to indicate an unstable temper when an alloy ages spontaneously at room temperature after solution treatment. This designation is specific only when the period of natural ageing is indicated, e.g., W½ h.

Several designations involving additional digits have been assigned to stress-relieved tempers of wrought products.

- Tx51—stress relieved by stretching. Applies to products that are stress relieved after quenching by stretching the following amounts: plate 0.5–3% permanent set; rod, bar and shapes 1–3% permanent set. These products receive no further straightening after stretching. Additional digits are used in the designations for extruded rod, bar, shapes, and tube as follows: Tx510 applies to products that receive no further straightening after stretching; Tx511 applies where minor straightening after stretching is necessary to comply with standard tolerances for straightness.
- Tx52—stress relieved by compressing. Applies to products that are stress relieved after quenching by compressing to produce a nominal permanent set of 2.5%.
- Tx53—stress relieved by thermal treatment.

In the above designations, the letter x represents digits, 3, 4, 6, or 8, whichever is applicable.

In cases where wrought products may require heat treatment by the user, the following temper designations have been assigned.

- T42—solution treated, quenched, and naturally aged.
- T62—solution treated, quenched, and artificially aged.

Compositions and tensile properties of selected aluminium alloys are included in Tables 4.2–4.5. As an illustration of the variation in tensile properties that may be obtained when the same alloy is prepared under different temper conditions, Table 4.1 provides typical results for the commonly used Al–Mg–Si alloy 6063.

In the British system of nomenclature, the form of the product is denoted by the letters: B for bar and screw stock; C for clad plate, sheet, or strip; E for bars, extruded round tube, and sections; F for forgings and forging stock; G for wire; J for longitudinally welded tube; R for rivet stock; S for plate, sheet, and strip; and T for drawn tube. The condition of the product with regard to strain hardening or heat treatment is denoted by suffixes: M as manufactured; O annealed; H1–H8 the degrees of strain hardening in increasing order of

Table 4.1 Tensile properties of alloy 6063 in different temper conditions

Temper condition	0.2% proof stress (MPa)	Tensile strength (MPa)	Elongation (% in 50 mm)
0	50	90	30
T1	90	150	20
T31		180	12
T32		205	8
T33	240	260	20
T34	325	340	15
T4	90	170	22
T5	180	220	12
T6	215	240	12
T81	230	250	11
T82	255	260	9
T83	270	280	8
H112	90	150	20
H14	95	160	18
H18	150	200	8

From Australian Aluminium Development Council Handbook, 1994.

strength, with two additional categories, H68 applicable only to wire, and H9 for extra-hard electrical wire. The heat treatment tempers are as follows.

TB—solution treated, quenched, and naturally aged (formerly designated W).
TD—solution treated, cold worked, and naturally aged (applicable only to wires and formerly designated WD).
TE—artificially aged for after cooling from a high-temperature-forming process (formerly P).
TF—solution treated, quenched, and artificially aged (formerly WP).
TH—solution treated, quenched, cold worked, and artificially aged (applicable only to wire and formerly designated WDP).

The combinations of letters and numbers enable an aluminium alloy to be identified and its form and condition described. For example, HE9–TF is heat-treatable composition 9 (Al–Mg–Si) in the form of bar, extruded round tube or section, in the fully heat-treated condition, i.e., solution treated, quenched, and artificially aged. The equivalent designation in the IADS would be 6063–T6, which does not define the form of the product.

4.3 NON-HEAT-TREATABLE ALLOYS

Wrought compositions that do not respond to strengthening by heat treatment mainly comprise the various grades of aluminium as well as alloys with manganese or magnesium as the major additions, either singly or in combination (Table 4.2). Approximately 95% of all aluminium flat rolled products (sheet,

Table 4.2 Compositions of selected Non-heat-treatable (NHT) wrought aluminium alloys

IADS designation	Si		Fe	Cu	Mn	Mg	Zn	Cr	Ti	Other
1100	1.0 Si	+	Fe	0.05–0.20	0.05		0.10			Al min 99.0
1200	1.0 Si	+	Fe	0.05	0.05		0.10		0.05	Al min 99.0
1145	0.55 Si	+	Fe	0.05	0.05	0.05	0.05		0.03	Al min 99.45
1199	0.006		0.006	0.006	0.002	0.006	0.006		0.002	Al min 99.99
3003	0.60		0.70	0.05–0.20	1.0–1.5		0.10			
3004	0.30		0.70	0.25	1.0–1.5	0.8–1.3	0.25			
3005	0.60		0.70	0.30	1.0–1.5	0.20–0.6	0.25	0.10		
3105	0.60		0.70	0.30	0.3–0.8	0.20–0.8	0.40	0.20	0.10	
5005	0.30		0.70	0.20	0.20	0.50–1.1	0.25	0.10		
5050	0.40		0.70	0.20	0.10	1.1–1.8	0.25	0.10		
5052	0.25		0.40	0.10	0.10	2.2–2.8	0.10	0.15–0.35		
5454	0.25		0.40	0.10	0.50–1.0	2.4–3.0	0.25	0.05–0.20	0.20	
5456	0.25		0.40	0.10	0.50–1.0	4.7–5.5	0.25	0.05–0.20	0.20	
5056	0.30		0.40	0.10	0.05–0.2	4.5–5.6	0.10	0.05–0.20		
5082	0.20		0.35	0.15	0.15	4.0–5.0	0.25	0.15	0.10	
5182	0.20		0.35	0.15	0.20–0.50	4.0–5.0	0.25	0.10	0.10	
5083	0.40		0.40	0.10	0.40–1.0	4.0–4.9	0.25	0.05–0.25	0.15	
5383	0.25		0.25	0.20	0.70–1.0	4.0–5.2	0.40	0.25	0.15	0.20Zr
5059	0.45		0.50	0.25	0.60–1.2	5.0–6.0	0.20	0.25	0.20	0.05–0.20Zr
5086	0.40		0.50	0.10	0.20–0.7	3.5–4.5	0.25	0.05–0.25	0.15	
8001	0.17		0.45–0.70	0.15				0.05		0.09–1.3Ni
8006	0.40		1.2–2.0	0.30	0.30–1.0	0.10	0.10			
8010	0.40		0.35–0.7	0.10–0.30	0.10–0.8	0.10–0.50	0.40	0.20	0.10	
8011	0.50–0.9		0.6–1.0	0.10	0.10	0.05	0.10	0.05	0.08	
8280	1.0–2.0		0.70	0.7–1.3	0.10		0.05			5.5–7.0Sn 0.20–0.7Ni
8081	0.7		0.70	0.7–1.3	0.10		0.05		0.10	18–22Sn

Compositions are in % maximum by weight unless shown as a range or a minimum.

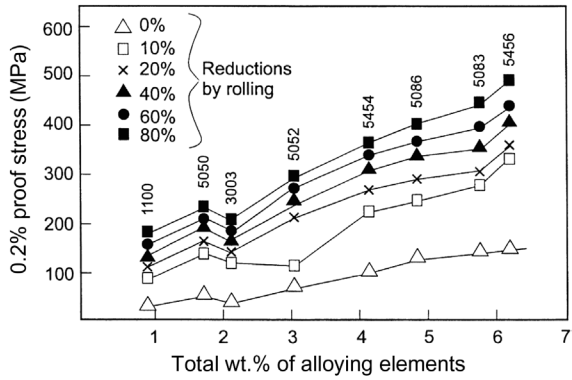


Figure 4.15 Attainable yield strengths of NHT alloys with different levels of cold work. Courtesy R. E. Sanders Jr., Alcoa, USA.

plate, and foil) are made from these three alloy groups. Packaging, transportation, and building and construction represent the largest usage of NHT sheet and the three major criteria for selecting and developing these products are:

1. structural—based on strength and durability;
2. formability—based on complexity and productivity in making the final part;
3. surface quality—based on finishing characteristics, reflectivity, or general appearance.

Each product has a particular balance of these requirements.

NHT alloys can provide a very wide range of tensile properties and Fig. 4.15 shows that yield strengths between 20 and 500 MPa are possible from the 1xxx, 3xxx, and 5xxx classes of alloys fabricated in tempers ranging from the annealed "O" to the severely cold worked H19 conditions. Strength is developed by strain hardening, usually by cold working during fabrication, in association with dispersion hardening (Al–Mn), and/or solid solution hardening (Al–Mg) or both (Al–Mn–Mg). Typical mechanical properties are given in Table 4.3 although it should be noted that some NHT alloys are used in applications for which other properties are the prime consideration. The miscellaneous alloys in the 8xxx series mostly do not respond to heat treatment and are used for specific purposes such as bearings and bottle caps. An Al–1Zn alloy designated 7072 serves as cladding to protect a number of other alloys, e.g., 2219, 7075, from corrosion (Section 4.1.4), and for some fin stock. Several Al–Si alloys are available in the 4xxx series one of which, 4343 (Al–7.5Si), is used mainly for cladding on brazing sheet. This series is also used for welding electrodes and brazing rods. The commercial forms in which NHT alloys are available and some typical applications are included in Table 4.3. All are readily weldable and have a high resistance to corrosion in most media.

Table 4.3 Tensile properties of selected NHT wrought aluminium alloys

IADS designation	Temper	0.2% Proof stress (MPa)	Tensile strength (MPa)	Elongation (% in 50 mm)	Typical application
1100	0	35	90	35	Sheet, plate, tube, wire, spun hollow-ware, food equipment
	H18	150	165	5	
1145	0	35	75	40	Foil, sheet, semi-rigid containers
	H18	115	145	5	
1199	0	10	45	50	Electrical and electronic foil
	H18	110	115	5	
3003	0	25	110	30	Sheet, plate, foil, rigid containers, cooking utensils, tubes
	H18	185	200	4	
3004	0	70	180	20	Sheet, plate, rigid containers
	H38	250	280	5	
3005	0	55	130	25	Higher-strength foil, roofing sheet
	H18	225	240	4	
3105	0	55	120	24	General sheet material, plate, extrusions
	H18	195	215	3	
5005	0	40	125	30	General sheet material, high-strength foil, electrical conductor wire
	H18	195	200	4	
	H38	185	200	5	
5050	0	55	145	24	Sheet and tube, rip tops for cans
	H38	200	220	6	
5052	0	90	195	25	Sheet, plate, tubes, marine fittings
	H38	255	270	7	
5454	0	120	250	22	
	H34	240	305	10	
5456	0	160	310	24	Special-purpose sheet, plate, extrusions, pressure vessels, marine applications such as hulls and superstructures, dump-truck bodies, cryogenic structures
	H24	280	370	12	
5056	0	150	290	35	
	H38	345	415	15	
5083	0	145	290	22	
	H343	280	360	8	
5383	0	145	290	17	
	H321	220	305	10	
5086	0	115	260	22	
	H34	255	325	10	
8001	0	40	110	30	Sheet, tubing for water-cooled nuclear reactors
	H18	185	200	4	

Some of the essential features of the individual classes of alloys are discussed as follows. More details concerning special products and applications, e.g., electrical conductors (ECs), are considered in the Section 4.6.9.

4.3.1 Super-purity and commercial-purity aluminium (1xxx series)

This group includes super-purity (SP) aluminium (99.99%) and the various grades of commercial-purity (CP) aluminium containing up to 1% of impurities or minor additions (e.g., 1145, 1200). The materials have been utilized as wrought products since the industry was first developed and the CP grades are available in most forms. Tensile properties are low and annealed SP aluminium has a proof stress of only 7–11 MPa. Applications include ECs for which there are several compositions (see Section 4.6.9), chemical process equipment, foil (Section 4.6.5), architectural products requiring decorative finishes, and lithographic plates.

4.3.2 Al–Mn and Al–Mn–Mg alloys (3xxx series)

In general, the 3xxx series of alloys is used when moderate strength combined with high ductility and excellent corrosion resistance is required. Commercial Al–Mn alloys contain up to 1.25% manganese although the maximum solid solubility of this element in aluminium is as high as 1.82%. This limitation is imposed because the presence of iron as an impurity reduces the solubility and there is a danger that large, primary particles of Al_6Mn will form with a disastrous effect on local ductility. The only widely used binary Al–Mn alloy is 3003 which is supplied as sheet. The presence of finer manganese-containing intermetallic compounds confers some dispersion hardening, and the tensile strength of annealed 3003 is typically 110 MPa compared with 90 MPa for CP aluminium (1100), with corresponding increases in the work hardened tempers. This alloy is commonly used for foil, cooking utensils, and roofing sheet.

The addition of magnesium provides solid solution strengthening and the dilute alloy 3105 (Al–0.55Mn–0.5Mg), which is readily fabricated, is widely used in a variety of strain hardened tempers. Higher levels of manganese and magnesium are present in 3104 (Al–1.1Mn–1.05Mg–0.15Cu) which raises the tensile strength to 320 MPa in the H19 condition. This alloy is used for manufacturing beverage cans, which is currently the largest single use of the metals aluminium and magnesium (Section 4.6.5).

4.3.3 Al–Mg alloys (5xxx series)

Aluminium and magnesium form solid solutions over a wide range of compositions and wrought alloys containing from 0.8% to slightly more than 5% magnesium are widely used. Strength values in the annealed condition range from 40 MPa yield and 125 MPa tensile for Al–0.8Mg (5005) to 160 MPa yield and 310 MPa tensile for the strongest alloy 5456 (Table 4.3). Elongations are

relatively high and usually exceed 25%. The alloys work harden rapidly at rates that increase as the magnesium content is raised (e.g., Fig. 2.6). As shown in Fig. 4.15, fully work hardened 5456 (H19 temper) may have a yield strength close to 500 MPa although ductility and formability are limited.

The alloys may exhibit some instability in properties which is manifest in two ways. If the magnesium content exceeds 3–4%, there is a tendency for the β phase, Mg_5Al_8, to precipitate in slip bands and grain boundaries which may lead to intergranular attack and SCC in corrosive conditions. Precipitation of β occurs only slowly at ambient temperatures but is accelerated if the alloys are in a heavily worked condition, or if the temperature is raised. Small additions of chromium and manganese, which are present in most alloys and raise the recrystallization temperatures, also increase tensile properties for a given magnesium content. This offers the prospect of using alloys with reduced magnesium contents if precipitation of β is to be avoided. For example, alloy 5454 contains 2.7% Mg, 0.7% Mn, and 0.12% Cr, and has tensile properties similar to those expected from a binary alloy having as much as 4% magnesium.

The second problem is that work hardened alloys may undergo what is known as age softening at ambient temperatures. Over a period of time, the tensile properties fall due to localized recovery within the deformed grains and, as mentioned in the "Temper or heat treatment nomenclatures" section, a series of H3 tempers has been devised to overcome this effect. These tempers involve cold working to a level slightly greater than desired and then stabilizing by heating to a temperature of 120–150°C. This lowers the tensile properties to the required level and stabilizes them with respect to time. The treatment also reduces the tendency for precipitation of β in the higher magnesium alloys.

The 5xxx series alloys were first developed in the 1930s when there was a need for sheet materials with higher strengths, weldability, good formability, and higher levels of corrosion resistance. The first appears to be the alloy 5052 (Al–2.5Mg–0.25Cr) and since then there has been continuing development of stronger alloys with higher magnesium contents, most of which also contain manganese. A well-known example is 5083 (Al–4.5Mg–0.7Mn–0.15Cr) and other compositions based on this alloy are discussed in the Section 4.6.3. One more recent change has been the deliberate addition of zinc in amounts ranging up to 1.5% with the aim of increasing strength and corrosion resistance (e.g., alloy 5059). However, there is evidence that high zinc levels may cause localized corrosion in the heat affected zones of welded components.

Because of their relatively high strengths in the annealed condition, Al–Mg alloys with higher levels of magnesium are candidates for the rapidly growing area of automotive sheet (Section 4.6.2). However, the fact they are susceptible to surface markings arising from Lüders band formation means that they may be restricted in use for inner panels. If this problem can be avoided, these alloys are capable of being polished to a bright surface finish, particularly if made from high-purity aluminium, and are used for automotive trim and architectural components.

Al–Mg alloys are widely used for welded applications. In transportation, structural plate is used for dump truck bodies, large tanks for carrying petrol, milk and grain, and pressure vessels, particularly where cryogenic storage is involved. Their high corrosion resistance makes them suitable for the hulls of small boats and for the superstructures of ocean-going vessels (Section 4.6.3). These alloys are also widely used for ballistic armor plate in lightweight military vehicles.

4.3.4 Miscellaneous alloys (8xxx series)

This series contains several dilute alloys, e.g., 8001 (Al–1.1Ni–0.6Fe) which is used in nuclear energy installations where resistance to corrosive attack by water at high temperatures and pressures is the desired characteristic. Its mechanical properties resemble 3003. Alloy 8011 (Al–0.75Fe–0.7Si) is used for bottle caps because of its good deep drawing qualities and several other dilute compositions are included in the range of EC materials (Section 4.6.9). This alloy and other dilute compositions containing transition metal elements, such as 8006 (Al–1.6Fe–0.65Mn), are used for producing foil (Section 4.6.5) and finstock for heat exchangers (Section 4.5.2). In each of these alloys, the most important contribution to strengthening comes from dispersion hardening which commonly accounts for 30–40 MPa of the values for proof stress and tensile strength. Solid solution strengthening is the next most important factor providing estimated increments of 2–10 MPa in proof stress of 5–20 MPa in tensile strength.

Alloys such as 8280 and 8081 serve an important role as bearing alloys based on the Al–Sn system that are now widely used in motor cars and trucks, particularly where diesel engines are involved. These alloys are considered in some detail in Section 4.6.7. Lithium-containing alloys, designated 8090 and 8091, are described in Section 4.4.6.

4.4 HEAT-TREATABLE ALLOYS

Wrought alloys that respond to strengthening by heat treatment are covered by the three series 2xxx (Al–Cu, Al–Cu–Mg), 6xxx (Al–Mg–Si), and 7xxx (Al–Zn–Mg, Al–Zn–Mg–Cu). All depend on age hardening to develop enhanced strength properties and they can be classified into two groups: those that have medium strength and are readily weldable (Al–Mg–Si and Al–Zn–Mg), and the high-strength alloys that have been developed primarily for aircraft construction (Al–Cu, Al–Cu–Mg, and Al–Zn–Mg–Cu), most of which have very limited weldability. Compositions of representative commercial alloys are given in Table 4.4, and Table 4.5 provides typical properties, the forms in which they are available, together with some common applications.

Table 4.4 Compositions of selected heat-treatable wrought aluminium alloys

IADS designation	Si	Fe	Cu	Mn	Mg	Zn	Cr	Ti	Other
2001	0.20	0.20	5.2–6.0	0.15–0.50	0.20–0.45	0.10	0.10	0.20	0.05Zr, 0.003 max. Pb
2011	0.40	0.70	5.0–6.0			0.30			0.02–0.6Bi, 0.2–0.6Pb
2014	0.5–1.2	0.70	3.9–5.0	0.40–1.2	0.20–0.8	0.25	0.10	0.15	0.2Zr + Ti
2017	0.20–0.8	0.70	3.5–4.5	0.4–1.0	0.4–0.8	0.25	0.10	0.15	0.2Zr + Ti
2618	0.10–0.25	0.9–1.3	1.9–2.7		1.3–1.8	0.10		0.04–0.10	0.9–1.2Ni
2219	0.20	0.30	5.8–6.8	0.20–0.40	0.02	0.10		0.02–0.10	0.05–0.15V, 0.10–0.25Zr
2519	0.25	0.30	5.3–6.4	0.10–0.50	0.05–0.40	0.1		0.10	0.05–0.15V, 0.10–0.25Zr
2021	0.20	0.30	5.8–6.8	0.20–0.40	0.02	0.10		0.02–0.10	0.10–0.25Zr
2024	0.50	0.50	3.8–4.9	0.30–0.9	1.2–1.8	0.25	0.10	0.15	0.20Zr + Ti
2124	0.20	0.30	3.8–4.9	0.30–0.9	1.2–1.8	0.25	0.10	0.15	0.20Zr + Ti
2324	0.10	0.12	3.8–4.4	0.30–0.6	1.2–1.6	0.20		0.10	
2025	0.50–1.2	1.0	3.9–5.0	0.40–1.2	0.05	0.25	0.10	0.15	
2036	0.50	0.50	2.2–3.0	0.10–0.40	0.30–0.6	0.25	0.10	0.15	
2048	0.08	0.10	4.8–5.4	0.45–0.8	0.7–1.1	0.25		0.06	0.08–0.15Zr, 0.4–0.7Ag
2060	0.07	0.07	3.4–4.5	0.10–0.50	0.6–1.1	03–0.5		0.10	0.6–0.9Li, 0.05–0.15Zr, 0.05–0.5Ag
6005	0.60–0.9	0.35	0.10	0.10	0.40–0.6	0.10		0.10	
6022	0.80–1.5	0.05–0.2	0.01–0.11	0.02–0.1	0.45–0.7	0.25	0.1	0.15	
6060	0.30–0.6	0.10–0.3	0.10	0.10	0.35–0.6	0.15	0.05	0.10	
6063	0.20–0.6	0.35	0.10	0.10	0.45–0.9	0.10	0.10	0.10	
6463	0.20–0.6	0.15	0.20	0.05	0.45–0.9	0.05			
6061	0.40–0.80	0.70	0.15–0.40	0.15	0.8–1.2	0.25	0.04–0.35	0.15	
6151	0.6–1.2	1.0	0.35	0.20	0.45–0.8	0.25	0.15–0.35	0.15	
6351	0.7–1.3	0.50	0.10	0.40–0.8	0.40–0.8	0.20		0.20	
6262	0.40–0.8	0.70	0.15–0.40	0.15	0.8–1.2	0.25	0.04–0.14	0.15	0.40–0.7Bi, 0.40–0.7Pb

(*Continued*)

Table 4.4 Compositions of selected heat-treatable wrought aluminium alloys (Continued)

IADS designation	Si	Fe	Cu	Mn	Mg	Zn	Cr	Ti	Other
6009	0.16–1.6	0.50	0.15–0.6	0.2–0.8	0.40–0.8	0.25	0.10	0.10	
6010	0.8–1.2	0.50	0.15–0.6	0.2–0.8	0.6–1.0	0.25	0.10	0.10	
6111	0.6–1.1	0.40	0.50–0.9	0.10–0.45	0.50–1.0	0.15	0.10	0.10	
6013	0.60–1.0	0.50	0.60–1.1	0.20–0.8	0.80–1.2	0.25	0.10	0.10	
6016	1.0–1.5	0.50	0.20	0.20	0.25–0.6	0.20	0.10	0.15	
6056	0.7–1.3	0.50	0.50–1.1	0.4–1.0	0.6–1.2	0.25	0.10–0.7		0.20Ti + Zr
6082	0.70–1.3	0.50	0.10	0.40–1.0	0.60–1.0	0.20	0.25	0.10	
7003	0.30	0.35	0.20	0.30	0.5–1.0	5.0–6.5	0.20	0.20	0.05–0.25Zr
7004	0.25	0.35	0. 05	0.20–0.7	1.0–2.0	3.8–4.6	0.05	0.05	0.10–0.20Zr
7005	0.35	0.40	0.10	0.20–0.7	1.0–1.8	4.0–5.0	0.06–0.20	0.01–0.06	0.08–0.20Zr
7009	0.20	0.20	0.6–1.3	0.10	2.1–2.9	5.5–6.5	0.10–0.25	0.20	0.25–0.40Ag
7010	0.10	0.15	1.5–2.0	0.30	2.2–2.7	5.7–6.7	0.05		0.11–0.17Zr
7016	0.10	0.12	0.45–1.0	0.03	0.8–1.4	4.0–5.2	0.35	0.15	0.10–0.25Zr
7017	0.35	0.45	0.20	0.05–0.5	2.0–3.0	4.0–5.2	0.35	0.15	0.10–0.25Zr, 0.15 min. Mn + Cr
7020	0.35	0.40	0.20	0.05–0.5	1.0–1.4	4.0–5.0	0.10–0.35		0.08–0.20Zr, 0.08–0.25Zr + Ti
7039	0.30	0.40	0.10	0.10–0.40	2.3–3.3	3.5–4.5	0.15–0.25	0.10	
7049	0.25	0.35	1.2–1.9	0.20	2.0–2.9	7.2–8.2	0.10–0.22	0.10	
7449	0.12	0.15	1.4–2.1	0.20	1.8–2.7	7.5–8.7			
7050	0.12	0.15	2.0–2.6	0.10	1.9–2.6	5.7–6.7	0.04	0.06	0.08–0.15Zr
7055	0.12	0.15	2.0–2.6	0.10	1.8–2.3	7.6–8.4	0.05	0.06	0.08–0.25Zr
7075	0.40	0.50	1.2–2.0	0.30	2.1–2.9	5.1–6.1	0.18–0.28	0.20	0.25Zr + Ti
7475	0.10	0.12	1.2–1.9	0.06	1.9–2.6	5.2–6.2	0.18–0.25	0.06	
7178	0.40	0.50	1.6–2.4	0.30	2.4–3.1	6.3–7.3	0.18–0.35	0.20	
7085	0.06	0.08	2.0–2.6	0.04	1.2–1.8	7.0–8.0	0.04	0.06	0.08–0.15Zr
7090*	0.12	0.15	0.6–1.3		2.0–3.0	7.3–8.7			1.0–1.9Co, 0.20–0.50O

Table 4.5 Tensile properties and applications of selected heat-treatable wrought aluminium alloys

IADS designation	Temper	0.2% Proof stress (MPa)	Tensile strength (MPa)	Elongation (% in 50 mm)	Typical applications
2011	T6	295	390	17	Screw machine parts
2014	T6	410	480	13	Aircraft structures
2017	T4	275	425	22	Screw machine fittings
2618	T61	330	435	10	Aircraft parts and structures for use at elevated temperatures. 2219 is weldable
2219	T62	290	415	10	
	T87	395	475	10	
2024	T4	325	470	20	Aircraft structures and sheet. Truck wheels
	T6	395	475	10	
	T8	450	480	6	
2124	T8	440	490	8	Aircraft structures
2025	T6	255	400	19	Forgings, aircraft propellers
2036	T4	195	340	24	Automotive body panels
2048	T85	440	480	10	Aircraft structures
6005	T5	270	305	12	General-purpose extrusions
6060	T5	195	215	17	
6016	T4	105	210	26	Automobile body sheet
6063	T6	215	240	12	Architectural extrusions, pipes
6061	T6	275	310	12	Welded structures
6151	T6	295	330	17	Medium-strength forgings
6009	T4	130	250	24	Automobile body sheet
	T6	325	345	12	
6010	T4	170	290	24	
6111	T4	160	290	25	
6013	T4	185	315	25	Aircraft sheet
6082	T5	260	300	15	Extrusions
	T6	285	315	12	Plate
7004	T6	340	400	12	Medium-strength welded structures
7005	T53	345	395	15	
7016	T6	315	360	12	
7020	T4	225	340	18	
	T6	310	370	15	
7039	T61	345	415	13	
7001	T6	625	675	9	Aircraft structures
7009	T6	470	535	12	
7010	T6	485	545	12	
7049	T73	470	530	11	
7050	T736	510	550	11	
7075	T6	500	570	11	
	T73	430	500	13	
	T76	470	540	12	
7475	7651	560	590	12	
7178	T6	540	610	10	
7055	T7751	610	630	12	
7085	T7651	475	510	7	
7090[a]	T7E71	580	620	9	Aircraft parts
7091[a]	T7E69	545	590	11	

[a]Alloys prepared by powder metallurgy techniques.

4.4.1 Al–Cu alloys (2xxx series)

Although the complex changes that occur during the ageing of Al–Cu alloys have been studied in greater detail than any other system, there are actually few commercial alloys based on the binary system. Alloy 2011 (Al–5.5Cu) is used where good machining characteristics are required, for which it contains small amounts of the insoluble elements lead and bismuth that form discrete particles in the microstructure and assist with chip formation. Alloy 2025 is used for some forgings although it has largely been superseded by 2219 (Al–6.3Cu) which has a more useful combination of properties and is also available as sheet, plate, and extrusions. Alloy 2219 has relatively high tensile properties at room temperature together with good creep strength at elevated temperatures and high toughness at cryogenic temperatures. In addition, it has excellent welding properties and has been used for fuel tanks for storing liquefied gases that serve as propellants for missiles and space vehicles. Response to age hardening is enhanced by strain hardening prior to artificial ageing (T8 temper) and the yield strength may be increased by as much as 35% as compared with the T6 temper (Table 4.5).

Modified versions of 2219 have been developed with the United States in order to meet requirements for increased tensile properties. One such alloy is designated 2021 which, as rolled plate, has a yield strength of 435 MPa, tensile strength of 505 MPa, and elongation of 9% with no reported sacrifice of weldability or toughness at low temperatures. Increased strength has been achieved by minor or trace additions of 0.15% cadmium and 0.05% tin which have the well-known effect of refining the size of the semi-coherent θ′ precipitate that forms on ageing in the medium temperature range (~130–200°C) (see Section 2.2.4). However, the toxicity of cadmium causes concern and production of this alloy has been banned in some countries. A second alloy is 2519, in which a minor amount of magnesium (e.g., 0.2%) modifies the precipitation process, resulting in greater age hardening.

The role of minor elements in modifying precipitation in an aged alloy based on the aluminium–copper system has also been exploited in an experimental alloy to promote improved strength at room and elevated temperatures. This alloy is based on 2219 but has controlled additions of 0.4 wt% (0.1 at.%) silver and magnesium (0.4–0.5%) which change the precipitation process. A typical composition is Al–5.8Cu–0.45Mg–0.4Ag–0.3Mn–0.15Zr. Instead of the phases θ″ and θ′ which precipitate on the $\{100\}_\alpha$ planes when 2219 is artificially aged, thin plates of a finely dispersed precipitate form on the $\{111\}_\alpha$ planes of the silver-containing alloy (Fig. 4.16). This phase, which has been designated Ω, has an orthorhombic structure (Table 2.2) and has proved to be relatively stable at temperatures up to approximately 200°C. As shown in Fig. 2.20, nucleation of Ω is facilitated in Al–Cu–Mg alloys having high Cu:Mg ratios due to rapid clustering of magnesium and silver atoms that occurs immediately artificial ageing is commenced. The Ag–Mg clusters do not have any well-defined shape at the start but evolve into more distinct platelets on $\{111\}_\alpha$ planes during further ageing. Once Ω precipitates have formed, the silver and

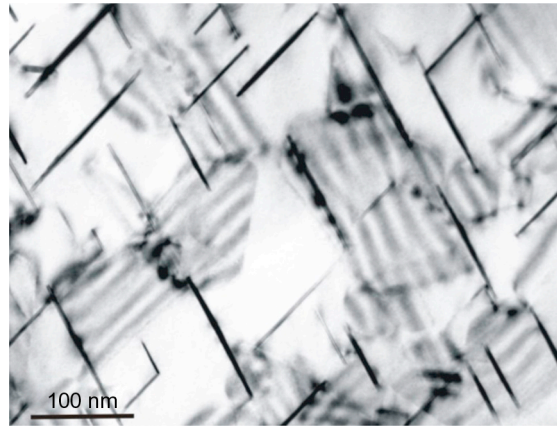


Figure 4.16 Plates of the Ω phase precipitated on the $\{111\}_\alpha$ planes in an Al–Cu–Mg–Ag alloy. Courtesy B. C. Muddle.

magnesium atoms diffuse to the broad Ω/matrix interface. There have been controversial reports on the thickness of the segregation layer. Early studies made by atom probe field ion microscopy revealed that silver and magnesium atoms were segregated into a single atomic layer. Subsequent work concluded that these atoms form a double layer in the Ω/matrix interface. More recent observations made by the atomic-resolution Z-contrast imaging technique of scanning transmission electron microscopy confirmed the existence of the double layer in the Ω/matrix interface (Fig. 4.17A). However, in the double layer that separates the Ω phase from the aluminium matrix, silver atoms are all confined in a single layer that is adjacent to the aluminium matrix whereas the copper atoms are in the next layer that is close to the precipitate (Fig. 4.17B). The silver atoms in the monolayer have a graphene-like hexagonal arrangement, with magnesium atoms located in the center of individual hexagons. The composition of this layer is Ag_2Mg. First-principles calculations indicated that the magnesium atoms in the layer stabilize the interfacial structure and hence the thermal stability of the Ω precipitate. Segregation of Ag and Mg atoms has been observed at all thicknesses of the Ω. Plates and it is presumed that the presence of these layers facilitates precipitate nucleation by reducing the interfacial energy. The presence of these layers at the surfaces of the Ω plates also restricts ledge formation thereby minimizing thickening at temperatures up to 200°C.

Alloys based on the Al–Cu–Mg–Ag system develop yield strengths that may exceed 500 MPa which compares with 290 and 395 MPa for alloy 2219 in the T6 and T87 conditions, respectively. In Fig. 4.18, accelerated stress-rupture tests suggest that the creep performances of four extruded Al–Cu–Mg–Ag alloys aged to the T6 condition are generally superior to those of three commercial 2xxx series alloys. As mentioned in the Section 2.5.6, it has been demonstrated that creep resistance can be further improved if aluminium alloys are

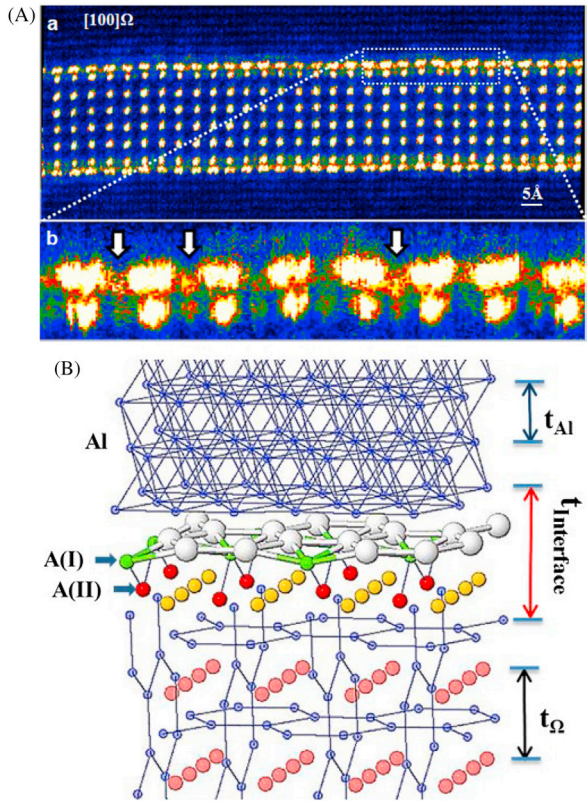


Figure 4.17 Segregation of a single layer of Ag atoms in the Ω/matrix interface. Atoms of Ag, Mg, Cu, and Al are colored in white, green, red/yellow/orange, and blue, respectively, in the schematic diagram. From Kang, SJ *et al.*: *Acta Mater.*, 81, 501, 2014.

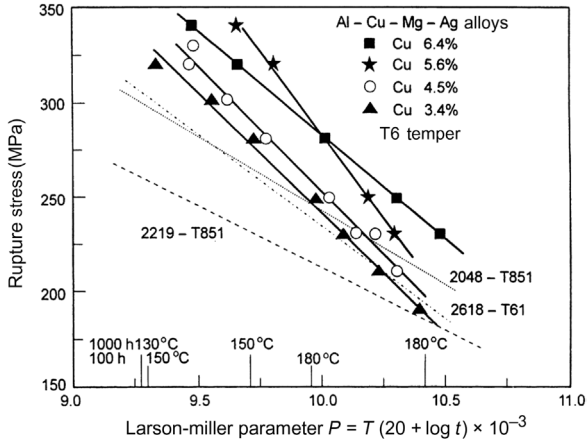


Figure 4.18 Larson–Miller plots of stress-rupture results for four alloys with compositions Al–3.4 to 6.4Cu–0.45Mg–0.40Ag–0.30Mn–0.18Zr, and for three commercial 2xxx series alloys. Equivalent positions for several temperatures after exposure times of 100 and 1000 h are shown on the horizontal axis. From Polmear, IJ *et al.*: *Mater. Sci. Technol.*, 15, 861, 1999.

tested in the underaged condition. As an example, the alloy Al–5.6Cu–0.45Mg–0.40Ag–0.30Mn–0.18Zr, underaged at 185°C for a time to reach 90% of its T6 0.2% proof stress, has shown zero secondary creep at 130°C during prolonged exposure for 20,000 h at a relatively high stress of 200 MPa. Several high-strength aluminium alloys containing these small additions of silver and magnesium have recently been registered including the nominal compositions 2039 (Al–5.0Cu–0.6Mg–0.38Ag–0.38Mn–0.18Zr) and 2040 (Al–5.1Cu–0.8Mg–0.55Ag–0.68Mn–0.11Zr). Alloy 2040 has recently been approved for the manufacture of critical aircraft wheels.

4.4.2 Al–Cu–Mg alloys (2xxx series)

These alloys date from the accidental discovery of the phenomenon of age hardening by Alfred Wilm, working in Berlin in 1906, who was seeking to develop a stronger aluminium alloy to replace brass for the manufacture of cartridge cases for guns. His work led to the production of an alloy known as Duralumin (Al–3.5Cu–0.5Mg–0.5Mn) which was quickly used for structural members for Zeppelin airships, and later for aircraft (Section 4.6.1). A modified version of this alloy (2017) is still used, mainly for rivets, and several other important alloys have been developed which are now widely used for aircraft construction. An example is 2014 (Al–4.4Cu–0.5Mg–0.9Si–0.8Mn) in which higher strengths have been achieved because the relatively high silicon content increases the response to hardening on artificial ageing. Typical tensile properties are 0.2% proof stress 320 MPa and tensile strength 485 MPa. Another alloy, 2024, in which the magnesium content is raised to 1.5% and the silicon content is reduced to impurity levels, undergoes significant hardening by natural ageing at room temperature and is frequently used in T3 or T4 tempers. It also has a high response to artificial ageing, particularly if cold worked prior to ageing at around 175°C, e.g., 0.2% proof stress 490 MPa and tensile strength 520 MPa for the T86 temper.

These and other 2xxx alloys in the form of sheet are normally roll-clad with aluminium or Al–1Zn (Fig. 4.8) in order to provide protection against corrosion, and the tensile properties of the composite product may be some 5% below those for the unclad alloy. Much greater reductions in strength may occur under fatigue conditions. For example, cladding 2014 sheet may reduce the fatigue strength by as much as 50% for tests conducted in air and under reversed plane bending. Differences between clad and unclad alloys are much less under axial loading conditions, or if the materials are tested as part of a structural assembly. Under corrosion-fatigue conditions, the strength of unclad sheet may fall well below that of the clad alloy. The adverse effect of cladding on fatigue strength in air is due mainly to the ease by which cracks can be initiated in the soft surface layers and a number of harder cladding materials have been investigated.

Microstructural features that influence toughness and ductility have been considered in Section 2.5.2. Fig. 4.19 shows that, for equal values of yield strength, alloys in the 2xxx series have lower fracture toughness than those of

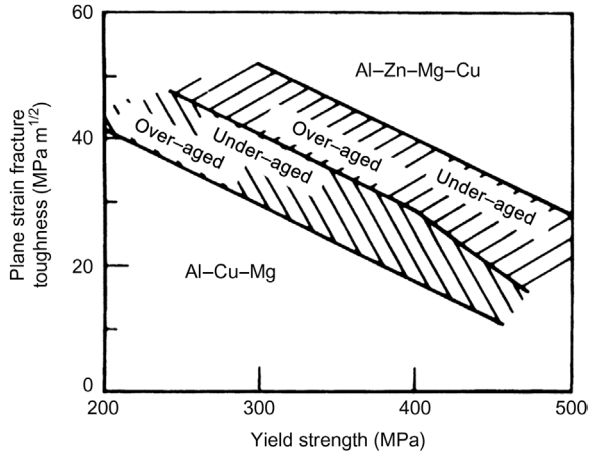


Figure 4.19 Relationships of plane strain fracture toughness to yield strength for the 2xxx and 7xxx series of alloys. From Develay, R: *Metals Mater.*, 6, 404, 1972.

Table 4.6 Effect of purity on the fracture toughness of some high-strength wrought aluminium alloys.

					Fracture toughness (MPa $m^{1/2}$)	
Alloy and temper	%Fe maximum	%Si maximum	0.2% proof stress (MPa)	Tensile strength (MPa)	Longitudinal	Short transverse
2024–T8	0.50	0.50	450	480	22–27	18–22
2124–T8	0.30	0.20	440	490	31	25
2048–T8	0.20	0.15	420	460	37	28
7075–T6	0.50	0.40	500	570	26–29	17–22
7075–T73	0.50	0.40	430	500	31–33	20–23
7175–T736	0.20	0.15	470	540	33–38	21–29
7050–T736	0.15	0.12	510	550	33–39	21–29

From Speidel, MO: *Metall. Trans.*, 6A, 631, 1975.

the 7xxx series (Al–Zn–Mg–Cu). This is attributed to the larger sizes of intermetallic compounds in the 2xxx alloys. Improvements in both fracture toughness and ductility can be obtained by reducing the levels of iron and silicon impurities as well as that of copper, all of which favor formation of large, brittle compounds in the cast materials. This led to the development of alloys such as 2124 (iron 0.3% maximum, silicon 0.2% maximum, as compared with levels up to 0.5% for each of these elements in 2024) and 2048 (copper reduced to a nominal value of 3.3% and impurities iron and silicon reduced to 0.2% and 0.15% maximum, respectively). Some comparative properties are shown in Fig. 2.41 and Table 4.6. High-toughness versions of older alloys such as 2024 are now being used as sheet, plate, and forgings in several modern aircraft.

Table 4.7 Effects of interrupted ageing and secondary hardening on the mechanical properties of selected aluminium alloys.

Alloy[a] and treatment[b]	0.2% proof stress (MPa)	Tensile strength (MPa)	Elongation (%)	Fracture toughness[c] (MPa $m^{1/2}$)
2014–T6	414	488	5	26.9
2014–T6I6	436	526	10	36.2
6061–T6	267	318	13	36.8
6061–T6I6	299	340	13	58.4
6061–T6I4	302	341	16	43.2
7050–T6	546	621	14	37.6
7050–T6I6	574	639	14	41.1
7050–T6I4	527	626	16	52.0
8090–T6	349	449	4	24.2
8090–T6I6	391	512	5	31.0
357–T6	287	325	7	25.5
357–T6I6	341	375	5	26.0
357–T6I4	280	347	8	35.9

After Lumley, RN *et al.*: *Mater. Sci. Technol*., 19, 1, 2003, and *Proc. 9th Inter. Conf. on Aluminium Alloys*, *Mater. Forum*, IMEA, 85, 2004.

[a]Wrought alloys except for casting alloy 357. Compositions in Tables 4.4 and 5.2, respectively.

[b]T6 involves single stage artificial ageing to peak strength at appropriate temperatures. T6I6 is a designation indicating that the T6 temper has been interrupted by quenching and holding the alloys for a prescribed time at 65°C, after which artificial ageing to peak strength is resumed. T6I4 is a designation indicating that T6 temper has been interrupted by quenching and holding the alloys for a long time at 65°C. In this case, artificial ageing is not resumed.

[c]Fracture toughness tests on wrought alloys in S-L orientation. All tests under plane strain conditions except for alloy 6061.

Experimental interrupted ageing treatments involving secondary precipitation (Section 2.3.5) have also been found to increase fracture toughness in the Al–Cu–Mg alloy 2014 and a number of other commercial aluminium alloys. Moreover, these improvements may be accompanied by increased tensile properties despite the fact that toughness and strength are usually inversely related. Results given in Table 4.7 compare these properties for selected wrought alloys, and the casting alloy 357 (Al–7Si–0.5Mg), that were given standard T6 or interrupted ageing treatments. Increases in fracture toughness by using the latter treatments were as follows: 2014 34.5%; 6061 58.6% and 17.4%; 7050 9.3% and 38.3%; 8090 28.1%; 357 2.0% and 38.8%.

Relationships between rate of growth of fatigue cracks and stress intensity for the alloys 2024–T3 and 7075–T6 are shown in Fig. 4.20. Other 2xxx series alloys show similar rates of crack propagation to 2024–T3 over most of the range of test conditions. In general, these alloys have rates of crack growth that are close to one-third those observed in the 7xxx series alloys.

It is now common to use precracked specimens to assess comparative resistance of alloys to SCC since this type of test avoids uncertainties associated

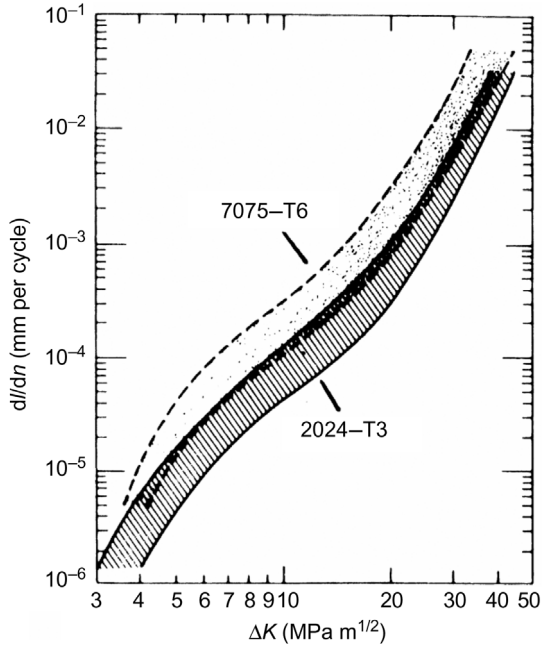


Figure 4.20 Comparative fatigue crack growth rates for 2024–T3 and 7075–T6 in air of varying humidity. From Hahn, GT and Simon, R: *Eng. Fract. Mech.*, 5, 523, 1973.

with crack initiation. Relationships between crack growth rate and stress intensity in tests on several 2xxx series alloys are shown in Fig. 4.21. It is clear that there is a large variation in threshold stress intensities for different alloys, while the crack velocity plateaus are similar. Thus the ranking of these alloys is best obtained from measurements of the threshold stress intensities (K_{1scc} values). In the naturally aged tempers T3 and T4, the 2xxx series are prone to SCC. The alloy 2014 in the T6 temper is also susceptible, whereas the more recent alloy 2048 in the T8 temper is much more resistant to this form of cracking.

Interest in supersonic aircraft such as Concorde stimulated a need for a sheet alloy with improved creep strength on prolonged exposure, e.g., 50,000 h, at temperatures around 120°C. Such a material was developed from a forging alloy known widely as RR58 (2618) which itself had been adapted from an early casting alloy (Al–4Cu–1.5Mg–2Ni) known originally in England as Y alloy. The alloy 2618 has the nominal composition Al–2.2Cu–1.5Mg–1Ni–1Fe, in which the copper and magnesium contribute to strengthening through age hardening, whereas nickel and iron form the intermetallic compound Al_9FeNi which promotes dispersion hardening and assists in stabilizing the microstructure. One refinement was the addition of 0.2% silicon, which both increases the hardening associated with the first stage in the ageing process (GPB zones) and

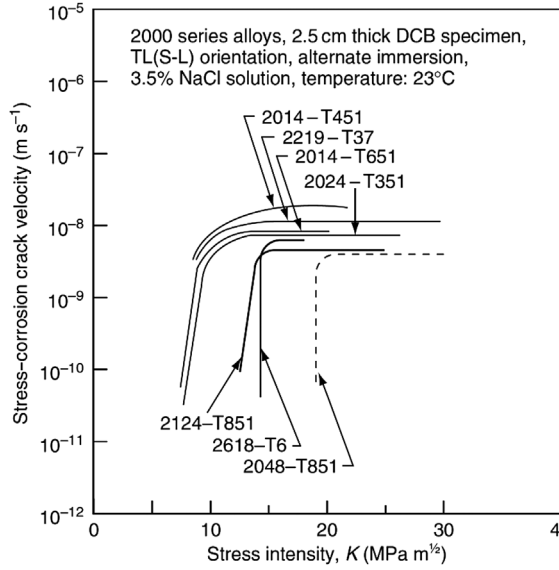


Figure 4.21 Crack propagation rates in stress–corrosion tests using precracked specimens of 2xxx alloys exposed to an aqueous solution of 3.5% NaCl. Double cantilever beam (DCB) specimens selected from short transverse direction of 25 mm thick plate and wet with the solution twice a day. From Speidel, MO: *Metall. Trans A*, 6A, 631, 1975.

promotes formation of a more uniform dispersion of the S′ (or S) phase (Table 2.3). Both these changes improve the creep properties of the alloy on long-term exposure at temperatures of 120–150°C.

Lower-strength Al–Cu–Mg alloys have been investigated as possible sheet materials for automotive applications and these are discussed in Section 4.6.2. One example is 2036 which has nominal copper and magnesium contents of 2.5% and 0.45%, respectively.

4.4.3 Al–Mg–Si alloys (6xxx series)

Al–Mg–Si alloys are widely used as medium-strength structural alloys which have the additional advantages of good weldability, corrosion resistance, and immunity to SCC. Just as the 5xxx series of alloys comprise the bulk of sheet products, the 6xxx series are used for the majority of extrusions, with smaller quantities being available as sheet and plate (Fig. 4.22). In commercial alloys, magnesium and silicon are added either in what are called “balanced” amounts to form quasi-binary Al–Mg_2Si alloys (Mg:Si 1.73:1), or with an excess of silicon above that needed to form Mg_2Si. The commercial alloys may be divided into three groups and a guide to the strength levels that may be attained in the T6 condition is shown as contours drawn on a compositional plot in Fig. 4.23.

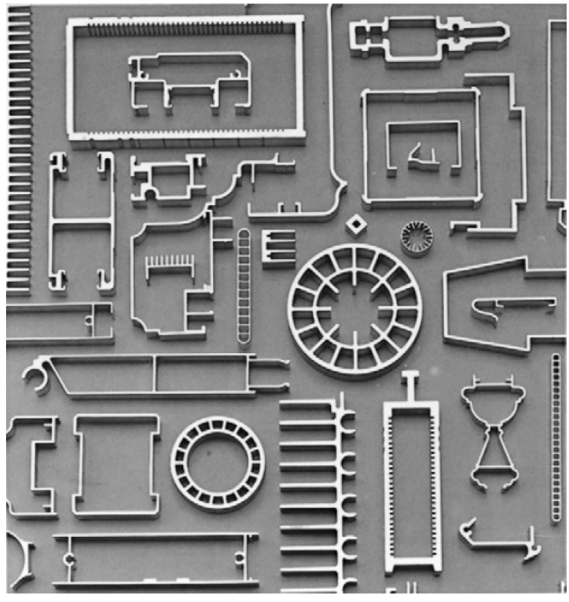


Figure 4.22 Examples of extruded sections made from Al–Mg–Si alloys. Courtesy Sumitomo Metal Industries Ltd.

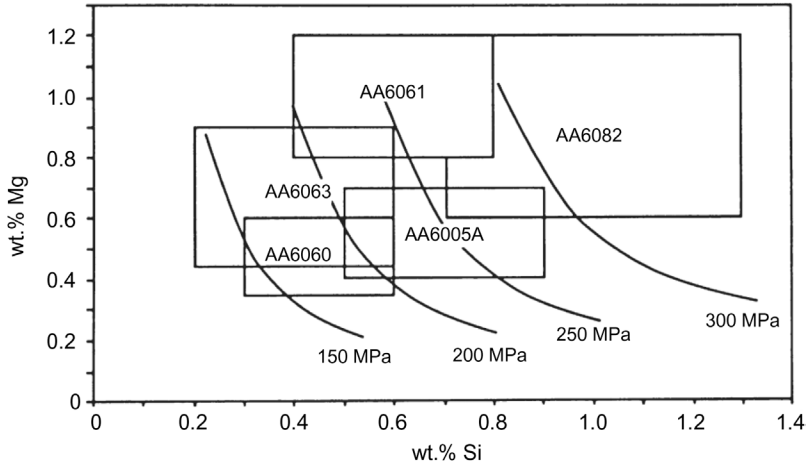


Figure 4.23 The compositional limits of some common 6xxx alloys, together with contours, representing common peak aged (T6) values of yield strength. From Court, SA *et al.*: *Proc. of 4th Inter. Conf. on Aluminium Alloys*, Atlanta, GA, USA, Sanders, TH and Starke, EA (Eds.), 1, 395, 1994.

The first group comprises alloys with balanced amounts of magnesium and silicon adding up to between 0.8% and 1.2%. These alloys can be readily extruded and offer a further advantage in that they may be quenched at the extrusion press when the product emerges hot from the die, thereby eliminating the need to solution treat as a separate operation. Quenching is normally achieved by means of water sprays, or by leading the product through a trough of water. Thin sections (3 mm) can be air-cooled. Moderate strength is developed by age hardening at 160–190°C and one alloy, 6063, is perhaps the most widely used of all Al–Mg–Si alloys. In the T6 temper, typical tensile properties are 0.2% proof stress 215 MPa and tensile strength 245 MPa. These alloys find particular application for architectural and decorative finishes and, in this regard, they respond well to clear or color anodizing as well as to the application of other surface finishes. A high-purity version, 6463, in which the iron content is kept to a low level (0.15%), responds well to chemical brightening and anodizing for use as automotive trim.

The other two groups of Al–Mg–Si alloys contain magnesium and silicon in excess of 1.4%. They develop higher strength on ageing and, because they are more quench sensitive, it is usually necessary to solution treat and water quench as separate operations after extrusion. One group, which is particularly popular in North America, has balanced compositions and a common example is 6061 (Al–1Mg–0.6Si) to which is added 0.25% copper to improve mechanical properties together with 0.2% chromium to offset any adverse effect copper may have on corrosion resistance. These alloys are widely used as general-purpose structural materials. The alloys in the other group contain silicon in excess of that needed to form Mg_2Si and the presence of this excess promotes an additional response to age hardening by both refining the size of the Mg_2Si particles and precipitating as silicon. The higher silicon contents may reduce ductility and cause intergranular embrittlement which is attributed in the tendency for this element to segregate to the grain boundaries. However, the presence of chromium (alloy 6151) and manganese (6351) helps to counter this effect by promoting fine grain size and inhibiting recrystallization during solution treatment. These alloys are used as extrusions and forgings. A more recent example of a high silicon alloy is 6082 (Al–1Si–0.9Mg–0.7Mn) which is a structural material used widely in Europe.

As mentioned in Section 2.3.4, there is strong experimental evidence that the actual atomic ratios Mg:Si in the intermediate precipitates that contribute maximum age hardening in Al–Mg–Si alloys are close to 1:1 rather than the expected 2:1 present in the equilibrium precipitate β (Mg_2Si). It has been suggested, therefore, that the balanced alloys actually have magnesium contents in excess of that needed to promote the required age-hardening response. This led to the design of a new series of alloys in which the magnesium contents were reduced in order to improve the hot working characteristics and increase productivity without compromising mechanical properties. As an example, the tensile properties of the readily extrudable alloy 6060, with a modified composition (Al–0.35Mg–0.5Si), are found to be comparable with those of the popular alloy 6063 (Al–0.5Mg–0.4Si), whereas extrusion speeds may be up to 20% greater.

Higher strengths may be achieved in Al–Mg–Si alloys by increasing the copper content and the alloy 6013 (Al–1Mg–0.8Si–0.8Cu–0.35Mn) has a 0.2% proof stress of 330 MPa for the T6 temper. This compares with a 0.2% proof stress of 275 MPa for the widely used alloy 6061 which has a maximum copper content of 0.25%. Another alloy is 6111 (Al–0.75Mg–0.85Si–0.7Cu–0.3Mn). These alloys are hardened by the presence of the Q phase ($Al_5Cu_2Mg_8Si_6$) that precipitates in addition to the phases which form in ternary Al–Mg–Si alloys (Table 2.3). The alloys have been promoted for automotive and aircraft applications. Because of the higher copper contents, the alloys may show some susceptibility to intergranular corrosion that is associated with the formation of precipitate-free zones at grain boundaries (see Section 2.2.3) which are depleted of copper and silicon and, as a consequence, are anodic with respect to the grains. This problem can be reduced by using a proprietary T78 temper which involves a controlled amount of overageing.

Al–Mg–Si alloys are normally aged at about 170°C and the complete precipitation process is now recognized as being perhaps the most complex of all age-hardened aluminium alloys (Table 2.3). Early clustering of silicon atoms has been detected prior to the formation of GP zones which can influence subsequent stages of precipitation. For example, during commercial processing, there may be a delay at room temperature between quenching and artificial ageing which may modify the mechanical properties that are developed. In alloys containing more than 1% Mg_2Si, a delay of 24 h causes a reduction of up to 10% in tensile properties as compared with the properties obtained by ageing immediately. However, such a delay can enhance the tensile properties developed in compositions containing less than 0.9% Mg_2Si. These effects have been attributed to clustering of solute atoms and vacancies that occurs at room temperature, and to the fact that the GP zones solvus (Section 2.2.2) is above 170°C for the more highly alloyed compositions. With these alloys, the precipitate which develops directly from the clusters formed at room temperature is coarser than that developed in alloys aged immediately after quenching, with a consequent adverse effect on tensile properties. The reverse occurs in alloys containing less than 0.9% MgSi. The addition of small amounts of copper (e.g., 0.25%) lessens the adverse effects of delays at room temperature by promoting an increased response to artificial ageing.

As with the 2xxx series, there is an Al–Mg–Si alloy (6262) containing additions of lead and bismuth to improve machining characteristics. Although the machinability of this alloy is below the Al–Cu alloy 2011, it is not susceptible to SCC and is preferred for more highly stressed fittings.

4.4.4 Al–Zn–Mg alloys (7xxx series)

The Al–Zn–Mg system offers the greatest potential of all aluminium alloys for age hardening although the very high-strength alloys always contain quaternary additions of copper to improve their resistance to SCC (Section 4.4.5).

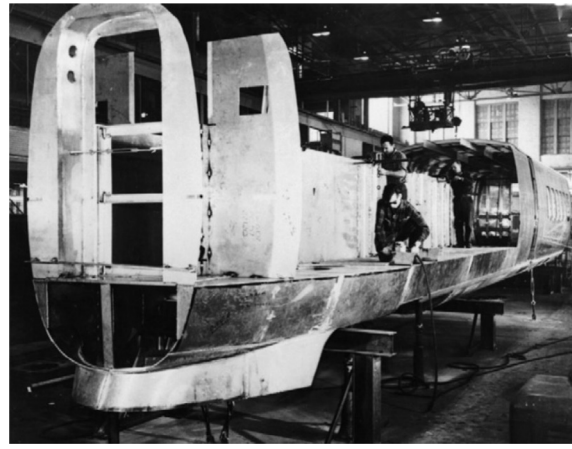


Figure 4.24 Railway carriage made from a welded Al–Zn–Mg alloy.

There is, however, an important range of medium-strength alloys containing little or no copper that have the advantage of being readily weldable. These alloys differ from most other weldable aluminium alloys in that they age harden significantly at room temperature. Moreover, the strength properties that are developed are relatively insensitive to rate of cooling from high temperatures, and they possess a wide temperature range for solution treatment, i.e., 350°C and above, with the welding process itself serving this purpose. Thus there is a considerable recovery of strength after welding and tensile strengths of around 320 MPa are obtained without further heat treatment. Yield strengths may be as much as double those obtained for welded components made from the more commonly used Al–Mg and Al–Mg–Si alloys.

Weldable Al–Zn–Mg alloys were first developed for lightweight military bridges but they now have commercial applications, particularly in Europe, e.g., Fig. 4.24. Elsewhere, their use has been less widespread for fear of possible SCC in the region of welds. Many compositions are now available which may contain 3–7% zinc and 0.8–3% magnesium (Zn+ Mg in the range of 4.5–8.5%) together with smaller amounts (0.1–0.3%) of one or more of the elements chromium, manganese, and zirconium. These elements are added mainly to control grain structure during fabrication and heat treatment although it has been claimed that zirconium also improves weldability. Minor additions of copper are made to some alloys but the amount is kept below 0.3% to minimize both hot cracking during the solidification of welds and corrosion in service. Compositions of representative weldable Al–Zn–Mg alloys are given in Table 4.8 for different categories of tensile strength.

Improvements in resistance to SCC have come through control of both composition and heat treatment procedures. With respect to composition, it is well known that both tensile strength and susceptibility to cracking increase as the

Table 4.8 Zinc and magnesium contents and ratios in some Al–Zn–Mg and Al–Zn–Mg–Cu alloys

	Alloy	Zn (%)	Mg (%)	Zn + Mg (%)	Zn/Mg ratio
Medium strength	7104	4.0	0.7	4.7	5.7
weldable	7008	5.0	1.0	6.0	5.0
Al–Zn–Mg alloys	7011	4.7	1.3	6.0	3.7
	7020	4.3	1.2	5.5	3.6
	7005	4.5	1.4	5.9	3.2
	7004	4.2	1.5	5.7	2.8
	7051	3.5	2.1	5.6	1.7
Higher strength	7003	5.8	0.8	6.6	7.2
weldable	7046	7.1	1.3	8.4	5.5
A1–Zn–Mg alloys	7039	4.0	2.8	6.8	1.4
	7017	4.6	2.5	7.1	1.8
High strength	7049	7.7	2.5	10.2	3.1
Al–Zn–Mg–Cu	7050	6.2	2.3	8.5	2.7
alloys	7010	6.2	2.5	8.7	2.5
	7475	5.7	2.3	8.0	2.5
	7001	7.4	3.0	10.4	2.5
	7075	5.6	2.5	8.1	2.2
	7055	8.0	2.05	10.05	3.9
	7085	7.5	1.5	9.0	5.0

Zn+ Mg content is raised and it is necessary to seek a compromise when selecting an alloy for a particular application. It is generally accepted that the Zn+ Mg content should be less than 6% in order for a weldable alloy to have a satisfactory resistance to cracking, although additional controls may be required. It has also been proposed that the Zn:Mg ratio is important and, with respect to these two elements, there is experimental evidence which suggests that the maximum resistance to SCC occurs if this ratio is between 2.7 and 2.9 (Fig. 4.25). As given in Table 4.8, few of the existing commercial alloys do in fact comply with this proposed ratio. Small amounts of copper and, more particularly, silver have been shown to increase resistance to SCC but the addition of silver is considered too great a cost penalty for this range of alloys.

Two changes in heat treatment procedures have led to a marked reduction in susceptibility to SCC in the weldable alloys. One has been the use of slower quench rates, e.g., air cooling, from the solution treatment temperature which both minimizes residual stresses and decreases differences in electrode potentials throughout the microstructure. This practice has also had implications with regard to composition as there has been a tendency to use 0.08–0.25% zirconium to replace chromium and manganese for the purpose of inhibiting recrystallization because this element has the least effect on quench sensitivity (Fig. 4.13). This characteristic is thought to arise because zirconium forms small,

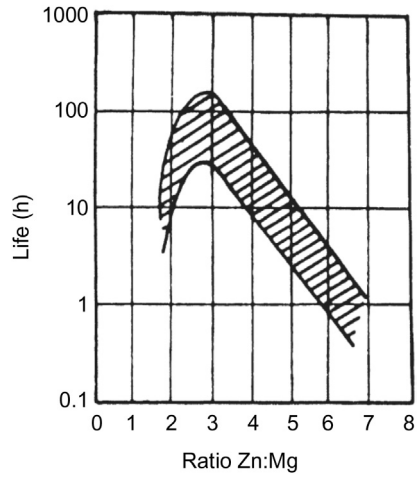


Figure 4.25 Effect of Zn:Mg ratio on the susceptibility of Al–Zn–Mg alloys to SCC. From Gruhl, W: *Inter. Congress on Aluminium Alloys in the Aircraft Industry*, Turin, 1976.

insoluble particles of Al_3Zr, whereas chromium and manganese combine with some of the principal alloying elements to form $Al_{12}Mg_2Cr$ and $Al_{20}Cu_2Mn_3$, respectively, thereby removing them from solid solution. The other change has been to artificially age the alloys, sometimes to the extent of using a duplex treatment of the T73 type.

The Al–Zn–Mg alloys are normally welded with an Al–4.5Mg+ Mn filler wire although some compositions are available which contain both zinc and magnesium. Although problems with intercrystalline SCC of welded structures in service are now comparatively rare, when this does occur, the cracks normally form close to the weld bead/parent alloy interface in what has become known as the "white zone" (Fig. 4.26). This is a region within the parent metal that has undergone partial liquation and in which the zinc and magnesium contents vary considerably (Fig. 4.26). It is also one into which elements added to the filler wire can diffuse, at least in part, but the influence of filler composition on SCC has not been studied in detail.

For most welded aluminium alloys, the weld beads are electronegative with respect to the adjacent heat affected zones and parent metal. Thus the weld beads act sacrificially (i.e., they are preferentially corroded) thereby protecting the surrounding, more vulnerable regions from corrosive attack. This situation is in fact reversed with the 7xxx series of alloys as it is the weld bead that is electropositive. The surrounding regions therefore require special protection and traditional methods have involved the use of paints and sprayed coatings. Success has also been achieved by the novel technique of completing the welding operation with a capping pass using a filler wire containing the elements tin, indium, or gallium. These elements lower the electrode potential of the

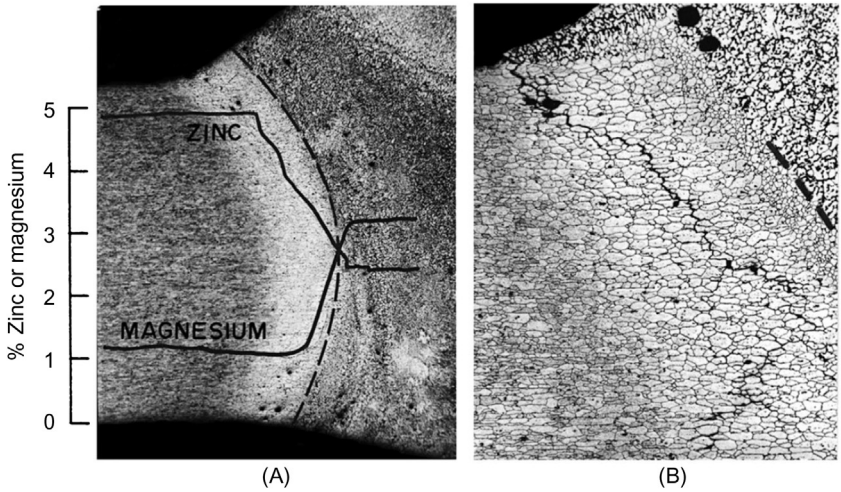


Figure 4.26 (A) Section showing interface between parent metal and weld bead. The "white zone" of the parent metal is revealed by deep etching with 20% HNO_3. The compositions of the parent metal and filler wire were Al–4.9Zn–1.2Mg and Al–4.5Mg, respectively. Variations in the zinc and magnesium contents were determined by microprobe analysis × 15; (B) intercrystalline cracking within the white zone × 40. From Cordier, H and Polmear, IJ: *Proc. of Eurocor 77*, Soc. Chemical Industry, London, 1979.

aluminium in the weld bead so that it becomes electronegative (i.e., protective) with respect to the surrounding regions. The role of these so-called activating elements is discussed in detail in Section 4.6.10.

4.4.5 Al–Zn–Mg–Cu alloys (7xxx series)

These alloys have received special attention because it has long been realized that they have a particularly high response to age hardening. For example, Rosenhain and his colleagues at the National Physical Laboratory in Britain in 1917 obtained a tensile strength of 580 MPa for a composition Al–20Zn–2.5Cu–0.5Mg–0.5Mn when the value for Duralumin was 420 MPa. However, this alloy and others produced over the next two decades proved to be unsuitable for structural use because of a high susceptibility to SCC. Because of the critical importance of Al–Zn–Mg–Cu alloys for aircraft construction, this problem has been the subject of continuing research and development and will now be considered in some detail.

Military needs in the late 1930s and 1940s for aircraft alloys having higher strength/weight ratios eventually led to the introduction of several Al–Zn–Mg–Cu alloys of which 7075 is perhaps the best known. Later this alloy and equivalent materials such as DTD 683 in Britain were also accepted for the construction of most civil aircraft. Stronger alloys, e.g., 7178–T6, tensile

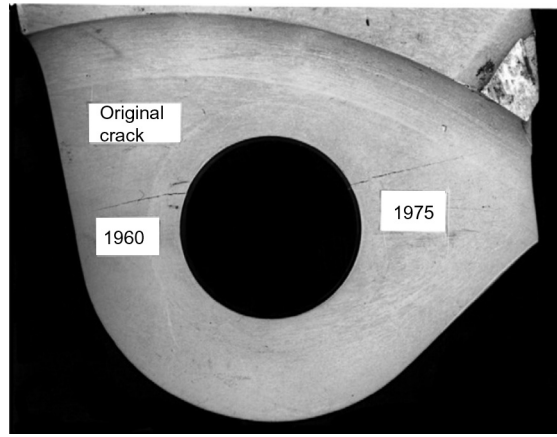


Figure 4.27 Stress–corrosion cracks in a cold-water quenched Al–Zn–Mg–Cu alloy forging.

strength 600 MPa, were introduced for compressively stressed members and another alloy 7079–T6 was developed particularly for large forgings for which its lower quench sensitivity was an advantage. However, continuing problems with SCC, notably in an early alloy 7079–T6, which was later withdrawn from production, and deficiencies in other properties stimulated a need for further improvements. Some aircraft constructors, in fact, reverted to using the lower-strength alloys based on the Al–Cu–Mg system even though a significant weight penalty was incurred.

Until then it had been the usual practice to cold-water quench components after solution treatment which could introduce high levels of residual stress. An example is shown in Fig. 4.27 in which machining of the end lug of a cold-water quenched aircraft forging exposed the underlying residual tensile stresses that contributed to SCC. It is interesting to note that, although cracking within the bore was first detected when the forging was in service, the cracks in the sides of the lugs propagated subsequently after the forging had been removed and exposed to corrosive atmospheres on separate occasions many years apart. Because of the problem of quenching stresses, some attempt was made in Britain to use chromium-free alloys for forgings and other components that could not be stress-relieved. Such alloys could accommodate a milder quench, e.g., in boiling water, without suffering a reduced response to ageing.

Another early practice was to give a single ageing treatment at temperatures in the range 120–135°C at which there was a high response to hardening due to precipitation of GP zones (Section 2.2.1). It was known that ageing these alloys at a higher temperature of 160–170°C, at which the phase η' (or η) formed, did result in a significant increase in resistance to SCC but tensile properties were much reduced (see curve a in Fig. 4.28). Subsequently, a duplex ageing treatment designated the T73 temper was introduced in which a finer dispersion of

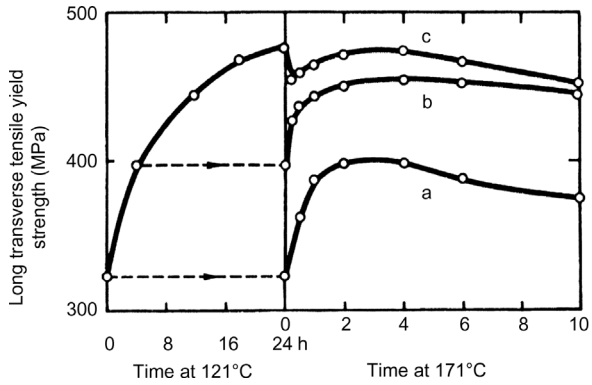


Figure 4.28 Comparison of yield strengths (0.2% proof stress) of 7075 plate resulting from isothermal (171°C) (curve a) and two-stage (121°C/171°C) (curve b) precipitation heat treatments. The enhanced yield strength for the alloy 7050 given a two-stage treatment is shown in curve c. From Hunsicker, HY: *Rosenhain Centenary Conf. on the Contribution of Physical Metallurgy to Engineering Practice*, The Royal Society, London, 1976.

the η′ (or η) precipitate could be obtained through nucleation from preexisting GP zones. As shown in Fig. 4.28 (curve b) tensile properties of 7075–T73 are about 15% below those for the T6 temper but now the resistance to SCC is greatly improved. For example, tests on specimens loaded in the short transverse direction have shown the alloy 7075 aged to the T73 temper to remain uncracked at stress levels of 300 MPa whereas, in the T6 condition, the same alloy failed at stresses of only 50 MPa in the same environment. Confidence in the T73 temper was demonstrated by the use of 7075–T73 for critical aircraft components such as the large die forging as shown in Fig. 4.29. Another duplex ageing treatment, designated T76, has been applied successfully to 7xxx alloys to increase resistance to exfoliation (layer) corrosion (Fig. 2.37).

The use of alloys given the T73 temper required that some aircraft components be redesigned and weight penalties were incurred when replacing alloys aged to the T6 temper. For this reason, much research has been directed to the development of alloys that could combine a high resistance to SCC with maximum levels of tensile properties. Some success was achieved with the addition of 0.25–0.4% silver as this element modifies the precipitation process in alloys based on the Al–Zn–Mg–Cu system enabling a high response to age hardening to be achieved in a single ageing treatment at 160–170°C. One German commercial high-strength alloy designated AZ74 (7009), which contained this element, was used for some forgings in two European aircraft manufactured in the 1970s. More recently, an alloy 7050 (Al–6.2Zn–2.25Mg–2.3Cu–0.12Zr) was developed by Alcoa in the United States in which the level of copper normally present in alloys such as 7075 was raised in order to increase the strengthening associated with the second stage of the T73 treatment (curve c in Fig. 4.28).



Figure 4.29 Die-forged 7075–T73 integral center engine support and vertical stabilizer spar for the McDonnell-Douglas DC-10 aircraft. Four similar forgings were used in each aircraft. From Hunsicker, HY: *Rosenhain Centenary Conf. on the Contribution of Physical Metallurgy to Engineering Practice*, The Royal Society, London, 1976.

Modern derivatives of 7050 are another high-strength alloy 7150 which had marginally higher amounts of Zn and Mg, and the later alloys 7055, 7449, and 7085 all of which have significantly higher levels of zinc (8% compared with 6.2%).

Another heat treatment has been developed which enables alloys such as 7075 to exhibit the high level of tensile properties expected of the T6 condition combined with SCC resistance equal to the T73 condition. This is known as retrogression and re-ageing (RRA) which involves the following stages for 7075:

1. Apply T6 treatment, i.e., solution treatment at 465°C, cold-water quench, age 24 h at 120°C.
2. Heat for a short time (e.g., 5 min) at a temperature in the range 200–280°C and cold-water quench.
3. Reage 24 h at 120°C.

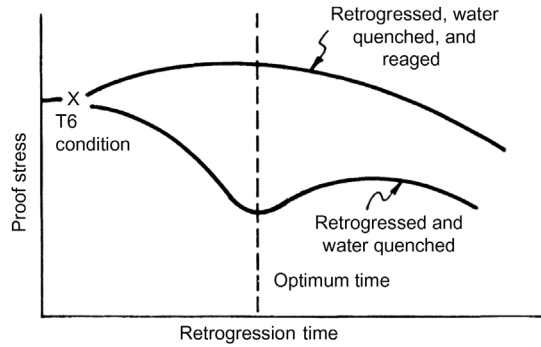


Figure 4.30 Schematic representation of the effects of RRA on the proof stress of an alloy such as 7075. From Kaneko, RS: *Met. Progr.*, 41(4), 1980.

Tensile property changes are shown schematically in Fig. 4.30. It is generally accepted that the RRA treatment results in a microstructure having a matrix similar to that obtained for a T6 temper, combined with grain boundary regions characteristic of a T73 temper in that precipitates are larger and more widely separated. Reduced susceptibility to SCC has been attributed to this latter change (Section 2.5.4). However, because of the short time interval initially proposed for stage (2), e.g., 1–5 min, an RRA treatment was difficult to apply to thick sections. More recently, the time and temperature conditions for this stage of the process have been optimized (e.g., 1 h at 200°C) and the RRA treatment has been given the commercial temper designation T77. It has been applied to the highly alloyed composition 7055 (Al–8Zn–2.05Mg–2.3Cu–0.16Zr) that has been used for structural members of the wings of the Boeing 777 passenger aircraft (Section 4.6.1).

As mentioned in Section 4.1.5, thermomechanical processing offers another method of optimizing the properties of age-hardened alloys. Fig. 4.31 shows, schematically, a way of combining ageing with deformation with the objective of achieving dislocation strengthening to compensate for the loss in strength that normally occurs during the overageing part of the T73 treatment mentioned earlier. Deformation is achieved by warm working after a T6 ageing treatment and before overageing. It has been reported that thermomechanical processing of some 7xxx alloys in this way can result in an improvement of some 20% in strength with no loss in toughness, or vice versa. However, commercial implementation has presented difficulties because of problems in controlling temperature and level of deformation that has to be carried out on material which is already in the age-hardened condition.

Other compositional changes have been made. One example is a reduction of the levels of the impurities iron and silicon in alloys such as 7075 (Fe+ Si 0.90% maximum) to a combined maximum of 0.22% in the higher purity alloy 7475 (Table 4.4). 7475 also has the manganese content reduced from 0.30%

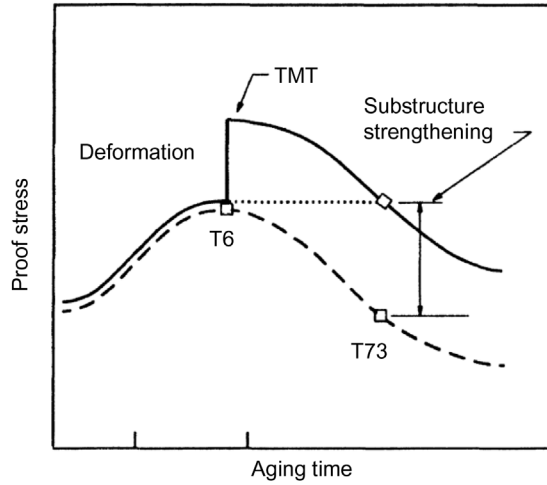


Figure 4.31 Schematic representation of FTMT strengthening of a 7xxx alloy. From Paton, NE and Sommer, AW: *Proc. of 3rd Inter. Conf. on Strength of Metal and Alloys*, Metals Society, London, 1, 101, 1973.

maximum to 0.06% maximum, whereas the content of the other alloying elements is essentially the same as 7075. The size and number of intermetallic compounds that assist crack propagation are much reduced in 7475 and, for similar T735 heat treatments and tensile properties, the fracture toughness (K_{1c}) values may exceed 50 MPa $m^{1/2}$ whereas a typical figure for 7075 is 30 MPa $m^{1/2}$. There is a cost penalty of around 10% for producing 7475 but it has been widely used in aircraft.

Another modification has been to use 0.08–0.25% zirconium as a recrystallization inhibitor in place of chromium or manganese, or in combination with smaller amounts of these elements, in order to reduce quench sensitivity so that slower quench rates can be used without loss of strength on subsequent ageing. Examples are the alloys 7050, 7150, 7055, 7085, and the British alloy 7010. This is also particularly important for alloys used for thick plate since cost reductions are possible if large builtup assemblies can be replaced by machined monolithic structures.

Overall, the progress that has been achieved in combating SCC in the 7xxx series materials through alloy development and changes in heat treatment can be appreciated from results for some compositions shown in Fig. 4.32. Contrary to the 2xxx series alloys (Fig. 4.21), improvements have come from large changes to the plateau values for crack growth rate rather than from increases in levels of the threshold stress intensity needed to initiate cracks.

Reference has already been made to the fact that 7xxx series alloys tend to show higher values of fracture toughness than the 2xxx series (e.g., Fig. 4.20).

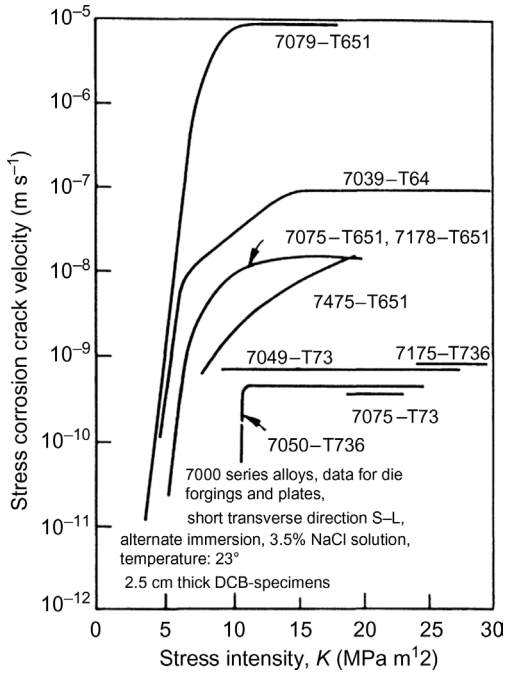


Figure 4.32 Crack propagation rates in stress–corrosion tests on 7xxx alloys. Test conditions as described for Fig. 4.21. DCB specimens prepared from short transverse directions of die forgings and plates. From Speidel, MO: *Metall. Trans. A*, 6A, 631, 1975.

Further improvements have been achieved, some examples of which are shown in Fig. 4.33. Here the inverse relationship between fracture toughness and tensile yield strength is shown for the older alloys 7075–T651 and 7178–T651. Modifications to alloying additions, purity, and heat treatment have allowed relatively high values of fracture toughness to be sustained in alloys such as 7150–T651 and 7055–T7751 despite increasing levels of yield strength. As mentioned earlier, one compositional trend has been to raise the Zn:Mg ratios which have increased from 2.25 for the early alloy 7075 to 2.7 for 7050, 3.9 for 7055, and as high as 5.0 for latest alloy 7085. Another change has been to increase copper contents from values around 1.5% to within the range 2.0–2.6% which has been found to improve resistance to SCC. Furthermore, the allowable limits on manganese, chromium, and the impurities iron and silicon have each been reduced to below 0.1% or less. In 7085 (Fe 0.08%, Si 0.06%), the consequent reduction in intermetallic compounds in the microstructure has resulted in lowering this alloy's quench sensitivity so that very thick sections (e.g., 150 mm) can be heat treated and still record tensile properties higher than earlier aircraft alloys such as 7050. This development was a major factor in the selection of 7085 for the large extruded wing spars and die-forged wing rib components for the European A380 Airbus (Section 4.6.1).

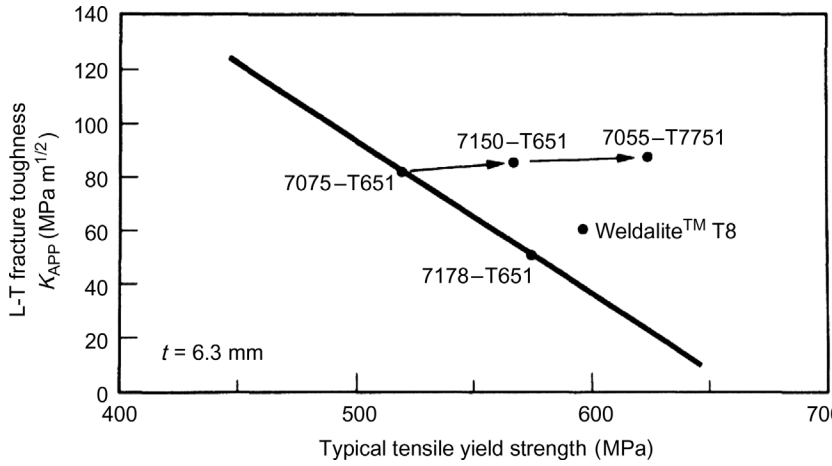


Figure 4.33 Strength–toughness relationships for 7xxx series alloys in form of rolled plate. From Hyatt, MV and Axter, SE: *Proc. Inter. Conf. on Recent Advances in Sci. & Eng. of Light Metals*, Japan Inst. for Light Metals, Sendai, 274, 1993.

As shown in Table 4.7, the alloy 7050 responds to secondary precipitation which has increased both the tensile and fracture toughness properties to levels higher than those obtained using a single stage, T6 temper. Similar responses have been observed with other 7xxx series alloys such as 7075 (Fig. 4.33).

4.4.6 Lithium-containing alloys

Lithium has a high solid solubility in aluminium with a maximum of approximately 4% (16 at.%) at 610°C. This is significant because of the low density of this element (0.54 g cm^{-3}) which means that, for each 1% addition, the density of an aluminium alloy is reduced by 3%. Lithium is also unique among the more soluble elements in that it causes a marked increase in the Young's modulus of aluminium [6% for each 1% added (Fig. 4.34)]. Moreover, binary alloys containing lithium respond well to age hardening due to precipitation of an ordered, metastable phase δ′ (Al_3Li) that is coherent and has a particularly small misfit with the matrix (Fig. 4.35). In more complex alloys that contain copper, significant hardening can also result from precipitation of the semi-coherent, hexagonal phase T_1 (Al_2CuLi) and sometimes θ′ (Al_2Cu) or S′ (Al_2CuMg). Because of all these attractive features, various countries have spent several decades attempting to develop commercial lithium-containing alloys as a new generation of low-density, high-stiffness materials for use in aircraft structures. For much of this time, however, these endeavors were frustrated because the lithium-containing alloys tended to display a number of problems including poor ductility and fracture toughness as well as pronounced anisotropy of mechanical properties. Some were also susceptible to

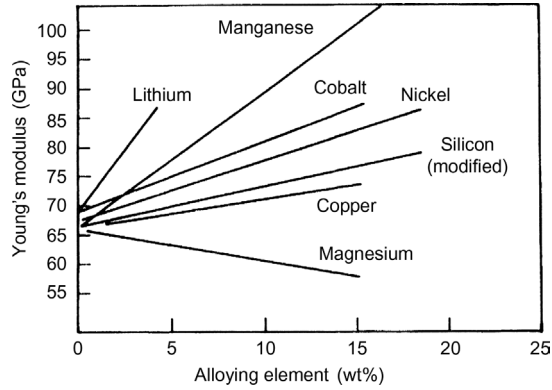


Figure 4.34 Effects of alloying elements on the Young's modulus of binary aluminium alloys.

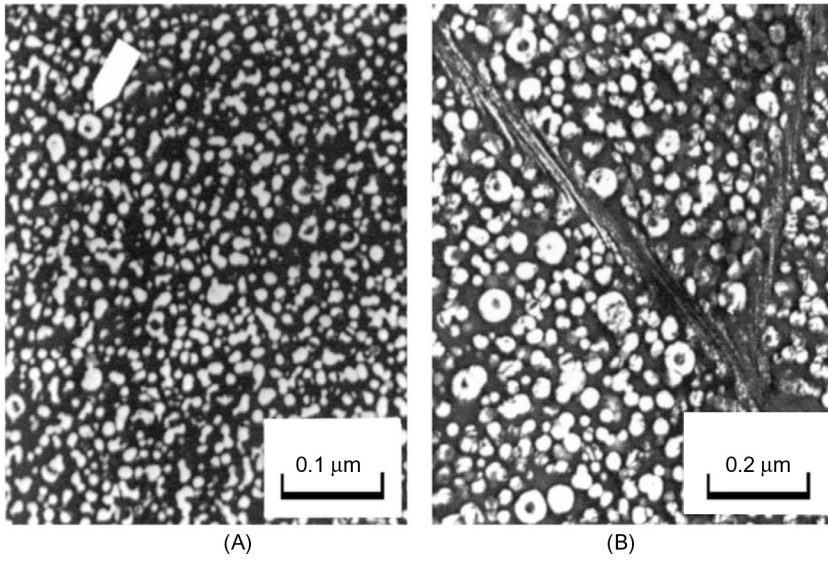


Figure 4.35 (A) Particles of δ′ precipitate in an Al–Li–Mg–Zr alloy aged at 190°C. The arrow indicates a δ′ precipitate that has nucleated on an Al_3Zr dispersoid particle. (B) Shearing of δ′ precipitates leading to strain localization in a deformed Al–Li–Zr alloy. (A) Courtesy P. J. Gregson and (B) courtesy D. J. Lloyd.

embrittlement. Before describing various alloy developments, reasons for these disappointing properties will be discussed.

Aged binary Al–Li alloys can suffer from low ductility and toughness due to severe strain localization which arises because coherent δ′ precipitates are readily sheared by dislocations moving on preferred slip planes (Fig. 4.35B). Stress concentrations arising from this effect may induce cracking along grain

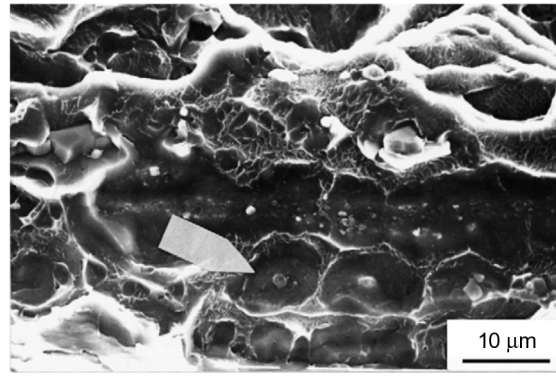


Figure 4.36 Fracture surface of 2090–T8 extrusion with 7.2 ppm alkali metal impurities showing the presence of brittle "islands" along partially recrystallized grain boundaries. Courtesy S. P. Lynch.

boundaries as shown schematically in Fig. 2.21A. Accordingly, much of the work on these alloys has involved the investigation of other solute elements that will form additional precipitates or small dispersoids capable of dispersing moving dislocations more homogeneously.

Another factor that is now recognized as an early cause for reducing ductility and fracture toughness in lithium-containing alloys has been the presence of alkali metal impurities (notably sodium and potassium) in grain boundaries. In other aluminium alloys, these elements are removed into innocuous, solid compounds by elements such as silicon, whereas they react preferentially with lithium when this element is present. Observations of the fracture surfaces of partially or fully recrystallized alloys have revealed the presence of intergranular brittle "islands," the number and size of which increases with increasing levels of these impurities above 3–5 ppm (Fig. 4.36). These brittle islands are composed of second-phase particles covered with films of the alkali metals which may be liquid at ambient temperatures. Lithium-containing alloys produced by conventional melting and casting techniques typically contain 3–10 ppm of alkali metal impurities. However, these levels can be reduced to below 1 ppm by vacuum melting and refining which has been shown to improve fracture properties at room temperature (Fig. 4.37) It is the special processing required during melting and casting to control both impurity levels and the reactivity of lithium that places a significant cost premium on the production of the lithium-containing alloys.

Susceptibility to intergranular fracture and embrittlement in some lithium-containing alloys has also been attributed to other factors including hydrogen embrittlement, the presence of large area fractions of a grain boundary phase δ (AlLi), or formation of soft, precipitate-free zones adjacent to grain boundaries during the ageing treatment. Yet another problem that may arise is associated with secondary age hardening (Section 2.3.5) in some alloys. As shown in Fig. 4.38A, significant increases in hardness may occur if the alloys are

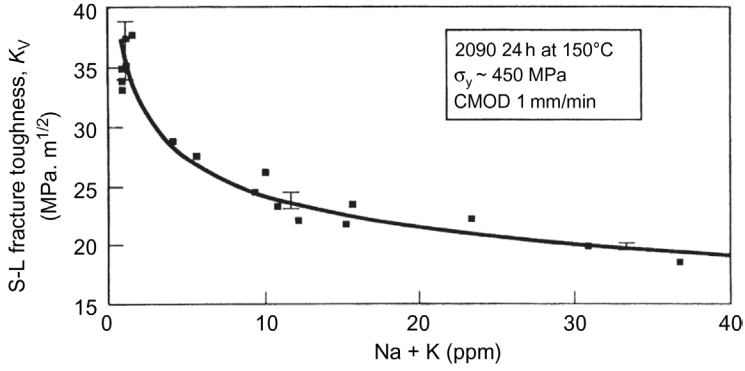


Figure 4.37 Effect of alkali metal impurities on short transverse (S-L) fracture toughness of a 2090 alloy extrusion. (CMOD denotes "crack mouth opening displacement.") From Sweet, ED *et al. Proc. 4th Inter. Conf. on Aluminium Alloys*, Atlanta, GA, USA, Sanders, TH and Starke, EA (Eds.), p. 321. 1994.

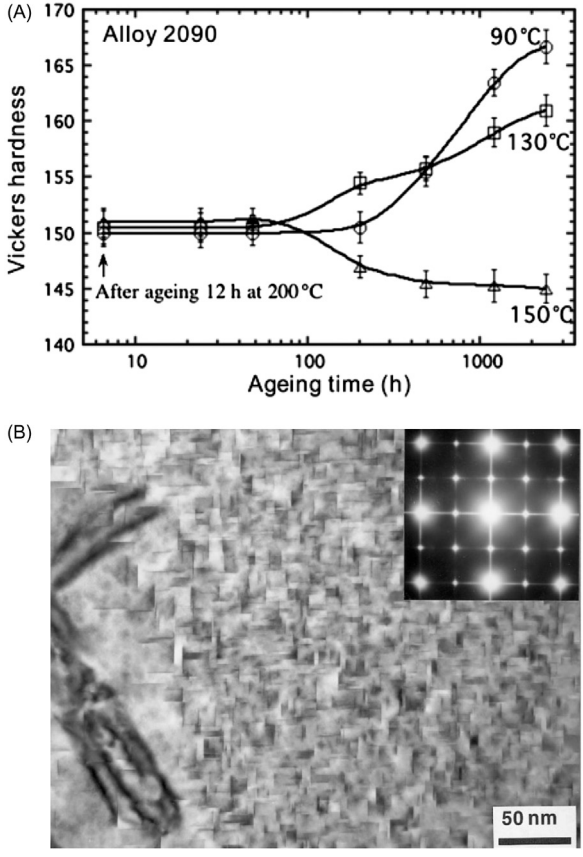


Figure 4.38 (A) Ageing curves of alloy AA2090 during secondary ageing at 90°C, 130°C, and 150°C, after initial ageing at 200°C for 12 h. (B) Distribution of precipitates after secondary ageing at 90°C for 150 days. From Gao, X *et al.: Proc. of the Biennial Conf. of the Inst. of Mater. Eng. Australasia*, Melbourne, p. 573, 1998.

Table 4.9 Nominal compositions of selected lithium-containing aluminium alloys

	Alloy	Major alloying elements				Other
		Li	Cu	Mg	Zr	
First generation	2020	1.3	4.5	–	–	0.5Mn, 0.25Cd
	1420[a]	2.1	–	5.2	0.11	–
	1421[a]	2.1	–	5.2	0.11	0.17Sc
Second generation	2090	2.2	2.7	–	0.12	–
	2091	2.0	2.15	1.5	0.10	–
	8090	2.4	1.3	0.9	0.10	–
	8091	2.6	1.9	0.9	0.12	–
	8092	2.4	0.65	1.2	0.12	–
	1460[a]	2.25	2.9	–	0.11	0.09Sc
Third generation	2195	1.0	4.0	0.40	0.11	0.4Ag
	2196	1.75	2.9	0.5	0.11	0.4Ag
	2094	1.1	4.8	0.5	0.11	0.4Ag
	2097	1.5	2.8	–	0.12	035Mn
	2098	1.05	3.5	0.53	0.11	0.43Ag
	2099	1.8	2.7	0.30	0.09	0.3Mn, 0.7Zn
	2199	1.8	2.6	0.30	0.09	0.3Mn, 0.55Zn
	2050	1.0	3.55	0.40	0.10	0.35Mn, 0.45Ag
	2055	1.15	3.7	0.40	0.11	0.3Mn, 0.5Zn, 0.4Ag
	2060	0.75	3.95	0.85	0.11	0.3Mn, 0.4Zn, 0.28Ag
	2076	1.5	2.3	0.5	0.11	0.33Mn, 0.28Ag

[a]CIS designation.

subject to prolonged exposure to elevated temperatures lower than that used for ageing. This secondary hardening is due to the formation of GP zones and precipitation of very fine particles of δ′ phase (Al_3Li) in matrix regions adjacent to grain boundaries and between precipitates formed from the primary ageing at higher temperature (Fig. 4.38B). These changes may significantly reduce ductility and toughness. The secondary precipitation of GP zones and δ′ phase may lead to narrower precipitation-free zones and may also cause highly localized deformation in the region and brittle intergranular fracture. The embrittlement problem can be eliminated if the secondary aged products are heat treated again at the primary ageing temperature to dissolve the secondary precipitates.

Three generations of lithium-containing alloys are now recognized during their development and representative nominal compositions of each group are given in Table 4.9. It has been the first two generations that tended to suffer from the problems mentioned earlier and it will be noted that all but the first commercial alloy 2020 had lithium contents exceeding 2%. Most of the third-generation alloys have been developed since the 1990s and those listed are all commercially available. Each has a reduced lithium

content as well as tighter controls on the levels of impurity elements such as iron and silicon that may otherwise form coarse intermetallic compounds. Several of these alloys have attracted the attention of the aerospace industries and are replacing conventional aluminium alloys for some critical parts of existing or new civil and military aircraft and space vehicles. Various types of the three generations of lithium-containing aluminium alloys will be considered below.

Al–Cu–Li The first commercially available alloy to contain lithium was 2020 which was produced by Alcoa in the United States in the late 1950s. Copper both reduced the solid solubility of lithium so that precipitation of δ′ was enhanced and led to co-precipitation of phases such as GP zones and θ′ that form in binary Al–Cu alloys. Alloy 2020 combined high room temperature mechanical properties (e.g., 0.2% PS 520 MPa) with good creep strength at temperatures as high as 175°C. It also has an elastic modulus 10% higher than other aluminium alloys. The alloy was used for wing skins for one type of US military aircraft but production was subsequently abandoned in 1974 because of its low toughness properties. A well-known example of a second-generation alloy is the high strength alloy 2090 which had a lower copper content and higher Li:Cu ratio than 2020. In addition to δ′, this alloy was hardened by the precipitate T_1 which forms as thin plates on the $\{111\}_\alpha$ planes (Fig. 4.39). Plates of the θ′ phase (Al_2Cu) may also form on the $\{100\}_\alpha$ planes. The T_1 precipitate is similar in appearance to the Ω phase mentioned earlier (Fig. 4.16), but its aspect ratio is much larger than the latter.

T_1 phase was originally proposed to have a hexagonal structure, with its *c*-axis being about four times of the spacing of the closest packed planes of the aluminium matrix. However, recent observations made by atomic-resolution Z-contrast scanning transmission electron microscopy and first-principles calculations indicated that the *c*-axis of the hexagonal structure of the T_1 precipitate is about six times larger than the spacing of the closest packed planes of the aluminium matrix (Fig. 4.39B). This structure is isomorphous to that determined for the monolithic T_1 alloy. In the T_1 structure, lithium atoms occupy three separate layers that are parallel to the basal plane, and copper atoms are located in the two layers that separate the lithium layers. While the isothermal section of the ternary Al–Cu–Li phase diagram indicates that T_1 is an equilibrium phase at temperatures typically used for solution treatment, the T_1 precipitates formed in Al–Cu–Li alloys are found to be metastable and are replaced by T_B (Al_7Cu_4Li) and T_2 (Al_6CuLi_3) phases after prolonged ageing in the temperature range 200–300°C.

The formation of either T_1 or θ′ inside aluminium grains involves a large shear strain. Therefore, nucleation of T_1 and θ′ is difficult and occurs preferentially on dislocation lines. For this purpose, alloy 2090 is normally cold worked before artificial ageing (T8 temper) to promote a more uniform distribution of

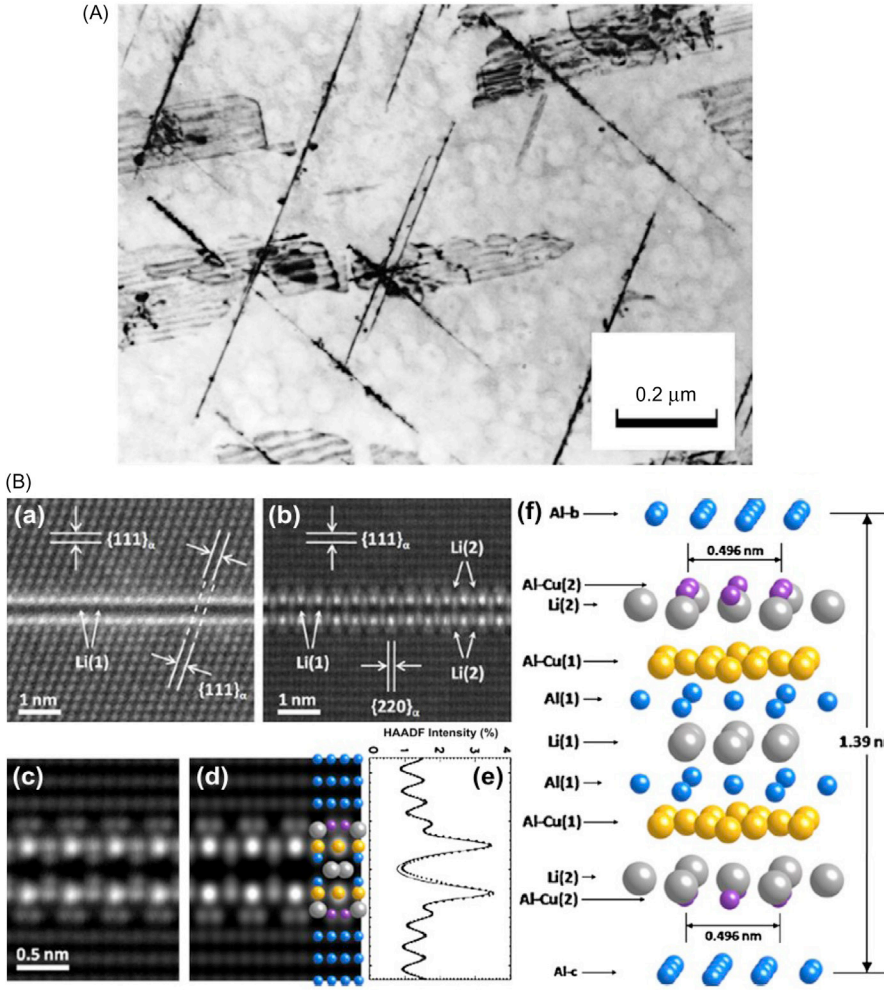


Figure 4.39 (A) Thin plates of the T_1 (Al_2CuLi) in an Al–Li–Cu–Zr alloy overaged (500 h) at 170°C. (B) Atomic-resolution high-angle annular dark-field scanning transmission electron microscopy images and simulated images and the structural model of T_1. (A) Courtesy P. J. Gregson. (B) From Dwyer, C *et al.*: *Applied Phys. Lett.*, 98, 201909, 2011.

each. Zirconium additions, nominally 0.12%, are also made which form fine dispersoids of Al_3Zr that help disperse dislocations and control recrystallization and grain size. One other effect of this element is that nucleation of some of the δ′ precipitates occurs on these dispersoids (see arrow, Fig. 4.35A). Taken overall, zirconium increases both tensile properties and toughness.

Al–Li–Cu–Mg In Britain and France, early attention was focused mainly on the development of alloys based on the quaternary Al–Li–Cu–Mg system. One example is the medium-strength alloy 8090 for which ageing at temperatures close to 200°C leads to co-precipitation of the semi-coherent phases T_1 and S′ in addition to coherent δ′. The S′(S) precipitates (Al_2CuMg) form as laths that also are not readily sheared by dislocations, thereby promoting more homogeneous slip. Since these precipitates also nucleate with difficulty, Al–Li–Cu–Mg alloys are again normally used in the T8 temper. In the 1980s, the second-generation alloy 8090 (S.G. 2.53) was adopted for most of the fuselage and main frame of what was then the Westland Augusta EH 101 helicopter (Fig. 4.40) at a time when weight savings of about 200 kg were urgently needed. Most third-generation alloys are based on the Al–Cu–Li–Mg system and all have lower levels of lithium and magnesium (Table 4.9). Several contain a small amount of silver and others (2099, 2199, and 2055) have an addition of zinc which is reported to improve corrosion resistance.

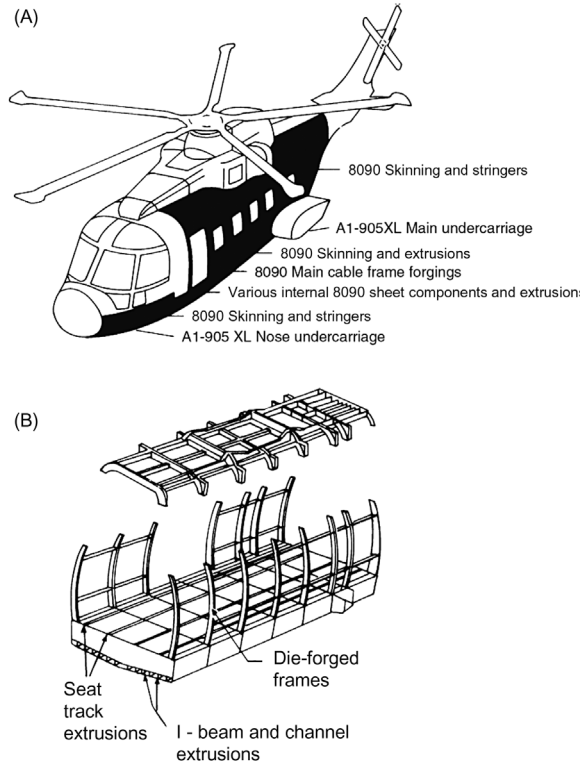


Figure 4.40 Application of alloy 8090 in (A) the fuselage and (B) the lift frame of the EH101 helicopter. From Grimes, R: *Metall. Mater.*, 8, 436, 1992.

Al–Li–Cu–Mg–Ag The cost of launching payloads into low Earth orbit has been estimated to be approximately US$8000 per kg so that there is a large incentive to reduce the weight of space vehicles through the use of lighter and stronger alloys. Because of this, attention in the United States was directed at the prospect of using lithium-containing alloys for the large, welded fuel tanks to replace the existing alloys 2219 and 2014. Some Al–Cu–Li alloys had proved to be weldable and it was then found that minor additions of silver and magnesium could promote significant increases in tensile properties in the manner described for Al–Cu alloys in Section 4.4.1. For Al–Cu–Li–Mg–Ag alloys with lithium contents around an optimum level of 1–1.3%, the source of this high strength resides in the ability of a combination of these minor additions to stimulate nucleation of finer dispersions of the T_1 phase which coexists with S′ and θ′ in the peak hardened condition.

The role of silver and magnesium in the precipitation of the T_1 phase is considered to be similar to that in the precipitation of Ω phase. However, there were conflicting reports on whether silver and magnesium segregate into the T_1 precipitate or just T_1/matrix interface. Recent work based on atom probe tomography indicated that silver and magnesium segregate only to the T_1/matrix interface at all ageing times, including the earliest stages (Fig. 4.41). A very recent study made by atomic-resolution Z-contrast scanning transmission electron microscopy and energy dispersive X-ray spectroscopy revealed the existence of a single layer of silver atoms in the T_1/matrix interface, similar to that observed in the Ω/matrix interface.

Precipitates of T_1, S′, and θ′ form on different matrix planes, and each is effective in impeding dislocation gliding. While the T_1 precipitate may be sheared by dislocations during plastic deformation, its large aspect ratio can provide a remarkably strong strengthening effect (Section 2.2.5). These features led to the development by Martin Marietta Company of an alloy known as Weldalite 049 (Al–6.3Cu–1.3Li–0.4Mg–0.4Ag–0.18Zr) which may exhibit tensile properties exceeding 700 MPa in the T6 and T8 conditions. On a

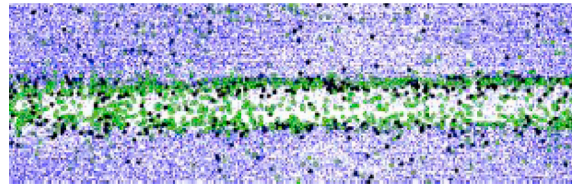


Figure 4.41 Atom probe map showing segregation of silver atoms in the T_1/matrix interface in alloy AA2198. Thickness of T_1 plate is about 2.5 nm. Green and black dots represent magnesium and silver atoms respectively. From Araullo-Peters, V *et al.*: *Acta Mater.*, 66, 199, 2014.



Figure 4.42 Large external liquid fuel tank for launching the US Space Shuttle to which the orbiter vehicle and solid fuel boosters are attached. Courtesy NASA.

strength:weight basis, an equivalent steel would need to have a tensile strength exceeding 2100 MPa so that Weldalite 049 can be said to be the first ultrahigh-strength aluminium alloy to be produced from conventionally cast ingots.

A lower copper variation of this alloy, 2195–T6, was 5% lighter and 30% stronger than the alloy 2219–T8 that was used for constructing the first version of the large, disposable, external fuel tank used for launching the US Space Shuttle. As shown in Fig. 4.42, this tank is 47 m long, has a diameter of 8.5 m, and originally weighed 34,500 kg. A redesign reduced its weight by 4500 kg and the adoption of alloy 2195 for the final so-called Super Light Weight External Tank resulted in a further weight reduction of 3400 kg. These changes had the potential to achieve huge cost savings by allowing payloads to be increased which, in turn, may have reduced the number of missions needed during construction of the International Space Station. Each launch has been said to have cost several hundred million US dollars.

Several other high strength Al–Li–Cu–Mg–Ag alloys are also available as sheet, plate, extrusions, and forgings. One example is 2050 that was developed as a medium to high strength, damage tolerant, corrosion, and stress–corrosion-resistant alloy that was intended to outperform the property balance of the 2xxx thin plate and 7xxx thick plate alloys traditionally used for aircraft construction. 2050 has a higher copper content than 2090, whereas the lithium content has been reduced to a maximum value of 1.3% to avoid formation of the δ' precipitate which was considered to be detrimental to stability at elevated temperatures. The combination of silver and magnesium again enhances nucleation of the T_1 precipitate which both accelerates ageing and increases the response to hardening during heat treatment.

Al–Li–Mg Russian workers have given particular attention to this system since the 1960s when the properties of the alloy 1420 (Al–5%Mg–2%Li–0.5%Mn) were evaluated and patented. Magnesium also has the effect of reducing the solubility of lithium but its main role appears to be that of solid solution strengthening. It was hoped that this element may increase the misfit between δ′ particles and the matrix but no significant change was observed. For alloys containing more than 2% magnesium that are aged at relatively high temperatures, a non-coherent, cubic phase Al_2LiMg is formed. However, this phase precipitates preferentially in grain boundaries and can have an adverse effect on ductility. Thus the addition of magnesium does not tend to improve the toughness of binary Al–Li alloys. Alloy 1420 has relatively low strength (0.2% PS, 280 MPa), but its corrosion resistance is high and it has been used successfully for welded sections of at least one military aircraft produced in the former Soviet Union some time ago. Higher strengths (0.2% PS, 360 MPa) were developed in a modified alloy 1421. This alloy also contains 0.18% of the expensive element scandium which forms fine, stable dispersions of the phase Al_3Sc that is isomorphous with Al_3Zr and promotes additional strengthening and creep resistance.

4.5 JOINING

Aluminium can be joined by most methods used for other metals including welding, brazing, soldering, bolting, riveting, and adhesive bonding. Welding and brazing will be considered in some detail and the other methods only referred to briefly.

Mechanical joining by fasteners is covered by a range of engineering codes and poses no real technical problems. Aluminium alloy rivets are normally selected so that their mechanical properties closely match those of the material to be joined. Most commercial rivets are produced from one of the following alloys: 1100, 2017, 2024, 2117, 2219, 5056, 6053, 6061, and 7075. They are usually driven cold and some, e.g., 2024, if solution treated and quenched shortly before use, will gradually harden by ageing at room temperature. Alloy 2024–T4 is commonly used for aluminium bolts or screws although steel fasteners are generally cheaper. Such fasteners must be coated to prevent galvanic corrosion of the aluminium, and plating with nickel, cadmium, or zinc is generally used depending upon the corrosive environment. Under severe conditions, stainless steel fasteners are preferable.

Adhesive bonding is particularly suitable for aluminium because of the minimal need for surface preparation. For general bonding with low-strength adhesives, and in field applications, surfaces may be prepared by mechanical abrasion using wire brushes, abrasive cloths, or grit or shot blasting. Where higher bond strengths are required, solvent degreasing is essential and this may need to be followed by some form of chemical treatment. This may involve

immersion in an acid bath such as an aqueous solution of sodium dichromate and sulfuric acid, or anodizing which thickens the oxide film and provides an excellent surface for bonding. Adhesives include epoxy and phenolic resins, and a range of elastomers.

Soldering involves temperatures below about 450°C and tends to be troublesome because aggressive chemical fluxes are needed to remove the oxide film. Problems with corrosion may occur if these fluxes are not completely removed, or if galvanic effects arise in service because the low-melting-point solders have compositions quite different from the aluminium alloys.

4.5.1 Welding

Oxyacetylene welding was widely used for the joining of aluminium alloys following the development in 1910 of a flux that removed surface oxide film. However, as such fluxes contain halides, any residues can cause serious corrosion problems and this form of fusion welding has been superseded except for a limited amount of joining of thin sheet.

The process requirements for welding aluminium are:

1. an intense and localized heat source to counter the high thermal conductivity, specific heat, and latent heat of this metal;
2. the ability to remove the surface oxide film which has a high melting point (about 2000°C) and may become entrapped to form inclusions in the weld bead;
3. a high welding speed to minimize distortion arising because of the relatively large coefficient of thermal expansion of aluminium;
4. a low hydrogen content because of the high solubility of this gas in molten aluminium, which can lead to porosity in the weld bead after solidification has occurred (Section 4.1.1).

Arc welding The two main processes in use today are TIG, i.e., tungsten inert gas (also known as GTA or gas tungsten arc) and MIG, i.e., metal inert gas (also known as GMA or gas metal arc) in which a shroud of inert gas, commonly argon, replaces the chemical flux. The heat source is an electric arc struck between the workpiece and either a non-consumable electrode (TIG), or consumable metal wire (MIG) as shown schematically in Fig. 4.43. Current flows in the arc due to ionization of the inert gas and it is the ionized particles which disrupt the oxide film and clean the surface. TIG welding is mostly carried out manually although the use of mechanized equipment is increasing where higher welding speeds can offset the greater cost of the facility. Where necessary, filler metal is introduced as bare wire. In MIG welding the consumable electrode is fed into the weld pool automatically through a water-cooled gun and the whole process is normally mechanized. It is favored for volume production work, particularly on material thicker than 4 mm. MIG welding of thin-gauge aluminium presents problems because of the relatively thin wire that

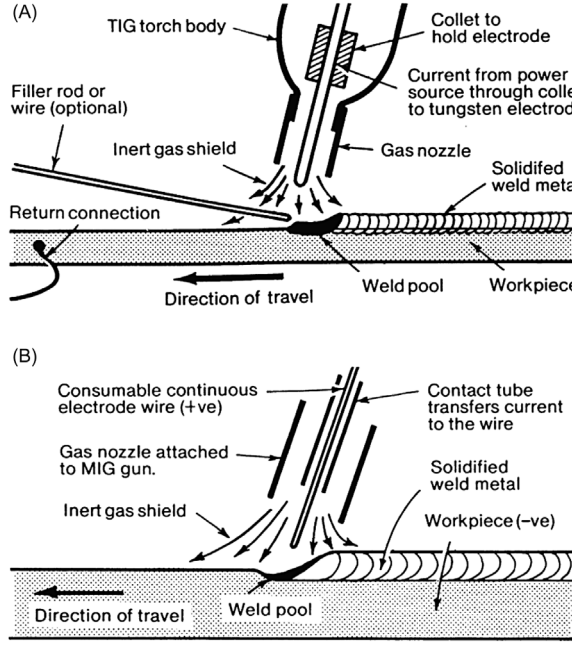


Figure 4.43 Essential features of (A) TIG or GTA and (B) MIG or GMA welding processes. Courtesy WTIA.

would need to be used at normal welding speed which is difficult to handle, or because welding speeds become too high with the thicker wires. For this purpose, the pulsed MIG process has been devised in which transfer of metal from the wire tip to the weld pool occurs only at the period of the pulse or peak in welding current. During the intervals between pulses, a background current maintains the arc without metal transfer taking place.

The weldability of the various wrought alloys was mentioned when the individual classes were discussed. Essentially, all are weldable with the exception of most of the 2xxx series and the high-strength alloys of the 7xxx series. An example of a welded structure is shown in Fig. 4.24. The strengths of NHT alloys after welding are similar to their corresponding strengths in the annealed condition irrespective of the degree of cold working prior to welding. This loss of strength is due to annealing of the zone adjacent to the weld and can only be offset by selecting a weldable alloy such as 5083 which has comparatively high strength in the annealed condition. This accounts for the popularity of this series of alloys for welded constructions. When a heat-treatable alloy is welded, there is a drop in the original strength to that approximating the T4 condition. The metallurgical condition of this softened zone is complex and may include

regions that are partly annealed, solution treated, and overaged, depending upon the actual alloy, speed of welding, material thickness, and joint configuration. As in the case of the medium-strength 7xxx alloys (Section 4.4.4), some natural ageing can occur in parts after welding, but the overall strength of the welded joint is not usually restored to that of the unwelded alloy. The presence of the range of metallurgical structures adjacent to welds can lead to localized corrosive attack of some alloys in severe conditions (e.g., Fig. 4.26B).

Filler alloys must be selected with due regard to the composition of the parent alloys and common fillers are listed in Table 4.10. Generally speaking, selection is based primarily on ease of producing crack-free welds of the highest strength possible. However, in some cases, maximum resistance to corrosion or stress–corrosion, or the ability of the weld to accept a decorative or anodized

Table 4.10 Aluminium filler alloys for general-purpose TIG and MIG welding of wrought alloys

Base metal welded to base metal	7005	6061 6063 6351	5454 5154A	5086 5083	5052	5005 5050A	3004 Alclad 3004	1100 3003 1200
1100								1100[a]
1200	5356[b]	4043	4043[b]	5356[a]	4043[b]	4043[b]	4043[b]	1200[a]
3003								
3004								
Alclad 3004	5356[b]	4043[b]	5356[b]	5356[b]	5356[a,b]	4043[b]	4043[b]	
5005								
5050A	5356[b]	4043[c]	5356[b]	5356[b]	4043[b]	4043[b,d]		
5052	5356[b]	5356[a,b]	5356[c]	5356[b]	5356[c]			
5083								
5086	5356[b]	5356[b]	5356[b]	5356[b]				
5154A	5356[b]	5356[a,c]	5356[a,c]					
5454	5356[b]	5356[a,c]	5356[a,c]					
6061								
6063	5356[b]	4043[c]						
6351								
7005	5039[b]							

For alloy compositions, see Tables 4.2 and 4.4 except 4043 Al–5Si: 5356 Al–5Mg–0.1Cr–0.1Mn; 5039 Al–Mg–2.8Zn–0.4Mn–0.15 Cr; 5154A A1–3.5Mg–0.3Mn.

[a]4043 may be used for some applications.

[b]5356 or 5556 may be used.

[c]5154A, 5356, and 5556 may be used. In some cases, they provide improved color match after anodizing treatment; higher weld ductility; higher weld strength; improved stress–corrosion resistance.

[d]Filler metal with the same analysis as the base metal is sometimes used.

finish compatible with the parent alloy, may be required. Softening of the heat affected zones adjacent to aluminium alloy welds also reduces fatigue properties and this effect is accentuated when weld geometry leads to a concentration of cyclic stress in these softened regions, e.g., at weld toes. One consequence is that the fatigue strengths of welded joints tend to show little difference from one another.

Surface treating by peening in the region of weld toes to induce residual compressive stresses is a recognized method for improving the fatigue performance of welded steel components and structures. However, such a procedure is less used for aluminium alloys, presumably because they are normally softer and the peening process may cause unacceptable surface damage. Shot peening can be effective for components that can be introduced into a suitable chamber. Another technique which has shown promise for application in the field is to use a portable needle gun in which long steel needles are vibrated back and forth by compressed air. The resulting surface suffers only superficial damage and this practice has, for example, been used successfully to reduce the incidence of fatigue cracking in welded aluminium rail wagons.

Another method is to smooth out the contour of weld toes so that cyclic stress concentrations are reduced. This can be achieved by using a portable TIG welding gun to remelt the critical toe regions after the earlier MIG welding has been completed (Fig. 4.44). Providing the heat associated with this dressing operation does not introduce undesirable levels of residual stress, fatigue performance may be significantly improved. An example of the beneficial effects of TIG dressing in delaying or preventing the onset of fatigue cracking in a fillet welded aluminium alloy specimen is shown in Fig. 4.45. In this case, fatigue lives over a wide cyclic stress range have been increased by three to five times.

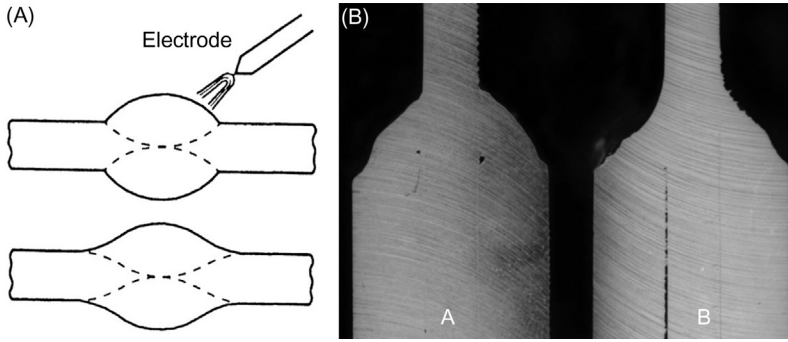


Figure 4.44 (A) Representation of TIG dressing to smooth the contour of weld toes; (B) cross section of fillet welds showing (A) undressed welds and (B) the effect of TIG dressing these welds.

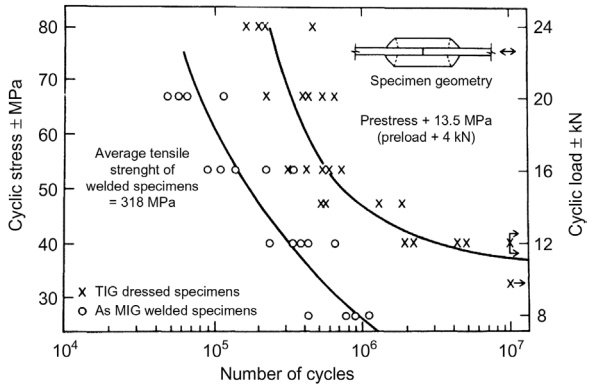


Figure 4.45 Stress/number of cycles (*S*/*N*) curves for TIG dressed and undressed fillet welded specimens. From Polmear, IJ and Wilkinson, DR: *Weld. J.*, 62(3), 785, 1983.

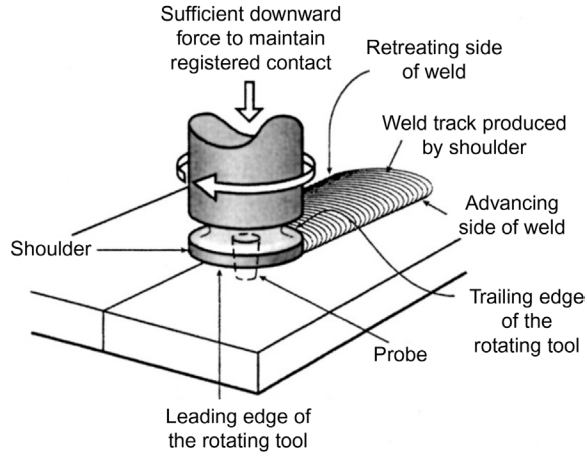


Figure 4.46 FSW process. Courtesy The Welding Institute, UK.

Friction stir welding Friction stir welding (FSW) is a solid-state process, invented at The Welding Institute in England in the early 1990s, which is particularly well suited to joining aluminium alloys that are difficult to fusion weld. A schematic illustration of the welding process is shown in Fig 4.46. Components to be joined (mainly sheet or plate) need to be symmetrical. They are securely clamped to a rigid table and a specially designed rotating tool (probe) is forced into and traverses down the joint line. The tool, which is made of a hard steel and is non-consumable, consists of a profiled pin with a concentric larger diameter shoulder. The depth of penetration is controlled by the tool shoulder and the length of the pin. Welding speeds may be comparable with those experienced with fusion welding processes.

The material being joined is rapidly friction heated within the solid state to a temperature at which it is easily plasticized. The frictional heat is produced from a combination of contact with the rotating shoulder and downward from the leading edge to the trailing face of the pin; it then cools to form the solid-state joint. Because of the extreme levels of plastic deformation involved, which are not unlike that experienced in equal channel angular pressing (Section 8.8), a very fine, dynamically recrystallized microstructure (e.g., grain sizes 2–10 μm) is obtained in the weld zones. Welds are stronger, comparatively defect-free and, because the heat generated is much less than for fusion welding, residual stresses are reduced. Furthermore, since there is no melting, undesirable brittle and low melting point eutectic phases are not formed. It is for these reasons that the more highly alloyed compositions, such as the 7000 series alloys, and even complex metal matrix composites, can be welded by FSW. It is also possible to weld dissimilar aluminium alloys. Another advantage over fusion welding is that environmental hazards associated with fume and spatter are eliminated.

FSW can be automated and used to produce symmetrical butt and lap joints including corner configurations. Another important advance has been to use a modified rotating toll to join thin sheets that may buckle severely if fusion welded, or for welding together metal sheets of differing thicknesses. Armor plate that is FSW has been shown to be more resistant to cracking under ballistic impact. One early major application was the welding of the 47 m long, Al–Cu–Li–Mg–Ag alloy "Super Light Weight" fuel tanks that was used for launching the US Space Shuttle (Fig. 4.42). Now FSW is being widely used for the production of aluminium alloy marine vessels and railroad trains.

Laser welding Resistance spot welding is the most important joining method used for assembling stamped automotive steel sheet sections. With aluminium alloy sheet components however, the presence of the relatively thick surface oxide film causes excessive pitting of the welding electrodes requiring them to be changed frequently. The oxide film may also have an adverse effect on the strength of the spot-welded joints. Laser welding is showing promise as an alternative to spot welding when assembling aluminium alloy structures.

Laser welding is a comparatively new method of joining in which the laser beam is focused onto the workpiece producing a metal-vapor filled cavity, or "keyhole." A molten metal layer, that forms in dynamic equilibrium with the metal vapor, establishes the weld pool which is then translated rapidly through the thickness of the workpiece. Melting takes place at the leading edge of the cavity and solidification occurs at the rear. Filler compositions are similar to those used in arc welding. Because of the high power density of what is a narrow beam, the overall heat input during laser welding is less that in conventional fusion welding, so that the widths of the fusion and heat affected zones are both reduced. Welding speeds are high (e.g., 5–8 m/min for thin sections) and thermal distortion of joints is less. Because of these characteristics, laser

welding is particularly well suited to joining sheet materials and it is now being used in the aircraft and automotive industries.

Two types of lasers are used for welding which differ in the way the beam is generated. One involves a gaseous CO_2 device and the other is a solid-state system comprising a neodymium yttrium–aluminium garnet (Nd-YAG) crystal. The latter has generally proved more suitable for welding light metals and alloys. Because of the narrow fusion zone, severe thermal cycles of heating and cooling may be involved when laser welding thicker sections and the major concerns are possible hot cracking, loss of alloying elements, and porosity.

4.5.2 Brazing

Brazing involves the use of a filler metal having a liquidus above about 425°C but below the solidus of the base metal. Most brazing of aluminium and its alloys is done with aluminium-base fillers at temperatures in the range 560–610°C. The NHT alloys that have been brazed most successfully are the 1xxx and 3xxx series and the low magnesium members of the 5xxx series. Of the heat treatable alloys, only the 6xxx series can be readily brazed because the solidus temperatures of most of the alloys in the 2xxx and 7xxx series are below 560°C. These alloys can, however, be brazed if they are clad with aluminium or the A1–1Zn alloy 7072. Most commercial filler metals are based on the Al–Si system with silicon contents in the range 7–12%. Sheet alloys to be joined by brazing may first be clad or roll-bonded to the filler metal which is particularly convenient for mass producing complex assemblies such as automotive heat exchangers. For other situations, the filler metals can be applied separately in the form of wire, thin sheet, or as dry or wet powders.

Brazing of aluminium was first made possible through the development of fluxes that dissolve the surface oxide film and protect the underlying metal until the joining operation is completed. Fluxes are compounded so that they melt just before the brazing alloy and they commonly comprise a mixture of alkaline earth chlorides and fluorides. Such fluxes may leave a corrosive residue which must be removed and this can present difficulties with assemblies containing narrow passage ways, pockets, etc. More recently, non-corrosive fluxes based on the compound potassium aluminofluoride have been developed.

The easiest method of heating and fluxing aluminium joints simultaneously is to immerse the whole assembly in a bath of molten flux that is maintained at the brazing temperature (e.g., 540°C). The assemblies are usually preheated to avoid cooling the flux bath and to shorten the processing time, which usually involves several minutes. This procedure is known as dip or flux bath brazing. It suffers from the disadvantage that corrosion problems may arise in service if the flux is not completely removed.

Furnace brazing of aluminium alloy components has become common because of the high volume that can be handled on a continuous production

line. This method is used for the assembly of automotive radiators and other heat exchangers in accessories such as air conditioners and oil coolers that were formerly made from copper. Two processes are employed: controlled atmosphere brazing (CAB) that uses a non-corrosive flux and vacuum brazing which is flux-free. The latter has the advantages that no costs are involved for the flux and cleaning is less important, although the surfaces to be joined must be prepared with more care. CAB is conducted in an atmosphere that usually contains the inert gas nitrogen. The flux, which melts and dissolves the aluminium oxide films, becomes inactive in the presence of magnesium so that the filler must be magnesium-free and it is desirable for the aluminium alloys being joined to have low contents of magnesium. On the contrary, vacuum brazing requires the presence of magnesium, at least in the filler, in order to disrupt the oxide films and promote wetting in the absence of a flux. In both processes, the components are assembled and placed in the furnace that is already at the brazing temperature of around 595°C.

Limitations on the magnesium contents of alloys to be CAB brazed has led to the development of compositions for use for the tubes, fins, and header tanks of automotive heat exchangers. Examples are as follows:

Tubes—alloy 3005: Al–1.2Mn–0.40Mg–0.35Fe–0.30Si–0.15Cu
Fins—alloy FA6815: Al–1.6Mn–1.5Zn–0.85Si–0.25Fe–0.15Zr
Headers—alloy FA7827–Al–0.7Si–0.45Mg–0.3Cu–0.25Fe–0.15Ti.

The alloys for fins and headers were developed in Sweden. Like all aluminium alloys for heat exchangers, strengthening relies on a combination of solid solution and dispersion hardening, supplemented in some instances by precipitation hardening.

Aluminium may be successfully brazed to many other metals including carbon steels, stainless steels, copper, nickel, and titanium. Special filler alloys and melting conditions may be required and care must be taken to apply protective coatings to the final assembly for protection against galvanic corrosion.

4.5.3 Soldering

Soldering is distinguished from brazing in that the metals or alloys being joined are not themselves melted. For aluminium alloys, the filler metal, or solder, melts below a temperature of 450°C. Thus, aluminium-base fillers are not used and most are alloys of zinc, tin, cadmium, and lead; examples are Zn–10Cd (melting range 265–400°C), Sn–30Zn (199–311°C), and Pb–34Sn–3Zn (195–256°C). Fluxing must again be used to remove surface oxide films. Whereas it is possible to solder all aluminium alloys, this method of joining is not commonly used. The quality of joints varies with composition and, for the wrought series of alloys, generally decreases in the following order: 1xxx, 3xxx, 6xxx, 2xxx, and 7xxx.

4.5.4 Diffusion bonding

Diffusion bonding is an attractive means of joining because there is minimal disturbance to the microstructures of the parent alloys. Another advantage is the prospect of joining different alloys, or even dissimilar materials. With aluminium alloys, however, the presence of the chemically stable oxide film makes it difficult to achieve such a bond.

It is possible to disrupt a surface oxide film by imposing plastic deformation, but early work on diffusion bonding of aluminium alloys revealed that the minimum amount needed was around 40% before bonds of reasonable strength could be obtained. Another approach has been to use alloys containing active elements such as lithium or magnesium which serve to weaken or decompose the oxide films during the bonding process. More recently a method has been developed which is known as transient liquid phase (TLP) diffusion bonding. This process involves interposing a thin (e.g., 5–10 μm) layer of copper between the surfaces to be joined which are lightly clamped in an evacuated chamber and heated close to the Al–Cu eutectic temperature of 548°C for times of around 10 min. Local melting and solute diffusion occurs and, by imposing a temperature gradient across the reaction zone, a sinusoidal/cellular interface is formed which both increases the surface area of the interface and disperses the oxide particles. Bonds with alloys such as 6082 have shown shear strengths equal to that of the parent material. Successful bonds have also been prepared between this alloy and a metal matrix composite containing SiC particles.

4.6 SPECIAL PRODUCTS

4.6.1 Aircraft alloys

Designers of aircraft require materials that will allow them to produce lightweight, cost-effective structures that are durable and damage tolerant at ambient, subzero and occasionally elevated temperatures. As mentioned earlier, strong aluminium alloys date from the accidental discovery of the phenomenon of age hardening by Alfred Wilm in Berlin in 1906. His work led to the development of the wrought alloy known as Duralumin (Al–3.5Cu–0.5Mg–0.5Mn) which was quickly adopted in Germany for structural sections of Zeppelin airships, and for the Junkers F13 passenger aircraft that first flew in 1919. Since that time, wrought aluminium alloys have been the major materials for aircraft construction which, in turn, has provided much stimulus for alloy development. Duralumin was the forerunner of a number of 2xxx series alloys including 2014 and 2024 that are still used today. The other major aircraft group of alloys is the 7xxx series, with some 6xxx series and lithium-containing aluminium alloys now being used as lighter weight substitutes.

Material selection for structural applications in aircraft depends mainly on a variety of performance requirements that are summarized for a typical passenger aircraft in Fig. 4.47. Examples of older and newer alloys that have been used for various parts of the modern Airbus A380 aircraft are given in Table 4.11.

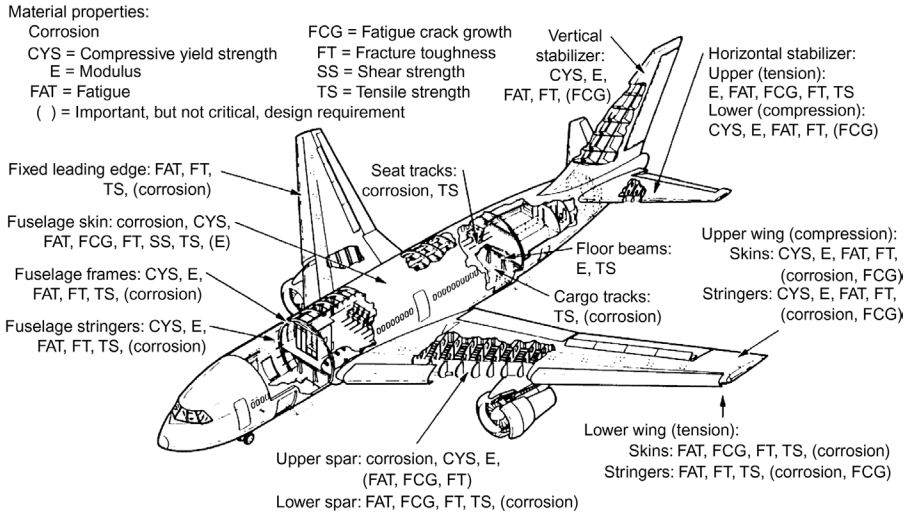


Figure 4.47 Property requirements for structural members of a typical passenger aircraft. From Staley, JT and Lege, DJ: *Journal de Physique IV*, 3, 179, 1993.

Table 4.11 Advanced aluminium alloys and their main applications for the modern Airbus A380-800 and A380-800F passenger aircraft.

From	Alloy/temper	A380 application
Plates	7056–T7951	Upper wing panels
	7449–T7951	Upper wing
	2024A–T351	Lower wing reinforcement
	2050–T84	Lower wing reinforcement
	2027–T351	Lower outer wing panel
	7010–T7651	Upper outer wing panel, heavier gauge wing ribs
	7040–T7451	Fuselage main frames, cockpit window frames, beams, fittings
	7449–T7651	Lower gauge wing ribs
	7040–T751	Wing spars
	7085–T7651	Wing spar and rib structures
	7255–T7951	Upper wing
Heavy	7449–T79511	Upper wing stringers
sections	2027–T3511	Lower wing stringers
	2196–T8511	Floor beams
Small	7349–T6511	Seat rails, stiffeners of center wing box
sections	7349–T76511	Fuselage stiffeners
	2024HS–T432	Fuselage frames
	6056–T78	Fuselage stiffeners
	6056–T6	Fuselage stiffeners
	2196–T8511	Floor structure, fuselage stiffeners
Sheets	6056–T78	Pressure bulkhead below cockpit floor
	6156Cl–T6	Fuselage panels
	6013–T651	Fuselage
Extrusions	2099–T83	Fuselage
	2099–T81	Lower wing skin

From Lequeu, Ph, Lassince, Ph and Warner, T: *Adv. Mater. Process.*, July, p. 41, 2007; Bryant, JD, Alcoa, USA.

The fuselage in modern aircraft is a semi-monocoque (continuous skin) structure made up of the outer skin to sustain cabin pressure (tension) and shear loads, longitudinal stringers (longerons) to carry longitudinal tension and compression loads caused by bending, circumferential frames to maintain fuselage shape and redistribute loads into the skin, and bulkheads to carry concentrated loads (Fig. 4.48). Strength, stiffness, resistance to fatigue crack initiation and propagation, corrosion resistance, and fracture toughness are all important. Traditionally, the alloy 2024 in the cold worked and naturally aged (T3) temper has been favored for the skin of passenger aircraft because of its high damage tolerance. This property has been progressively improved with the introduction of the compositions 2224, 2324, and 2524 in which the impurity levels have been reduced, and tighter controls have been placed on the contents of the major alloying elements copper, magnesium, and manganese. All Al–Cu–Mg and Al–Zn–Mg–Cu sheet alloys have the disadvantage that they must be clad to prevent corrosion and most cannot be fusion welded. On the other hand, some weldable lithium-containing sheet alloys such as 2199 do not require cladding and can provide a weight reduction of between 10% and 20%. Unclad 6xxx series sheet alloys that are also corrosion-resistant and weldable have been introduced. These are significantly cheaper and provide a more modest weight reduction of 3%. The copper-containing Al–Mg–Si alloys 6013 and 6056 have been used because of their higher strengths, although initially both showed some susceptibility to intergranular corrosion because of the presence of anodic precipitate-free zones. This problem has been minimized with the development of a proprietary T78 temper and these alloys have been introduced into parts of the fuselages of the Boeing 777 and European Airbus 380 aircraft. Fuselage stringers are usually made from formed sheet or extrusions using 7xxx series alloys such as 7075–T6, 7150–T77, and the lithium-containing alloy 2099–T83. More recently, sheet panels used for parts of the fuselage of the Airbus 340 and cross beams and seat tracks in the fuselage of the Airbus 380 aircraft have also been made from the lithium-containing alloy 2099–T83 extrusions. Weight savings as much as 20% have been achieved using these components, the economics of which had to be assessed against the higher cost of this alloy when compared with that of the traditional medium- and high-strength aluminium alloys.

The airframe of modern passenger aircraft such as Airbus A380 requires the use of more advanced high-strength and high damage-tolerant alloys. As mentioned in Section 4.4.5 the Al–Zn–Mg–Cu alloy 7085, which has low quench sensitivity during heat treatment, was developed for use for thicker sections (Fig. 4.48). Another example is the Al–Li–Cu–Mg–Ag alloy 2050–T84 which was designed to outperform the property balance of 2xxx thin plate alloys and 7xxx thick plate alloys. It has lower amounts of Li and reduced quench sensitivity that has allowed it to be produced in thicker gauges than most other Al–Li alloys. This third-generation Al–Li alloy was approved for use in lower wing structures of A380-800 and A380-800F.

Wings are essentially beams that experience bending during flight. The upper surfaces are loaded primarily in compression and high compressive yield strength is therefore a key property. Here the focus has been to develop

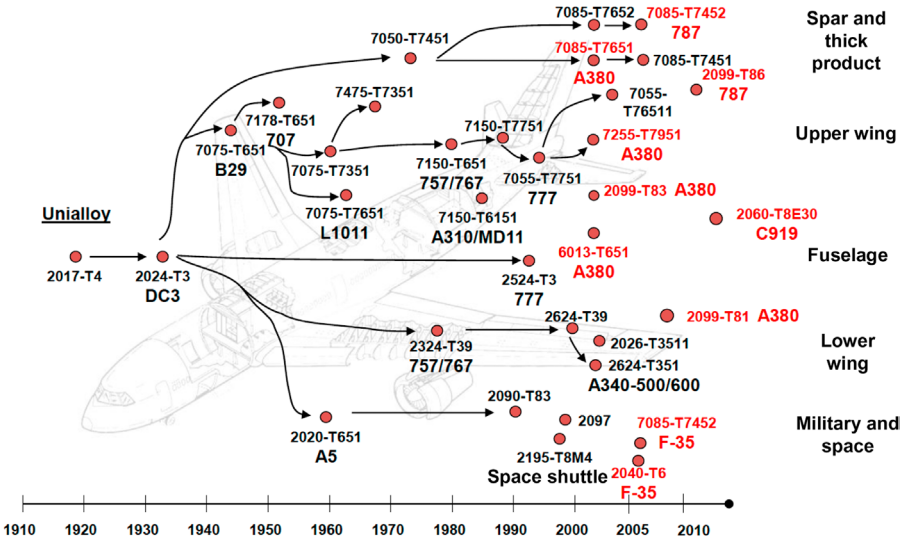


Figure 4.48 Historical record of aluminium alloys and tempers used for passenger and military aircraft. Courtesy J. D. Bryant, Alcoa, USA.

wing skins with higher strengths and Fig. 4.48 shows most of the incremental improvements that have occurred since the introduction of aluminium alloys to aircraft in 1919. The lower wing skins are in tension during flight and more emphasis must be placed on properties in addition to yield strength such as fatigue resistance and toughness. Alloys that have been used include 2024–T3 and more recently 2324–T39, both in the form of rolled plate. The selection of alloys for internal members, such as wing spars, is dependent upon their positions with respect to compressive and tensile loading regimes.

A new process called creep age forming (CAF) was developed which offered substantial cost benefits for the production of curved aluminium alloy components, such as large wing panels for aircraft. In CAF, the forming operation is combined with artificial ageing by elastically loading the component onto a former using a combination of mechanical clamping and vacuum bagging, and then holding for a fixed time at one or more ageing temperatures (typically in the range 150–190°C). Stress relaxation occurs by creep so that the component undergoes permanent deformation. Allowance must be made for significant springback that may occur when the component is released because the ageing conditions needed to achieve the required mechanical properties are insufficient to relax fully the elastic stresses. Advantages of CAF include accuracy, reproducibility, and the ability to produce multiple curvatures in complex components close to near net shape in a single procedure. CAF has been applied successfully to alloys of the 2xxx and 7xxx series, as well as to the lithium-containing alloy 8090. It is being used for the production of upper wing panels of several civil and military aircraft, including the Airbus 380, for which the wing panels are up to 34 m long, 2.8 m wide, and have thicknesses varying from 3 to 28 mm.

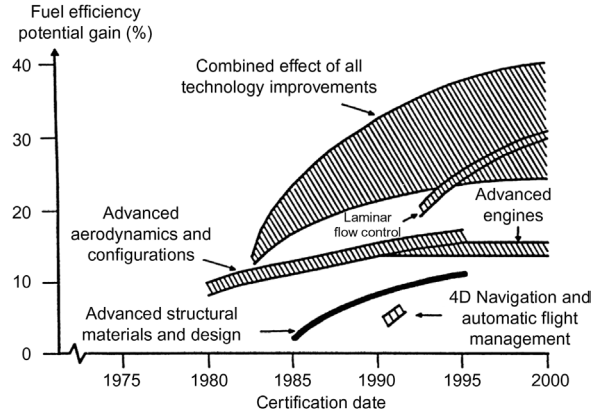


Figure 4.49 Relative contributions of different technological advances to improved fuel efficiency of aircraft. Courtesy of C. J. Peel, QinetiQ.

The empennage (tail) consists of a horizontal stabilizer, a vertical stabilizer, elevators, and rudders. The horizontal stabilizer is like an upside-down wing whose span is often about half that of the wing. Both the upper and lower surfaces are often in compression due to up and down bending so that modulus of elasticity in compression is the most important property. Sheet, plate, and extrusions of 7075–T6, 2024–T3, have traditionally been used in the empennage although high-stiffness, fiber-reinforced materials are now being adopted.

The relative contribution that improved structural materials have made to reducing costs of operating passenger aircraft through improved fuel efficiency is shown schematically in Fig. 4.49. Reducing the weight of materials is a constant aim, but the designer must first ensure that a proposed new material meets the property requirements for a particular structural component. Furthermore, any additional material costs should not exceed the savings expected from using less fuel, and from other possible economies such as reduced maintenance. In this regard, the Boeing Airplane Company has developed a formula that is useful when evaluating projected weight savings for recurring materials costs:

$$\Delta Q = \frac{1}{u}\left[\frac{\Delta P}{\left(\frac{W_o}{W_c} - 1\right)} - P_o\right]$$

P_o = Price per kg of baseline material
ΔP = Difference in price per kg between candidate and baseline material
W_o = Weight of baseline part
W_c = Weight of candidate part
u = Material utilization, i.e., ratio between part and purchased material weight
ΔQ = Cost difference per kg of weight saved

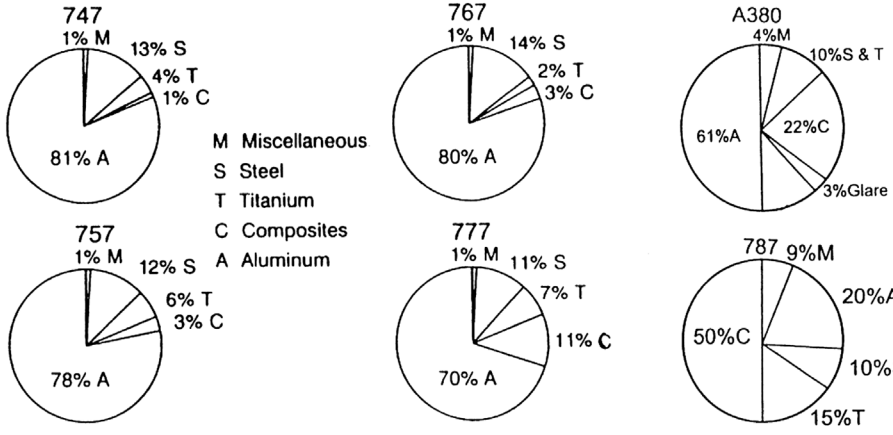


Figure 4.50 Structural materials used in selected passenger aircraft. Courtesy M.V. Hyatt and A. S. Warren, Boeing Airplane Company, and E. Grosjean, Airbus Industrie.

In recent years, the aluminium industry has faced strong competition from alternative lightweight materials, notably fiber-reinforced organic composites. Predictions made in the 1980s suggested that the aluminium content of civil passenger aircraft could fall from around a traditional figure of around 80% to less than 50% within a decade. Even more drastic reductions were expected for military aircraft. This latter prediction has proved to be correct for combat aircraft which fly at supersonic speeds that cause significant aerodynamic heating during flight, and require the use of titanium alloys or other materials for much of the skin and structure. However, as shown in Fig. 4.50, aluminium alloys have retained their dominant position with recent passenger aircraft with the exception of the Boeing 787. The Boeing 777 has 70% aluminium alloys in its structure and the larger Airbus A380 has 61%, although the wing still has retained more than 80%. A major change with the design of this latter aircraft has been the use of carbon-fiber-reinforced polymers for much of the critical center wing box, which is said to allow a weight saving of 1.5 tonnes compared to using the most advanced aluminium alloys. Parts of the fuselage and much of the empennage (tail) are made from another fiber-reinforced composite materials called GLARE laminate (see Section 8.1.1). The actual division of materials in the A380 is aluminium alloys 61%, fiber-reinforced polymer composites 22%, titanium and steel 10%, GLARE laminates 3%, surface protection compounds 2%, and miscellaneous 2%. For the Boeing 787, the radical decision was made to reduce weight by using carbon fiber epoxy resin composites for the primary structure and the overall aluminium content has been reduced to only 20%. Here the aim was to achieve 20% better fuel efficiency and improve corrosion resistance. Manufacturing costs and cabin noise in flight have also been reduced.

4.6.2 Automotive sheet and structural alloys

Serious attention to weight savings in motor vehicles first arose in the 1970s following steep increases in oil prices imposed by Middle Eastern countries. More recently, impetus has come from legislation in some countries to reduce the levels of exhaust emissions through improved fuel economies. In this regard, each 10% reduction in weight is said to correspond to a decrease of 5.5% in fuel consumption. Moreover, each kilogram of weight saved is estimated to lower CO_2 emissions by some 20 kg for a vehicle covering 170,000 km.

The two strategies to save weight have been to build smaller vehicles (so-called downsizing) and to use lighter materials (lightweighting). The extent to which each has been adopted has depended on factors such as customer preference and levels of fuel tax in various countries. More recently, the use of lighter materials has been further stimulated by the need to offset weight penalties associated with the demand for accessories such as air conditioners and emission control equipment, as well as additional safety features to provide more protection to occupants.

Particular attention has focused on the replacement of steel and cast iron by aluminium alloys which usually results in weight savings of 40–50%. In this regard, the average aluminium content of motor vehicles built in North America has risen from 3 kg in 1947 to 20 kg in 1960, 54 kg in 1980, 117 kg in 2000, and 181 kg in 2015 (Fig. 4.51) and an estimated 250 kg in 2025. A similar trend has been followed in Western Europe and in Japan. The global automobile industry (excluding China) consumed 2.87 million tonnes of aluminium in 2014 which is estimated to rise to about 4.5 million tonnes by 2020.

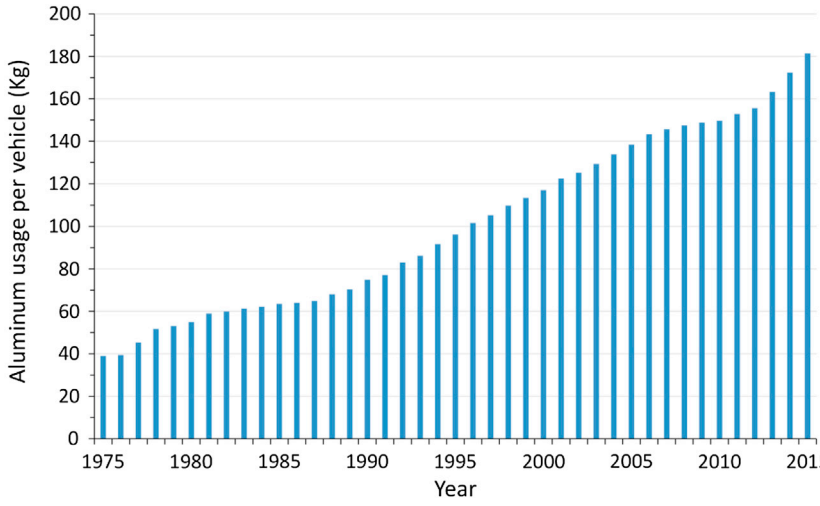


Figure 4.51 Past average and present use of aluminium alloys per vehicle in North America.

A controlling factor in materials selection is cost, and an additional premium of up to US$3 for each kilogram of weight saved has been considered to be acceptable for mass-produced cars. This restriction is accommodated more readily with lower-cost aluminium castings for engine components, transmission housings, and wheels which currently account for about two-thirds of the aluminium used worldwide in cars. For wrought components, steel generally costs less than US$1 per kg as compared with US$3–4 for aluminium alloy sheet and extrusions. Luxury cars such as Rolls-Royce, Rover, and Porsche have for many years made use of aluminium alloys for bonnets and other body panels. Now competition with steel has become intense for both body sheet and structural members in mass-produced cars.

The main property requirements for automotive sheet are:

- sufficient strength for structural stability, fatigue resistance, dent resistance, and crash worthiness;
- good formability for stretching, bending and deep drawing, as well as the ability to control anisotropy and spring back;
- good surface appearance, e.g., freedom from Lüders bands;
- easy joining by welding, clinching, riveting, brazing, and adhesive bonding;
- high corrosion resistance;
- ease of recycling.

Formability, notably the capacity for sheet to be drawn, is a critical requirement. This property is controlled by the crystallographic texture developed on rolling, as well as the work hardening exponent n and the R-value (ratio of width to thickness strain), both of which should be as large as possible (Section 2.1.3). An optimum combination of strength and formability requires careful control of alloy composition, working, and heat treatment.

The first alloys selected for automotive sheet were 3004, 5052, and 6061. However, the low strength of 3004, problems with Lüders band formation drawing of some 5xxx series alloys, and the limited formability of 6061 led to the development of new compositions such as the copper-containing alloys 2008 and 2036, and other 6xxx series alloys including 6009 and 6010 (Table 4.12). Now focus for producing the so-called body in white vehicle is on the use of the NHT Al–Mg alloys or several Al–Mg–Si alloys of the 6xxx series that respond to age hardening.

The main advantages of Al–Mg alloys are their relatively high strength combined with good formability which arise from solution strengthening and capacity for extensive strain hardening. In this regard, these alloys have a high stain-hardening exponent n (~0.30) which is important in drawing operations because it serves to reduce metal flow in locally strained regions. One disadvantage that remains is the tendency to serrated yielding during stretching and drawing that may cause Lüders bands to form which disfigure the surface of a sheet. This phenomenon arises because of the pinning of dislocations by

Table 4.12 Typical mechanical properties and formability indices for aluminium automotive sheet alloys

Alloy	Nominal composition	0.2% proof stress (MPa)	Elongation (%)	η	R
2008–T4	0.9Cu–0.65Si–0.4Mg	126	28	0.25	0.70
2036–T4	2.6Cu–0.45Mg–0.25Mn	195	24	0.30	0.65
5754–0	3.1Mg	100	28	0.30	0.75
5052–0	2.5Mg–0.25Cr	90	25	0.30	0.75
5182–0	4.5Mg–0.35Mn	140	30	0.31	0.75
5022–T4	3.7Mg–0.35Cu	135	30	0.30	0.65
6009–T4	1.1Si–0.6Mg–0.35Mn	125	27	0.22	0.64
6010–T4	1Si–0.8Mg–0.5Mn–0.4Cu	165	24	0.22	0.70
6016–T4	1.25Si–0.4Mg	120	28	0.27	0.60
6111–T4	0.85Si–0.75Mg–0.7Cu–0.3Mn	160	26	0.26	0.56

From Hirsch, J: *Mater. Sci. Forum*, 242, 33, 1997.
η, strain hardening exponent; R, ratio of width to thickness strain.

magnesium atoms and can often be overcome during sheet production by giving a final light cold rolling pass that increases dislocation density. It is also less of a problem with more dilute alloys such as 5754 (Al–3.1Mg). A second disadvantage is some loss of some strength that may occur due to partial annealing during the paint bake cycle (e.g., 30 min at 180°C). This problem can be minimized by copper additions which induce clustering so that some rapid hardening occurs during the first few minutes at such temperatures (Section 2.3.2). An example of an Al–Mg–Cu alloy is 5022 (Al–3.7Mg–0.35Cu).

Neither of the above problems occurs in 6xxx alloys and paint baking may in fact lead to some increase in strength due to age hardening. Yield strengths may exceed those of the 5xxx series alloys (Table 4.12) but formability is somewhat less (n values 0.22–0.27). Levels of magnesium, silicon, and, more recently, copper must be optimized to achieve a required combination of properties. Surplus amounts of silicon have been found to have positive effects on response to age hardening as well as to formability. For these reasons, the alloy 6016 has gained favor with European manufacturers. In North America, attention has been directed more to the addition of copper which increases age hardening and improves the strain-hardening characteristic of Al–Mg–Si alloys, although there are concerns about adverse effects on corrosion properties. One such alloy is 6111. Pre-ageing some 6xxx series alloys for short times at temperatures such as 100°C has been shown to increase the so-called paint bake response, i.e., ageing during this brief cycle is accelerated which results in additional hardening.

Stronger alloys are regarded as being more suitable for outer panels whereas the lower strength but more formable alloys, such as the earlier composition 5182 (Al–4.5Mg–0.35Mn), are preferred for more complex inner panels. At the

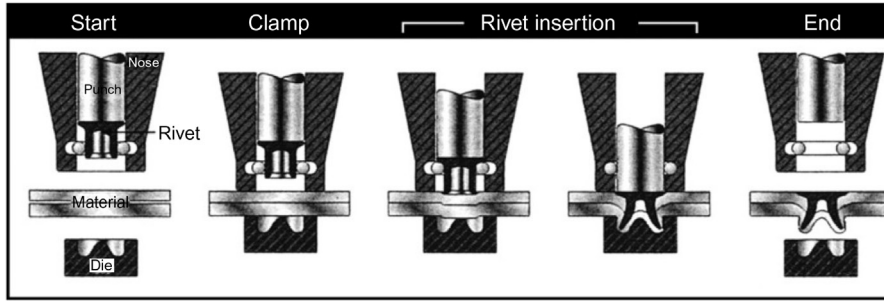


Figure 4.52 Self-pierce riveting insertion process for sheet joining. Courtesy HENROB Corporation.

same time, there is an advantage to be gained if the combinations of alloys in the same assembly have compositions that are fairly similar in order to facilitate scrap separation during recycling.

Aluminium body sheet alloys usually have yield strengths equal to or better than most plain carbon steel sheet alloys and the respective work hardening exponents are similar (typically $n = 0.22$–0.25). However, steel sheet displays much better formability because ductilities (e.g., 40%) and R-values (1.6 compared to 0.75) are significantly higher than those of the aluminium sheet alloys. Another disadvantage with aluminium alloy sheet has been the difficulty of using traditional spot-welding techniques during assembly. Frequent changes of the tips in the welding electrodes have been necessary and, even then, the strength and fatigue resistance of the spot welds do not compare well with those in steel sheets. This has led to the development of techniques for continuous adhesive bonding of flanges, often combined with less frequent spot welds to improve peel strength and hold the structure together while the adhesive cures. This practice has become known as weld bonding and has the additional advantage of increasing the overall stiffness. Another advance has been the development of an improved method of self-piercing riveting (SPR) so that leakproof joints can be made (Fig. 4.52). SPR is a cold-forming process in which the rivet is driven through the top sheet(s) and upset on a die so that the rivet penetrates the innermost sheet without piercing it. Being a non-thermal process, SPR can be used after coating or painting with virtually no esthetic or other damage. Joints are claimed to be 30% stronger than those produced by spot welding and fatigue resistance can be up to 10 times better. Furthermore, sheets of different materials can be easily joined. When combined with adhesive bonding, the joining system has become known as rivbonding.

Although aluminium alloy sheet has been used for many years for body panels in some automobiles such the Rolls-Royce and the Land Rover in Britain, the first production vehicle to utilize aluminium for the body in a broad and systematic way was the Honda Acura NSX sports car that was introduced in 1990. The primary structure weighed 210 kg which represented a saving of

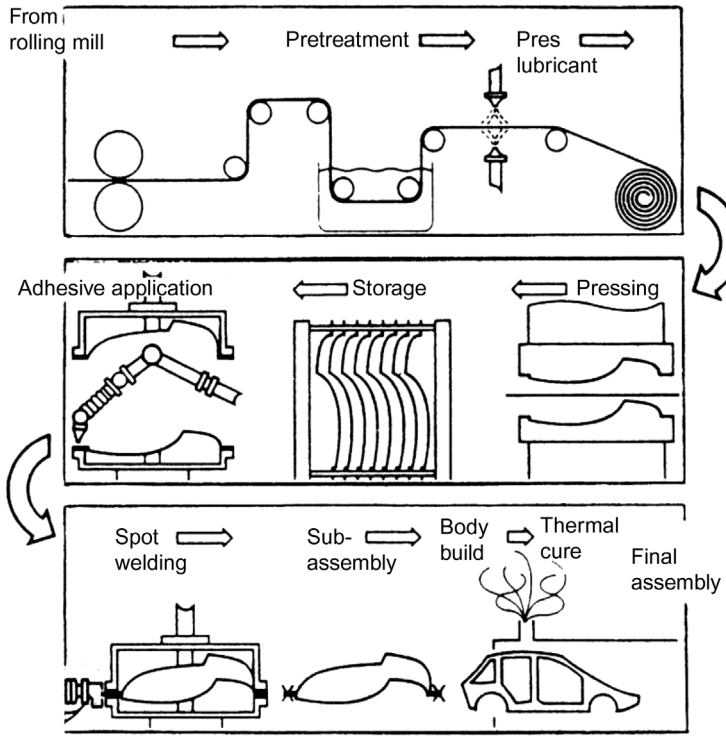


Figure 4.53 Prototype assembly line for producing adhesively bonded aluminium alloy motor car panels. From Shearby, PG *et al.*: *Aluminium '86*, Sheppard, T. (Ed.), Institute of Metals, London, 543, 1986.

an estimated 140 kg over an equivalent steel construction. The Alcan and Ford Companies have made extensive use of bonded sheet for load-bearing members in the conventional monocoque design of their aluminium intensive vehicle. Behind this approach has been the belief that existing manufacturing and assembly facilities used for fabricating automotive panels from steel sheet can be retained and easily adapted to handle aluminium alloy sheet. The body and exterior panels are 200 kg lighter than would be the case had steel sheet been used. So far as assembly is concerned, Fig. 4.53 shows one production route developed for a prototype manufacturing line which uses the low-strength, corrosion-resistant, and highly formable Al–Mg alloy 5052–O. It is necessary to pretreat the surface of sheet to improve its adhesive properties and to use a lubricant during pressing of panels that is compatible with the adhesive. Furthermore, the adhesive itself has to provide a necessary combination of shear, peel, and impact strength, and to retain these properties over a temperature range of −40°C to 120°C so as to cope with climatic variations and heat generated in the engine compartment.

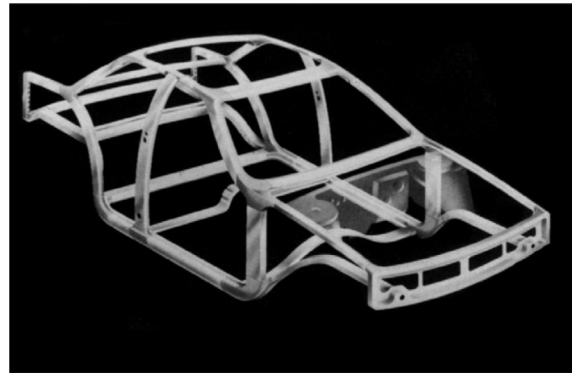


Figure 4.54 Alcoa extruded aluminium alloy space frame.

The Alcoa Company decided to follow a more radical approach to design which has involved the concept of a space frame comprised mainly of hollow aluminium alloy extrusions interconnected at die cast nodes by robotic welding techniques (Fig. 4.54). The extrusions are made from 6xxx series alloys and the nodes are produced by pressure die casting an Al–Si alloy into evacuated dies to minimize porosity and improve fracture toughness to levels well above those normally found for castings. A plant to exploit this technology was built in Soest in Germany to produce components and subassemblies for the Audi Company whose A8 vehicle was released in 1994. Fewer than 100 extrusions and nodes were needed for the primary body structure compared with as many as 300 stampings that would be required for a comparable structure made from steel. Several methods have been used to attach the external aluminium alloy body panel to the space frame including shielded argon arc welding, resistance spot welding, punch riveting, clinching, and adhesive bonding. Arc welding has been considered in Section 4.5.1 and clinching is a technique for joining two sheet panels by bending over the edges. The all-aluminium body used 55% sheet, 25% extrusions and 20% castings which reduced the overall weight by 40%. Another model, the Audi AL2, was also produced in which cost savings were made because of a simpler design whereby the extruded members were kept as straight as possible, the number of joint castings was reduced, and the several hundred spot-welded or clinched joints were completely eliminated.

Economic analysis suggests that space frame technology has a cost advantage for low volume production (up to 60,000–80,000 vehicles per year), whereas the use of stamped sheet components becomes less expensive for higher volumes. Several other companies have been developing vehicles with aluminium alloy bodies made from stamped sheet components. As examples, Chrysler in the United States, in collaboration with Reynolds Metals, has built a version of its Neon model in which the use of stamped aluminium alloys for the body has resulted in a weight reduction of 270 kg, and General Motors have adopted the same strategy to reduce the weight of their EV1 electric vehicle.

Another use of wrought 6xxx alloys is for drive shafts which are gaining acceptance and commonly result in weight savings of around 6 kg. Higher-strength alloys are required for bumper bars and bumper reinforcements for which use has been made of Al–Zn–Mg and Al–Zn–Mg–Cu alloys of the 7xxx series. An example is 7029–T5 (Al–4.7Zn–1.6Mg–0.7Cu) which was derived from compositions traditionally used for aircraft construction. This alloy has the following mechanical properties: 0.2% proof stress 380 MPa, tensile strength 430 MPa, and elongation 15%. Impurity levels are kept low to improve toughness and bright finishing characteristics.

Two other factors that influence the selection of materials for car bodies are safety (or crashworthiness) and capacity for recycling. Stiffness is a prime concern when considering the deflection of panels or structures and this parameter is directly related to elastic modulus which places aluminium alloys at an apparent disadvantage with respect to steels. What is more significant, however, is that stiffness of a component also varies with the cube power of thickness. As a general rule, when an aluminium structure is half the weight of an equivalent steel structure, the gauge of the sheet or the wall thickness of components is some 50% greater which provides for enhanced rigidity and crush resistance, particularly for tubular sections. With respect to recycling, aluminium scrap has the advantage of relatively high intrinsic value, particularly if similar alloys can be contained and remelted within a closed loop. One early estimate was that, if aluminium comprised only 6% of the weight of a motor car, this could still represent as much as 30% of the recycled value (Section 1.1.4).

A manufacturing innovation, which was developed in the steel industry in the 1990s, is the use of welded "tailored blanks" to produce complete sections of automobiles. This method has become possible because of advances in laser welding which enable panels of varying thicknesses, and sometimes of different alloys, to be joined together. Various aluminium alloys have been selected for this purpose and different joining processes have been examined that may permit combinations of aluminium alloys and steel to be used. The aim with the tailored blanks has been to enable designers to reduce weight and improve rigidity in precise locations where this is needed.

4.6.3 Shipping

The position of the ship's center of buoyancy above the center of mass determines its stability. For passenger vessels, the use of aluminium alloys makes possible an increase in the volume and height of the superstructure without loss of stability which, in turn, allows for the inclusion of more passenger decks than is possible with an equivalent design built in steel.

The introduction of significant tonnages of aluminium alloys for ship building dates back to the end of World War II. An early major advance was made with the passenger liner SS United States of 54,200 tonnes displacement which



Figure 4.55 Ocean-going ferry constructed from 5xxx series aluminium alloys. Courtesy INCAT, Tasmania, Australia.

was launched in 1952 and contained around 2000 tonnes of aluminium alloy plate and extrusions in its superstructure. This change in design gave savings of 15–20% in weight and 8% in fuel so that this vessel quickly captured the speed record for crossing the Atlantic Ocean. Although the overall use of aluminium has generally been less, this trend has continued with liners such as the Queen Elizabeth II, and with modern cruise ships. During recent years, there has been a worldwide demand for high speed, ocean-going ferries, and other coastal vessels that has led to construction of all aluminium designs commonly 50–80 m long and capable of speeds of exceeding 80 kmh. One example of a vehicular ferry is shown in Fig. 4.55.

Although there is no pressing need to exploit the weight advantages of aluminium alloys in cargo ships, their good welding characteristics and cryogenic properties (no ductile/brittle transition) have led to their use for the large spherical tanks that are distinctive features of vessels transporting liquefied natural gases. The other use of aluminium alloys in shipping is with naval vessels because of the need to reduce weight high up, especially for masts and structures carrying radar aerials. Some parts of the superstructures of many of these naval vessels have also been constructed from aluminium alloys leading to accusations that this makes them prone to fire damage through the "burning" of aluminium. This is incorrect because bulk aluminium does not burn in air, nor does it support combustion.

The alloys most commonly used for plate are the 5xxx series based on the composition 5083 (Al–4.5%Mg–0.7%Mn) in the hot-rolled, cold-stretched, and stabilized condition. These alloys readily weldable and show a good combination of strength and corrosion resistance. A more recent alloy is 5383 (Table 4.2) for which the nominal levels of magnesium and manganese have been slightly raised, as have the allowable amounts of the impurities zinc and copper, whereas the iron and silicon impurities are reduced. The advantages claimed for

5383 over 5083 are that the proof stress and tensile strength are 12–14% higher both before and after welding, and that the corrosion resistance is improved. Further increases in pre- and postweld tensile properties have been reported for a European alloy known as ALUSTAR in which the 5083 composition has been adjusted to allow a zinc content as high as 1.3%. The minimum level for the proof stress in the welded condition is set at 160 MPa which compares with 140 and 125 MPa, respectively, for the alloys 5383 and 5083. Friction stir welding (see Section 4.5.1) is proving to be a useful method for distortion-free joining of long symmetrical plate sections in all these alloys.

Further weight savings are possible with the development of composite panels involving a combination of flat and corrugated sheets, the latter being manufactured by standard roll-forming methods. CORALDEC is the trademark of one such assembly in which the flat top and bottom sheets are laser welded to the central corrugated sheets. These panels have been used for construction of accommodation and vehicle decks in fast ferry catamarans. Advantages of up to 25% in weight savings are claimed over extruded panels made from 6xxx series alloys such as 6005 and 6082.

4.6.4 Building and construction

Significant use of aluminium and its alloys for building materials commenced some 70 years ago after the end of World War II. Since then consumption has increased steadily in most countries and this segment is now the major market in China which is the world's two of the three largest consumer of aluminium. Advantages of aluminium include its good decorative appearance, high corrosion resistance in most environments, lightness, ease of fabrication, and the fact that extruded sections can be easily prepared for the provision of double glazing or the insertion of insulation and blinds. Competitive disadvantages of aluminium when compared with steel are cost, relatively low elastic modulus which means that beams and other supports must be thicker, the need for greater protection from fires due to the lower melting point of aluminium, and the higher coefficient of thermal expansion which requires more allowance to be made for movement, particularly in extreme climates. Most of these disadvantages are more apparent with plastics which are another major competitor for many building products.

Applications include facades, roofing, guttering, window frames, sun shades, curtain walls, and balustrades. Foil is often used as a moisture barrier in house construction. Aluminium alloys are also often used as external cladding to retain spalled fragments and disguise discoloration in old stone and concrete buildings. More limited use is being made to construct small bridges. The alloys in most common use for rolled products are those based on the 5xxx series (e.g., 5005–H34 for surface critical anodized architectural sheet) and 3xxx series (e.g., 3105–H1 for painted gutters and house siding), whereas extrusions are usually made from the 6xxx series (e.g., 6063–T6 for door and window frames).

4.6.5 Packaging

During the last three decades, the use of aluminium in packaging has increased to the extent that, at times, it has been the largest market for this metal. As shown in Fig. 1.5, packaging was the second largest consumer of aluminium in the advanced economies in 2013. This situation has arisen because aluminium is an attractive container for food and beverages since it has generally high corrosion resistance, offers good thermal conditions, and is impenetrable by light, oxygen, moisture, and microorganisms. Furthermore, simple alloy compositions can be used that are easy to both fabricate and recycle. The largest production items are beverage cans and foil.

Canstock The entry of aluminium into the can market occurred in 1962 with the introduction of the tear-end tab, or the so-called easy-open end, which was used for steel beverage cans. This was followed by the two-piece, all-aluminium can with a seamless body that is produced from sheet by cupping followed by drawing and ironing the side walls. Since then growth in use of the all-aluminium can has been phenomenal and now accounts for more than three-quarters of all the aluminium used for packaging. In 2015, the amount of can stock produced worldwide was estimated to be 5.3 million tonnes which would have been sufficient to manufacture close to 300 billion cans. This represents the largest single use of aluminium for the one product. As mentioned in Section 1.1.4, efficient recycling has been a key economic factor in guaranteeing the competitive success of aluminium for canstock.

Aluminium canstock was first made from the alloy 3004 (Al–1.25Mn–1.05Mg) which was in its annealed condition. Demands for thinner gauges were then met by cold rolling in several stages to what is called the H19 temper. More recently this alloy was replaced by 3104 (Al–1.1Mn–1.05Mg–0.15Cu) which has a slightly reduced Mn content and usually higher Mg and/or Cu to improve ironing performance and maintain sufficient strength in the finished can.

Sheet for canstock is mostly produced by rolling large DC cast ingots (Fig. 4.3) and the following is a typical processing cycle:

1. Homogenization of the ingots, usually at two temperatures (e.g., 570°C followed by slow cooling to 510°C) to obtain a desirable distribution of primary particles (Al_6(Fe,Mn) and α-Al(Fe,Mn,Si)), and the finer dispersoids, e.g., Al_6(Fe,Mn). This helps to control recrystallization in (4) below.
2. Hot rolling at 450°C to reduce the thickness from around 600 to 25 mm.
3. Warm rolling to a so-called hot-band thickness of 2.5 mm, during which the grain structure develops a preferred orientation as shown in Fig. 4.56. During this process, the temperature of the strip is controlled to ensure that it will recrystallize in the coil after exit from the tandem rolling mill.
4. Cooling to room temperature and cold rolling in several stages to the final gauge size of around 0.30 mm. At this stage the sheet is in the H10 condition and the typical mechanical properties are 0.2% PS 290 MPa, TS 310 MPa, and elongation of 10%.

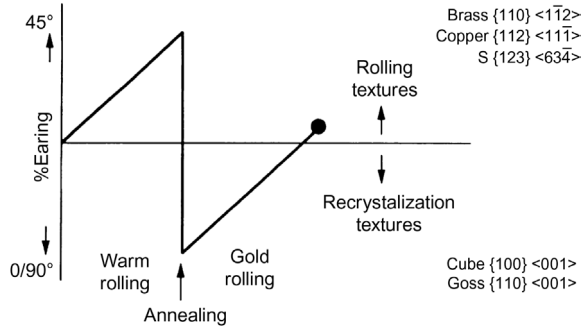


Figure 4.56 Progressive development of textures and earing during the processing of 3004–H19 canstock.

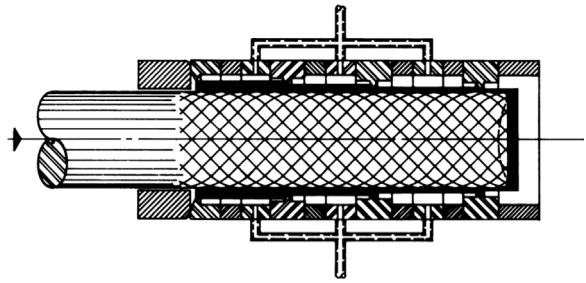


Figure 4.57 One stage in the drawing and ironing of a seamless aluminium alloy can.

What is critical is control of sheet texture to minimize earing (Section 2.1.4) during the final deep drawing and ironing of the can. This is achieved by promoting the formation of a cube (0–90°) texture in recrystallized grains which then serves to balance the 45° texture that develops during subsequent cold rolling (Fig. 4.56). What is finally desired is consistent slight positive earing of less than 2.5% in each can.

One stage in the demanding process of drawing and ironing of the can body is shown schematically in Fig. 4.57. It can be seen that ironing involves the progressive squeezing of the metal between an inner punch and outer dies that have decreasing internal diameters. Machines are now available that can punch out as more than 500 cans each minute. Lubrication is important, as is the presence of primary particles of the relatively hard intermetallic compound α-Al(Fe,Mn,Si) in the sheet that serves to wipe away aluminium debris which may have been transferred to the dies during the ironing process. This latter phase, the composition of which may vary between α-$Al_{12}(Fe,Mn)_3Si$ and α-$Al_{15}(Fe,Mn)_3Si_2$, forms from the interaction of silicon in solid solution in the matrix with primary $Al_6(Fe,Mn)$ particles during homogenization.

The thickness of final gauge sheet for can making has been reduced from 0.50 mm in the 1960s to 0.44 mm in the early 1970s, 0.30 mm in the early

1990s, and to a current average of 0.255–0.270 mm in North America. This progressive thinning, or lightweighting, has been crucial because of the relatively high cost of aluminium. Careful attention must be given to the design of cans which, in effect, are small pressure vessels that must withstand internal pressures of some 600 kPa when they contain gasified beverages. Wall thicknesses vary depending on location in the can and may be as thin as 0.10 mm in the central regions of the side walls. It is necessary, therefore, to filter the molten aluminium during casting to remove inclusions and to control the size of primary intermetallic particles both of which might otherwise cause pinholing or perforation of the sheet during can making. These requirements also apply to the production of foil.

Thickness reductions and cost savings have also been achieved with can ends (end stock) through improved designs and the use of stronger alloys. Typical thicknesses were around 0.335 mm in the 1970s and are now usually within the range 0.200–0.220 mm. In the mid-1980s, a typical yield strength for the can end alloy 5182 (4.5Mg–0.04Mn) was 320 MPa which has been raised to 370 MPa by gradually increasing the level of magnesium above the specified limit of 5%, increasing the manganese content, and allowing small increases in minor elements such as copper.

Foil Due to its capability of being cold rolled to very thin gauges, aluminium foil is widely used as an effective barrier to light, water vapor, and gases. Foil is commonly defined as rolled sheet having a thickness less than 0.200 mm. Products range from light gauge foil, e.g., 0.01 mm thick, for domestic and other uses to thicker foil for semirigid containers. In laminated products with plastic or paper films, thin-gauge aluminium foil is also an ideal packaging material for applications such as pharmaceuticals and food containers. The amount of foil stock produced worldwide in 2015 was 6.1 million tonnes.

Historically, 1xxx aluminium alloys such as 1145, 1100, and 1200 have been widely used. However, the need for alloys with greater levels of strength and ductility has led to the development of alloys with higher levels of iron, manganese, and silicon which can therefore contain higher volume fractions of intermetallic compounds. These compounds can control the microstructure during recovery and recrystallization during annealing resulting in an attractive combination of properties after final cold rolling. One example is the alloy 8011 which is widely used for household foil in the United States.

The major advance in foil production has been the development of methods for rolling at high speeds while maintaining close control of thickness. Rolls capable of handling coil stock weighing as much as 10 tonnes and operating at speeds in excess of 40 $m\,s^{-1}$ are now common. The coil stock is produced by rolling semi-continuously cast ingots (Fig. 4.3) or, more economically, continuously cast strip (Figs. 4.4B and 4.5) and then cold-rolling to a strip thickness of about 0.5 mm. Foil is produced by further cold-rolling the strip in several stages in a continuous mill, the material being pack-rolled double in the last stage if very light gauges, e.g., 0.025 mm, are needed. Most foil is then softened by annealing.

One of a number of coating treatments such as laminating with paper, lacquering, printing, and embossing may then be applied for purposes such as advertising.

A common problem associated with foil production from twin roll cast strip is the tendency for alloying elements to segregate to the center of the strip during casting. This centerline segregation occurs because, during rapid solidification, the shearing action of the rolls squeezes the interdendritic liquid toward the center of the strip. The result is that this zone contains higher amounts of the relatively hard Al–Fe–Si intermetallic compounds, which if not reduced in size by further thermal treatments and cold working, may perforate the final foil and produce an unacceptable number of pinholes. For most applications, a pinhole limit of less than 500 per m^2 and sizes below 20 μm is required. Centerline segregation may also reduce foil strength and cause higher foil tearing at the mill.

4.6.6 Powder metallurgy products

Powder metallurgy technology provides a useful means for fabricating near net shape components, thereby enabling the costs associated with machining to be minimized. This aspect is discussed further in the "Powder metallurgy processes" section. Another advantage is that microstructures are generally finer than those present in alloys prepared by normal ingot metallurgy, which may result in improved mechanical properties and corrosion resistance.

Normal processing involves the production of powders which are then cold pressed and sintered at elevated temperatures (e.g., 500°C). Recently several novel techniques have been developed which have enabled new, and sometimes unconventional, alloys to be produced, thereby extending the range of properties available from powder compacts. One method is spray forming which is discussed later in this section; others include rapid solidification processing and mechanical alloying, which are described in Chapter 8, Novel materials and processing methods. In all cases, much of the developmental work was carried out in aluminium-based materials.

Aluminium powders were first produced as flakes by ball milling and resulted in a number of fatal fires and explosions because of the highly exothermic nature of finely dispersed aluminium. Safer milling methods are now available but most powders are currently produced by "atomization" in which the molten aluminium (alloy) issuing from an orifice is broken up into very small droplets by a stream of high-velocity air or an inert gas. The droplets solidify as a fine powder which is collected in the chamber and graded for size. A problem is that aluminium is always covered by a tenacious oxide film and the thickness on atomized powders can vary from 5 to 15 nm. Although this film cannot be removed, it may be disrupted by sintering in the presence of magnesium. Magnesia has a lower free energy of formation than alumina and magnesium metal can partially reduce alumina to form a spinel $MgAl_2O_4$. This reaction serves to rupture the oxide which exposes the underlying aluminium metal and facilitates sintering. Less than 0.2% magnesium is required.

As mentioned earlier, the direct production of components from powders normally involves cold compaction in dies followed by sintering. Allowance must be made for shrinkage. Alternatively, if powder alloy billet is required, then the following stages are usually involved:

1. Compacting the powder in an aluminium can.
2. Vacuum degassing and hot pressing. This step may require sealing the can which is later removed by machining.
3. Fabricating the powder alloy billet by the normal processes of extrusion, forging, or rolling.
4. Heat treatment.

Although they are more expensive to produce, powder metallurgy billets are now available weighing several hundred tonnes.

Conventional processing One of the early products produced by powder metallurgy techniques was the material known as SAP that was developed in Switzerland. SAP is an Al–Al_2O_3 alloy prepared by pressing and sintering finely ground flakes of aluminium, and the final microstructure may contain an oxide content as high as 20% in the form of Al_2O_3 particles dispersed in the aluminium matrix. The sintered compacts can be hot-worked by extrusion, forging, and rolling to give a product which, using Al–15Al_2O_3 as an example, may have room temperature properties of 0.2% PS 240 MPa, TS 345 MPa, with 7% elongation. These properties are relatively low but the fact that the oxide is stable up to the melting point means that creep strength is superior to conventional aluminium alloys at temperatures above about 200–250°C. Although SAP was once considered as a possible skin material for high-speed aircraft which would suffer aerodynamic heating, it has found relatively few applications and its major use has been for fuel element cans in certain nuclear fission reactors which use organic coolants. For this purpose, its creep strength, corrosion resistance, low capture cross section for neutrons, and absence of radioactive isotopes are special advantages. The material is also a candidate for part of the internal structure of experimental nuclear fusion reactors which may employ the deuterium–tritium fuel cycle.

A wider range of powders is now available including premixes which give compositions that tend to mimic several wrought alloys normally produced from cast ingots. Compositions of common commercial powder metallurgy alloys are given in Table 4.13. It will be noted that most are based on the wrought Al–Mg–Si and Al–Cu–Mg alloys 6061 (Al–1Mg–0.6Si–0.28Cu) and 2014 (Al–4.4Cu–0.6Mg–0.85Si–0.8Mn). A common feature is that all but one contain magnesium which reacts with the surface Al_2O_3 film during sintering to form spinel $MgAl_2O_2$. This disrupts the film and exposes underlying metal which facilitates the sintering process. Another common feature is that they all respond to age hardening.

Table 4.13 Compositions of commercial powder metallurgy aluminium alloys

Alloy	Cu	Mg	Si
602	–	0.6	0.4
601	0.25	1.0	0.6
6711	0.25	1.0	0.8
321	0.2	1.0	0.5
202	4.0	–	–
2712	3.8	1.0	0.75
201	4.4	0.5	0.6
2014	4.4	0.5	0.8
13	4.5	0.5	0.2
123	4.5	0.5	0.7

Since these alloys were not specifically designed to be sintered, it is to be expected that opportunities will exist to improve processing conditions through compositional changes. For example, it has been shown the sintering response of the Al–Cu–Mg alloys can be enhanced by microalloying additions of the low melting point elements tin, lead, bismuth, or antimony. Each of these elements has a high diffusivity in aluminium and a high vacancy binding energy. They therefore diffuse into aluminium ahead of the alloying element copper and will bind preferentially with vacancies. This has the effect of reducing the rate at which alloying elements in the premix powders diffuse into aluminium thereby allowing the TLP to persist for longer times which improves densification. Alloys based on the Al–Zn–Mg–Cu system (7xxx series) do not have good sintering characteristics and have been little used as powder metallurgy materials. However, for the composition Al–8Zn–2.5Cu–1Cu, it has been demonstrated that a very small addition (0.01 at.%) of lead will greatly improve the sintering process and reduce porosity (Fig. 4.58).

Improvements have also been made with lubricants used during pressing of the compacts which have reduced the earlier problems of excessive wear of punches and dies. Better combinations of strength and resistance to both corrosion and SCC have been obtained for small forgings and extrusions made from prealloyed, atomized powders than the corresponding products made from ingot metal. In addition, it has been possible to blend into the powder elements that could not be readily added to conventional alloys. One example has been the addition of cobalt to an Al–Zn–Mg–Cu alloy which produces a fine dispersion of the phase Al_9Co_2 in the powder metallurgy product. Commercial alloys such as 7090 and 7091 (Table 4.4) are now available and, as shown in Fig. 4.59, grain size is much reduced as compared with that for a similar type of alloy produced from an ingot. Tensile properties are increased (Table 4.5) and the presence of fine dispersions of the phase Al_9Co_2 along grain boundaries is claimed to reduce the rate of crack propagation in conditions that favor fatigue or SCC.

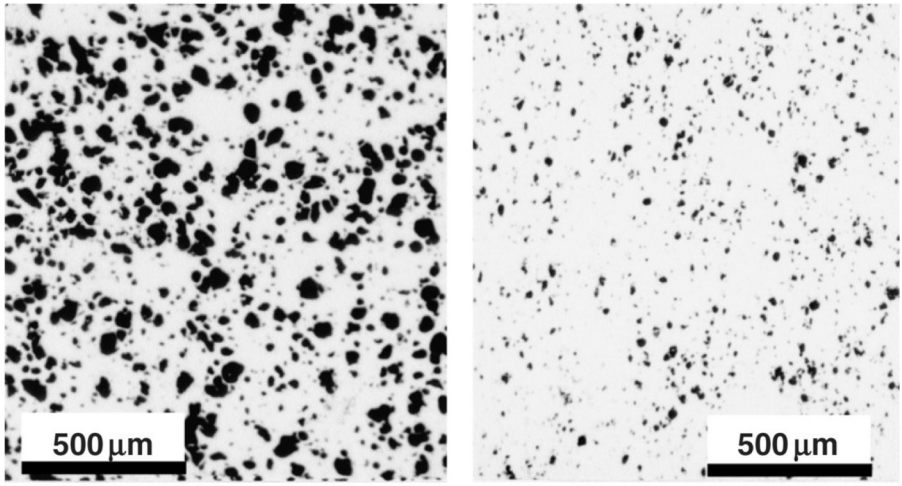


Figure 4.58 Optical micrographs of unetched sections of sintered alloys (A) Al–8.5Zn–2.5Mg–1Cu and (B) Al–8.5Zn–2.5Mg–1Cu–0.07Pb showing the effect of a microaddition of lead in reducing porosity. Courtesy G. B. Schaffer.

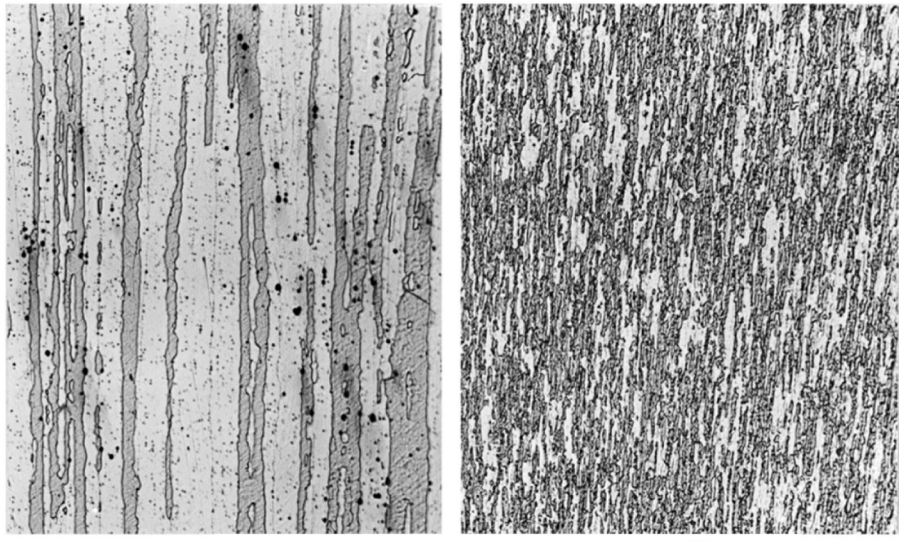


Figure 4.59 Microsections of extrusions produced from (A) 7475 ingot and (B) 7091 powder metallurgy compacts × 100. Courtesy J. T. Staley, Alcoa Research Laboratories.

Powder metallurgy techniques are also enabling the creation of materials with improved tribological properties. Wear resistance can be improved by blending prealloyed aluminium powder with hard particles, such as silicon carbide, whereas the incorporation of solid lubricants reduces the friction. In this regard, experiments have shown that the inclusion of up to 4 wt% of graphite reduces the friction coefficient of powder metallurgy aluminium alloys to values below that of gray cast iron.

Spray forming This method, which is known more generally as the Osprey Process, involves atomization of molten alloys by a stream of high-velocity gas such as nitrogen. However, in this case, the resulting spray of droplets is deposited on a rotating collector plate to produce a compact preform (Fig. 4.60). Cooling of the molten droplets in flight and on impact is fast and solidification rates may be as high as 10^3–10^4 °C s^{-1}. Preforms, which may be 98–99% of the theoretical density, have refined microstructures with respect to the sizes of grains and primary intermetallic compounds.

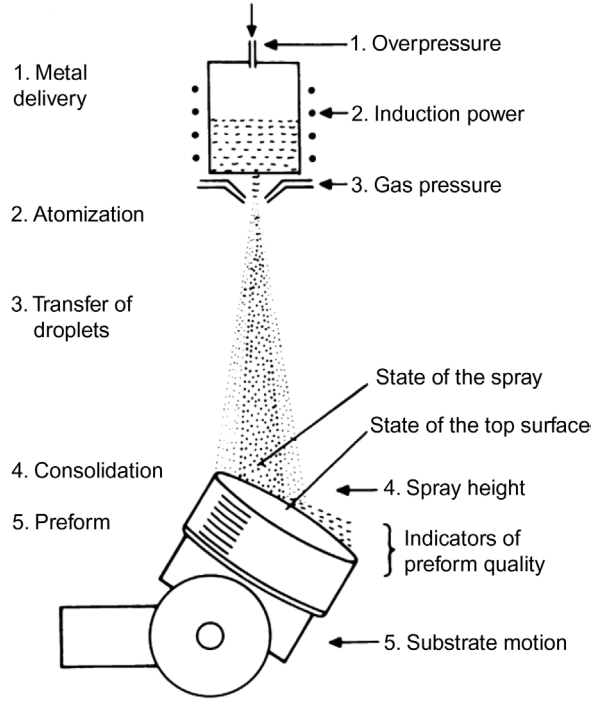


Figure 4.60 Schematic illustration showing spray forming by deposition of molten droplets on to a rotating collector plate. Courtesy D. Apelian.

The fast rate of solidification also provides the opportunity for increasing the supersaturation of alloying elements and a number of experimental compositions have been produced. Examples are Al–11Zn–Mg–Cu–X and Al–20Si–Cu–X, where X is one or more of the transition metals such as iron, chromium, nickel, manganese, and zirconium. In the T6 condition, one of the former alloys has shown the following tensile properties: 0.2% PS 760 MPa, TS 775 MPa, and elongation 8% which are significantly greater than those for the normal 7xxx series alloys. Higher values of fracture toughness and fatigue strength are also possible. The other composition is a hypereutectic Al–Si–Cu alloy and mechanical properties (e.g., T.S. 480 MPa) are again much greater than those of the equivalent conventionally cast alloy (Section 5.2.3) due mainly to the finer dispersion of the primary silicon phase. Wear resistance, which is a feature of these particular alloys, is also increased.

Spray forming offers a number of advantages:

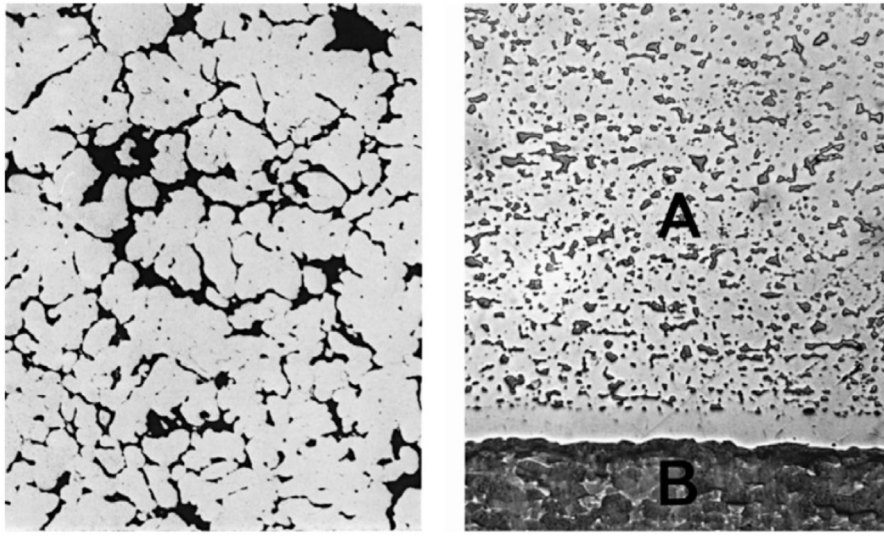
1. Some of the steps involved in normal powder processing are eliminated.
2. Preforms may be fabricated by forging, extrusion, etc.
3. It should be possible to produce alloys with controlled variation in composition (graded materials).
4. Particulates (e.g., SiC) may be injected into the gas stream to produce metal matrix composites directly (Section 8.1.3).
5. The process may be modified to allow direct production of sheet and tube.

Several spray-forming facilities have been constructed and preforms are available weighing a few hundred kilograms. However, it is necessary to appreciate that the alloys carry a significant cost premium so that potential applications are likely to be confined to specialized products. Loss of powder due to overspray beyond the confines of the collector plate is also difficult to control and can have a significant effect on the efficiency of alloy production.

4.6.7 Aluminium alloy bearings

The development of aluminium alloys for bearings dates back to the 1930s when the high thermal conductivity, corrosion resistance, and fatigue resistance of aluminium were recognized. Compositions containing 2–15% copper were then the most successful and the structure of the alloys comprised hard intermetallic compounds in a softer aluminium matrix. Although they were adopted for a number of applications, their relatively high hardness was a disadvantage with regard to certain property requirements, e.g., conformability to rotating shafts. Al–Sn alloys offered the alternative prospect of a softer bearing alloy and compositions with up to 7% tin were introduced. These are still used. They were first produced by casting solid bearings but the high coefficient of thermal expansion of aluminium made retention of fit with steel shafts virtually impossible at the operating temperatures of modern engines. Consequently, most current aluminium alloy bearings are backed with steel.

Early work revealed that the seizure resistance of Al–Sn bearings continued to improve as the tin content was raised to levels of 20% or more. However,



(A) (B)

Figure 4.61 (A) Continuous grain boundary film of tin in a cast Al–30Sn–3Cu alloy (× 120); (B) microstructure of Al–20Sn–1Cu (A) roll bonded to steel (B) via an aluminium interlayer. (A) From Liddiard, EAG: *The Engineers Digest*, 1955. (B) Courtesy G. C. Pratt. The Glacier Metal Co Ltd (× 150).

the full potential of these alloys could not then be realized because, regardless of the method of casting, tin contents in excess of 7% resulted in the formation of low-strength, grain boundary films of tin (Fig. 4.61A). Eventually it was discovered that these films could be fragmented and dispersed along the boundaries if the alloys were cold worked and recrystallized during processing. For alloys with tin contents below 15%, the tin then appears as discrete particles in the grain corners. However, if the alloy contains more than 16% tin, this phase remains continuous in the boundaries where three grains meet producing what is known as a reticular structure.

Bonding the bearing alloy to a steel backing presented further problems because intimate contact was prevented by the tenacious Al_2O_3 film, until it was found that this film could be dispersed by severe cold rolling. Moreover, if the tin content exceeded 7%, smearing of the tin occurred during machining. This meant that pure aluminium cladding had to be incorporated during rolling to form an interface with the steel (Fig. 4.61B).

Current practice for producing steel-backed, Al–Sn bearings commonly involves the following procedures:

1. Either chill casting the alloy on a copper plate to promote directional solidification of a slab approximately 300 mm thick, or semi-continuously casting a similar slab which is cut into lengths in order to machine top and bottom.

2. Cladding top and bottom with pure aluminium by heavily cold rolling in stages to produce a bonded composite having a thickness between 4% and 10% of the original dimension. This treatment also elongates the tin particles.
3. Cold roll-bonding this composite to the steel backing, contact being made via the pure aluminium interface. The configuration of the rolls is arranged so that the bearing alloy is more heavily worked than the steel backing so as to prevent the latter being unduly hardened.
4. Annealing at 350°C for 1 h which recrystallizes the bearing alloy and coalesces the tin either into discrete globules in the grain corners or to form the reticular structure.

A content of 20% tin is often regarded as the optimal level and, in Europe, the most common automotive plain bearing has the composition Al–20Sn–1Cu. An alloy with 30Sn–1Cu is widely used in bushes, and in conditions where lubrication is marginal. These particular alloys offer the added advantage of not requiring a Pb–Sn or Pb–Sn–Cu overlay that is needed to protect Cu–Pb, and some other bearings, from corrosion by chemicals present in modern lubricating oils.

In Japan, especially, the Al–20Sn alloy has been modified by reducing the tin content to 15–17% and adding 2–4% silicon. Hard silicon particles are formed within the grains which have the particular advantage of polishing the widely used spheroidal graphite cast iron crankshafts.

Other aluminium alloys have been developed as bearing materials and particular interest has been shown in substituting cheaper lead for tin. Lead is also claimed to promote development of a better film of lubricant than tin so that Al–Pb alloys exhibit lower frictional characteristics and have a higher resistance to seizure. One example is an alloy Al–9Pb–3Si–1Cu. However, the preparation of alloys based on the Al–Pb system by conventional casting methods presents special difficulties because of gravity segregation of heavy lead, and the fact that this element is immiscible in both liquid and solid aluminium. Unconventional methods have been used including stir casting, rheocasting, rapid solidification, powder metallurgy, and spray deposition, all of which are discussed elsewhere. Each is capable of improving the homogeneity of the dispersion particles of lead although some methods may introduce unacceptable levels of porosity. Hot extrusion has been found to improve homogeneity and reduce porosity in Al–Pb alloys with increased lead contents up to 20%. Another group of alloys that are based on the Al–Si system have been shown to offer greater fatigue strength than Al–Sn alloys and are used in some high-speed diesel engines.

4.6.8 Superplastic alloys

Superplasticity is the ability of certain materials to undergo abnormally large extensions (commonly 1000% or more) without necking or fracturing. After

many years as a laboratory curiosity, the phenomenon has now attracted commercial interest because of the possibility of forming complex shapes in a small number of operations using relatively inexpensive tooling.

The usual requirement for a material to show superplastic characteristics is the presence of roughly equal proportions of two stable phases in a very fine dispersion, e.g., grain size 1–2 μm, which must be maintained at the working temperature. Such materials are commonly eutectics or eutectoids and the eutectic alloys Al–33Cu and Al–35Mg exhibit the phenomenon although neither has commercial potential. One eutectic composition that did show early promise was Al–5Ca–5Zn, which was developed in Canada. However, tensile properties at room temperature were relatively low and all the aluminium alloys currently in commercial use have their grain structures stabilized by fine particles.

One example is a modified version of the corrosion-resistant alloy 5083 (Al–4.5Mg–0.7Mn–0.15Cr), known as 5083 SPF, in which the fine grain structure is controlled by submicron, manganese-bearing particles. This alloy has relatively low tensile properties (0.2% PS 150 MPa, TS 300 MPa) and more attention has been given to compositions that respond to age hardening after forming. In this regard, it was known that Al–5Cu can recrystallize to give a fine grain size. However, this structure is not stable at temperatures of 400–500°C where superplastic flow might be expected, because most of the Al_2Cu particles that might restrict grain growth have redissolved. The possibility of adding a third element that might form small stable particles was then considered, and zirconium was found suitable for this purpose. A composition Al–6Cu–0.5Zr was subsequently developed which was found to be superplastic in the temperature range 420–480°C and, under the name of Supral 100, this material is now being used to produce products such as those shown in Fig. 4.62.



Figure 4.62 Examples of products produced by superplastic forming of the alloy Al–6Cu–0.5Zr. Courtesy T. I. Superform Ltd.

The production route for the alloy is basically similar to that used for manufacturing conventional aluminium alloy sheet, although some changes are necessary in order to achieve adequate supersaturation of zirconium. Higher casting temperatures (~800°C) are used and the semi-continuous, DC casting process is modified so that the rate of solidification is increased. The cast slabs are sometimes clad with pure aluminium during the hot-rolling stage for subsequent corrosion protection, and reduction to sheet is not greatly different from standard practice. Zirconium precipitates as small particles of a metastable, cubic phase Al_3Zr and the fine-grained structure develops during superplastic deformation at temperatures between 420°C and 480°C. Strain rates are of the order of $5 \times 10^{-3}\,s^{-1}$ and, although the flow stresses are greater than those needed to form thermoplastics, similar methods of fabrication can be used. Once a component has been formed, it can be strengthened by precipitation hardening using standard heat treatment operations. Mechanical tests on clad 1.6 mm sheet of the alloy Al–6Cu–0.5Zr after solution treating, quenching, and ageing 16 h at 165°C have given values of 0.2% PS 300 MPa, TS 420 MPa, with 5% elongation. Similar figures for the alloy in the as-formed condition are 125 MPa, 200 MPa, and 7% respectively.

Attention has also been directed at achieving superplastic behavior in high-strength aluminium alloys of the 7xxx series in which it has been shown that thermomechanical processing by the ITMT route (Section 4.1.5) can produce very fine grain sizes (e.g., 10 μm) in rolled components. As shown in Fig. 4.63, the treatment requires the alloy (e.g., 7475) to be overaged at a relatively high temperature after homogenization so that coarse (e.g., 1 μm) η phase precipitates are formed. The alloy is then warm-worked (e.g., 80% reduction at 200°C) which causes intense deformation zones to form around the larger precipitates. These regions then provide sites at which recrystallization occurs during subsequent solution treatment leading to a fine grain size. This treatment also causes

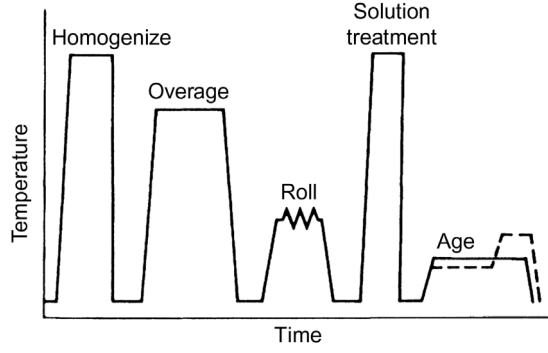


Figure 4.63 Schematic diagram of an ITMT used to achieve very fine grain size in alloy 7475. From Paton, NE *et al.*: *Metall. Trans. A*, 12A, 1267, 1981.

the large precipitates to redissolve. The alloy is then water quenched and artificially aged in the usual way to develop the normal high-strength properties.

The major benefits of such a fine-grained 7475 alloy are improved formability and resistance to SCC. The microstructure is amenable to a degree of superplasticity at appropriate strain rates and temperatures so that elongations exceeding 500% have been achieved. The process presents some handling problems but it does make possible the superplastic forming of complex airframe shapes in conventional high-strength sheet alloys.

In each of the examples mentioned earlier, the strain rates needed to achieve superplasticity are quite slow (e.g., 5×10^{-3}–$10^{-4}\,s^{-1}$) which limits productive output. Moreover, although tooling is usually inexpensive, the superplastic aluminium alloys themselves usually carry a significant cost penalty when compared with conventional sheet alloys, many of which possess relatively good cold-forming characteristics. To date, these factors have limited applications to niche markets, notably in the aircraft industry. What is required is the development of less expensive alloys that exhibit superplastic deformation at higher strain rates of $10^{-2}\,s^{-1}$ or less. If such alloys become available, then there are opportunities to expand to mass produce components that are normally difficult to form, particularly in the automotive industry.

4.6.9 Electrical conductor alloys

The use of aluminium and its alloys as ECs has increased significantly in recent decades, due mainly to fluctuations in the price and supply of copper. The conductivity of EC grades of aluminium and its alloys average about 62% that of the International Annealed Copper Standard (IACS) but, because of its lower density, aluminium will conduct more than twice as much electricity for an equivalent weight of copper. As a consequence, aluminium is now the least expensive metal with a conductivity high enough for use as an EC and this situation is unlikely to change in the future.

Aluminium has virtually replaced copper for high-voltage overhead transmission lines although the relatively low strength of the EC grades requires that they be reinforced by including a galvanized or aluminium-coated high-tensile steel core with each cable. Aluminium is also widely used for insulated power cable, especially in underground systems. In this case, instead of the substitution of copper wires by aluminium, each strand of wire is usually replaced by a solid aluminium conductor which is continuously cast by the Properzi process (Section 4.1.2) and sector shaped by rolling (Fig. 4.64). Cable manufacture is thus simplified and economies are also achieved with insulating materials. For other applications, e.g., wiring for electric motors, communication cables or power supply to buildings, properties such as tensile strength and ductility also become critical requirements and growth in the use of aluminium has been slower.

Stronger alloys such as some heat-treatable Al–Mg–Si compositions have been used as ECs for a number of applications but their conductivity is



Figure 4.64 An underground cable consisting of four-core solid aluminium conductors, insulated with polyvinyl chloride (PVC) and enclosed in lead, then in steel to protect against mechanical damage, and lastly in PVC as an outer layer.

relatively low (55% IACS or less). In general, alloying elements which are either in solid solution or present as finely dispersed precipitates cause significant increases in resistivity so that these methods of strengthening tend to be unacceptable for aluminium conductors. Work hardening is less deleterious in this regard, but conductors strengthened in this way tend to exhibit poor thermal stability and may be susceptible to mechanical failure in service. For these reasons, attention has been directed to alternative methods by which adequate strengthening can be achieved while retaining a relatively high electrical conductivity (>60% IACS).

As mentioned in Section 2.1.2, aluminium is amenable to substructure strengthening and much of the developmental work has been directed at stabilizing the substructure with low volume fractions of finely dispersed intermetallic compounds. These compounds also assist in improving ductility in the final product by increasing strain hardening which delays localized deformation and necking. It is necessary for the compounds to be uniformly distributed and this presents some difficulties because they precipitate in the interdendritic regions during casting. Casting methods must be used which ensure a rapid rate of solidification as this reduces the dendrite arm spacing and refines the microstructure. Extensive deformation during rod production and wire drawing

Table 4.14 Compositions and typical properties of some aluminium alloy EC wires

	Alloy	Yield strength (MPa)	Tensile strength (MPa)	Elongation in 250 mm (%)	Electrical conductivity (% IACS)
Old alloys	EC (99.6Al)	28	83	23	63.4
	5005–H19 (Al–0.8Mg)	193	200	2	53.5
	6201–T81 (Al–0.75Mg–07Si)	303	317	3	53.3
Newer alloys	Triple E (Al–0.55Fe)	68	95	33	62.5
	Super T (Al–0.5Fe–0.5Co)	109	129	25	61.1
	8076 (Al–0.75e–0.15Mg)	61	109	22	61.5
	Stabiloy (Al–0.6Fe–0.22Cu)	54	114	20	61.8
	Nico (Al–0.5Ni–0.3Co)	68	109	26	61.3
	8130 (Al–0.6Fe–0.08Cu)	61	102	31	62.1

From Starke, EA Jr.: *Mater. Sci. Eng*., 29, 99, 1977.
Note: All alloys except 5005 and 6201 are in annealed condition (O-temper).

further assists in distributing the compounds. Rod production involves hot working at a temperature at which dynamic recovery occurs during processing, thereby ensuring the formation of subgrains rather than cells, and the work-hardening exponent n approaches 0.5.

The general trend to increase the level of electrical currents carried by transmission lines leads to higher operating temperatures and may cause softening through changes to alloy microstructure. Zirconium in solid solution is known to have a particularly strong effect in stabilizing grain structure by raising recrystallization temperatures but this element causes a marked decrease in electrical conductivity (1% reduction for each 0.03% present). Work in Japan has shown that this effect may be partly offset by adding trace amounts of rare earth elements, such as yttrium, and ECs are available with a rating of 60% IACS which are capable of continuous operation at 150°C.

The compositions and properties of some newer conductor alloys are compared with those of the older EC materials in Table 4.14. Additions such as iron and nickel have been selected because they have a very low solubility in aluminium, they form stable compounds and they cause relatively small increases in resistivity when out of solution. The presence of magnesium in the alloy 8076 leads to improved creep resistance. The success of the new products has been reflected in their increased usage for electrical wire.

4.6.10 Electric storage batteries

Aluminium-air batteries As mentioned in Chapter 1, large amounts of electrical energy are required to reduce alumina to aluminium. Aluminium has therefore been regarded as an energy bank, providing this energy can be released by electrochemical conversion to aluminium hydroxide. A particularly attractive way

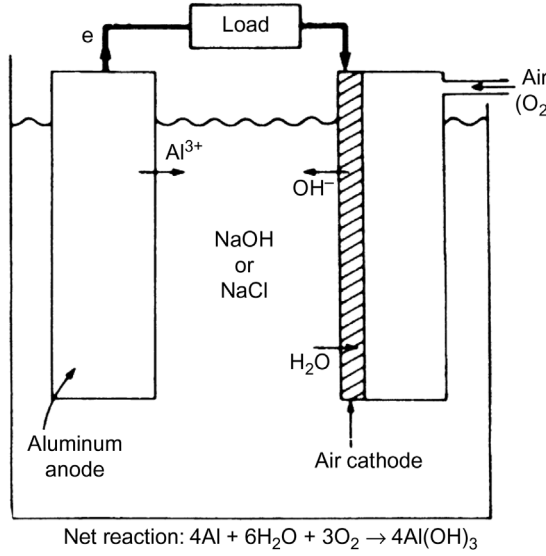


Figure 4.65 Concept of aluminium/air electric storage battery. From Fitzpatrick, N and Scamans, GM: *New Scientist*, 1517, 17 July, 1986.

of making this conversion is to couple an aluminium anode through an aqueous electrolyte to an air electrode which is supplied with an inexhaustible supply of the cathode reactant (oxygen) from air. In such an arrangement, the theoretical specific energy ($W\,h\,g^{-1}$) of aluminium is 8.1. Only lithium has a higher value but lithium anodes are more difficult to fabricate and use safely.

The concept of the aluminium/air battery is simple and is shown in Fig. 4.65. The electrolyte may be either a neutral chloride (e.g., NaCl) or an alkali (e.g., NaOH) and the net reaction is $4Al + 6H_2O + 3O_2 \rightarrow 4Al(OH)_3$. The battery is non-rechargeable electrically but mechanical refueling is also conceptually easy since it only involves the regular addition of water and removal of the solid reaction products, together with the occasional replacement of the aluminium anodes. Major reasons for delays in the commercial exploitation of the system have been the development of cheap and efficient electrodes together with a convenient system for separating and removing the reaction products. Another problem is minimizing the parasitic corrosion of the aluminium electrode when the battery is on open circuit. One possible solution could be to integrate the battery with a flowing electrolyte system which allows the electrolyte to be stored separately from the cell when it is not in use.

The fact that the aluminium anode is protected by an adherent, insulating oxide film has been a key barrier to overcome before controlled dissolution can occur in an electrolyte. Initially it was necessary to use relatively expensive super-purity aluminium (99.995%) to which was added small amounts

(e.g., 200 ppm) of the so-called activating elements such as tin, indium, or gallium. However, a cheaper Al–Sn–Mg anode exhibiting the desired characteristics has since been developed and it has become possible to use lower-purity aluminium. Experiments have revealed that, when an aluminium/air battery is operating, the current actually comes from very small areas on the surface of the anode. Modification of aluminium electrochemistry occurs when these activating elements are in solid solution, and dissolution at appropriate anode potentials results in the rejection and deposition of the more noble alloying element on to the anode surface. Once this has occurred, rapid surface diffusion and agglomeration of these atoms appears to take place under the aluminium oxide film. Localized defilming results allowing rapid dissolution of aluminium by galvanic action rather than by the much slower process of ionic transport through the oxide layer. If this so-called superactive state can be sustained, the anodes show high coulombic efficiencies over a wide range of current density (15 to $>1000\,\mathrm{mA\,cm^{-2}}$). What needs to be avoided is the "hyperactive" state in which current densities may reach $4\,\mathrm{A\,cm^{-2}}$ and undesirable copious amounts of hydrogen are evolved.

An Al–Sn–Mg anode exhibiting the desired characteristics was patented by Alcan in 1988 and development since then has concentrated on strategies that would allow the use of lower-purity aluminium. Essentially this has involved coping with iron impurities and up to 40 ppm can now be tolerated which has more than halved the cost of the aluminium.

The air cathodes have also presented significant manufacturing problems. One form consists of a current collector composed of a nickel wire mesh on to which is pressed a mixture of carbon and fluorocarbon resin. Oxygen from the air can diffuse into the carbon so that it comes into contact with the electrolyte. The coatings are formulated so that the electrolyte penetrates the cathode through the hydrophilic layer to the mesh, but cannot leak through the hydrophobic layer to the air. Catalysts are incorporated in the cathode to improve performance. It has also been necessary to develop a method for continuous production of the cathodes from low-cost materials. This has been achieved by rolling the various layers together as a laminate and cathodes 280 mm wide and only 0.5 mm thick have been produced in rolls up to 90 m in length.

Individual cells generate approximately 1.4 V and they are connected in series to give the desired power output. Efficiency is limited by the electrolyte mainly because the dissolved aluminium forms soluble complexes with either chloride or hydroxyl ions, thereby showing down precipitation of the aluminium hydroxide. Precipitation can be encouraged by additives and by seeding in a crystallizer through which the electrotype must be pumped in order to be regenerated.

Interest in the aluminium/air battery was first stimulated by its potential as a power unit for electric vehicles. Using an alkaline electrolyte, this battery was seen as a viable alternative to the internal combustion engine so far as acceleration, refueling time, and range were concerned. Specific energy yields of

amounting to $4\,W\,h\,g^{-1}$ were obtained and it has been demonstrated that such a battery is capable of providing the power needed to drive a conventional sized motor car about 300 km between stops for water to replenish the alkaline electrolyte, and 2000 km before the aluminium anode needs replacement. To date, however, the system has not proved to be competitive with engines powered by petroleum fuels. One more limited application has been the use of aluminium/air batteries as reliable and compact reserve units to back up d.c. electrical systems.

Aluminium-ion batteries The advent of commercial batteries based on the reactive, ultralight metal lithium in 1991 has led to their widespread use in consumer electronics, portable tools, medical equipment, small electric vehicles, and some aerospace applications. Lithium-ion batteries are also rechargeable, have a high energy density, and individual cells have a discharge voltage of 3.5–4 V which is convenient because they can readily substitute for lead-acid batteries. Because of these attractive features, they are a leading contender for powering future electric vehicles. Disadvantages are the high cost of lithium, the fact that this metal is a scarce and so far has only been found in a few remote locations worldwide. There are also concerns that lithium-ion batteries can be a fire hazard which has led to their withdrawal from civil aircraft operated by some airlines.

Aluminium-ion batteries do not share these particular problems. They also have the advantage that the metal is trivalent so that, when it is ionized, three electrons are liberated compared with one for lithium which potentially gives these batteries a higher charge capacity. However despite many years of research, the performance of aluminium-ion batteries has been disappointing because they have a discharge voltage less than half that for the lithium-ion batteries and their storage capacity is less. Furthermore cathodes, that were mostly made from solid graphite, have tended to disintegrate in service which has limited the battery's capacity for recharging to about 100 cycles. Recently in 2013 however, a research group at Stanford University in California has announced the development of a prototype aluminium-ion battery that appears to overcome some of these problems.

The key feature of this new battery is the use of a foamed graphite cathode together with the usual aluminium anode and an organic liquid electrolyte containing mobile $AlCl_4^-$ ions. During charging, these ions diffuse to the cathode where they are readily stored within the open graphite structure. On discharging, the ions will then be easily released so that they can readily migrate to the aluminium anode where they combine to form Al_2Cl_7. As a consequence, it has been found that the battery can be completely recharged safely in less than 60 s which is claimed to be nearly 100 times faster than the maximum charge rate for a lithium-ion battery. Furthermore it has also been demonstrated that the

new aluminium-ion battery can be recycled at least 7500 times with very little loss of its storage capacity whereas the lithium-ion battery is reported to have a durability of about 1000 cycles. Another feature is that the discharge voltage of the new battery has been increased to between 2 and 2.5 V depending on the state of charge. The charge storage capacity of the aluminium-ion battery is about $70\,A\,h\,kg^{-1}$ which is still only approximately half of the capacity of the lithium-ion battery. Nevertheless, it has been suggested that, with further development, this cheaper new battery may also be suitable for use in electric vehicles and for storing power within an electrical grid.

FURTHER READING

Lumley, RN, (Ed.): *Fundamentals of Aluminium Metallurgy: Production, Processing and Applications*, Woodhead Publishing Limited, Cambridge, UK, 2011.

Altenpohl, D: *Aluminium: Technology, Applications and Environment*, 6th ed., TMS, Warrendale, PA, USA, 1998.

Davis, JR et al. *ASM Specialty Handbook on Aluminium Alloys*, ASM International, Materials Park, OH, USA, 1993.

Hatch, JE, (Ed.): *Aluminium: Properties and Physical Metallurgy*, ASM, Cleveland, OH, USA, 1984.

Mondolfo, LF: *Aluminium Alloys: Structure and Properties*, Butterworths, London, 1976.

Van Horn, KR, Ed. *Aluminium*, Vols. 1–3, ASM, Cleveland, OH, USA, 1967.

Kim, NJ: Designing with aluminium alloys. In Totten, GE Xie, L, and Funatani, K, (Eds.): *Handbook of Mechanical Alloy Design*, Marcel Dekker Inc., New York, NY, USA, pp 441, 2004.

Greer, AL: Grain refinement of alloys by inoculation of melts, *Philos. Trans. R. Soc. Lond. A*, 361, 479, 2003.

Quested, TE: Understanding mechanisms of grain refinement of aluminium alloys by inoculation, *Mater. Sci. Technol.*, 20, 1357, 2004.

The Aluminium Association Inc., *International Alloy Designations and Chemical Composition Limits for Wrought Aluminium and Wrought Aluminium Alloys*, The Aluminium Association Inc., New York, NY, USA, 2004.

The Aluminium Association Inc., *Tempers for Aluminium Alloy Products*, The Aluminium Association Inc., New York, NY, USA, 2004.

Nie, JF, Morton, AJ and Muddle, BC (Eds.): *Proc. 9th Inter. Conf. on Aluminium Alloys*, Brisbane, Australia, Mater. Forum, Inst. of Mater. Eng. Australasia, 2004.

Gregson, PJ and Harris, SJ (Eds.): *Proc. 8th Inter. Conf. on Aluminium Alloys*, Cambridge, UK, Mater. Sci. Forum, Vols. 396–402, 2002.

Starke Jr, EA, Sanders Jr, TH and Cassada, WA (Eds.): *Proc. 7th Inter. Conf. on Aluminium Alloys*, Charlottesville, VA, USA, Mater. Sci. Forum, Vols. 331–337, 2000.

Sato, T Kumai, S, Kobayashi, T, and Murakami, Y, (Eds.): *Proc. 6th Inter. Conf. on Aluminium Alloys*, Japan Inst. of Light Metals, Toyohashi, Japan, 1998.

Driver, JH, Dubost, B, Durand, F, Fougeres, R, Guyot, P, Sainfort, P and Suery, M (Eds.): *Proc. 5th Inter. Conf. on Aluminium Alloys*, Grenoble, France, Mater. Sci. Forum, Vols. 217–222, 1996.

Prasad, NE, Gokhale, AA and Wanhill, RJH: *Aluminium–Lithium Alloys: Processing, Properties, Applications*, Butterworth-Heinemann, Oxford, UK, 2014.

Mishra, RS: Friction stir processing technologies, *Adv. Mater. Struct.*, 152, 2003.

Zhao, H, White, DR and DebRoy, T: Laser welding of automotive aluminium alloys, *Int. Mater. Rev.*, 44, 238, 1999.

Karlsson, A: Braze clad aluminium materials for automotive heat exchangers—some recent developments, *Inter. Conf. on Aluminium, INCAL '98*, New Delhi, India, 1998.

Staley, JT: History of wrought aluminium alloy development. In Vasudevan, AK and Doherty, RD, (Eds.): *Treatise on Materials Science and Technology, Vol. 31, Aluminium Alloys—Contemporary Research and Applications*, Academic Press, New York, NY, USA, pp 3, 1989.

Sanders, RE, Baumann, SF and Stumpf, HC: History of wrought aluminium alloy development. In Vasudevan, AK and Doherty, RD, (Eds.): *Treatise on Materials Science and Technology, Vol. 31, Aluminium Alloys—Contemporary Research and Applications*, Academic Press, New York, NY, USA, p. 65, 1989.

Starke, EA Jr, and Staley, JT: Application of modern aluminium alloys to aircraft, *Progr. Aerospace Sci.*, 32, 131, 1996.

Williams, JC and Starke, EA, Jr: Progress in structural materials for aerospace systems, *Acta Mater.*, 51, 5775, 2003.

Davies, G: *Materials for Automobile Bodies*, Elsevier, London, 2003.

Bottema, J and Miller, WS: Aluminium in transport replacing weight with intelligence, *Mater. Australasia*, 37(2), 15, 2004.

Bryant, AJ: Aluminium at sea, *Light Metal Age*, 59, 2001.

Hosford, WF and Duncan, JL: The aluminium beverage can, *Sci. Am.*, 271(3), 48, 1994.

Pratt, GC: Materials for plain bearings, *Int., Mater. Rev.*, 18, 62, 1973.

Grimes, R: Superplastic forming: evolution from metallurgical curiosity to major manufacturing tool, *Mater. Sci. Technol.*, 19, 3, 2003.

Egan, DR, Ponce de León, C, Wood, RJK, Jones, RL, Stokes, KR and Walsh, FC: Developments in electrode materials and electrolytes for aluminium-air batteries, *J. Power Sources*, 235, 293, 2013.

Lin, MC, Gong, M, Lu, B, Wu, Y, Wang, DY, Guan, M, Angell, M, Chen, C, Yang, J, Hwang, BJ and Dai, H: An ultrafast rechargeable aluminium-ion battery, *Nature*, 520, 324, 2015.

5

CAST ALUMINIUM ALLOYS

Aluminium is one of the most versatile of the common foundry metals and the ratio of cast to wrought aluminium alloy products is increasing primarily because of the larger amounts of castings being used for automotive applications. This ratio varies from country to country and in 2014 it was approximately 1:3 in North America. Of this about 50% by weight is cast from secondary alloys some of which is blended with primary alloy to control the iron content and other impurity elements. A wide range of cast aluminium alloys is available for commercial use and, for example, over 300 compositions were registered with the US Aluminium Association in 2015. The most widely used are those based on the Al–Si, Al–Si–Mg, and Al–Si–Cu systems.

Apart from light weight, the special advantages of aluminium alloys for castings are the relatively low melting temperatures, negligible solubility for all gases except hydrogen, and the good surface finish that is usually achieved with final products. Most alloys also display good fluidity and compositions can be selected with solidification ranges appropriate to particular applications. The major problem with aluminium castings is the relatively high shrinkage that occurs in most aluminium alloys during solidification. Allowance for this must be made in the design of molds in order to achieve dimensional accuracy in castings, and to avoid or minimize hot tearing, residual stresses, and shrinkage porosity. These problems are considered in Section 3.4.

As with wrought materials, there are cast alloys which respond to heat treatment and these are discussed later. It should be noted, however, that pressure diecastings are not normally solution treated because blistering may occur due to the expansion of air entrapped during the casting process. Moreover, there is the possibility of distortion as residual stresses are relieved. Recently, a modified heat-treatment process has been developed allowing pressure diecastings to be heat treated. The modified treatment involves the use of a short solution treatment at lower temperatures before conventional quenching and ageing steps. More than 100% increase in 0.2% proof stress has been achieved in some alloys. (More details are provided in Section 3.5.2.)

In all areas, except creep, castings normally have mechanical properties that are inferior to wrought products and these properties also tend to be much more

Light Alloys. DOI: http://dx.doi.org/10.1016/B978-0-08-099431-4.00005-1
Copyright © 2017 Ian Polmear, David StJohn, Jian-Feng Nie, Ma Qian.
Published by Elsevier Ltd. All rights reserved.

variable throughout a given component. As it is common practice to check tensile properties by casting separate test bars, it is necessary to bear in mind that the results so obtained should be taken only as a guide. The actual properties of even a simple casting may be 20–25% lower than the figures given by the test bar.

The demand for greater assurance in meeting a specified level of mechanical properties within actual castings has led to the concept of "premium quality" castings and represents a major advance in foundry technology. Specifications for such castings require that guaranteed minimum property levels are met in any part of the casting and match more closely those obtained in test bars. Mechanical properties previously thought unattainable have been achieved through strict control of factors such as melting and pouring practices, impurity levels, grain size, and, in the case of sand castings, the use of metal chills to increase solidification rates. Certain radiographic requirements may also need to be met. Moreover, castings are submitted in batches/lots and if one casting selected at random fails to meet specification requirements, all are rejected. Premium quality castings are more expensive to produce although they may be economic if wrought components can be replaced. Some of the improved procedures have been translated into more general foundry practices.

Because of their relatively low melting points which are below 660°C, and their ease of handling, aluminium and its alloys have been model materials for developing several novel casting processes. Examples are rheocasting and squeeze casting which both promote improved mechanical properties in products. These are discussed in Sections 3.5.3 and 3.5.4.

5.1 DESIGNATION, TEMPER, AND CHARACTERISTICS OF CAST ALUMINIUM ALLOYS

No internationally accepted system of nomenclature has so far been adopted for identifying aluminium casting alloys. However, the Aluminium Association of the United States introduced a revised system which has some similarity to that adopted for wrought alloys and this is described in the following section. Details are also given of the traditional British system.

5.1.1 US Aluminium Association System

This Association now uses a four-digit numerical system to identify aluminium and aluminium alloys in the form of castings and foundry ingot. The first digit indicates the alloy group in Table 5.1.

In the 1xx.x group, the second two digits indicate the minimum percentage of aluminium, e.g., 150.x indicates a composition containing a minimum of 99.50% aluminium. The last digit, which is to the right of the decimal point, indicates the product form with 0 and 1 being used to denote castings and ingot, respectively.

In the 2xx.x to 9xx.x alloy groups, the second two digits have no individual significance but serve as a number to identify the different aluminium alloys in

Table 5.1 Four-digit system for aluminium and its alloys

	Current designation	Former designation
Aluminium, 99.00% or greater	1xx.x	
Aluminium alloys grouped by major alloying elements:		
Copper	2xx.x	1xx
Silicon with added copper and/or magnesium	3xx.x	3xx
Silicon	4xx.x	1–99
Magnesium	5xx.x	2xx
Zinc	7xx.x	6xx
Tin	8xx.x	7xx
Other element	9xx.x	7xx
Unused series	6xx.x	

the group. The last digit, which is to the right of the decimal point, again indicates product form. A modification to the above grouping of alloys is used in Australia in which the 6xx.x series is allocated to Al–Si–Mg alloys. For example, 356 is AA601 and 357 is AA602.

When there is a modification to an original alloy, or to the normal impurity limits, a serial letter is included before the numerical designation. These letters are assigned in alphabetical sequence starting with A but omitting I, O, Q, and X, the X being reserved for experimental alloys. The temper designations for castings are the same as those used for wrought products (see Fig. 4.14). This does not apply for ingots.

5.1.2 British system

Most alloys are covered by the British Standard 1490 and compositions for ingots and castings are numbered in no special sequence and have the prefix LM. The condition of castings is indicated by the following suffixes:

M	As-cast
TB	Solution treated and naturally aged (formerly designated W)
TB7	Solution treated and stabilized
TE	Artificially aged after casting (formerly P)
TF	Solution treated and artificially aged (formerly WP)
TF7	Solution treated, artificially aged, and stabilized (formerly WP-special)
TS	Thermally stress relieved

The absence of a suffix indicates that the alloy is in ingot form.

There are also some aerospace alloys which are covered separately by the L series of British Standards and formerly by a system of DTD specifications that was discontinued in 1999. These specifications, which are not systematically

grouped or numbered, are concerned with specific compositions and often with particular applications. In both cases, the condition of the casting is not indicated by a suffix and is identified only by the number of the alloy.

The features of the different types of aluminium casting alloys are discussed in succeeding sections and are classified according to the major alloying element that is present, e.g., Al–Si and Al–Mg. Because of the problems of identification in different countries, individual alloys are represented by their basic compositions. It will be noted that castings in commercial-purity aluminium are not considered separately because their only major use is for certain electrical applications which were discussed in Chapter 4, Wrought aluminium alloys.

Although many different casting alloys are available, the number used in large quantities is much smaller. In Britain, for example, most cast aluminium alloy components are made from only four alloys designated LM2, LM4, LM6, and LM21. A representative list of alloy compositions is given in Table 5.2 together with the type of casting process for which they are used. Some mechanical properties and the relative ratings of the various casting characteristics are given in Table 5.3.

Selection of alloys for castings which are produced by the various casting processes depends primarily upon composition which, in turn, controls characteristics such as solidification range, fluidity, and susceptibility to hot cracking. Sand castings impose the least limitation on choice of alloy and commonly used alloys are 208 (Al–4Cu–3Si), 413 (Al–11.5Si), 213 (Al–7Cu–2Si–2.5Zn), and 356 (Al–7Si–0.3Mg). Alloys 332 (Al–9Si–3Cu–1Mg) and 319 (Al–6Si–4Cu) are favored for permanent mold castings, whereas 380 (Al–8.5Si–3.5Cu) and 413 (Al–11.5Si) are most commonly used for pressure diecastings. In the latter case, the prime consideration is a low melting point which increases production rates and minimizes die wear.

In order of decreasing castability, the groups of alloys can be classified in the order 3xx, 4xx, 5xx, 2xx, and 7xx. Corrosion resistance is also a function of composition and the copper-free alloys are generally regarded as having greater resistance than those containing copper. The 8xx series is confined to Al–Sn-bearing alloys which are discussed in Section 4.6.7.

5.2 ALLOYS BASED ON THE ALUMINIUM–SILICON SYSTEM

Alloys with silicon as the major alloying addition are the most important of the aluminium casting alloys mainly because of the high fluidity imparted by the presence of relatively large volumes of the Al–Si eutectic. Fluidity is also promoted because of the high heat of fusion of silicon (~1810 $kJ\,kg^{-1}$ compared with ~395 $kJ\,kg^{-1}$ for aluminium) which increases "fluid life" (i.e., the distance the molten alloy can flow in a mold before being too cold to flow further), particularly in hypereutectic compositions. Other advantages of castings based on the Al–Si system are high resistance to corrosion, good weldability, and the fact that the silicon phase reduces both shrinkage during solidification and the coefficient of thermal expansion of the cast products. However, machining may present difficulties because of the presence of hard silicon particles in

Table 5.2 Compositions of selected aluminium casting alloys

Association number	BS 1490 LM number	Casting process	Si	Fe	Cu	Mn	Mg	Cr	Ni	Zn	Ti	Other
150.1	LM 1	Ingot	a	a	0.10					0.05		99.5 Al min
201.0		S	0.10	0.15	4.0–5.2	0.20–0.50	0.15–0.55				0.15–0.35	Ag 0.40–1.0
208.0		S	2.5–3.5	1.2	3.5–4.5	0.50	0.10		0.35	1.0	0.25	
213.0		PM	1.0–3.0	1.2	6.0–8.0	0.6	0.10		0.35	2.5	0.25	
	LM 4	S and PM	4.0–6.0	0.8	2.0–4.0	0.20–0.6	0.15		0.30	0.50	0.20	
238.0		PM	3.5–4.5	1.5	9.0–11.0	0.6	0.15–3.5		1.0	1.5	0.25	
242.0	LM 14	S and PM	0.7	1.0	3.5–4.5	0.35	0.15–03.5	0.25	1.7–2.3	0.35	0.35	
295.0		S	0.7–1.5	1.0	4.0–5.0	0.35	0.03			0.35	0.25	
308.0		PM	5.0–6.0	1.0	4.0–5.0	0.50	0.10			1.0	0.25	
319.0	LM 21	S and PM	5.5–6.5	1.0	3.0–4.0	0.50	0.10		0.35	1.0	0.25	
328.0		S	7.5–8.5	1.0	1.0–2.0	0.20–0.6	0.20–0.6	0.35	0.25	1.5	0.25	
A332.0	LM 13	PM	11.0–13.0	1.2	0.50–1.5	0.35	0.7–1.3		2.0–3.0	0.35	0.25	
355.0	LM 16	S and PM	4.5–5.5	0.6[b]	1.0–1.5	0.50[b]	0.40–0.6	0.25		0.35	0.25	
356.0	LM 29	S and PM	6.5–7.5	0.6	0.25	0.35	0.20–0.40			0.35	0.25	
A356.0	LM 25	S and PM	6.5–7.5	0.20	0.20	0.10	0.20–0.40			0.10	0.20	
357.0		S and PM	6.5–7.5	0.15	0.05	0.03	0.45–0.60			0.05	0.20	Be 0.04–0.07
360.0	LM 9	D	9.0–10.0	2.0	0.6	0.35	0.40–0.6		0.50	0.50		
380.0	LM 24	D	7.5–9.5	2.0	3.0–4.0		0.50	0.10	0.50	3.0		
A380.0	LM 24	D	7.5–9.5	1.3	3.0–4.0	0.50	0.10		0.50	3.0		
390.0	LM 30	D	16.0–18.0	1.3	4.0–5.0	0.10	0.45–0.65			0.10	0.20	
	LM 6	S, PM and D	10.0–13.0	0.6	0.10	0.50	0.10		0.10	0.10	0.10	
413.0	LM 20	D	11.0–13.0	2.0	1.0	0.35	0.10		0.50		0.50	
	LM 2	D	9.0–11.5	1.0	0.7–2.5	0.50	0.30		0.50	2.0	0.20	
443.0	LM 18	S	4.5–6.5	0.8	0.6	0.50	0.05	0.25		0.50	0.25	
514.0	LM 5	S	0.35	0.50	0.15	0.35	3.5–4.5			0.15	0.25	
518.0		D	0.35	1.8	0.25	0.35	7.5–8.5		0.15	0.15		

(*Continued*)

Table 5.2 Compositions of selected aluminium casting alloys (Continued)

Association number	BS 1490 LM number	Casting process	Si	Fe	Cu	Mn	Mg	Cr	Ni	Zn	Ti	Other
520.0	LM 10	S	0.25	0.30	0.25	0.15	9.5–10.6			0.15	0.25	
535.0		S	0.15	0.15	0.05	0.1–0.25	6.2–7.5				0.10–0.35	
705.0		S and PM	0.20	0.8	0.20	0.40–0.6	1.4–1.8	0.2–0.4		2.7–3.3	0.25	
707.0		S and PM	0.20	0.6	0.20	0.40–0.6	1.4–1.8	0.2–0.4		4.0–4.5	0.25	
712.0		PM	0.15	0.50	0.25	0.10	0.50–0.65	0.4–0.6		5.0–6.5		
713.0		S and PM	0.25	1.18	0.40–1.0	0.6	0.20–0.50	0.35	0.15	7.0–8.0	0.25	
850.0		S and P	0.7	0.7	0.7–1.3	0.10	0.10		0.7–1.3		0.20	Sn 5.5–7.0

S, sand casting; PM permanent mold (gravity die) casting; D, pressure diecasting. *Notes*: Compositions are in % maximum by weight unless shown as a range.
[a]Ratio Fe:Si minimum of 2:1.
[b]If iron exceeds 0.45%, manganese content must be less than one-half the iron content.

Table 5.3 Mechanical properties and foundry characteristics of selected casting alloys

Aluminium Association number	BS 1490 LM number	Casting process	Temper	0.2% Proof stress (MPa)	Tensile strength (MPa)	Elongation (% in 50 mm)	Casting characteristics					
							Fluidity	Pressure tightness	Resistance to hot tearing	Corrosion resistance	Weldability	Machining
201.0		S[a]	T6	345	415	5.0	C	D	D	D	C	B
208.0		S	T533	105	185	1.5	B	B	B	D	B	C
213.0		PM	T533	185	220	0.5	B	C	C	E	C	B
	LM4	S	T21	95	175	3.0	B	B	B	C	C	B
		PM	T6	230	295	2.0						
242.0	LM14	PM	T6	230	295	1.0	C	C	D	D	D	B
295.0		PM	T61	195	260	4.0	C	D	D	D	C	B
319.0	LM21	S	T21	125	185	1.0	B	B	B	C	B	C
		PM	T21	125	200	2.0						
		S and PM	T61	240	260	0.5						
332.0	LM13	PM	T65	295	325	0.5	B	C	A	C	B	B
355.0	LM16	S	T4	125	210	3.0	B	B	B	C	B	B
		PM	T4	140	245	6.0						
		PM	T6	235	280	1.0						
356.0	LM25	S	T6	205	230	4.0	B	A	A	B	B	C
		PM	T6	225	240	6.0						
357.0		S	T6	275	345	3.0	B	A	A	B	B	C
		PM	T6	295	360	6.0						
360.0	LM9	S	T5	110	185	2.0	A	B	A	B	B	C
		S	T6	215	255	–						
		PM	T5	130	245	2.5						
		PM	T6	265	310	1.0						
	LM6	S	F1	65	185	8.0	A	B	A	A	B	C
		PM	F1	90	205	9.0						

(*Continued*)

Table 5.3 Mechanical properties and foundry characteristics of selected casting alloys (Continued)

Aluminium Association number	BS 1490 LM number	Casting process	Temper	0.2% Proof stress (MPa)	Tensile strength (MPa)	Elongation (% in 50 mm)	Casting characteristics					
							Fluidity	Pressure tightness	Resistance to hot tearing	Corrosion resistance	Weldability	Machining
		D	F1	130	250	2.5						
413.0	LM20	D	F1	140	265	2.0	A	A	A	B	A	C
443.0	LM18	S	F1	65	130	5.0	B	A	A	A	B	C
		PM	F1	70	160	6.0						
514.0	LM5	S	F1	80	170	5.0	C	D	C	A	C	B
		PM	F1	80	230	10.0						
518.0		D	F1	130	260	10.0	D	E	C	A	A	A
520.0	LM10	S	T1	175	320	15.0	D	E	B	A	E	B
535.0		S	F	145	275	13.0	D	E	C	A	A	A
705.0		S	T1	130	240	9.0	D	C	E	B	D	A
707.0		S	T1	185	255	3.0	D	C	E	B	D	A
713.0		S	T5	175	235	4.0	D	C	E	B	D	A

Tensile properties for all alloys generally represent "best practice" in casting procedures. Ratings for casting characteristics A through to E in decreasing order of merit.

Notes: S, sand casting; PM, permanent mold (gravity die) casting; D, pressure diecasting.

[a]Results for sand cast alloys obtained from separately cast test bars.

the microstructure. Commercial alloys are available with hypoeutectic and, less commonly, hypereutectic compositions.

The eutectic is formed between an aluminium solid solution containing just over 1% silicon and virtually pure silicon as the second phase. The eutectic composition has been a matter of debate but experiments with high purity binary alloys has shown it to be Al–12.6Si, with the transformation occurring at 577.6°C. Slow solidification of a pure Al–Si alloy produces a very coarse microstructure in which the eutectic comprises large plates or needles of silicon in a continuous aluminium matrix (Fig. 5.1A and B). The eutectic itself

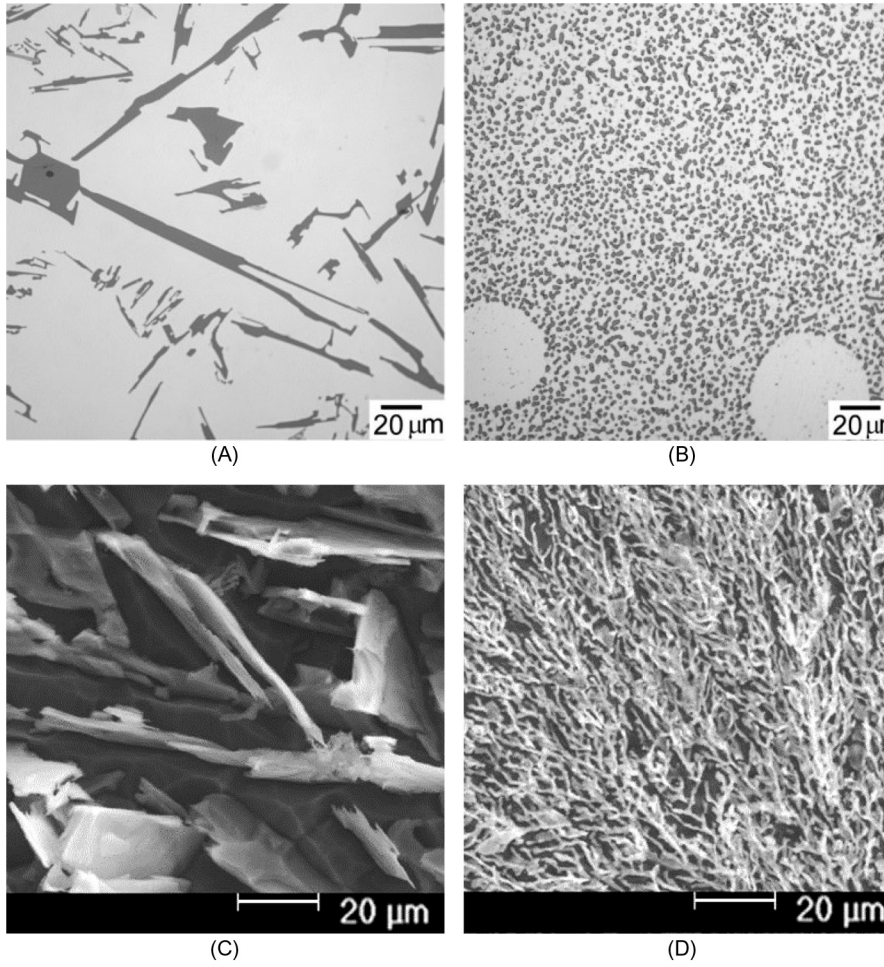


Figure 5.1 As-cast binary Al–10 wt% Si alloy in the following conditions (A) unmodified, (B) modified by 130 ppm strontium, (C) SEM image of unmodified silicon flakes, and (D) SEM image of 140 ppm Sr-modified fibrous silicon. (A) and (B) are from Dahle, AK *et al.*: *Mater. Sci. Eng. A*, 413, 243, 2005; (C) and (D) are from McDonald, SD *et al.*: *Metall. Mater. Trans. A*, 35A, 1829, 2004.

is composed of individual cells within which the silicon particles appear to be interconnected. Alloys having this coarse eutectic exhibit low ductility because of the brittle nature of the large silicon plates. Rapid cooling, as occurs during permanent mold casting, greatly refines the microstructure and the silicon phase assumes a fibrous form with the result that both ductility and tensile strength are much improved. The eutectic may also be refined by the process known as modification.

5.2.1 Modification

The widespread use of Al–Si alloys for other types of castings derives from the discovery by Pacz in 1920 that a refinement or modification of microstructure, similar to that achieved by rapid cooling, occurred when certain alkali fluorides were added to the melt prior to pouring (Fig. 5.1C).

As given in Table 5.4, mechanical properties may be substantially improved due to refinement of the microstructure and to a change to a planar interface during solidification which minimizes porosity in the casting. Fracture toughness is also significantly raised (Fig. 5.2).

For many years, modification of alloys based on the Al–Si system was achieved only by the addition of sodium salts or small quantities (0.005–0.015%) of metallic sodium to the melt although the actual amount of sodium needed may be as little as 0.001%. The mechanism by which the microstructure and, more particularly, the size and form of the silicon phase are modified has been the subject of much research. Controversy still remains although most theories involve possible effects of sodium on the nucleation and/or growth of eutectic silicon during solidification.

Sodium will depress the eutectic temperature by as much as 12°C and a finer fibrous silicon microstructure is produced. Depression of the eutectic temperature implies that sodium reduces the potency of nucleating sites for the eutectic phases, notably Si. Silicon is readily nucleated on the surface of AlP particles formed by reaction of aluminium with impurity amounts of phosphorus. Because of the crystallographic similarity between the two phases, AlP is a potent nucleant for silicon with recent research showing that nucleation

Table 5.4 Mechanical properties of Al–13 wt% Si alloy

Condition	Tensile strength (MPa)	Elongation (%)	Hardness (Rockwell B)
Normal sand cast	125	2	50
Modified sand cast	195	13	58
Normal chill cast	195	3.5	63
Modified chill cast	200	8	72

From Thall, BM and Chalmers, B: *J. Inst. Met.*, 77, 79, 1950.

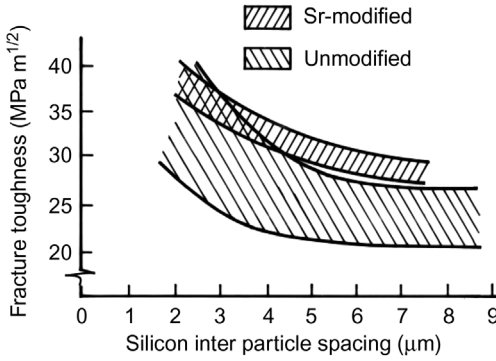


Figure 5.2 Fracture toughness of alloy 357 (Al–7Si–0.5Mg). Castings solidified over a range of cooling rates, with and without strontium modification. From Chadwick, GA: *Metals Mater.*, 2, 693, 1986.

occurs almost immediately the melt reaches the eutectic temperature. On the other hand, an excessive level of phosphorus can lead to the formation of a third, granular type of microstructure containing large particles of silicon which results in poor mechanical properties. Accordingly, a possible explanation for the behavior of sodium is that it neutralizes the effect of phosphorus, probably by the preferential formation of the compound NaP which coats the AlP particles that form before silicon forms at the eutectic temperature. In a similar way, the phenomenon known as over-modification, whereby coarse silicon particles may reappear when an excess of sodium is present, has been attributed to formation of another compound, AlNaSi, which once again provides sites for the easy nucleation of silicon.

Several theories have been proposed to account for the possible effect of sodium on the growth of silicon. For example, it has been suggested that sodium segregates at the periphery of growing silicon plates and prevents, or poisons, further growth. Another theory involves twinning of the silicon plates. Normally, crystal growth in diamond cubic systems, such as silicon, tends to be highly anisotropic, leading to the plate or flake form. If the plates are twinned, then the so-called twin plane reentrant angle mechanism of growth may operate in which the grooves between the planes act as preferred sites for the attachment of silicon atoms. Growth is then promoted in other crystallographic directions. Twin density is known to be much greater in modified alloys and this is thought to produce numerous alternative growth directions thereby leading to the desirable fibrous form of the silicon. What is uncertain is the mechanism by which sodium promotes twinning. One suggestion is that the greater undercooling known to occur in the modified alloys may induce significant stresses in the silicon plates due to the large (6:1) difference in the coefficients of thermal expansion between this phase and aluminium. Restricted growth theories do not, however, account for over-modification when coarsening of silicon occurs in the presence of an excess of sodium.

The use of sodium as the modifying agent does present founding problems because the fluidity of the melt is reduced, but the major difficulty is its rapid and uncertain loss through evaporation or oxidation. It is therefore necessary to add an excess amount and difficulties in controlling the content in the melt can lead to under- or over-modification of the final castings. For the same reason, the effects of modification are lost if Al–Si castings are remelted which prevents foundries being supplied with premodified ingots. Attention was therefore directed at alternative methods and modification today is carried out mostly by using additions of strontium. The amounts needed vary with the silicon content of the alloy and range from 0.015% to 0.02% for hypoeutectic permanent mold castings and slightly more for sand castings that solidify more slowly, or for alloys with higher silicon contents. Strontium is added as an Al–Sr or Al–Si–Sr master alloy which also refines the Al–Si eutectic and results in castings having tensile properties comparable with those obtained when using sodium. Loss of strontium through volatilization during melting is much less and the modified microstructure can be retained if alloys are remelted. Over-modification is also less of a problem with strontium because excess amounts are taken into compounds such as Al_3SrSi_3, Al_2SiSr_2, and Al_4Si_2Sr. Yet another advantage of strontium additions is that they suppress formation of primary silicon in hypereutectic compositions which may improve their ductility and toughness. This effect is not observed when sodium is used. Additions of antimony (e.g., 0.2%) also cause modification but result in a lamellar rather than a fibrous eutectic.

As for sodium, debate continues regarding the mechanism of modification by strontium. Recent studies indicate that modification is the result of a complex interaction between a number of factors. It has been shown that the growth rate of a eutectic grain's solid–liquid interface is an important factor related to cooling rate and the degree of undercooling necessary for the nucleation of silicon. A higher degree of undercooling, whether formed by suppression of silicon's nucleation temperature or a higher cooling rate, causes the eutectic grains to grow at a faster rate producing a modified fibrous silicon structure. As occurs with sodium, the addition of strontium poisons the AlP particles thus suppressing the nucleation temperature of silicon and therefore nucleation of a eutectic grain. Once silicon forms, the eutectic grain's interface will grow much faster than it would have if silicon were to be nucleated at the equilibrium eutectic temperature by AlP. Also, due to the large degree of suppression of the nucleation temperature, the number of grains nucleated is much smaller with large distances between them allowing the growth rate to remain high maintaining a modified structure. This is illustrated in Fig. 5.3A which shows an ingot of a strontium-modified Al–Si alloy where nucleation of the eutectic grains only occurs on the walls of the ingot. The lower nucleation rate is probably related to a much larger nucleation-free zone (see Section 3.3.1) preventing further nucleation in the vicinity of the initial nucleation event.

Supporting information comes from recent studies on the effect of ternary elements, in particular copper, on the eutectic microstructure. Copper is

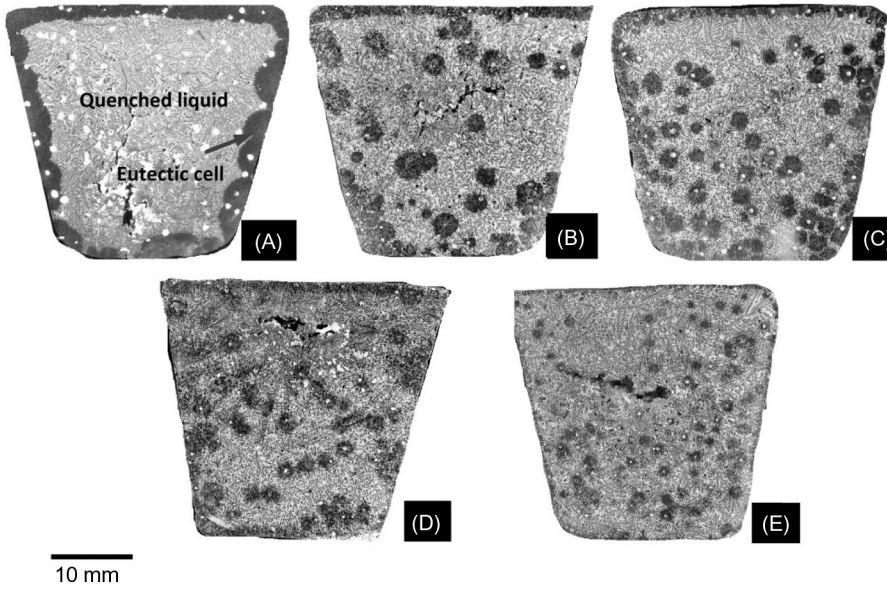


Figure 5.3 Macrographs of quenched Sr-modified samples: Al–10Si with (A) 0Cu, (B) 1Cu, (C) 2Cu, (D) 4Cu, and (E) 6Cu. The samples are cooled in air until partly solidified before quenching in water. The dark areas are the eutectic grains (A) that nucleate on the mold walls and grow into the melt. (B) to (E) are with 1–6% Cu showing the nucleation occurring in the bulk of the melt with the number of eutectic grains increasing with Cu addition. From Darlapudi, A *et al.*: *J. Alloys Compounds*, 646, 699, 2015.

rejected at the Al–Si interface into the liquid forming a concentration gradient resulting in constitutional undercooling. As shown in Fig. 5.3, the constitutional undercooling increases the nucleation rate of strontium-modified silicon and the more copper that is added the more nucleation events occur. Because the nucleation temperature is still low, the eutectic grains initially grow quickly with a modified structure. However, in this case, the copper solute eventually begins to accumulate between the growing grains reducing the amount of constitutional undercooling which in turn reduces the driving force for growth. It was found that, as the velocity of the eutectic grain–liquid interface decreases, the modified silicon becomes unmodified and adopts a flake-like morphology. Fig. 5.4 is a micrograph showing the modified to unmodified transition. Taken overall, modification of Al–Si alloys results in changes to both the processes of nucleation and growth of silicon in the eutectic.

One of the unfortunate effects of adding strontium is an increase in porosity as observed in Fig. 5.3, reducing the strength and ductility of the alloy. In cases where too much strontium modifier is added, this phenomenon can be observed with the naked eye and is sometimes referred

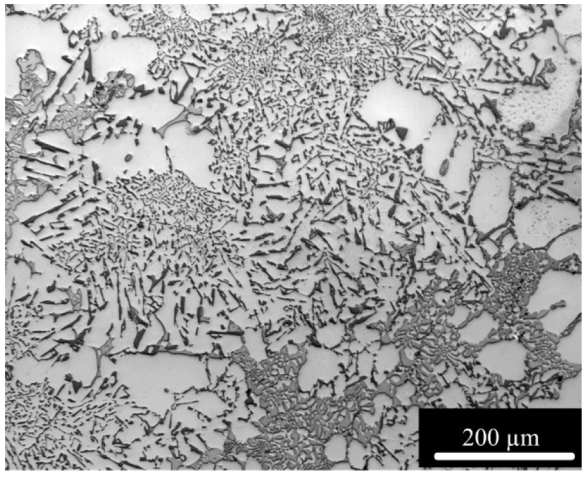


Figure 5.4 Micrograph of a strontium-modified Al–10Si–8Cu alloy showing the transition from fibrous to flake-like silicon during the growth of the eutectic phase. From Darlapudi, A *et al.*: *J. Crystal Growth*, 433, 67, 2016.

to by founders as salt and pepper porosity. This porosity is formed due to shrinkage of the liquid between the eutectic grains which are growing through a network of primary aluminium dendrites without access to sufficient feed liquid. This can be controlled by reducing the level of strontium addition and improving casting design.

5.2.2 Binary Al–Si alloys

Binary Al–Si alloys up to the eutectic composition retain good levels of ductility, providing the iron content is controlled to minimize the formation of large, brittle plates of the compound β-AlFeSi. In this regard, additions of manganese have been found to be beneficial because this element favors the formation of finer α-AlFeSi phase which has the so-called Chinese script morphology. An accepted rule in industry is that the Mn:Fe ratio needs to be at least 0.5:1 for β-AlFeSi to be suppressed, although the latter phase has been observed in alloys with Mn:Fe ratios as high as 1:1. However, such high levels of manganese can be a disadvantage since they may promote formation of greater volume fractions of intermetallic compounds than are present for the same levels of iron. This follows because α-AlFeSi contains a lower atomic percentage of iron so that it is possible for larger colonies of this phase to form than the β-AlFeSi it replaces. Thus, the preferred strategy is to keep the iron levels as low as possible in the first place.

If the silicon content is below 8%, modification is not necessary to achieve acceptable levels of ductility because the primary aluminium phase is present

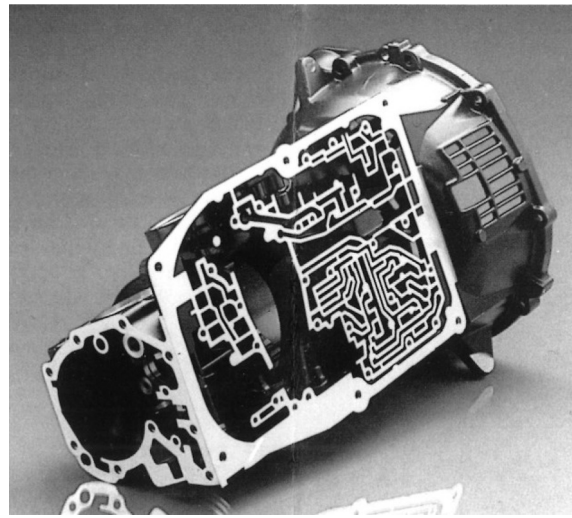


Figure 5.5 Thin-walled cast Al–Si alloy automotive transmission casing. Courtesy Vereinigte Aluminium-Werke, A. G. Bonn.

in relatively large amounts. The eutectic composition, which has a high degree of fluidity and low shrinkage on solidification, has particular application for thin-walled castings, e.g., Fig. 5.5. As a class, the alloys are used for sand and permanent mold castings for which strength is not a prime consideration, e.g., domestic cookware, pump casings, and certain automobile castings, including water-cooled manifolds.

When as-cast alloys containing substantial amounts of silicon are subjected to elevated temperatures, they suffer growth due to precipitation of silicon from solid solution. Dimensional stability can be achieved by heating for several hours in the temperature range 200–500°C prior to subsequent machining or use, and tempers of the T5 or T7 types should be given to castings which are to be used at temperatures of 150°C or above.

5.2.3 Al–Si–Mg alloys

Large quantities of sand and permanent mold castings are made from the Al–Si–Mg alloys 356 or LM25 (Al–7Si–0.3Mg) and 357 (Al–7Si–0.5Mg) in which the small additions of magnesium induce significant age hardening through precipitation of phases that form in the Al–Mg–Si system (Table 2.3). For example, the yield strengths of these alloys in the T6 condition are more than double that of the binary alloy containing the same amount of silicon. The alloys also respond well to secondary precipitation (Section 2.3.5). Moreover, they display excellent corrosion resistance. Both alloys are used for critical castings for aircraft such as the engine support pylon as shown in Fig. 5.6, and precision cast

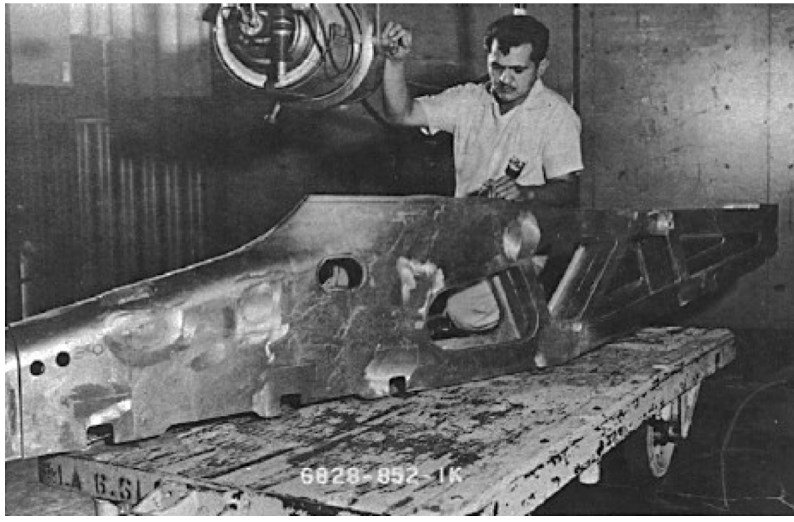


Figure 5.6 Pylon for a fighter aircraft prepared by premium casting techniques. Courtesy Defence Materials Information Center, Columbus, OH, USA.

wing flap tracks for models of the European Airbus series. Automotive components include cylinder heads and wheels.

The critical nature of some of these applications has required more attention to be paid to relationships between microstructure and fracture characteristics. Tensile fracture of Al–Si–Mg castings has been shown to initiate mainly by cracking of eutectic silicon particles as a result of stresses imposed during plastic deformation of the softer aluminium matrix. While solution treatment has the beneficial effect of fragmenting and spheroidizing the silicon particles in alloys that are well modified, it has little effect on the coarser particles in the unmodified condition. The higher magnesium content of alloy 357 increases the response to age hardening and results in higher tensile properties but there is the disadvantage in that relatively large particles of an intermetallic compound π ($Al_5Si_6Mg_8Fe_2$) may form (Fig. 5.7). These particles tend to crack preferentially when the alloy is strained which may reduce the ductility of 357 when compared with the lower magnesium alloy 356. The π phase also removes magnesium so that the yield stress is less than expected. Another result is that, as shown for alloy 357 in Table 4.7, secondary precipitation can be used to increase the tensile properties and fracture toughness of both cast and wrought Al–Si–Mg alloys.

Studies of fatigue properties of the alloy 356 have revealed that, unlike wrought aluminium alloys, the relationship between alternating stress and time to failure is essentially the same for the as-cast and heat-treated (age-hardened) conditions. This behavior is illustrated in Fig. 5.8 in which specimens machined from continuously cast billets were tested in the as-cast condition, and after

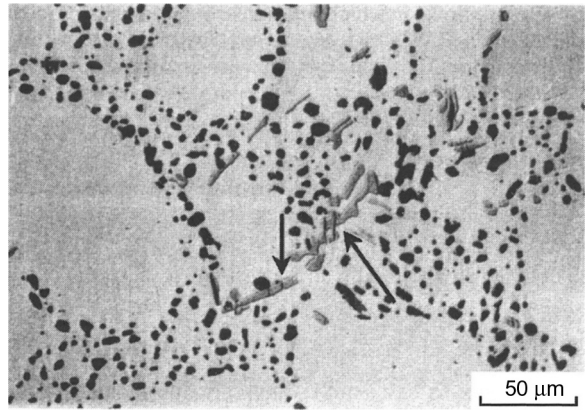


Figure 5.7 Microstructure of alloy 357 showing relatively large π phase particles together with smaller eutectic silicon particles. As shown by the arrows, the π phase particles have cracked preferentially when the cast alloy was deformed. Courtesy Q. G. Wang.

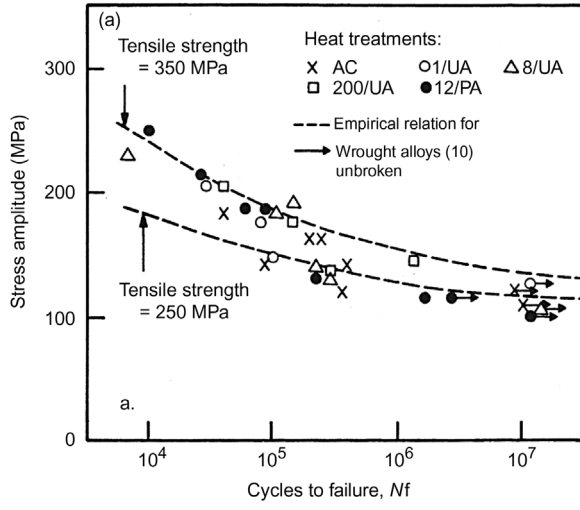


Figure 5.8 Fatigue lifetime (*S*/*N*) data for the casting alloy 356 ($R = -1$). AC = as-cast condition. 1/UA, 8/UA, 200/UA = alloys solution treated for 1, 8, or 200 h at 540°C, preaged 48 h at room temperature, and underaged 4 h at 155°C. 12/PA = alloy solution treated 8 h at room temperature and aged 6 h at 165°C (T6 temper). Wrought alloy curves shown as dotted lines. From Couper, M. J. *et al.*, *Fatigure Fract. Eng. Mater. Struct.*, **13**, 213, 1990.

solution treatment at 540°C for times ranging from 1 to 200 h to change the size of the eutectic silicon phase. These alloys were then quenched into water at 80°C, preaged at room temperature for 48 h, and either underaged 4 h at 155°C, or to peak strength after 6 h at 165°C. Tensile properties varied greatly

from 0.2% proof stress of 120 MPa and tensile strength of 250 MPa for the as-cast state, to a 0.2% proof stress of 250 MPa and tensile strength of 320 MPa when aged to peak strength. Nevertheless, the fatigue results all fell on the same curve. As shown in the figure, this contrasts with results for a wrought alloy for which an increase in tensile strength from 250 to 350 MPa was accompanied by improved fatigue performance.

The insensitivity of fatigue strength of cast alloys to heat treatment arises because fatigue cracks are always initiated at casting defects, notably shrinkage porosity and oxide films. Thus, the fatigue strength of castings tends to be defined by the maximum size of defects, whereas it is the volume fraction of defects that controls yield strength and ductility. Reducing the size of casting defects will increase fatigue life up to the stage that the initiation of cracks occurs normally in persistent slip bands at some surface (Section 2.5.3). This situation is considered to hold for all aluminium alloys cast under industrial conditions.

5.2.4 Al–Si–Cu alloys

The addition of copper to cast Al–Si alloys also promotes age hardening and increases strength. Copper also improves machinability but castability, ductility, and corrosion resistance are all decreased. Commercial Al–Si–Cu alloys have been available for many years and compromises have been reached between these various properties (Table 5.3). Compositions lie mostly within the ranges 3–10.5% silicon and 1.5–4.5% copper. The higher silicon alloys (e.g., Al–10Si–2Cu) are used for pressure diecastings, whereas alloys with lower silicon and higher copper (e.g., Al–3Si–4Cu) are used for sand and permanent mold castings. The strength and machinability of some of these castings is often improved by artificial ageing (T5 temper). In general, the Al–Si–Cu alloys are used for many of the applications listed for the binary alloys but where higher strength is needed. One example is the use of alloy 319 (Al–6Si–3.5Cu) for die cast (permanent mold) automotive engine blocks and cylinder heads in place of cast iron. As with the wrought alloys, some compositions contain minor additions of elements such as bismuth and lead which improve machining characteristics.

More complex compositions are available where special properties are required. One example is the piston alloys for internal combustion engines, e.g., 332 (Al–12Si–1Cu–1Mg–2Ni) in which nickel, in particular, improves elevated temperature properties by forming stable intermetallic compounds that cause dispersion hardening. Another example is the range of hypereutectic compositions such as 390 (Al–17Si–4Cu–0.55Mg) which have been used for sand and permanent mold castings of all-aluminium alloy automotive cylinder blocks. Here the main direction of the developmental programs has been the desire to eliminate using cast iron sleeves as cylinder liners which is the case in several production engines. Alloy 390 is also used for parts in automotive automatic

transmissions and for casting numerous small engines for lawn mowers and chain saws. BMW in Germany designed and manufactured a lightweight automobile engine until 2015 that has cylinders cast in alloy 390 that serve as a core around which the engine block is sand cast in a magnesium alloy (Fig. 5.9). Another advantage of 390 is its low coefficient of expansion reducing the likelihood of thermal fatigue failures.

In all these applications, it is necessary to incorporate, in the eutectic matrix, sufficient quantities of hard primary silicon particles to provide high wear resistance in the cylinders during service, and yet keep the dispersion low enough to avoid serious problems with machining. It is also necessary to ensure that the primary silicon is well refined. This can be achieved by adding a small amount of phosphorus to the melt which reacts with aluminium to form small, insoluble particles of AlP. As mentioned earlier, this compound has lattice spacings similar to those of silicon, and the particles serve as nuclei on which the primary particles can form (Fig. 5.10). The final microstructure is not unlike that of some modern metal matrix composites (e.g., Fig. 8.7). Phosphorus is available as Cu–P pellets, a proprietary Al–Cu–P compound, or phosphorus-bearing salts, and it is usual to aim for a retained level of between 0.002% and 0.004%. An excess should be avoided because the AlP particles tend to agglomerate and may become entrapped as undesirable inclusions in a casting if they are not removed by fluxing or filtering. Another characteristic of alloy 390 is its particularly high heat of fusion. Although this has the desirable effect of increasing fluidity during casting, cycle times for permanent mold and pressure diecastings are increased which reduces productivity. Tool life is also decreased as a consequence of the higher temperatures experienced.

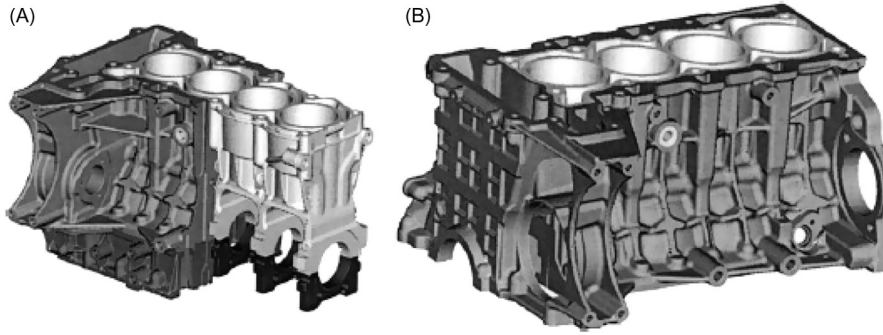


Figure 5.9 Lightweight BMW magnesium alloy automotive engine block containing cast aluminium alloy 390 cylinders. (A) Cutaway section and (B) engine block with cylinders in place. Courtesy J.-M. Ségaud, BMW Group.

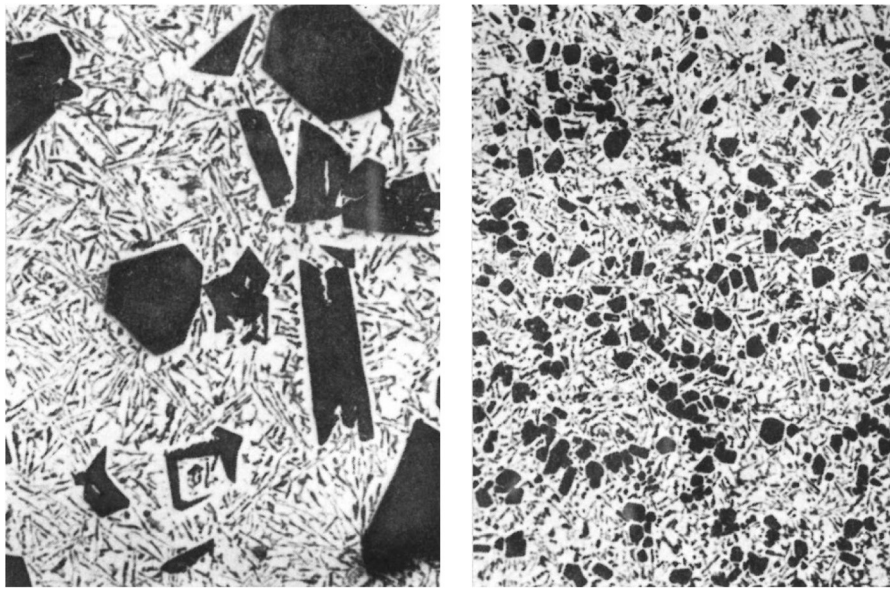


Figure 5.10 Effect of minor additions of phosphorus in refining the size of the primary silicon plates in the hypereutectic alloy 390: (A) no phosphorus and (B) small addition of phosphorus (× 100). From Jorstad, JL: *Met. Soc. AIME*, 242, 1219, 1968.

5.3 ALLOYS BASED ON THE ALUMINIUM–COPPER SYSTEM

Alloys with copper as the major alloying addition were the first to be widely used for aluminium castings although many have now been superseded. Most existing compositions contain additional alloying elements. As a group, these alloys may present casting problems, e.g., hot tearing, and it is also essential to design casting systems to provide generous feeding during solidification to ensure soundness in the final product. The alloys respond well to age-hardening heat treatments.

Several compositions are available which have elevated temperature properties that are superior to all other classes of aluminium casting alloys. Examples are 238 (Al–10Cu–3Si–0.3Mg), which is used for permanent mold casting of the soleplates of domestic hand irons, and 242 (Al–4Cu–2Ni–1.5Mg), which has been used for many years for diesel engine pistons and air-cooled cylinder heads for aircraft engines. Each alloy relies on a combination of precipitation hardening together with dispersion hardening by intermetallic compounds to provide stability of strength and hardness at temperatures up to around 250°C.

The highest strength casting alloy is 201 which has the nominal composition Al–4.7Cu–0.7Ag–0.3Mg (Table 5.2). A similar European alloy, known as Avoir, also contains 1.3%Zn. Although susceptible to hot tearing during casting, these alloys show a high response to age hardening due to precipitation of the finely dispersed Ω phase (Fig. 4.16) that is described in Section 4.4.1. Using premium

quality casting techniques, guaranteed properties of 345 MPa proof stress and 415 MPa tensile strength with a minimum elongation of 5% have been obtained from a variety of castings heat treated to the T6 temper, and values as high as 480 MPa proof stress and 550 MPa tensile strength with 10% elongation have been recorded. These tensile properties are much higher than can be obtained with any other aluminium casting alloys and compare well with the high-strength wrought alloys. The alloys may be susceptible to stress–corrosion cracking in the T6 condition but resistance is greatly improved by heat treating to a T73 temper. Because of the expense of adding silver, alloys 201 and Avoir are used only for military and other specialized applications.

5.4 ALUMINIUM–MAGNESIUM ALLOYS

This group contain several essentially binary alloys together with some more complex compositions based on Al–4Mg. Their special features are a high resistance to corrosion, good machinability, and attractive appearance when anodized. Most show little or no response to heat treatment.

Casting characteristics are again less favorable than for Al–Si alloys and more control must be exercised during melting and pouring because magnesium increases oxidation in the molten state. In this regard, special precautions are needed when sand casting as steam generated from moisture in the sand will react to produce MgO and hydrogen, which results in roughening and blackening of the surface of the casting. This mold reaction can be reduced by adding about 1.5% boric acid to the sand which forms a fused, glassy barrier to the steam produced within the mold. An alternative method is to add small amounts (0.03%) of beryllium to the alloy, which results in the formation of an impervious oxide film at the surface. Beryllium also reduces general oxidation during melting and casting although special care must be taken because of the potentially toxic nature of BeO. As a group, Al–Mg alloys also require special care with gating, and large risers and greater chilling are needed to produce sound castings.

The magnesium contents of the binary alloys range from 4% to 10%. Most are sand cast although compositions with 7% and 8% magnesium have limited application for permanent mold and pressure diecastings. Al–10Mg responds to heat treatment and a desirable combination of high strength, ductility, and impact resistance may be achieved in the T4 temper. The castings must be slowly quenched from the solution treatment temperature otherwise residual stresses may lead to stress–corrosion cracking. In addition, the alloy tends to be unstable, particularly in tropical conditions, leading to precipitation of Mg_5Al_8 (perhaps Mg_2Al_3) in grain boundaries which both lowers ductility and may cause stress–corrosion cracking after a period of time. Consequently, other alloys such as Al–Si–Mg tend to be preferred unless the higher strength and ductility of Al–10Mg are mandatory.

Casting characteristics are somewhat improved by ternary additions of zinc and silicon and alloys such as Al–4Mg–1.8Zn and Al–4Mg–1.8Si can be diecast for parts of simple design.

5.5 ALUMINIUM–ZINC–MAGNESIUM ALLOYS

Several binary Al–Zn alloys have been used in the past but all are now obsolete except for compositions which are used as sacrificial anodes to protect steel structures in contact with seawater. Engineering alloys currently in use contain both zinc and magnesium, together with minor additions of one or more of the elements copper, chromium, iron, and manganese.

The as-cast alloys respond to ageing at room temperature and harden over a period of weeks. In this condition, or when artificially aged or stabilized after casting, the proof stress values range from 115 to 260 MPa and the tensile strength range from 210 to 310 MPa, depending upon composition. Casting characteristics are relatively poor and the alloys are normally sand cast because the use of permanent molds tends to cause hot cracking.

One advantage of the alloys is that eutectic melting points are relatively high which makes them suitable for castings that are to be assembled by brazing. Other characteristics are good machinability, dimensional stability, and resistance to corrosion. The alloys are not recommended for use at elevated temperatures because overaging causes rapid softening.

FURTHER READING

Van Horn, K, Ed. *Aluminium*, Vols. 1–3, ASM, Cleveland, OH, USA, 1967.

Davis, JR and Associates, *ASM Specialty Handbook on Aluminium Alloys*, ASM International, Materials Park, OH, USA, 1993.

Hatch, JE: *Aluminium: Properties and Physical Metallurgy*, ASM International, Materials Park, OH, USA, 1984.

Wang, W, Makhlouf, M and Apelian, D: Aluminium die casting alloys: alloy composition, microstructure, and properties–performance relationships, *Int. Mater. Rev.*, 40, 221, 1995.

Lumley, R, (Ed.): *Fundamentals of Aluminium Metallurgy: Production, Processing and Applications*, Woodhead Publishing, Cambridge, UK, 262, 2011.

Sigworth, GK: *Best Practices in Aluminium Metalcasting*, American Foundry Society, 2014.

McDonald, SD, Dahle, A, Taylor, J and StJohn, D: Eutectic grains in unmodified and strontium-modified hypoeutectic aluminium–silicon alloys, *Metall. Mater. Trans. A*, 35A, 1829, 2004.

Mazahery, A and Shabani, MO: Modification mechanism and microstructural characteristics of eutectic Si in casting Al–Si alloys: a review on experimental and numerical studies, *JOM*, 66, 726, 2014.

Liang, S and Schmid-Fetzer, R: Nucleants of eutectic silicon in Al–Si hypoeutectic alloys: β-(Al, Fe, Si) or AlP phase, *Metall. Mater. Trans. A*, 45A, 5308, 2014.

Darlapudi, A, McDonald, SD, Terzi, S, Prasad, A, Felberbaum, M and StJohn, DH: The influence of ternary alloying elements on the Al–Si eutectic microstructure and the Si morphology, *J. Cryst. Growth*, 433, 67, 2016.

Ye, H: An overview of the development of Al–Si–alloy based material for engine applications, *J. Mater. Eng. Performance*, 12, 288, 2003.

Jorstad, JL: Hypereutectic Al–Si alloy parts manufacturing: practical processing techniques, Dahle, A (Ed.), *Proc. 1st Inter. Light Metals Technology Conf.*, 93, 2003.

6

MAGNESIUM ALLOYS

6.1 INTRODUCTION TO ALLOYING BEHAVIOR

Magnesium is readily available commercially with purities exceeding 99.8% but it is rarely used for engineering applications without being alloyed with other metals. Key features that dominate the physical metallurgy of the alloys are the hexagonal structure of magnesium and the fact that its atomic diameter (0.320 nm) is such that it enjoys favorable size factors with a diverse range of solute elements. Aluminium, zinc, cerium, silver, thorium, yttrium, and zirconium are examples of widely different elements that are present in commercial alloys.

Solubility data for binary magnesium alloys are given in Table 6.1 with the first section containing elements used in commercial compositions. Apart from magnesium and cadmium which form a continuous series of solid solutions, the magnesium-rich sections of the phase diagrams show peritectic or, more commonly, eutectic systems. A wide range of intermetallic compounds may form with the three most frequent types of structures being as follows:

1. AB. Simple cubic CsCl structure. Examples are MgTl, MgAg, CeMg, SnMg, and it will be seen that magnesium can be either the electropositive or the electronegative component.
2. AB_2. Laves phases with ratio $R_A/R_B = 1.23$ preferred. Three types exist, namely:
   $MgCu_2$ (fcc, stacking sequence abcabc)
   $MgZn_2$ (hex., stacking sequence abababab)
   $MgNi_2$ (hex., stacking sequence abacaba)
3. CaF_2. fcc. This group contains Group IV elements and examples are Mg_2Si and Mg_2Sn.

Magnesium's close-packed hexagonal structure has a *c*/*a* ratio of approximately 1.623. Its close-packed plane is (0001), and its close-packed directions are $<11\bar{2}0>$. The shortest lattice vectors are 1/3 $<11\bar{2}0>$. The perfect

Light Alloys. DOI: http://dx.doi.org/10.1016/B978-0-08-099431-4.00006-3
Copyright © 2017 Ian Polmear, David StJohn, Jian-Feng Nie, Ma Qian.
Published by Elsevier Ltd. All rights reserved.

Table 6.1 Solubility data for binary magnesium alloys

Element	at.%	wt%	System
Lithium	17.0	5.5	Eutectic
Aluminium	11.8	12.7	Eutectic
Calcium	0.82	1.35	Eutectic
Scandium	~15	~24.5	Peritectic
Titanium	0.1	0.2	Peritectic
Manganese	1.0	2.2	Peritectic
Zinc	2.4	6.2	Eutectic
Gallium	3.1	8.4	Eutectic
Strontium	0.03	0.11	Eutectic
Yttrium	3.75	12.5	Eutectic
Zirconium	1.0	3.8	Peritectic
Silver	3.8	15.0	Eutectic
Cadmium	100	100	Complete SS
Indium	19.4	53.2	Peritectic
Tin	3.35	14.5	Eutectic
Lanthanum	~0.04	~0.23	Eutectic
Cerium	0.1	0.5	Eutectic
Neodymium	~1	~3	Eutectic
Samarium	~1	~6.4	Eutectic
Gadolinium	4.53	23.49	Eutectic
Terbium	4.6	24.0	Eutectic
Thulium	6.3	31.8	Eutectic
Ytterbium	1.2	8.0	Eutectic
Gold	0.1	0.8	Eutectic
Thallium	15.4	60.5	Eutectic
Lead	7.75	41.9	Eutectic
Bismuth	1.1	8.9	Eutectic
Thorium	0.52	4.75	Eutectic

From Massalski, TB: *Binary Phase Diagrams*, 2nd Ed., Vols. 1–4, ASM International, Metals Park, OH, USA, 1990; Nayeb-Hashemi, AA and Clark, JB: *Phase Diagrams of Binary Magnesium Alloys*, ASM International, Metals Park, OH, USA, 1988.

dislocations are those with Burgers vectors in the basal plane, Burgers vectors perpendicular to the basal plane, or Burgers vectors that are the sum of these two types. Basal slip (Fig. 6.1) is the dominant deformation mode in magnesium and its alloys at room temperature or temperatures less than 200°C due to its lower critical resolved shear stress (CRSS). However, the basal slip provides only two independent slip systems, which are insufficient to allow individual magnesium grains to plastically deform to meet the shape changes imposed by their neighbors. Therefore, non-basal slip on prismatic or pyramidal planes may also occur at room temperature, but at much higher stresses or in orientations that favor the operation of such a deformation mode (Fig. 6.2). The CRSS of

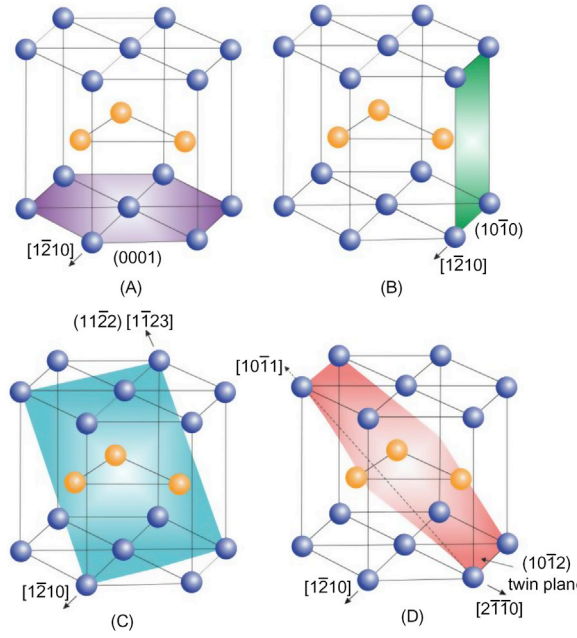


Figure 6.1 (A) Basal slip, (B) prismatic slip, (C) {11$\bar{2}$2} <11$\bar{2}$3> pyramidal slip, and (D) {10 $\bar{1}$2} twinning in Mg. Courtesy Z. R. Zeng.

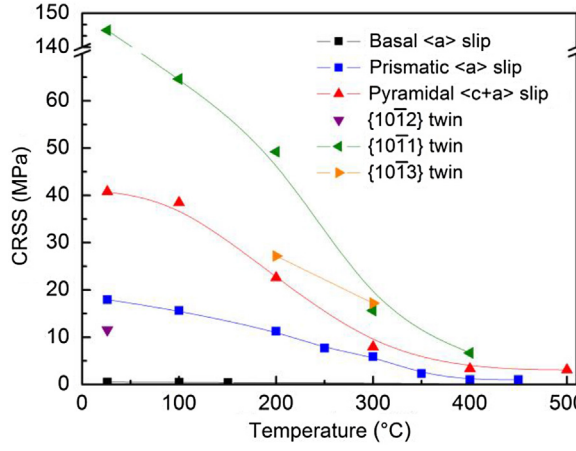


Figure 6.2 CRSS values for different slip and twinning modes and their variation with temperature.

these non-basal slip modes are about 50–100 times greater than that of basal slip at room temperature.

In addition to basal, prismatic and pyramidal slip, twinning also plays an important role in the plastic deformation of magnesium and its alloys. A deformation twin grows or shrinks under shear stress to generate a shape change and an orientation change. A variety of twinning modes have been reported for magnesium alloys, with twin planes on $\{10\bar{1}1\}$, $\{10\bar{1}2\}$, $\{10\bar{1}3\}$, $\{10\bar{1}4\}$, $\{10\bar{1}5\}$, $\{30\bar{3}4\}$, $\{11\bar{2}1\}$, and $\{11\bar{2}4\}$, the most commonly observed being the $\{10\bar{1}2\}$ twins. The formation and growth of the $\{10\bar{1}2\}$ twins lead to an extension along the *c*-axis (Fig. 6.1D), and hence they are often called extension twins. The $\{10\bar{1}1\}$ and $\{10\bar{1}3\}$ twins are observed less frequently in plastically deformed magnesium alloys. In contrast to the $\{10\bar{1}2\}$ twin, the latter two types of twins cause a contraction along the *c*-axis, and they are often described as contraction twins. The CRSS of these contraction twins are much higher than that of the extension twins. For polycrystalline magnesium alloys, the $\{10\bar{1}1\}$ contraction twins are much more frequently observed than $\{10\bar{1}3\}$ twins. Homogeneous nucleation of deformation twins inside a magnesium grain is extremely difficult. Instead, they often nucleate at grain boundaries and preexisting twin boundaries. Once nucleated, they can propagate readily within the grain, often extending from one side of the grain to the other side.

There are a number of factors affecting slip and twinning in magnesium alloys. These factors include temperature, grain size, grain orientation (texture), solute atoms, and second-phase particles. At room temperature, the CRSS value to activate basal slip in pure magnesium is significantly lower than those for prismatic and pyramidal slip (Fig. 6.2). The $\{10\bar{1}2\}$ twins are easier to activate than the $\{10\bar{1}1\}$ and $\{10\bar{1}3\}$ twins. The CRSS value is almost independent of temperature for basal slip but decreases significantly with temperature for other deformation modes. It is for this reason that magnesium and its alloys are thermomechanically processed at warm to high temperatures to maximize the number of deformation modes to facilitate the plastic deformation (Section 6.5). Alloying additions may alter the CRSS values for different slip and twinning modes, therefore influencing plastic deformation, and also change the recrystallization texture of thermomechanically processed magnesium alloys (Section 6.5).

General directions in the development of die cast, sand cast, and wrought magnesium alloys for specific requirements are summarized in Fig. 6.3. A special feature has been the successful introduction of several rare earth (RE) elements, notably cerium, neodymium, and yttrium into a number of commercial magnesium alloys. Most RE elements have high solid solubilities in magnesium because their atomic sizes are favorable, and they have electron negativities (e.g., Ce 1.21, Nd 1.19, and Y 1.20) similar to magnesium (1.20). These elements increase the strength of magnesium and its alloys, particularly at elevated temperatures.

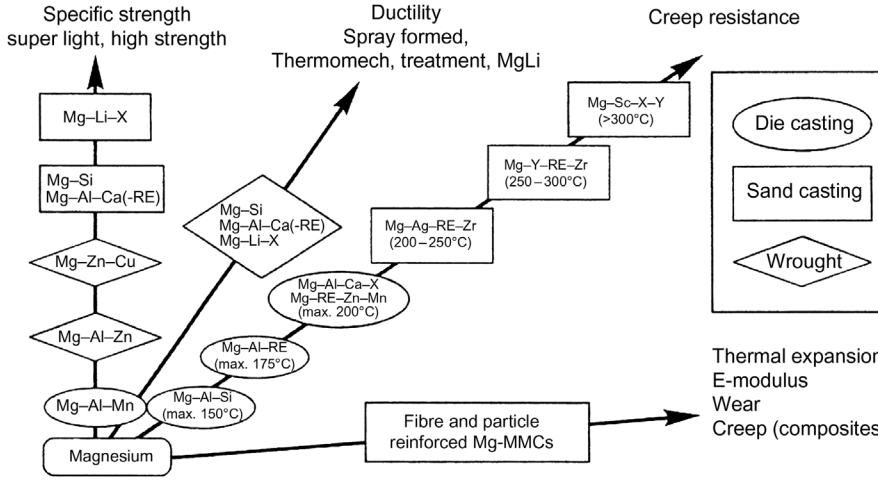


Figure 6.3 Directions in the development of magnesium alloys. From Mordike, BL and Ebert, T: *Mater. Sci. Eng. A*, 302, 37, 2001.

Cast magnesium alloys have always predominated over wrought alloys, particularly in Europe where, traditionally, they have comprised 85–90% of all products. The first alloying elements used commercially were aluminium, zinc, and manganese, and the Mg–Al–Zn system is still the one most widely used for castings. The first wrought alloy was Mg–1.5Mn that was produced as sheets, extrusions, and forgings, but this material has largely been superseded. General effects of alloying elements that may be present in commercial magnesium alloys are summarized in Table 6.2.

Early Mg–Al–Zn castings suffered severe corrosion in wet or moist conditions which was significantly reduced with the discovery, in 1925, that small additions (0.2 wt%) of manganese gave increased resistance. The role of this element was to remove iron and certain other heavy metal impurities into relatively harmless intermetallic compounds, some of which separate out during melting. In this regard, classic work by Hanawalt and colleagues has shown that the corrosion rate increases abruptly once the so-called tolerance limits are exceeded: these are 5, 170, and 1300 ppm for nickel, iron, and copper, respectively. An example of this behavior is illustrated in Fig. 6.4.

Another problem with early magnesium alloy castings was that grain size tended to be large and variable, which often resulted in poor mechanical properties, microporosity, and, in the case of wrought products, excessive anisotropy of properties. Values of proof stress also tended to be particularly low relative to tensile strength. In 1937, Sauerwald, in Germany, discovered that zirconium had an intense grain-refining effect on magnesium, although several years elapsed before a reliable method was developed to alloy this metal. Paradoxically, zirconium could not be used in most existing alloys because it

Table 6.2 General effects of elements used in magnesium alloys

Alloying element	Melting and casting behavior	Mechanical and technological properties	Corrosion behavior I/M produced
Ag		Improves elevated temperature tensile and creep properties in the presence of REs	Detrimental influence on corrosion behavior
Al	Improves castability, tendency to microporosity	Soli solution hardener, precipitation hardening at low temperatures (<120°C)	Minor influence
Be	Significantly reduces oxidation of melt surface at very low concentrations (<30 ppm), leads to coarse grains		
Ca	Effective grain-refining effect, slight suppression of oxidation of the molten metal	Improves creep properties, ideal for developing biomaterials	Detrimental influence on corrosion behavior
Cu	System with easily forming metallic glasses, improves castability		Detrimental influence on corrosion behavior, limitation necessary
Fe	Magnesium hardly reacts with mild steel crucibles		Detrimental influence on corrosion behavior, limitation necessary
Li	Increases evaporation and burning behavior, melting only in protected and sealed furnaces	Solid solution hardener at ambient temperatures, reduces density, enhances ductility	Decreases corrosion properties strongly, coating to protect from humidity is necessary
Mn	Control of Fe content by precipitating Fe–Mn compound, refinement of precipitates	Increases creep resistance	Improves corrosion behavior due to iron control effect
Ni	System with easily forming metallic glasses		Detrimental influence on corrosion behavior, limitation necessary
REs	Improves castability, reduces microporosity	Solid solution and precipitation hardening at ambient and elevated temperatures, improve elevated temperature tensile and creep properties	Improves corrosion behavior

Si	Decreases castability, forms stable silicide compounds with many other alloying elements, compatible with Al, Zn, and Ag, weak grain refiner		Detrimental influence
Sn	Increases ductility	Solid solution hardener, less effective in precipitation hardening	Detrimental influence on corrosion behavior
Sr	Increases castability, reduces microporosity	Improves creep resistance, ideal for developing biomaterials	Detrimental influence on corrosion behavior
Th	Suppresses microporosity	Improves elevated temperature tensile and creep properties, improves ductility, most efficient alloying element	
Y	Grain-refining effect, increases ignition temperature of molten metal	Improves elevated temperature tensile and creep properties	Improves corrosion behavior
Zn	Increases fluidity of the melt, weak grain refiner, tendency to microporosity	Precipitation hardening, improves strength at ambient temperatures tendency to brittleness and hot shortness unless Zr refined	Minor influence, sufficient Zn content compensates for the detrimental effect of Cu
Zr	Most effective grain refiner, incompatible with Si, Al, and Mn, removes Fe, Al, and Si from the melt	Improves ambient temperature tensile properties slightly	

Modified from Neite, G *et al.*: Magnesium-based alloys in materials science and technology: a comprehensive treatment. Cahn, RW, Haasen, P and Kramer, EJ (Eds.), Vol. 8, *Structure and Properties of Non-Ferrous Alloys*, VCH, Weinheim, Germany, p. 113, 1994.

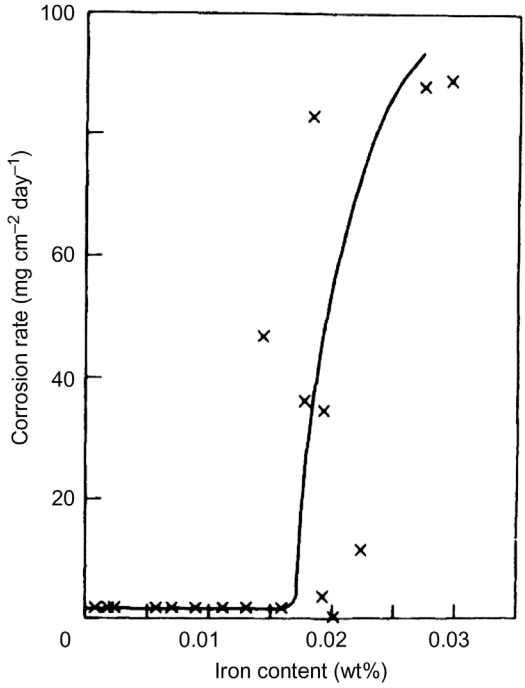


Figure 6.4 Effect of iron on corrosion of pure magnesium (alternate test in 3% NaCl). From Hanawalt, JD *et al.*: *Trans.AIME*, 147, 273, 1942.

was removed from solution due to the formation of stable compounds with aluminium and manganese. This led to the evolution of a completely new series of cast and wrought zirconium-containing alloys that were found to have much improved mechanical properties at both room and elevated temperatures. Compositions, tensile properties, and the general characteristics of various commercial cast and wrought magnesium alloys are given in Tables 6.3 and 6.4. These are considered here and divided into two groups depending on whether or not they contain the grain-refining element zirconium.

A second characteristic of alloy systems in which solubility is strongly influenced by atomic size factors is that solid solubility generally decreases with decreasing temperature. Such a feature is a necessary requirement for precipitation hardening and most magnesium alloys are amenable to this phenomenon although the responses are significantly less than is observed in some aluminium alloys. Precipitation processes are usually complex and are not completely understood, especially the early stage. Probable precipitation sequences in alloys of commercial interest are given in Table 6.5. A feature of the ageing process in several alloys is that the early stage involves the formation of solute clusters with short-range ordered structures such as that shown in Fig. 6.5. The oversized RE atoms tend to segregate into a single column along the

[0001] direction of the magnesium matrix, and to form a pair of such columns, to minimize the elastic strain associated with individual RE atoms. This pair of columns is the fundamental building block of all cluster types and GP zones observed experimentally in Mg–RE alloys. Such solute clusters have compact forms and rational orientations, and are quite different from the long-standing notion that solute clusters are cloud-like.

Another common feature of the ageing process in the Mg–RE alloys is that the peak-age stage involves the formation of a precipitate with a $D0_3$ (Mg_3RE) crystal structure that is coherent with the magnesium lattice. The precipitate forms as plates parallel to $\{10\bar{1}0\}$ planes of the magnesium matrix (Fig. 6.6A) and is very effective in impeding dislocation slip and twinning. It is significant to note that a substantial increase in precipitate plate aspect ratio will create an essentially continuous network of precipitates (Fig. 6.6B) that may give rise to substantially higher strengths. The strengthening effects of the prismatic precipitate plates in magnesium alloys are similar to those described for aluminium alloys (Section 2.2.5).

Various solute species cause solid solution strengthening of magnesium by increasing the CRSS for slip along the basal planes. Special attention has been given to Mg–Al and Mg–Zn alloys and, as shown in Fig. 6.7, zinc is approximately three times more effective, on an atomic per cent basis, than aluminium in increasing the yield strength for alloys that are in the solution treated and quenched condition. After correcting for effects arising from changes in grain size for different compositions, the yield strength of Mg–Al alloys has been found to increase linearly with c^n, where c is the atom concentration and n = 1/2–2/3. Solid solution strengthening is also significant in the aged alloys and, for Mg–Al alloys aged to peak strength, it has been shown that about half the aluminium atoms available for precipitation still remain in solid solution.

6.2 ALLOY DESIGNATIONS AND TEMPERS

No international code for designating magnesium alloys exists although there has been a trend toward adopting the method used by the American Society for Testing Materials. In this system, the first two letters indicate the principal alloying elements according to the following code: A—aluminium; B—bismuth; C—copper; D—cadmium; E—rare earths; F—iron; G—magnesium; H—thorium; J—strontium; K—zirconium; L—lithium; M—manganese; N—nickel; P—lead; Q—silver; R—chromium; S—silicon; T—tin; W—yttrium; X—calcium; Y—antimony; Z—zinc; V—gadolinium. The letter corresponding to the element present in greater quantity in the alloy is used first, and if they are equal in quantity the letters are listed alphabetically. The two (or one) letters are followed by numbers which represent the nominal compositions of these principal alloying elements in weight %, rounded off to the nearest whole number, e.g., AZ91 indicates the alloy Mg–9Al–1Zn the actual composition ranges being 8.3–9.7Al and 0.4–1.0Zn. A limitation is that information concerning other intentionally added elements is not given, and the

Table 6.3 Nominal composition, typical tensile properties, and characteristics of selected magnesium casting alloys

ASTM Designation	Nominal composition								Condition	Tensile properties			Characteristics
	Al	Zn	Mn	Si	Ca	Sr	RE (MM)	Sn		0.2% Proof stress (MPa)	Tensile strength (MPa)	Elongation (%)	
AZ63	6	3	0.3						As-sand cast	75	180	4	Good room-temperature strength and ductility
										110	230	3	
AZ81	8	0.5	0.3						As-sand cast	80	140	3	Tough, leaktight castings
									T4	80	220	5	With 0.0015 Be, used for pressure die casting
AZ91	9.5	0.5	0.3						As-sand cast	95	135	2	General-purpose alloy used for sand and die castings
									T4	80	230	4	
									T6	120	200	3	
									As-chill cast	100	170	2	
									T4	80	215	5	
									T6	120	215	2	
AM50	5		0.3						As-die cast	125	200	7[a]	High-pressure die castings
AM20	2		0.5						As-die cast	105	135	10[a]	Good ductility and impact strength
AS41	4		0.3	1					As-die cast	135	225	4.5[a]	Good creep properties to 150°C
AS21	2		0.4	1					As-die cast	110	170	4[a]	Good creep properties to 150°C
AE42	4		0.3				2		As-die cast	122	238	12	Good creep properties to 150°C
AE44	4		0.3				4		As-die cast	130	252	13	Good creep properties to 150°C
AJ52	5		0.3			2			As-die cast	126	231	9	Good creep properties to 150°C
AXJ530	5		0.3		3	0.2			As-die cast	188	242	4	Good creep properties to 150°C
AXJ810	8		0.3		1.1	0.3			As-die cast	162	240	7	Good creep properties to 150°C
AXJT7201	6.5		0.3		2	0.4		1	As-die cast	180	221	4	Good creep properties to 150°C
EZ41		0.5					3.7		As-die cast	175	186	4	Good creep properties to 150°C

ZK51	4.5			0.7					T5	140	235	5	Sand castings, good room-temperature strength and ductility
ZK61	6			0.7					T5	175	275	5	As for ZK51
ZE41	4.2			0.7	1.3				T5	135	180	2	Sand castings, good room-temperature strength, improved castability
ZC63	6	0.5	3						T6	145	240	5	Pressure-tight castings, good elevated temperature strength, weldable
EZ33	2.7			0.7	3.2				Sand cast T5	95	140	3	Good castability, pressure-tight weldable, creep resistant to 250°C
									Chill cast T5	100	155	3	
QE22				0.7		2.5		2.5	Sand or chill cast T6	185	240	2	Pressure tight, weldable, high proof stress to 250°C
WE54				0.5		3.25[b]		5.1	T6	200	285	4[a]	High strength at room and elevated temperatures, good corrosion resistance
WE43				0.5		3.25[b]		4	T6	190	250	7[a]	Weldable
EZ31	0.5			0.7	1	1.7			T6	130	206	3	Sand castings, good creep resistance
	0.3			0.5		2.8	1.4		T6	170	280	5	Sand castings, good creep resistance

AXJ810 (MRI153M); AXJ7201 (MRI230D); EZ41 (AM-SC1); EV31 (Elektron 21).

[a]Values quoted for tensile properties are for separately cast test bars and may not be realized in certain parts of casting.

[b]Contains some heavy metal rare earth elements; RE, rare earth element; MM, misch-mental.

Table 6.4 Nominal composition, typical tensile properties, and characteristics of selected wrought magnesium alloys

ASTM designation	Nominal composition							Condition	Tensile properties			Characteristics
	Al	Zn	Mn	Zr	Ce	Cu	Li		0.2% Proof stress (MPa)	Tensile strength (MPa)	Elongation (%)	
AZ31	3	1	0.3 (0.20 min)					Sheet, plate O	120	240	11	Medium-strength alloy, weldable, good formability
								H24	160	250	6	
								Extrusions F	130	230	4	
AZ61	6.5	1	0.3 (0.15 min)					Extrusions F	180	260	7	High-strength alloy, weldable
								Forgings F	160	275	7	
AZ80	8.5	0.5	0.2 (0.12 min)					Forgings T6	200	290	6	High-strength alloy
AM30	3		0.4					Extrusions F	146	246	28	Medium-strength alloy
ZM21		2	1					Sheet, plate O	120	240	11	Medium-strength alloy good formability good damping capacity
								H24	165	250	6	
								Extrustions	155	235	8	
								Forgings	125	200	9	
ZK30		3		0.6				Forgings T6	215	300	9	High-strength alloys, weldable
								Extrusions T6	240	290	14	
ZK60		6		0.6				Forgings T6	235	315	8	Good formability
								C	280	320	12	
ZEK 100		1.4		0.1	0.1			Sheet O	203	234	24	Good formability
ZMC711		6.5	0.75			1.25		Extrusions T6	300	325	3	High-strength alloy
LA141	1.2		0.15 min				14	Sheet, plate T7	95	115	10	Ultra-lightweight (specific gravity 1.35)

M1	1.5					Sheet, plate F	70	200	4	Low- to medium-strength alloy, weldable, corrosion resistant
						Extrusions F	130	230	4	
						Forgings F	105	200	4	
ME10	1		0.4			Extrusions F	184	259	25	
ME20	2		0.5			Sheet	163	241	18	
ME21	2		0.7			Extrusions	210	240	20	
						Extruded sheet	230	270	13	
WE43		0.5			3	4	Extrusions T6	160	260	6	High temperature
WE54		0.5			3.5	5.25	Forgings T6	180	280	6	Creep resistance
WV67		0.5		7		6	Extrusions T5	310	410	9	High-strength alloy for elevated temperature applications

ME10 (AM-EX1); (Elektron 21); WV67 (Elektron 675).

Table 6.5 Probable precipitation processes in magnesium alloys

Mg–Al	SSSS →	β ($Mg_{17}Al_{12}$) bcc ($1\bar{4}3m$, $a = 1.06$ nm); $(0001)_\alpha$ plate/lath				
Mg–Al–Ca	SSSS →	ordered GP zones hcp $a = 0.556$ nm Monolayer $(0001)_\alpha$ disc	→ C15 (Al_2)Ca fcc, $Fd\bar{3}m$ $a = 0.802$ nm $(0001)_\alpha$ plate			
Mg–Zn	SSSS →	GP zones	→ β_1' (Mg_4Zn_7) Monoclinic, B/2m $a = 2.60$ nm $b = 1.43$ nm $c = 0.52$ nm $\gamma = 102.5°$ $[0001]_\alpha$ rod	→ β_2' ($MgZn_2$) hcp, $P6_3/mmc$ $a = 0.52$ nm $c = 0.86$ nm $(0001)_\alpha$ plate	→ β (MgZn) Monoclinic $a = 1.61$ nm $b = 2.58$ nm $c = 0.88$ nm $\beta = 112.4°$	
Mg–Zn–Al[a]	SSSS →	GP zones	→ *i* Icosahedral or approximant Diamond shape	→ Φ and /or T Φ: orthorhombic, Pbcn $a = 0.90$ nm $b = 1.70$ nm $c = 1.97$ nm $(0001)_\alpha$ lath	T: bcc, $Im\bar{3}$ $a = 1.40$ nm	
Mg–Nd	SSSS →	Ordered clusters and GP zones	→ β′ (Mg_7Nd) Orthorhombic $a = 0.64$ nm $b = 1.14$ nm $c = 0.52$ nm Lenticular shape	→ β_1 (Mg_3Nd) fcc, $Fm\bar{3}m$ $a = 0.74$ nm $\{10\bar{1}0\}_\alpha$ plate	→ β ($Mg_{12}Nd$) Tetragonal, I4/mmm $a = 1.03$ nm $c = 0.59$ nm $[0001]_\alpha$ rod	→ β_c ($Mg_{41}Nd_5$) Tetragonal, I4/m $a = 1.47$ nm $c = 1.04$ nm

Mg–Nd–Zn	SSSS →	Ordered GP zones hcp $a = 0.556$ nm Monolayer $(0001)_\alpha$ disc	→ γ' ($Mg_5(Nd,Zn)$) hcp, $P\bar{6}2m$ $a = 0.55$ nm $c = 0.52$ nm $(0001)_\alpha$ plate	→ γ (possibly $Mg_3(Nd,Zn)$) fcc $a = 0.70$ nm Plate on irrational plane	
Mg–Gd(–Y)	SSSS →	Ordered clusters and GP zones	→ β' (Mg_7Gd) Orthorhombic $a = 0.65$ nm $b = 2.27$ nm $c = 0.52$ nm Lenticular shape	→ β_1 (Mg_3Gd) fcc, $Fm\bar{3}m$ $a = 0.73$ nm $\{10\bar{1}0\}_\alpha$ plate	→ β (Mg_5Gd) fcc, $Fm\bar{3}m$ $a = 2.23$ nm $\{10\bar{1}0\}_\alpha$ plate
Mg–Y	SSSS →	ordered clusters and GP zones	→ β' (Mg_7Y) Orthorhombic $a = 0.65$ nm $b = 2.27$ nm $c = 0.52$ nm Globular shape	→ β ($Mg_{24}Y_5$) bcc, $I\bar{4}3m$ $a = 1.13$ nm $\{10\bar{1}0\}_\alpha$ or $\{31\bar{4}0\}_\alpha$ plate	
Mg–Y–Nd	SSSS →	Ordered clusters and GP zones	→ β' ($Mg_{12}YNd$) Orthorhombic $a = 0.64$ nm $b = 2.24$ nm $c = 0.52$ nm Globular shape	→ β_1 ($Mg_3(Nd, Y)$) fcc, $Fm\bar{3}m$ $a = 0.74$ nm $\{10\bar{1}0\}_\alpha$ plate	→ β ($Mg_{14}Nd_2Y$) fcc, $Fm\bar{3}m$ $a = 2.20$ nm $\{10\bar{1}0\}_\alpha$ plate
Mg–Gd–Zn[b]	SSSS →	γ'' ($Mg_{70}Gd_{15}Zn_{15}$) Ordered hcp, $P\bar{6}2m$ $a = 0.56$ nm $c = 0.44$ nm $(0001)_\alpha$ plate	→ γ' (MgGdZn) hcp, $P\bar{3}ml$ $a = 0.32$ nm $b = 0.78$ nm $(0001)_\alpha$ plate	→ γ ($Mg_{35}Gd_4Zn_3$) Ordered hcp, 14H $a = 1.11$ nm $c = 3.65$ nm $(0001)_\alpha$ plate	

(*Continued*)

Table 6.5 Probable precipitation processes in magnesium alloys (Continued)

Mg–Y–Zn	SSSS →	I_2 stacking fault $(0001)_\alpha$ plate →	γ′ ($MgYZn$) hcp, $P\bar{3}ml$ $a = 0.32\,nm$ $c = 0.78\,nm$ $(0001)_\alpha$ plate →	γ ($Mg_{35}Y_4Zn_3$) Ordered hcp, 14H $a = 1.11\,nm$ $c = 3.65\,nm$ $(0001)_\alpha$ plate		
Mg–Y–Ag–Zn	SSSS →	GP zones Monolayer $(0001)_\alpha$ disc →	γ″ Ordered hcp, $P\bar{6}2m$ $a = 0.56\,nm$ $c = 0.78\,nm$ $(0001)_\alpha$ plate →	γ′ hcp, $P\bar{3}ml$ $a = 0.32\,nm$ $c = 0.78\,nm$ $(0001)_\alpha$ plate →	γ + δ γ: ordered hcp, 14H $a = 1.11\,nm$ $c = 3.65\,nm$ $(0001)_\alpha$ plate	δ: fcc, $Fd\bar{3}m$ $a = 1.59\,nm$

fcc, face-centered cubic.

[a]Precipitation process is not well studied.

[b]Low Gd:Zn weight ratio and low Gd content.

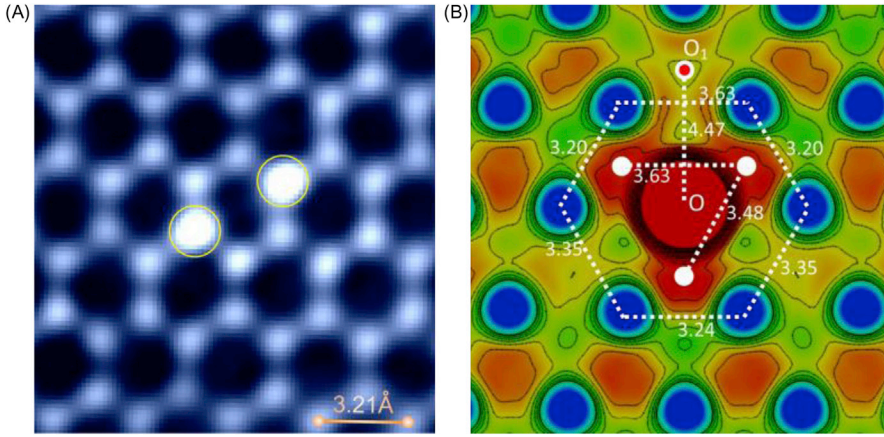


Figure 6.5 (A) Z-contrast scanning transmission electron micrograph showing a solute cluster in an aged Mg–Nd alloy. (B) Valence electron charge density plot of a basal plane passing through a single substituted Nd atom (position O) in the magnesium lattice. From Nie, JF *et al.*: *Acta Mater.*, 106, 260, 2016.

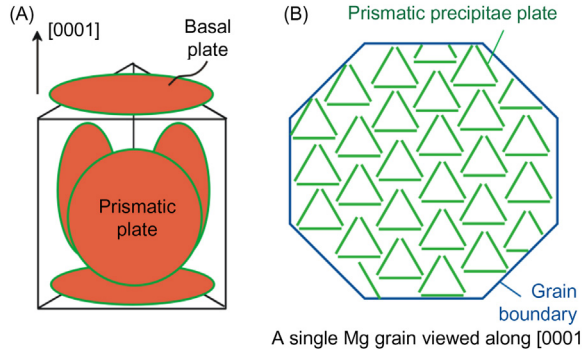


Figure 6.6 Near-continuous network of prismatic and basal precipitate plates in (A) can divide a single magnesium grain into many near-isolated blocks in (B). From Nie, JF: *Metall. Mater. Trans. A*, 43, 260, 2012.

system may need to be modified on this account. Suffix letters A, B, C, etc. refer to variations in composition within the specified range. This system will be used when discussing alloys in this book.

The heat-treated or work-hardened conditions, i.e., tempers, of alloys are specified in the same way that has been described for aluminium alloys in Section 4.2. Commonly used tempers are T5 (alloys artificially aged after casting), T6 (alloys solution treated, quenched, and artificially aged), or T7 (alloys solution treated and stabilized).

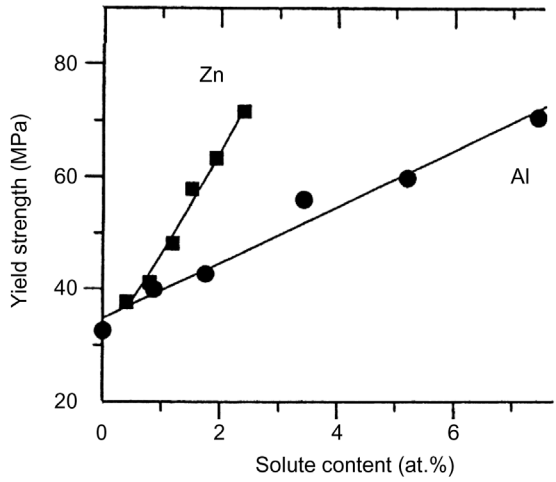


Figure 6.7 Solid solution strengthening of binary Mg–Al and Mg–Zn alloys. From Abbott, TB *et al.*: *Handbook of Mechanical Design*, Totten, GE *et al.* (Eds.), Marcel Dekker Inc., New York, NY, USA, 487, 2004.

6.3 ZIRCONIUM-FREE CASTING ALLOYS

6.3.1 Alloys based on the magnesium–aluminium system

The Mg–Al system has been the basis of the most widely used magnesium casting alloys since these materials were introduced in Germany during the First World War. Most alloys contain 8–9% aluminium with small amounts of zinc, which gives some increase in tensile properties, and manganese, e.g., 0.3%, which improves corrosion resistance (Section 6.1). The presence of aluminium requires that the alloys be grain refined by superheating or inoculation. A section of the Mg–Al phase diagram together with a summary of the effects of composition and heat treatment on tensile properties of an alloy similar to AZ80A is shown in Fig. 6.8, and other property data are included in Table 6.3.

In the as-cast condition, the β phase $Mg_{17}Al_{12}$ appears in alloys containing more than 2% aluminium. A network of β forms around grain boundaries as the aluminium content is increased (Fig. 6.9A) and ductility decreases rapidly above approximately 8% (Fig. 6.8). In more slowly cooled castings, discontinuous precipitation of the β phase may occur at grain boundaries with the formation of a cellular or pearlitic structure (Fig. 6.9B). Annealing at temperatures around 420°C causes the cellular constituent and all or part of the β phase along grain boundaries to redissolve leading to solid solution strengthening. Interdendritic coring (Fig. 6.9A) is also reduced and both tensile strength and ductility are significantly improved. Discontinuous precipitation of lamellae of the β phase is considered to be undesirable in Mg–Al alloys subject to creep conditions and attempts have been made to prevent its formation by adding

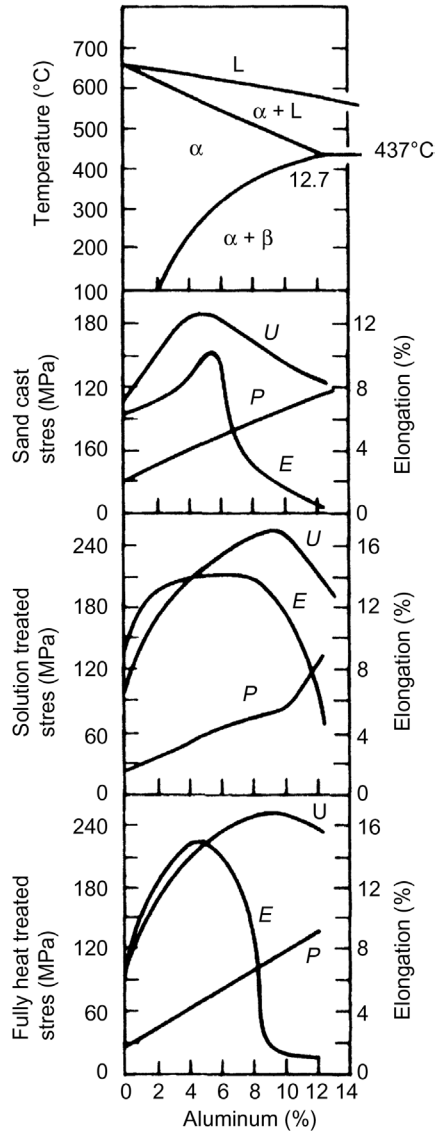


Figure 6.8 Relation of properties to constitution in the Mg–Al alloys, showing effects of composition and heat treatment on the tensile properties of sand cast AZ80A alloy. *P* = 0.2% proof stress, *U* = tensile strength, and *E* = elongation. From Fox, FA: *J. Inst. Metals*, 71, 415, 1945.

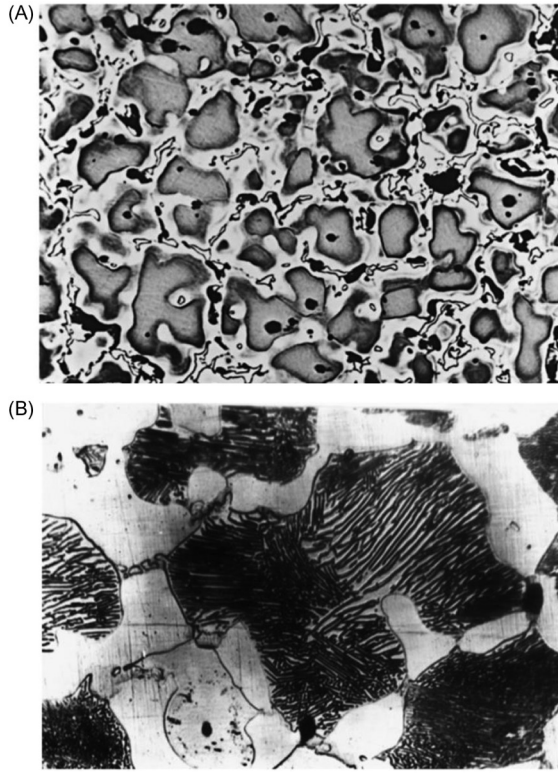


Figure 6.9 Cast structures in alloy AZ80: (A) chill cast alloy with the β phase ($Mg_{17}Al_{12}$) present in the grain boundaries. Note also the interdendritic aluminium-rich coring (white) around the edges of the α grains (gray) (× 200) and (B) discontinuous precipitation in more slowly cooled alloys (× 500). Courtesy Magnesium Elektron.

micro-alloying elements. So far, the only effective addition has been a trace of gold (~0.1 at.%) which apparently segregates in grain boundaries and suppresses the growth of discontinuous precipitates, perhaps because of the strong interaction that is known to occur between gold and aluminium atoms. As a consequence of this change in microstructure, creep resistance is improved although the use of such an expensive element is not a practical solution to this problem. Discontinuous precipitation may also be eliminated by adding high concentrations of zinc to Mg–Al alloys but the Mg–Zn–Al alloys also show only moderate creep resistance.

Because the solid solubility of aluminium in magnesium decreases from a maximum of 12.7 wt% at 437°C to around 2% at room temperature (Fig. 6.8), it might be expected that ageing treatments would induce significant precipitation hardening. However, as given in Table 6.5, supersaturated solid solutions of Mg–Al alloys transform directly to the equilibrium precipitate β on artificial

ageing, without the appearance of GP zones or an intermediate precipitate. The β phase mainly forms as coarse laths on the basal planes of the α-Mg matrix and the response to age hardening is relatively poor. Accordingly, alloys based on this system are generally used in the as-cast or as-cast and annealed conditions.

The addition of zinc to Mg–Al alloys causes some strengthening although the amount of zinc is limited because of an increase in susceptibility to hot cracking during solidification. Actual levels of zinc are inversely related to the aluminium contents and two examples of alloys are AZ63 (Mg–6Al–3Zn–0.3Mn) and AZ91 (Mg–9Al–0.7Zn–0.2Mn). AZ91 is the most widely used of all magnesium alloys. As mentioned earlier, the corrosion resistance of this and related alloys is adversely affected by the presence of cathodic impurities such as iron and nickel and, for some purposes, strict limits have now been placed on these elements. Higher-purity versions such as AZ91E (Fe 0.015% max., Ni 0.001% max., and Cu 0.015% max.) have corrosion rates in salt fog tests which are as much as 100 times lower than for AZ91C so that they become comparable with those for some aluminium casting alloys.

Requirements for specific property improvements have stimulated the development of alternative die casting alloys. For applications where greater ductility and fracture toughness are required, a series of high-purity alloys with reduced aluminium contents are available. Examples are AM60, AM50, and AM20 (Table 6.3). The improved properties arise because of a reduction in the amount of $Mg_{17}Al_{12}$ around grain boundaries. Such alloys are used for automotive parts including wheels, seat frames, and steering wheels. Fig. 6.10 shows a seat frame for a Mercedes Benz roadster which has been produced from five AM20 and AM50 alloy die castings and has a weight of 8.3 kg. It is claimed that a comparable steel seat would weigh an estimated 35 kg and require between 20 and 30 stampings and weldments. An added advantage of the magnesium alloy seat is its extra stiffness which has allowed the safety belt and belt mechanism to be attached and incorporated in the back rest.

Cast Mg–Al and Mg–Al–Zn alloys show some susceptibility to microporosity but otherwise have good casting qualities and resistance to corrosion is generally satisfactory. They are suitable for use at temperatures up to 110–120°C above which creep rates become unacceptable (Figs. 6.11 and 6.12). This behavior is attributed to the fact that magnesium alloys undergo creep mainly by grain boundary sliding and the phase $Mg_{17}Al_{12}$, which has a melting point of approximately 460°C and is comparatively soft at lower temperatures, does not serve to pin boundaries. Accordingly, commercial requirements have led to the development of other alloys based on the Mg–Al system.

Creep properties of Mg–Al alloys may be improved by lowering the aluminium content and introducing silicon which has the effect of reducing the amount of $Mg_{17}Al_{12}$. Providing solidification rates are fast, such as in pressure die casting, the silicon combines with some of the magnesium to precipitate fine and relatively hard particles of Mg_2Si in grain boundaries, rather than

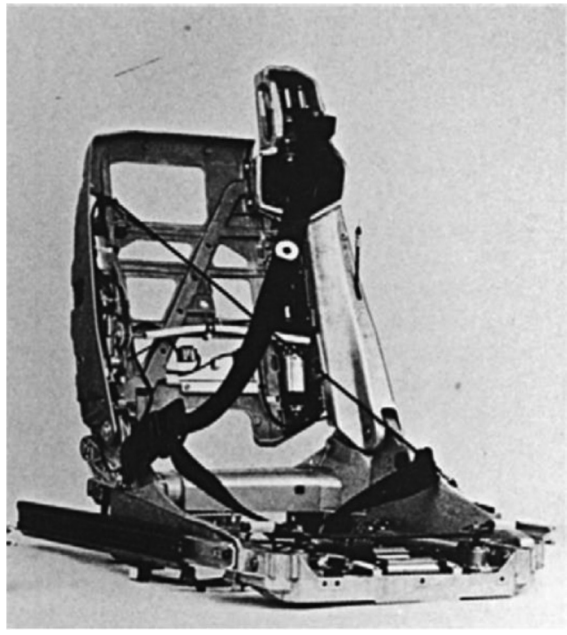


Figure 6.10 Die cast magnesium alloy seat frame.

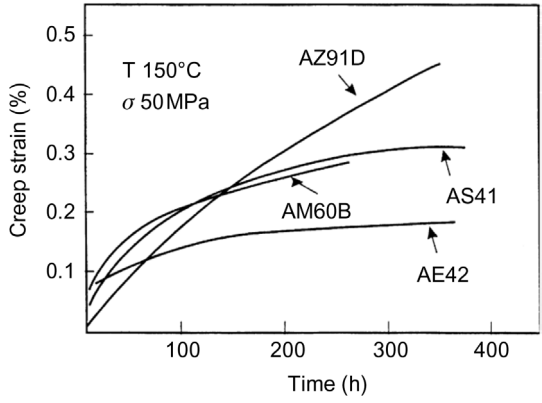


Figure 6.11 Creep strain vs time for commercial magnesium die casting alloys based on the Mg–Al system. Tests at 150°C and a stress of 50 MPa. From Han, Q. *et al.*, *Philos. Mag.*, 84, 3843, 2004.

forming this phase in its coarse, Chinese script morphology that is detrimental to mechanical properties. Small additions of calcium (e.g., 0.1%) also help suppress this undesirable form of Mg_2Si. Two examples are the commercial alloys AS41 (Mg–4.5Al–1Si–0.3Mn) and AS21(Mg–2.2Al–1Si–0.3Mn). As shown in

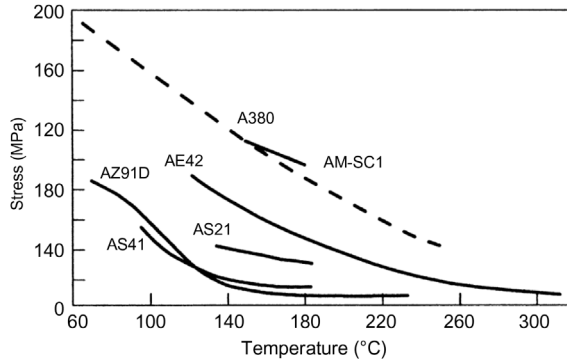


Figure 6.12 Stress for 0.1% creep strain in 100 h for commercial magnesium die casting alloys based on the Mg–Al system, the Mg–RE–Zn sand cast alloy designated AM-SC1, and the aluminium die casting alloy 380. From Waltrip, JS: *Proc. 47th Ann. World Magnesium Conf.*, 1990, Inter. Magnesium Assoc., p. 124, 1990; Bettles, CJ *et al.*: *Magnesium Technology 2003*, Kaplan, HI (Ed.), TMS, Warrendale, PA, USA, p. 223, 2003.

Fig. 6.12, alloy AS21 with the lower content of aluminium performs better than AS41, but it is more difficult to cast because of reduced fluidity. These alloys were exploited on a large scale in the rear engine of various models of the famous Volkswagon Beetle motor car in which the replacement of the cast iron crank case and transmission housing with magnesium alloys saved some 50 kg in weight. Such a saving was critical for the road stability of such a vehicle.

The creep properties of Mg–Al–Si alloys still fall well below those of competing die cast aluminium alloys such as A380 (Fig. 6.12) and attention has been directed at other alloying additions, notably the RE and alkaline earth elements that form relatively stable intermetallic dispersoids in their as-cast microstructures. While the individual solubility of some of these elements in molten magnesium is quite high, their mutual solubility is usually much less if several elements are present. The challenge in developing more creep-resistant die casting alloys is to retain enough of the elements in solution to give some solid solution hardening, while maximizing both the volume fraction and spatial distribution of dispersoids. At the same time, the alloys must show acceptable castability and corrosion resistance.

As shown in Table 6.1, magnesium forms solid solutions with a number of RE elements and magnesium-rich sections of the respective phase diagrams all contain simple eutectics. Because of this, the binary alloys have good casting characteristics since the presence of the relatively low melting point eutectics as networks in grain boundaries tends to suppress microporosity. RE elements are comparatively expensive and the most economical way of making these additions is to use naturally occurring misch-metals based on cerium (e.g., 50%Ce–20%La–15%Nd–5%Pr) or neodymium (e.g., 80%Nd–16%Pr–2%Gd–2% others) although the use of these compounds still imposes a significant cost penalty.

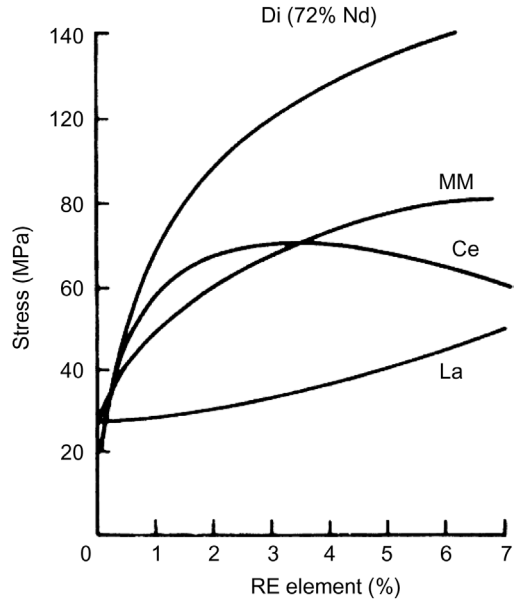


Figure 6.13 Effect of various RE metals on the stress for 0.5% extension in 100 h at 205°C. Fully heat-treated Mg–RE alloys. From Leontis, TE: *TAIMME*, 35, 968, 1949.

Individual RE elements have differing effects on the response of magnesium alloys to heat treatment with the mechanical properties generally increasing in the order of lanthanum, misch-metal, cerium, and didymium (72% neodymium). This effect is demonstrated for creep extension curves (Fig. 6.13) and probably corresponds to an increasing solid solubility of the elements in magnesium. It should also be noted that cerium is in fact marginally better than misch-metal over the useful addition range of these elements, i.e., below 3%, but the expense of separating individual RE elements from misch-metal is normally not justified.

Generally Mg–Al–RE alloys are only suitable for die casting because fast cooling is needed to form a relatively fine dispersion of the compound $Al_{11}RE_3$, rather than coarser particles of Al_2RE. $A1_{11}RE_3$ forms as lamellae within the interdendritic regions of the matrix. One composition, AE42 (Mg–4Al–2RE–0.3Mn), has a good combination of mechanical properties including creep strength that is superior to the Mg–Al–Si alloys (Figs. 6.11 and 6.12). However, the creep properties of AE42 deteriorate rapidly above 175°C, because of the relatively high level of aluminium retained in the α-Mg matrix after die casting.

Improvement in creep resistance of AE42 was achieved by adding more RE elements, which led to the development of alloy AE44 (Mg–4Al–4RE). The better creep resistance exhibited by AE44 (Fig. 6.14A) is attributed to an increased amount of intermetallic phases and a reduced level of aluminium

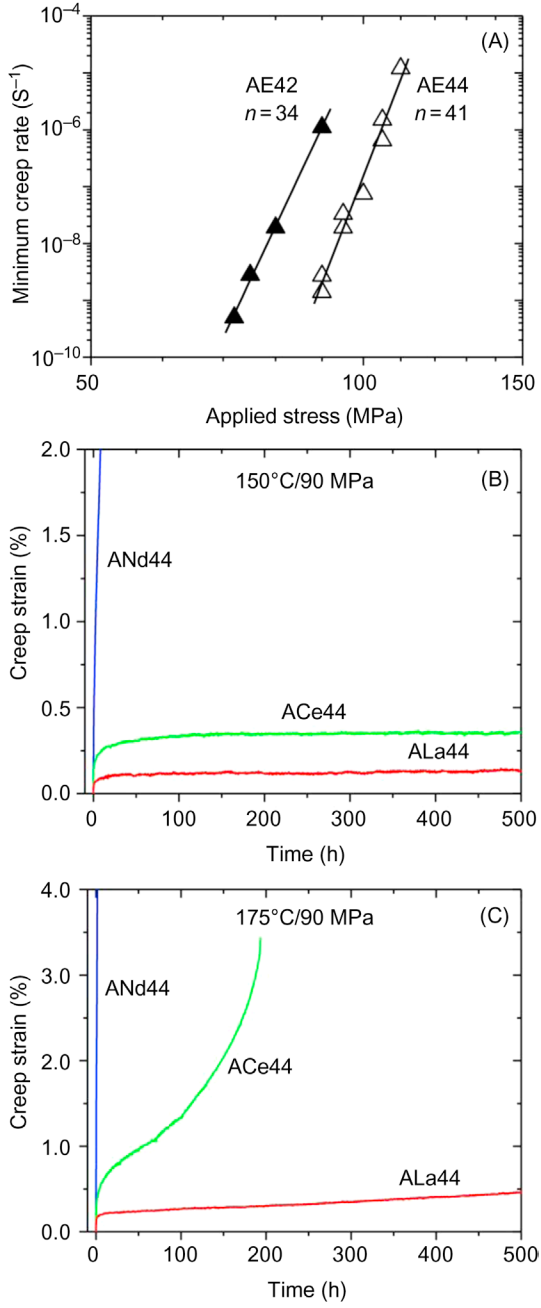


Figure 6.14 (A) Variation of minimum creep rate as a function of applied stress at 175°C for AE44 and AE42. (B, C) Creep curves of die cast AE44 alloys at 150°C and 175°C under an applied stress of 90 MPa. (A) From Zhu, SM *et al.*: *Metall. Mater. Trans. A.*, 43, 4137, 2012. (B, C) From Zhu, SM *et al.*: *Adv. Eng. Mater.*, 18, 932, 2016.

saturation in the α-Mg matrix because of the higher content of RE. As in AE42, $Al_{11}RE_3$ is the predominant intermetallic phase in AE44, and Al_2RE is the minor one. Both $Al_{11}RE_3$ and Al_2RE phases have good thermal stability, with no significant decomposition or coarsening occurring at temperatures up to 200°C. Recent studies indicate that the choice of RE elements has strong influence on the creep resistance of die cast AE44 alloy: the lanthanum-containing alloy is the most creep-resistant, followed by the cerium-containing alloy and the neodymium-containing alloy (Fig. 6.14B and C). This trend in creep resistance is similar to the tensile strengths measured from these alloys at room temperature and 150°C. The observed differences in creep resistance cannot be accounted for by the thermal stability of $Al_{11}RE_3$ phase as reported previously. The volume fraction of intermetallic phases is considered to be a contributing factor for the observed differences in creep resistance and strength. A more recent study indicates that minor additions of manganese enhance the age hardening response and the strength of die cast AE44 alloys. The manganese-containing alloys can be strengthened by a T5 temper without any loss of ductility.

Alkaline earth additions of calcium and strontium to Mg–Al alloys have been studied, with and without the presence of RE elements, as another way to improve creep resistance. For example, it has been claimed that, with the die cast alloy AM50 (Mg–5Al–0.3Mn), the minimum creep rate at 150°C may be reduced by three orders of magnitude by the addition of 1.7%Ca. A more detailed comparison of the effects of aluminium, alkaline earth and RE elements on the properties and cost of magnesium die casting alloys is shown schematically in Fig. 6.15. Both calcium and strontium have low solubilities in magnesium and form stable particles of Al_2Ca or Al_4Sr, mainly at grain boundaries. When RE elements are also present, the $Al_{11}RE_3$ phase forms within the grains that reduces dislocation slip. Calcium is cheaper than strontium although the latter element is claimed to have the advantage of promoting higher tensile properties at elevated temperatures. Both elements have some adverse effects on castability and may also increase the susceptibility of castings to hot tearing.

A number of new alloys were produced, some of which have been found in industrial applications. Examples are AX81 (Mg–8Al–1Ca), AXE522 (Mg–5Al–2Ca–2RE), and AJ62 (Mg–6Al–2.3Sr). Some, such as MRI 153 and 230D that have been developed by collaboration between the companies Dead Sea Magnesium and Volkswagon AG, are known only by their proprietary designations. Properties of some of these alloys are summarized in Table 6.6 in which comparisons can be made with the commonly used magnesium alloys AZ91, AS21, AS41, and AE42, and with the aluminium casting alloy 380. The new magnesium alloys have room-temperature tensile properties similar to, or exceeding those of other alloys based on the Mg–Al system, but show improved creep strengths at temperatures in the range 150–175°C, and are generally more resistant to corrosion. Small additions of zinc are known to improve metal flow during casting which has led to the development of another series of creep-resistant alloys of which one designated ZAXE05613

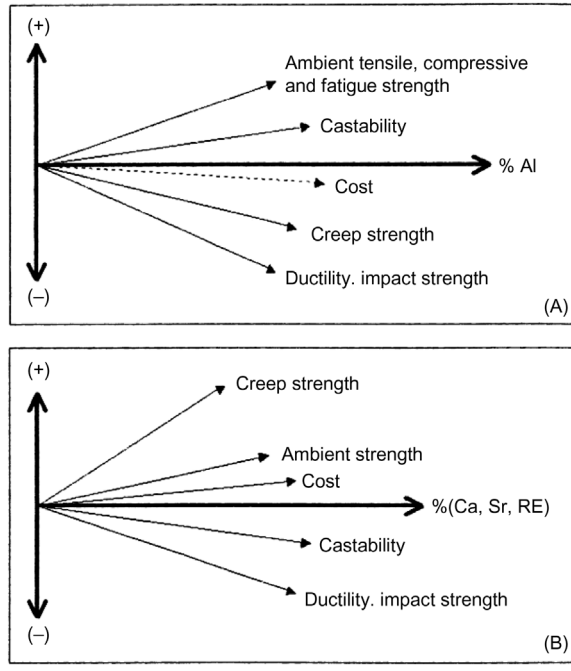


Figure 6.15 General effects of (A) aluminium and (B) alkaline and RE elements on the properties and cost of die cast magnesium alloys. From Aghion, E *et al.*: *Mater. Sci. Forum*, 419–422, 407, 2003.

(Mg–0.5Zn–6Al–1Ca–3RE) is an example. An important innovation has been the selection of the strontium-containing alloy AJ62, that was developed in Canada, for use in the lightweight composite engine for one model of a motor car being produced by BMW in Germany. As shown in Fig. 5.9, this magnesium alloy is used for the engine block which is cast around an aluminium–silicon alloy A390 core containing the cylinders.

It has been shown the Mg–Al alloys with high zinc contents may have attractive die casting characteristics combined with tensile and corrosion properties that exceed traditional alloys such as AZ91. Composition ranges for these potential alloys are shown in Fig. 6.16 and alloys with zinc contents as high as 12%, e.g., Mg–12Zn–4Al, have been investigated. Studies of the alloy Mg–8Zn–4Al have shown that the as-cast microstructure contains a high-volume fraction of primary intermetallic compounds, most of which are a quasi-crystalline phase with the approximate composition $Mg_9Zn_4Al_3$. Such phases lack the translational long-range order of the crystalline state and may display unique properties; in particular a very high hardness. The amount of this phase decreases on homogenizing at 325°C, and quenching from this temperature followed by ageing at 150–200°C promotes age hardening through

Table 6.6 Summaries of properties of experimental and commercial die cast magnesium alloys and the aluminium casting alloy 380

Alloy	Composition	Tensile properties 20°C			Tensile properties 150°C			Tensile properties 175°C			%Tensile creep at 50 MPa, 200 h		Salt spray corrosion rate
		YS (MPa)	TS (MPa)	Elong. (%)	YS (MPa)	TS (MPa)	Elong. (%)	YS (MPa)	TS (MPa)	Elong. (%)	150°C	175°C	mg cm^{-2} day^{-1}
A380	Al–8.5Si–3.5Cu	168	290	3	155	255	6	151	238	8.5	0.08	–	0.34
AZ91D	Mg–9Al–1Zn	150	222	3	105	160	18	89	138	21	2.7	a	0.10
AS21	Mg–2Al–1Si	121	210	5.5	87	120	27	78	110	23	0.19	1.27	–
AS41	Mg–4Al–1Si	138	206	5	94	154	20	85	127	22	0.05	2.48	0.16
AE42	Mg–4Al–2RE	137	225	10.5	100	160	22	86	135	23	0.06	0.33	0.21
AX51	Mg–5A1–1Ca	128	192	7	102	161	7	–	–	–	–	–	–
AX52	Mg–5A1–2Ca	161	228	13	–	–	–	133	171	23	–	–	–
AJ52	Mg–5A1–2Sr	134	212	6	108	164	14	100	141	18	0.04	0.05	0.09
AJ62	Mg–6Al–2.2Sr	143	240	7	116	166	27	103	143	19	0.05	0.05	0.11
MRI153M	–	170	250	6	135	190	17	112	139	3.5	0.18	–	0.09
MRI230D	–	180	235	5	150	205	16	–	–	–	–	–	0.10

From Pekguleryuz, MO and Kaya, AA: *Proc. of 6th Inter. Conf. Magnesium Alloys and Their Applications*, Kainer KU (Ed.), Wiley-VCH Verlag GmbH, Germany, 74, 2004; Luo, AA: *Mater. Sci. Forum*, 419–422, 59, 2003; and Aghion, E *et al*.: ibid. p. 409.

[a]Failed after 80 h.

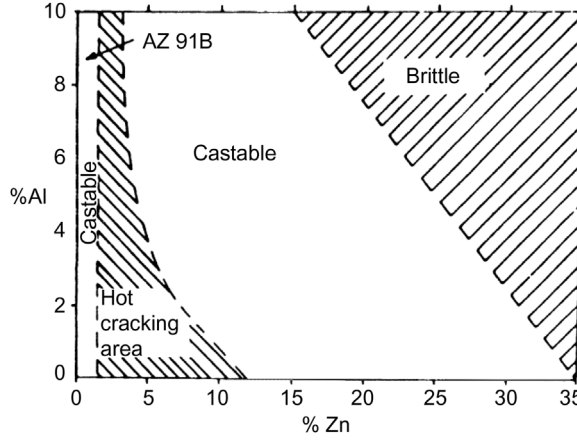


Figure 6.16 Potential composition ranges of Mg–Al–Zn alloys for die casting. From Foerster, GS: *Proc. of 33rd Annual Meeting International Magnesium Association*, Montreal, Quebec, Canada, 1976.

precipitation of a finely dispersed, diamond-shaped phase that also appears to have a quasi-crystalline structure (Section 8.4). The addition of 0.5% calcium is reported to result in the replacement of the primary quasi-crystalline phase with a crystalline cubic phase in the as-cast microstructure, and to stimulate precipitation of an additional rod-like phase when the alloy is aged. Although the presence of calcium does not increase maximum hardness, the rate of overageing at 200°C is much reduced and creep resistance is improved. For example, the creep strain after 100 h at 150°C and a stress of 60 MPa is 0.5×10^{-3} which compares with 0.21×10^{-2} for the ternary Mg–Zn–Al alloy.

6.3.2 Magnesium–zinc based alloys

As mentioned in Section 6.1, zinc causes more solid solution strengthening than an equal atomic percent of aluminium but its solubility is much less (Table 6.1). Mg–Zn alloys also respond to age hardening and, as shown in Table 6.5, the ageing process is complex and may involve four stages. The GP zones solvus for the alloy Mg–5.5Zn lies between 70°C and 80°C, and pre-ageing below this solvus before ageing at a higher temperature (e.g., 150°C) refines the size and dispersion of rods of the coherent phase $MgZn_2$ that may form from the GP zones. Maximum hardening is associated with the presence of this coherent phase. However, binary Mg–Zn alloys are not amenable to grain refining by superheating or inoculation, and are prone to microporosity. As a consequence, they are not used for commercial castings.

Minor additions may modify precipitation in Mg–Zn alloys. Examples are the elements calcium and strontium which accelerate the rate of ageing but delay overageing, refine the sizes, and increase the number densities of

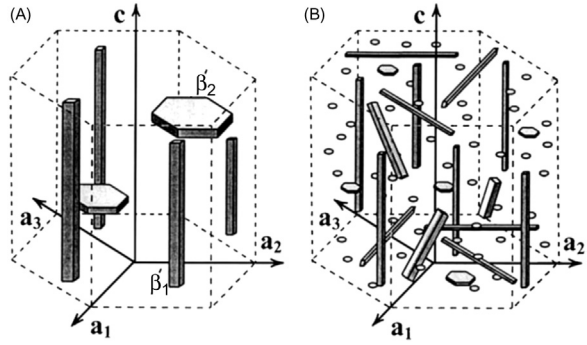


Figure 6.17 Schematic representations of the precipitate sizes, morphologies, and habit planes with respect to the α-Mg matrix for (A) Mg–4Zn and (B) Mg–4Zn–0.35Ca aged for 2.7 h at 177°C. Courtesy of C. J. Bettles and M. A. Gibson.

precipitates that form. The resulting microstructure is shown schematically in Fig. 6.17.

The addition of copper to binary Mg–Zn alloys causes a marked improvement in ductility and induces a relatively large response to age hardening. The copper-containing alloys exhibit tensile properties similar to alloy AZ91 (e.g., 0.2% PS 130–160 MPa, TS 215–260 MPa, and ductility 3–8%) but have the advantage that these properties are more reproducible. Elevated temperature stability is also improved.

One typical sand casting alloy is designated ZC63 or ZCM630 (Mg–6Zn–3Cu–0.5Mn). It has been found that progressive addition of copper or cobalt to Mg–Zn alloys raises the eutectic temperature (Fig. 6.18) which is important because it permits the use of higher solution treatment temperatures, thereby ensuring maximum solution of zinc and copper. The structure of the eutectic is also changed from being completely divorced in binary Mg–Zn alloys, with the Mg–Zn compound distributed around grain boundaries and between dendrite arms, to truly lamellar in the ternary copper-containing alloys.

On solution treatment, partial dissolution of the eutectic occurs leaving rounded rods or platelets within the α-matrix. It is this structure that is believed to improve the ductility of the alloy. A typical heat treatment cycle involves solution treatment for 8 h at 440°C, hot water quench, followed by ageing for 16–24 h at 180–200°C. Two main precipitates have been identified, β'_1 (rods) and β'_2 (plates), which appear to be similar in structure to the phases observed in binary Mg–Zn alloys. However, the density of precipitates is much greater and more uniform when copper or cobalt is present (Fig. 6.19). Peak hardening occurs around 200°C when both these precipitates are present. Manganese is added because it has been found to stabilize the ageing response and to reduce the rate of overageing.

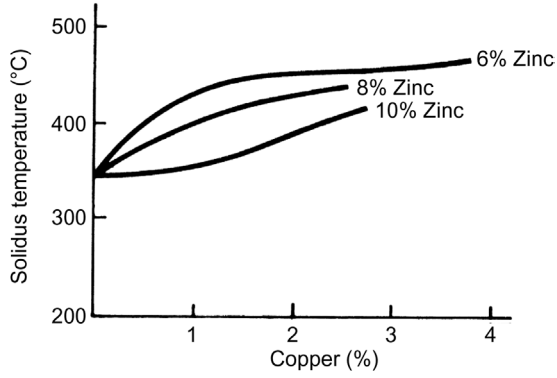


Figure 6.18 Effect of copper in raising the eutectic temperature of Mg–Zn alloys. From Unsworth, W and King, JF: *Magnesium Technology*, p. 25, Institute of Metals, London, 1987.

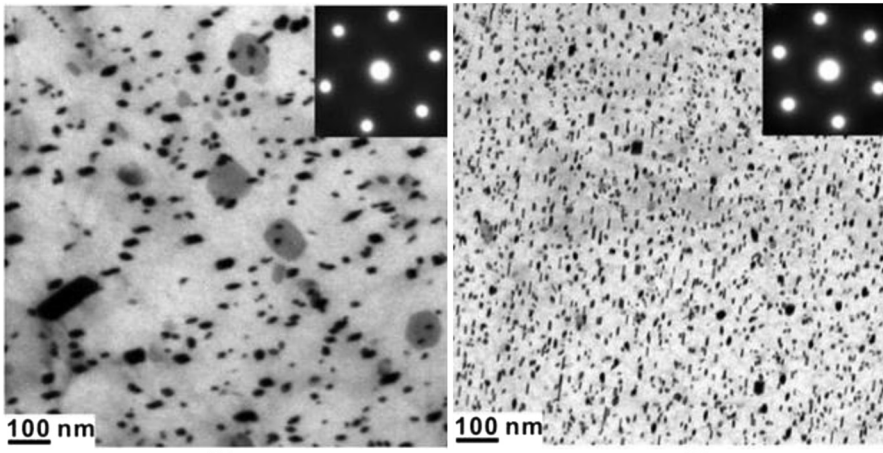


Figure 6.19 Comparison of precipitate densities in (A) Mg–8Zn and (B) Mg–8Zn–0.6Co alloys peak-aged at 150°C. From Geng, J *et al.*: *Scr. Mater.*, 64, 506, 2011.

The addition of copper to Mg–Al–Zn alloys has a detrimental effect on corrosion resistance but this appears not to be the case in Mg–Zn–Cu alloys. This may be attributed to the incorporation of the copper in the eutectic phase as $Mg(Cu,Zn)_2$. Fatigue strength in the unnotched condition (e.g., endurance limit 10^7 cycles of ± 90 MPa) is better than that of Mg–Al–Zn alloys, while the notched values are comparable.

A number of Mg–Zn–Cu castings have been produced under practical foundry conditions using sand, gravity die, and precision casting techniques. This work has confirmed that the alloy has good casting characteristics, notably its freedom from microshrinkage, which enables pressure tight castings to

be produced without impregnation. Castings can be welded using the standard tungsten inert gas technique. Taken overall, these alloys would seem to offer significant improvements over the traditional Mg–Al–Zn alloys for critical high-strength castings. It was thought that they would find particular application in the automotive industry, but they are not commercially available, presumably because of the corrosion problem.

6.3.3 Magnesium–RE–zinc alloys

Mg–RE–Zn alloys Since Mg–Al- and Mg–Zn-based alloys have limited creep resistance, efforts have been made to develop Mg–RE–Zn alloys for elevated temperature applications. MEZ (Mg–2.5RE–0.5Zn–0.35Mn) was developed by Magnesium Elektron for high-pressure die castings. This alloy has better creep resistance than AE42 at temperatures above 150°C, but has low tensile yield strength and ductility at room temperature. The choice of RE elements has significant influence on the tensile properties and creep resistance of die cast Mg–RE alloys. By optimizing the RE composition, a new Mg–RE-based die casting alloy, designated EZ41 (Mg–1.63La–0.97Ce–0.96Nd–0.11Y–0.5Zn) and also known as AM–HP2, was developed about 10 years ago. This alloy exhibits excellent creep resistance at temperatures 150–200°C (Table 6.3).

Mg–Y–Zn alloys Zinc additions to Mg–Y alloys significantly reduce the equilibrium solid solubility of yttrium in magnesium. Therefore, the Mg–Y–Zn alloys have a lower volume fraction of solid-state precipitates, and they exhibit little response to age hardening. In the early studies of these alloys, I_1 intrinsic stacking faults were reported to form on the basal plane of the magnesium matrix phase. Similar planar defects were also observed in an early study of Mg–Th–Zn alloys aged at 300–400°C, and they were also reported to be stacking faults. In recent studies, it was found that the stacking faults reported in earlier studies are actually precipitates of γ' or 14H phase (Table 6.5). The γ' phase has a disordered hexagonal structure that is similar to that in Mg–Gd–Zn alloys (Section 6.4.3). It forms as thin plates which have a very large aspect ratio. The Shockley partial dislocations associated with the formation of these thin plates make them appear as stacking faults. The 14H is an equilibrium phase in the Mg–Y–Zn system. It has a long-period stacking ordered (LPSO) structure (Fig. 6.20), and forms as thin plates with a large aspect ratio.

In 2001, Y. Kawamura and coworkers developed an Mg–Y–Zn alloy by combined processes of rapid solidification and conventional hot extrusion. This alloy exhibits an impressively high 0.2% proof strength exceeding 600 MPa and elongation to fracture of 5%. The intermetallic particles in this alloy are 50–250 nm in diameter, and they have LPSO structures. These LPSO structures are thought to be responsible for the ultra-high strength. These structures have been found to form in Mg–RE–X systems where RE represents yttrium,

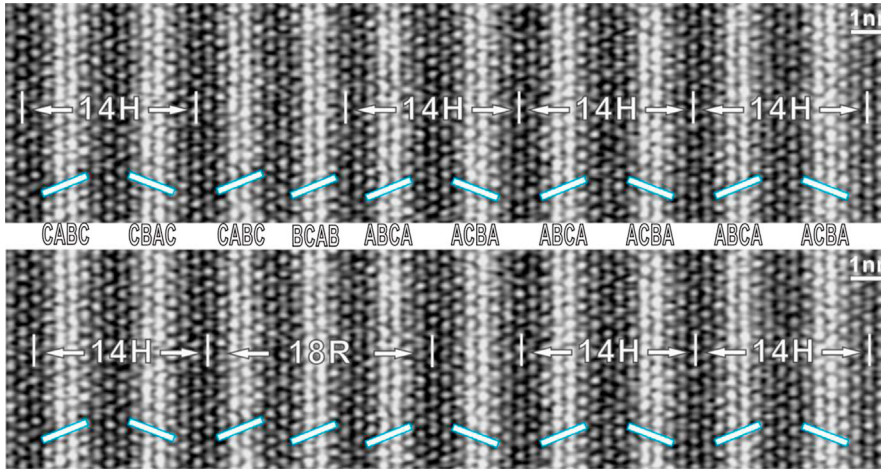


Figure 6.20 Z-contrast scanning transmission electron micrograph showing complex LPSO structures in an Mg–Y–Zn alloy. From Zhu, YM *et al.*: *Scr. Mater.*, 60, 980, 2009.

gadolinium, dysprosium, holmium, erbium, thulium, or terbium, elements that have larger atomic size than magnesium, and X represents zinc, copper, nickel, cobalt, or aluminium, elements with smaller atomic size than magnesium. In most of these alloy systems, the intermetallics have an 18R (another type of LPSO) structure in the as-cast condition, and a 14H structure in the heat-treated condition. Other types of LPSO structures such as 24R and 10H have also been found in Mg–RE–X alloys, but they are rare in the alloy microstructures. A major issue that limits commercialization of these alloys is their cost. One avenue to reduce their cost is to utilize misch-metal rather than particular purified RE elements for alloying constituents. A yttrium-rich misch-metal-based alloy containing extensive regions of 14H phase has been developed and it exhibited good strength and ductility: approximately 300 MPa and 27% elongation at 250°C. However, it would be of commercial interest to be able to develop RE-free alloys with these same LPSO-type structures that offer such excellent strength and ductility properties.

6.4 ZIRCONIUM-CONTAINING CASTING ALLOYS

The maximum solubility of zirconium in molten magnesium is 0.6% and as binary Mg–Zr alloys are not sufficiently strong for commercial application, the addition of other alloying elements has been necessary. The selection of these elements has been governed by three main factors:

1. Compatability with zirconium
2. Foundry characteristics
3. Properties desired of the alloy.

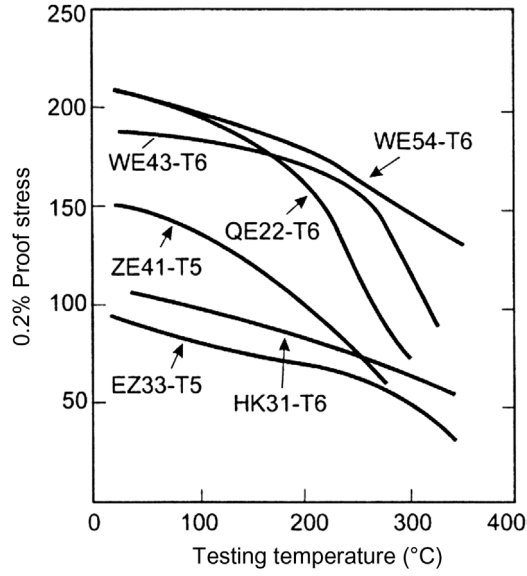


Figure 6.21 Effect of temperature on the 0.2% proof stress of sand cast magnesium alloys grain refined by zirconium and age hardened. Courtesy Magnesium Elektron.

With respect to (1), a prerequisite is the absence of elements such as aluminium and manganese that effectively suppress the liquid solubility of zirconium in magnesium. Elements that do not interfere with the grain refining effect of zirconium include zinc, RE elements, thorium, silver, yttrium, and calcium. So far as (3) is concerned, improved tensile properties, including higher ratios of proof strength to tensile strength, and enhanced creep resistance, have been the two principal objectives in an alloy development that has been driven by the aerospace industries. Developments in various countries have been rather similar and Table 6.4 and Figs. 6.21 and 6.22 compare the elevated temperature proof stresses of some of these alloys.

6.4.1 Magnesium–zinc–zirconium alloys

The ability to grain refine Mg–Zn alloys with zirconium led to the introduction of alloys such as ZK51 (Mg–4.5Zn–0.7Zr) and the higher-strength ZK61 (Mg–6Zn–0.7Zr) that are normally used in the T5 and T6 tempers, respectively. However, the fact that these alloys are susceptible to microporosity, and are not weldable, has severely restricted their practical application.

6.4.2 Magnesium–RE–zirconium alloys

Further improvements in the creep resistance of magnesium alloys have been achieved by taking advantage of the high solid solubility of yttrium (maximum

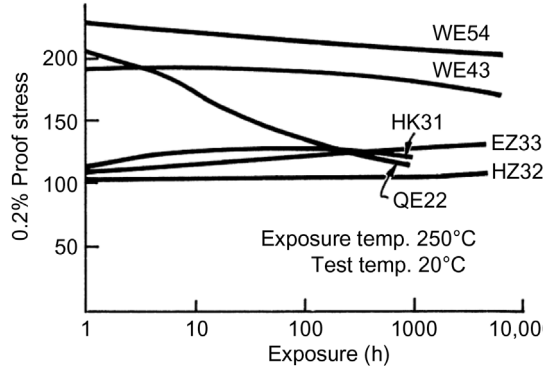
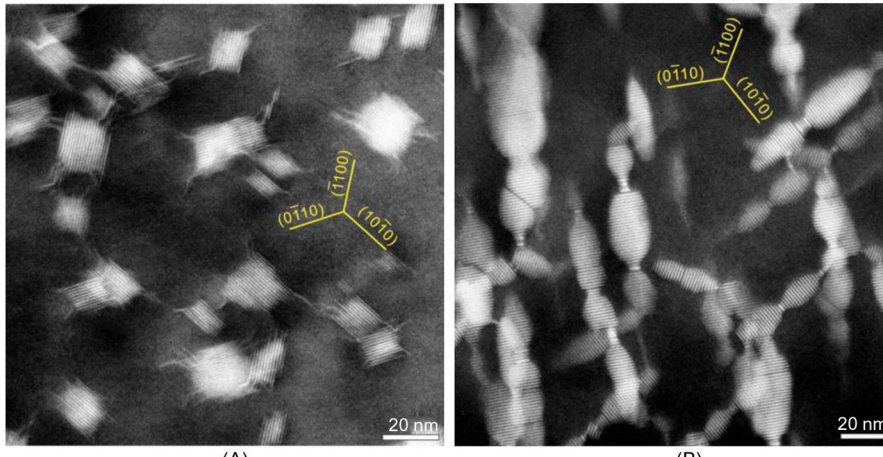


Figure 6.22 Effect of exposure at 250°C on the 0.2% proof stress at room temperature for several creep-resistant magnesium alloys containing zirconium.



(A) (B)

Figure 6.23 Z-contrast scanning transmission electron micrographs showing β′ precipitates in aged (A) Mg–8 wt%Y and (B) Mg–15 wt%Gd alloys. From Liu, H *et al.*: *Acta Mater.*, 61, 453, 2013.

12.5 wt%). Yttrium is particularly effective in solid solution strengthening and Mg–Y alloys also respond to age hardening at relatively high ageing temperatures. The precipitates formed in peak-aged samples of binary Mg–Y alloys appear to be β′ that has a body-centered orthorhombic structure and an Mg_7(NdY) composition (Fig. 6.23A).

The addition of neodymium to Mg–Y alloys significantly enhances the age hardening response. A series of Mg–Y–Nd–Zr alloys have been developed which combine high strength at ambient temperatures with good creep resistance at temperatures up to 300°C. At the same time, the heat-treated alloys

Table 6.7 Comparative corrosion resistance of WE54–T6 and other magnesium and aluminium alloy castings after immersion in seawater for 28 days

Alloy type/designation		Weight loss ($mg\,cm^{-2}\,day^{-1}$)
Magnesium casting alloys	WE54–T6	0.08–02
	ZE41–T5, EZ33–T5	2–4
	AZ91–T6	6–10
Aluminium casting alloys	A356, A357	0.04–0.08

From Unsworth, W and King, JF: *Magnesium Technology*, p. 25, Inst. of Metals, London, 1987.

have a resistance to corrosion which is superior to that of other high-temperature magnesium alloys, and comparable with many aluminium-based casting alloys (Table 6.7). From a practical viewpoint, pure yttrium is expensive; it is also difficult to alloy with magnesium because of its high melting point (1522°C) and its strong affinity to oxygen. Subsequently, it was found that a cheaper yttrium-rich misch-metal containing around 75% of this element, together with heavy RE metals such as gadolinium and erbium, could be substituted for pure yttrium. Melting practices were also changed because the standard fluxes based on alkali and alkaline earth halides resulted in the loss of yttrium by reaction with $MgCl_2$. It is therefore necessary to process the alloys in an inert atmosphere of argon and 0.5 vol.% SF_6.

Precipitation in Mg–Y–Nd alloys is again complex (Table 6.5). Extremely fine GP zones are formed on ageing below 200°C. However, the T6 treatment normally involves ageing at 250°C, which is above the solvus for GP zones and leads to precipitation of three other metastable phases. Initial decomposition involves precipitation of fine plates of an as-yet unidentified phase on the $\{11\bar{2}0\}_\alpha$ planes, and globular particles of the body-centered orthorhombic phase β' that has an $Mg_7(NdY)$ composition. With continued ageing, the first precipitate is gradually replaced by relatively coarse plates of a face-centered cubic (fcc) phase that forms on the prismatic $\{1\bar{1}00\}_\alpha$ planes in contact with the β' particles (Fig. 6.24). This phase, which has been designated β_1, is claimed to be the major hardening precipitate in Mg–Y–Nd alloys aged to peak strength at 250°C. It has the composition $Mg_3(Nd,Y)$ and is similar to other Mg_3X phases (X = Nd, La, Ce, Pr, and Sm) that may form when alloying magnesium with the RE elements. The observation that β_1 plates always form heterogeneously at the sites of β' particles suggests that it is energetically difficult for β_1 to nucleate, and it has been found that cold work prior to ageing (T8 temper) promotes the formation of β_1 at the expense of β'. This increases the response to age hardening. Continued ageing at 250°C leads to gradual precipitation of the equilibrium β phase on the $\{1\bar{1}00\}_\alpha$ planes, which may form by in situ transformation

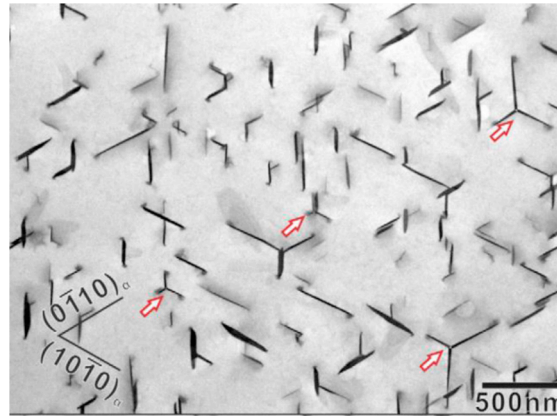


Figure 6.24 Transmission electron micrograph showing β_1 precipitate plates in aged WE54 alloy. From Xu, Z *et al.*: *Acta Mater.*, 75, 122, 2014.

from β_1. It is reported to have the composition $Mg_{14}Nd_2Y$. The fact that some of these phases contain such a high amount of magnesium helps promote high-volume fractions of precipitates.

Maximum strengthening combined with an adequate level of ductility was found to occur in an alloy containing approximately 6% yttrium and 2% neodymium, and the first commercially available alloy was WE54 (Mg–5.25Y–3.5RE(1.5–2Nd)–0.45Zr). In the T6 condition (Fig. 4.14), typical tensile properties at room temperature are 0.2% PS 200 MPa, TS 275 MPa, elongation 4%, and it showed elevated temperature properties superior to existing magnesium alloys (Figs. 6.21 and 6.22). It was revealed, however, that prolonged exposure to temperatures around 150°C led to a gradual reduction in ductility to levels that were unacceptable and this change was found to arise from the slow, secondary precipitation of GP zones throughout the grains. Subsequently it was shown that adequate ductility can be retained with only a slight reduction in overall strength if the yttrium content is reduced and the neodymium content is increased. On the basis of this work, an alternative composition WE43 (Mg–4Y–2.25Nd–1Heavy RE–0.4 min Zr) was developed. Because of its high strength at elevated temperatures, WE43 is being used for some cast components in racing car engines and for aeronautical applications such as helicopter transmission casings.

In recent years, a number of Mg–Gd–Y–Zr experimental alloys have been developed that have superior strength to the WE alloys. The solid solubility of gadolinium in magnesium is several times higher than that of neodymium at 550°C, and it decreases with temperature. Hence it can be added in larger quantities to obtain a higher volume fraction of precipitates. The Mg–Gd–Y–Zr alloys usually contain higher concentrations of gadolinium and yttrium, typically

in the range 10–16 wt%. They have stronger age hardening response than the WE alloys when aged to a T6 temper. The precipitation reactions in these alloys appear to be identical to that observed in the WE alloys. Because gadolinium is quite expensive, these alloys may be restricted to aerospace applications.

Recent work has revealed that micro-alloying additions of zinc (e.g., 0.05%) may increase the creep strength of Mg–Y alloys because zinc appears to suppress non-basal slip that occurs at high temperatures. This suggests that it may be possible to reduce the cost of these alloys by lowering the yttrium content without sacrificing their excellent creep properties. Another interesting observation is that the crystal structures, atomic radii, and electronegativities of yttrium and gadolinium are identical. Gadolinium is present in small quantities in yttrium-containing misch-metal, and a study has been conducted on some alloys with larger additions of this RE element. Binary Mg–Gd alloys show a rapid response to age hardening at high ageing temperatures which is attributed to nucleation of a higher volume fraction of relatively stable precipitates (Fig. 6.23B) that appear to be isomorphous with those formed in Mg–Y system. A proprietary Mg–Nd–Gd–Zn–Zr alloy, Elektron 21, has been developed which has mechanical and corrosion properties similar to WE43 and is claimed to have better castability because it is less prone to oxidation during melting. It shows excellent properties up to 300°C. The heavy RE element terbium also has a high solid solubility in magnesium and binary alloy Mg–20Tb has shown a 0.2% proof stress in the range 220–250 MPa at 300°C.

The comparatively rare and costly light element, scandium (SG 3.0) is another element having a particularly high solubility in magnesium (maximum of ~24.5 wt% or 15 at.%) and it also increases the melting point of the α-Mg solid solution. Furthermore, because of its relatively high melting point (~1541°C), scandium is assumed to have a low diffusivity in magnesium. Creep properties much superior to the alloy WE43 at high temperatures (e.g., 350°C) have been reported for experimental alloys such as Mg–Sc–Mn.

6.4.3 Magnesium–RE–zinc–zirconium alloys

These alloys also show good casting characteristics because the presence of the RE elements promotes the formation of relatively low melting point eutectics that improve fluidity and tend to prevent microporosity. In the as-cast condition, the alloys generally have cored α grains surrounded by grain boundary networks. Ageing causes precipitation to occur within the grains and the generally good creep resistance they display is attributed both to the strengthening effect of this precipitate and the presence of the grain boundary phases (Fig. 6.25).

The properties of Mg–RE alloys are enhanced by adding zirconium to refine grain size and further increases in strength occur if zinc is present as well. One commonly used alloy is ZE41 (Mg–4.2Zn–1.3Ce–0.6Zr) that develops moderate strength when given a T5 ageing treatment which is maintained up to 150°C. One application has been helicopter transmission housings (Fig. 6.26).

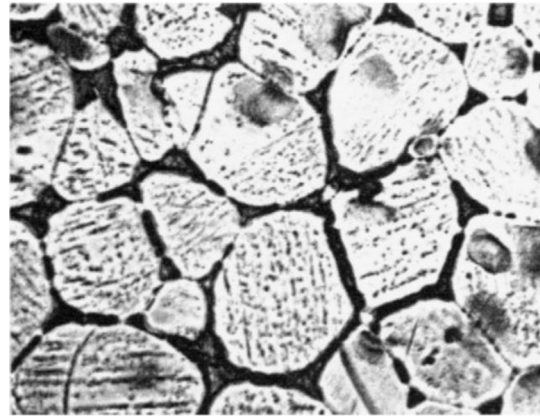


Figure 6.25 Mg–RE–Zn–Zr alloy EZ33 as-cast and aged 8 h at 350°C (T5 temper) (× 500).

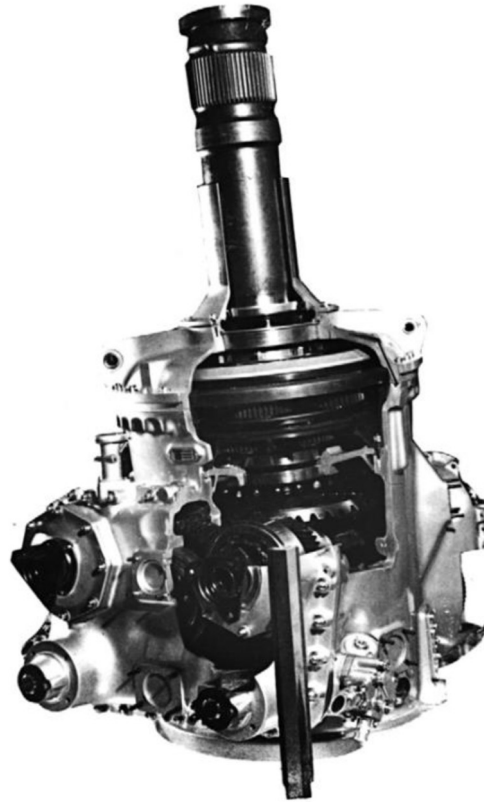


Figure 6.26 Cutaway section of the magnesium alloy gearcase in the Sud-Aviation Super Frelon helicopter. Casting is made from the Mg–Zn–RE–Zr alloy ZE41 and weighs 133 kg as-cast and 111 kg finish machined. Courtesy Magnesium Industry Council.

Higher tensile properties combined with good creep strength at temperatures up to 250°C have been achieved in the alloy EZ33 (Mg–3RE–2.5Zn–0.6Zr).

The precipitation processes in Mg–RE systems are not completely understood. Particular attention has been paid to Mg–Nd alloys in which four stages have been detected (Table 6.5). Most hardening is associated with formation of the coherent β' and β_1 phases. Loss of coherency of these two phases occurs close to 250°C and is associated with a marked increase in creep rate. The β_1 phase is prone to nucleation on dislocation lines when the alloys are aged in the range 200–300°C. It is possible that the MgRE (Ce) alloys have a similar ageing sequence which leads to the eventual formation of an equilibrium precipitate that is either $Mg_{12}Ce$ or $Mg_{17}Ce_2$.

The role of zinc with respect to strengthening is uncertain. It is likely that independent formation of Mg–Zn precipitates occurs although part of the zinc is associated with RE elements in constituents that form at grain boundaries. The effect of zirconium is thought to be confined to its role in grain refinement.

It might be thought that by starting with a high zinc content, e.g., 6%, and adding sufficient RE metals, e.g., 3%, an alloy could be produced which could combine the high tensile properties of ZK51 with the castability and freedom from microporosity of EZ33. Unfortunately such an alloy composition proves to be unusable since the low solidus temperature precludes solution heat treatment and the elongation, at 3% RE, is almost nil. Realizing that the low ductility was connected with a brittle grain boundary phase, it occurred to P. A. Fisher to decompose the latter by diffusing hydrogen into the alloy at a high temperature, thereby precipitating the RE metals as hydrides and enabling the zinc to be taken into solution (Fig. 6.27A, B). After final precipitation treatment in which a needle-like phase forms in the grains (Fig. 6.27C), castings in this alloy show high tensile properties with freedom from microporosity, together with high elongation values and outstanding fatigue resistance, which is an altogether remarkable combination of properties. The effect of the hydrogen treatment on tensile properties is shown for the Mg–6Zn–2RE composition in Table 6.8.

The final alloy developed in this way has the composition Mg–5.8Zn–2.5RE–0.7Zr (ZE63). It has found limited but important usage in the aircraft industry. The rate of penetration of hydrogen is about 6 mm in 24 h at a temperature of 480°C and a pressure of 1 atm. Penetration can be accelerated by increasing the gas pressure, but the slowness of the hydriding step has hitherto restricted use of the alloy to castings with fairly thin sections.

Magnesium Elektron in England developed an alloy designated MEZ (Mg–2.5RE–0.5Zn–0.35Mn) that has potential automotive applications such as gear boxes and oil pans. This alloy was designed for use in high-pressure die castings and therefore does not require grain refining. Zinc was added to improve castability. The tensile properties are lower than for the alloy AE42 (Section 6.4.1) but MEZ shows superior creep resistance, especially at temperatures above 150°C. This latter behavior is attributed to the presence of a more stable compound in grain boundaries that has the general formula $Mg_{12}RE$ and is probably $Mg_{12}(La_{0.43}Ce_{0.57})$ in which partial substitution of zinc for magnesium may occur.

Although special attention has been given to the development of magnesium alloys for high-pressure die casting, this method of manufacturing is not necessarily the best for casting an engine block. Design variations can be accommodated more readily when using permanent mold or sand casting. Moreover, because such castings usually contain less porosity, they are amenable to heat

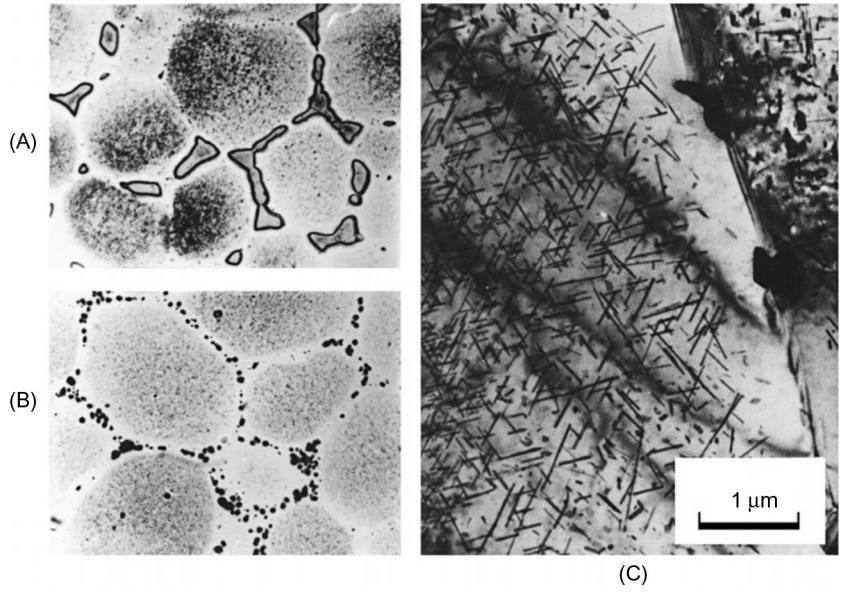


Figure 6.27 Effect of hydriding on the microstructure of the alloy ZE63: (A) as-cast microstructure; (B) alloy heat treated in hydrogen atmosphere at 480°C and given T6 temper (× 300); and (C) thin-foil electron micrograph showing massive RE hydrides in the grain boundary and needles within the grains which are probably ZrH_2 (× 13,000). (B) Courtesy Magnesium Elektron and (C) courtesy K. J. Gradwell.

Table 6.8 Tensile properties of cast test bars of the alloys ZK61 and ZE62 after solution treatment in an atmosphere of SO_2 and wet H_2

Alloy	Heat treatment: Solution treatment 24 h 500°C; aged 64 h 125°C	Tensile properties		
		0.2% Proof stress (MPa)	Tensile strength (MPa)	Elongation (% in 5 cm)
ZK61 (Mg–6Zn–0.7Zr)	SO_2	186	271	3.5
	H_2	183	252	2.5
ZE62 (ZK61+2%RE)	SO_2	94	173	3.8
	H_2	181	306	12.0

From Fisher, PA *et al.*: *Foundry*, 95(8), 68, 1967.

treatment to improve their mechanical properties because there is little danger of swelling and blistering. Several programs were carried out to design and evaluate permanent mold and sand cast magnesium alloys for possible use in lightweight engines.

One such development involved groups in Australia, Germany, Austria, and England that was focused on producing a cost-effective, sand cast alloy based on the Mg–RE system for cylinder blocks and crank cases. This alloy has been designated AM–SC1. It has the nominal composition Mg–2.7RE–0.5Zn–Zr, which is similar to MEZ. However, a special combination of RE elements has been used to promote creep resistance. It has a microstructure after a T6 temper (Fig. 4.14) that is generally similar to MEZ and has an intermetallic phase dispersed around the grain boundaries and triple points to minimize grain boundary sliding at the operating temperature of around 150°C. However, the fine-scale precipitates are much denser than those in MEZ. The influence of grain size and testing temperature on tensile properties are provided in Table 6.9.

Since the new alloy must compete with the cast aluminium alloys A319 (Al–6Si–3.5Cu) and A380 (Al–8.5Si–3.5Cu), it was considered that the target values for the critical creep and fatigue properties should at least equal the values for these two alloys. These target values and the actual properties achieved for AM–SC1 aged to a T6 temper were as follows:

1. Stress to give 0.1% creep strain after 100 h: target 110 MPa at 150°C and 90 MPa at 177°C, actual values 115 and 100 MPa, respectively (Fig. 6.12).
2. Fatigue limit after 5×10^7 cycles at 25°C, $R = -1$: target 50 MPa, actual value 75 MPa.

While engine blocks do not require a high level of tensile yield strength, it is vital that the compressive yield strength and creep resistance of an alloy are adequate to minimize relaxation, especially in bolted assemblies. The compressive yield strength of AM–SC1, which is 133 MPa at 20°C, remains unchanged up to 177°C. Bolt load retention properties at 150°C were found to be similar to aluminium alloy A319 and superior to the die cast magnesium alloy AE42.

Table 6.9 Tensile properties of AM–SC1 aged to T6 temper as a function of grain size and testing temperature

Grain size (μm)	Test temperature (K)			
	294	373	423	450
536	86.3 ± 2.1	74.3 ± 4.5	74.3 ± 1.5	74 ± 4.6
337	107 ± 2.0	92.7 ± 5.7	86.7 ± 4.7	90.3 ± 12.3
235	117.3 ± 3.2	102 ± 3.6	91 ± 7.5	100.3 ± 1.5
110	126 ± 6.6	120.2 ± 6.3	113.9 ± 6.5	113.4 ± 2.9
46	130.1 ± 3.6	124.1 ± 9.6	128.2 ± 2.8	114.2 ± 7.1

From Bettles, CJ *et al.*: *Mater. Sci. Eng. A*, 505, 6, 2009.

The alloy was successfully road tested in the engine block of a small three cylinder diesel engine installed in a Volkswagon Lupo automobile. The block, that has separate hypereutectic Al–Si alloy cylinder liners and reinforced main bearing housings, weighs only 14 kg. In 2004, the AM–SC1 alloy was selected by the US Automobile Materials Partnership for the sand cast cylinder block in their Magnesium Intensive Engine Research Project. For this purpose, a V6 engine block has been specially designed which incorporates cast iron cylinder liners. However, the magnesium engine block didn't proceed to anything commercial, and the AM-SC1 (now known as SC1) alloy is produced only in small quantities for foundry use mainly in Europe.

Mg–Gd alloys containing less than 6 wt% gadolinium have poor age hardening response at 200–250°C due to lower volume fractions of precipitates. The addition of 1–2 wt% zinc to the Mg–Gd alloys can significantly enhance the age hardening response and creep resistance. In the T6 temper condition (Fig. 4.14), the Mg–6Gd–2Zn–0.6Zr alloy has a tensile 0.2% proof strength of 137 MPa at room temperature and 124 MPa at 175°C. The creep resistance (stress to produce 0.1% strain at 100 h) of this alloy is well above 90 MPa at 175°C and approaches 90 MPa at 200°C. This significant improvement in tensile and creep properties is associated with a uniform and dense distribution of basal precipitate plates (Fig. 6.28) that do not form in binary Mg–Gd alloys.

The precipitation process in Mg–Gd–Zn alloys at 200–250°C involves the formation of metastable γ'' and γ' phases (Table 6.5) and the peak hardness

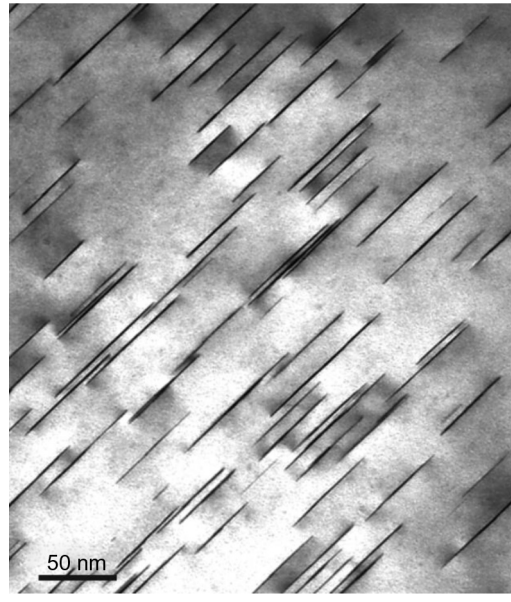


Figure 6.28 Transmission electron micrograph showing precipitate plates in Mg–6Gd–2Zn–0.6Zr alloy aged 3.5 h at 250°C. From Nie, JF *et al.*: *Scr. Mater.*, 53, 1049, 2005.

of Mg–Gd–Zn alloys is associated with the γ″ precipitates. Both these phases form as plate-shaped particles on the basal plane of the magnesium matrix. Most precipitates in the peak-aged condition are γ″ that has an ordered hexagonal structure, and an $Mg_{14}Gd_3Zn_3$ composition. The thickness of the γ″ plates is often of a single unit cell height. This phase is fully coherent with the matrix in its habit plane, but with a relatively large negative misfit strain in the normal direction. GP zones have been reported to form in Mg–11.5Gd–2.4Zn and Mg–8.8Gd–2.4Zn alloys, but latest studies suggested that these are actually the γ″ precipitate.

Continued ageing at 250°C leads to gradual replacement of γ″ by γ′ which has a disordered hexagonal structure and MgGdZn composition. The γ′ plates are perfectly coherent with the matrix phase in their habit plane and in the direction normal to their habit plane. Their thickness is always of a single unit cell height, and their aspect ratio is considerably larger than that of γ″. The γ′ phase is also a metastable phase, but it is remarkably resistant to thickening during isothermal ageing at 250°C. For example, it is still less than 1 nm in thickness and remains the dominant precipitate phase in the microstructure after 1000 h ageing at 250°C.

6.4.4 Alloys based on the magnesium–silver system

The importance of this class of alloys stems from the discovery by Payne and Bailey that the relatively low tensile properties of age-hardened Mg–RE–Zr alloys could be much increased by the addition of silver. Room-temperature tensile properties were obtained which were similar to those of the high-strength Mg–Zn–Zr alloys, such as ZK51, with the experimental alloys having superior casting and welding characteristics. Substitution of normal cerium-rich misch-metal with didymium misch-metal (average composition 80%Nd, 16%Pr, 2%Gd, 2% others) gave a further increase in strength which was attributed to the presence of neodymium. Several commercial compositions were subsequently developed having tensile properties which exceeded those of any other magnesium alloys at temperatures up to 250°C, and were comparable to the high-strength aluminium casting alloys.

The most widely used alloy has been QE22 (Mg–2.5Ag–2RE(Nd)–0.7Zr) for which the optimal heat treatment is: solution treatment for 4–8 h at 525°C, cold-water quench, age 8–16 h at 200°C. If these alloys contain less than 2% silver, the precipitation process appears to be similar to that occurring in Mg–RE alloys and involves the formation of Mg–Nd precipitates. However, for higher silver contents, this element apparently modifies precipitation and increases the volume fraction of particles that are formed (Fig. 6.29). The precipitation process in these alloys has not been clearly established, although two independent precipitation processes have been reported, both of which lead ultimately to the formation of an equilibrium phase of probable composition $Mg_{12}Nd_2Ag$. Maximum age hardening and creep resistance are associated with the presence of nano-precipitates in the microstructure.

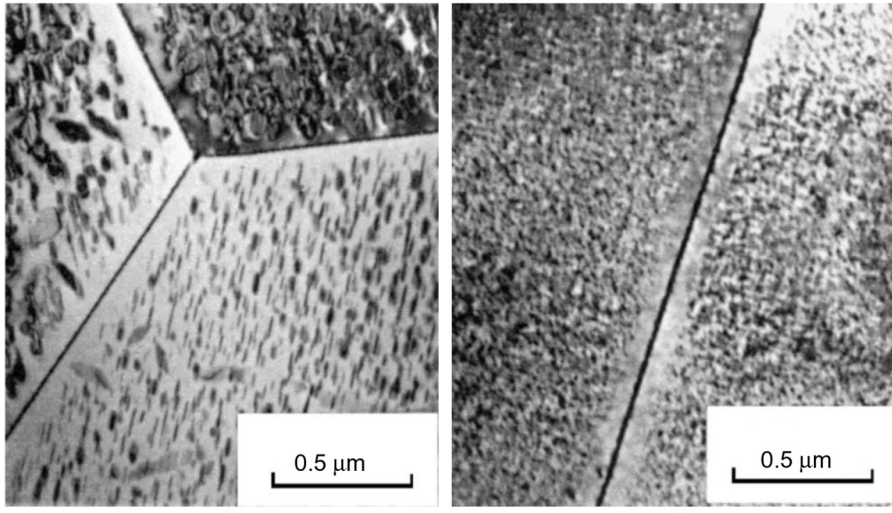


Figure 6.29 Thin-foil electron micrographs showing the effect of silver on precipitate size in Mg–RE(Nd)–Zr alloys aged to peak hardness at 200°C: (A) EK21 (Mg–2.5RE(Nd)–0.7Zr) and (B) QE22 (Mg–2.5Ag–2RE(Nd)–0.72Zr). Courtesy K. J. Gradwell.

Alloy QE22 has been used for a number of aerospace applications, e.g., aircraft landing wheels, gearbox housings, and helicopter rotor fittings. Its superior tensile properties over most magnesium alloys are maintained to 250°C (Fig. 6.21) although it is only considered to be resistant to creep at temperatures up to 200°C. The alloys are relatively expensive and attempts have been made to replace at least some of the silver with copper. This work has met with some success despite the relatively low solubility of copper in magnesium (maximum of 0.55% at the eutectic temperature) although no practical alloys have so far been produced.

Mg–Gd–Zr and Mg–Y–Zr alloys with gadolinium or yttrium less than 6 wt% are not age hardenable during isothermal ageing at 200–250°C. Recent studies have indicated that the addition of silver to these alloys can generate a remarkable age hardening response for silver concentrations at and above 2 wt%. While the hardening effect can be further enhanced if a small concentration of zinc is also added to the Mg–Gd–Zr alloys, the addition of zinc does not appear to affect the age hardening response of Mg–Y–Zr alloys. The enhanced hardening response is associated with a dense distribution of nanoscale basal precipitate plates of γ''. These nanoscale precipitate plates appear similar to those in the Mg–Gd–Zn, Mg–Ce–Zn, Mg–Nd–Zn, and Mg–Ca–Zn alloys. With prolonged ageing at elevated temperatures, these γ'' plates are gradually replaced by γ' and 14H. The γ' phase has a structure that is similar to that in Mg–Gd–Zn alloys. It is relatively stable during isothermal ageing at 350°C. The temperature range 300–350°C is probably above the solvus line of γ'' but below the solvus line of γ'.

6.4.5 Alloys based on the magnesium–thorium system

It has been known for some time that additions of thorium also confer increased creep resistance to magnesium alloys and cast and wrought compositions were developed for service at temperatures as high as 350°C (Figs. 6.21 and 6.22). As with the RE elements, thorium improves casting properties and, in the as-cast condition, the ternary alloy HK31 (Mg–3.2Th–0.7Zr) has a microstructure similar to the Mg–RE–Zr alloys. Thorium-containing alloys are normally given a T6 ageing treatment and investigations of the precipitation processes have also revealed similarities with those for the Mg–RE–Zr alloys. Although GP zones are likely to occur at low temperatures, none have been identified and the precipitation sequence has been described as:

$$\text{SSSS} \rightarrow \beta'' \rightarrow \beta' \rightarrow \beta(Mg_{23}Th_6)$$

The phase β'' has an ordered $D0_{19}$ structure and occurs as thin disks which are coherent with the matrix. There is dispute as to whether the formula of this compound is $MgTh_3$ or Mg_3Th, although the latter would provide the low-energy interfaces with the matrix. This phase may transform directly to the equilibrium β phase although two semi-coherent polymorphs β'_1 and β'_2 have been detected which form on dislocation lines in cold-worked alloys. The presence of zirconium directly favors the formation of one or both of these phases as they precipitate on dislocations generated around zirconium-containing compounds. All these phases, as well as the equilibrium precipitate, appear to be resistant to coarsening at temperatures up to 350°C.

Again, in parallel with alloys based on the Mg–RE system, thorium-containing alloys have been developed to which zinc has been added, e.g., HZ32A (Mg–3Th–2.2Zn–0.7Zr). The addition of zinc further increases creep strength (Fig. 6.22) and a Th:Zn ratio of 1.4:1 appears to be optimal in this regard. Zinc promotes formation of an acicular phase in grain boundaries and the good creep properties of alloy HZ32 are attributed, at least in part, to the presence of this phase.

Thorium-containing alloys were used in early missiles and spacecraft but they are now generally considered obsolete for environmental reasons. In England, alloys having as little as 2% of thorium are classified as being radioactive and therefore require special handling procedures which increases the complexity and cost of manufacturing products.

6.5 WROUGHT MAGNESIUM ALLOYS

6.5.1 Introduction

Interest in wrought magnesium alloys peaked in the 1930s and 1940s when significant amounts were used in military aircraft. For example, magnesium alloy sheet was once used for some 50% of the fuselage of two large American

bombers amounting 5500 kg in weight. Seven hundred kilograms of forgings were also used. Since then there has been very little interest in wrought alloys which have consumed less than 1% of the annual output of magnesium metal. The largest application of flat products has been for AZ31 (Mg–3Al–1Zn–0.3Mn) alloy photoengraving plate because of the high reactivity of magnesium to acid etching, whereas sacrificial anodes for cathodic protection of steel structures has been the main extruded product. Only recently has there been a large-scale, global interest in developing new wrought products and this has been stimulated mainly by the potential applications in the automotive industry.

Because of its hexagonal crystal structure, magnesium possesses fewer slip systems than fcc aluminium which restricts its ability to deform, particularly at low temperatures. At room temperature, deformation occurs mainly by slip on the basal planes in the close-packed $<11\bar{2}0>$ directions and by twinning on the pyramidal $\{10\bar{1}2\}$ planes (Fig. 6.1). With stresses parallel to the basal planes, twinning of this type is only possible in compression whereas, with stresses perpendicular to the basal planes, it is only possible in tension. Above about 250°C, additional pyramidal $\{10\bar{1}1\}$ slip planes become operative so that deformation becomes much easier and twinning is less important. Production of wrought magnesium alloy products is, therefore, normally carried out by hot working.

Currently wrought materials still account for only about 1% of magnesium consumption and are produced mainly by rolling, extrusion, and press forging at temperatures in the range 300–500°C. Rolling is usually required to be carried out in a number of stages, and extrusion speeds are five to ten times slower than is possible with aluminium alloys. Some general remarks can be made concerning the way properties vary in different directions in the final wrought products.

1. Since the elastic modulus does not show much variation in different directions of the hexagonal magnesium crystal, preferred orientation has relatively little effect upon the modulus of wrought products.
2. Rolling tends to orient the basal planes parallel to the surface of sheet with the $<10\bar{1}0>$ directions in the rolling direction (RD). Extrusion at relatively low temperatures tends to orient the basal planes and also the $<10\bar{1}0>$ directions approximately parallel to the direction of extrusion.
3. Because twinning readily occurs when compressive stresses are parallel to the basal plane, wrought magnesium alloys tend to show lower values of longitudinal proof stress in compression than in tension. The ratio may lie between 0.5 and 0.7 and, since the design of lightweight structures involves buckling properties which, in turn, are strongly dependent on compressive strength, the ratio is an important characteristic of wrought magnesium alloys. The value varies with different alloys and is increased by promoting fine grain size because the contribution of grain boundaries to overall strength becomes proportionally greater.

4. Strengthening of wrought products by cold-reeling in which alternate tension and compression occurs can cause extensive twinning through compression, with a marked reduction in tensile properties.

As with cast alloys, the wrought alloys may be divided into two groups according to whether or not they contain zirconium. However, it is proposed here to consider the alloys with regard to the form of the wrought product. Compositions and mechanical properties are summarized in Table 6.4. Discussion of the ageing behavior is included only where the compositions differ significantly from the cast alloys.

Wrought thorium-containing alloys such as HM21 (Mg–2Th–0.8Mn) have been used for manufacturing missile and spacecraft components which require creep resistance at temperatures up to 350°C. However, as mentioned earlier, these alloys are now considered to be obsolete for environmental reasons.

6.5.2 Sheet alloys

At one stage there was only one company worldwide that was producing sheet on a commercial scale. Now a German company is producing thick plate and sheet with a minimum thickness of 1 mm to a width of 1850 mm. Magnesium alloy sheets are produced by stages including casting, homogenization, machining, and repeated hot rolling. Some may also undergo cold rolling, annealing, or an ageing treatment at the end of hot rolling. Slabs for hot rolling are usually produced by direct chill casting. They are homogenized for up to 24 h in the temperature range 300–500°C, depending on alloy composition. The purpose of the homogenization treatment is to dissolve intermetallic particles resulting from the casting process and to achieve a uniform distribution of alloying elements. After the homogenization treatment, the slabs are machined to certain sizes and then hot rolled. Hot rolling is initially carried out in a reversing breakdown mill at temperatures 300–500°C with a typical thickness reduction of 10% per pass to avoid any cracking. Several intermediate reheats are often necessary due to the low volumetric heat content of magnesium and the relatively limited process window of hot rolling. Apart from the primary aim of thickness reduction, the initial stage of hot rolling schedule also serves to break down the original coarse microstructure into fine grains by dynamic recrystallization. This is possible because the hot rolling temperature is usually above the recrystallization temperature of the processed alloy. Finishing rolling is usually carried out at lower temperatures to achieve the best combination of surface quality, dimensional accuracy, and mechanical properties. Some alloys are cold rolled at final gauge, but the thickness reduction is generally less than 5%.

The rollability and formability of magnesium alloy sheet is significantly influenced by hot rolling parameters, such as temperature, thickness reduction per pass, rolling speed, and alloy composition. At higher temperatures, more deformation modes such as non-basal slip and $\{10\bar{1}1\}$ twinning become

activated and operative during hot rolling process (Section 6.1). These additional deformation modes, combined with an accelerated dynamic recrystallization process and grain growth, give rise to better rollability of magnesium sheet. The higher-temperature hot rolling also leads to weaker basal texture by spreading the basal poles more broadly along the sheet RD. The weaker texture, in turn, results in improved stretch formability and plastic anisotropy. For example, AZ31 sheet rolled at 450°C has higher stretch formability and lower plastic anisotropy than that rolled at 390°C.

A larger thickness reduction per pass leads to a higher degree of plastic deformation, which, in turn, leads to finer sizes of recrystallized grains and more homogeneous microstructure. The finer recrystallized grains are caused by increased nucleation rate of recrystallization in the highly strained state. A weaker basal texture may also be generated with a larger rolling reduction which also usually generates a larger fraction of shear bands. These shear bands are highly strained regions where more randomly oriented grains nucleate and therefore weaker texture may develop.

Increased rolling speeds lead to a significant improvement of rollability. For example, it has been reported that ultra-high speed rolling in the range of 450–2000 m min^{-1} can result in a remarkable improvement in the rollability of the alloy AZ31. At such high speeds, the sheet thickness reduction per pass can be increased up to 60% without surface cracking, even when rolling is done at relatively low temperatures (200–350°C). However, these rolling speeds are too fast to be of practical use in an industrial hot rolling plant. A larger thickness reduction per pass (~80%) is possible for alloy ZK60 at a rolling speed of 26 m min^{-1} and in the range of 250–400°C. The improved rollability at high rolling speeds is attributed to the activation of more deformation modes at higher strain rates together with the occurrence of dynamic recrystallization.

The as-cast or homogenized microstructures are usually destroyed after repeated deformation and recrystallization. However, they may be partially inherited in the final microstructure if the number of rolling reduction is relative low, especially for twin-roll cast strips.

Mg–Al based alloys The early sheet alloy was AZ31, and is still the most widely used magnesium alloy for applications at room or slightly elevated temperatures. AZ31 is strengthened by strain hardening and is weldable, although weldments should be stress-relieved to minimize susceptibility to stress–corrosion cracking (SCC).

Mg–Zn based alloys Higher room-temperature properties can be obtained with the British alloy ZK31 (Mg–3Zn–0.7Zr) but weldability is limited. Three lower strength alloys ZM21 (Mg–2Zn–1Mn), ZE10 (Mg–1.2Zn–0.2RE), and ZEK100 (Mg–1.4Zn–0.1RE–0.1Zr) are weldable and do not require stress relieving. ZE10 has the highest toughness of any magnesium sheet alloy. In recent years, a number of experimental alloys have been developed based on

the Mg–Zn system, including Mg–1.5Zn–0.2Ce and Mg–1.5Zn–0.1Ca (wt%). The addition of small amounts of RE elements or calcium to Mg–Zn alloys weakens the basal texture and thus improves sheet formability. These alloys exhibit superior stretch formability that is even comparable to that of 6000 series aluminium alloys. However, they have not been commercialized because of their low strength properties. A recent study indicates that annealing of plastically deformed Mg–0.8Zn–0.2Ca alloy can lead to remarkable strengthening, rather than softening. The strengthening increment is more than 20% of the yield strength of the original sheet and may arise from the pinning of gliding dislocations by GP zones and solute atoms that might have segregated there during the annealing treatment. Note that annealing of strain-free sheet of the same alloy in the same temperature range has no strengthening effect, i.e., this alloy is not age hardenable in this condition. Mg–Zn–Ca alloys with zinc content more than 1.5 wt% do become age hardenable. The combination of better rollability, weakened basal texture, age hardenability, and low-cost renders these alloys an interesting prospect for commercial sheet development.

Mg–Mn based alloys Three commercial alloys have been developed based on the Mg–Mn system: MlA (Mg–1.5Mn), ME20 (Mg–2Mn–0.5Ce), and ME21 (Mg–2Mn–0.7Ce). The M1A alloy is now little used although sheet of ME21 alloy is sometimes produced by extrusion through a die rather than by rolling. Raising the manganese content increases strength as well as improving corrosion resistance and weldability. The addition of RE elements also improves the formability by weakening the basal texture although these alloys have so far found only limited applications.

Mg–Li based alloys The Mg–Li system has attracted attention for many years as a possible basis for very lightweight sheet and plate. Lithium with a relative density of 0.53 g cm^{-3} is the lightest of all metals and the Mg–Li phase diagram (Fig. 6.30) shows this element to have extensive solid solubility in magnesium. Moreover, only about 11% lithium is needed to form a new β phase, which has a body-centered cubic (bcc) structure, thereby offering the prospect of extensive cold formability. The slope of the (α + β)/β phase boundary suggests that selected compositions may show age hardening. Early work on binary alloys revealed that traces of sodium caused grain boundary embrittlement but this problem was overcome with the availability of high-purity lithium. A second difficulty was that the binary alloys became unstable and overaged at slightly elevated temperatures (50–70°C) resulting in excessive creep under relatively low loads. Greater stability has since been achieved by adding other elements and one composition LA141 (Mg–14Li–1Al), which was developed in the United States and is weldable, has been used for armor plate and for aerospace components. Elevated temperature stability can also be improved by the addition of 0.5% Si. A number of wrought alloys were developed in Russia including two designated MA18 and MA21 that were registered in 1983.

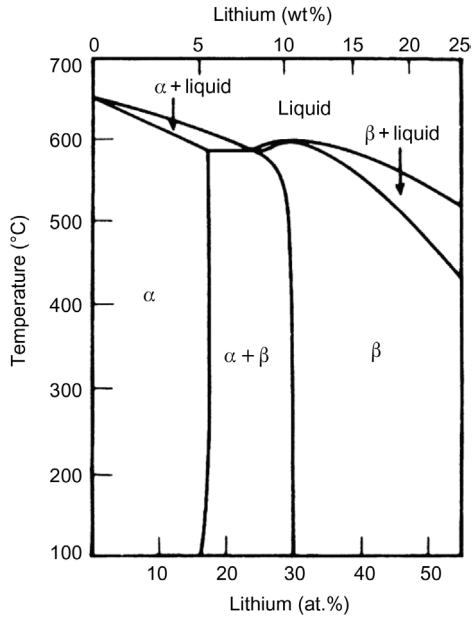


Figure 6.30 Section of binary Mg–Li equilibrium diagram. From Freeth, WA and Raynor, GV: *J. Inst. Metals*, 82, 575, 1953–54.

MA18 (Mg–10.8Li–2.25Zn–0.75Al–0.25Ce) has a bcc lattice, whereas MA21 (Mg–8.75Li–4.8Al–4.5Cd–1.5Zn–0.08Ce) has a mixed hcp/bcc structure. These alloys are also weldable and some properties are summarized in Table 6.10.

Minimum strength properties in Table 6.10 concern large forgings, die forgings, and extruded bars, whereas maximum properties are for warm rolled thin sheets and other thin shapes and tubes. Billets weighing up to 3 tonnes have been cast in special gas shielded melting facilities.

Sheet texture Hot rolled sheets of conventional alloys such as AZ31 and ZM21 exhibit strong basal texture, with a preferred orientation of basal planes parallel to the sheet plane (Fig. 6.31A). The strong basal texture leads to unsatisfactory formability at or near to room temperature, and therefore considerable efforts have been made to weaken the basal texture. It is now known that dilute additions of calcium or RE elements can weaken the basal texture after recrystallization. However, they do not cause any texture weakening effect during cold rolling. They only delay the development of a strong basal texture by reducing the growth of deformation twins.

Magnesium alloys containing RE elements do not tend to form a strong basal textures during hot or warm rolling. Increased concentrations of such RE elements up to even 0.1 at.% in magnesium lead to a spread of basal poles along

Table 6.10 Properties of the Russian alloys MA18 and MA21

Alloy	Density ($g\,cm^{-3}$)	0.2% Proof stress (MPa)	Tensile strength (MPa)	Elongation (%)	Elastic modulus (GPa)
MA18	1.48	90–180	140–210	10–30	45–46
MA21	1.60	130–220	200–260	6–20	45–46

From Elkin FM and Davydov, VG: *Proc. of 6th Inter. Conf. on Magnesium Alloys and Their Applications*, Wiley-VCH, p. 94, 2004.

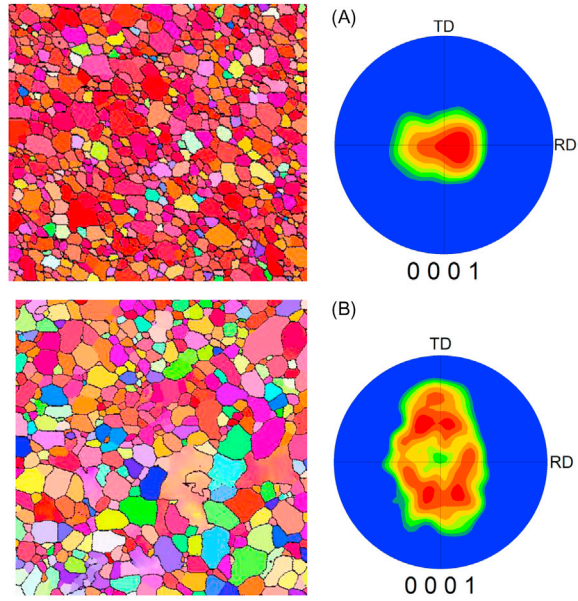


Figure 6.31 Electron backscatter diffraction orientation maps and (0002) pole figures showing microstructures and corresponding textures of annealed (A) AZ31 and (B) Mg–0.8Zn–0.2Ca alloy. Courtesy Z. R. Zeng.

the RD. The combined additions of RE elements and zinc, or calcium and zinc, give rise to a further weakened but different texture in which the basal poles are tilted along the transverse direction (TD) (Fig. 6.31B).

The weakened recrystallization texture in magnesium alloys containing RE elements or calcium has been proposed to be related to particle stimulated nucleation (PSN), shear band induced nucleation (SBIN) (Fig. 2.4), deformation twin induced nucleation (DTIN), and the more uniform growth of recrystallized grains with randomized orientations. In studies of recrystallization behaviors of aluminium alloys, second-phase particles were observed, and PSN was subsequently postulated to be the cause of weakened texture in these alloys. In magnesium alloys, particles have been reported to provide heterogeneous nucleation sites

for recrystallized grains with randomized orientations, which results in a weakened recrystallization texture. However, subsequent studies have suggested that the texture weakening is not caused by second-phase particles, because texture weakening is also observed in magnesium alloy sheet that contains essentially no second-phase particles.

In plastically deformed and annealed magnesium alloys, recrystallized grains formed inside shear bands also have relatively randomized orientations, and the growth of these grains leads to a weakened basal texture. Because a large fraction of shear bands was often observed after plastic deformation of RE-containing magnesium alloys, SBIN has been considered to be critical for the occurrence of weakened texture. However, shear bands are also observed in RE-free magnesium alloys, but these alloys have a strong recrystallization texture.

Deformation twins have been reported to provide heterogeneous nucleation sites for recrystallized grains in magnesium alloys. DTIN is based on the assumption that twins can act as nucleation sites for recrystallized grains with randomized orientations. It has been reported that RE additions promote more deformation twins, which provide more nucleation sites for recrystallized grains with randomized orientations. It has also been suggested that DTIN is important to the development of weakened recrystallization texture in RE-containing alloys. However, it is to be noted that the recrystallized grains that have nucleated inside twins do not grow beyond the twin size. It is for this reason that the effectiveness of DTIN on texture weakening is likely to be limited.

Recent studies indicate that $<11\bar{2}0>$ recrystallized grains, defined as those whose $<11\bar{2}0>$ axes are nearly parallel to the RD and *c*-axes are almost parallel to the *c*-axes of the deformed parent grains, grow preferentially during recrystallization in AZ31 and some binary Mg–Zn and Mg–Ca alloys. Because of the preferential growth of the $<11\bar{2}0>$ grains at the expense of grains with other orientations, the resultant recrystallization texture is dictated by the orientations of these $<11\bar{2}0>$ grains. Since in the cold-rolled condition, most deformed grains have their *c*-axis parallel to the normal direction of sheet, and the $<11\bar{2}0>$ grains that nucleate during recrystallization inherit the *c*-axis orientations of their parent grains, the strong basal texture of the cold-rolled sample is subsequently preserved by the preferential growth of the $<11\bar{2}0>$ grains.

The preferential growth of recrystallized $<11\bar{2}0>$ grains is suppressed in some Mg–Zn–Ca alloys, where uniform growth of recrystallized grains occurs and hence a weakened basal texture is obtained. The suppression of the preferential grain growth is most likely to be related to the preferential segregation of calcium and zinc atoms to high-energy boundaries of $<11\bar{2}0>$ grains that would otherwise grow preferentially during recrystallization. The phenomenon of solute segregation to grain boundaries has been found in a number of magnesium alloys. It is possible that high-energy grain boundaries have a stronger solute segregation than low-energy grain boundaries and that it is the stronger

segregation of calcium and zinc atoms in the grain boundaries of the $<11\bar{2}0>$ grains that eliminates their preferential growth. It is generally expected that high-energy boundaries would have a stronger solute segregation than low-energy boundaries. Stronger solute segregation would lead to more significant reduction in the grain boundary energy and hence larger reduction in grain boundary mobility. The solute segregation also exerts a drag effect on grain boundary migration, and therefore, the preferential solute segregation to the high-energy boundaries is likely to exert a stronger drag effect, which gives rise to a greater pinning force to grain boundary migration.

Sheet anisotropy One of the major issues of magnesium sheets is the anisotropy of their mechanical properties. Table 6.11 provides tensile properties of ZEK100 sheets tested along the RD, TD, and at 45° to the RD. The change in tensile properties along different directions is related to the sheet texture and the relative ease of plastic deformation along these directions. Sheet anisotropy is influenced greatly by alloying additions, even for the similar alloy systems. For example, ZEK100 sheet with different RE additions have quite different levels of anisotropy after warm rolling and annealing (Table 6.11). The yield stress obtained along the RD is much higher than that obtained from the TD. The ductility is lowest for the RD and greatest for the TD in all alloys, except for the cerium-containing alloy. The highest ductility, together with an ultimate

Table 6.11 Room-temperature tensile properties of warm rolled and annealed ZEK100 sheet

Alloys	Orientation	TYS (MPa)	UTS (MPa)	TYS/UTS	Elongation to failure (%)
	Rd	131	234	0.56	17
Ce series	45	110	237	0.46	23
	TD	115	222	0.52	13
	Rd	123	241	0.48	23
La series	45	108	240	0.42	25
	TD	96	243	0.34	25
	Rd	111	243	0.46	28
Nd series	45	101	234	0.43	28
	TD	84	238	0.35	29
	Rd	88	229	0.38	29
Gd series	45	78	227	0.34	30
	TD	66	233	0.28	32
	Rd	131	233	0.56	19
MM series	45	108	243	0.49	25
	TD	99	247	0.43	25

From Al-Samman, T and Li, X: *Mater. Sci. Eng. A*, 528, 3809, 2011.
TYS, tensile yield stress at $\varepsilon = 0.2\%$.

tensile strength (UTS) of 233 MPa, is achieved in the gadolinium-containing sheet that was tested along the TD. The Nd addition leads to isotropic ductility: 0.28 for the RD and 45° direction, and 0.29 for the TD.

The addition of light RE elements such as cerium, lanthanum, neodymium, or misch-metal leads to a weak basal texture that is characterized by a broad scattering of basal poles toward the sheet TD. In contrast, the gadolinium addition gives rise to a different type of RE texture, which is characterized by a soft off-basal orientation with even lower intensity. Because of this unique sheet texture, a remarkable improvement in the room temperature ductility is achieved in the gadolinium-containing sheet despite the coarsest grain size relative to the other RE-containing alloys.

Sheet formability Sheet forming process involves stretch forming and deep drawing in which magnesium sheet undergoes a variety of strain paths. Stretch forming and deep drawing are often used to obtain information about specific features of the sheet formability. Fig. 6.32 shows the stretch formability of different magnesium alloys measured by the Erichsen cupping test at room temperature, which is indicated by limiting dome height (LDH) values. The stretch formability of magnesium alloys containing RE elements, lithium or calcium, as well as the texture-modified AZ31 alloy, is better than or comparable to those of 5xxx and 6xxx aluminium sheet alloys at a similar strength level. In general, the stretch formability of those magnesium alloys that have low yield strengths

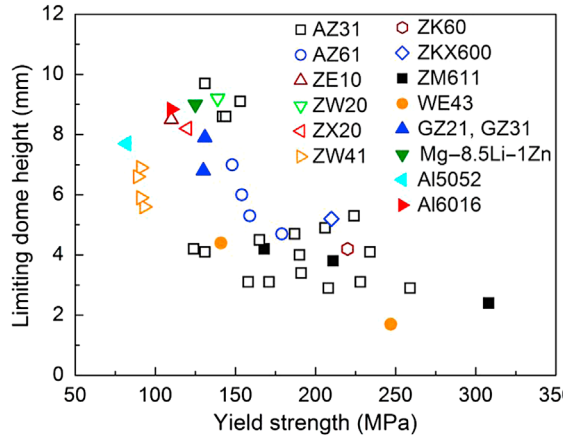


Figure 6.32 Room-temperature longitudinal yield strength and LDH of representative magnesium sheet alloys. From Suh, BC *et al.*: *Scr. Mater.*, 84–85, 1, 2014; Bhattacharjee, T *et al.*: *Mater. Sci. Eng. A*, 609, 154, 2014; Schneider, R *et al.*: *IOP Conf. Series: Mater. Sci. Eng.*, 74, 012014, 2015.

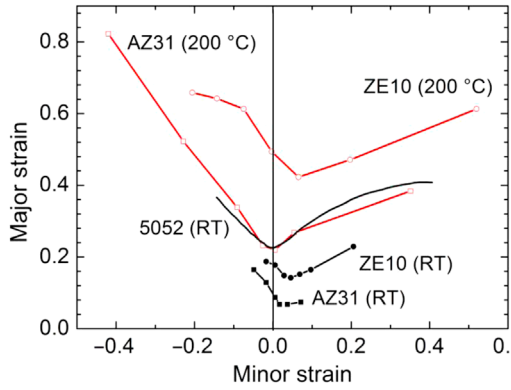


Figure 6.33 Forming limit diagram for sheets of AZ31, ZE10, and aluminium alloy 5052. AZ31 and ZE10 are tested at room temperature (RT) and 200°C. From Stutz, L *et al.*: *Magnesium Technology 2011*, p. 373, TMS, USA, 2011 and Australian Aluminium Council.

(100–170 MPa) is comparable to that of some commercial aluminium alloys (LDH ≈ 7–11), but higher-strength magnesium alloys exhibit poor stretch formability.

Forming limit curves for annealed sheets (1.5 mm thick) of AZ31 and ZE10 alloys, tested at a speed of 1 mm s^{-1} and at room temperature and 200°C, are shown in Fig. 6.33. For the purpose of comparison, the forming limit curve for the annealed sheet of the Al–Mg–Mn alloy 5052 is also shown in the figure (Section 2.1.3). Both magnesium alloys have equiaxed recrystallized grains of approximately 10 μm in diameter. AZ31 has a strong basal texture, while ZE10 has a weakened basal texture with basal poles spreading along the TD. Sheets of these two alloys have forming characteristics that are inferior to the aluminium alloy sheet at room temperature. The formability of AZ31 at room temperature is very poor. An increase of testing temperature to 200°C leads to a significant increase in formability under strain paths of both negative and positive minor strains. The ZE10 alloy has a better formability than AZ31 at both room and elevated temperatures under conditions of plane-strain and biaxial stretching. It also has a better deep drawability than AZ31. Testing results from other temperatures such as 150°C and 250°C indicate that the formability of ZE10 at room temperature is even higher than AZ31 at 150°C under the condition of plane-strain or biaxial stretching.

While ZE10 has better formability, it has a greater susceptibility to earing than AZ31. It is unclear whether this problem is related to its low Lankford value (r). In general, low R values tend to increase the tendency to fracture around the cup corner and are not beneficial for deep drawing. The problem may also be related to the rather complex stress states occurring during deep drawing, which may result in operation of various deformation and failure modes depending on the alloy microstructure. Apart from the failure near the cup corner, failure also occurs frequently near the top of the cup, especially in

alloys with a strong basal texture and strong tension–compression asymmetry. This has been attributed to bending/unbending-induced twinning/detwinning near the die radius during deep drawing. The relationship between drawability and R value is not straightforward, but it is generally accepted that magnesium alloys with random texture and accompanying low-planar anisotropy have better drawability at room temperature. Lower R values also correlate with better stretch formability.

The formability of magnesium sheet can be improved by high-temperature hot rolling, reverse rolling (reversing the sheet direction after each rolling pass), or cross rolling. For example, reverse-rolled AZ31 sheet has more isotropic mechanical properties than unidirectionally rolled sheets due to its more homogeneous grain structure. Cross rolling of AZ31 sheet leads to a weakened basal texture and enhanced formability.

Only limited cold forming can be carried out with sheet alloys and typical minimum bend radii vary from 5 to 10T, where T = thickness of sheet, for annealed material, and from 10 to 20T for the hard-rolled condition. Thus, for even simple operations, hot forming within the temperature range 230–350°C is preferred. Under these conditions sheet can be formed by pressing, deep drawing, spinning, and other methods using relatively low-powered machinery. A number of deep drawn automotive sheet panels in alloys such as AZ31 have been produced for prototype testing. Indicative weight savings are 50% compared with the same panels made from steel, and 15% when compared with aluminium. This alloy has also been shown to exhibit superplasticity if processing is carefully controlled. If the overall cost of producing magnesium alloy sheets can be reduced, this feature may offer unique opportunities for forming complex automotive body panels.

6.5.3 Extrusion alloys

During the past 15 years, considerable research efforts have been made worldwide to develop magnesium extrusions for automotive applications, but the current usage of these products is still very low. This is mainly because the productivity of magnesium alloy extrusions is much lower than that of aluminium alloys and hence the cost is higher. Furthermore, the extruded magnesium products often have tension–compression yield asymmetry: the compressive yield strength may be only half of the tensile yield strength (Fig. 6.34). Such problems have to be solved for any larger usage of magnesium extrusion alloys.

As with aluminium alloy extrusions, magnesium alloy extrusions are produced by stages of melting, alloying, casting, homogenization, extrusion, and stretching. Some may also undergo an ageing treatment at the end of processing. Billets for extrusion are traditionally produced by direct chill casting, and their diameters vary from 150 to over 550 mm. After being cut into the required length, the billets are homogenized, preheated to 300–450°C, then extruded into solid or hollow profiles of various shapes by direct, indirect, or

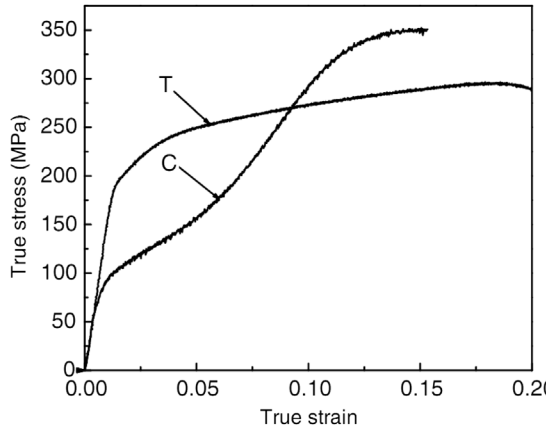


Figure 6.34 Tensile and compressive stress–strain curves of extruded AZ31 (T and C represent tension and compression, respectively, along the extrusion direction). From Yin, SM *et al.*: *Scr. Mater.*, 58, 751, 2008.

hydrostatic extrusion. Direct extrusion is most commonly used by the manufacturing industry. In this process, the billet temperature is 25–50°C below the operation temperature. After extrusion, the profiles must be straightened in the extrusion direction to meet requirements of straightness and twist tolerances. The stretching operation is generally carried out in the range 200–300°C, but can be applied at room temperature to improve mechanical properties of the extruded products. For example, the application of a 0.5% stretch can increase the tensile yield strength of ZK60A alloy from 239 to 264 MPa without affecting the ductility. Age hardenable alloys are usually cooled rapidly by forced air after exiting the die and subsequently artificially aged in the range 100–200°C to further increase their strength. AZ alloys containing a low amount of alloying elements are used in the as-extruded state. Products of AZ80A and ZK60A alloys are normally treated to a T5 condition. ZK60A, WE43, and WE54 alloys can be fully heat treated by applying a T6 cycle (Fig. 4.14). The influence of different T5 tempers on a ZK60A profile is given in Table 6.12.

The extrudability of magnesium alloys is usually measured by the speed of the operation, which, itself, depends on the temperature, extrusion ratio, and alloy composition. It may vary between 0.5 and 30 m min^{-1}. While an extrusion speed approaching 30 m min^{-1} is possible for basic shapes with lower extrusion ratios, or for low-strength alloys, it may drop by a factor of 10 or more for complex shapes with higher extrusion ratios, or for high-strength alloys. In general, the extrusion speed for magnesium alloys is five to ten times lower than those used for most aluminium alloys, and the operation needs to be carried out at a higher pressure. In addition to the higher cost of billets, the extruded magnesium profiles are more expensive than comparable aluminium sections. The

Table 6.12 Influence of heat treatment on tensile properties of extruded profiles of ZK60A

Alloy	Heat treatment cycle	UTS (MPa)	YS (MPa)	*E* (%)
ZK60A-F	As-extruded	288	238	6.5
ZK60A-T5	150°C/24 h air quenched	345	281	2.8
ZK60A-T5	200°C/16 h furnace cooled	289	244	5.2
ZK60A-T5	400°C/8 h furnace cooled	248	191	14.6

From Closset, B: *Magnesium Technology*, Springer, p. 289, 2006.

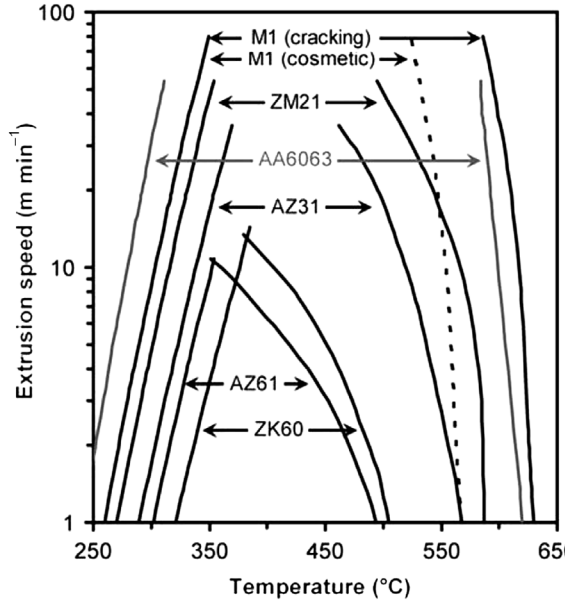


Figure 6.35 Comparison of extrusion limits for different magnesium alloys and aluminium alloy AA6063. From Atwell, DL and Barnett, MR: *Metall. Mater. Trans. A*, 38, 3032, 2007.

use of higher extrusion temperatures permits higher speeds and lower pressure, but is often restricted by incipient melting and hot cracking (also known as hot shortness). This is because most magnesium alloys have higher alloying contents that lead to lower solidus temperatures, and hence local melting in the billet may occur during processing at higher temperatures. Hot cracking can also occur at low extrusion temperatures if a magnesium alloy contains low melting point constituents. In this case, the constituents need to be fully dissolved by homogenization heat treatment before the extrusion.

The range of speed and temperature over which a magnesium alloy can be extruded without any visible surface defects constitutes the extrusion limit diagram, also known as the operation or processing window for this alloy. An extrusion limit diagram (Fig. 6.35) provides a convenient way to assess the

extrudability of magnesium alloys. At lower billet temperatures, the limit of the extrusion speed is restricted by the balance between the hot working flow stress of the alloy and the load limit of the press; a lower flow stress permits a higher extrusion speed unless the load limit of the press is reached. At higher billet temperatures, the maximum extrusion speed is limited by the onset of hot cracking on the product surface. The appearance of hot cracking is related to the solidus temperature of the alloy; a higher solidus temperature permits a higher extrusion speed and a higher billet temperature before incipient melting and hot cracking occur on the surface of the product.

Alloy composition is also a crucial factor in controlling extrudability of magnesium alloys. To increase the extrudability, the alloying content needs to be reduced. It has been reported that, by reducing the aluminium content in Mg–Al–Zn alloys from 3% to 1%, the extrusion pressure can be reduced by approximately 11%, while by decreasing the zinc content from 1% to 0%, the extrusion pressure decreases by approximately 4%. The leaner alloy AZ11 has a significantly larger processing window and therefore can be extruded at much higher speeds. A comparison of the extrusion limits of some commercial magnesium alloys and aluminium alloy AA6063 is shown in Fig. 6.35. Under similar processing conditions, such as billet size and extrusion ratio, heavily alloyed AZ61 and ZK60 have very small processing windows, but leaner alloys AZ31 and ZM21 have larger processing windows. Alloy M1 has the leanest composition, and its extrusion limit window is similar to that of AA6063. In general, the extrusion limit window becomes larger when the total alloying content is reduced.

Mg–Al based alloys Mg–Al–Zn extrusion alloys are used with aluminium content between 1% and 8%, the strongest alloy, AZ81 (Mg–8Al–1Zn–0.7Mn) showing some response to age hardening if heat treated after fabrication. Decreasing the aluminium content reduces hot working flow stress and hot cracking susceptibility and thus makes the alloy easier to extrude, but concomitantly it narrows the freezing range and makes the alloy billet more difficult to cast. Therefore, an optimal aluminium content of 3% is used, and AZ31 is often selected as a general-purpose extruded alloy. The extrusion of AZ31 may reach a speed of $20\,\mathrm{m\,min^{-1}}$, which is an order of magnitude higher than that for AZ81. The addition of zinc to the Mg–Al alloys can provide some strengthening, but it lowers the solidus temperature of the alloy and hence increases susceptibility of hot cracking. Alloy AM30, which was developed in recent years without any zinc addition, has better extrudability than its counterpart alloy AZ31. It can be extruded 20% faster and has a 50% increase in room-temperature ductility with similar strength.

Alloys based on the Mg–Al–Zn–Mn–Ca system were reported to have high extrusion speeds and were patented in the 1960s. The aluminium content in these alloys is less than 1.75 wt%, the zinc content is 0.6 wt%, and the calcium content is limited to 0.6 wt%. Extrusion speeds of $15–30\,\mathrm{m\,min^{-1}}$ are possible when either aluminium or calcium is at its maximum concentration

and the others are in relatively low concentrations. These alloys have adequate strength but suffer from tension–compression yield asymmetry (Fig. 6.34). More recently, a leaner alloy with a composition of Mg–0.3Al–0.21Ca–0.47Mn was developed for fast extrusion. With an extrusion ratio of 20:1 and an extrusion temperature of 500°C, this alloy can be extruded at a remarkable speed of $60\,m\,min^{-1}$ without any visible surface defects. The product has a tensile yield strength of 170 MPa and a total elongation of 16%, which are compatible with those of AZ31 extruded at much lower speeds. Unlike AZ31, this alloy responds to age hardening at 200°C. After a T5 temper, the yield strength of this alloy is increased to 207 MPa, with a slight reduction in ductility to 13%. The strength improvement is caused by the formation of single-layer GP zones on the basal plane of the magnesium matrix.

One alloy was specifically developed as a canning material for use in the British gas-cooled Magnox nuclear reactors. This has the composition Mg–0.8Al–0.005Be and the fuel element cans are impact extruded with integral cooling fins, as shown in Fig. 6.36, or machined from a finned extrusion. The spiral shape is obtained by hot twisting after extrusion. The selection of magnesium alloy was made because the metal has a relatively low capture cross section for thermal neutrons (0.059 barns), is resistant to creep and corrosion by the carbon dioxide coolant at the operating temperatures (180–420°C), and, contrary to aluminium, does not react with the uranium fuel. The addition of aluminium provides some solid solution strengthening, whereas the trace amount of beryllium improves oxidation resistance.

Similar to magnesium alloy sheets, magnesium extrusions develop a strong texture during processing, especially for alloys based on the Mg–Al system. During warm or hot extrusion of AZ and AM series alloys, the basal planes of randomly oriented grains are rotated so that they are approximately parallel to the extrusion direction, and the $<10\bar{1}0>$ axes parallel to the extrusion direction. Hence, the products generally have a strong fiber texture. For this type of texture, basal slip is not favored under both tension and compression loading along the extrusion direction. Instead, $\{10\bar{1}2\}$ twinning occurs readily upon compressive loading, and the yield stress is much lower than the tensile yield stress

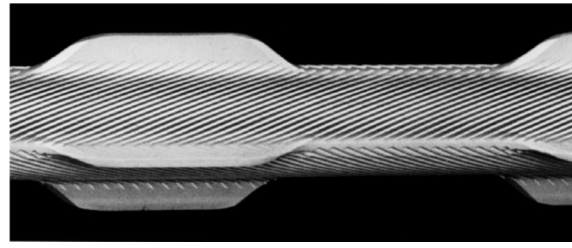


Figure 6.36 Part of extruded magnesium alloy fuel can from a British Magnox nuclear reactor.

Table 6.13 Tensile and compression strengths of extruded bars of magnesium alloys

Alloy	Condition	Tensile (longitudinal)			Compression (longitudinal) 0.2% Proof Stress (MPa)	Tensile (transverse)		
		0.2% Proof Stress (MPa)	Tensile Strength (MPa)	Elongation (%)		0.2% Proof Stress (MPa)	Tensile Strength (MPa)	Elongation (%)
AZ31	F	180	250	14	110	110	225	13
AZ61	F	220	300	12	130	137	294	12
AZ80	F	240	340	10	145	170	323	11
ZK30	T6	240	290	14	190	220	280	16
ZK60	T6	280	320	12	230	250	310	14
WE43	T6	170	260	12	165	165	250	14
WE54	T6	190	280	10	180	185	275	13

From Becker, J *et al.*: *Magnesium Alloys and Their Applications*, DGM, p. 15, 1998; Closset, B: *Magnesium Technology*, Springer, p. 289, 2006.

(Fig. 6.34). The ratio of compressive and tensile strengths may lie between 0.5 and 0.7 and, since the design of lightweight structures involves buckling properties which, in turn, are strongly dependent on compressive strength, this ratio is an important characteristic of wrought magnesium alloys. The ratio varies in different alloys and is increased by promoting fine grain size because the contribution of grain boundaries to overall strength becomes proportionally greater.

The strong basal texture in extruded AZ alloys leads to anisotropic mechanical properties. The tensile yield strength obtained from a direction perpendicular to the extrusion direction is 30–40% lower than that measured in the extrusion direction (Table 6.13). In comparison, the difference for ZK alloys is significantly smaller, particularly when the alloy has a higher alloying content and is in the T6 condition. The commercial magnesium alloys WE54 and WE43 do not suffer from the yield strength anisotropy problem. Their tensile properties are quite uniform when tested along the directions parallel and perpendicular to the extrusion direction.

As crack propagation normal to the basal plane is more difficult than along directions in the basal plane, an extrudate having a precrack normal to the extrusion direction has a higher value of plane-strain fracture toughness than that having a precrack parallel to the extrusion direction. The plain-strain fracture toughness, K_{IC}, of AZ31 is 22 and 16 MPa m$^{1/2}$, respectively, in these two cases. These two values have been obtained for a grain size of approximately 14 μm. The variation of grain size does not seem to cause any substantial change in fracture toughness. For example, the plain-strain fracture toughness value is only changed from 23 to 25 MPa m$^{1/2}$ when the grain size changes from 15 to 4 μm. Table 6.14 provides fracture toughness values of commonly used magnesium and aluminium wrought alloys. Heat treatments lead to a significant reduction in fracture toughness for magnesium alloys.

Table 6.14 Fracture toughness of extruded plat bars of magnesium and aluminium alloys

Alloy	Condition	Fracture toughness K_{IC} [MPa m$^{1/2}$]	
		L–T	T–L
AZ80	F	23	20
AZ80	T6	16	14
AZ61	F	24	20
ZK30	T6	16	16
WE54	T6	16	17
AA6082	T6	36	29
AA7075	T6	29	24

Becker, J *et al*.: *Magnesium Alloys and Their Applications*, DGM, p. 15, 1998; Closset, B: *Magnesium Technology*, Springer, p. 289, 2006.

The fatigue properties of three wrought magnesium alloys are shown in Fig. 6.37. For a similar level of cyclic stress, the fatigue life of ZK60 is considerably longer than AZ31 alloy in both air and 3.5% NaCl solution saturated with $Mg(OH)_2$. It should be noted that extruded magnesium alloys usually have a significantly longer fatigue life than die cast magnesium alloys.

It has been shown recently that it is possible to develop high-strength magnesium extrusion alloys based on the Mg–Al–Ca–Mn system. One experimental alloy has a composition of Mg–3.5Al–3.3Ca–0.4Mn, and it exhibits a tensile yield strength of 410 MPa, a tensile strength of 420 MPa and an elongation to fracture of 5.6% when tested in the as-fabricated condition. The compressive yield strength is 350 MPa, giving rise to a yield asymmetry ratio of 0.83. The tensile yield strength of the as-extruded alloy is approaching that of the Mg–10Gd–5.7Y–1.6Zn–0.7Zr alloy, even though this alloy does not contain any expensive alloying elements and the total alloying content is significantly less than that in the latter alloy. The high strength achieved in this alloy is attributed to a strong basal texture and nanoscale precipitates. The microstructure of this alloy has a mixed distribution of equiaxed recrystallized grains and elongated un-recrystallized grains. The recrystallized grains are approximately 1 μm in size, and their volume fraction is about 68%. The orientations of both recrystallized and un-recrystallized grains lead to low Schmidt factors that make basal slip difficult to occur. The un-recrystallized grains contain nanoscale precipitate plates and spheres. The combined analysis from transmission electron microscopy and three-dimensional atom probe suggests that the plate-shaped precipitates are probably Al_2Ca and the spherical particles are rich in aluminium, manganese, and calcium with a yet to be identified structure. Both types of precipitates form dynamically during hot extrusion at 350°C.

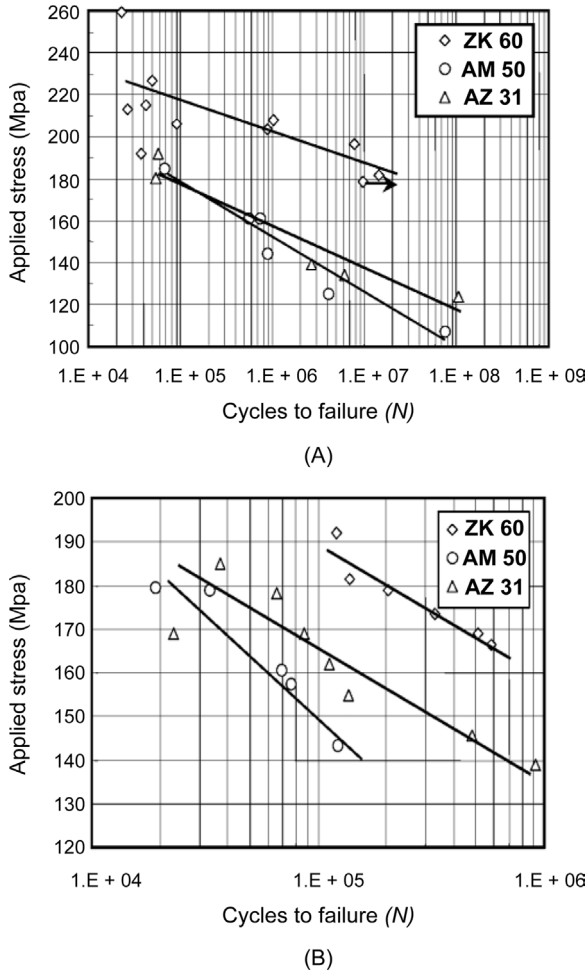


Figure 6.37 σ–N curves for extruded magnesium alloys ZK60, AM50, and AZ31 in (A) air and (B) 3.5% NaCl solution saturated with $Mg(OH)_2$. From Eliezer, A *et al.*: *Mater. Manu Processes*, 20, 75, 2005.

Mg–Zn based alloys A number of commercial alloys have been developed based on the Mg–Zn system. These alloys include ZK60, ZK30, ZMC711, and ZM21. The alloy ZM2l can be extruded at high speeds and is the cheapest magnesium wrought alloy available. Alloy ZMC711 was developed by the Magnesium Elektron in early 1980s as a weldable high-strength extrusion alloy. It has moderate tensile yield strength in the as-fabricated condition. However, in the fully heat-treated condition, this alloy exhibits a tensile yield strength of over 300 MPa together with elongation to fracture of 3% and it was the strongest wrought magnesium alloy at that time. This alloy receives little attention

nowadays due to its poor corrosion resistance. Alloys ZK60 and ZK30 are both grain refined by zirconium. They have good formability due to the fine and uniform as-cast grain size. Adding zirconium increases the extrudability of Mg–Zn alloys. The maximum extrusion speed of Mg–6Zn–0.8Zr alloy is about an order of magnitude higher than that of Mg–6Zn alloy. This is presumably because zirconium increases the solidus temperature of the Mg–Zn alloys. For ZK series alloys, a reduction of the zinc content from 6.8% to 3.8% can increase the extrusion speed by a factor of three. Manganese may also be added to binary Mg–Zn alloys, and a resultant alloy ZM21 can be extruded at speeds up to $20\,m\,min^{-1}$. For Mg–Zn-based alloys with lower zinc contents, the as-extruded microstructures usually contain a mixed distribution of equiaxed fine recrystallized grains and coarse elongated un-recrystallized grains, unless the alloys are extruded at fast speeds or high temperatures. The size and area fraction of the recrystallized grains both increase with an increase in the extrusion speed, leading to a decrease in the yield strength and an increase in elongation.

The Mg–Zn–Ce system has also been used to develop extrusion alloys. Alloys containing higher zinc contents are prone to hot cracking and oxidation during processing and hence they have poor extrudability. The extrudability of these alloys is dramatically increased by decreasing the zinc content. The extrudability of ZE50 alloy approaches that of AZ31. A further decrease in the zinc content leads to even better extrudability. The maximum extrusion speed of ZE20 (Mg–2%Zn–0.2%Ce) alloy is about 25% higher than that of AZ31 when extrusion is carried out at 400°C, and this speed is compatible to that for AM30. The ZE20 alloy has a tensile yield strength of 135 MPa, an UTS of 225 MPa, and a ductility of 27% that is significantly higher than those of AZ31 and AM30.

ZK60 is commonly used in the T5 condition. Its tensile yield strength increases substantially, with some reduction in elongation, after ageing at 150°C. Heat treatments at higher temperatures lead to reduction in strength, even though the elongation to fracture is significantly improved. Alloy ZK60 can also be fully heat treated by applying a T6 cycle. Tensile yield strength after an appropriate T6 treatment is usually higher than that obtained from T5 tempers. Similar to AZ series alloys, the ZK series alloys also have a strong basal texture after extrusion. This basal texture leads to anisotropic mechanical properties. For extruded cylindrical rods of alloy ZK60, the tensile yield strength along the extrusion direction can be twice that obtained normal to the extrusion direction, or that obtained from compression along the extrusion direction.

Alloy ZK61 (Mg–6Zn–0.7Zr), which is normally aged after extrusion, develops the highest room-temperature yield strength among the commonly used wrought magnesium alloys. It also offers the advantage that tensile and compressive yield strengths are closely matched. The lower zinc alloys ZK21 and ZM21 (Mg–2Zn–1Mn) are widely used where higher extrusion rates (e.g., $40\,m\,min^{-1}$) are desired. The highest strength recorded for a wrought magnesium alloy is believed to be for the composition Mg–6Zn–1.2Mn (ZM61) in the form

of heat treated extruded bar. The alloy shows a high response to age hardening, and solution treatment at 420°C, water quenching and duplex ageing below and above the GP zones solvus (24 h at 90°C and 16 h at 180°C) results in the following tensile properties: 0.1% PS 340 MPa; TS 385 MPa; with an elongation of 8%. Similar properties have been achieved with the alloy that is based on the Mg–Zn–Cu system which has the advantage of faster extrusion speeds than ZM61. This alloy is Mg–6.5Zn–1.25Cu–0.75Mn (ZCM711) which is given a T6 heat treatment (solution treat 8 h at 435°C, hot water quench, age 24 h at 200°C). On a strength/weight basis, these alloys have properties comparable to some of the strongest wrought aluminium alloys.

Additions of silver and calcium to Mg–Zn alloys have been reported to remarkably enhance the age hardening response. Silver alone can enhance the age hardening response, but this effect is less significant than when silver is added together with calcium. The role of silver in precipitation is unclear whereas calcium and zinc are known to form co-clusters in the very early stage of ageing. These co-clusters are reported to provide heterogeneous nucleation sites at which strengthening precipitates form at a later stage of the ageing process. A representative alloy is Mg–6.1Zn–0.4Ag–0.2Ca–0.6Zr that is usually extruded at a very slow speed at 350°C and develops a strong fiber texture, with the basal planes of individual magnesium grains aligned approximately parallel to the extrusion direction. Their microstructures contain a mixture of fine-scale recrystallized grains and coarse un-recrystallized grains. The zirconium addition significantly retards both the recrystallization process and the growth of recrystallized grains. In the as-fabricated condition, the tensile yield strength is about 290 MPa, together with elongation to fracture of 17%. The compressive yield strength is 246 MPa, leading to a tension–compression yield asymmetry value of 0.85. A T6 treatment does not change the partially recrystallized grain microstructure but stimulates precipitation of nanoscale rods of β'_1 phase. In the T6 condition, the tensile yield strength is 325 MPa and the elongation to failure is 14%. It is understood that the Mg–6.1Zn–0.4Ag–0.2Ca–0.6Zr alloy has yet to be commercialized.

Mg–Mn–RE based alloys An alloy with high extrudability has been developed in recent years based on the Mg–Mn–RE system. This alloy contains 1 wt% manganese and 0.4 wt% cerium-rich misch-metal and is designated ME10 (also known as AM-EX1). At a billet temperature of 370°C, the extrusion speed limit of this alloy is twice that of AZ31. Tensile yield strength and UTS are compatible with those of AZ31 and T6 tempered aluminium alloy AA6063. Alloy AM-EX1 also has significantly improved elongation to fracture and reduced tension–compression asymmetry.

A problem of using leaner alloy compositions to obtain better extrudability is that the yield strength of the products may not be sufficiently high for practical applications. For most magnesium alloys, there is an inverse relationship between tensile yield strength of extrudate and processing speed. This problem may be overcome through reducing the grain size which can be achieved

by appropriate micro-alloying additions. For example, the addition of 0.4 wt% cerium-rich misch-metal to an extruded Mg–1Mn alloy can decrease the grain size from 26 to 6 μm. However, a further addition of 0.5 wt% aluminium to the resultant Mg–Mn–RE alloy eliminates the grain-refining effect of the RE addition and leads to a much larger grain size.

Mg–RE based alloys This group has several commercial and experimental alloys that combine high tensile strength and creep resistance at elevated temperatures. The commercial alloys include WE54, WE43, and Elektron 675 (Mg–6Y–7Gd–0.5Zr), all of which were developed by the Magnesium Elektron. Among these three alloys, Elektron 675 has the highest elevated temperature tensile yield strength. It also has excellent fatigue strength, corrosion resistance, ignition resistance, and can be machined easily. All of these alloys contain a large amount of RE elements and hence they have to be extrudeded at very low speeds. All have strong response to age hardening and they are normally heat treated after extrusion. Due to the high costs of some of the alloying elements and processing, these alloys are mainly used for defense, military aircraft, and specialized applications.

Elektron 675 ingots are usually produced by casting into cylindrical water-cooled molds. The as-cast microstructure comprises magnesium grains that are about 60 μm in size and has second-phase particles of β-Mg_5(Gd,Y) in grain boundaries. The solvus temperature of the β phase is about 525°C, hence the homogenization treatment is usually carried out for 8 h at this temperature to allow complete dissolution of the β particles. Due to the presence of a high concentration of RE elements, the alloy has to be extruded at much higher temperatures (425–500°C) and lower speeds (0.55–1.2 m min^{-1}) than the usual for magnesium alloys.

The final microstructure of Elektron 675 varies significantly with extrusion temperature. When production is carried out in the range 425–460°C (well below the β solvus), the as-fabricated microstructure contains a banded distribution of fine and coarse grains along the extrusion direction. The bands of fine grains are associated with stringers of β particles, with bands of coarse grains between them (Fig. 6.38). This banding becomes less obvious when the alloy is extruded at higher temperatures such as 500°C and the grain size is much larger. Extrusions done in the range 425–500°C exhibit weak textures. For products extruded at 460°C and a 10:1 ratio, their crystallographic textures are similar to what is commonly observed in non-RE-containing magnesium extrusions, but the texture intensity is much weaker. Products made at higher temperatures have slightly different textures with the $<11\bar{2}1>$ directions on the basal plane are parallel to the extrusion direction. This texture is similar to those commonly observed in extruded binary Mg–RE alloys. For extrusions produced at 425–475°C but have higher extrusion ratios (e.g., 17:1), an unusual texture is formed with the prismatic planes parallel to the extrusion direction, i.e., basal planes are perpendicular to the extrusion axis. This prismatic texture

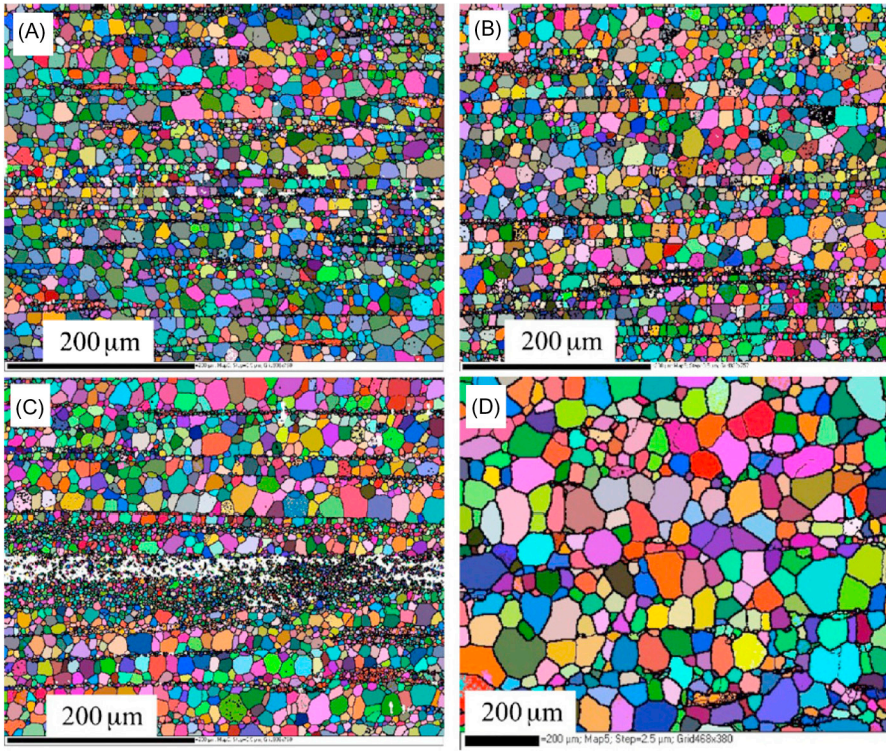


Figure 6.38 As-extruded microstructures of Elektron 675. (A) Extrusion at 425°C, 1.2 m min^{-1} speed and 17:1 ratio; (B) extrusion at 475°C, 1.2 m min^{-1} and 17:1; (C) extrusion at 460°C, 1.1 m min^{-1} and 10:1; and (D) extrusion at 500°C, 0.55 m min^{-1} and 10:1. Extrusion direction is horizontal. From Robson, JD *et al.*: *Mater. Sci. Eng. A*, 528, 7247, 2011.

is strengthened in all extrusions after solution treatment and all have almost no tension–compression yield asymmetry. Even when some asymmetry is observed, it is opposite to the usual one in the sense that the compression yield strength is higher, rather than lower, than the tension yield strength. The elimination of tension–compression yield asymmetry maybe related to the weak texture and factors such as a change in CRSS for various deformation modes.

A T5 or T6 temper is usually applied to the Elektron 675 extrusions for higher strength. The T6 temper involves a solution treatment for 2 h at 525°C, water quenching, and subsequent ageing for 16 h at 250°C. This heat treatment does not change the grain size and texture of products, but enables strengthening precipitates to form. In the T6 condition, the tensile yield strength is about 310 MPa, UTS is 410 MPa, and elongation to fracture is approximately 9%. These mechanical properties remain remarkably stable at elevated temperatures. For example, the tensile yield strength is still over 300 MPa when tested at 200°C.

The Mg–RE system offers the greatest potential for developing ultra-high strength wrought magnesium alloys via grain refinement and age hardening. A remarkably stronger alloy (Mg–10Gd–5.7Y–1.6Zn–0.7Zr) was developed experimentally in 2009. This alloy contains a higher concentration of RE elements and zinc, and consequently it has to be produced by a much lower extrusion speed. In this condition, this alloy has a tensile yield strength of 419 MPa and a compression yield strength of 400 MPa. The alloy responds to age hardening at 200°C and after 64 h both tensile and compressive yield strengths are dramatically increased without any loss of ductility. In the T5 condition, this alloy exhibits a tensile yield strength of 473 and elongation to fracture of 8.0%, together with a compressive yield strength of 524 MPa and elongation to fracture of 6%. The UTS and ultimate compressive strength are 542 and 595 MPa, respectively. These properties are superior to those of high-strength aluminium alloy AA2024 in a T8 condition (TYS of 450 MPa, UTS of 480 MPa, elongation to fracture of 6%, respectively). The T5 treatment causes the precipitation of β' phase in a dense distribution in the magnesium matrix and hence a dramatic enhancement in strength. The sizes of recrystallized grains in the as-extruded and the T5 conditions are approximately 1 μm. While there is a strong basal texture, the tension–compression asymmetry is eliminated in both as-extruded and T5 conditions. The rather small grain size and the presence of nanoscale precipitate plates are thought to suppress the initiation of deformation twinning upon compressive loading.

Hydrostatic extrusion In the belief that the availability of cost-effective extruded sections is essential if magnesium alloys are to be used more widely for structural applications, a consortium from the European Community is investigating the use of hydrostatic extrusion. In this process, a billet is forced through a die opening by means of a pressurized fluid as is shown in Fig. 6.39. Unlike conventional direct or indirect extrusion, there is no metallic contact between the ram and the billet so that the only billet-tooling contact is with the die cone. Plastic deformation takes place under high hydrostatic pressure and, as lubrication is almost ideal, no significant friction is involved. This contrasts with conventional extrusion is which frictional forces and shearing within the billet add considerably to the mechanical work that is required. Thus the thermal effects associated with the dissipation of this mechanical work are less during hydrostatic extrusion which reduces the danger of incipient melting of the billet material and allows processing to be done at higher speeds.

Hydrostatic extrusion was first developed in the 1960s as a means for increasing the ability to cold work relatively brittle materials. It is now also used for applications involving warm and hot working including the production of copper tubing, copper-clad aluminium wire, and for compacting ceramic superconductors. Hot hydrostatic extrusion trials involving the magnesium alloys M1, AZ31, and ZM21 have shown that speeds five to ten times faster than those used for conventional extrusion are possible. Grain sizes are finer

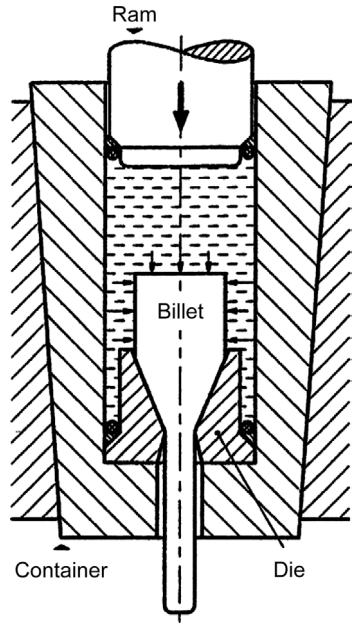


Figure 6.39 Arrangement for hydrostatic extrusion. From Sillekens, WH and Bohlen, J: *Proc. 6th Inter. Conf. on Magnesium Alloys and Their Applications*, Wiley-VCH, p. 1046, 2004.

and more uniform and tensile properties are reported to be comparable with those for alloys prepared by conventional extrusion.

6.5.4 Forging alloys

Forgings represent a comparatively small part of the inventory of wrought magnesium products and can only be fabricated from alloys with fine-grained microstructures. They tend to be made from the higher-strength alloys AZ80 and ZK60 if they are to be used at ambient temperatures, or WE43 (and formerly HM21) for elevated temperatures applications. Alloys that show rapid grain growth at the forging temperature are subsequently forged in stages at successively lower temperatures. Forgings are often specified when a component has an intricate shape and is required to have a strength higher than can be achieved with castings. Press forging is more common than hammer forging and it is often the practice to pre-extrude the forging blanks to refine the microstructure.

6.6 ELECTROCHEMICAL ASPECTS

6.6.1 Corrosion and protection

Magnesium has a normal electrode potential at 25°C of –2.30 V, with respect to the hydrogen electrode potential taken as zero, which places it high in the

Table 6.15 Results of 2.5-year exposure tests

Material	Corrosion rate (mm year^{-1})	Tensile strength after 2½ years (% loss)
Marine atmosphere		
Aluminium alloy 2024	0.002	2.5
Magnesium alloy AZ31	0.018	7.4
Mild steel	0.150	75.4
Industrial atmosphere		
Aluminium alloy 2024	0.002	1.5
Magnesium alloy AZ31	0.028	11.2
Mild steel	0.025	11.9
Rural atmosphere		
Aluminium alloy 2024	0.000	0.4
Magnesium alloy AZ31	0.013	5.9
Mild steel	0.015	7.5

From *Metals Handbook*, Vol. 2, 9th Ed. , ASM, Cleveland, OH, USA, 1979.

electrochemical series. However, its solution potential is lower, e.g., –1.7V in dilute chloride solution with respect to a normal calomel electrode, due to polarization of the surface with a film of $Mg(OH)_2$. The oxide film on magnesium offers considerable surface protection in rural and most industrial environments and the corrosion rate of magnesium lies between aluminium and mild steel (Table 6.15). Essentially it is the high susceptibility to impurities and lack of passive film stability in solutions below pH 10.5 that accounts for most corrosion problems in magnesium alloys. Tarnishing occurs readily and some general surface roughening may take place after long periods. However, unlike some aluminium alloys, magnesium and its alloys are virtually immune from intercrystalline attack because the grain centers are usually anodic with respect to grain boundary regions.

Magnesium is readily attacked by all mineral acids except chromic and hydrofluoric acids, the latter actually producing a protective film of MgF_2 which prevents attack by most other acids. In contrast, magnesium is very resistant to corrosion by alkalis if the pH exceeds 10.5, which corresponds to that of a saturated $Mg(OH)_2$ solution. Chloride ions promote rapid attack of magnesium in aqueous solutions, as do sulfate and nitrate ions, whereas soluble fluorides are chemically inert. With organic solutions, methyl alcohol and glycol attack magnesium whereas ethyl alcohol, oils, and degreasing agents are inert.

The corrosion behavior of alloys varies with composition. Where alloying elements form grain boundary phases, as is generally the case in casting alloys, corrosion rates are likely to be greater than those occurring with pure magnesium. As mentioned earlier, the first magnesium alloys suffered rapid attack in moist conditions due mainly to the presence of more noble metal

impurities, notably iron, nickel, and copper (Fig. 6.4). Each of these elements, or compounds they form, act as minute cathodes in the presence of a corroding medium, creating microgalvanic cells with the relatively anodic magnesium matrix. Nickel and copper are not usually a problem in current alloys due to the very low levels of these elements present in primary magnesium. Iron tends to be more troublesome as there is always a risk of pickup from crucibles which are made from mild steel. However, the potential detrimental effect of iron in zirconium-free alloys is reduced by adding manganese (as $MnCl_2$) to the melt. This element combines with the iron and settles to the bottom of the melt or forms intermetallic compounds which, depending on the Fe: Mn ratio, reduces the cathodic effect of the iron. This ratio should not exceed 0.032. Zirconium has a similar effect in those alloys to which it is added. As mentioned earlier, Mg–Al–Zn and Mg–Al alloys are particularly susceptible to the presence of impurities and the widely used alloy AZ91C has largely been superseded by higher-purity versions known as AZ91D for pressure die casting and AZ91E for gravity die casting which have stricter limits for the nickel, iron, and copper contents. Further improvements are possible by applying a T6 ageing treatment. Alloys AZ91D and AZ93E exhibit corrosion rates which are similar to those of comparable cast aluminium alloys.

Some magnesium alloys may be susceptible to SCC which is especially severe in chromate–chloride solutions. Special attention has been paid to alloys based on the Mg–Al system. Cracking is usually transgranular and involves discontinuous cleavage on microstructural features that have been identified as twin boundary interfaces and various preferred crystallographic planes. There is general agreement that hydrogen embrittlement is the dominant mechanism. Zirconium-containing alloys are less susceptible and SCC only occurs at stresses approaching the yield stress of the alloy concerned. Wrought products are more likely to undergo SCC than castings and it is desirable to stress-relieve components that may be exposed to potential corrodents.

It is common practice to protect the surface of magnesium and its alloys and such protection is essential where contact with other metals may lead to galvanic corrosion. Methods available for magnesium are given as follows:

1. Fluoride anodizing—this involves alternating current anodizing at up to 120 V in a bath of 25% ammonium bifluoride which removes surface impurities and produces a thin, pearly white film of MgF_2. This film is normally stripped in boiling chromic acid before further treatment as it gives poor adhesion to organic treatments.
2. Chemical treatments involving pickling and conversion of the oxide coating—components are dipped in chromate solutions which clean and passivate the surface to some extent through formation of a film of $Mg(OH)_2$ and a chromium compound. Such films have only slight protective value, but form a good base for subsequent organic coatings.

3. Electrolytic anodizing, including proprietary treatments that deposit a hard ceramic-like coating which offers some abrasion resistance in addition to corrosion protection, e.g., Dow 17, HEA, and MGZ treatments—such films are very porous and provide little protection in the unsealed state but they may be sealed by immersion in a solution of hot dilute sodium dichromate and ammonium bifluoride, followed by draining and drying. A better method is to impregnate with a high-temperature curing epoxy resin (see (4)). Resin-sealed anodic films offer very high resistance to both corrosion and abrasion, and, in some instances, can even be honed to provide a bearing surface. Impregnation is also used to achieve pressure tightness in castings that are susceptible to microporosity.
4. Sealing with epoxy resins—in this case, the component is heated to 200–220°C to remove moisture, cooled to approximately 60°C, and dipped in the resin solution. After removal from this solution, draining and air-drying to evaporate solvents, the component is baked at 200–220°C to polymerize the resin. Heat treatment may be repeated once or twice to build up the desired coating thickness which is commonly 0.025 mm.
5. Standard paint finishes—the surface of the component should be prepared as in (1)–(4), after which it is preferable to apply a chromate-inhibited primer followed by good quality top coat.
6. Vitreous enameling—such treatments may be applied to alloys which do not possess too low a solidus temperature. Surface preparation involves dipping in a chromate solution before applying the frit.
7. Electroplating—several stages of surface cleaning and the application of pre-treatments, such as a zinc conversion coating, are required before depositing chromium, nickel, or some other metal.

Magnesium alloy components for aerospace applications require maximum protection; schemes involving chemical cleaning by fluoride anodizing, pre-treatment by chromating or anodizing, sealing with epoxy resin, followed by chromate primer and top coat are sometimes mandatory.

6.6.2 Cathodic protection

Due to its very active electrode potential, magnesium and its alloys can be used to protect many other structural materials from corrosion when connected to them in a closed electrical circuit. Magnesium acts as an anode and is consumed sacrificially, thereby offering protection to metals such as steel. Magnesium metal and, more commonly, the alloys AZ63 and M1A (Mg–1.5Mn) which offer higher relative voltages are used for this purpose. Examples of areas where cathodic protection is used are ships' hulls, pipelines, and steel piles. It should be noted, however, that magnesium and its alloys are not used to protect oil rigs because of the potential incendive sparking risk. The anodes are usually produced by extruding the magnesium alloys.

6.7 FABRICATION OF COMPONENTS

6.7.1 Machining

Magnesium and its alloys are the most machinable of all structural materials. This applies with respect to depth of cut, speed of machining, tool wear, and relative amounts of power required for the equipment being used (Table 6.16). Magnesium is normally machined dry but, where very high cutting speeds are involved and there is a possibility of igniting fine turnings, it may be necessary to employ a coolant. For this purpose, mineral oils must be used because water-based coolants may react chemically with the swarf. Good tool life is experienced providing cutting edges are kept sharp and generous rake clearance angles (usually 7° minimum) are used. Sharp tools also reduce the possibility of fires due to frictional heat.

Magnesium alloys can be chemically machined or milled by pickling in 5% H_2SO_4 or in dilute solutions of HNO_3 or HCl. Some alloys also lend themselves to contour etching and AZ31 is widely used for the production of printing plates.

6.7.2 Joining

Early magnesium alloys were gas welded with an oxyacetylene torch and required careful fluxing to minimize oxidation. Apart from the normal difficulties associated with such a process, extensive corrosion of welds was common when the flux was incompletely removed by the cleaning methods applied. Since then, virtually all magnesium welding has been done using inert gas-shielded tungsten arc (TIG, tungsten inert gas) or consumable electrode (MIG, metal inert gas) processes (Section 4.5.1). Increasing interest in using magnesium alloys in automobiles is requiring more attention to be given to alternative welding methods. Spot welding is possible but so far has been little used. Some success has also been achieved with laser welding and with friction stir welding (Section 4.5.1) and both these methods have been used experimentally to join dissimilar magnesium alloys or magnesium alloys to aluminium alloys.

Table 6.16 Comparative machinability of metals

Metal	Relative power required[a]	Rough turning speeds ($m\,s^{-1}$)	Drilling speeds (5–10 mm drill) ($m\,s^{-1}$)
Magnesium	1	up to 20	2.5–8.5
Aluminium	1.8	1.25–12.5	1–6.5
Cast iron	3.5	0.5–1.5	0.2–0.65
Mild steel	6.3	0.65–3.3	0.25–0.5
Stainless steel	10.0	0.3–1.5	0.1–0.35

From *Machining*, Magnesium Elektron Handbook.
[a]1 = lowest.

Comparisons can be made between the welding characteristics of magnesium and aluminium alloys. As with aluminium, the solubility of hydrogen in magnesium deceases significantly as it solidifies which can lead to porosity in weld beads. The fact that the viscosity and surface tension of molten magnesium are both lower than that of molten aluminium can cause increased sputter during welding and reduce the surface quality of welded regions. Furthermore, the relatively high vapor pressure of liquid magnesium can lead to higher evaporative losses during welding, particularly in alloys containing zinc. On the other hand, the combination of lower heat capacity and heat of fusion of magnesium means that less energy is consumed during welding and offers the potential to achieve higher welding speeds.

Both cast and wrought magnesium alloy products can be welded and the weldability of different alloys has already been compared in Tables 6.3 and 6.4. In general, filler rods are of the same composition as the parent alloys are desirable although the use of a more highly alloyed rod with lower melting point and wider freezing range is sometimes beneficial to minimize cracking. Castings are often preheated to 250–300°C to reduce weld cracking during solidification, and stress-relieving may be desirable after welding is completed.

The design of mechanical joints in magnesium and its alloys is qualified by the vital consideration of galvanic corrosion. This problem precludes direct contact with most other metals and special coatings or insulating materials must be used as separating media. Care must also be taken in the design of joints to avoid crevices, grooves, and such like, where water and other corrosive materials can collect.

6.8 TRENDS IN APPLICATIONS

As mentioned in Chapter 1, The light metals, annual production of magnesium in the Western World was relatively constant at close to 250,000 tonnes during much of the 1990s. Of this total, more than half was used as an addition to various aluminium alloys and only some 40,000 tonnes was actually consumed to produce structural magnesium alloys, mainly as die castings. In recent years, consumption of magnesium has been increasing and an estimated 900,000 tonnes was produced worldwide in 2015, about 80% of which came from China. Annual shipments of die castings were estimated to have risen to 290,000 tonnes in 2015 and some of the products made from magnesium alloys are shown in Fig. 6.40.

A comparative analysis of Western World markets for magnesium alloys in 1966 and for the period 1981–1992 by F. Hehmann revealed that the number of individual applications actually fell from an estimated 198 to 161. The latter figure could be reduced further to 125 if automotive applications were classified into representative groups. Major changes included substantial reductions in the aeronautical and missile markets (totals of 96 applications in 1966 and only 23 in 1981–1992), whereas there were marked increases in the surface

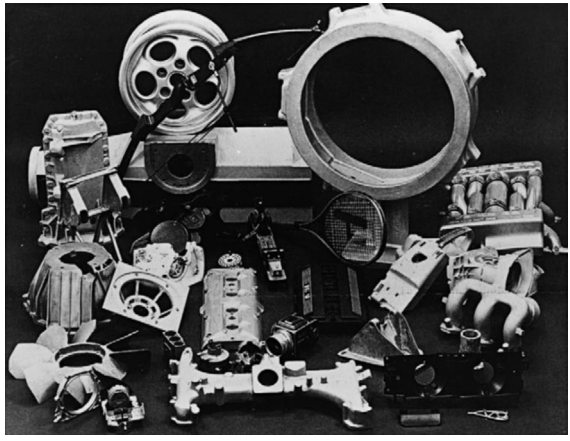


Figure 6.40 Range of products made from magnesium alloys. Courtesy Hydro Magnesium.

transport area. This latter trend has continued during the past decade as market demands for magnesium have become linked more and more to developments in the automotive industry.

In the aeronautical industry, airframe applications in new designs have virtually disappeared and significant uses of magnesium alloys have been confined to castings for engine and transmission housings, notably for helicopters. Historically, the so-called Volkswagon Beetle motor car has represented the largest single market for magnesium alloys which were used for engine crank case and transmission housing castings weighing a total of 17 kg. As was mentioned earlier, this resulted in a weight saving of some 50 kg when compared with using traditional cast iron which was critical for improving the stability of this rear-engined vehicle. A total of 21,559,464 vehicles were produced between 1934, when production commenced in Germany, and when it finally ceased in 2003, in Mexico. Large increases in the price of magnesium in the mid-1970s led to its replacement, at least in part, by aluminium alloy castings. Before then a total of more than 400,000 tonnes of magnesium had been consumed.

While magnesium products have been used in military aircraft for many years, they have little use in civil aircraft interiors due to flammability restrictions from the US Federal Aviation Administration (FAA). In 2013, the results of the magnesium full-scale testing and the progress demonstrated in the development of the lab scale test method led FAA announce that it would now allow magnesium in aircraft seats providing the requirements and conditions as set out in the Special Conditions are satisfied. Two years later, the US Society of Automotive Engineers, which develops standards for the aviation industry, revised its AS8049 standard that now reads “magnesium alloys may be used in aircraft seat construction provided they are tested to and meet the flammability performance requirements in the FAA Fire Safety Branch document.” WE43

and EV31 are the only two alloys that have passed extensive flammability tests conducted by the FAA, including seven full-scale airplane interior tests. Magneium Elektron and an Italian manufacturer of aircraft interiors started producing 16G-compatible seats with major structural components made from WE43. These seats provide a significant weight reduction compared to commonly used aluminium alloys and the first batch are scheduled to enter service in the near future.

Current interest in possible applications of magnesium alloys in automobiles has been stimulated by continuing demands to lower weight, thereby reducing fuel consumption and pollution. A target being pursued in some countries has been to develop a vehicle that consumes only 3 liters of fuel to travel 100 km. In this regard, the mass-dependent component of fuel consumption is the key factor since it contributes approximately 60% to the total. With the engine block for example, weight savings of 35% and 75%, respectively, are possible if it can be cast from a magnesium alloy rather than from an aluminium alloy or cast iron.

Although there has been an average annual increase in the use of magnesium alloys in automobiles of some 15% during the past 15 years and predicted 10% use from 2015 to 2020, this only represents a change from around 1 to 5 kg per vehicle. This compares with current consumption of 120 kg each for aluminium and plastics in a vehicle weighing 1500 kg that is produced in North America. Cost is a major factor limiting the wider use of magnesium (Chapter 1). A European survey has suggested that the wider use of magnesium in automobiles requires the following cost goals to be achieved: castings < cost of aluminium alloy castings + 30%, and sheet and extruded components to be half their current costs.

Examples of some current global applications of magnesium alloy automotive components are die cast steering wheels and steering column components, instrument panels, seat frames (Fig. 6.10), small motor housings, door handles, pedals, various brackets, engine valve cover, and oil pan. In 2014, Renault Samsung Motors, together with Korean steel company POSCO, developed a magnesium sheet and announced to use it for the walls of VIP back seats and the trunks of upgraded SM7 vehicles. In 2015, Porsche selected magnesium sheet for the roof of its new model of the 911 GT3 after tests on magnesium, aluminium, and carbon-fiber-reinforced polymers. Much larger consumption will be involved with the wider use of magnesium alloys for powertrain components such as the die cast gearbox casing as shown in Fig. 6.41. As mentioned in Section 6.3.1, developments were made with sand cast engine blocks (Fig. 5.9). Table 6.17 summarizes potential automotive applications for magnesium alloys together with the technical challenges they present.

On the basis of relative densities, it has been generally accepted that magnesium can become an effective substitute for aluminium if the price ratio falls below 1.5:1. During the last three decades, this ratio has varied between 1.5 and 2.5. What may favor magnesium in the future is a greater appreciation of the cost savings that are possible through savings in energy in casting (estimated

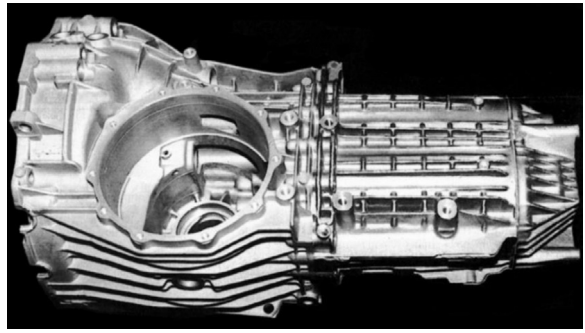


Figure 6.41 Die cast AZ91 magnesium alloy gearbox casing. Courtesy Volkswagen AG.

Table 6.17 Potential magnesium alloy automotive applications and their technical challenges

System	Product	Technical challenges
Interior	Airbag housing	Improved casting process
	Window regulator housing	Rapid prototyping
	Glove box	Design for magnesium
Body	Door frame/inner	Thin-wall design
	A&B pillar	Thin-wall design
	Hatchack frame	Joining and welding
	Spare tyre jack	
Chassis	Wheel	High-strength alloy development
	Control arm	New casting processes
	Rack and pinion housing	(Squeeze and semi-solid metal casting)
	Brackets for rail frames	Low-cost coatings
	Spare tyre rim	
Powertrain	Automatic transmission case	Creep-resistant alloy development
	Engine block	Design for magnesium
	Crankcase	Fastening strategy
	Oil pan	Engine coolant compatibility
	Starter housing	
	Oil/water pump housing	
	Intake manifold	
	Engine mount	

From Luo, AA: *JOM*, 56(2), 42, 2002.

to be up to 30%) and machining (up to 45%) when calculated on a volumetric basis. Improved methods of recycling magnesium alloy scrap are another area in which there is a potential for cost savings in the use of this metal.

Other areas in which the use of magnesium is expanding can be categorized as appliances and sporting goods. As two examples, there has been a trend to use magnesium alloy die castings for producing thin-walled computer housings

and mobile telephone casings where lightness, ability to be thin-wall cast, and the provision of electromagnetic shielding are special advantages. Magnesium alloys have also been used to cast the frames of lightweight bicycles.

In recent years, magnesium alloys have received increasing attention for potential applications in the fields of vascular intervention and orthopedic trauma fixation. In 2016, Magnesium Elektron and BIOTRONIK, a world-leading manufacturer and distributor of cardio- and endo-vascular medical devices, announced a partnership in the development of SynerMag bioresorbable magnesium alloys for cardiovascular application. The SynerMag bioabsorbable alloy has already undergone a number of in vitro and in vivo evaluations. The two companies started in 2006 a joint research and development program on the development of a bioresorbable magnesium coronary scaffold. A product of this program is the SynerMag 410 alloy system that is now being used as the platform material in the BIOTRONIK magnesium scaffold, the world's first clinically proven magnesium-based bioresorbable scaffold. The latest generation BIOTRONIK magnesium scaffold has been clinically evaluated.

One unexpected and exciting development was the discovery, in 2001, that the magnesium alloy (compound) MgB_2 exhibits superconductivity at approximately 40 K (−233°C). This critical temperature (T_c) is nearly twice that at which more traditional metallic superconductors, such as Nb_3Sn, can operate and offers the prospect of cooling with liquid hydrogen or neon rather than using more expensive liquid helium. Moreover, when doped with carbon or other impurities, MgB_2 was reported to have a current-carrying capacity in the presence of magnetic fields which is at least equal or better than that of these other metallic compounds. MgB_2 wires can be formed by reacting magnesium vapor with boron fibers at temperatures of 1000°C, or by synthesizing powder mixtures of these two elements in thin tubes. Possible applications could include superconducting magnets, power lines, and sensitive magnetic field detectors.

Polycrystalline magnesium alloys usually exhibit a small pseudo-elasticity effect, with a recoverable strain of up to 0.4%. This pseudo-elasticity is caused by the reversal of deformation twins during unloading. One recent discovery indicates that polycrystalline Mg–Sc alloys, with more than 18 at.% scandium in the alloy to allow a metastable β phase of scandium solid solution to be retained upon quenching from high temperature, show a surprisingly large super-elasticity with recoverable strain of 4.4% at −150°C. The super-elastic strain is caused by stress-induced martensitic transformation from the metastable β phase. These alloys also exhibit the shape memory phenomenon (Fig. 6.42). If the alloy sheet is deformed into a round shape at the temperature of liquid nitrogen, it will

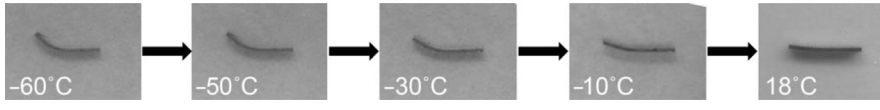


Figure 6.42 Shape memory phenomenon of a β-type Mg–Sc alloy. From Ogawa, Y *et al.*: *Science*, 22 July, 353(6297), 368, 2016.

return into its initial flat condition upon heating. This phenomenon appears to be caused by reversible transformation from martensite to the parent β phase. The density of these β-type Mg–Sc alloys is only about $2\,g\,cm^{-3}$, which is one-third of those of TiNi shape memory alloys that are now widely used. However, due to the large amounts of scandium in the alloy, these alloys are much more expensive than commercial shape memory alloys and may be restricted to possible applications in the aerospace industry.

FURTHER READING

Emley, EG: *Principles of Magnesium Technology*, Pergamon, London, 1966.

Raynor, GV: *The Physical Metallurgy of Magnesium and its Alloys*, Pergamon, London, 1959.

Roberts, CS: *Magnesium and Its Alloys*, Wiley, New York, NY, USA, 1960.

Avedesian, MM and Baker, H: *ASM Specialty Handbook: Magnesium and Magnesium Alloys*, ASM International, Materials Park, OH, USA, 1999.

Nayeb-Hashemi, AA and Clark, JB: *Phase Diagrams of Binary Magnesium Alloys*, ASM International, Materials Park, OH, USA, 1988.

Kainer, KU, (Ed.): *Magnesium Alloys and Technologies*, Wiley-VCH, Weinheim, Germany, 2003.

Mordike, BL and Kainer, KU, (Eds.): *Proc. 4th Int. Conf. on Magnesium Alloys and Their Applications*, Werkstoffe Informationsgesellschaft, Frankfurt, Germany, 1998.

Nie, JF: Precipitation and hardening in magnesium alloys, *Metall. Mater. Trans. A*, 43, 3891, 2012.

Zhu, SM, Easton, MA, Abbott, TB, Nie, JF, Dargusch, MS, Hort, N and Gibson, MA: Evaluation of magnesium die-casting alloys for elevated temperature applications: microstructure, tensile properties, and creep resistance, *Metall. Mater. Trans. A*, 46, 3543, 2015.

Luo, AA, (Ed.): *Magnesium Technology*, TMS, Warrendale, PA, USA, 2004.

Kainer, KU, (Ed.): *Proc. 6th Inter. Conf. on Magnesium Alloys and Their Applications*, Wiley-VCH, Weinheim, Germany, 2004.

Neite, G, Kubota, K, Higashi, K and Hehmann, F: Magnesium-based alloys, Cahn, RW, Haasen, P and Kramer, EJ (Eds.), *Materials Science and Technology—A Comprehensive Treatment*, Vol. 8, Matucha, KH (Ed.), *Structure and Properties of Non-Ferrous Alloys*, 113, 1996.

Nie, JF: Viewpoint on phase transformations and deformation in magnesium alloys, *Scr. Mater.*, 48, 981, 2003.

Rokhlin, LL: *Magnesium Alloys Containing Rare Earth Metals: Structure and Properties*, Taylor and Francis, London, 2003.

Pekguleryuz, MO and Kaya, AA: Creep resistant magnesium alloys for powertrain applications, *Magnesium Alloys Containing Rare Earth Metals: Structure and Properties*, Taylor and Francis, London, 2003.

Abbott, TB, Easton, MA and Caceres, CH: Designing with magnesium: alloys, properties, and casting processes. In Totten, GE Xie, L, and Funatani, K, (Eds.): *Handbook of Mechanical Alloy Design*, Marcel Dekker, Inc., New York, NY, USA, 2004.

Han, Q, Kad, BK and Viswananathan, S: Design perspectives for creep-resistant magnesium die-casting alloys, *Philos. Mag.*, 84(36), 3843, 2004.

Westengen, H: Magnesium: alloying and magnesium alloys: properties and applications, *Encyclopedia of Materials Science and Technology*, Elsevier Science Ltd., 2001.4745, 2001.

Friedrich, HE and Mordike, BL: *Magnesium Technology*, Springer, Berlin, 2006.

Bettles, C and Barnett, M: *Advances in Wrought Magnesium Alloys*, Woodhead Publishing, Oxford, 2012.

Suh, BC, Shim, MS, Shin, KS and Kim, NJ: *Scr. Mater.*, 84–85(1), 2014.

Robson, JD, Twier, AM, Lorimer, GW and Rogers, P: *Mater. Sci. Eng. A*, 528, 7247, 2011.

Makar, GL and Kruger, J: Corrosion of magnesium, *Int. Mater. Rev.*, 38(3), 138, 1993.

Brown, RF: Magnesium wrought and fabricated products: yesterday, today, and tomorrow. In Kaplin, HI, (Ed.): *Magnesium Technology 2002*, TMS, Warrendale, PA, USA, pp 155, 2002.

Schumann, S and Friedrich, H: Current and future use of magnesium in the automotive industry, *Mater. Sci. Forum*, 419–422, 51, 2003.

7

TITANIUM ALLOYS

7.1 INTRODUCTION

Stimulus for the development of titanium alloys since 1948 came initially from the aerospace industry when there was a critical need for new materials with higher strength-to-weight ratios at elevated temperatures. As mentioned in Chapter 1, the high melting point of titanium (1668°C, 138°C higher than that of iron) was taken as a strong indication that, titanium alloys would show good creep strengths over a wide range of temperature. Although subsequent investigations revealed that this temperature range was narrower than expected, titanium alloys now occupy a critical position in the materials inventory of the aerospace industries (Fig. 1.6) and around 40% of titanium is used in this way globally. Another important property of titanium alloys is their superior resistance to corrosion, especially in corrosive media that contain chloride ions. Consequently, they have found essential applications in chemical processing, marine engineering, pharmaceutical manufacturing, and many other industry sectors. In addition, titanium alloy prostheses are commonly used for implanting in the human body today due to their excellent biocompatibility and bio-corrosion resistance in body fluids together with their relatively low Young's modulus. This chapter will deal with titanium alloys for these applications and concentrate on wrought titanium alloys, which currently account for more than 95% of the titanium usage.

Titanium has a number of features that distinguish it from the other light metals and make its physical metallurgy both complex and interesting.

1. At 882.5°C, pure titanium undergoes an allotropic transformation from a hexagonal close-packed (hcp) structure (α) to a body-centered cubic (bcc) phase (β) that remains stable up to the melting point. The transformation temperature changes with the addition of alloying elements.

Light Alloys. DOI: http://dx.doi.org/10.1016/B978-0-08-099431-4.00007-5
Copyright © 2017 Ian Polmear, David StJohn, Jian-Feng Nie, Ma Qian.
Published by Elsevier Ltd. All rights reserved.

2. Titanium is a transition metal with an incomplete shell in its electronic structure, which enables it to form solid solutions with most substitutional elements having a size factor within ±20%. Also because of its electron configuration ($3d^2 4s^2$), titanium is paramagnetic as only some spins of its unpaired 3d electrons will be oriented by the external field.
3. Titanium and its alloys react with all interstitial elements, including oxygen, nitrogen, and hydrogen over a wide range of temperature, and the solubility of these interstitial elements can be signficant. For example, titanium can dissolve up to 14.25%O at 600°C and 7.6%N at 1083°C, which rarely happens with the other metals. Consequently, the oxide film or skin dissolves into the titanium matrix underneath as temperature increases.
4. In its reactions with other elements, titanium may form solid solutions and compounds with metallic, covalent, or ionic bonding. At high temperatures, only two solid materials, yttria and molybdenum, do not react with or react very slowly with titanium. This makes it difficult to find a suitable crucible material for melting titanium and its alloys and for handling them in the molten state.

In general, alloying of titanium is dominated by the ability of elements to stabilize either of the α or β phase (see Section 7.4 for other requirements for the formulation of different β-titanium alloys). This behavior, in turn, is related to the number of bonding electrons, i.e., the group number, of the element concerned. Alloying elements with electron/atom ratios of <4 stabilize the α phase, elements with a ratio of 4 are neutral, while elements with ratios >4 are β-stabilizing. These alloying elements can be introduced to titanium in different combinations leading to α, near-α, α−β, near-β, metastable β, and β-titanium alloys.

7.1.1 Classification of titanium alloys

Titanium alloys can be divided into two broad groups, commercially pure (CP) titanium and titanium-based alloys. CP titanium materials are essentially pure titanium (≥99%, Table 7.1), and they are often classified into Grades 1 to 4 according to their oxygen, iron, carbon, nitrogen, and hydrogen levels (Tables 7.1 and 7.2), which determine their strengths, ductility, and corrosion resistance. Their characteristics will be discussed in Section 7.2.2. Titanium alloys are obtained from adding one or more alloying elements to high-purity titanium or CP titanium.

Titanium alloy phase diagrams are often complex and some are still incomplete. However, the titanium-rich sections of pseudo-binary systems enable them to be classified into three simple types, as shown in Fig. 7.1. Elements that dissolve preferentially in the α phase expand the α phase field thereby raising the α/β-transus (Fig. 7.1A). There are only five elements that behave in this way, namely aluminium, oxygen, nitrogen, carbon, and gallium, known as α-stabilizing elements. Aluminium and oxygen are the two most important α-stabilizers. Tin, and silicon

Table 7.1 Chemical compositions, densities, and typical tensile properties of selected titanium alloys at room temperature

Alloys	Al	Sn	Zr	Mo	V	Cr	Other	ρ (g cm^3)	Condition	YS (MPa)	UTS (MPa)	El. (%)
α-Alloys												
Grade 1/Ti35A							≤0.18O, ≤0.2Fe, 99.5Ti	4.51	Mill-annealed 675°C	170	240	24
Grade 2/Ti50A							≤0.25O, ≤0.3Fe, 99.2Ti	4.51	Mill-annealed 675°C	275	344	20
Grade 3/Ti65A							≤0.35O, ≤0.3Fe, 99.1Ti	4.51	Mill-annealed 675°C	377	440	18
Grade 4/Ti75A							≤0.4O, ≤0.5Fe, 99.0Ti	4.51	Mill-annealed 675°C	480	550	15
Grade 7/Ti75A							≤0.25O, ≤0.3Fe, 0.2Pd	4.50	Mill-annealed 675°C	275	344	20
Grade 15							0.5Ni–0.05Ru	4.51	Mill-annealed ~675°C	380	483	18
KS120Si							0.3O–0.5Fe–0.6Si	4.51	Mill-annealed ~650°C	650	750	10
IMI 317	5	2.5						4.46	Annealed 900°C	800	860	15
IMI 230							2.5Cu	4.56	ST(α) aged 475°C	630	790	24
Near-α alloys												
8–1–1	8			1	1			4.37	Annealed 780°C	980	1060	15
IMI 679	2.25	11	5	1			0.25Si	4.84	ST(α+β) aged 500°C	990	1100	15
IMI 685	6		5	0.5			0.25 Si	4.49	ST(β) aged 550°C	900	1020	12
6–2–4–2S	6	2	4	2			0.2Si	4.54	ST(α+β) aged 590°C	960	1030	15
Ti–11	6	2	1.5	1			0.3Bi–0.1Si	4.45	Annealed 750°C then aged 595°C	940	1040	19
IMI 829	5.5	3.5	3	0.3			INb-0.3Si	4.61	ST(β) aged 625°C	860	960	15
Ti–1100	6	2.75	4	0.4			0.45Si	4.50	ST(β) aged 600°C	895	1000	10
IMI 834	6	4	3.5	0.5			0.35Si–0.7Nb	4.59	ST (α+β) aged 650°C	905	1035	10

(*Continued*)

Table 7.1 Chemical compositions, densities, and typical tensile properties of selected titanium alloys at room temperature (Continued)

Alloys	Al	Sn	Zr	Mo	V	Cr	Other	ρ (g cm^3)	Condition	YS (MPa)	UTS (MPa)	El. (%)
Ti–5111	5	1	1	1	1		0.1Si	4.43	25.4 mm plate β roll 954°C 1 h air-cooled	720	835	13
α–β Alloys												
Ti–6–4 (IMI 318)	6				4		≤0.2O	4.42	Mill-annealed ~740°C	880	950	14
									ST (α+β) aged 500°C	1100	1170	10
Ti–6–4	6				4		≤0.13O, ELI	4.42	Mill-annealed ~740°C	790	860	15
Ti–6–7	6						7Nb, ≤0.5Ta	4.52	Mill-annealed ~740°C	800	900	10
IMI 550	6	2	4	0.5				4.60	ST (α+β) aged 500°C	1000	1100	14
IMI 680	2.25	11	4	0.2				4.86	ST (α+β) aged 500°C	1190	1310	15
α–β Alloys												
Ti–74	7			4					940°C 1 h WQ 650°C 16 h	1035	1170	10
Ti–6–6–2	6	2			6		0.7 (Fe, Cu)	4.54	ST (α+β) aged 550°C	1170	1275	10
Ti–6–2–4–6	6	2	4	6				4.68	ST (α+β) aged 590°C	1170	1270	10
IMI 551	4	4		4			0.5Si	4.62	ST (α+β) aged 500°C	1200	1310	13
Ti–6–2–2–2-2	6	2	2	2		2	0.25Si	4.65	950°C 8 h WQ 540°C 8 h			
Corona-5	4.5			5		1.5		4.54	Annealed 815°C after β processing	930	1030	14
Ti–62S	6						2Fe–0.1Si	4.4 4	α–β forged plus RA	945	986	18
									β forged plus RA	945	986	15
Ti–8Mn							8Mn	4.72	Mil-annealed 700°C	860	945	15

β-Alloys												
Ti–13–11–3	3				13	11		4.87	ST(β) aged 480°C 36 h	1200	1280	8
Beta III		4.5	6	11.5				5.07	ST(β) duplex aged 480	1315	1390	10
Ti–8–8–2–3	3			8	8		2Fe	4.85	and 600°C	1240	1310	8
Transage 129	2	2	11		11			4.81	ST(β) aged 580°C	1280	1400	6
Beta C	3		4	4	8		6	4.82	ST(β) aged 540°C	1130	1225	10
Ti–10–2–3	3				10		2Fe	4.65	ST(β) aged 580°C	1250	1320	8
Ti 21S	3			15			2.7Nb–02Si	5.34	ST(β) aged 560°C	1170	1240	8
KS15–5–3	3		5	15			≤0.35Fe, ≤0.0.2O	5.01	STA forgings	1103	1250	5
Ti 17	5	2	2	4		4		4.65	800°C 4 h WQ 635 8 h	1170	1240	8
TB2	5			5	5	3	0.4Fe	4.65	ST(α+β) aged 650°C	1174	1236	13
Ti–5583	3			5	5	8		4.83	STA (800°C 4 h AC 538°C 8 h-AC)	1100	1370	7
Ti–15333	3	3			15	3		4.78	790°C 15 min AC 538°C 4–16 h	1050	1160	11
Alloy C					35	15		5.30	Stable β alloy	900	960	20
Ti40					25	15	0.3Si	5.18	Stable β alloy	830	900	8
VT22	5			5	5	1	1Fe	4.65	ST(α+β) aged 650°C	1200	1280	8
Gum Metal			Ti–23Nb–0.7Ta–2Zr–1O in mole per cent (mol.%)					5.60	Cold-worked heat treated	1400	1500	8

ELI, extra low interstitial; YS, 0.2% yield stress; UTS, ultimate tensile strength; EI., elongation +; RA, recrystallization annealing; WQ, water quenched; STA, solution treated and aged; ST(α), ST (α+β), and ST(β) correspond to solution treatments in the α, α+β, and β-phase fields, respectively; AC, air-cooled.

Table 7.2 Classification of CP titanium

Composition (wt%)	Grade 1	Grade 2	Grade 3	Grade 4
O	≤0.18	≤0.25	≤0.35	≤0.5
Fe	≤0.2	≤0.3	≤0.3	≤0.5
H	≤0.015	≤0.015	≤0.015	≤0.015
N	≤0.03	≤0.03	≤0.05	≤0.05
C	≤0.1	≤0.1	≤0.1	≤0.1
Ti	≥99.5	≥99.2	≥99.1	≥99

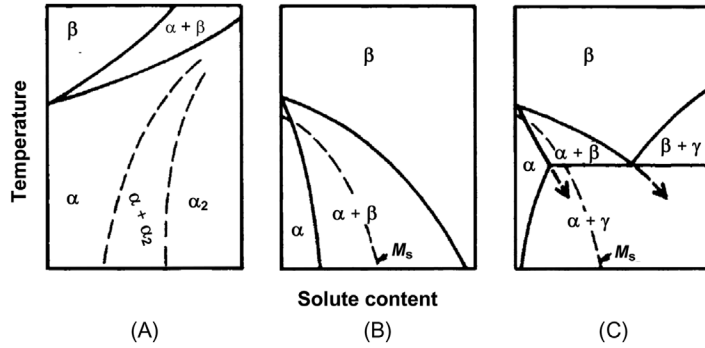


Figure 7.1 Basic types of phase diagrams for titanium alloys. The dotted phase boundaries in (A) refer specifically to the Ti–Al system. The dotted lines in (B) and (C) show the martensite start (M_s) temperatures. Alloying elements favoring the different types of phase diagrams are (A) Al, O, N, C, Ga; (B) Mo, W, V, Ta, Nb; (C) Cu, Mn, Cr, Fe, Ni, Co, Si, H, Pd.

do not strongly affect the stability of either the α or β phase at low addition levels and are often regarded as neutral. As for zirconium, it also used to be regarded as neutral. However, the Ti–Zr binary phase diagram produced using the established Pandat™ CompuTherm database suggests that, zirconium should be treated as a β-stabilizer as the β-transus decreases with increasing zirconium on the titanium-rich side. Research has confirmed that zirconium plays the role of a β-stabilizer in Ti–Nb based alloys.

Elements which depress the α/β-transus and stabilize the β phase may be classified into two groups: those which form binary alloys of the β-isomorphous type (Fig. 7.1B), and those which favor the formation of a eutectoid alloy (β→α+γ, Fig. 7.1C). The latter group includes chromium, iron, copper, nickel, manganese, cobalt, hydrogen, and palladium, which have low or negligible solubility in the α phase. It should be noted, however, that the eutectoid reactions in

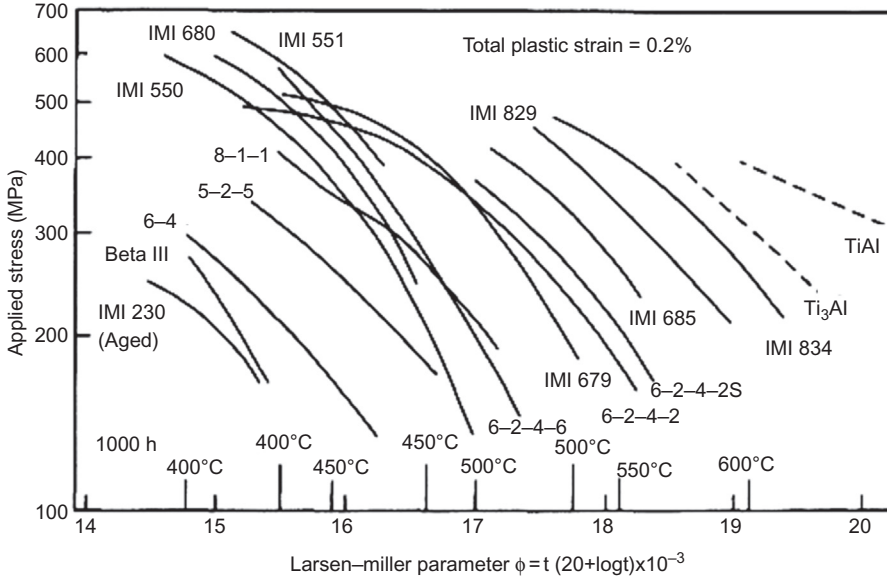


Figure 7.2 Creep curves of some commercial titanium alloys. Courtesy IMI Titanium.

a number of titanium alloys (e.g., Ti–Fe, Ti–Mn) are sluggish so that, in practice, no eutectic reactions are observed even under slow furnace cooling conditions. These alloys behave as if they conformed to the β-isomorphous phase diagram (Fig. 7.1B); hence the arrows shown in Fig. 7.1C. Hydrogen strongly promotes the formation of the β phase. As a result, β-Ti(H) can form at 298°C vs at 882.5°C in high-purity titanium. Of the substitutional β-stabilizing elements, molybdenum, vanadium, and chromium are commonly used, while tungsten is little used because of its high density and tendency to segregate during alloy preparation. Iron is a potent β-stabilizer, but its addition is typically limited to 2.0% due also to its tendency to segregate during ingot solidification (Section 7.4.1). An addition of more than 6% chromium can cause similar problems. The potency of each element in stabilizing the β phase is ranked according to the approximate critical minimum addition of each element needed to retain 100% β on water quenching (Section 7.4.1).

It is customary to classify titanium alloys into three main groups, designated α, α–β, and β, which will each be considered Sections 7.2–7.4. The compositions and a selection of properties of representative titanium alloys in each group are listed in Table 7.1. In addition, the creep characteristics of a number of these alloys are shown in Fig. 7.2 because this property has dominated much alloy development. Both Table 7.1 and Fig. 7.2 should be consulted in conjunction with the foregoing discussions in which special consideration is given to commercial compositions and the roles of particular alloying elements.

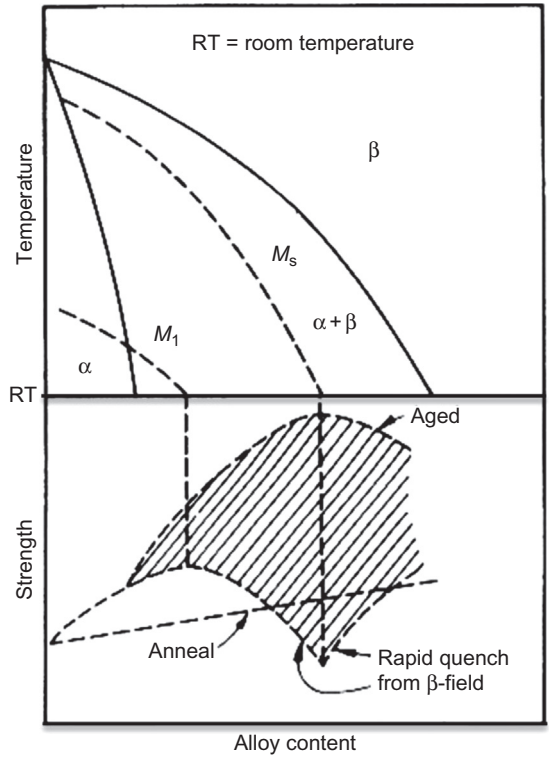


Figure 7.3 Schematic diagram for the heat treatment of β-isomorphous titanium alloys and resulting tensile strength vs alloy content. From Morton, PH: *Rosenhain Centenary Conference on the Contribution of Metallurgy to Engineering Practice*, The Royal Society, London, 1976.

7.1.2 Basic principles of heat treatment

The properties of titanium alloys are determined primarily by the morphology, volume fraction and individual properties of the two phases α and β. Although the first alloys that will be discussed (α-alloys) show little response to heat treatment, it is desirable to examine the general principles of heat treatment that are involved, even though they relate mainly to the α–β and β groups. This is possible by considering the effects of alloy content on the β to α transformation in a typical binary β-isomorphous system, as shown in Fig. 7.3. Also included is a schematic diagram which depicts trends in tensile strength with respect to alloy content resulting from different heat-treatment procedures.

Titanium alloys are heat treated for a variety of reasons:

1. Stress relieving, e.g., in the range 480–650°C for the alloy Ti–6Al–4V.
2. Sub-transus annealing for improved strength–ductility combinations, creep resistance, fracture toughness, or stabilizing annealing for phase stability, and/or dimensional stability when exposed to elevated temperatures in service.

3. β-Annealing (slightly above the β-transus in most cases) for improved fracture toughness, creep resistance, and reduced notch sensitivity (tensile strength and ductility normally decrease).
4. Solution treatment and ageing (STA) to achieve high tensile yield strength (≥1100 MPa) with reasonable ductility (elongation ≥10%) and excellent fatigue strength (e.g., 700 MPa at $R = 0.1$ for STA Ti−6Al−4V).

α−Ti alloys show little response to sub-transus annealing, STA or β-annealing, which apply primarily to α–β and near-β alloys. These treatments will be discussed in the following three sections for different titanium alloys with a special focus on Ti–6Al–4V, which is the most widely used alloy in industry.

Apart from the diffusionless composition–invariant $\beta \rightarrow \alpha'$ martensitic transformation, the other composition-invariant transformation that also occurs in titanium alloys is the $\beta \rightarrow \alpha_m$ massive transformation. The diffusional activity occurs mainly at or only across the advancing interfaces in this transformation. Therefore it may also be regarded as interface-controlled. Other phase transformations that occur in titanium alloys, and the related microstructural evolution processes during heating, cooling, or isothermal holding, are all diffusion-controlled. Knowledge of the diffusion rates of alloying elements and self-diffusion rates of titanium in both the α and β phases is therefore important. Some typical features of the self-diffusion and the diffusion of alloying elements in titanium are summarized here:

- The self-diffusion rate in the high-temperature bcc β phase is about three orders of magnitude faster than that in the low-temperature hcp α phase.
- The self-diffusion rate in β shows a non-Arrhenius plot with an upward curvature, which is best described using two exponential terms such as:

$$D_{Ti}^{\beta} = A_1 \exp\left(-\frac{Q_1}{RT}\right) + A_2 \exp\left(-\frac{Q_2}{RT}\right)$$

where $A_1 = 3.58 \times 10^{-4}\,\mathrm{cm^2\,s^{-1}}$, $A_2 = 1.09\,\mathrm{cm^2\,s^{-1}}$, $Q_1 = 130\,\mathrm{kJ\,mol^{-1}}$ (1.35 eV), $Q_2 = 251\,\mathrm{kJ\,mol^{-1}}$ (2.60 eV), and $R = 8.314\,\mathrm{J\,K^{-1}\,mol^{-1}}$. This implies that the self-diffusion in the β phase is controlled by two or more mechanisms. The same behavior occurs with zirconium and hafnium. In contrast, the self-diffusion rate in the α phase shows an Arrhenius plot. An experimental description based on the Ti[44] measurements is given by:

$$D_{Ti}^{\alpha} = 7 \times 10^{-10} \exp\left(-\frac{23859\,J\,mol^{-1}}{RT}\right)(\mathrm{cm^2\,s^{-1}})$$

- The diffusion rates of transition metals such as iron, nickel, cobalt, manganese, and chromium in α-titanium are three to five orders of magnitude faster than the self-diffusion rate of titanium (Fig. 7.4). These

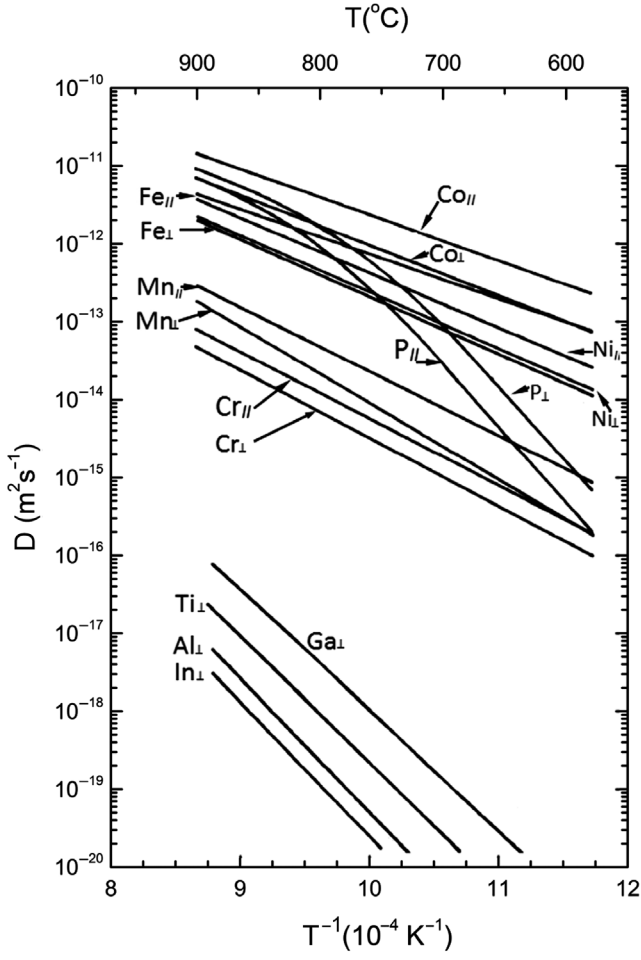


Figure 7.4 Self- and impurity-diffusion coefficients in α-titanium, where the subscripts || and ⊥ stand for parallel and perpendicular to the *c*-axis of the α-titanium lattice, respectively. From Perez RA *et al.*: *Mater. Trans.*, 44, 2, 2003.

transition metals diffuse even one to three orders of magnitude faster than interstitial oxygen, carbon, and nitrogen in α-titanium. The mechanisms for their fast diffusion rates in α-titanium remain unclear. Their diffusion rates in the β phase are also faster than the self-diffusion rate of titanium but the difference is less prominent (about one order of magnitude faster only).

- The diffusion rates of iron, nickel, cobalt, manganese, and chromium parallel to the *c*-axis of α-titanium are faster than that perpendicular to the *c*-axis (Fig. 7.4).
- Aluminium is a slow diffuser in both the α and β phases. In addition, the Arrhenius plot of the impurity diffusion coefficient of aluminium in the β-titanium phase also exhibits an upward curvature.
- Zirconium is also a slow diffuser in the α phase, but its diffusion rate is similar to the self-diffusion rate of titanium in the β phase.
- Vanadium, molybdenum, niobium, tantalum, tungsten, and tin are slow diffusers in both the α and β phases.
- Hydrogen exhibits very high diffusion rates in both the α and β phases, which can lead to hydrogen embrittlement, stress–corrosion cracking (SCC), and corrosion fatigue in titanium alloys that are exposed to humid environments. The very high diffusion rates of hydrogen in the α phase are desired only when titanium is hydrogenated for the production of titanium hydride (TiH_2) powder or hydride–dehydride (HDH) titanium powder. They are essential feedstock powder materials for titanium powder metallurgy (PM) (Section 7.5.8). In addition, TiH_2 powder is also widely used in the production of porous metals or metal foams.

Empirical rules of diffusion suggest that the addition of a faster diffusing solute tends to enhance the diffusion rates of both the solvent and other solute atoms, while the opposite effect occurs for the addition of a slower diffusing element. Of the four transition metals mentioned earlier, iron as an impurity exists in all titanium-based materials and is also introduced as an alloying element to a number of titanium alloys (Table 7.1). Chromium is a common alloying element. A small amount of nickel (<1.0%) can be found in several commercial titanium alloys, e.g., the highly corrosion-resistant α-titanium alloy Ti–0.5Ni–0.05Ru (Table 7.1). Manganese as an alloying element is mainly used in alloys Ti–8Mn (Table 7.1) and Ti–(1–4)Al–(1–1.5)Mn. The effects of these fast diffusing impurities or alloying elements can be significant on the diffusion phenomena in both the α and β phases during heat treatment or in service at elevated temperatures. Consequently, they are excluded from creep-resistant or high-temperature near-α titanium alloys (see Section 7.2.3). For example, the iron and nickel contents in Ti–6Al–2.75Sn–4Zr–0.4Mo–0.45Si (Ti–1100) are limited to 0.03% and 0.02%, respectively, for elevated temperature applications at ~600°C.

7.2 α-ALLOYS

7.2.1 General

α-Alloys generally exhibit excellent weldability, low-to-medium tensile strength accompanied with reasonably high ductility and notch toughness (e.g., by the Charpy impact test). Notch sensitivity resistance is an important

property for titanium components with holes, threads, and sharp edges. In addition, they possess very low ductile-to-brittle transition temperatures and have long been used for cryogenic vessels and components. Near-α titanium alloys are known for their high-temperature creep strength and oxidation resistance up to ~600°C. These alloys are, however, not heat treatable.

Aluminium and oxygen are the two premier α-stabilizing elements. The addition of aluminium is typically limited to 6% in order to avoid the formation of the brittle phase Ti_3Al (α_2). For example, ageing of Ti–Al alloys containing above 5–6%Al at elevated temperatures can lead to the formation of finely dispersed and ordered α_2 particles. The phase α_2 is coherent with the lattice of the α phase over a broad range of temperatures and has the $D0_{19}$ (hexagonal) crystal structure. Continuous ageing causes α_2 to coarsen. In α-alloys with complex compositions, the misfit between α and α_2 can be larger than that in Ti–Al alloys. Therefore, nucleation of α_2 becomes more difficult and it tends to form heterogeneously. This nonuniform dispersion appears to have a less deleterious effect on ductility. There is a general agreement concerning the location of the $\alpha/(\alpha+\alpha_2)$ phase boundary up to 800°C, but uncertainty exists as to whether α_2 forms by peritectoid reaction involving β and an intermediate compound TiAl, or by phase separation of α at higher temperatures (see Fig. 7.1A).

Research has revealed that the intense hardening effect of oxygen atoms in pure α-titanium is attributed to the interaction between oxygen and the core of screw dislocations that mainly glide on prismatic planes. However, increasing oxygen lowers ductility so that its content is often limited to ~0.25%. In particular, oxygen promotes the formation of the brittle Ti_3Al phase into which it partitions preferentially in Ti−Al-based alloys. For example, an increase in oxygen content from 600 to 1200 ppm decreases the room temperature tensile elongation of the alloy Ti–8Al, aged at 695°C for 200 h, from 20% to 1%, due to the formation of Ti_3Al. Even in the α−β alloy Ti–6Al–4V, doubling the oxygen content from 0.25% to 0.5% was found to promote the formation of the brittle Ti_3Al when slowly cooled from the β phase field. Carbon and nitrogen are α-stabilizers as well. They both raise the β-transus at which α completely transforms to β. On the other hand, hydrogen as an interstitial impurity element and a β-stabilizer lowers the β-transus.

α-Alloys are usually divided into three subgroups, depending upon whether they are entirely single phase α, near-α (containing some β-stabilizers), or respond to a conventional age-hardening reaction (e.g., Ti–Cu alloys with 2.5%Cu in particular). When aluminium is used as the principal α-stabilizing element, there is a practical limit to the addition of other α-stabilizers in order to avoid the formation of Ti_3Al. This quantity, known as the *aluminium equivalent* or *ordering parameter*, may be calculated empirically from the composition as follows:

$$\text{Al equivalent} = \text{Al} + \frac{1}{3}\text{Sn} + \frac{1}{6}\text{Zr} + 10(\text{O} + \text{C} + 2\text{N})$$

The aluminium equivalent should be limited to ~9%. In this formula, silicon and zirconium are included as α-stabilizers, because it is believed that they can retard the rates of the α→β transformation. However, as pointed out in Section 7.1.1, zirconium is essentially a β-stabilizer, rather than a neutral element. In that regard, the inclusion of zirconium may need to be reassessed.

The low ductility of α alloys containing the α_2 phase has been a disappointment as the strengthening of nickel-based superalloys is essentially dependent on microstructures containing a rather similar coherent phase $Ni_3(Ti,Al)$ or γ′. The only element reported to improve the ductility of α_2 in titanium alloys is gallium (an α-stabilizer). Although some gallium-containing alloys have been produced, the high cost of this element and problem with melting make their applications impractical.

In the presence of hydrogen, titanium hydrides may form as long thin plates in CP titanium and alloyed α-titanium. These brittle hydrides risk facilitating certain fracture phenomena and are usually detrimental to the mechanical properties of titanium alloys (see Section 7.7). They have the nominal composition TiH_2 but the hydrogen-to-metal ratios may vary from 1.5 to 1.99. The basic δ hydride is face-centered cubic (CaF_2 structure), while a face-centered tetragonal ε hydride forms below 37°C, which has a *c/a* ratio <1. A third γ hydride has been observed to form in the α phase at low hydrogen concentrations, which is metastable and also has a face-centered tetragonal structure with a *c/a* ratio equal to 1.09. Additionally, a strain-induced, body-centered cubic hydride has been reported to form on the $\{10\bar{1}0\}$ slip planes during deformation of α solid solutions. A large volume expansion of as much as 18% accompanies hydride formation, which may entail the generation of dislocations in the surrounding matrix.

Contrary to what has been mentioned earlier, research has also shown that both hydrogen and oxygen may be used as effective alloying elements for the fabrication of strong and ductile titanium alloys. For example, an extruded PM titanium alloy having the composition Ti–0.97O–0.11H has reportedly achieved tensile strength of ≥1100 MPa and elongation of ≥20%. These properties are superior to those of Ti–6Al–4V and many other titanium alloys listed in Table 7.1 while offering lower cost.

7.2.2 Fully-α alloys

The commonly used α alloys include CP titanium Grades 1 through 4 (Table 7.2), which are in effect Ti−O−Fe alloys, Ti−Pd alloys (Grades 7, 11, and 17, Table 7.3), as well as the ternary alloy Ti–5Al–2.5Sn and its variants. Their tensile properties at room temperature are given in Table 7.1. In fact, CP titanium alloys are not always fully-α alloys. For example, grain boundary (GB) β phases can form in CP titanium containing 0.12%Fe. In general, since these alloys are essentially single phase, tensile strength is relatively low but their high thermal stability leads to reasonable creep strength in the upper

Table 7.3 Corrosion-resistant titanium–palladium (Ti–Pd) alloys

Composition (wt%)	Grade 7	Grade 11	Grade 17
Pd	0.12–0.25	0.12–0.25	0.04–0.08
O	≤0.25	≤0.18	≤0.18
Fe	≤0.30	≤0.20	≤0.20
H	≤0.015	≤0.015	≤0.015
N	≤0.03	≤0.03	≤0.03
C	≤0.1	≤0.1	≤0.1
Ti	Balance	Balance	Balance

temperature range (Fig. 7.2). In addition, they are weldable and can exhibit good ductility down to very low temperatures (e.g., −253°C). Since it is usually necessary to hot-work these alloys at temperatures below the α/β-transus in order to prevent excessive β grain growth, their formability as hcp structure can be limited due to their high rate of strain hardening.

α-Alloys can be produced in three different forms (Fig. 7.5), which are discussed in the following conditions:

1. Equiaxed α-grains that are formed when the alloys are worked and annealed in the α phase field (Fig. 7.5A). Grain sizes tend to be relatively small because grain growth is inhibited due to the comparatively low temperatures that are involved and to the presence of impurities which pin GBs. Yield strength (σ_{YS}) at room temperature can be predicted from the average grain size (d) according to the Hall–Petch relationship, e.g., the equation for Grade 1 CP titanium (Ti−50A, Table 7.1) is:

$$\sigma_{YS} = 231 + 10.5\mathrm{d}^{-1/2}\,(\mathrm{MPa})$$

2. Quenching of an α-alloy from the β phase field can produce the hcp martensitic phase α′ (Fig. 7.5B). The martensite contains a high density of dislocations and consists of colonies of plates or laths separated by low angle boundaries. The transformation is characterized by a habit plane near $\{334\}_\beta$. There is negligible hardening associated with the production of α′ martensite because α′ and α have the same lattice structure (hcp) and similar lattice parameters (the lattice distortion is negligible, unlike the formation of martensite in carbon steels). In addition to the martensitic transformation, the composition-invariant $\beta \rightarrow \alpha_m$ massive transformation can also occur as mentioned in Section 7.1.2. α_m, α′, and α all have the same hcp lattice.
3. Slow cooling from the β phase field causes α to form as Widmanstätten plates (Fig. 7.5C). In high-purity alloys, this structure is referred to as serrated α, whereas, if β-stabilizers or impurities such as hydrogen are present, α-laths or α-colonies (parallel α-laths) with different orientations may form producing a "basket-weave" effect (Fig. 7.5D).

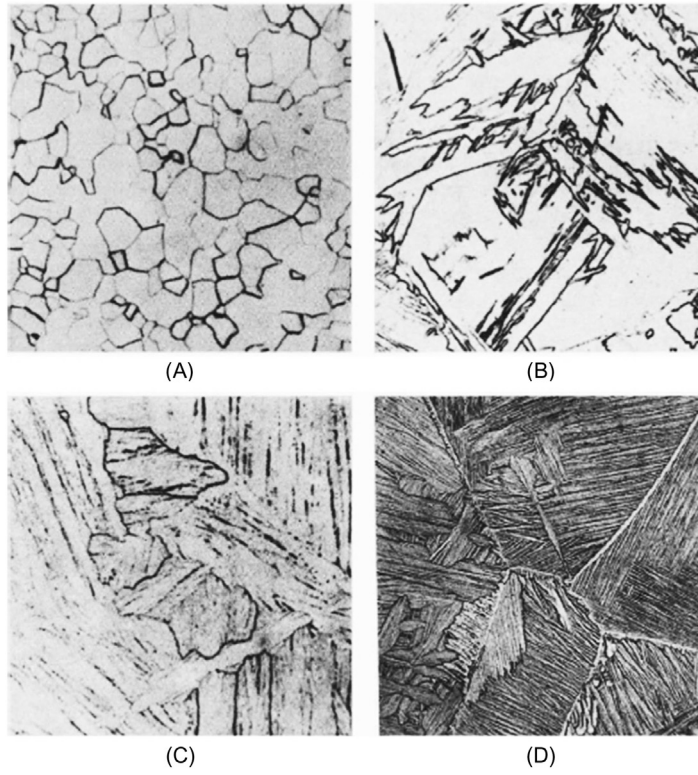


Figure 7.5 Microstructure of CP titanium: (A) annealed 1 h at 700°C showing equiaxed grains of α (× 100); (B) quenched from β phase field showing martensitic α′ (× 150); (C) air-cooled from the β phase field showing Widmanstatten plates of α (× 100); (D) near-α alloy IMI 685 (Ti–6Al–5Zr–0.5Mo–0.25Si) air-cooled from the β phase field showing a basket-weave configuration of Widmanstatten plates of the α phase delineated by small amounts of the β phase. (C) Courtesy W. K. Boyd and (D) courtesy IMI Titanium.

β-Annealed α-alloys exhibit lower values of tensile strengths, fatigue strength, and ductility at room temperature, than those having a fine equiaxed grain structure. For low-cycle fatigue strength, there is an empirical relation:

$$\text{Fatigue strength at } 5 \times 10^4 \text{ cycles} \propto 0.1\% \text{ proof stress} \times \log R_A$$

where R_A is reduction of area in tensile tests. This is a useful guide in rating α-alloys. On the other hand, cooling from the β-field can lead to improved values of fracture toughness and higher creep resistance compared to α-alloys with an equiaxed grain structure. These trends in mechanical properties which arise from the shape and size of the grains, and from the structure of the grain boundaries, are important as they are characteristics of many other titanium alloys.

CP titanium alloys (Table 7.2) are second only to the α−β Ti−6Al−4V in applications. They are widely used in marine engineering, chemical processing, health care, aerospace, architectural, and many other industries. Famous architectural examples include the National Grand Theatre of China in Beijing (the egg-shaped titanium shell used 60 tonnes of CP titanium sheet products), and the external titanium cladding of the Guggenheim Museum in Bilbao, Spain. As shown in Table 7.2, four grades of CP titanium are available. Grade 1 (0.18O–0.2Fe) has the lowest strength and displays excellent cold formability so that it can be deep drawn. It is mainly used in marine engineering and chemical industries. Grade 2 (0.25O–0.3Fe) has tensile strength between 390 and 540 MPa and is the most widely used CP titanium alloy because of its excellent formability, moderate strength, and superior corrosion resistance. Examples include condensers, evaporators, reaction vessels for chemical processing, tubing and tube headers in desalinization plants and heat exchangers, cryogenic vessels, and many medical applications. Grade 3 (0.35O–0.3Fe) is confined mainly to pressure vessels. Grade 4 (0.5O–0.5Fe) has the highest tensile strength (650−690 MPa) of the CP titanium, similar to that of annealed stainless steels. However, they are 40% lighter and offer superior corrosion resistance. Further substantially improved resistance to corrosion can be achieved by small additions of palladium (≤0.25%, Table 7.3), which will be discussed in Section 7.7.4.

Use of the α-alloy Ti–5Al–2.5Sn has gradually declined as alloys with better forming properties and higher creep resistance have become available. One continuing application, however, has been cryogenic storage tanks which require the use of titanium alloys with high strength and toughness at low temperatures. For this purpose, extra low interstitial (ELI) Ti–5Al–2.5Sn has been developed to increase the toughness of the alloy, which has been used to store liquid hydrogen (−253°C). α-Titanium alloy pressure vessels have become standard for fuel storage at cryogenic temperatures in a number of space vehicles, because their specific strengths are approximately double those of aluminium alloys and stainless steel at these temperatures.

7.2.3 Near-α alloys

This class of forging alloys was initially developed to meet demands for higher operating temperatures in the compressor section of aircraft gas-turbine engines as part of the continuing quest for improved performance and efficiency. They possess higher tensile strengths at room temperature than the fully-α alloys, and show the greatest creep resistance of all titanium alloys at temperatures above ~400°C. Early near-α titanium alloys are the American composition Ti−8Al−1Mo−1V (Ti−8−1−1), and the British alloy Ti−6Al−5Zr−0.5Mo−0.25Si (IMI 685) used for the forged gas-turbine compressor disk or wheel (Fig. 7.6).

As shown by the formulation of Ti−8−1−1, near-α alloys usually contain up to 2% β-stabilizers, which introduce small amounts of the β phase to improve forgeability. However, these additions are normally too small to

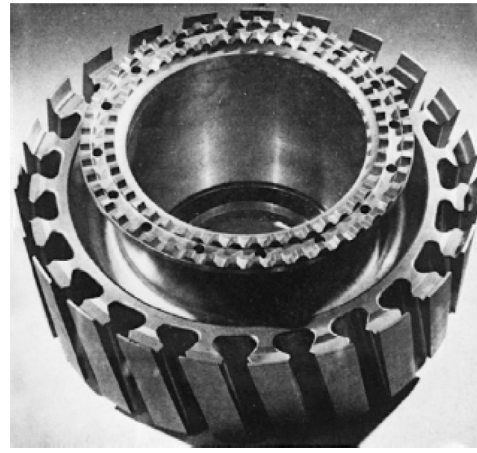


Figure 7.6 Forged compressor disk or wheel made from the near-α IMI 685 (Ti–6Al–5Zr –0.5Mo–0.25Si). Courtesy Rolls Roys Ltd.

provide significant strengthening through the decomposition of the retained β phase (Fig. 7.3).

An empirical expression has been proposed to denote those near-α titanium alloy compositions giving maximum creep strength:

$$36 - 2.6(\%\text{Al}) - 1.1(\%\text{Sn}) - 0.7(\%\text{Zr}) - 27(\%\text{Si}) \\ -3(\%\text{Mo equivalent}) \leq 10$$

The Mo equivalent, which offers an empirical indication of the β phase stability of a β-titanium alloy (see Section 7.4), is estimated by:

$$\text{Mo equivalent} = 1.0(\%\text{Mo}) + 0.67(\%\text{V}) \\ +0.44(\%\text{W}) + 0.28(\%\text{Nb}) + 0.22(\%\text{Ta}) \\ +2.9(\%\text{Fe}) + 1.6(\%\text{Cr}) - 1.0(\%\text{Al})$$

Most near-α alloys are forged and heat treated in the α+β phase field so that primary α-grains are always present in the microstructure. Improved creep performance can be achieved in special compositions by carrying out forging in the β phase field (i.e., β forging). The two near-α alloys which currently show the best creep resistance or maximum operating temperatures (590–600°C) are similar in composition, namely IMI 834 (Ti–5.8Al–4Sn–3.5Zr–0.5Mo–0.7Nb–0.35Si), introduced in 1984, and Ti–1100, introduced in 1988. However, they are forged in the α+β and β phase fields, respectively. Another unique near-α alloy is Ti–6Al–2Nb–1Ta–0.8Mo (Ti–621/0.8), introduced around 1956. The alloy has excellent fracture toughness in marine environments and resistance to seawater SCC, used mainly in deep submersible crafts for the US Navy. It is

now appropriate to consider the metallurgical synthesis of alloy compositions of some important near-α alloys.

Alloys heat treated in α+β phase field One of the first alloys specifically designed to meet creep requirements was the composition Ti–11Sn–2.25Al–5Zr–1Mo–0.2Si (IMI 679), introduced in 1962. Development occurred in three well-defined stages. The first was to determine the maximum amounts of α-stabilizers that could be added without a severe loss of ductility. It was recognized that, although tin caused less solid solution hardening than aluminium at room temperature, it became a more effective strengthener as the temperature was raised. Tin also had the advantage that higher amounts could be tolerated without causing formation of the embrittling α_2 phase, although large additions would increase density and prevent the alloy from being welded. In actual practice, the total content of tin and aluminium was limited by a tendency for the alloys to become susceptible to hydrogen embrittlement. A ternary composition Ti–11Sn–2.25Al was therefore selected. Zirconium was added to provide further solid solution strengthening of the α phase.

The second stage of development was to introduce a β-stabilizer that would both promote some response to heat treatment and render the alloy more forgeable without adversely affecting creep properties. For this purpose, 1% molybdenum was selected. Finally, sufficient silicon was added to further increase strength and creep resistance, mainly by dissolving in the α phase in which evidence shows that silicon segregates to, and reduces the mobility of, dislocations.

A parallel development in the United States led to the alloy Ti−8−1−1 (Table 7.1), introduced in 1960, slightly earlier than IMI 679. It had a lower density, was weldable, and had better forging characteristics because of the higher content of β-stabilizers. However, this alloy has an ordering parameter or aluminium equivalent in excess of 9, which led to problems of instability and loss of ductility because of the tendency to form the α_2 phase after long time exposure at elevated temperatures. In 1966, another American alloy was introduced as a compromise which was known as Ti−6242 (Ti–6Al–2Sn–4Zr–2Mo). Ti−6242 has an outstanding combination of tensile strength, creep strength, fracture toughness, and high-temperature stability for long-term service at temperatures up to 540°C. Its primary application is gas-turbine compressor components such as blades, disks, and impellers. It has also been used in sheet metal form for engine afterburner structure and for various hot airframe skin applications.

Ti−6242 and IMI 834 are two commonly used near-α alloys in aircraft engines. Later, an addition of 0.1%Si was made and this silicon-containing alloy is designated Ti–6242S. It was introduced in 1970. This amount of silicon has an optimal effect in reducing creep deformation (Fig. 7.7) and is presumed to correspond to the limit of supersaturation in this alloy. Nevertheless, the minimum in the curve shown in Fig. 7.7 is unexpected. The effect of silicon in improving creep performance can be seen by comparing the curves for Ti–6242 and Ti–6242S in Fig. 7.2. Ti–6242S is widely used in the United States where high creep resistance is required.

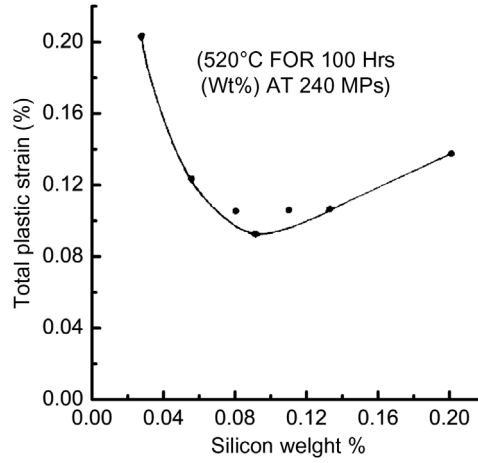


Figure 7.7 The effect of minor additions of silicon on creep strain in the alloy Ti-6242 (Ti–6Al–2Sn–4Zr–2Mo). From Seagle, SR et al.: Metals Eng. Quart., p. 48, February 1975.

All these alloys are forged in the α+β phase field. The recommended heat treatment is to solution treat at a temperature at which the alloy consists of approximately equal proportions of the α and β phases, e.g., 900°C for IMI 679 and 1010°C for Ti−8−1−1. For maximum creep strength, the alloys are air-cooled to form a bimodal microstructure of equiaxed grains of primary α and Widmanstätten α, which forms by nucleation and growth from β (Fig. 7.8A). Faster cooling may cause the high-temperature β phase to transform to martensitic α′ (e.g., in thin sections), which increases tensile strength, although creep resistance is reduced at the upper end of the temperature range (>450°C). The alloys are then normally given a stabilizing treatment within the range 500–590°C.

β-Heat treated alloys Forging of titanium alloys in the β phase field offers the advantage of easier deformation because of the higher working temperatures and the bcc structure. However, this practice, and the subsequent heat treatment of the alloys in this phase field, is normally avoided because excessive grain growth often occurs, which adversely affects ductility at room temperature.

The near-α alloy IMI 685 is an example of a composition developed to explore the opportunities of both β-forging and β-heat treatment. The α/β-transus is 1020°C and quenching from 1050°C produces laths of martensitic α′ which are delineated by thin films of retained β (Fig. 7.8B). Subsequent ageing at 500–550°C reduces quenching stresses and causes some strengthening. Martensitic α′ decomposes into α and the microstructure comprises laths of α bounded by a fine dispersion of particles. Electron diffraction studies have indicated that these particles may be either body-centered cubic ($a = 0.33$ nm) which is the normal β-titanium structure, or face-centered cubic ($a = 0.44$ nm).

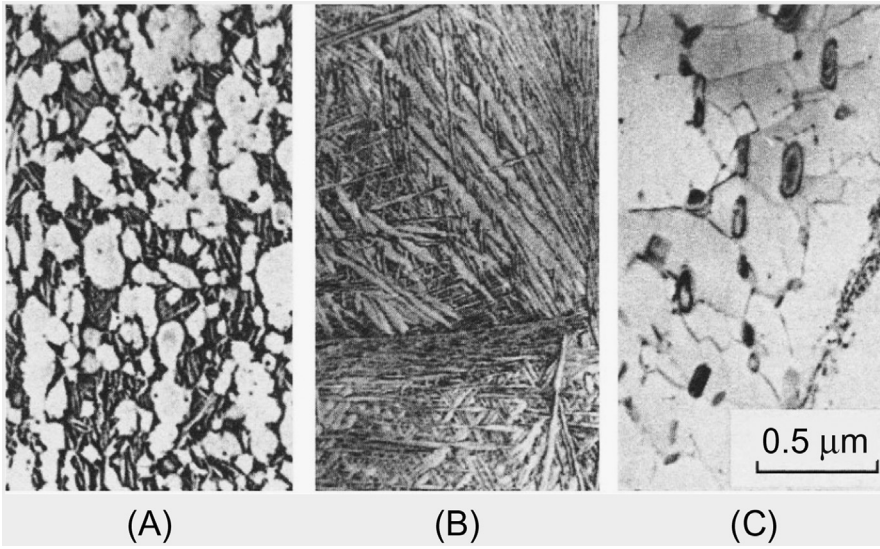


Figure 7.8 (A) Alloy IMI 679 (Ti–11Sn–2.25Al–5Zr–1Mo–0.2Si) air-cooled from the α+β phase field. The white phase is primary α and the other is Widmanstatten α plus β (× 500); (B) alloy IMI 685 (Ti–6Al–5Zr–0.5Mo–0.25Si) oil-quenched from the β phase field showing laths of the martensitic α′ phase delineated by small amounts of the β phase (× 75); (C) IMI 685 quenched from the β phase field and aged at 850°C showing particles of the phase $(Ti,Zr)_5Si_3$. Courtesy IMI Titanium (× 30,000).

It is probable that some β-particles form from the decomposition of the martensitic α′ and then grow into inter-lath films. This was observed in the decomposition of martensitic α′ in Ti–6Al–4V. Little is known of the other phase except that it contains titanium, molybdenum, and silicon. If ageing is carried out at higher temperatures, e.g., 850°C, softening occurs, and it is possible to observe the precipitate $(Ti,Zr)_5Si_3$ which forms on dislocation networks in the boundaries between the α laths (Fig. 7.8C).

Creep resistance is high in the range 450–520°C and is at a maximum if quenching rates in the range 1–10°C s^{-1} are used (Fig. 7.9). In this condition, the basket-weave morphology, e.g., Fig. 7.5D, is present in the microstructure. In thick sections, or with slower quenching rates, the microstructure can contain coarse, aligned laths of α which reduce room temperature ductility and increase the rate of crack propagation in low-cycle fatigue (Section 7.7).

As compared with earlier alloys, the essential features of the composition IMI 685 are as follows:

1. Tin is replaced by a lower amount of aluminium to reduce density while maintaining the ordering parameter within safe limits.
2. The content of the β-stabilizer molybdenum is halved which reduces the amount of the β phase, the presence of which leads to lower creep resistance.

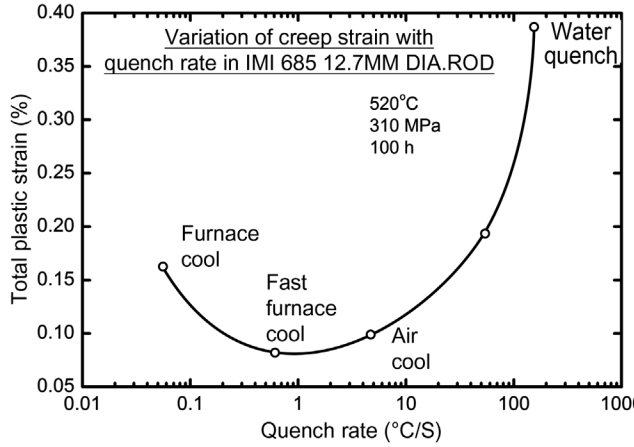


Figure 7.9 Effect of cooling rate from the β phase field on creep strain of alloy IMI 685 (Ti–6Al–5Zr–0.5Mo–0.25Si). From Blenkinshop, PA et al.: Titanium and Titanium Alloys, Proc. 3rd Inter. Conf. on Titanium, Williams, JC and Belov, AF (Eds.), Plenum Press, p. 2003, 1982.

3. Zirconium is added to provide solid solution strengthening of the α phase.
4. The level of silicon is increased slightly to allow for its greater solubility at the higher β-heat-treatment temperature.

A near α-alloy IMI 829 (Ti–5.5Al–3.5Sn–3Zr–0.3Mo–1Nb–0.3Si) was introduced in 1980 with enhanced creep strength (Fig. 7.2) and an upper operating temperature of 580°C. This alloy is also heat treated in the β phase field, or just below the β-transus, so that a small amount of the α phase (e.g., 5 vol.%) is retained to pin GBs and minimize β grain growth. Niobium is considered to confer oxidation resistance superior to that of the earlier near-α alloys. Oxidation or even burning is a limiting factor when considering long-term exposure at such temperatures. Section 7.4.2 will discuss the development of two burn-resistant β-titanium aerospace alloys.

A further marginal increase in operating temperature has been achieved with a later alloy, IMI 834, which has the slightly changed composition Ti–5.8Al–4Sn–3.5Zr–0.5Mo–0.7Nb–0.35Si, and has been used as high-pressure compressor disks in aircraft engines. The alloy chemistry has been tailored to allow a greater degree of flexibility in heat treatment and to optimize both creep and fatigue strength. With respect to heat treatment, it is important that such alloys can be held at temperatures very close to the β-transus to retain some α phase without requiring impractical levels of temperature control. The microstructure is similar to that shown in Fig. 7.8A except that the amount of the primary α phase is reduced to 5–10 vol.%. As shown in Fig. 7.10, the slope of the so-called β-transus approach curve for IMI 834 is less than that for IMI 829, which has the effect of widening the allowable temperature range to obtain the microstructure containing a small amount of the α phase. This change is attributed to the presence of the minor

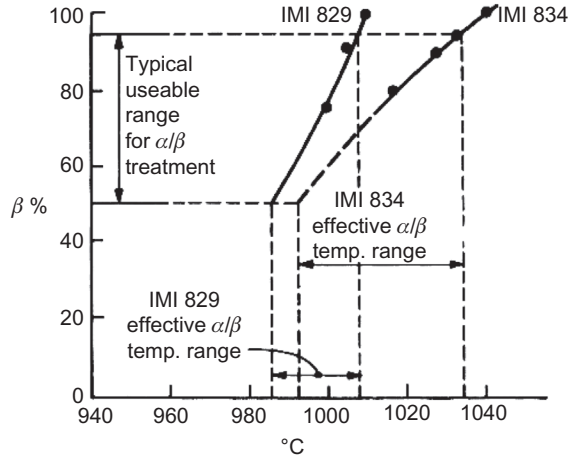


Figure 7.10 β-Transus approach curves for IMI 829 (Ti–5.5Al–3.5Sn–3Zr–0.3Mo–1Nb–0.3Si) and IMI 834 (Ti–5.8Al–4Sn–3.5Zr–0.5Mo–0.7Nb–0.35Si). Courtesy P.A. Blenkinshop.

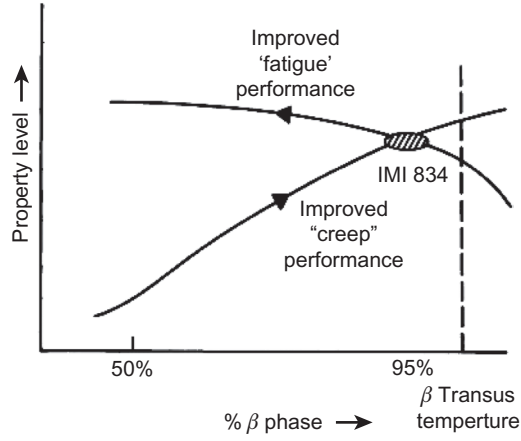


Figure 7.11 Schematic representation of the effect of α or β phase proportion on the creep and fatigue properties of IMI 834. Courtesy P.A. Blenkinshop.

amount of carbon. The effects of the different proportions of the α and β phases on creep and fatigue properties of IMI 834 are shown schematically in Fig. 7.11. It should be noted that this figure also serves as a useful reminder that alloy design is of necessity a compromise; maximization of one particular property, such as creep resistance, is often achieved at the expense of some other properties.

The alloy Ti−1100 is normally forged in the β region and then directly aged. The microstructure is similar to that shown in Fig. 7.8B. Prolonged

exposure of Ti−1100 at relatively high temperatures (e.g., 600°C) causes two precipitates to form; one is the coherent, ordered phase α_2 (Ti_3Al) that nucleates homogeneously within the martensitic α′ laths, and the other is the silicide $(Ti,Zr)_5Si_3$ that forms at the interfaces. Some increase in proof stress and loss of ductility is observed which is more marked in tests carried out at ambient than at elevated temperatures. This effect is attributed mainly to the presence of the α_2 phase. These two precipitates have also been observed in alloy IMI 834 exposed under similar conditions. In the late 1990s, the alloy Ti−1100 was modified with an addition of 0.1% yttrium in China, designated as Ti−600, which has been used to manufacture automotive engine valves for racing cars since 2008. The introduction of 0.1% yttrium refines the microstructure and improves the ductility, stability, and elevated temperature properties of the alloy. In addition, it changes the precipitation location of titanium silicides in the microstructure. Additive manufacturing of this yttrium-containing Ti−1100 alloy or Ti−600 by selective electron beam melting (SEBM) resulted in the formation of fine (50−200 nm) Y_2O_3 dispersoids in the matrix.

It seems probable that, with the development of the alloys IMI 834 and Ti−1100, the limit has been reached in optimizing the composition of the near-α alloys. To achieve further increases in operating temperatures of titanium-based materials, recourse to new approaches to alloy development or manufacturing processes such as additive manufacturing will be needed.

7.2.4 Ti–Cu age-hardening alloy

Ti–Cu is a β-eutectoid system. It was recognized that the titanium-rich end of the Ti−Cu phase diagram offered potential for developing an alloy that may respond to age hardening. This follows because the solubility of copper in α-titanium reduces from 2.1% at the eutectoid temperature of 798°C to 0.7% at 600°C and to a very low value at room temperature. Moreover, it seemed possible that such an alloy could be cold-formed after solution treatment when in a relatively soft condition and then strengthened by ageing.

Ti–Cu alloys were investigated in Britain where hot-forming facilities were limited and the composition Ti–2.5Cu (designed as IMI 230, also known as TIMETAL 230 now) was developed as a cold formable and heat-treatable sheet material. IMI 230 possesses excellent cold formability and its product forms include sheet, forgings, and extrusions. They are used in the annealed condition for fabricating components such as bypass ducts of gas-turbine engines.

IMI 230 is of special interest in that it is one of very few titanium alloys that can be strengthened by a classical age-hardening reaction. Solution treatment is carried out at 805°C for 1 h and is followed by air cooling (sheet) or oil quenching to room temperature. A duplex ageing treatment was recommended by IMI Titanium, which comprised nucleation (first ageing) at 400°C for 8−24 h with air cooling, followed by growth (second ageing) for 8 h at 475°C with air

cooling again. It promotes precipitation of a fine dispersion of the metastable Ti_2Cu which is coherent with the β-matrix (Fig. 7.12) and forms on the $\{10\bar{1}1\}$ planes. A shorter and more economic ageing cycle has also been proposed. A moderate increase of 150–170 MPa in tensile strength is achievable by ageing. Strength properties can be further enhanced if the alloys are cold formed prior to ageing and, in this condition, compare favorably with the α-alloy Ti–5Al–2.5Sn which requires hot forming.

Ti–2.5Cu is weldable and its strength may be recovered providing the duplex ageing treatment is applied after welding. Fig. 7.13 shows an application which is a casing for a gas turbine engine that is constructed by welding together forged rings and vanes formed from IMI 230 sheet.

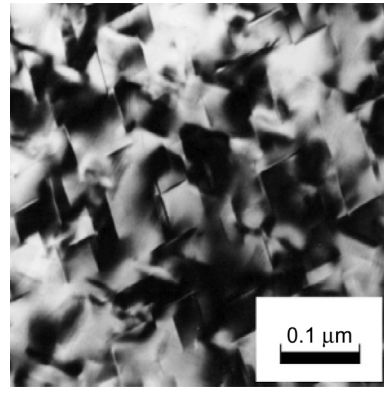


Figure 7.12 Coherent plates of Ti_2Cu zones in an aged IMI 230 (Ti–2.5Cu) alloy. Courtesy IMI Titanium.

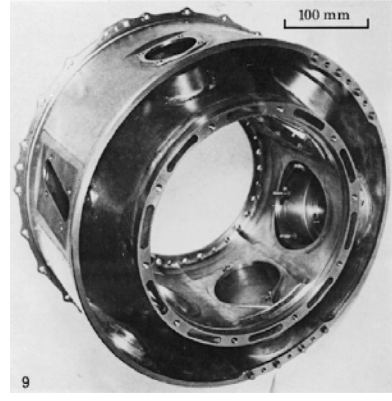


Figure 7.13 Welded IMI 230 (Ti–2.5Cu) alloy casting from a Rolls Royce/SNECMA Olympus engine. Courtesy Rolls Royce Ltd.

Since IMI 230 is a binary Ti−2.5Cu alloy, it was anticipated that additions of other elements, singly or together, may induce a further response to age hardening. However, extensive investigation has failed to reveal any addition having this desired effect.

7.3 α–β ALLOYS

7.3.1 Introduction to Ti−6Al−4V and other common α–β alloys

In the late 1940s, it was realized that binary Ti−Al alloys containing <2.5%Al were inadequate in strength, while those containing more than 7.5% aluminium had insufficient ductility. This led to a search for new titanium alloys that were both strong and ductile. In addition, there was a great need from the US defense industry to replace steels with lightweight titanium alloys for a variety of important applications, for example, as impact-resistant ordnance materials. However, none of the titanium alloys available at that time exhibited sufficient resistance to intense impact (impact toughness). Prior to the invention of Ti−6Al−4V, iron, manganese, or chromium was often selected as the third alloying element for titanium alloys containing aluminium. However, the resulting alloys all exhibited severely decreased tensile ductility. Vanadium was chosen because it showed little adverse effect on ductility while improving tensile strength. Ti−6Al−4V was invented during the period from 1952 to 1954 by Stanley Abkowitz in the United States (US Patent 2,906,654). Today Ti−6Al−4V alone makes up more than half the usage of titanium-based materials worldwide.

Two grades of Ti−6Al−4V are produced commercially, Grade 5 and Grade 23 (ELI). Table 7.4 lists their compositions, liquidus, β-transus, and density values in both the solid and liquid states. It should be noted that, the specifications of Ti−6Al−4V allow aluminium to vary from 5.5% to 6.75% and vanadium from 3.5% to 4.5%. Ti−6Al−4V is the nominal composition only. The range of vanadium was dictated by the weldability of the alloy. When the need for weldability overrides strength and ductility, the vanadium content should be limited to 4%. Conversely, when weldability is not a prime concern, the vanadium content can go up to 6% for higher tensile strength. The aluminium content was

Table 7.4 Ti−6Al−4V in Grade 5 and Grade 23 (ELI)

Grade	Al	V	O	Fe	C	H	N	Other impurities total (each)
5	5.5–6.75	3.5–4.5	≤0.20	≤0.30	≤0.08	≤0.015	≤0.05	≤0.4 (≤0.1)
23 (ELI)	5.5–6.5	3.5–4.5	≤0.13	≤0.25	≤0.08	≤0.0125	≤0.03	≤0.3 (≤0.1)

Liquidus (T_l): 1650 ± 150°C. Beta trances: 996 ± 14°C. Density at room temperature: 4.42–4.43 g cm^{-3}. Liquid density: $\rho = 4122 - 0.254\,(T - T_l)$ kg m^{-3} over 1661 K ≤ T ≤ 1977 K.

limited to 7.0% because, according to Abkowitz, beyond which "the ductility of the resulting alloy drops to such an extent that the forming and drawing qualities thereof are below the minimum regarded as essential in many industrial and ordnance applications."

Ti–6Al–4V is fully heat treatable but it is most commonly used in the mill-annealed condition, including as large fan blades in jet engines (Fig. 7.14) and bulkheads (closed-die forgings measuring 3.8 m long by 1.7 m wide weighing 1600 kg) in the Lockheed F-22 military aircraft. Ti–6Al–4V is also hardenable in sections up to 25.4 mm thick and it is therefore also used in the STA condition, e.g., as fasteners in aircraft. STA Ti–6Al–4V possesses superior tensile and fatigue strength. Table 7.5 lists the minimum tensile properties of

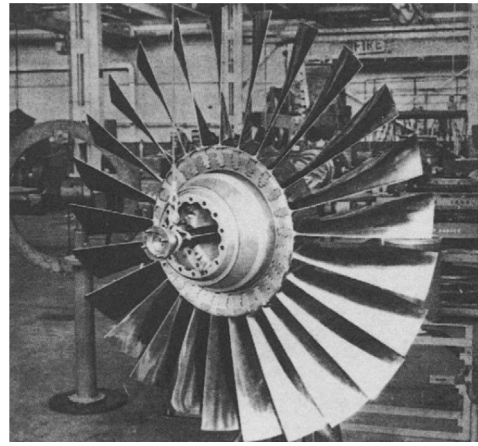


Figure 7.14 Forged IMI 318 (Ti–6Al–4V) blades from the low-pressure stage of the Rolls Royce/SNECMA Olympus 593 jet engine. Courtesy Rolls Royce Ltd.

Table 7.5 Minimum tensile properties and typical fatigue strength of Ti–6Al–4V at room temperature

Bar or billet diameter (mm)	Condition	UTS (MPa)	YS (MPa)	El. (%)	R_A (%)	Specification	Fatigue strength (MPa)
General	Mill-annealed	895	828	10	25	ASTM B348	400–680
<12.7	STA	1137	1068	10	20	Mil-T-9047G	700
12.7–25.4	STA	1103	1034	10	20	Mil-T-9047G	700

Mill-annealed: equiaxed α (elongated cross-sectional) plus ~10 vol.% β. STA: ~30–40 vol.% equiaxed α-grains (elongated cross-sectional) plus a fine lamellar α/β matrix from decomposed α′. El., elongation; RA, reduction of area.

mill-annealed Ti−6Al−4V and STA Ti−6Al−4V at room temperature together with their fatigue properties. Grade 23 ELI Ti−6Al−4V offers better ductility but lower strength than Grade 5 Ti−6Al−4V, and can be made into a wide variety of product forms, including coils, strands, wires, or flat wires. In particular, it is the premier titanium alloy used for dental and medical applications. Examples include orthopedic pins and screws, orthopedic cables, ligature clips, surgical staples, springs, orthodontic appliances, in-joint replacements, cryogenic vessels for medical storage, and bone fixation devices. With the increasing acceptance of metal additive manufacturing (3D printing), it is common practice today to produce ELI Ti−6Al−4V implants (knee, hip, neck, shoulder, spine, heel, skull, etc.) by additive manufacturing.

A range of other α−β alloys are in use today (Table 7.1), including Ti−6246, Ti−62222, Ti−62S, Ti−74, Ti−3Al−2.5V, Ti–662, IMI 551, and Corona-5. They were developed for different purposes. For example, Ti−6246 can be heat treated to higher strength in greater section sizes than Ti−6Al−4V. This alloy is used in intermediate (mid-pressure) compressor stages of turbine engines for disks and blades, seals, and also for airframe parts. It is a widely used α−β titanium alloy in aircraft engines. Ti−62222 is hardenable up to a section thickness of 100 mm (heavy sections) and offers superior strength, fracture toughness, and elevated temperature properties compared to Ti−6Al−4V. It accounts for 10% of the total titanium usage in the US Air Force F-22 jet fighter. Ti−62S has tensile properties and processing characteristics equivalent to, or better than, those of Ti−6Al−4V but with a lower cost. Most α−β alloys contain elements to stabilize and strengthen the α phase, together with 4–6% of β-stabilizers which allow substantial amounts of the β phase to be retained on cooling from the β- or α+β phase fields.

The common β-stabilizers that confer solid solution strengthening of the β phase are given in Table 7.6, but these effects are relatively small. Table 7.6 also gives the minimum solute concentration needed to give complete retention of the β phase on quenching of binary alloys to room temperature. More detailed information in this regard can be found in Section 7.4 (Table 7.9). Strength properties of the α−β alloys can be enhanced by subsequent ageing,

Table 7.6 Solid solution strengthening and β-stabilizing capacity of commonly used β-stabilizers

	Element (wt.%)							
	V	Cr	Mn	Fe	Co	Ni	Cu	Mo
Solid solution strengthening (MPa wt%$^{-1}$)	19	21	34	46	48	35	14	27
Minimum alloy content to retain β on quenching (%)	14.9	6.3	6.4	3.5	7	9	13	10

From Hammond, C and Nutting, J: *Metal Sci.*, 11, 474, 1977.

e.g., tensile strength exceeding 1400 MPa has been achieved. However, few compositions can sustain these levels of strength in thick sections because of the hardenability effects on quenching, which are aggravated by the low thermal conductivity of titanium (Table 1.1). β-Titanium alloys, to be discussed in Section 7.4, can offer deep hardenability due to the high contents of the β-stabilizers.

It is proposed now to consider the structure–property relationships in α−β alloys that are developed by heat treatment. In addition to Fig. 7.3, Table 7.7 summarizes experimentally determined critical cooling rates for phase transformations ($\beta \rightarrow \alpha'$, $\beta \rightarrow \alpha$, $\beta \rightarrow \alpha_m$) in three different compositions of Ti−6Al−4V and the corresponding microstructural features. Also, Fig. 7.15 gives a schematic continuous cooling diagram for Ti–6Al–4V solution treated at 1050°C. Together they provide a useful basis for understanding the effects of cooling rate on phase transformations in α−β alloys. The critical cooling rate reported for the $\beta \rightarrow \alpha'$ martensitic transformation in Ti−6Al−4V varies from 18°C s^{-1} to 425°C s^{-1} and so does the $\beta \rightarrow \alpha'$ start temperature (M_s, from 575°C to 800°C) due to different aluminium, vanadium, and impurity contents (Table 7.7), and experimental errors.

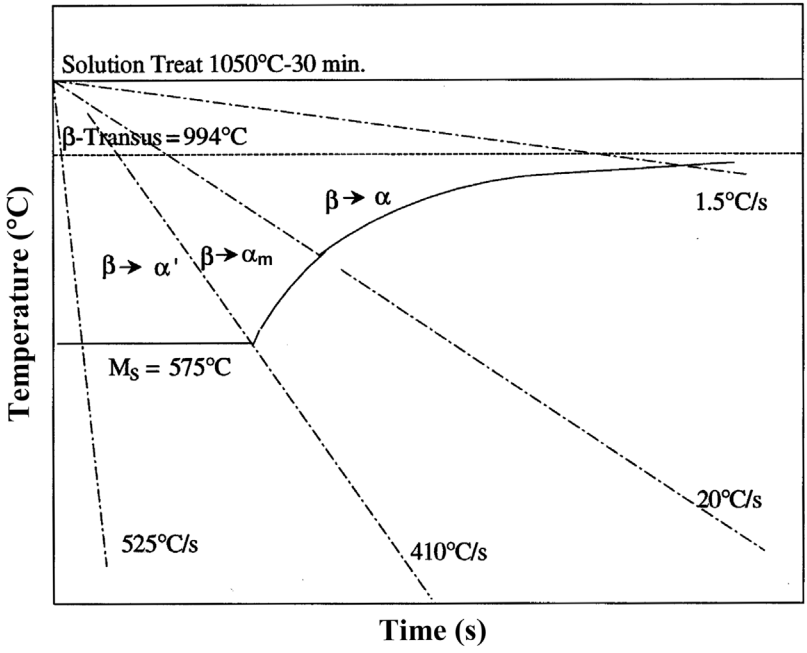


Figure 7.15 Effect of cooling rate on phase transformations in Ti−6Al−4V. From Ahmed, T and Rack, HJ: *Mater. Sci. Eng.* A243, 206, 1998.

Table 7.7 Critical cooling rates for phase transformations in Ti−6Al−4V when cooled from the β phase field

Composition	Critical cooling rate R (°C s^{-1})	Transformation	Microstructure (GB)
	$R \geq 23.1$	β→α′	Fully martensitic (α′)
Ti−6.5Al−4.4V	$7.3 < R < 23.1$	β→α	Lamellar α–β and GB α
(0.13O–0.15Fe–0.023C)	$0.065 < R < 7.3$	β→α	Lamellar α–β and GB α
–0.017N–0.0024H	$0.015 < R < 0.065$	β→α	Coarse lamellar α–β and GB α
Quenched from 1020°C	$R \leq 0.012$	β→α	Equiaxed α with β
Ti–6.1Al–4.3V	$R \geq 18.0$	β→α′	Fully martensitic (α′)
(0.16Fe–0.01C)	$3.5 < R < 18.0$	β→α	Lamellar α–β and GB α
Quenched from 1027°C	$R < 2.0$	β→α	Lamellar α–β and GB α
Ti–6.04Al–4.03V	$420 < R < 525$	β→α′	Fully martensitic (α′)
(0.12Fe–0.09O–0.03C–0.009N–0.023H)	$20 < R < 420$	β→α_m	Massive transformation (patch-like α_m phases)
Quenched from 1050°C	$R < 20$	β→α	Coarse lamellar α–β and GB α

7.3.2 Annealing treatments

The α−β titanium alloys can acquire a wide variety of microstructures by annealing treatments. The major purposes are to increase fracture toughness, ductility at room temperature, dimensional and thermal stability, creep resistance, or fatigue strength. The commonly used annealing treatments are described briefly in the following sections.

β-Annealing This refers to heating the alloy into the β phase field for an isothermal hold, followed by furnace or air cooling, or water quenching for thick sections to avoid the formation of coarse GB α phase. The purpose is to improve fracture toughness. Since β-annealing often leads to coarse prior-β grains, both the annealing temperature and time should be kept to the minimum. In general, slow cooling results in coarse lamellar α–β and GB α (Fig. 7.16A), where the α-laths nucleate at the prior-β GBs and grow inward as large α-colonies. Increasing cooling rate promotes the formation of finer and shorter α-laths. In addition, owing to the increased driving force, i.e., the increased cooling rate, α-colonies not only nucleate and grow from the prior-β GBs but also from the boundaries of the newly formed α colonies. Such developments lead to the formation of a basket-weave microstructure (Fig. 7.16B).

β-Annealed α−β alloys show reduced ductility and tensile strenghts but improved fracture toughness. They also exhibit reduced fatigue crack growth rates (see Fig. 7.19). The α-colony size, α-lath width, and prior-β grain size all affect the mechanical properties. Small prior-β grains produce small α-colonies. For lamellar α–β Ti−6Al−4V, its yield strength (σ_{YS}) and α-lath width (d, in μm) follows an approximate Hall–Petch relationship $\sigma_{YS} \approx 775+163d^{-1/2}$.

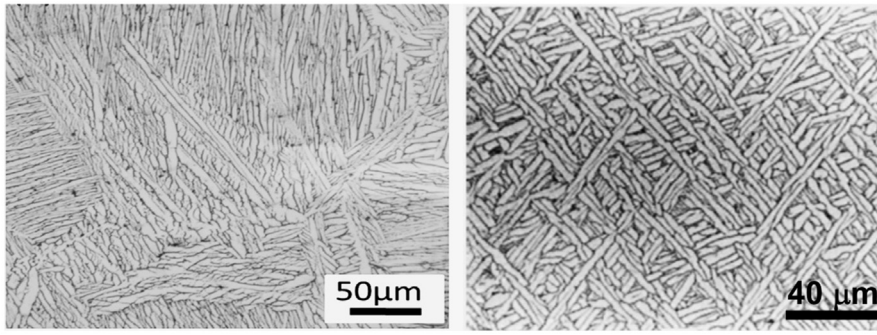


Figure 7.16 β-annealed Ti–6Al–4V. (A) Lamellar α–β with GB α, cooled at 0.42°C s^{-1} from 1100°C × 10 min. (B) Cooled from the β phase field at more than 1°C s^{-1} (estimated) showing a basket-weave α–β microstructure. (A) From Matsumoto, H et al.: Mater. Sci. Eng. A, 661, 68, 2016 and (B) courtesy Rolls Royce Ltd.

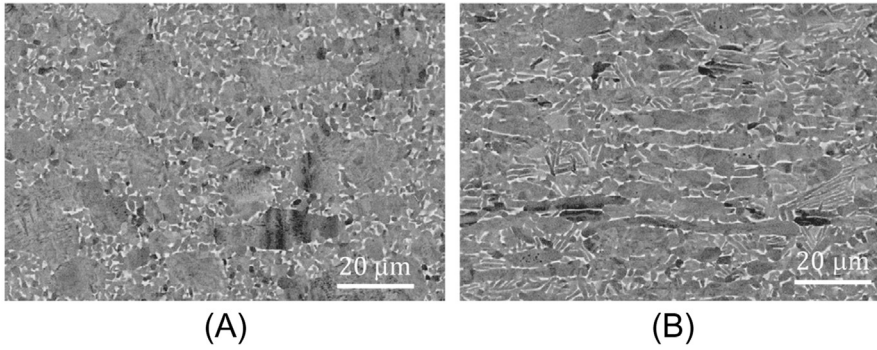


Figure 7.17 Backscattered electron images of the microstructure of mill-annealed Ti–6Al–4V: (A) plan view consisting of globular α and irregular β (bright) phases and (B) cross-sectional view consisting of elongated α and irregular β (bright) phases. From Mulay, RP *et al.*: *Mater. Sci. Eng. A*, 666, 43, 2016.

Mill annealing The isothermal hold is typically carried out in the range 700–800°C for Ti–6Al–4V for 1–4 h, followed by air cooling. For the similar α–β alloy Ti–3Al–2.5V, it is performed in the range 649–760°C for 1–3 h and then air-cooled to room temperature, while for Ti–6242, the mill annealing temperatures can be in the range 704–843°C. Mill annealing is an incomplete annealing treatment and the purpose is to retain the wrought-state microstructure, which consists of elongated α phase and irregular β phase particles (Fig. 7.17), for desired strength properties.

The maximum annealing temperature is determined by the stability of the β phase, which changes with temperature due to variations in the vanadium and aluminium contents. For example, the equilibrium composition of the β phase in Ti−6Al−4V is predicted to be Ti−4.3Al−9.8V at 845°C, which changes to Ti−4.0Al−13.0V at 795°C, and further to Ti−3.6Al−17.0V at 745°C according to the Pandat™ CompuTherm database. For Ti−6Al−4V, the critical annealing temperature is at ~845°C. When annealed at temperatures above 845°C, the β phase in Ti−6Al−4V is not retained during subsequent cooling, either by water quenching or furnace cooling, due to its low vanadium content or low stability.

Recrystallization annealing Similar to β-annealing, this treatment serves primarily to improve fracture toughness. The alloy is usually heated into the upper end of the α+β field for an isothermal hold up to 2 h, followed by furnace cooling. For Ti–6Al–4V, it is annealed at 955°C for 2 h. The resulting α and β phases are both essentially dislocation free, which gives the name recrystallization annealing. Recrystallization annealing leads to a bimodal microstructure (Fig. 7.18A). If furnace cooling leads to ordering and formation of the α_2 phase, it should be terminated at ~760°C and replaced by air cooling. Recrystallization annealing has been applied to other α–β alloys as well (e.g., Ti–62S, Table 7.1). In fact, the process has largely replaced β-annealing as it offers similar advantages but without causing excessive β grain growth so that the ductility can be maintained.

Duplex annealing A typical duplex annealing schedule for Ti–6Al–4V includes 870–950°C for 0.2–1.0 h, air cooling, and 680–730°C for 2–4 h, air

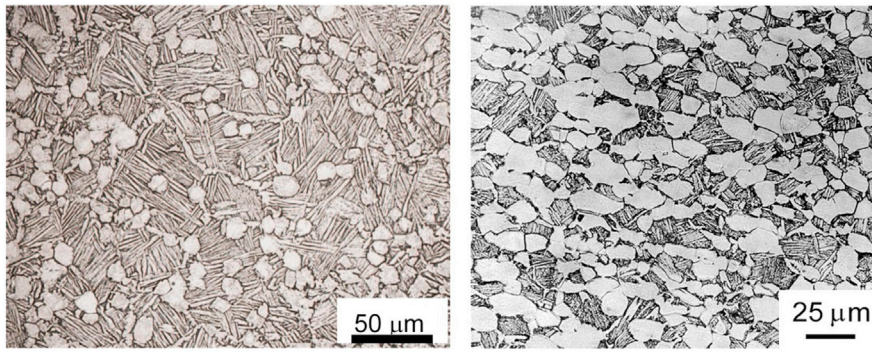


Figure 7.18 Bimodal (primary α and lamellar α–β) Ti–6Al–4V. (A) Recrystallization annealing: heated to 950°C at 0.05°C s^{-1}, held for 20 min, and cooled at 0.9°C s^{-1} to room temperature. (B) Duplex annealing: 925°C × 1 h, fan air-cooled, and 700°C × 2 h, air-cooled. (A) From Dabrowski, R: Archives Metall. Mater., 56, 217, 2016 and (B) from Nalla RK *et al.*: *Inter. J. Fatigue*. 24, 1047, 2002.

cooling again. The first anneal serves to control the α phase fraction and morphology, while the second anneal allows precipitation of acicular secondary α phase in the metastable β phase. For Ti–6242, the first stage annealing is carried out at 900°C, while the second stage is conducted at 785°C. A third stage annealing treatment is sometimes also applied to Ti–6242 at 595°C, which can be regarded as a further stabilization annealing treatment (see below). Duplex annealing also produces a bimodal microstructure (Fig. 7.18B), which offers improved fracture toughness and creep resistance. For example, duplex-annealed Corona-5 achieved plane strain fracture toughness of 155 MPa $m^{1/2}$ for tensile strength of 950 MPa.

Stabilization annealing This treatment is essentially similar to the second stage of duplex annealing. The purpose is to enhance the stability of the β phase in order to make the alloy capable of resisting further transformation during services at elevated temperatures. For example, in order to obtain the maximum creep resistance and stability, the first annealing treatment for Ti–8–1–1 begins at 25–55°C below the β-transus (15–25°C below the β-transus for Ti–6–2–4–2S, Table 7.1), followed by air cooling or water quenching. The subsequent stabilization annealing treatment is carried out at ~300–450°C below the β-transus.

Stress-relief annealing The purpose is to alleviate residual stresses resulted from previous cold- or hot-forming or heat-treatment processes. For example, it is common practice to apply stress-relief annealing to fixtures to remove springback or warpage. For α–β Ti–6Al–4V, stress-relief annealing is performed at 480–650°C in air for 1–4 h, followed by air cooling. As for Ti–3Al–2.5V, it is carried out at 316–649°C in air for for 0.5–3 h, followed by air cooling.

7.3.3 Properties of annealed α–β alloys

The α−β alloys are mostly used in the mill-annealed or forged-and-annealed condition (Fig. 7.17) but their mechanical properties also depend on whether forging was conducted in the β or α+β field. Table 7.8 compares the properties of Ti−6Al−4V forged in these two regimes. Although the tensile properties are similar, the samples forged in the α+β field (equiaxed grains) are more ductile, whereas both fracture toughness and fatigue strength are notably higher in the β-forged and β-annealed condition (acicular Widmanstätten microstructures).

β-Annealed Ti–6A1–4V shows slower rates of crack propagation than mill-annealed Ti–6A1–4V (Fig. 7.19A). This effect is attributed to the slower progress of cracks through the Widmanstatten microstructure, particularly at stress intensities below a critical value (T in Fig. 7.19A), at which desirable crack branching occurs within packets of the α-laths (Fig. 7.19B). These trends have already been noted when considering α-alloys. However, it should be pointed out that the low-cycle (high-stress) fatigue strength of β-annealed Ti–6Al–4V is

Table 7.8 Properties of Ti−6Al−4V forgings after annealing at 705°C for 2 h

	Forging treatment (β = 1005°C)[a]	
	α+β Phase field	β Phase field
Tensile ultimate (MPa)	978	991
Tensile yield (MPa)	940	912
Tensile elongation (%)	16	12
Reduction in area (%)	45	22
Fracture toughness (MPa $m^{1/2}$)	52	79
10^7 fatigue limit[b]	±494	±744

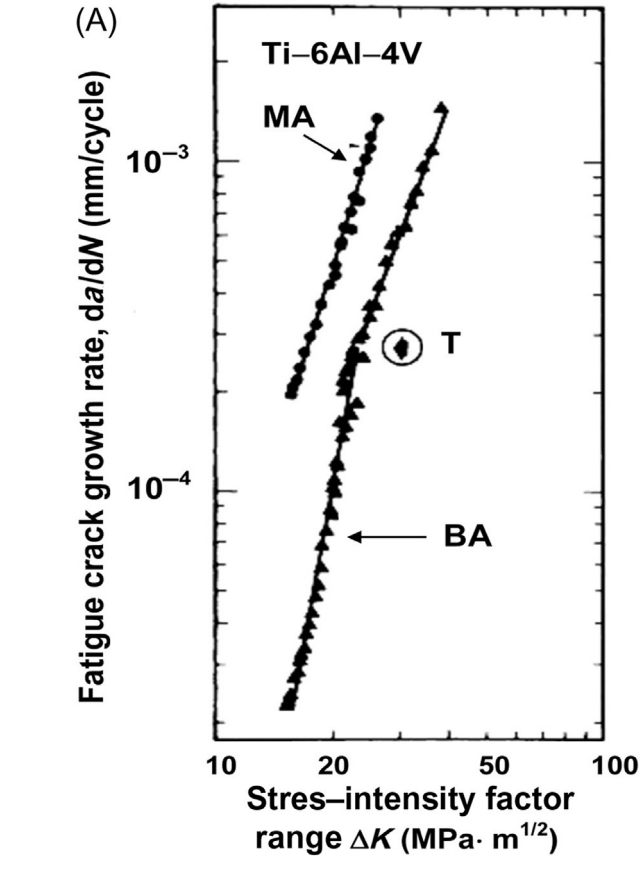
[a]Annealed 2 h at 705°C, air-cooled after forging.
[b]Axial loading: smooth specimens, $K_t = 1.0$.

inferior to that of the mill-annealed condition (Fig. 7.20) as the fatigue strength appears to depend more on the resistance to fatigue crack initiation than the rates of crack propagation. In general, the fatigue strength of a titanium alloy is proportional to yield strength (Section 7.7.2) but its fracture toughness decreases with increasing yield strength (Section 7.7.3). β-Annealing leads to reduced yield strength. At elevated temperatures, the fatigue performance can be adversely affected by enhanced oxidation along phase boundaries, which can permit premature crack initiation along surface-connected, acicular-α interfaces. In order to achieve balanced creep and fatigue properties in α−β alloys, a bimodal microstructure consisting of ~30 vol.% of equiaxed α-grains and 70 vol.% of lamellar α−β has been found to be useful for rotating components, such as compressor disks, that operate at high temperatures.

7.3.4 Quenching from β phase field

The range of properties of α−β alloys can be extended by quenching from the β phase field and then ageing at elevated temperatures to decompose the quenched microstructure. The possible reactions and resulting microstructures on quenching may be summarized as in Fig. 7.21.

The most common titanium martensite is the hcp α′-type. It usually forms as colonies of parallel-sided plates or laths in two-dimensional (2D) morphology (Fig. 7.22A), the boundaries of which consist of walls of dislocations. The internal regions are also heavily dislocated. With increasing solute content, which lowers the M_s temperature, these colonies tend to decrease in size and many degenerate into individual plates which are randomly oriented. These plates have a lenticular or acicular morphology (2D morphology, Fig. 7.22B) and are internally twinned on $\{10\bar{1}1\}$ planes. The orientation relationship between the β phase and α′-martensite is $(110)_\beta // (0001)_{\alpha'}$; $[111]_\beta // [11\bar{2}0]_{\alpha'}$, and the habit planes for the untwinned and twinned planes are $\{334\}_\beta$ and $\{344\}_\beta$,



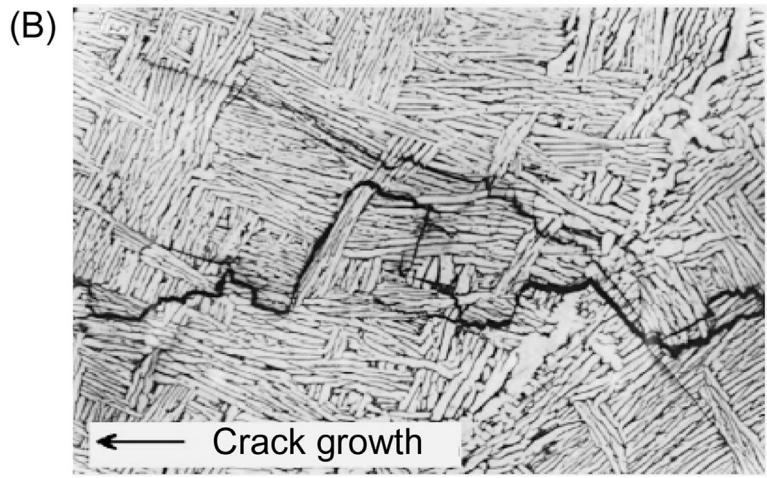


Figure 7.19 (A) Fatigue crack growth rates for rolled plates of Ti–6Al–4V in β-annealed (BA) and mill-annealed (MA) conditions. β-Annealing: 0.5 h at 1038°C, air-cooled. Tests conducted at 5 Hz using compact tension specimens. Ratio of minimum to maximum load (R) = 0.1. (B) Branching of fatigue cracks within the Widmanstatten packets of the α-laths. (A) From Yoder, GR et al.: Metall. Trans. A, 8, 1973, 1977 and (B) courtesy J. Ruppen and A. J. McEvily (× 225).

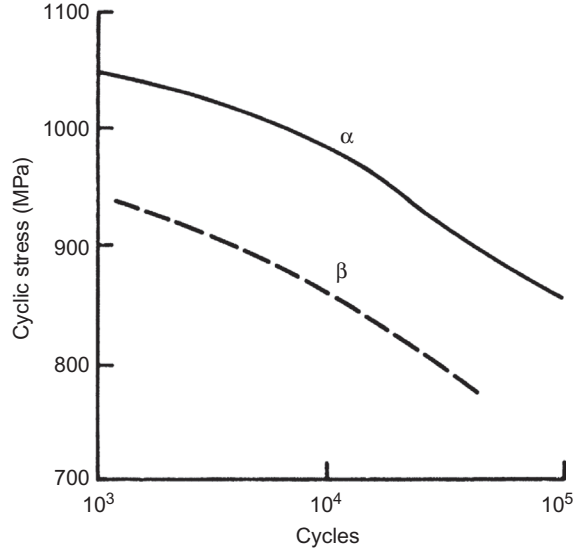


Figure 7.20 Comparison of low-cycle fatigue lives of Ti–6Al–4V in (α+β)-annealed and β-annealed condition. From Blenkinshop, PA *et al.*: *Titanium Science and Technology*, *Proc. 5th Inter. Conf. on Titanium*, Lutjering, G Zwicker, U, Bunk, W (Eds.): p. 2323, DGM, Oberursel, 1985.

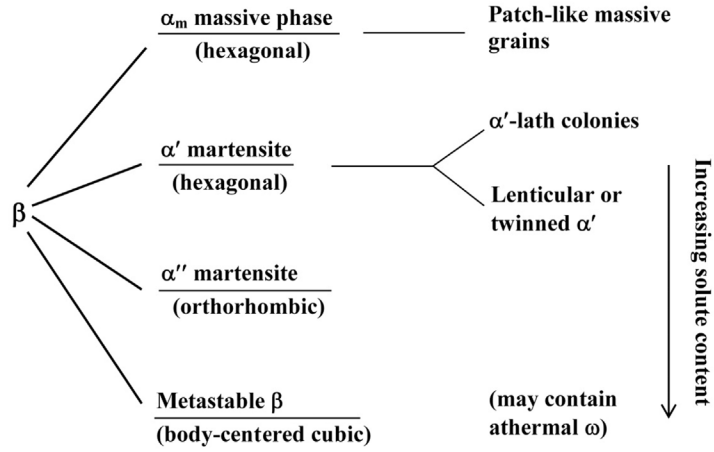


Figure 7.21 Possible reactions from the β phase in titanium alloys on water quenching.

respectively. Since α′ and α have the same lattice structure (hcp) and similar lattice parameters, the β→α′ transformation in titanium alloys offers only limited strengthening through solid solution strengthening (α′ is supersaturated) and the formation of fine and short α′-laths.

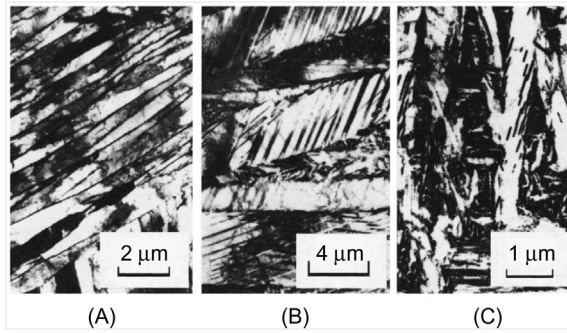


Figure 7.22 TEM images showing the structure of titanium alloy martensites: (A) hcp α′ laths in Ti−1.8Cu quenched from 900°C; (B) hcp lenticular α′ containing twins in Ti−12V quenched from 900°C; (C) orthorhombic α″ in Ti−8.5Mo−0.5Si quenched from 950°C. From Williams, JC: Titanium Science and Technology, Jaffee, RI and Burte, HM (Eds.): Plenum Press, New York, NY, USA, Vol. 3, 1973.

The 3D morphology of α′ martensite in Ti−6Al−4V additively manufactured by selective laser melting (SLM) has been studied using focused ion beam and scanning electron microscopy techniques. Individual α′ martensite phases were reconstructed from slice data to reveal their 3D morphology. The α′-martensite exhibited flat and irregular 3D shapes (patch-like) in different sizes. For example, the thickness ranged from <50 nm to a few hundred nanometers.

The second type of titanium martensite (α″) has an orthorhombic structure and a similar lattice correspondence with the β phase. It is also internally twinned (Fig. 7.22C), with twins forming on the $\{111\}_{\alpha''}$ planes. Its approximate lattice parameters are $a = 0.298$ nm, $b = 0.494$ nm, and $c = 0.464$ nm in Ti−8.5Mo−0.5Si quenched from 950°C. Fig. 7.23 illustrates the crystal structures of β, α″, and α (or α′) phases and their lattice correspondences.

The transition from α′ to α″ occurs in alloys with increasing solute content (Fig. 7.21), as well as with decreasing M_s temperature. The critical solute content for the α′/α″ boundary is dependent on solute type. For example, α′-forms in Ti−Mo binary alloys containing up to 2 at.%Mo, whereas in Ti−Nb binary alloys, the borderline is ~6 at.%Nb. The α′/α″ boundary for Ti−Ta binary alloys is ~9 at.%Ta. α″ does not seem to form in Ti–V binary alloys, although it forms if aluminium is added. For example, formation of α″ has been reported in Ti−6Al−4V when quenched from clearly below 845°C, e.g., 745°C at which the β phase has the approximate equilibrium composition Ti−3.6Al−17.0V. Whereas α″ tended to be neglected in earlier studies, its importance is now recognized, especially in the development of shape memory and superelastic β-titanium alloys (Section 7.4.3). Both properties are associated with the reversible transformation between β and α″. The presence of α″ lowers tensile ductility in titanium alloys,

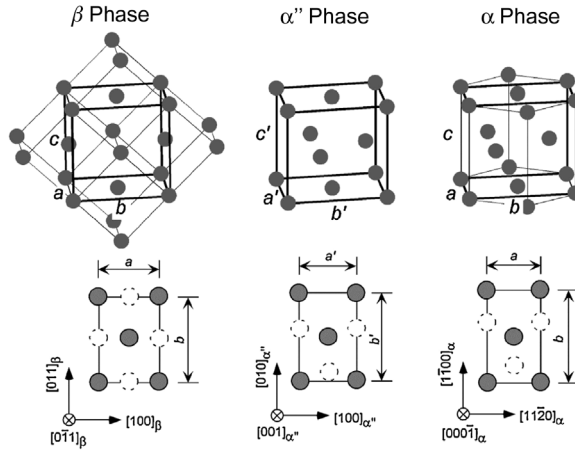


Figure 7.23 Crystal structures of β, α″, and α (or α′) phases and their lattice correspondences. From Kim, HY and Miyazaki, S: Mater. Trans., 56, 625, 2015.

although it does have the advantage of being a favorable precursor in producing a very uniform distribution of the α phase following subsequent heat treatment.

Depending on the heat treatment or manufacturing processes, α″ martensite can be formed in the following three ways:

1. Decomposition of metastable β (see Section 7.4.1) during quenching: β→α″
2. Decomposition of retained β by intermediate transformation during isothermal ageing, e.g., through β→β (lean) + β (rich)→α″ + β (rich). In addition, a short-time holding of the retained β (e.g., 30 s), at either the ω-formation temperature or a higher temperature but just before the α-phase forms (through lattice softening), can facilitate the subsequent β→α″ transformation on quenching.
3. Stress-induced transformation of retained β: β→α″ + twinned β.

If the M_s and M_f fall above and below room temperature, respectively, then a mixed microstructure containing lenticular α′ or α″ martensite may be formed together with retained β. Another feature is that metastable β may contain a fine dispersion of a metastable phase ω (Section 7.3.6, Figs. 7.27 and 7.28), the formation of which cannot be suppressed even at fast quenching rates.

In addition to martensitic transformations, the other composition-invariant transformation, β→α_m massive transformation, may also occur in α−β alloys at slower quenching rates from the β phase field (see Fig. 7.15). Limited diffusional activities are involved at the advancing interfaces. The resulting α_m grains are patch-like and they can form at different locations, e.g., at or across β GBs or inside β grains (Fig. 7.24). It should be pointed out that martensite laths often form together with the α_m grains due to local fast cooling rates.

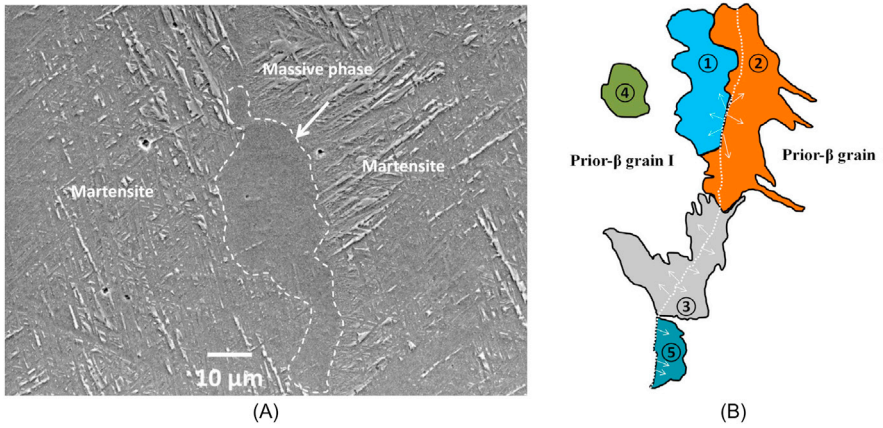


Figure 7.24 (A) Formation of α′-martensite phase and α_m massive phase in Ti–6Al–4V additively manufactured by SEBM. (B) Schematic illustration of the formation of massive grains (1–5) in Ti–6Al–4V based on experimental observations. From Lu, SL *et al.*: *Acta Mater.* 104, 303, 2016.

If the alloys contain a sufficient amount of β-stabilizing elements to bring the M_s temperature below room temperature, then a fully metastable β phase microstructure can be retained. This will be discussed in Section 7.4.

A double solution treatment combined with either water quenching or air cooling has also been proposed. The initial solution treatment is conducted below the β-transus to control the volume fraction of the primary α phase (similar to duplex annealing). A range of microstructures can be produced (Fig. 7.25). For example, the use of double-solution treatment, particularly in conjunction with air cooling, promotes the formation of coarse, acicular plates of the α phase, which are effective for branching cracks and improving fracture toughness.

The surfaces of the titanium alloy components absorb oxygen, carbon, nitrogen, and other impurities during solution annealing. It is necessary to remove the surface layer afterwards, a hard and brittle oxygen-stabilized α phase layer, known as the α-case. Solution annealing is therefore best performed in vacuum because of surface contamination, which is not always visible. This often requires removal of a sufficient surface layer in order to expose uncontaminated metal, which can be an issue for thin sections. Consequently, solution annealing times and temperatures should be minimized. In addition, it may be necessary to complete solution annealing in vacuum. Another issue is hydrogen pickup during solution annealing. A titanium alloy surface can readily react with water vapor at solution annealing temperatures and the hydrogen thus liberated will be immediately absorbed in the surface and diffuse deep into the metal. This serves as another reason for limiting solution treatment time and temperature or for vacuum annealing.

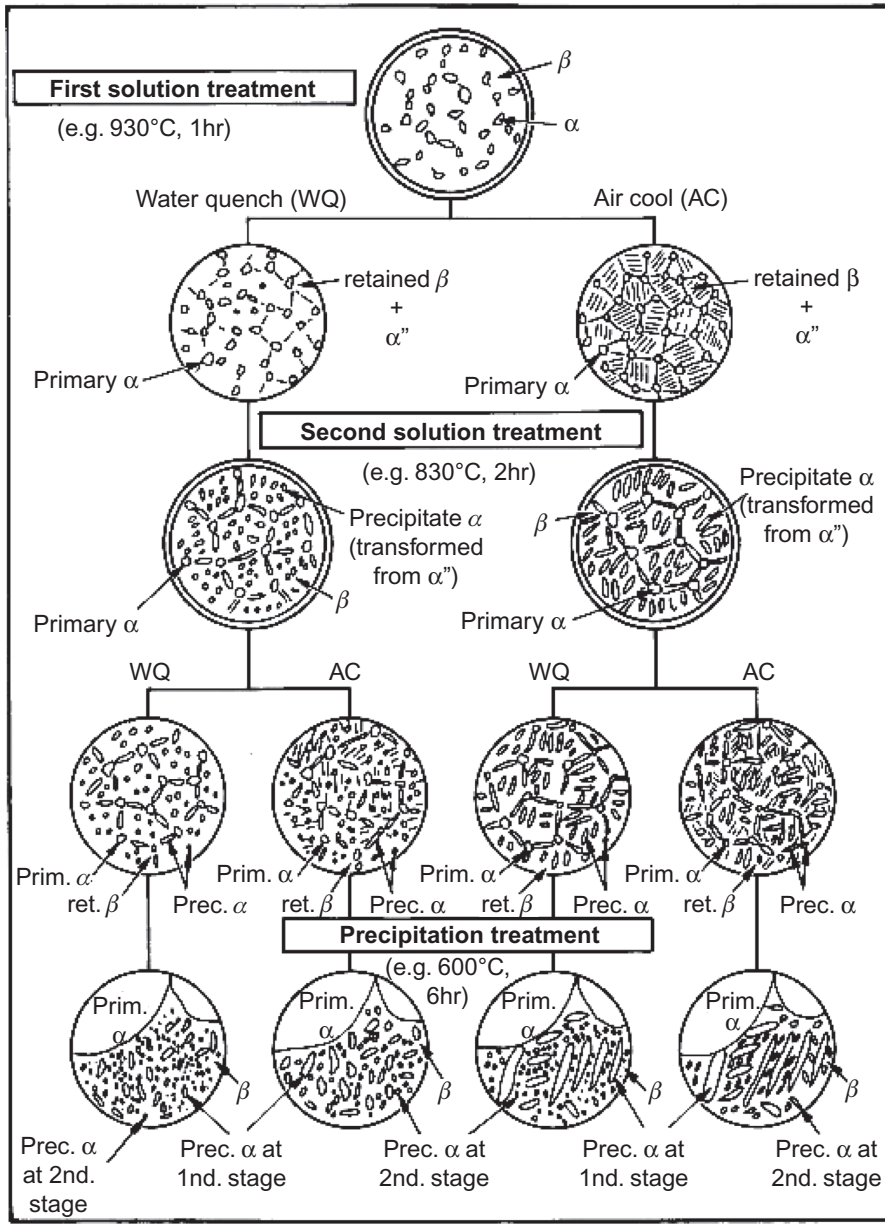


Figure 7.25 Schematic diagram showing range of microstructures obtained by double-solution treatment and either water quenching (WQ) or air cooling (AC) followed by an ageing treatment. From Murakami, Y: Titanium '80 Science and Technology, Kimura, H and Izumi, Q (Eds.): AIME, Warrendale, PA, USA, p. 153, 1980.

Quenched alloys are normally aged to decompose the retained β phase to allow the precipitation of fine and dispersed α phase particles for desired strength, fracture toughness, or fatigue properties. It is now appropriate to consider the changes that may occur during ageing.

7.3.5 Ageing of titanium martensites

The martensitic α′ phase is supersaturated but with negligible lattice distortion. It is unstable and is normally subjected to a subsequent ageing treatment. Precipitation in the retained β phase may also occur in the same process when the retained β phase exists. It appears that, on water quenching, the β→α′ transformation can readily occur to nearly completion unless the section is too thick. For example, the retained β phase is not always detectable by both X-ray diffraction and electron microscopy. The M_s temperature for Ti−6Al−4V is generally taken as 800°C but other values have also been used (see Fig. 7.15) due probably to different aluminium, vanadium, and impurity contents (e.g., the M_s temperature for Ti−0.3O was measured to be ~860°C). The ageing temperature is alloy dependent. For water-quenched Ti−6Al−4V, it is recommended to be 480−595°C for 4−8 h, while for both Ti−6Al−2Sn−4Zr−6Mo and Ti−5Al−2Sn−2Zr−4Mo−4Cr, in the range 580−605°C for 4−8 h, all followed by air cooling.

The reactions during ageing can be complex and the various types are shown in Fig. 7.26. These reactions lead to a wide range of microstructures.

α′ *martensite* (hexagonal close packed)

β-isomorphous alloys: $\alpha' \rightarrow \alpha + \beta$

β-eutectoid alloys:
- Alloys with slow eutectoid reactions (e.g. Ti–Fe): $\alpha' \rightarrow \alpha + \beta \rightarrow \alpha +$ compound
- Alloys with fast eutectoid reactions (e.g. Ti–Cu): $\alpha' \rightarrow \alpha +$ compound (may form in several stages)

α″ *martensite* (orthorhombic)

- Decomposition of α″ by both spinodal decomposition and reverse martensitic transformation during cooling and ageing: $\alpha'' \rightarrow \alpha''_{lean} + \alpha''_{rich} \rightarrow \alpha''_{lean} + \beta \rightarrow \alpha + \beta$
- Decomposition of α″ in the normal (i.e. reverse) way: $\alpha'' \rightarrow \beta \rightarrow \alpha + \beta$

Figure 7.26 Illustration of decomposition of titanium martensites during ageing of titanium alloys containing different solute elements. Decomposition of α″: from Welsch, G, Boyer, R, and Collings, EW: Materials Properties Handbook: Titanium Alloys, ASM International, Materials Park, OH, USA, p. 1053, 1993.

In β-isomorphous alloys, α′ decomposes into β and α through β forming as fine precipitates at martensite plate boundaries, or at internal substructures such as twins. In β-eutectoid alloys, α′ may decompose into the α phase and an intermetallic compound, although the formation of this compound may take place in several stages. However, in systems such as Ti−Fe and Ti–Mn where the normal eutectoid reaction is sluggish, the martensite decomposes first by forming β and α, with the intermetallic compound appearing only slowly at a later stage.

Ageing of α″ martensite may occur by two mechanisms (Fig. 7.26). In alloy compositions in which $M_s(\alpha'')$ occurs at a relatively high temperature, decomposition of α″ may proceed by both spinodal decomposition and reverse martensitic transformation. The resulting microstructure consists of α and β phases (Fig. 7.26). Further ageing may lead to the formation of some α phase particles at the prior β-GBs and lamellar α−β in the matrix. In alloys having an $M_s(\alpha'')$ temperature close to room temperature, the α″ reverts to the β phase, which then decomposes by a mechanism that is characteristic of the particular ageing temperature. Decomposition of metastable β phase during ageing is discussed in the next section.

7.3.6 Decomposition of metastable β during ageing

Decomposition of the β phase that is retained on quenching to the equilibrium α phase occurs only at relatively high temperatures probably because of the difficulty of nucleating the hcp α phase from bcc β-matrix. Accordingly, intermediate decomposition products are usually formed and the possible reactions are summarized and discussed here:

Medium alloy content

$100 - 500°C \qquad \beta \rightarrow \beta + \omega \rightarrow \beta + \alpha$

Concentrated alloys

$200 - 500°C \qquad \beta \rightarrow \beta + \beta_1 \rightarrow \beta + \alpha$

$> 500°C \qquad \beta \rightarrow \beta + \omega \rightarrow \beta + \alpha$

The ω phase Athermal ω phase may form in the β phase during quenching of some compositions by a displacement reaction. More commonly, the ω phase precipitates isothermally as a very fine dispersion of ellipsoidal or cuboidal particles (Fig. 7.27A) when alloys containing metastable β are isothermally aged at temperatures in the range 100–500°C. The ranges of stability of both types of ω phase are shown schematically in a β-isomorphous phase diagram (Fig. 7.27B), but there is some evidence that the athermal ω phase can also form during heating to the isothermal ageing temperature. In addition, it has been found that the ω phase can also be stress-induced as plate-like precipitates, e.g., in a zirconium–niobium alloy, under extremely high strain-rate compressive loading conditions (e.g., shock loading).

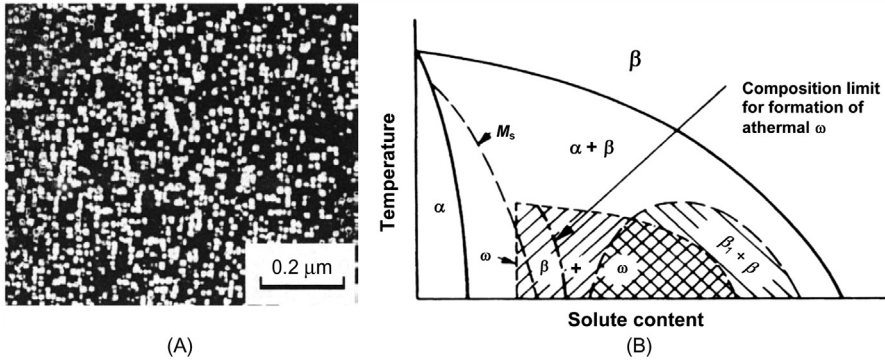


Figure 7.27 (A) Cuboids of the ω phase in a Ti–11.5Mo–4.5Sn–6Zr alloy. (B) Schematic β-isomorphous alloy phase diagram showing an M_s curve and the ranges of stability of ω, β, and β_1. (A) From Williams, JC: Titanium Science and Technology, Jaffee, RI. and Burte, HM (Eds.), Plenum Press, New York, NY, USA, Vol. 3, 1973.

The ω phase has attracted special attention because its presence can cause severe embrittlement of the alloy concerned. In a more positive vein, strengthening of Ti–10–2–3 through the precipitation of the ω phase instead of the α phase has been found to retard fatigue crack propagation significantly. This retardation has been attributed to changes in slip character. In addition, ω particles have been beneficial in the specialized field of superconducting titanium–niobium alloys (e.g., Ti–45Nb and Ti–47Nb, Section 7.4.3) as they are effective in flux-pinning. Consequently, a large improvement in the critical current densities can develop, which may be sustained in the presence of an external magnetic field.

Studies of the isothermal ω phase have revealed the following characteristics:

1. ω forms rapidly as homogeneously nucleated, coherent precipitates with a large volume fraction (Fig. 7.27A).
2. The ω particles are cuboidal in shape (cube face//$\{100\}_\beta$) if there is high misfit and ellipsoidal (long axes// $<111>_\beta$) if misfit is low.
3. Most results suggest that ω has a hexagonal (not hcp) lattice structure (Fig. 7.28B) with a *c*/*a* ratio of 0.612. The changes in lattice structure from β to ω are schematically illustrated in Fig. 7.28. The unit cell of the ω phase (Fig. 7.28D) can be regarded as originating from four adjacent layers of $\{222\}_\beta$ (*d*-spacing $= \frac{\sqrt{3}}{6}\, a_\beta$) after a small shuffle along the direction $<111>_\beta$ (see Fig. 7.28C). Hence the *d*-spacing of $(0001)_\omega$ is equal to three times the *d*-spacing of $\{222\}_\beta$, i.e., $c_\omega = \frac{\sqrt{3}}{2}\, a_\beta$ (see Fig. 7.28C and D). The presence of ω phase precipitates in β matrix can be found by electron diffraction patterns

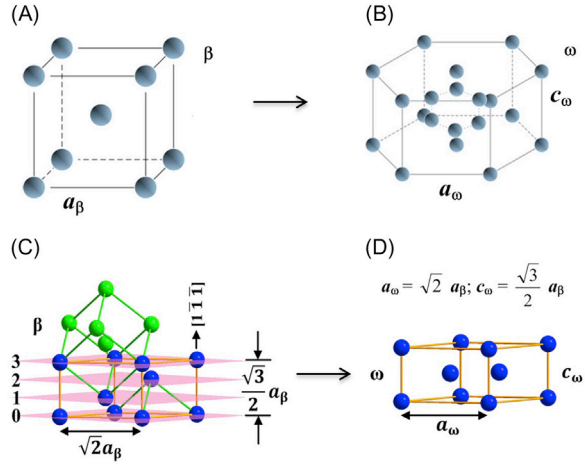


Figure 7.28 (A) Bcc lattice of β-Ti, (B) hexagonal lattice of ω-Ti, (C) relationship between bcc β and hexagonal ω prior to small shuffle along the direction $[1\,\bar{1}\,\bar{1}]$ and (D) unit cell of ω-Ti after the small shuffle along $[1\,\bar{1}\,\bar{1}]$ in (C). The unit cell in (D) represents a third of the hexagonal lattice of ω-Ti in (b). a_β, a_ω, and c_ω are lattice parameters. Adapted from Yan, M *et al.*: *Metall. Mater. Trans.* A 44, 3961, 2013 and Lai, MJ *et al.*: *Acta Mater.* 92, 55, 2015.

along zone axes $<113>_\beta$ and $<110>_\beta$. The orientation relationship between β and ω can be defined as $(0001)_\omega // \{222\}_\beta$ or $\{111\}_\beta$: $<11\bar{2}0>_\omega // <110>_\beta$.

4. Partitioning of solute occurs during ageing leading to depletion of ω and enrichment of the β-matrix. The terminal composition of ω in aged binary titanium alloys is related to the group number of the solute in the periodic table because the electron-to-atom ratios of all ω phases have been found close to 4.2:1. Thus the possibility exists that ω is an electron compound.
5. Dislocations have little or no mobility in ω which accounts for the embrittlement of alloys having high volume fractions of this phase. It is interesting to note, however that, even in alloys displaying no macroscopic ductility, the fracture surfaces show exceedingly small dimples which are indicative of some ductility at a microscopic scale. Thus the possibility exists that the potent hardening associated with ω may be used to practical advantage although no progress has been made in this regard.

The formation of isothermal ω may be minimized or avoided by control of the ageing conditions, as well as by varying alloy composition. The significance of both ageing temperature and composition is apparent from Fig. 7.27B. The upper temperature limit of stability of ω in most binary alloys is close to 475°C and the range of stability decreases as the solute content is raised. This latter effect is attributed to a relative increase in the stability of the β phase and

it should be noted that this effect can arise from the presence of both α- and β-stabilizers. For example, ω forms in Ti–V binary alloys, but is usually absent in the important ternary alloy Ti–6Al–4V (conversely, α″ does not seem to form in Ti–V binary alloys, but it forms if aluminium is added, Section 7.3.4). This is one reason why most α−β and β-titanium alloys contain at least 3%Al.

β Phase separation Separation of the β phase into two bcc phases of different compositions is favored in alloys which contain sufficient β-stabilizers to prevent ω formation during low temperature ageing, and which transform only slowly to the equilibrium phase α under these conditions (Fig. 7.27B). This transformation is thought to occur during ageing of a wide range of alloys but has received only limited attention, because it is not considered to be important in commercial alloys. The phases that form have been designated as β (matrix) and β_1 (occasionally as β_1 and β_2, respectively), which occurs as a uniformly dispersed, coherent precipitate. Again there is partitioning of solute between the two phases, which leads to enrichment of the β-matrix and depletion of β_1 during treatment.

Formation of equilibrium α phase Ageing of alloys containing metastable β can, under certain circumstances, result in the direct nucleation of the α phase. Alternatively this phase may form indirectly from either the ω- or β_1 phase. The route that is followed controls the morphology and distribution of the α phase and thus could have a marked effect on properties. The α phase that forms directly from β can have two distinct morphologies. It may occur as coarse Widmanstätten plates in a β-matrix in relatively dilute binary alloys aged at temperatures above the range for ω formation, and in more complex alloys containing substantial amounts of aluminium. In such cases, ductility may be adversely affected and deformation prior to ageing is desirable so as to obtain a more uniform distribution of α. Alternatively, a fine dispersion of α in a β-matrix is obtained when alloys containing β-stabilizers are aged at temperatures above which phase separation of β occurs.

When α forms in alloys comprising β+ω phases, the mechanism of nucleation depends upon both the relative misfit between these two phases as well as the ageing temperature. If the misfit is low, α nucleates with difficulty, and it forms at the β-GBs. If the misfit is high, then α tends to nucleate at β/ω interfaces. High ageing temperatures encourage α to form directly from the ω phase. Continued ageing of alloys that have undergone β phase separation into $\beta+\beta_1$ leads to the nucleation of the α phase within the β phase particles. Thus the final α phase distribution is determined by the distribution of β_1. Although this reaction may, inadvertently, play a part in the heat treatment of some commercial α–β-titanium alloys, it has not been studied in detail.

7.3.7 Solution treated and aged (STA) α–β alloys

α−β alloys in the STA condition can offer much higher strength than in the mill-annealed condition. Therefore they can be used for more demanding applications such as fasteners. The STA schedule for Ti−6Al−4V consists of solution annealing in the α+β phase field (e.g., 10 min at 940°C), followed by water quenching, and ageing (e.g., 4 h at 510−540°C). The resultant bimodal microstructure comprises equiaxed α-grains (~30−40 vol.%) in a matrix of fully transformed β, and possesses superior tensile and fatigue properties as listed in Table 7.5. However, its ductility, stress–corrosion resistance, and fracture toughness are inferior to those of the mill-annealed Ti−6Al−4V. Overageing is practiced occasionally, referred to as STOA. Ti−6Al−4V in the STOA condition offers lower strength than STA Ti−6Al−4V but improved ductility and fracture toughness. Product forms of Ti−6Al−4V in the STA condition include forgings, plates, and rods.

In addition to Ti−6Al−4V, the STA process has also been applied to other α−β-forging alloys for applications that require greater strength such as aircraft engine mounting brackets and undercarriage components. Owing to the increased use of β-stabilizers, the M_f temperature is depressed well below room temperature in these alloys, and significant amounts of β phase are retained. Common examples of these alloys include Ti–6Al–2Sn–4Zr–6Mo (Ti−6246), Ti–6Al–6V–2Zr–0.7 (Fe, Cu) (Ti–662), Ti–4Al–4Sn–4Mo–0.5Si (IMI 551), and Ti–4.5Al–5Mo–1.5Cr (Corona-5). Full strengthening is again usually obtained by solution annealing in the α+β field, followed by water quenching, and subsequent ageing to transform the retained β phase.

7.4 β-ALLOYS

7.4.1 Basic physical metallurgy

β-Titanium alloys are generally defined as those containing sufficient β-stabilizing elements to enable the β phase to be retained in a metastable condition by water quenching to room temperature. This means that the amount of these elements is sufficient to avoid passing through the M_s temperature during water quenching. Fig. 7.29 illustrates the M_s curve, the position of the approximate critical minimum amount of the β-stabilizer needed to retain 100% β phase on water quenching (β_c), and the β-transus curve (β_s) on a pseudo-binary phase diagram of Ti−X (X: a β-stabilizer).

Highly alloyed compositions to the right of the β-transus curve (β_s) in Fig. 7.29 are considered to be stable β-titanium alloys. Since these compositions are in the single β phase field, no response is expected to ageing. Only a few such alloys exist, e.g., Alloy C (Ti−35V−15Cr) in the United States and its variant Ti−25V−15Cr−0.3Si in China. Alloy compositions that place them between β_c and β_s in Fig. 7.29 are commonly referred to as metastable β-titanium alloys,

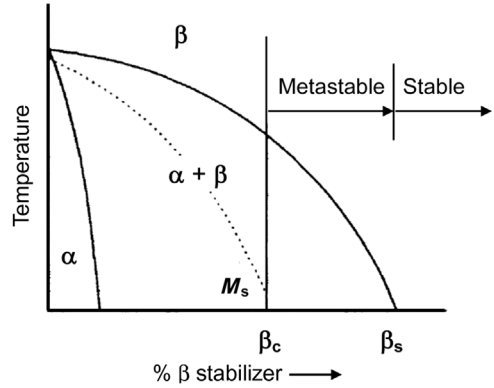


Figure 7.29 Pseudo-binary β-isomorphous phase diagram showing locations of metastable and stable β-titanium alloys. β_c refers to the critical minimum addition of a β-stabilizer to retain 100% β on water quenching. β_s denotes the β-transus. From Bania, PJ: *JOM*, 7, 16, 1994.

Table 7.9 Potency of β-stabilizers in titanium

β-Stabilizer	Type	β_c (wt%)[a]	$\Delta\beta_{Transus}$ (°C)[b]
Mo	Isomorphous	10.0	−8.3
V	Isomorphous	15.0	−5.5
W	Isomorphous	22.5	−13.8
Nb	Isomorphous	36.0	−10.6
Ta	Isomorphous	45.0	−15.6
Fe	Eutectoid	3.5	0
Cr	Eutectoid	6.5	−2.8
Cu	Eutectoid	13.0	−5.6
Ni	Eutectoid	9.0	4.4
Co	Eutectoid	7.0	3.3
Mn	Eutectoid	6.5	4.4
Si	Eutectoid	–	21.1

From Bania, PJ: *JOM*, 7, 16, 1994.
[a]Approximate wt% needed to retain 100% β on water quenching.
[b]Approximate amount of β-transus reduction per wt% of addition.

because they are still within the α−β two phase field, and α phase can precipitate upon ageing leading to improved mechanical properties.

Table 7.9 lists the commonly used β-stabilizers and their β_c values. Iron is the most potent β-stabilizer by this criterion. Between the two groups of β-stabilizers considered in Table 7.9, the eutectoid stabilizers are generally more potent than the isomorphous group. Additionally, all the five isomorphous β-stabilizers considered reduce the β-transus temperature of respective Ti−X binary alloys per wt% of addition, while the eutectoid β-stabilizers are inconsistent in changing the β-transus.

Molybdenum is well known as a β-stabilizing element in titanium alloys. The critical minimum molybdenum content required to retain 100% β in Ti–Mo binary alloys on water quenching is at 10% for small samples (Table 7.9). By arbitrarily using this critical minimum molybdenum content as a point of reference, a single β phase stability parameter, designated *molybdenum equivalent* (Mo-Eq), was proposed by Paul. J. Bania to gauge the β phase stability on water quenching. A formula for calculating the Mo-Eq value was given in Section 7.2.3, in which the coefficient before each β-stabilizer reflects the ratio of the β_c value for molybdenum (i.e., 10.0) divided by the β_c value for the specific β-stabilizer. Aluminium was also included in the formula with its β_c value being arbitrarily taken as −10 in order to reflect its opposite effect on stabilizing the β phase. Based on the Mo-Eq values calculated for various titanium alloys, β-alloys have also been defined as those having a Mo-Eq value of ≥10. More specifically, the following classifications have been proposed:

1. Stable β-titanium alloys (Mo-Eq > 30)
2. Metastable β-titanium alloys (8 ≤ Mo-Eq ≤ 30)
3. β-rich α–β-titanium alloys (Mo-Eq < 8)
4. Near β-titanium alloys (5 ≤ Mo-Eq ≤ 10).

These terms are used interchangeably in literature. The overlaps between the Mo-Eq boundaries in these classifications arose from the fact that, they were suggested by different proposers, which reflects the empirical nature of these distinctions. However, the Mo-Eq value provides a simple and useful parameter for ranking the β phase stability in different titanium alloys on water quenching and predicting the microstructures to be produced.

β-Titanium alloy ingots are usually forged or rolled first in the β phase field, to a degree sufficient to enable recrystallization during forging or rolling in order to obtain a uniform fine microstructure, and then in the α+β phase field at 10−50°C below the transus. The purpose of this α+β finish forging is to control the distribution, morphology, and volume fraction of the primary α phase (α_P) particles, including the breakup of the GB and other coarse α_P particles that have formed during cooling after β-forging. The outcome depends on the starting microstructure, which is affected by the (i) β-forging temperature, (ii) the amount of deformation, (iii) the rate of deformation, and (iv) the subsequent cooling rate. Accordingly, a variety of different morphologies of the α_P particles can be obtained, including nearly continuous GB α_P particles and α-laths (light deformation), or, fragmented and deformed GB α_P particles and α-laths (e.g., deformation by 20% reduction or more). The distribution, morphology, and volume fraction of these α_P particles can be further manipulated by the solution treatment in the STA process. The α_P particles in the final microstructure are often around a few micrometers (e.g., ≤5 μm). When elongated α_P particles are preferred for higher fracture toughness, they can be up to ∼10 μm with an aspect ratio of greater than 3:1–4:1.

β-Titanium alloys offer the deepest hardenability of all titanium alloys due to their high solute contents. Accordingly, they are often used in the STA condition, with the exception of those stable β alloys which, like Alloy C, do not respond to ageing hardening. Table 7.10 summarizes the STA schedules for

Table 7.10 Premier β-titanium aerospace alloys in current production in the United States and Russia and their STA schedules

Alloy nominal composition	Developer, year	β-Transus (°C)	STA	Product form	Mo-Eq (%)
Ti–10V–2Fe–3V (Ti–10–2–3)	TIMET, 1971	790–805	760–780°C 1 h, WQ, 495–525°C 8 h	Forgings	9.5
Ti–5Al–5V–5Mo–3 Cr–0.5Fe (Ti–5553)	VSMPO, 1997	855–870	740–860°C 1 h, AC, 550–677°C 8 h	Forgings	9.6
Ti–15V–3Al–3Sn–3 Cr (Ti–15333)	TIMET, 1978	750–770	788–843°C 3–30 min, AC, 482–538°C 8–16 h	Strip	11.9
Ti-15Mo–2.7Nb–3 Al–0.2Si (Beta 21S)	TIMET, 1989	795–810	816–899°C 3–30 min AC, 593°C 8 h	Strip	12.8
Ti–3Al–8V–6Cr–4 Mo–4Zr (Beta C)	RTI, 1969	730	815–925°C 1 h, WQ, 455–540°C 8–24 h	Spring wire	16.0
Ti–35V–15Cr (Alloy C)	Pratt & Whitney, 1990	NA	850°C 2 h (no ageing)	Sheet	47.5

Adapted from Cotton, JD *et al.*: *JOM*, 67(6), 1281, 2015.
Mo-Eq, molybdenum equivalent; WQ, water quenching; AC, air cooling.

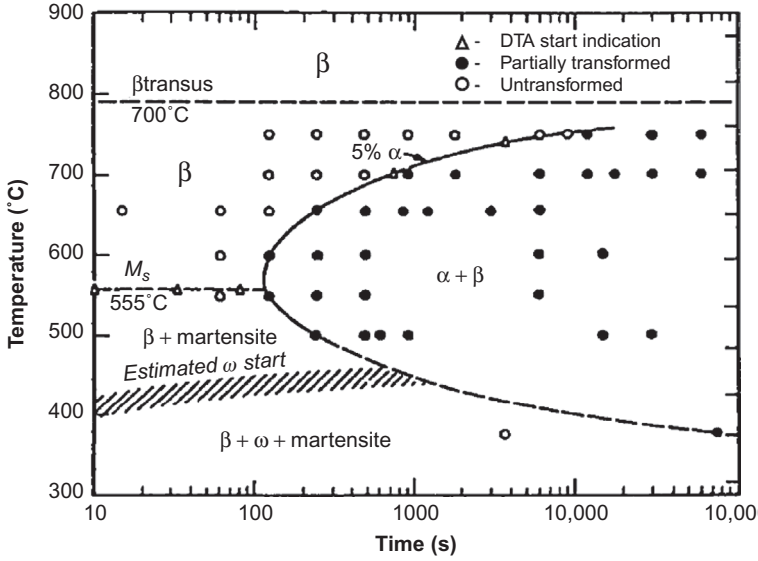


Figure 7.30 TTT diagram for Ti–10–2–3. From Cotton, JD *et al.*: *JOM*, 67(6), 1281, 2015.

selected β-titanium aerospace alloys in current production in the United States and Russia. Their mechanical properties can be found in Table 7.1. The isothermal phase transformation processes of these β-titanium alloys have been studied in detail for microstructural control by heat treatment. As an example, Fig. 7.30 shows the *time–temperature-transformation* (TTT) diagram for Ti–10–2–3 with defined phase boundaries for the formation of martensitic α′ phase ($M_s = 555°C$) and ω phase. The critical cooling rate at the nose of the TTT diagram is at $\sim 5°C\,s^{-1}$. Accordingly, water quenching is required to retain a sufficient amount of the β phase in Ti–10–2–3 in order to produce desired mechanical properties by subsequent ageing. For this reason, although Ti–10–2–3 is deep hardenable, the maximum section size is normally limited to ~75 mm. During ageing, the metastable β phase can decompose into either an α+β or an ω+β phase mixture (Fig. 7.30). In general, low temperatures and short ageing times produce a strong propensity for an isothermal decomposition that leads to an ω+β phase mixture. However, the ω phase is metastable and will transform after long ageing times or during ageing at higher temperatures to secondary α-precipitates.

Fig. 7.31 shows the typical microstructure of Ti–10–2–3 in the STA condition. It consists of fine α_P particles (mostly ≤5 μm with aspect ratios >3:1) in a matrix of aged β which contains a high volume fraction of very fine α precipitates (50–250 nm). The aligned, fragmented α_P particles are indicative of the α+β finish forging that was applied to the alloy. The morphology of the α_P particles affects the ductility (spherical preferred), fatigue properties (elongated

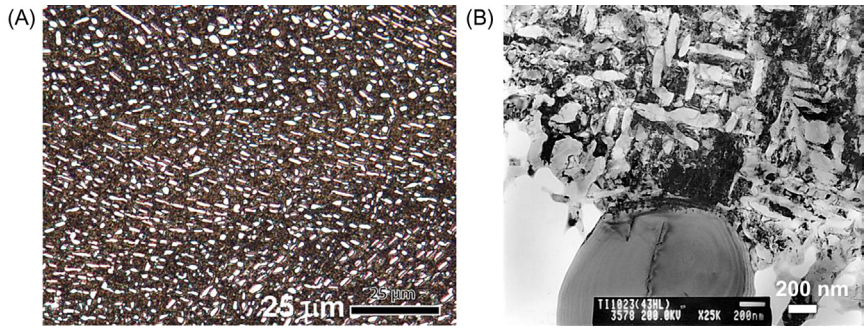


Figure 7.31 Ti–10–2–3 forging, STA condition: (A) Elongated primary α (light) in an aged β-matrix (dark, optical micrograph, × 600). (B) TEM bright-field image showing a globular primary α-particle (bottom) and a high volume fraction of fine aged α-precipitates. From Cotton, JD *et al.*: *JOM*, 67(6), 1281, 2015.

preferred), and fracture toughness (elongated preferred) of the alloy. The microstructures of other β-titanium alloys in the STA condition can be more complex. For example, the metastable Beta C alloy (Ti–3Al–8V–6Cr–4Mo–4Zr, Mo-Eq = 16.0) in the STA condition can contain α (hcp), β (bcc, solute-rich), β′(solute-lean β), ω, titanium chromide ($TiCr_2$), and silicide $(Ti,Zr)_5Si_3$ particles. Both the ω phase and $TiCr_2$ phase are embrittling. Therefore, special ageing practices have been developed to avoid them (e.g., using high ageing temperatures to avoid ω and short ageing times to avoid $TiCr_2$).

The extra processing steps that are required to deal with the embrittling ω- and $TiCr_2$ phases and other processing issues, e.g., ingot segregation and inadequate hardenability by air cooling, have led to the following design guidelines for β-titanium alloys:

1. Addition of selected elements, e.g., aluminium, zirconium, and tin, which tend to suppress or restrict the ω phase formation during heat treatment or welding by promoting nucleation of the α phase.
2. Limiting the use of chromium, which stabilizes the β-eutectoid transformation and can cause embrittlement because of the formation of $TiCr_2$ or other compounds. In addtion, excessive eutectoid stabilization leads to a sluggish response to age hardening, which is undesirable. Another reason of limiting the use of chromium is given below.
3. Minimal propensity for ingot segregation, which requires that the use of iron and chromium be restricted to 2% and 6%, respectively. Both elements can be readily rejected into the liquid ahead of the solid–liquid interface during solidification. Also, they both widen the solidus–liquidus gap. As a result, gross segregation can easily develop in ingot solidification, which is difficult

to eliminate by homogenization annealing. For example, the production of Ti−10−2−3 ingots is carried out in multiple melting steps. However, large iron-enriched "beta fleck" defects can still occur. Small ingots may allow higher iron and/or chromium, depending on property variability requirements.

4. Adequate hardenability without water quenching. Water quenching is often required in order to retain sufficient supersaturated β phase for subsequent effective strengthening by ageing. This limits the section size. In addition, although the β-transus is not significantly high (≤880°C, Table 7.10) for most β-titanium alloys, water quenching could still entail large residual stresses, which require additional stress-relief annealing before machining.
5. Promotion of plastic strain by slip rather than by a mechanism involving a strain-induced transformation to martensite. Alloys which deform primarily by slip have been found to possess better forming characteristics.

Finally, the specifications of most β-titanium alloys require both extra low oxygen (≤0.13%) and carbon (≤0.05%). The former requirement is necessary to maintain desired toughness and ductility at very high strength levels (e.g., 1600 MPa). The latter requirement arises from the high molybdenum, vanadium, or niobium contents, which can reduce the solubility of carbon in the β phase from 0.08% to <0.006% leading to the precipitation of GB carbides. This was observed in metastable β-alloy Ti−15V−3Al−3Cr−3Sn−0.046C after ageing at 500°C for 12 h and also in two other β-alloys Ti–15Mo−0.032C and Ti−(10-22)Nb−0.06C when cooled in furnace from the β-field. β-titanium alloys are generally less susceptible to hydrogen degradation than other titanium alloys at room temperature. Their hydrogen content is usually limited to ≤0.015%, although a lower hydrogen content is always preferred.

7.4.2 β-Titanium aerospace alloys

β-Titanium alloys were not widely recognized as a distinct group of alloys until the late 1950s. They attracted attention because of their potential superior forming characteristics anticipated from their bcc structure. Moreover, they offered the prospect of being cold-formed in the relatively soft β phase state with subsequent strengthening by ageing. Their increased hardenability is also highly desirable for hardening of thick sections. The high β-stabilizer contents did, however, cause problems with both the melting (multiple melting steps) and ingot solidification (segregation) processes, in addition to increased densities (e.g., ≥5.0 g cm^{-3}).

The first β-titanium aerospace alloy in production was the composition Ti−13V−11Cr−3Al, which can be solution treated, quenched, cold-formed, and aged at 480°C to achieve a tensile strength of 1300 MPa. This alloy has limited weldability because of the formation of the ω phase in the heat-affected zones. Moreover, it is unstable for long-term exposures to ≥200°C due to the potential precipitation of $TiCr_2$. The alloy was first used as the airframe alloy for the American SR-71 Blackbird aircraft designed to fly at speeds around 3200 km h^{-1}, at which aerodynamic heating precludes the use of aluminium

alloys. It was then used to make springs for multiple aircraft actuation systems. From about the mid-1980s, the alloy was superseded by the metastable Beta C alloy, which was developed in the 1960s and is easier to melt and solidify (with low segregation), and also easier to be cold-worked, hot-worked, and heat treated. In contrast, Ti−13V−11Cr−3Al was difficult to produce due to segregation of chromium during ingot solidification.

Apart from the Beta C alloy, the 1980s also saw the implementation of three near-β titanium alloys in commercial aircraft, namely, Ti−10−2−3, Ti−15−3−3−3, and VT 22 (Ti−5Al−5V−5Mo−1Cr−1Fe, Russia), which are all still used today in the aerospace industry. In particular, Ti−10−2−3 has proved to be one of the most forgeable β-titanium alloys (low flow stresses), and it also exhibits high resistance to edge cracking. These characteristics enable greater reductions between reheats, reduce labor-intensive conditioning operations, increase materials yield, improve efficiency, and lower processing cost. The low flow stress is a common feature of β-titanium alloys during hot working when compared with that required for the α–β alloy Ti−6Al−4V. This characteristic, which occurs over a wide range of strain rates, is shown in Fig. 7.32. It will be noted that the flow stresses for all three alloys in Fig. 7.32

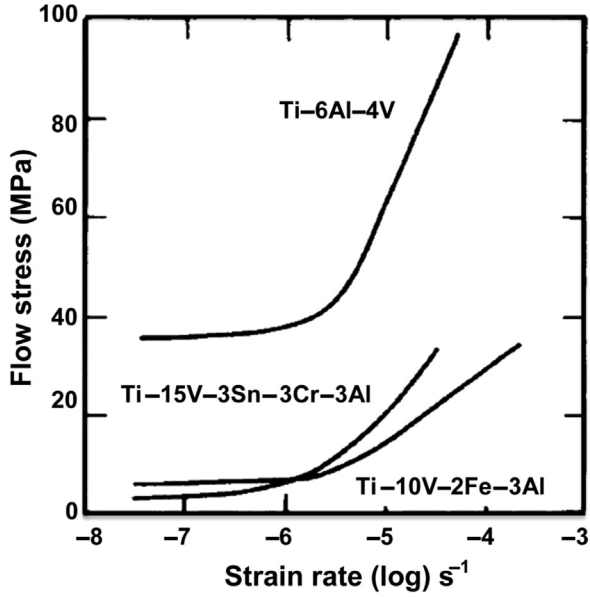


Figure 7.32 Relationship between flow stress and strain rate for titanium alloys hot-worked at 810°C. The flow stresses for all three alloys decrease to plateau values as the strain rates fall below $\sim 10^{-5}\,s^{-1}$. These plateau values correspond to the onset of superplastic behavior. Courtesy H.W. Rosenberg.

decrease to plateau values as the strain rates fall below $\sim 10^{-5}\,s^{-1}$. These plateau values correspond to the onset of superplastic behavior (Section 7.5.2).

Rapid oxidation and fires can occur occasionally in thin-wall titanium alloy parts in aircraft engines, or in titanium-based heat exchangers at elevated temperatures in a high-pressure air environment, due to mechanical reasons, e.g., a heavy rub between blades and stator vanes. The oxidation reaction is exothermic and can self-intensify causing titanium fires. The 1990s witnessed the implementation of two superior oxidation- or burn-resistant β-titanium alloys, namely, the metastable Beta 21S (Ti−15Mo−2.7Nb−3Al−0.2Si) and stable Alloy C. The ignition temperature of the Alloy C is 2991°C, compared with 1976°C for Ti−6Al−4V, due to its high chromium content, which contributes to the formation of a chromium-containing continuous protective oxide film. Beta 21S further offers excellent resistance to attack by aircraft hydraulic fluids. Both alloys have found unique applications in the aerospace sector, which will be described in some detail in Section 7.8.1.

The latest addition to the β-titanium alloy family is the near-β alloy Ti−5553 (Ti−5Al−5V−5Mo−3Cr−0.5Fe), developed in the late 1990s by the premier titanium producer in Russia, VSMPO. It was designed on the basis of the alloy VT 22 but for improved processability and performances as compared to both VT 22 and Ti−10−2−3. Its microstructure consists of 10–20 vol.% globular primary α in a matrix of aged β in the STA condition (similar to the STA microstructure shown in Fig. 7.31 for Ti−10−2−3). Fig. 7.33 shows its tensile properties vs ageing temperature. The fracture toughness (K_{IC}) of the alloy in the STA condition is $\sim 33\,MPa\,m^{1/2}$, which can be doubled by a

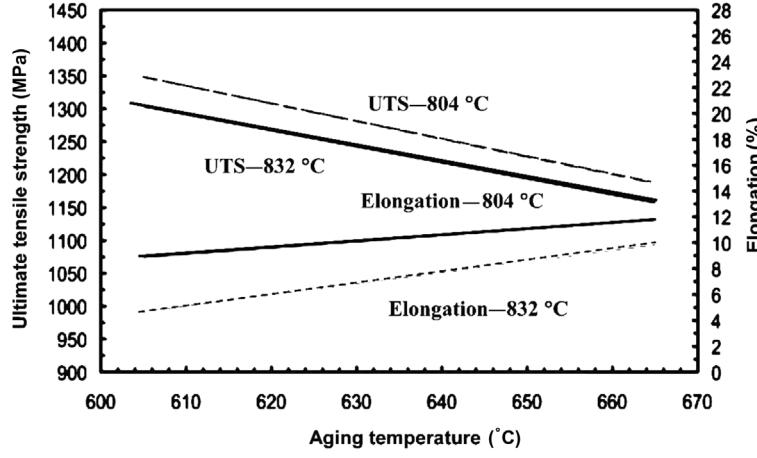


Figure 7.33 Ultimate tensile strength (UTS) and elongation vs ageing temperature (8 h) for 178 mm diameter and 89 mm long Ti−5553 billet, solution treated at either 804°C or 832°C. From Fanning, JC: *J. Mater. Eng. Perform.*, 14, 788, 2005.

β-annealing and ageing treatment for intermediate strengths. A modification of the alloy Ti−5553 containing 1% zirconium, designated Ti−55531, has reportedly been in production as well.

7.4.3 Specialty alloys

This section briefly discusses four groups of specialty titanium alloys, i.e., β-titanium biomedical alloys, β-titanium–niobium superconducting alloys, nickel–titanium shape memory alloys, and β-titanium superelastic alloys. They have all found important applications.

β-Titanium alloys containing niobium, tantalum, and zirconium as principal alloying elements are an emerging group of biomedical alloys. They offer lower modulus values (30−80 GPa; closer to that of human bone) and better biocompatibility (no toxic vanadium and aluminium) than the commonly used Ti−6Al−4V and CP Ti. Notable examples of such low modulus alloys include Ti−13Nb−13Zr, Ti−35Nb−5Ta−7Zr, Ti−29Nb−13Ta, and Ti−24Nb−4Zr−8Sn. In particular, the *d*-electron alloy design theory or molecular orbital design approach developed by Masahiko Morinaga has significantly accelerated the development of β-titanium biomedical alloys. This theory predicts some potential relationship between the β phase stability and the elastic modulus of titanium alloys through two characteristic parameters $\overline{B_0}$ and $\overline{M_d}$ defined by the following formulae:

$$\overline{B_0} = \sum X_i (B_0)_i \text{ and } \overline{M_d} = \sum X_i (M_d)_i$$

where X_i is the atomic fraction of a given alloying element, B_0 is the bond order which is a measure of the covalent bond strength between Ti and an alloying element, and M_d is the *d* orbital energy level which correlates with the electronegativity and metallic radius of the element. Each alloying element has specific values of B_0 and M_d. A $\overline{B_0} - \overline{M_d}$ diagram can then be constructed for existing titanium alloys together with their modulus values to allow predictions of new low-modulus β-titanium alloys. The $\overline{B_0} - \overline{M_d}$ diagram has proved to be a highly effective approach for the search of low-modulus β-titanium biomedical alloys.

β-Titanium–niobium or niobium–titanium superconducting alloys containing 44−55% titanium are premier superconducting materials in current industrial applications (≥90% of the usage). There are six prominent compositions, i.e., Nb−44Ti, Nb−46.5Ti, Nb−48Ti, Nb−50Ti, Nb−53Ti, and Nb−55Ti, of which the last three can be referred to as titanium-based alloys. In principle, they all belong to metastable β-titanium alloys by both their Mo-Eq values (14.0 for Nb−50Ti, 14.8 for Nb−53Ti, and 15.4 for Nb−55Ti), and their microstructures in the final wire product forms, which consist of the metastable β-Ti(Nb) phase and α-Ti(Nb) phase. ω phase particles can also form in these titanium–niobium superconducting alloys. As mentioned in Section 7.3.6, their formation can be beneficial as they are effective in flux-pinning, which can

improve the critical current densities that may be sustained in the presence of an external magnetic field.

The Ti−Nb binary superconducting alloys have a critical temperature of 10 K and are therefore used in liquid helium (−269°C or 4 K). Unlike other superconducting materials existing today, they have excellent tensile ductility, which enables them to be drawn into 0.5−1.0 mm diameter wires for a wide range of industrial applications. Examples include superconducting high-energy accelerators, magnetic resonance imaging diagnostic equipment, magnetic levitation high-speed train, magnetic concentrator, controlled nuclear fusion, magneto-hydrodynamic power generation, and magnetic propulsion systems.

Many β-titanium alloys can exhibit unique shape memory effects in the martensitic condition whereby, if deformed (up to a limit of ∼10% strain) below the M_s temperature, they are able to recover their original shapes when reheated to the so-called austenite region. The best-known shape memory alloy is a nickel–titanium binary alloy, referred to as nitinol, which contains titanium and nickel at approximately equal atomic percentages. According to Table 7.9, its Mo-Eq value falls in the range of stable β-titanium alloys.

Nitinol has been used in a number of engineering applications as fasteners, actuators, and couplings. For example, nitinol couplings have been designed to connect aircraft hydraulic lines, plumbing in submarines, and fittings to join steel pipes installed under the sea. The couplings are expanded ∼4% in the martensitic condition at liquid nitrogen temperatures and placed around tubes to be joined. After warming to room (or sea) temperatures, they contract producing a tight seal thereby providing a convenient alternative to welding or brazing. Nitinol also has application in certain prosthetic devices (Section 7.8.3). However, since nickel is a known allergen and it might also have carcinogen effects, a variety of nickel-free titanium-based shape memory alloys have been developed for different backgrounds. For example, alloys Ti–22Nb–8Ta (at.%), Ti–45Pt–5Co (at.%), Ti–45Pt–5Ru (at.%), Ti−30Ta−1Al (at.%), and Ti−30Zr (at.%) have all exhibited a shape memory effect based on the martensitic transformation β→α″. It remains to be a subject of considerable interest and practical importance.

Superelastic β-titanium alloys are a different group of shape memory alloys, which derive their superelasticity from the formation of stress-induced metastable martensitic α″ phase (β→α″) by loading and its reverse transformation (α″→β) by unloading. No change in temperature is thus needed for these alloys to recover their original shapes. A variety of superelastic Ti–Nb- and Ti–Mo-based β-alloys have been developed. Notable examples include Ti−(40.5–41.5)Nb binary alloys (close to the Ti−45Nb superconducting alloy), Ti−24Nb−4Zr−8Sn (Ti−2448), and the Gum Metal to be introduced below. Most current superelastic β-titanium alloys exhibit shape recovery strain up to only ∼3%.

The Gum Metal or GUMMETAL (Table. 7.1) is a novel β-titanium alloy. It exhibits a range of unique properties, including (1) low Young's modulus down to 40 GPa, (2) ultrahigh tensile strength up to 2000 MPa, (3) super-elasticity with more than 2.5% elastic deformability, and (4) super-plasticity with over 99.9%

cold workability. The alloy was originally developed as Ti–23Nb–0.7Ta–2Zr–1O (at.%), but it can exist over a range of compositions and can further include vanadium and hafnium. The design of this alloy was based on the *d*-electron alloy design theory mentioned previously. The Gum Metal is manufactured via a special PM process which requires substantial cold working. It can be used in the cold-worked or heat treated state and has found niche applications such as spectacles frames, bone implants, and lightweight spring.

7.5 FABRICATION

7.5.1 Hot working

The as-cast microstructure of consumable arc-melted ingots is sensitive to cracking, and the initial working is usually done by hot-press forging in the β phase field. Deformation is carried out at a relatively slow rate in large hydraulic presses, and the ingots may be press-forged to slabs ~150 mm thick for subsequent rolling to plate or sheet. They can also be pressed to round or square billets for processing to bar, rod, tube, extruded sections or wire. Rough forgings for components such as gas-turbine compressor disks can be pressed directly from ingots in multiple steps.

Above 550°C, titanium quickly absorbs oxygen and the oxide scale can actively dissolve into the titanium matrix underneath due to the high solubility of oxygen in titanium (e.g., 14.25% at 600°C). A brittle, subsurface layer (oxygen-enriched, known as the α case) may develop which can initiate surface cracks. Titanium also absorbs hydrogen, nitrogen, and carbon. For this reason, electric preheating furnaces are preferable to those fired by oil or gas. Chemical descaling, abrasive cleaning, and even machining, frequently combined with careful surface inspection, may be necessary before any further working operations are carried out.

Titanium alloys can be hot-worked to produce most of the shapes that can be obtained with steels and other metals. However, they are among the most difficult metallic materials to forge. In addition to shape forming, the forging process serves as a critical step to create the required microstructure for subsequent heat treatments in order to produce the final desired microstructure and properties (see Sections 7.2.3, 7.3.2 and 7.4.2). For this reason, the forging process parameters are often determined by also considering the heat treatment schedules to be applied to the alloy. Table 7.11 lists the typical forging temperature ranges for a variety of titanium alloys selected from different groups.

Although some preforming of titanium alloys may be undertaken by open-die forging, most forging operations normally involve closed dies in which the shaping of hot metal occurs completely within the walls or cavities of the two dies as they come together. Dies for closed-die forging are commonly preheated to 200–250°C for rapid operations, involving hammers or mechanical presses, and to around 425°C for slower working in hydraulic presses.

Table 7.11 Typical forging temperature ranges for selected titanium alloys

Nominal titanium alloy specification	β-Transus (°C)	Forging temperature (°C)
CP titanium (α-titanium alloy)	915	815–900 (α forging)
Ti–5Al–2.5Sn (α)	1050	900–1010 (α forging)
Ti–6Al–2Sn–4Zr–2Mo (Ti–6242, near-α)	990	1040–1120 (β forging) 900–975 (α+β forging)
Ti–5.8Al–4Sn–3.5Zr–0.5Mo–0.7Nb–0.35Si (IMI–834, near-α)	1010	980–1050 (β or α+β forging)
Ti–6Al–4V (Ti–6–4, α–β)	995	1010–1065 (β forging) 900–980 (α+β forging)
Ti–6Al–2Sn–2Zr–2Mo–2Cr (Ti–62222, α–β)	980	870–955 (α+β forging)
Ti–6Al–2Sn–4Zr–6Mo (Ti–6246, α–β)	940	950–1010 (β forging) 870–955 (α+β forging)
Ti–4.5Al–5Mo–1.5Cr (Corona-5, β-rich α–β)	925	930–970 (β forging) 845–915 (α+β forging)
Ti–10V–2Fe–3Al (Ti–10–2–3, near-β)	805	705–785 (α+β forging)
Ti–3Al–8V–6Cr–4Mo–4Zr (Beta C, metastable β)	795	705–980 (β or α+β forging)
Ti–15V–3Cr–3Al–3Sn (Ti–15333, metastable β)	770	705–925 (β or α+β forging)
Ti–11.5Mo–6Zr–4.5Sn (Beta III, metastable β)	745	705–955 (β or α+β forging)

Adapted from Dieter, GE *et al*.: *Handbook of Workability and Process Design, ASM International, Materials Park, OH, USA, 2003.*

Heating of dies is particularly critical when forming thin sections, otherwise the poor thermal conductivity of titanium can lead to localized chilling, which causes uneven metal flow or even cracking in a workpiece. Some novel hot-forming techniques have been developed. For example, assemblies of quite large dimensions can be produced by slow, isothermal forging (or creep forming) between heated dies, some of which can be made cost-effectively from cast ceramics. Metallic tooling is often much more expensive, particularly when the die faces need to be made from nickel- or cobalt-based superalloys in order to ensure adequate hardness and oxidation resistance at the relatively high forming temperatures, e.g., 850°C or higher.

Titanium alloys are susceptible to galling, namely, wear due to friction, during hot or cold working, which causes surface damage. Lubrication is therefore essential and care must be taken in selecting materials that do not react with titanium when heated. Suspensions of graphite or molybdenum disulfide are suitable for both types of operations, whereas glass or special ceramic-based

die coatings may be required for more severe processes such as hot extrusion for which the titanium billet temperature is usually in the range 1000–1250°C. At such high temperatures, the thermal insulation of the dies from overheating by the titanium billet is of equal importance to the lubrication effect. The lubrication film can help protect the billet surface from severe oxidation.

7.5.2 Superplastic forming

If creep forming is carried out at controlled strain rates of around 10^{-5}–$10^{-6}\,s^{-1}$, and at temperatures close to $0.6T_M$ (where T_M is the liquidus of the alloy in degrees Kelvin), then alloys having stable, small grain sizes (e.g., <5 μm) may exhibit superelasticity. Flow stresses can be very low (e.g., see Fig. 7.32) and components can be produced by simple methods similar to those used for thermoplastics. α–β Titanium alloys such as Ti–6Al–4V were early materials recognized as being superplastic and typical process parameters are 100–1000 kPa pressure applied at 900–950°C for 0.25–4 h. Such pressures, which are even lower for β-titanium alloys, can be achieved using an inert gas, e.g., argon, which may be introduced into one part of the mold cavity with titanium sheet serving as a deformable diaphragm that flows into the other part.

One disadvantage with the α–β alloys is the relatively high temperature at which superplastic forming has to be carried out in order that the required distribution of the α and β phases is obtained. One novel method for reducing this temperature is to exploit hydrogen as a temporary alloying element, known as thermo-hydrogen processing, based on the fact that titanium and its alloys readily absorb hydrogen at elevated temperatures (hydrogenation). Hydrogen can substantially lower the β-transus to ~350°C so that the required number of α and β phases for superplastic forming can be achieved at a reduced temperature. In practice, the alloy is first heated in an atmosphere of 4 vol.% hydrogen in argon and later degassed in vacuum to remove the hydrogen after forming is completed (dehydrogenation).

A clean titanium surface can easily diffusion bond to itself (Section 7.5.7) under processing conditions similar to those used for superplastic forming. Therefore forming and joining can be combined in one step to produce special products such as the truss section shown diagrammatically in Fig. 7.34.

7.5.3 Cold working

CP titanium and most other titanium alloys (excluding some β-alloys) in the annealed condition have a limited capacity to be cold-worked. For example, minimum bend radii for sheet are commonly one to three times the gauge thickness for CP titanium, two to four times for β-alloys, and three to six times for most other titanium alloys. One major problem is springback, which is a consequence of the low-modulus and relatively high-flow stresses of titanium and its alloys. In order to improve dimensional accuracy, cold forming is generally

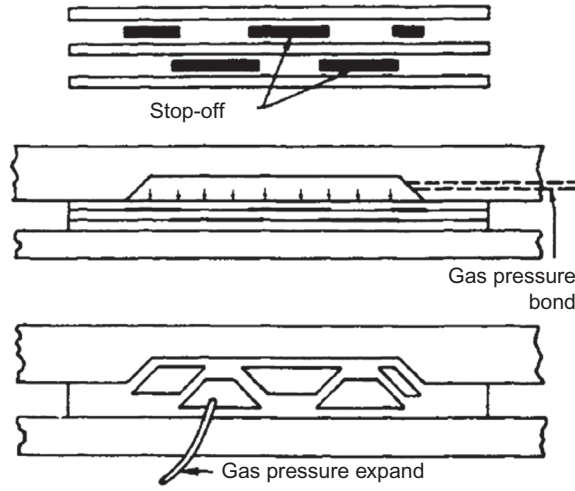


Figure 7.34 Manufacturing techniques using superplastic forming combined with diffusion bonding to produce a truss section. The stop-off material has been inserted where joining is not wanted. From Tupper, NG *et al.*: *J. Metals,* 30 (9), 7, 1978.

followed by hot sizing and stress relieving for periods of 0.25 h at temperatures around 650–700°C. Such treatments may also help to restore strength properties that are reduced in certain directions of some deformed alloys, which contain the hcp α phase in the manner described for wrought magnesium alloys in Section 6.6. The treatments may also cause changes to fine-scale features of the microstructure, but little is known of these effects.

7.5.4 Texture effects

The major cause of property anisotropy in aluminium alloys, that of aligned, coarse intermetallic compounds (Fig. 2.43), is normally absent in titanium alloys. However, those titanium alloys that contain a large amount of the hcp α phase may show marked elastic and plastic anisotropy if fabrication procedures produce a preferred orientation or texture in the grain structure. Such anisotropy may be reflected in the mechanical properties, and there is considerable interest in the prospect of controlled texture strengthening of titanium alloys. This introduces a potential third dimension to alloy development as an adjunct to composition and microstructure.

Three easy slip modes and six twinning modes exist in α-titanium and the former are shown in Fig. 7.35A. The slip vectors in each case are parallel to the basal planes {0001} so that, if stress is applied in the direction of the *c*-axis, there will be no critical resolved shear stress acting in this plane. There are, however, other slip systems which can operate so that the requirement of having five independent slip systems for general plasticity is fulfilled.

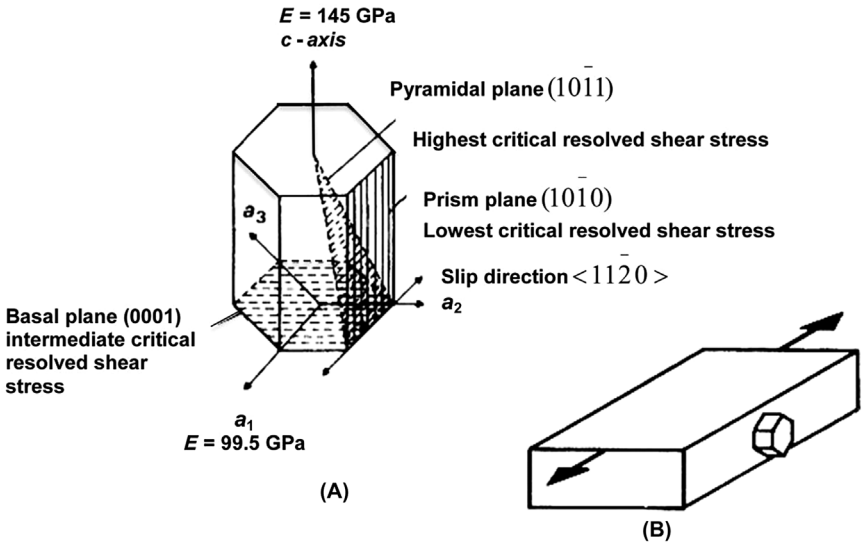


Figure 7.35 (A) Slip planes in α-titanium. (B) Alignment of hexagonal unit cell in α-titanium showing strongly preferred orientation after rolling.

The elastic moduli in the *c*- and *a*-directions of single crystals of α-titanium show a large variation from 145 to 99.5 GPa. Although this difference is less in polycrystalline alloys showing preferred orientation, the elastic moduli in the longitudinal, long transverse and short transverse directions (see Fig. 2.42) can still differ by as much as 30%. An example of the variation in tensile properties with stressing direction is shown for the alloy Ti–6Al–4V in Table 7.12. In this case, maximum texture strengthening has occurred in the long transverse direction and is associated with the alignment of basal planes normal to the forging plane (Fig. 7.35B), which is one of the two favored textures that may develop in rolled or forged titanium alloys. Fracture toughness and elastic modulus are also maximal in the long transverse direction.

Table 7.12 and Fig. 7.36 show that fatigue properties are lowest in the long transverse direction. This result has been attributed to the fact that Poisson's ratios are also sensitive to crystal orientation, these ratios being higher in the longitudinal and short transverse directions because stressing occurs parallel to the basal planes. Higher ratios imply greater constraint, which means that the levels of strain will be reduced and the fatigue strength enhanced in these two directions. The differences observed in fatigue strength in the longitudinal and short transverse directions have been attributed to relative changes in grain shapes that also occur during processing.

The other type of texture that may be developed in rolled or forged titanium alloys involves alignment of basal planes parallel to the rolling or forging plane, i.e., the *c*-axis is parallel to the short transverse direction. This texture can be

Table 7.12 Mechanical properties of a 57 mm thick × 235 mm wide forged and annealed Ti–6Al–4V plate

Testing conditions	Yield strength (MPa)	Tensile strength (MPa)	Elastic modulus (GPa)	Elongation (%)	Fatigue strength at 10^7 cycles (±MPa)
Longitudinal	834	910	114	17.5	496
Long transverse	934	986	128	17.0	427
Short transverse	893	978	114	12.5	565

From Bowen, AW: *Titanium Science and Technology*, Jaffee, RI and Burte, HM (Eds.), Plenum Press, New York, NY, USA, Vol. 2, 1271. 1973.

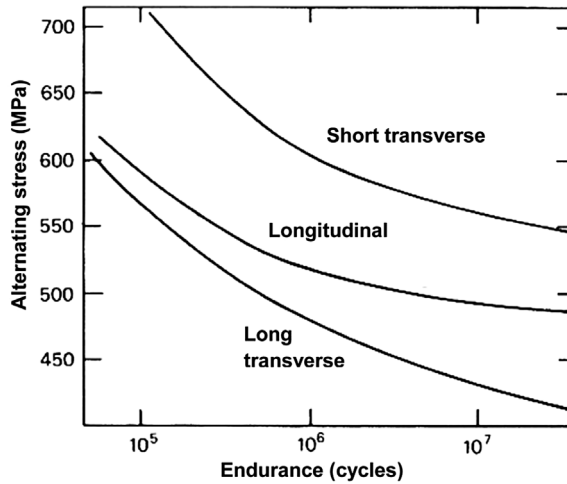


Figure 7.36 Rotating-cantilever fatigue (*S*/*N*) curves for three testing directions in a 57 mm thick × 235 mm wide, forged and annealed Ti–6Al–4V plate (Table 7.12). From Bowen, AW: Titanium Science and Technology, Jaffee, RI and Burte, HM. (Eds.), Plenum Press, New York, NY, Vol. 2, 1271, 1973.

beneficial in sheet metal forming involving biaxial tension when thinning by simple slip becomes difficult. Measurements have shown that *R*-values (Section 2.1) are high and may lie in the range 1–5, whereas they are less than 1 for aluminium alloys. This form of texture strengthening is also useful in applications such as pressure vessels which require high biaxial strength.

7.5.5 Machining

Titanium alloys are classified as hard-to-machine materials. The cost of machining usually accounts for ~30–40% of the total cost of manufacture of a titanium

component by the conventional ingot metallurgy-based processes. The high machining cost in conjunction with the large amount of titanium scrapped, which is not easy to recycle, served as a major driving force for the development of the metal additive manufacturing or 3D printing technology (Section 8.10).

The low thermal conductivity of titanium alloys, which is about one-sixth that of steels, hinders the conduction of heat away from the region being machined. This feature entails high tool tip temperatures and plastic deformation wear, which, in turn, lead to higher cutting forces. For example, at similar cutting speeds, the temperature developed at the cutting edge of a tungsten carbide tool was found to be ~700°C for titanium samples compared to ~540°C for steel samples. The consequence is immediate as titanium alloys react with most cutting tool materials at these or even lower temperatures. Tool lives will be shortened unless slower cutting speeds are used together with more efficient cooling operations.

Another tendency is that chips start to stick to the cutting edge (galling) at elevated temperatures due also to the high-chemical reactivity of titanium alloys. This problem not only disrupts the machining process but also risks reducing tool life, because fracture of the cutting edge may occur if the titanium chip is removed when the tool re-enters the workpiece on the next pass. Alternatively, cutting forces may be increased by a factor of several times which, when combined with the relatively low elastic modulus of titanium, can cause deflection of the workpiece resulting in tool vibration, chatter, and poor surface finish. Hence titanium is usually machined at slow speeds, efficiently cooled using cutting fluids to minimize tool tip temperature, and avoid rapid tool wear. Moreover, because of the tendency of titanium to gall or weld to other metals, sliding contact should be avoided, which means that deep cuts with sharp tools are often needed. Finally, it is necessary to ensure that both tool and workpiece are rigidly supported during machining.

The above features apply to the machining of all titanium-based materials, although machining conditions vary with different categories. Table 7.13 compares the actual ratios of machining times for CP titanium and typical α-, α+β-,

Table 7.13 Ratios of machining times for various titanium alloys compared with alloy steel AISI 4340

Titanium alloy	Hardness (BHN)	Turning (WC tool)	Face milling (WC tool)	Drilling (high-speed steel tool)
CP titanium	175	0.1:1	1.4:1	0.7:1
Near-α: Ti–8Al–1Mo–1V	300	1.4:1	2.5:1	1:1
α–β: Ti–6Al–4V	350	2.5:1	3.3:1	17:1
β: Ti–13V–11Cr–3Al	400	5:1	10:1	10:1

From Zlatin, N *et al.*: *Titanium Science and Technology*, Jaffee, RI and Burte, HM (Eds.), Plenum Press, New York, NY, USA, Vol. 2, p. 409, 1973.

and β-titanium alloys versus alloy steel AISI 4340 (hardness = 300 BHN). Alloy compositions can markedly affect the machinability of titanium alloys.

Much effort has been made to improve the machinability of titanium alloys. For instance, preheating the surface of a titanium workpiece by laser during machining, known as laser-assisted machining, can accelerate the machining speed of titanium by two to four times to the range of $100-200\,\mathrm{m\,min^{-1}}$. Chemical or electrochemical milling may also be used to remove unwanted titanium metal, but it will lead to an irreversible loss of expensive titanium alloys. In addition, the disposal of the used acid solutions can be problematic. The ultimate solution is to minimize the need for machining by near-net or net shape manufacturing.

7.5.6 Surface treatments

Titanium and its alloys are not hard enough to withstand abrasive wear (≤HRC 25 for unalloyed titanium, and ≤HRC 40 for most titanium alloys). This deficiency has hindered their broader applications. In addition, as mentioned in Section 7.5.5, titanium alloys also show poor tribological properties because they have a strong tendency to gall or weld to themselves, or to other metals, under conditions of sliding contact. In this context, traditional lubricants are often ineffective in overcoming this problem, and treatments such as anodizing or electroplating are also of limited value because surfaces treated in these ways are not able to withstand more than light loads.

More success has been achieved with physical vapor deposition (ion plating) and plasma processing, in which particular use has been made of surface coatings of titanium nitride (TiN). Physical vapor deposition involves reacting titanium vapor, which is sputtered from a separate source, with nitrogen ions generated by glow discharge in a nitrogen atmosphere. The operating temperature is commonly at ~500°C and the deposited coatings, which are typically 3 μm thick, provide a hard, smooth, and low-friction surface capable of withstanding modest loading conditions. Thicker coatings (e.g., 30 μm) may be obtained by plasma nitriding at a higher temperature of 700–850°C. In this technique, the titanium component is made the cathode in a low-pressure nitrogen glow discharge. As a result, the positive nitrogen ions are accelerated towards the negatively biased component surface where they react to form TiN.

Overall, no viable solutions are available as yet to markedly improve the wear resistance and tribological properties of titanium and its alloys.

7.5.7 Joining

Fusion welding The capacity of titanium alloys to be fusion-welded is related to microstructure and composition. General weldability is restricted to α-, near-α-, and to α–β alloys containing <20% of the β phase. Fusion, resistance, and flash-butt welding have all been used for titanium. Oxyacetylene and atomic hydrogen

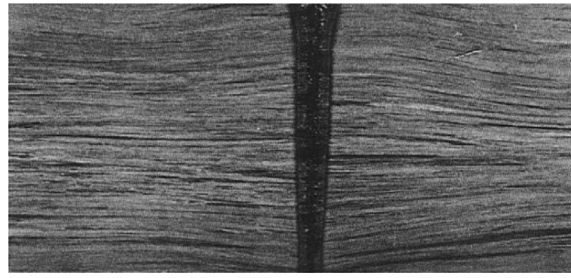


Figure 7.37 Polished and etched section of an electron beam butt-weld in a 50 mm thick Ti–6Al–4V plate. Courtesy Rolls Royce Ltd.

fusion welding is unsuitable because of gaseous contamination, but nonconsumable (tungsten inert gas welding) and consumable (metal inert gas welding) electrode techniques (Section 4.5.1), as well as electron beam and plasma arc processes are applicable. Open air techniques can be used but extra attention must be given to shielding the area being welded with an inert gas such as argon. In that regard, it is necessary to take special protective measures, e.g., supplying argon to the underside of the weld. In the case of complex assemblies, it is often preferable to weld in a glove-box type of chamber that can be filled with the inert gas. It is important to note that titanium cannot be fusion-welded to conventional structural materials such as steel, copper, and nickel alloys. Spontaneous cracking or brittleness is inevitable due to the formation of brittle intermetallic compounds.

Electron beam welding, which is carried out in a vacuum chamber, is well suited to titanium alloys, although the capital cost of the equipment is high. Specific powers are greater than those usable by other processes so that deep penetration combined with a narrow heat-affected zone is possible, e.g., Fig. 7.37 shows an electron beam butt-weld in 50 mm thick, rolled titanium alloy plate. Both electron beam and laser beam welding processes produce high integrity, narrow welds which minimize the risk of distortion.

Diffusion bonding Titanium-based materials are also amenable to joining by diffusion-bonding techniques since surface oxides are readily dissolved at the temperatures used, which are usually in the range 850–950°C, i.e. below the β-transus in α–β alloys. It is again necessary to exclude air during bonding, and the components being joined are held under low pressures of ~1 MPa for periods of 30–60 min. Diffusion readily occurs across the interface and it is usual for localized recrystallization to take place there. This is evident in Fig. 7.38. Joint strengths can reach ~90% those of the alloys being bonded.

Diffusion bonding can result in clear cost reductions by eliminating machining operations in the manufacture of intricate parts (see Fig. 7.45 for a major application). The technique also enables assemblies to be produced in alloys

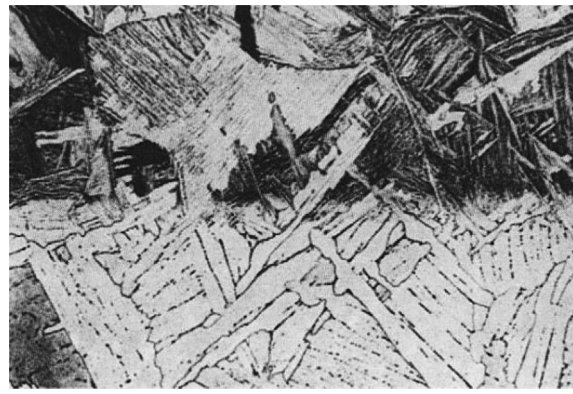


Figure 7.38 Micrograph of a diffusion-bonded joint between two different titanium alloys. The grain structure shows that localized recrystallization has occurred. The conditions were temperature 980°C; pressure 1.5 MPa; time 30 min. From Blanchet, B: Revue de Metallurgie, 71, 99, 1974) (× 100).

that are not normally regarded as being weldable. As mentioned in Section 7.5.2, diffusion bonding can be combined with superplastic forming in certain fine-grained alloys.

Brazing Titanium and its alloys can be brazed at around 1000°C in a protective atmosphere using materials such as silver, copper, and a special alloy Ti–15Cu–15Ni. An important use of brazing has been in the production of honeycomb structures (see Section 8.1.2) which offer a unique combination of stiffness and corrosion resistance at elevated temperatures. Many titanium honeycomb structures can also be easily produced today by metal additive manufacturing.

7.5.8 Powder metallurgy processes

Titanium or titanium alloy components can be produced directly from powder through a variety of PM processes. In addition to additive manufacturing, the three commonly used titanium PM processes include metal injection molding (MIM, net shape), hot isostatic pressing (HIP, net or near-net shape), and press-and-sinter process (conventional PM, near-net shape). All can lead to significant saving in machining and fabricating costs.

MIM is a net shape manufacturing process that is particularly suited to the manufacture of small and intricate titanium parts (e.g., ≤100 mm in size). In this process, fine spherical titanium or titanium alloy powder (≤45 μm) is mixed with ~40 vol.% of a binder (e.g., 55 wt% paraffin wax, 35wt% low-density polyethylene, and 10 wt% stearic acid) to comprise a feedstock.

Injection moulding is made at temperatures above the melting point of the binder (160−180°C). The binder is subsequently removed from the molded part through solvent debinding and thermal debinding. The last step is sintering of the debinded part at 1250−1350°C for 1−2 h, followed by furnace cooling. The total shrinkage after sintering is between 12% and 15%. The as-sintered density is in the range of 97−99% of the theoretical density.

HIP is the simultaneous application of high temperature and pressure to either metal powder for near-net manufacturing, or to solid metal parts to heal internal defects for improved mechanical properties and performance consistency. When applied to metal powder, the powder is first canned in sheet metal capsules, giving the product the desired shape. The capsules are then consolidated into full density through the simultaneous application of high temperature and pressure, e.g., 100−150 MPa at 910−930°C for 2−4 h for prealloyed Ti−6Al−4V powder (80−150 μm). A variety of net-shaped titanium parts have been fabricated by HIP for various applications, including Ti−6Al−4V compressor casings, airframe honeycomb structures, and upper-stage rocket engine impellers.

Both the MIM and HIP processes normally use prealloyed spherical powder. The MIM process requires use of finer spherical powder (≤45 μm) to ensure uniform shrinkage and high sintered density. Methods of preparing spherical titanium and titanium alloy powders include argon gas atomization, plasma rotating electrode process (PREP), and plasma atomization of titanium or titanium alloy wires. The PREP powder has the lowest internal porosity, while the gas-atomized power has the highest. However, it is challenging to produce fine (<45 μm) PREP spherical titanium or titanium alloy powders, due to both the low density of molten titanium (4.12 g cm^{-3} at 1700°C) and the maximum rotation speed that can be realized at present (≤18,000 rpm).

The press-and-sinter process is technically the simplest and economically the most attractive PM process. The process typically uses low-cost HDH titanium powder and other elemental powders or master alloy powder such as 60Al−40V as alloying additives. These powders are blended to achieve the desired alloy chemistry and compacted at room temperature to produce "green" shapes with relative densities of 75–85%. They are then sintered in a vacuum or a high-purity argon gas atmosphere at 1250−1350°C for 2−4 h, followed by furnace cooling. The as-sintered density varies in the range of 95−99% of the theoretical density. As-sintered titanium alloys can be further processed by HIP, extrusion, or forging for demanding applications.

The production process of HDH titanium powder is shown schematically in Fig. 7.39. For example, the hydrogenation process of small sponge particles (1–3 mm) can complete in 15 min at temperatures between 400°C and 550°C under four atmospheric pressures. The HDH titanium powder produced is angular, which can be converted into spherical powder through a plasma spheroidization process. Finally, the use of TiH_2 powder for the press-and-sinter PM process has proved to be promising, which can result in lower oxygen content

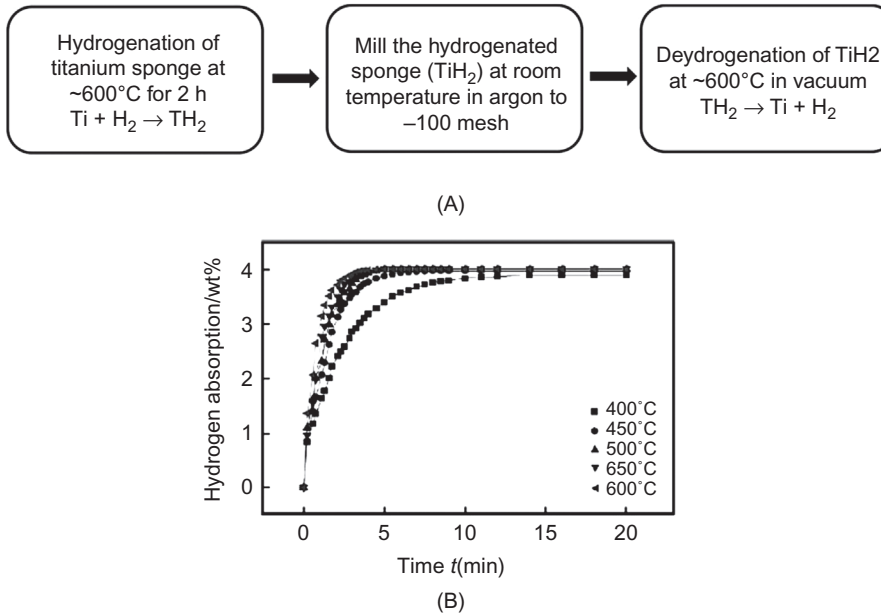


Figure 7.39 Schematic illustration of the production of HDH titanium powder (A) and hydrogenation of titanium sponge particles (1–3 mm) in hydrogen at different temperatures under four atmospheric pressures (B). Hydrogenation essentially completed after ~10 min at each temperature. From Chen, S *et al.*: *J. Functional Mater.*, 45, 11123, 2014.

and higher sintered density than the use of HDH titanium powder. Recently, hydrogen has been used to destabilize titanium (oxygen) solid solutions for the production of low-oxygen titanium powder through reaction with molten magnesium.

Apart from economies in materials and fabrication costs, PM techniques can offer other advantages. Uniformity of composition is greater because the chemical heterogeneity in cast billets is avoided. In addition, components produced from powders show no crystallographic texture or anisotropy of grain shape, and so are much more uniform in respect of mechanical properties. Another attribute is that ceramic reinforcements (e.g., TiB_2 and TiC) can be readily introduced to enable the fabrication of specialty titanium metal matrix composites. Significantly higher values of proof stress and tensile strength at room and elevated temperatures are possible, although ductility and toughness are normally less than that achieved for conventional wrought alloys. As shown in Fig. 7.40, the fatigue properties are intermediate between wrought alloys and castings. Recent developments have shown that strong (tensile strength $\geq$1000 MPa) and ductile (tensile elongation $\geq$15%) titanium metal matrix composites reinforced with TiB are achievable in the as-sintered state without

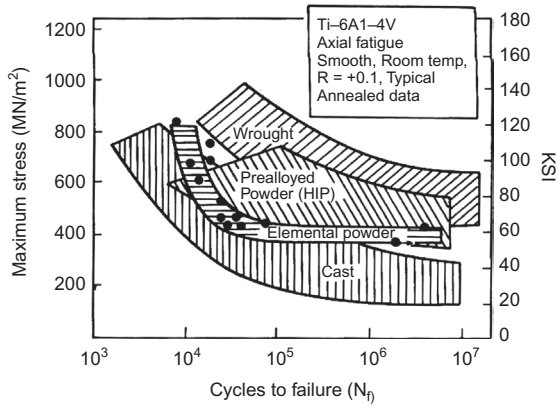


Figure 7.40 Comparative scatter bands for results of fatigue tests on annealed Ti–6Al–4V products fabricated by different processes. From Kelto, CA et al.: Powder Metallurgy of Titanium Alloys, Froes, FH and Smugeresky, JE (Eds.), *Met. Soc. AIME*, Warrendale, PA, USA, p. 1, 1980.

postprocessing. This may lead to more encouraging applications of PM titanium metal matrix composites in the future.

7.6 TITANIUM ALLOY CASTINGS

The high affinity of molten titanium for oxygen, nitrogen, and hydrogen requires that melting and pouring be carried out under vacuum. Consumable electrode vacuum arc or electron beam melting furnaces are commonly used (see Section 1.4). The range of molding materials is limited because of the acute reactivity of molten titanium. Rammed graphite is often used for this purpose. Effective mold coating materials are still under development. Lost wax investment casting is used to produce precision parts for the aerospace industry, one example being the intermediate compressor casings for several gas-turbine engines. The cost of each part is 15–35% lower than for the equivalent wrought component because of savings in materials and the costs of fabrication. The largest titanium alloys castings are those prepared for chemical equipment where rammed graphite molds are used. In the United States, for example, spherical valves up to 2.5 m in diameter and weighing as much as 1 tonne have been produced from titanium alloy castings. Impellors for pumps is another common application.

It is standard practice to apply HIP (Section 7.5.8) to titanium castings in order to remove porosity and ensure performance consistency for critical applications. On the F-22 Raptor aircraft, HIP-processed titanium castings are used on six large structures: the rudder actuator housing (one for each rudder), the canopy deck, the wing side-of-body forward and aft fittings

(four total, two for each wing), the aileron strongback (one for each aileron, two total), and the inlet canted frame (one each for the left and right inlets).

Static strength values for titanium alloy castings are similar to those for wrought titanium alloys with the same composition but the ductility is generally much lower. Low-cycle fatigue strength is within the normal range of distribution for wrought materials but above 10^6 cycles, the smooth bar fatigue strength is clearly lower. Notched fatigue strength (e.g., $K_t = 2.5$) is similar for both cast and wrought titanium alloys.

Two widely used titanium alloys for castings are the general purpose α−β alloy Ti–6Al–4V and α-alloy Ti–5Al–2.5Sn. The as-cast microstructure of Ti−6Al−4V typically consists of lamellar α−β and GB α, similar to that shown in Fig. 7.16A. Step-plate samples of Ti−6Al−4V (100 mm long, 50 mm wide, and 3−25 mm thick) in the as-cast condition (graphite molds) exhibited tensile strength of 958 ± 28 MPa, yield strength of 826 ± 8 MPa, and elongation of 7.3 ± 0.9%. Other cast titanium alloys include the α−β alloy Ti–6242 and the near-β alloy Ti–5553 (Table 7.1), which have lower castabilities but can develop higher tensile and fatigue strength. For example, Ti−5553 in the cast-HIP-and-further-heat treated condition can achieve ultimate tensile strength of 1158 MPa, yield strength of 1055 MPa, elongation of 9%, and fatigue strength of 780 MPa ($R = 0.1$). These properties compare well with those of many wrought titanium alloys.

7.7 ENGINEERING PERFORMANCE

7.7.1 Tensile and creep properties

Titanium alloys can achieve very high tensile properties. For example, cold-rolled and aged bars of the metastable β-alloy Beta 21S (Ti−15Mo−3Nb−3Al−0.2Si; 80% cold work, and aged at 482°C for 20 h) can attain tensile yield strength of ≥1400 MPa and tensile strength of ≥1700 MPa accompanied by 5.0% of elongation. In addition, most titanium alloys show very close tensile and yield strength values (Table 7.1). The uniquely high strength-to-density ratios of titanium alloys were shown in Fig. 1.6 over a broad temperature range. Besides, as mentioned in Section 7.2.2, α-titanium alloys can show high strength and toughness at very low temperatures (−253°C) for cryogenic storage vessels in space vehicles, and they are the material of choice for such applications.

The development of titanium alloys has also been driven by the desire to improve their creep performance (see Fig. 7.2). Near-α titanium alloys such as IMI 829, IMI 834, and Ti−1100 are available for long-term service at 550−600°C. These temperatures are close to the limit at which conventional titanium alloys can be used in air because oxidation or even burning becomes significant above 600°C. There are, however, titanium aluminide intermetallic alloys which show promise of being used at temperatures up to 1000°C (Section 8.9).

Table 7.14 Influence of microstructure and heat treatment on tensile and fatigue properties of Ti–6Al–2Sn–4Zr–6Mo

Condition	YS (MPa)	UTS (MPa)	El. (%)	R_A%	Fatigue strength at 10^7 cycles (MPa)	
					Smooth sample	Notched sample
10% equiaxed α annealed	1020	1109	15	37	620	289
10% equiaxed α STA	1116	1213	13	37	620	248
50% equiaxed α annealed	1061	1130	13	34	620	282
50% equiaxed α STA	1051	1240	14	42	675	276
50% equiaxed α STOA	1068	1144	14	41	620	262
50% equiaxed α STA	1096	1206	10	23	751	276
20% equiaxed α STA	1109	1206	11	26	620	282
β forged (no primary α), STA	1047	1199	7	13	675	262

Adapted from the TIMETAL datasheet. The stress ratio (R) was unspecified.
YS, yield strength; UTS, ultimate tensile strength; El., elongation; R_A, reduction of area; STA, solution treated and aged (885°C/1 h/AC + 595°C/8 h/AC; AC, air cooling); STOA, solution treated and overaged (885°C/1 h/AC + 705°C/1 h/AC); annealed, 705°C/1 h/AC.

7.7.2 Fatigue properties

Titanium and titanium alloys with isotropic microstructures can display fatigue properties comparable to those obtained with ferrous materials. The ratio of fatigue-strength-to-tensile-strength is in the range 0.50–0.65 for most titanium alloys (0.75–0.80 for near-β Ti–10–2–3). As with other metallic materials, the fatigue performance of titanium alloys is greatly influenced by microstructure (Table 7.14) and texture. In general, conditions which favor high toughness also tend to give low cyclic crack growth rates under fatigue loading. The effects of microstructure on fatigue crack propagation have been shown in Fig. 7.19 and Table 7.8, whereas the influence of grain direction (and texture) was demonstrated in Fig. 7.36 and Table 7.12. As mentioned in Section 7.3.2, coarse lamellar or basket-weave type microstructures are resistant to crack propagation, whereas a finer microstructure tends to be beneficial in delaying crack initiation. In that regard, heat treatment can play a critical role in producing the desired microstructure as shown in the following discussion with Table 7.14.

Bimodal microstructures can offer excellent fatigue strength as well as high tensile properties. For example, Ti–6Al–4V in the STA condition, which has a bimodal microstructure consisting of elongated primary α-particles in an aged α′-matrix (fine lamellar α+β), can achieve fatigue strength of ≥700 MPa, tensile strength of >1100 MPa, and elongation of >10% (Table 7.5). Table 7.14 provides the influence of microstructure and heat treatment on both the tensile and fatigue properties of the α–β alloy Ti–6246. Elongated primary α phase

particles reduce both the elongation and reduction of area but increases fatigue strength compared with the equiaxed primary α phase condition. For example, increasing the amount of equiaxed primary α from 10 to 50 vol.% increased fatigue strength from 620 to 675 MPa. With 10 vol.% of equiaxed primary α phase, the STA and low-temperature annealing (at 705°C) treatments produced the same relatively low fatigue strength (620 MPa), indicative of the importance of having elongated primary α phase particles for improved fatigue strength in the STA condition. Notched samples displayed much lower fatigue strength. Consequently, the influence of microstructure and heat treatment is less clearer due to the prominent influence of the notch. Fatigue strength can be anisotropic, especially when the microstructure is textured (Section 7.5.4).

β-Titanium alloys generally display good fatigue performance. For example, Ti−10−2−3 in the STA condition, which has a bimodal microstructure comprising elongated α_P (aspect ratio >3:1) in an aged β matrix (Fig. 7.31), can show very high fatigue strength (≥880 MPa). Under high-cycle, low-stress conditions, fatigue strength increases with yield strength (fracture toughness decreases with yield strength, refer to Fig. 7.42 in Section 7.7.3) up to levels at which fatigue cracks tend to initiate in soft regions in the microstructure, such as precipitate-free zones or α phase particles at GBs, where deformation becomes concentrated. In general, the crack growth rates in β-alloys are comparable to those of Ti–6Al–4V in the mill-annealed condition at high stresses, but slightly higher at low stresses.

A phenomenon which may be unique to certain titanium alloys is the effect of dwell periods, at high loads, on rates of growth of fatigue cracks. This effect is shown schematically in Fig. 7.41 and increases in the rates of growth, immediately after the dwell period, of as much as 50 times may occur as compared with results obtained in tests on the same alloy subjected to continuous sinusoidal stress cycles. Dwell effects are greatest in alloys containing substantial amounts of the α phase which have a preferred texture such that stressing is normal to the basal planes. On the other hand, they appear to be insignificant if stressing occurs parallel to the basal planes of the α phase, or if the microstructure is homogeneous and fine grained. Once again, special attention has been paid to the α−β alloy Ti–6Al–4V in which dwell effects have been found to decrease with increasing amounts of the β phase in the microstructure. In all cases, dwell effects disappear when stressing occurs above 75°C. They are generally considered to arise because of the presence of relatively high contents of hydrogen (more than 100 ppm) which, during the dwell period, diffuses to regions of localized hydrostatic tension ahead of advancing cracks. Such an accumulation of hydrogen apparently embrittles these regions, and it has even been suggested that brittle plates of TiH_2 may have formed.

It should also be noted that dwell periods may have the opposite effect of increasing fatigue strength if alloys contain low levels of hydrogen. Strain ageing may occur in this case, which is beneficial because it results in pinning of dislocations by atmospheres of hydrogen and/or other interstitial atoms.

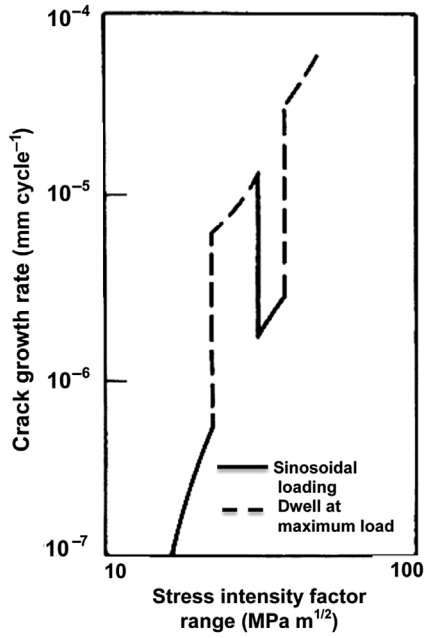


Figure 7.41 Schematic representation of the effect of dwell periods at maximum load on the rate of crack growth during fatigue tests on certain titanium alloys.

As mentioned in Section 7.5.5, titanium alloys are particularly sensitive to contact due to sticking or galling, a characteristic which may lead to fretting fatigue. Fretting itself is a form of wear that occurs when two surfaces, pressed together by an external load, are subjected to transverse cyclic loading so that one contacting face is cyclically displaced relative to the other face. Extremely small displacements may be involved and small fragments of metal and oxidation products may break off leading to surface pitting at which stresses may be concentrated. Fretting damage in titanium alloys can reduce fatigue life by factors of as much as eight times compared with a reduction factor of around three for similar damage in aluminium alloys.

One example where fretting can be a major concern is at the root fittings of titanium alloy blades in gas-turbine engines. Much attention has been given to alleviating the problem and one method involves the application of two thin coatings. One is a Cu–In–Ni alloy that is plasma sprayed on to the surface; after this the second, a phenolic resin which contains graphite and molybdenum disulfide as lubricants, is baked on.

7.7.3 Fracture toughness

The fracture toughness (K_{IC}) of a titanium alloy is affected by a range of factors including the alloy chemistry, microstructure, specimen geometry and size, and

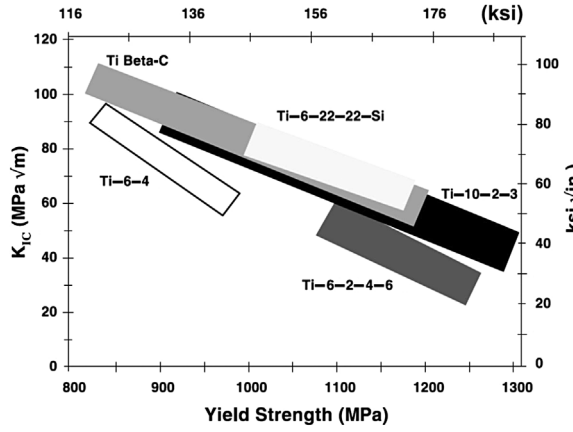


Figure 7.42 Fracture toughness vs yield strength for α–β alloys Ti–6–4, Ti–6246, and Ti–6–22–22–Si, near-β alloy Ti–10–2–3, and metastable β-alloy Beta C. From RTI Titanium Alloy Guide, p. 2, 2000.

measurement method. For example, the K_{IC} value obtained from the acoustic emission method can be different from that obtained according to the ASTM E399—12e3. Only the influence of microstructure is discussed briefly in this section. It has been generally established for titanium alloys that (1) an acicular microstructure leads to lower tensile strength and ductility but higher fracture toughness than an equiaxed microstructure, and (2) the fracture toughness improves with coarsening microstructure. Coarse lamellar or basket-weave type microstructures are therefore in favor for achieving higher fracture toughness and this has been confirmed in service. Some of the annealing treatments discussed in Section 7.3.2 were designed, to a large extent, for improving fracture toughness. The yield or ultimate tensile strength may be used as an approximate indication to predict the trend of fracture toughness. Fig. 7.42 shows the correlation between fracture toughness and yield strength for three α–β alloys, near-β alloy Ti–10–2–3, and metastable β-alloy Beta C. The nearly linear decreasing trend of fracture toughness with increasing yield strength underlines the importance of microstructural design and control for different performance requirements by hot forming and heat treatment.

7.7.4 Corrosion

Titanium is a highly reactive metal but, because of the presence of the very stable, self-healing titanium dioxide film (TiO_2), it exhibits excellent corrosion resistance in a wide variety of environments and is more resistant to attack than stainless steels under many circumstances. For example, it resists attack by oxidizing solutions, particularly those containing chloride ions as mentioned in Section 7.1. This unique property has led to its major applications in the chemical, pharmaceutical, and marine industries. Titanium also shows outstanding

resistance to atmospheric corrosion in both industrial and marine environments, and its resistance to seawater is virtually unsurpassed by other structural metals. It is further resistant to many acids and salt solutions. However, titanium is attacked in reducing environments in which the oxide film is unstable and cannot be repaired.

One of the most successful applications for titanium alloys is in handling wet chlorine gas, bleaching solutions containing chlorides, hypochlorite, and chlorine dioxide. However, titanium suffers catastrophic attack in dry chlorine gas, although as little as 50 parts per million of water will prevent this attack. For most chemical applications, strength is a secondary requirement and CP titanium is used. In order to cope with nonoxidizing acids such as sulfuric, hydrochloric, and phosphoric, or with some reducing conditions, several methods have been developed to improve the corrosion resistance of titanium. In particular, small additions of palladium ($\leq$0.25%) as mentioned in Section 7.2.2, and nickel (0.5%Ni) have proved to be highly effective in expanding the corrosion resistance of titanium alloys under reducing conditions. Moreover, small palladium additions can significantly increase crevice corrosion resistance of titanium and titanium alloys in hot aqueous chlorides (crevice corrosion of titanium alloys occurs mainly when they are exposed to hot aqueous chloride, bromide, iodide, or sulfate solutions). These findings have enabled the development of palladium-containing titanium alloys Grades 7 (IMI 260), 11, and 17 (Table 7.3), and nickel-containing alloys Grade 13 (low oxygen), Grade 14 (standard oxygen), and Grade 15 (medium oxygen, Table 7.1).

In Grade 7 or IMI 260 (Ti–0.2Pd), the role of palladium was to induce anodic passivation, which can reduce corrosion rates in some solutions by a factor of as much as 1000 times. A similar effect may be achieved by external anodic protection in which the potential of titanium is made more positive by connecting to either an electrical power source or to a more noble metal. In this regard, titanium has the particular advantage over stainless steel because it remains passive over a much wider range of potential. However, an addition of 0.2% palladium can double the price of CP titanium. As an alternative, the alloy Ti–0.5Ni–0.05Ru has been developed (Grade 15, Table 7.1). The influence of aluminium, vanadium, and molybdenum as major alloying elements on the general responses of titanium alloys has also been studied in reducing aqueous acid media. Vanadium and especially molybdenum with an addition of $\geq$4%Mo can markedly improve corrosion resistance while increasing aluminium content appears to be detrimental.

Ion plating is a method of coating in which some of the deposited particles are ionized, e.g., by passing through a plasma which assists in cleaning the surface of the substrate and improving the adhesion of the coating. In addition to raising the general corrosion resistance of titanium, ion plating may also increase wear resistance and fatigue strength. The technique has been used to coat titanium with a very thin (~1 μm) coating of platinum.

The major corrosion problem with titanium alloys is crevice corrosion which may take place in joints, seams, welds, under gaskets, under fouling, or deposits, where circulation of the corroding medium is restricted. Progressive acidification occurs in the crevice because of hydrolysis of corrosion products and destroys protective oxide film. The problem becomes worse at elevated temperatures. CP titanium is vulnerable to crevice corrosion, even at a neutral pH with temperatures >120°C. Again the addition of the noble metal palladium has been found to be beneficial, as has ion plating of surfaces with platinum. Proper design (e.g., avoid crevices) and maintenance (e.g., periodic cleaning to decrease chloride ions, fluid movement, and oxygen presence) can be equally important.

In principle, surface pitting may occur at inclusions or weak points that exist in the passive oxide film. However, this problem has rarely been observed in titanium alloys and may only be significant in halide-containing aqueous solutions which are at elevated temperatures.

7.7.5 Stress–corrosion cracking

The apparent stability and integrity of the oxide film in environments that caused SCC in more common structural alloys suggested that, titanium alloys may be very resistant to this phenomenon. For example, early investigators were unable to crack titanium alloy specimens that were stressed and exposed to boiling solutions of 42% $MgCl_2$ or 10% NaOH, both of which induce cracking in many stainless steels. However, a susceptibility issue to SCC was recognized in 1953 with the cracking of CP titanium in red fuming nitric acid, and further in 1955 when the unexpected failure of a titanium alloy undergoing a hot tension test was supposedly traced to chloride salts deposited from finger marks. Since then, it has been demonstrated in the laboratory that, most titanium alloys will undergo SCC in one or more environments (Table 7.15), and special attention has been given to the comparative performance of titanium alloys in aqueous halides, organic fluids, e.g., methanol, and hot salts. However, it must be emphasized that actual failures in service have been rare.

The resistance of titanium alloys to SCC is highly dependent on both alloy composition and microstructure. β-Isomorphous elements such as molybdenum, vanadium, niobium, and tantalum have proved to be particularly beneficial, while aluminium (>5%), tin, and the β-eutectoid, and compound-forming elements including chromium, manganese, and silicon, were found to be detrimental. Oxygen levels below 0.13% in Ti–6Al–4V (i.e., ELI) were found to be able to significantly increase the resistance to SCC. ELI Ti–6Al–4V is therefore commonly used in marine environments when good resistance to SCC is required. Near-α titanium alloy Ti–5111 (Table 7.1), which was developed for the US *Navy*, is immune to SCC in marine environments at room temperature. A modified version of the alloy, which is Ti–5111Pd containing 0.05%Pd,

Table 7.15 Some environments in which titanium alloys may be susceptible to SCC

Medium	Temperature (°C)	Examples of susceptible alloys
Cadmium	>320	T–4Al–4Mn
Mercury	Ambient	CP Ti (≥99%), Ti–6Al–4V
	370	Ti–13V–11Cr–3Al
Silver plate	470	Ti–5Al–2.5Sn, Ti–7Al–4Mo
Chlorine	290	Ti–8Al–1Mo–1V
Hydrochloric acid (10 vol.%)	35	Ti–5Al–2.5Sn
	345	Ti–8A1–1Mo–1V
Nitric acid (fuming only)	Ambient	CP Ti (≥99%), Ti–8Mn, Ti–6Al–4V, Ti–5Al–2.5Sn
Chloride salts	290–425	All commercial titanium alloys
Methanol	Ambient	CP Ti(≥99%), Ti–5Al–2.5Sn, Ti–6Al–4V, Ti–8Al–1Mo–1V, Ti–4Al–3Mo–1V
Trichloroethylene	370	Ti–5A1–2.5Sn, Ti–8Al–1Mo–1V
Seawater	Ambient	CP Ti–(≥99%), Ti–5Al–2.5Sn, Ti–6Al–4V, Ti–8Mn, Ti–11Sn–2.25Al–5Zr–1Mo–0.25Si, Ti–13V–11Cr–3Al, Ti–8Al–1Mo–1V

From Boyd, WK: *Proceedings of Conference on Fundamental Aspects of Stress–Corrosion Cracking*, Staehle, RW *et al.* (Eds.), Nat. Assoc. Corrosion Eng., p. 593, 1969.

offers considerably improved resistance to crevice corrosion and to corrosion in reducing acid environments, in addition to its immunity to SCC. It is the clear material of choice for submarine or similar applications where both toughness and corrosion resistance are essential.

Alloys Beta 21S and Beta C have also shown excellent resistance to SCC. The reason can be attributed to the difficulty in initiating cracks. Many titanium alloys are highly resistant to pitting corrosion whereas, in many other materials, the pits provide the stress concentration necessary to initiate SCC.

Titanium fasteners are used in many structural designs. SCC-induced failures are among the greatest concerns due to the lack of in situ inspection capability and the unpredictable nature of these failures. Experiences have indicated that, only a slight misalignment or a small degree of fastener head-to-flange nonperpendicularity may result in sufficient local stresses for SCC to progressively develop during service. The fastener system often shows no direct evidence of general corrosion attack. Accordingly, the use of highly SCC-resistant titanium alloys relevant to the specific service environment is critical for important fasteners.

It is apparent from Table 7.15 that, SCC in most titanium alloys is specific to a particular environment. However, it is possible to identify several trends related to composition and microstructure.

1. α-Titanium alloys generally show the greatest susceptibility to SCC. For example, CP titanium will crack in some environments if the level of oxygen in the metal is high. Aluminium contents in excess of 5–6% are considered detrimental and this is attributed primarily to the formation of the ordered phase α_2 (Ti_3Al), the presence of which changes the dislocation substructure that forms during deformation.
2. The addition of molybdenum and vanadium enhances the resistance to SCC. They increase the amount of the β phase and, as this phase appears to be immune from SCC in a number of α–β alloys, it has been proposed that it serves to arrest cracks that may be propagating in the more susceptible α phase. It should be noted, however, that elements such as manganese which stabilize β-eutectoid systems increase susceptibility to SCC.
3. Hydrogen is readily absorbed by titanium and is detrimental because a number of alloys are susceptible to hydrogen embrittlement, particularly in aqueous environments. Although the precise mechanism for embrittlement is uncertain, it seems likely to arise either from the formation of brittle titanium hydride or from the directed diffusion of hydrogen to highly stressed regions such as crack tips, thereby assisting crack propagation. Hydride formation seems to occur preferably in titanium alloys containing aluminium.
4. Quenching from the β phase field, which often gives acicular microstructures, generally confers greater resistance to SCC than slow cooling from the α+β field. This result is similar to that described for fatigue cracking in Section 7.3.1, and is again associated with crack branching (Fig. 7.19B). However, the reverse seems to hold for alloys exposed to halides at high temperatures, i.e., the so-called hot salt SCC.
5. A combination of plastic deformation and heat treatment is beneficial in reducing susceptibility to SCC because it refines the grain structure.
6. Ageing leading to precipitation of a second phase (e.g., ω or α) within β-grains can lower resistance to SCC.
7. As with aluminium alloys, wrought titanium products show a greater susceptibility to SCC in the short transverse direction.

7.7.6 Corrosion fatigue

The combination of the generally high fatigue strength of titanium alloys and their excellent resistance to corrosion suggests that they should perform well under conditions of corrosion fatigue and this has been found to be so. Special attention has been given to comparisons between Ti–6Al–4V and a 12%

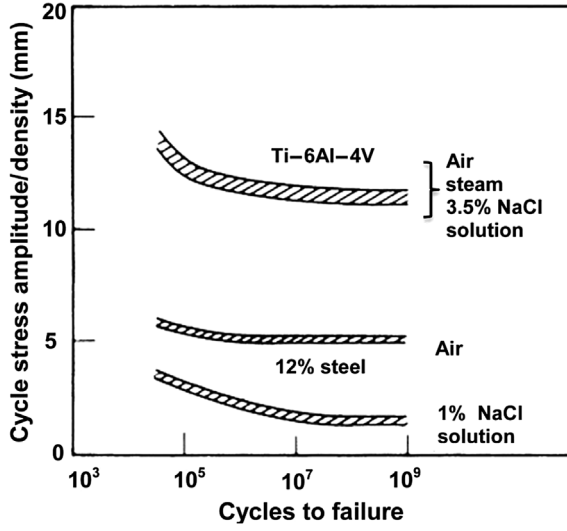


Figure 7.43 Fatigue property-to-density ratios of Ti–6Al–4V and 12% chromium steel tested in different environments. From Jaffee, RI: *Metall. Trans.*, 10A, 139, 1979.

chromium steel, because of the possible replacement of this steel by titanium alloys for the low-pressure sections of large steam turbines. The strength level at which titanium alloys could be put into service is some 25% higher than that for a 12% chromium steel. Taking into account this factor and the difference in relative density, the fatigue strength of Ti–6Al–4V tested in air is more than double that of the steel (Fig. 7.43). Moreover, whereas the titanium alloy is unaffected by testing in steam or in a solution of 3.5% NaCl, the fatigue strength of the steel tested in only 1% NaCl solution falls to one-eighth that of the titanium alloy. In addition to Ti–6Al–4V, CP titanium (Grades 1–4) and CP titanium containing minor additions of palladium (Grades 13–15) have all exhibited excellent resistance to corrosion fatigue. No significant reduction in fatigue strength has occurred in saltwater or seawater media.

Owing to their high tensile strength, β-titanium alloys have also been used in marine, offshore, and downhole applications. The excellent resistance to corrosion fatigue displayed by Ti–6Al–4V and CP titanium appears to apply to β-titanium alloys as well. No accelerated fatigue failure was observed on Beta C, Beta 21S, and Ti–l0–2–3 alloys in 3.5% NaCl brine at 25°C.

7.8 APPLICATIONS OF TITANIUM ALLOYS

7.8.1 Aerospace

The high specific strength of titanium alloys led to their introduction in aircraft gas turbines as early as 1952 when they were used for compressor blades and

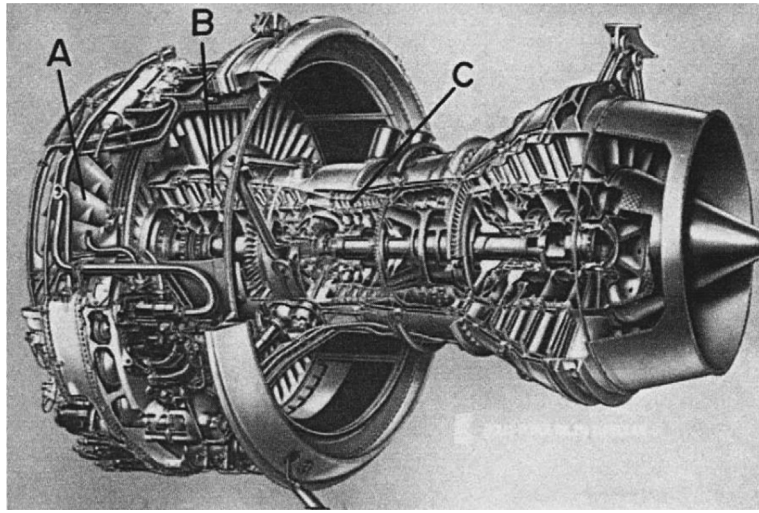


Figure 7.44 Sectional view of one model of the Rolls Royce RB 211 gas-turbine engine. A, fan blades; B, lower-pressure compressor; C, intermediate pressure compressor. Courtesy Rolls Royce Ltd.

disks in the famous Pratt and Whitney J57 engine. Immediate weight savings of ~200 kg were achieved. At the same time, in Britain, an alloy Ti–2Al–2Mn was used for the equally famous Rolls Royce Avon engine that powered such aircraft as the Comet and Canberra. Since then, titanium alloys have continued to be used in aircraft gas turbines, which now make up 20–25% of the weight of most modern engines. In particular, titanium alloys have played a major role in bypass (fan-jet) engines for which a large front fan is required (Figs. 7.14 and 7.44). Some fans are close to 3 m in diameter, and each solid blade may weigh more than 6 kg, which means that, when rotating in service, each blade exerts a pull of ~75 tonnes or more on the turbine disk or wheel. This has led to an innovation in design whereby the so-called wide-chord, hollow blade has been introduced to reduce weight. This blade comprises a honeycomb core covered by titanium alloy skins, which are diffusion bonded together to form an integral structure (Fig. 7.45).

In addition to the fan, titanium alloys are used for most of the blades and disks in the low and intermediate sections of the compressors of modern jet engines as shown, for example, in Fig. 7.44. Selection of the disk material is particularly critical as it is subjected to thermal stresses arising because of temperature differences between the hotter rim and cooler core, which are additional to the high loads imposed by the rotating blades. A high-performing disk material should have low values of coefficient of expansion and high values of low-cycle fatigue (LCF) strength in the operting environment. High-strength titanium alloys are the best materials for this application. In general, the $\alpha-\beta$

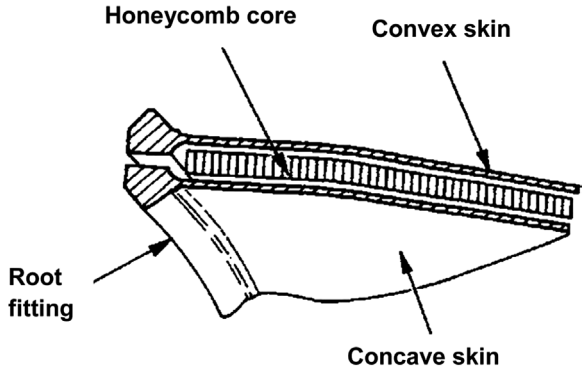


Figure 7.45 Expanded section showing construction of a wide-chord fan blade for an advanced gas-turbine engine. Titanium alloy skins are diffusion-bonded together in this structure. Courtesy J. F. Coplin, Rolls Royce Ltd.

alloy Ti–6Al–4V is favored for the fan and cooler parts of the compressor, whereas the near-α alloys are specified where greater strength and creep resistance are required. Other engine applications include the use of the CP titanium sheet for casings and ducting.

The use of titanium alloys for structural members in aircraft had also developed steadily before the early 1970s. For example, the Boeing 707 commercial aircraft, which first came into service in 1958, contained only 80 kg of titanium parts (0.5% of the structural weight). Subsequently, the Boeing 727 aircraft (1963) had 290 kg (1%), the Boeing 747 (1969) 3850 kg (2.8%), and the McDonnell-Douglas DC 10 (1971) 5500 kg (10%). However, it slowed down during the next two decades because of the high cost of titanium alloys relative to aluminium alloys. The Boeing 777 aircraft (1994) had just 9% of the total structural weight made from titanium and titanium alloys. Since then, titanium has made up 15% of the structural weight of the Boeing 787 aircraft, roughly 17,600 kg, which accounts for $17 million of the total cost of the $260 million aircraft, far more than other Boeing jetliners. However, some of the titanium alloy parts used in the Boeing 787 aircraft were made at an extremely high buy-to-fly ratio (the weight ratio between the raw material purchased for making a part and the weight of the final flying part itself). For example, the large titanium alloy structure that is used to join the wings to the body, known as the double plus chord, was manufactured at the buy-to-fly ratio of 40:1. Overall, the Airbus jetliners have used similar levels of titanium materials. For example, the Airbus A320 jetliner (1988) contained ~2200 kg of titanium parts (6% of the structural weight), and the same percentage (6% of the structural weight or 16,600 kg) was used in the Airbus double-decker jumbo jet A380 (2007). The usage was increased to 14% in the Airbus A350 XWB jetliner (2013),

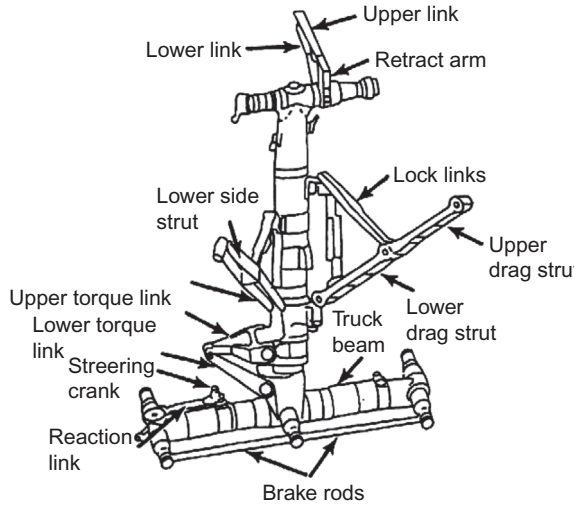


Figure 7.46 Main landing gear of the Boeing 777 aircraft made from near-β Ti–10–2–3 alloy forgings. Courtesy Boeing Commercial Aircraft, Seattle, WA, USA.

which contained ~16,000 kg of titanium parts. These include those used in the engines, landing gears, pylons, and door surroundings.

Titanium alloys were first used mainly as sheet for engine nacelles, exhaust shrouds, and fire walls where heating was significant. Apart from the applications discussed earlier, now they are also used for many other purposes. For example, most of the main landing gear of the Boeing 777 aircraft is made from high strength, near-β Ti–10–2–3 forged parts (Fig. 7.46) with weight savings of 270 kg over high-strength steel parts. In this aircraft, use has also been made of the stronger, and highly cold formable near-β alloy Ti–15–3–3–3, which replaces CP titanium for some 49 m of ducting. This allows thinner sheet to be used which enables further weight savings to be obtained. Other common applications include (i) thin straps wrapped around aluminium alloy fuselages to prevent the propagation of possible fatigue cracks, (ii) hydraulic tubing, kitchen, and toilet flooring where high corrosion resistance is required, and (iii) forgings of Ti–6Al–4V such as engine mountings, flap and slat tracks in wings, and undercarriage components.

The two oxidation-resistant β-titanium alloys discussed in Section 7.4.2, Beta 21S and Alloy C, have both found important applications in the aerospace industry. Applications of Beta 21S include the plug, nozzle, and aft cowl on the Pratt & Whitney 4084 engines for Boeing 777 and the Pratt & Whitney 4168 engines for Airbus 330. The heat shield of the compressor case in the latter engine is also fabricated from Beta 21S, which is ~114 cm in diameter and operates to nearly 650°C. The use of Beta 21S rather than Inconel 625 led to approximate weight reductions in the range up to 164 kg per Boeing 777 aircraft. Alloy

C has found applications in compressor stators and the thrust-vectored nozzle systems on the F119 engines for the US Air Force F-22 jet fighter.

Much greater use has been made of titanium alloys in military aircraft (e.g., 39% of the structural weight of the F-22 jet fighter) due to the high Mach number they were designed to fly at, which exceeds the capabilities of high-strength aluminium alloys (Mach number: ~2.2) due to strong aerodynamic heating. Here the most common location for the titanium alloys is in the engine bay, e.g., in the early McDonnell-Douglas F-15 aircraft. In this aircraft, some 7000 kg of titanium alloys was used which represents 34% of the structural weight compared with 48% for aluminium alloys. Newer alloys such as Ti–6Al–2Zr–2Sn–2M0–2Cr–0.25Si are used in the airframe of the US F-22 fighter aircraft. The mid-fuselage bulkhead, which makes up part of the wing box of this aircraft and measures 4.9 m × 1.8 m × 0.2 m, is one of the largest titanium alloy forgings ever made. Although this component only weighs 150 kg, it is forged from a cast ingot weighing almost 3000 kg. Complex structures such as the wing box of the swept-wing European Panavia Tornado fighter aircraft are also made largely from welded and machined titanium alloy forged plate, and the critical wing-pivot lug is a Ti–6Al–4V forging.

Considerable use has also been made of high-strength titanium alloy fasteners, and the large American military transport aircraft, the Lockheed C5A, uses 1.5 million such units out of a total of 2.2 million. This has resulted in a direct reduction in weight of 1 tonne, with an additional 3.5 tonnes being saved through consequent structural modifications that are possible by using titanium alloys fasteners. For military helicopters, titanium alloys are now also used for the fasteners. Similarly, titanium alloy fasteners have been used in the wing and fuselage assemblies of the Airbus A380 jet liner in order to reduce weight. For example, nearly 9000 titanium MaxiBolt Plus blind bolts were used to replace the stainless steel bolts in each carbon fiber vertical tail plane section (weight savings: 8.5 kg). In addition to fasteners, the Beta C alloy discussed in Section 7.4.2 remains to be the material of choice for aircraft springs due to its high tensile strength (1600 MPa) and relatively low density (4.81 g cm^{-3}).

Titanium alloys also have critical applications in helicopters. For example, the use of the high-strength, fatigue-resistant near-β Ti–10–2–3 for the rotor head of the Westland Super Lynx helicopter has enabled this vehicle to operate at gross weights some 45% higher than was intended in the original design. As shown in Fig. 7.47, this rotor head is assembled by bolting together three different forged components. Applications of titanium materials in the aerospace area have also been driven by the increased use of composite materials. When composite materials are made into useful structures, metallic interfaces and inserts are often required for joining with bearings and moving parts. Few materials are more compatible with composite materials than titanium due to stiffness mismatch and galvanic corrosion.

Some of the high costs associated with titanium alloys have arisen because of the use of fabrication methods originally developed for aluminium and its

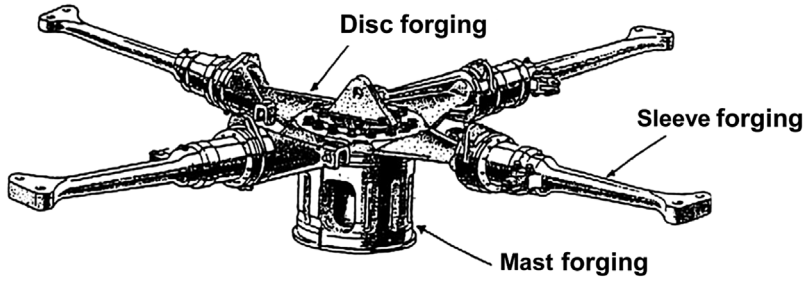


Figure 7.47 Super Lynx helicopter rotor head assembly made from forgings of the near-β Ti–10–2–3. Courtesy Agusta Westland.

alloys. For example, the sheet and rivet methods were initially used to fabricate a range of parts used in the F-15 aircraft. Subsequently, cost savings have been achieved using later models with new designs that used superplastic forming combined with diffusion bonding, thereby eliminating more than 700 parts and 10,000 fasteners. However, the effort to reduce the initial ownership cost of an aircraft has also forced aircraft makers to be very cautious about any unnecessary use of titanium. For example, Boeing has changed the cockpit window frame back to aluminium (with a special coating) from titanium and the frames of some doors to composite, also from titanium.

7.8.2 General applications

About 60% of the global production of titanium is currently used for non-aerospace purposes. As discussed in Section 7.7.3, it is the superior corrosion resistance of titanium and its alloys in many environments that leads to their selection for manufacturing chemical and pharmaceutical equipment and architectural applications. Although titanium alloys are usually more expensive than the materials they replace, their adoption is based on expected cost savings over the planned lifetime of the particular equipment or building. In areas such as for automotive components, military hardware, and sports equipment, high strength-to-weight ratios are usually the main attraction.

Chemical and pharmaceutical equipment The high resistance to general corrosion, pitting and crevice corrosion, and SCC in the presence of chlorides is the major reason for the selection of titanium and its alloys for most chemical and pharmaceutical engineering applications. They are uniquely suited to piping, valves, and pump casings for handling hot brine, bleaching agents, chlorinated hydrocarbons, and other strong chemicals at elevated temperatures. In general, they are much superior to stainless steels in these applications. Tubing for heat exchangers and steam condensers is another common application, because titanium alloys have higher corrosion and erosion resistance than the

traditional copper alloys they replace. CP titanium with thinner wall thicknesses, e.g., 0.5 mm, is usually used, which can actually result in improved heat transfer despite its intrinsically low thermal conductivity. Titanium can also be used for handling nitric, acetic, and organic acids, as well as acetone and wet bromine. In addition, it is normally stable in alkaline solutions up to a pH 12 at temperatures below 75°C.

One of the earliest industrial uses of titanium was based on the discovery that, even though this metal rapidly passivates under anodic conditions, the current will continue to flow through the surface oxide film if other metals are in contact with it. This effect was exploited by the metal finishing industry with titanium being used for jigs that support aluminium components during anodizing, and for anode baskets to hold parts to be plated with copper or nickel. Sheets of CP titanium are also used in the electrolytic refining of copper where they serve as starter blanks. A thin layer of copper is electrodeposited onto the starter blanks and then stripped off for transfer to the main production line to produce a thick copper electrode. Previously the material traditionally used for starter blanks was copper itself, but this had the disadvantage that corrosion occurred at the electrolyte level requiring the copper surface to be coated with oil to act as a parting agent. Titanium is not attacked by this copper sulfate/sulfuric acid solution because of the passivating effect of the cupric ions. Moreover, the oxide film on the titanium surface serves as the parting agent thereby eliminating the need for oil.

Power generation An area of future expansion is the use of titanium alloys for blading in the low-pressure section of large steam turbines. For many years, these blades have been forged from a 12% chromium steel and their size has become limited by the centrifugal loads imposed on the supporting rotors. This, in turn, limits the size of the turbines thereby preventing more efficient operation. As shown in Fig. 7.43, Ti–6Al–4V has corrosion-fatigue properties that are superior to this steel and, for comparable stresses, titanium alloy blades can be 40% longer. One German company has already produced Ti–6Al–4V blades that are 1.65 m in length. In addition, additively manufactured Ti–6Al–4V blades are under evaluation.

Erosion by wet steam is a particular problem in this section of the turbine, and titanium alloys also perform better than stainless steels, although they are not as resistant to wear as the stellite shields that are commonly bonded to the leading edges of the steel blades. Apart from increased cost, a disadvantage of the titanium alloy blades is their reduced stiffness due to lower elastic moduli. However, it is practical to alter their design so that more rigid positioning can be achieved.

Automotive A variety of automobile parts can be made from titanium alloys to reduce weight. However, their affordability has been a major obstruction. On average, for each kilogram of weight reductions, the aerospace industry is

willing to pay €10,000; the aircraft industry €1000, while the automotive industry €10 maximum in most cases. This dictates that their use in mass produced vehicles can only be justified if the advantages are exceptional. Examples of components are connecting rods, valves, valve springs, and turbocharger rotors in the engine and suspension springs (the Beta C alloy) and exhaust systems in the body.

Reducing the weight of reciprocating and rotating components in the engine can lower fuel consumption and consequent exhaust emissions. Connecting rods require high tensile and fatigue strengths, stiffness, and wear resistance. Titanium alloys present problems with the last two of these properties and need reinforcements with high modulus, and the use of special coatings on wear surfaces. Special attention has been paid to engine valves. Since the late 1990s, Toyota in Japan has used the Ti−6Al−4.5Sn−4.5Zr−1Mo−1Nb−0.2Si−0.3O–TiB composite (5 vol.%TiB) to make inlet and exhaust valves for a family car model and several models of motorbikes. The valves were 40% lighter than the heat-resistant steel valves. In addition, 16% of weight savings were also achieved from valve springs. As a result, the maximum engine revolutions were increased by 700 rpm and the noise generated in this range was reduced by 30%. Titanium aluminide (γ-TiAl) alloys (Section 8.9) have the potential to be used for automotive engine valves as well.

The relatively low modulus of titanium is an advantage for springs. A cost-effective β-titanium alloy, Ti–4.5Fe–6.8Mo–1.5Al, has been developed to make the two rear coil springs for one model of the Volkswagon Lupo motor cars, and each spring weighs only one half of the equivalent steel spring. Other common applications include CP titanium mufflers and exhaust pipes, which are also approximately half the weight of the equivalent mild steel or stainless steel components, but they offer a life expectancy of at least 12−15 years. An improved CP titanium alloy has been developed for these applications, which has the composition Ti–0.5Fe–0.6Si–0.15O, designated TIMETAL Exhaust XT. It exhibits superior resistance to oxidation and elevated temperature strength compared to other CP titanium alloys, and has been used to replace stainless steel in automotive and motorcycle exhaust applications.

Marine Both the high corrosion resistance in the presence of seawater and the high strength-to-weight ratios of titanium and its alloys make them an attractive prospect for use in marine environments such as offshore oil and gas platforms. Russia has been a leader in this regard. Stringent requirements that must be met include:

1. high strength and fracture toughness under static and dynamic loading conditions at temperatures as low as −50°C,
2. resistance to SCC,
3. resistance to erosion by sea ice,
4. fire resistance under conditions of hydrocarbon combustion,

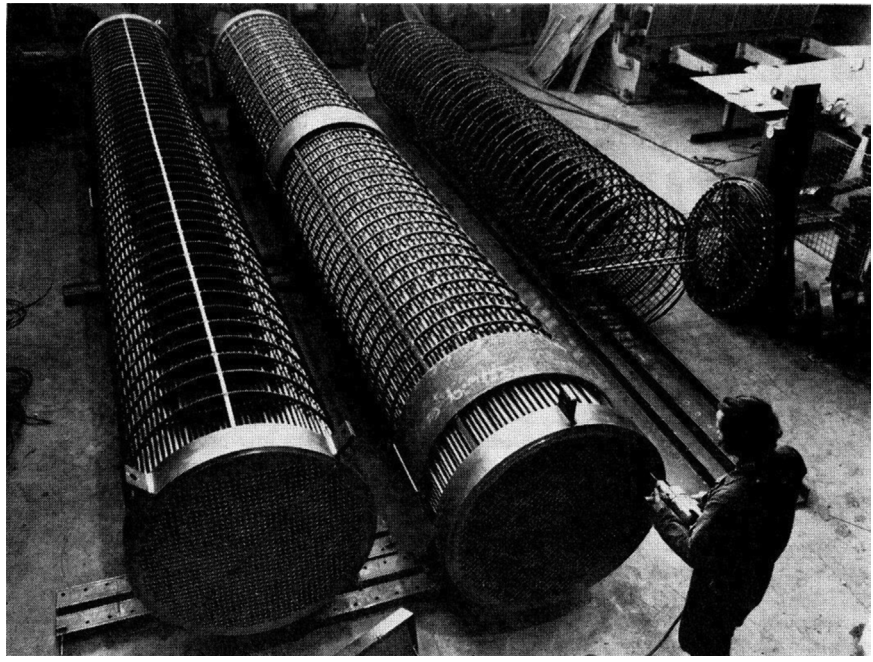


Figure 7.48 Tubing and baffles for oil/gas product coolers fabricated from CP titanium seamless tubes and plates. From *Metallurgist Mater. Technol.*, 9, 543, 1977.

5. resistance to the adsorption of hydrogen when in contact with other metals or with cathodic protection systems,
6. a capacity for repairs to be made without the need for postweld heat treatment.

Russia has developed several α and near-α titanium alloys especially for marine applications, examples being Ti–5.3Al–2Mo–0.6Zr and Ti–5.5Al–1.5V–1.4Mo. During the last two decades several thousands of tonnes of titanium alloys, mostly CP titanium and ELI Ti–6Al–4V, have also been used on oil platforms in the North Sea. Applications include heat exchangers, drilling risers, pipelines, valve castings, and fasteners. In the example shown in Fig. 7.48, seawater is used as the coolant and the tubing must resist attack by sulfide contaminants in the oil and gas.

During the 1970s and 1980s, the Russian Navy operated submarines with a hull completely manufactured from titanium. This allowed the thickness and weight of the hull to be reduced, which enabled these vessels to travel faster and dive deeper than any other in the world. Deep-sea submersible vessels made with titanium pressure hulls are now capable of diving more than 10,000 m deep.

Military hardware Ti–6Al–4V has been used for military armor applications in ground vehicles, particularly tanks, fighting vehicles, and personnel carriers in order to save weight due to its excellent ballistic characteristics, lightweight, corrosion resistance, and its ability to be easily fabricated. It has also been utilized in personal armor applications. Titanium machine guns and titanium silencers (additively manufactured) are also being used today. In addition, both Grade 2 CP titanium and Ti–5111 have found useful applications in naval ships.

Architectural As mentioned in Chapter 1, the use of panels of thin (0.35 mm) CP titanium sheet to clad the Guggenheim Museum in Bilbao, Spain, has drawn attention to its architectural attributes. Apart from its pleasing silver-gray color, titanium has low coefficients of thermal expansion and heat conductivity. The former, which is half that of stainless steel and one-third that of aluminium, minimizes thermal stresses, whereas the latter provides some opportunity to improve energy efficiency in buildings. Immunity from atmospheric corrosion guarantees long life and minimal maintenance requirements.

Sports The constant desire by golfers to hit balls greater distances has exposed a profitable niche market for titanium alloys. Having a larger head on woods and drivers is considered to be an advantage, and this has been achieved without increasing weight by using hollow designs made by lost wax investment casting of titanium alloys. Another application has been for lightweight racing bicycles and components that are made from α–β alloys Ti–3Al–2.5V and Ti–6Al–4V. Fig. 7.49 shows a titanium bicycle frame manufactured from Ti–3Al–2.5V seamless tubes, which offer excellent fatigue life, property consistency, and corrosion resistance (Ti–6Al–4V seamless tubes are more expensive due to increased manufacturing difficulty). CP titanium tennis and badminton rackets have also found a niche market. In addition, titanium valves, suspension springs, exhaust systems, and drive shafts have long been used in racing and limited production exotic sports cars.

In addition to the applications discussed earlier, titanium and its alloys have found important applications in seawater desalination, salt production, shipbuilding, deep-sea exploration, biofuel production, gas–oil separation, metallurgical engineering, paper manufacturing, food manufacturing, and other industries.

7.8.3 Dental and medical prostheses

As mentioned in Section 7.1, titanium and titanium alloys show excellent biocorrosion resistance in body fluids, which is superior to that of stainless steels. They also have a lower elastic modulus which makes them more compatible with the natural elasticity of bone. These factors, together with their high mechanical properties and acceptable tissue tolerance, have led to their wide use in medical and dental applications. One feature of particular importance is that,



Figure 7.49 A titanium bicycle frame manufactured using α–β Ti–3Al–2.5V seamless tubes.

titanium is one of the few materials which will not induce formation of a fibrous tissue barrier when placed in contact with healthy bone. This is desirable since it permits bone to grow close to the surface of an implant and to fill grooves or pores that may have been deliberately introduced to enable a device to become more firmly embedded. This is a particular advantage for dental prostheses and Fig. 7.50 illustrates a titanium implant embedded into a human jawbone into which an artificial tooth can be screwed. Yet another advantage is the fact that, the fatigue properties of titanium load-bearing devices are not reduced through contact with dilute saline solutions such as body fluids (0.9% NaCl).

One example of titanium in medical applications has been the early Starr–Edwards aortic heart valve in which a Dacron covered titanium cage contains a hollow, electron beam welded titanium ball (Fig. 7.51A). It should be noted that the ball has been designed to have a relative density similar to that of blood and it is preferred to a heavier silicone ball which has proved less satisfactory due to inertial effects. Fig. 7.51B shows a selection of other prostheses including an artificial hip joint, plates, and pins.

As mentioned in Section 7.4.3, a range of vanadium- and aluminium-free low-modulus titanium alloys have been developed to replace the widely used implant alloy Ti–6Al–4V. They show promise as next-generation implant alloys. For example, nickel-free more biocompatible shape memory alloys such as Ti–22Nb–8Ta (at.%) and Ti–30Ta–1Sn (at.%) may capture more applications for orthodontic devices because they are also pseudo-elastic. This property allows stress to remain constant over a wide range of strain, which means that braces on teeth require less frequent adjustment to compensate for the movement of teeth. Other examples include medical splints that can be formed into shapes to meet the unique needs of each individual patient and coiled

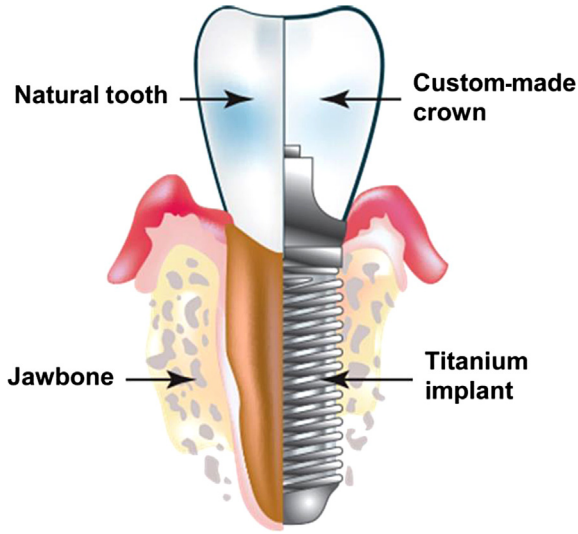
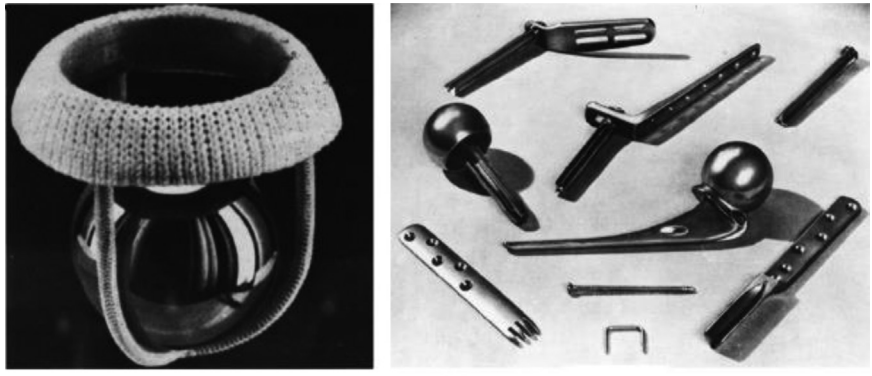


Figure 7.50 Schematic illustration of a titanium dental implant into a human jawbone. Courtesy Busch Dentistry, Seminole, FL, USA.



(A) (B)

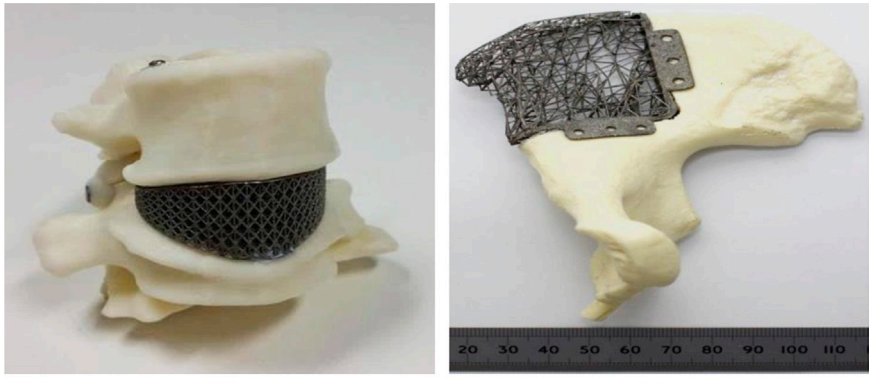
Figure 7.51 Prosthetic devices made from titanium and titanium alloys: (A) Starr–Edwards aortic heart valve. (B) Artificial joint, plate, and pins.

wire stents that are used to dilate narrowed blood vessels. These stents may be cooled, collapsed, inserted by means of a catheter to the desired location, and then allowed to expand by the heat of the bloodstream.

Metal additive manufacturing (Section 8.10) has been increasingly used to make various types of metallic implants as shown in Fig. 7.52. In addition, it has enabled the manufacture of titanium lattice structures with the same modulus of human bones to be repaired or replaced (Fig. 7.53). This has to some



Figure 7.52 ELI Ti–6Al–4V implants additively manufactured using SEBM. Courtesy Huiping Tang, State Key Laboratory of Porous Metal Materials, China.



(A) (B)

Figure 7.53 (A) An ELI Ti–6Al–4V spine implant additively manufactured using SLM. (B) Demonstration of bone repair with a SLM ELI Ti–6Al–4V lattice structure. (A) Courtesy Anatomics Pty Ltd, additively manufactured at RMIT University, Australia and (B) courtesy Milan Brandt, RMIT University, Australia.

extent changed the concept of the low-modulus-centered alloy design approach for the development of biomedical titanium alloys. Porous titanium structures made by conventional PM or dealloying processes can achieve the same but with much less design flexibility.

FURTHER READING

Lim, JY, McMahon, CJ, Pope, DP and Williams, JC: The effect of oxygen on the structure and mechanical behavior of aged Ti–8 wt pct Al, *Metall. Trans. A*, 7(1), 139, 1976.

Collings, EW: *Physical Metallurgy of Titanium Alloys*, ASM, Cleveland, OH, USA, 1984.

Duerig, TW, Allison, JE and Williams, JC: Microstructural influences on fatigue crack propagation in Ti–10V–2Fe–3Al, *Metall. Trans. A*, 16(5), 739, 1985.

Collings, EW: Introduction to titanium alloy design. In Walter, JL Jackson, MR, and Sims, CT, (Eds.): *Alloying*, ASM International, Materials Park, OH, USA, pp 257, 1988.

Welsch, G, Boyer, R and Collings, EW: *Materials Properties Handbook: Titanium Alloys*, ASM International, Materials Park, OH, USA, 1993.

Bania, PJ: Beta titanium alloys and their role in the titanium industry, *JOM*, 46(7), 16, 1994.

Boyer, RR: Aerospace applications of beta titanium alloys, *JOM*, 46(7), 20, 1994.

Titanium Metals Corporation (TIMETAL), Properties and processing of TIMETAL® 6-4, 1998

Donachie, MJ: *Titanium: A Technical Guide*, ASM International, Material Park, OH, USA, 2000.

Mantovani, D: Shape memory alloys: properties and biomedical applications, *JOM*, 52(10), 36, 2000.

RMI Titanium Company (RTI): *Titanium Alloy Guide*, 2000.

Ohmori, Y, Ogo, T, Nakai, K and Kobayashi, S: Effects of ω-phase precipitation on β→ α, α′′ transformations in a metastable β titanium alloy, *Mater. Sci. Eng.*, A312(1), 182, 2001.

Niinomi, M: Recent metallic materials for biomedical applications, *Metall. Mater. Trans. A*, 33, 477, 2002.

Kim, SK and Park, JK: In-situ measurement of continuous cooling β→α transformation behavior of CP-Ti, *Metall. Mater. Trans. A*, 33(4), 1051, 2002.

Saito, T, Furuta, T, Hwang, JH, Kuramoto, S, Nishino, K, Suzuki, N, Chen, R, Yamada, A, Ito, K, Seno, Y and Nonaka, T, et al: Multifunctional alloys obtained via a dislocation-free plastic deformation mechanism, *Science*, 300, 464, 2003.

Leyens, C and Peters, M: *Titanium and Titanium Alloys: Fundamentals and Applications*, Wiley-VCH Verlag GmbH, Weinheim, Germany, 2003.

Froes, FH: *Titanium: Physical Metallurgy, Processing, and Applications*, ASM International, Materials Park, OH, USA, 2015.

Dieter, GE, Kuhn, HA and Semiatin, SL: *Handbook of Workability and Process Design*, ASM International, Material Park, OH, USA, 2003.

Abdel-Hady, M, Hinoshita, K and Morinaga, M: General approach to phase stability and elastic properties of β-type Ti-alloys using electronic parameters, *Scr. Mater.*, 55(5), 477, 2006.

Lütjering, G and Williams, JC: *Titanium*, 2nd ed., Springer, Berlin, Germany,, 2007.

Tahara, M, Kim, HY, Inamura, T, Hosoda, H and Miyazaki, S: Effect of nitrogen addition on superelasticity of Ti–Zr–Nb alloys, *Mater. Trans.*, 50(12), 2726, 2009.

Yan, M, Luo, SD, Schaffer, GB and Qian, M: Impurity (Fe, Cl, and P)-induced grain boundary and secondary phases in commercially pure titanium (CP-Ti), *Metall. Mater. Trans. A*, 44, 3961, 2013.

Cotton, JD, Briggs, RD, Boyer, RR, Tamirisakandala, S, Russo, P, Shchetnikov, N and Fanning, JC: State of the art in beta titanium alloys for airframe applications, *JOM*, 67, 1281, 2015.

Qian, M and Froes, FH: *Titanium Powder Metallurgy: Science, Technology and Applications*, Butterworth-Heinemann, Elsevier, Waltham, MA, USA, 2015.

Froes, FH, Senkov, ON and Qazi, JI: Hydrogen as a temporary alloying element in titanium alloys: thermohydrogen processing, *Int. Mater. Rev.*, 49, 227, 2004.

Kim, HY and Miyazaki, S: Martensitic transformation and superelastic properties of Ti–Nb base alloys, *Mater. Trans.*, 56, 625, 2015.

Choda, T, Oyama, H and Murakami, S: Technologies for process design of titanium alloy forging for aircraft parts, *KOBELCO Technol. Rev.*(No. 33), 44, 2015.

Lai, MJ, Tasan, CC, Zhang, J, Grabowski, B, Huang, LF and Raabe, D: Origin of shear induced β to ω transition in Ti–Nb-based alloys, *Acta Mater.*, 92, 55, 2015.

Zhao, D, Ebel, T, Yan, M and Qian, M: Trace carbon in biomedical beta-titanium alloys: recent progress, *JOM*, 67, 2236, 2015.

Yu, Q, Qi, L, Tsuru, T, Traylor, R, Rugg, D, Morris, JW, Asta, M, Chrzan, DC and Minor, AM: Origin of dramatic oxygen solute strengthening effect in titanium, *Science*, 347, 635, 2015.

Zhang, Y, Fang, ZZ, Sun, P, Zhang, T, Xia, Y, Zhou, C and Huang, Z: Thermodynamic destabilization of Ti–O solid solution by H_2 and de-oxygenation of Ti using Mg, *J. Am. Chem. Soc.*, 138, 6916, 2016.

8

NOVEL MATERIALS AND PROCESSING METHODS

Service demands for improvements in the properties of engineering materials are unceasing and often exceed the capacity of conventionally processed alloys to respond. This situation has stimulated an interest in new compositions produced by a number of novel methods. Because of ease of handling, aluminium alloys, in particular, have often been chosen to model these new processes and the association of these materials with the advanced aerospace industries tends to place them at the forefront of emerging technologies. Accordingly, it is convenient to consider these new developments with reference to their impact on light alloy metallurgy. Many are experimental or at an early stage of commercial development and most involve cost premiums when compared with conventionally produced alloys that may be substantial.

8.1 COMPOSITES

One method of meeting these new demands, which has considerable historical precedent, is the practice of combining different materials to form composites with properties superior to those of the components either individually or additively. Laminates or sandwich panels and, more recently, metals reinforced with fibers or particulates are common examples.

8.1.1 Laminated composites

Three examples of laminated composites based on aluminium will be mentioned. One is a predominantly sheet product comprising a number of alternating layers of aluminium and plies, or prepregs, of fibers that are bonded together with resin to produce laminates that are notable for their resistance to crack propagation, particularly under fatigue conditions. Two products are

Light Alloys. DOI: http://dx.doi.org/10.1016/B978-0-08-099431-4.00008-7
Copyright © 2017 Ian Polmear, David StJohn, Jian-Feng Nie, Ma Qian.
Published by Elsevier Ltd. All rights reserved.

known as ARALL and GLARE and they use aramid and glass fibers, respectively. Both were developed mainly by the Delft University of Technology in conjunction with the Fokker Aircraft Company in the Netherlands. Each is produced using standard bonding procedures and the laminates may be formed, punched, riveted, or bolted like a normal metal. A cross section of a fiber-metal laminate is shown in Fig. 8.1.

One configuration of ARALL had three sheets of aluminium alloy 7075–T6, each 0.3 mm thick, and two 0.2 mm thick internal layers of unidirectional continuous aramid fibers in an epoxy resin prepreg giving a 1.3 mm composite sheet (Fig. 8.2A). In the longitudinal direction, the composite may have a TS as high as 800 MPa and an elongation of 2.5%, which compares with 570 MPa and 11% for monolithic 7075–T6 sheet. The elastic modulus is comparable

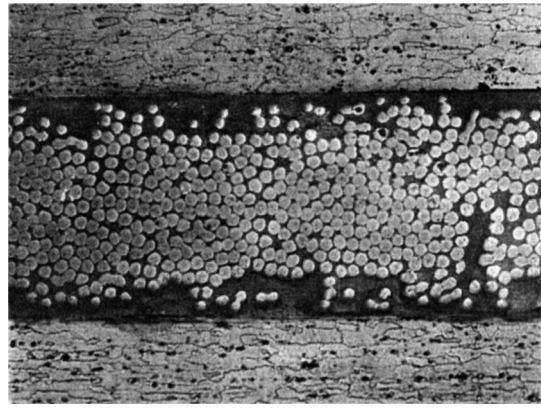


Figure 8.1 A fiber-metal laminate showing a cross section of fibers resin-bonded to thin sheets of aluminium (~× 80). Courtesy Delft University of Technology.

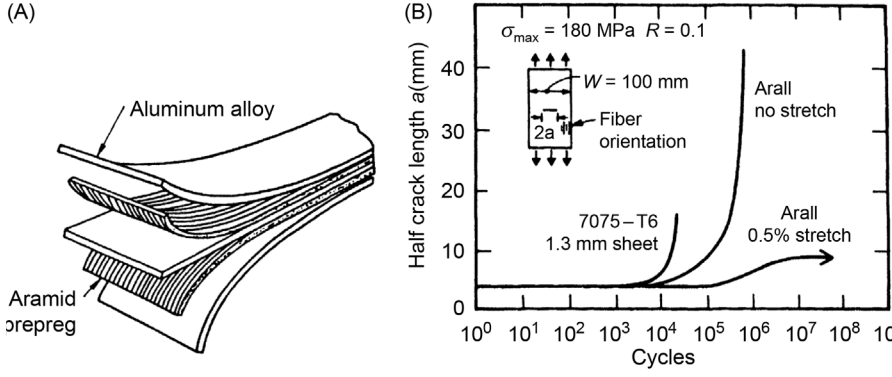


Figure 8.2 (A) ARALL laminate and (B) fatigue crack propagation behavior of ARALL compared with 7075–T6 sheet. Courtesy R. J. Bucci.

to 7075–T6 but the density is reduced to 2.35 g cm^{-3}, which is 18% less. The transverse properties are, however, much lower unless some of the fibers are suitably aligned in this direction.

Comparative rates of fatigue crack growth for precracked panels of this ARALL laminate and 7075–T6 sheet of the same thickness (1.3 mm), tested in the longitudinal direction are shown in Fig. 8.2B. In the unstretched condition (0.2% PS 496 MPa), the laminate panel exhibited fatigue lives some 10 times those of the 7075–T6 sheet due to a combination of factors which place restraint on crack opening in individual metal sheets and crack propagation to other sheets. Moreover, the laminate showed greater damage tolerance since it can accommodate a crack which is nearly three times longer before overload failure occurs. Stretching the laminate by 0.5% raises the 0.2% PS to 640 MPa and effectively prevents the crack propagating beyond a few millimeters after more than 10^7 test cycles.

ARALL was developed primarily for possible applications in aircraft wings. Further fatigue tests revealed that failure of the aramid fibers tended to occur at low test frequencies that simulated cycles associated with the pressurization of the fuselage. This fiber failure was attributed to insufficient bonding between fibers and the epoxy adhesive, as well as to damage that occurred under compressive loads. There was also a tendency for the aramid fibers to absorb moisture. Carbon fibers were considered as a possible replacement but there were concerns that attaching carbon to aluminium may lead to galvanic corrosion. The combination of glass fibers and aluminium did not pose such a problem and attention was directed to the sheet product that became known as GLARE (derived from GLAss-REinforced laminate).

GLARE is comprised of alternating layers of aluminium foils and continuous, unidirectional or biaxially oriented meshes of high-strength glass fibers impregnated with an epoxy resin adhesive. A laminate can be tailored to suit particular requirements by varying factors such as fiber-resin system, alloy type and thickness, stacking sequence, and fiber orientation. The layers are built up in a mold with localized reinforcements being included as required, after which the completed layup is bagged and evacuated before curing at 120°C. Densities range from 2.4 to 2.5 g cm^{-3} and so GLARE is about 10% lighter than conventional aluminium alloys. High static strengths can be achieved, particularly with unidirectional fibers, although elastic moduli are somewhat lower than for monolithic aluminium alloys because of the presence of the glass/epoxy resin layers.

Despite the additional material costs, which may be more than five times that of conventional monolithic aluminium alloy sheet, some 380 m^2 of GLARE is being used for upper fuselage panels in parts of the Airbus A380 aircraft (Fig. 8.3). The motivation for this selection is this composite's outstanding resistance to crack growth although there is also a useful weight saving of some 800 kg. Another minor advantage is a capacity to absorb acoustic vibration which is some three times higher than that for conventional aluminium alloys. Further applications have been investigated such as the use of GLARE for the leading edge of the empennage (vertical tail) to provide protection against bird impact.

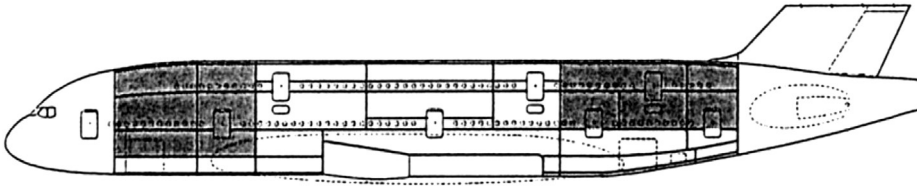


Figure 8.3 Locations of GLARE laminate sheet in the fuselage of the Airbus A380 passenger aircraft. Courtesy Airbus Industries.

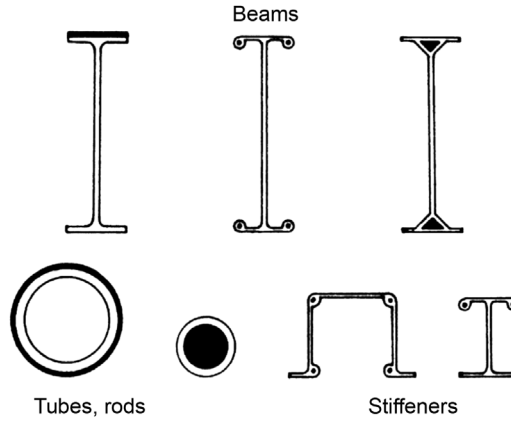


Figure 8.4 Aluminium alloy sections strategically reinforced with high-modulus fibers to increase stiffness. Courtesy Avco Systems Division.

A magnesium-based, laminated composite has been developed by sandwiching rolled foils (0.5–0.6 mm thick) of the alloy AZ31 (Mg–3Al–1Zn) between thin sheets of the polymer polyether ether ketone, that were produced as a prepreg reinforced with about 60 vol.% of continuous 7 μm diameter carbon fibers. Prior to lamination, the metal sheets were etched with chemicals to assist adhesion by roughening the surfaces. Composite panels were then produced by hot pressing. A five-layer panel had a density of 1.7 g cm^{-3} and a thickness of 2.7–2.8 mm. In the longitudinal direction, the tensile strength was 932 MPa, and the elastic modulus 75 GPa.

A second type of laminate is shown in Fig. 8.4. In this case, layers of high-modulus fibers, such as boron, are strategically placed and bonded to various structural sections to improve their stiffness.

8.1.2 Sandwich panels

Sandwich panels form a third type of laminate and they offer a particular combination of high rigidity and low weight. Such panels comprise thin facings which are secured, usually by adhesive bonding, to a relative thick, low-density

core material. From the design viewpoint, a sandwich panel is similar to an *I*-beam with the facings and core corresponding to the flanges and center web, respectively. The facings carry axial compressive and tensile stresses whereas the core sustains shear and prevents buckling of the facings under compressive loading.

Moment of inertia is a direct measure of stiffness or rigidity and it is interesting to compare values for a sandwich panel and a homogeneous isotropic plate of the same material as the facings of the panel. For example, a sandwich panel with two 0.5 mm thick facings of an aluminium alloy and a balsa wood core 6 mm thick would weigh 3.4 kg m^{-2}. A plate of the same alloy of the same size and weight would be 1.25 mm thick. The moment of inertia of the cross section of the plate I_p about its neutral axis, per unit width, is given by:

$$I_p = \frac{t_p^3}{12}$$

where t_p is the thickness of the plate. Neglecting the small effect of the core material, the moment of inertia of the sandwich panel, I_s, per unit width, is given by:

$$I_s = 2t_f\left(\frac{t_f + t_c}{2}\right)^2$$

where t_f is the thickness of the facings and t_c is the thickness of the core. For the sandwich panel and plate under consideration, $I_s = 10.5\,\text{mm}^4$ and $I_p = 0.162\,\text{mm}^4$. Thus the sandwich panel has the advantage of 65 times the rigidity of a solid plate having the same weight. It can also be shown that, for the aluminium alloy plate to have equal rigidity, it would weigh four times more than the sandwich panel.

Sandwich panels with cores of balsa wood or foamed plastic are now used for applications such as siding for refrigerated trucks and for a variety of aircraft components and containers. In this latter regard, even greater weight savings are possible by using a honeycomb core made from impregnated paper or aluminium alloy foil. The honeycomb is usually made by an expansion method (Fig. 8.5) which begins with stacking of sheets of foil on which adhesive stripes have been printed. The adhesive is cured and the block cut into slices which are then expanded to form the honeycomb panel. Honeycomb can be contoured to desired shapes by high-speed cutters and lightweight sandwich panels are used in aircraft for applications such as fuselage and wing panels, one example being leading-edge wing flaps, a section of which is shown in Fig. 8.6.

Sandwich panels have also been prepared using titanium alloy facings and honeycomb core. In this case it is possible to assemble the components by diffusion bonding (Section 7.5.7).

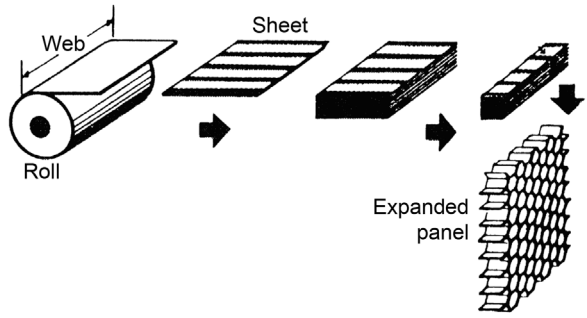


Figure 8.5 Expansion process for the manufacture of aluminium honeycomb cores for sandwich panels. Courtesy Hexel Aerospace.

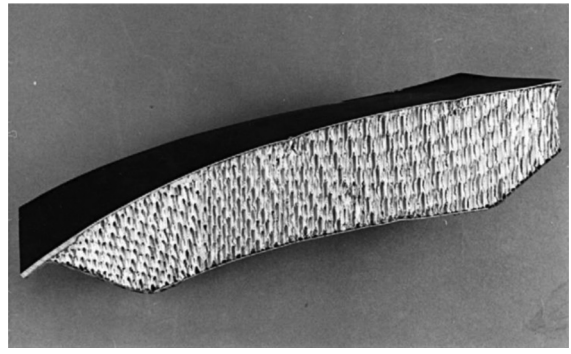


Figure 8.6 Section of honeycomb sandwich panel from an aircraft wing flap.

8.1.3 Metal–matrix composites

Aluminium alloys Fiberglass is the most widely known fiber-reinforced composite material but its use at even moderately elevated temperatures is severely restricted because the polymeric matrix degrades. Another limitation is the relatively low elastic modulus of such a matrix. In this regard, it should be noted that the elastic modulus E_c of a fiber-reinforced composite having continuous, unidirectional fibers is given by the rule of mixtures so that $E_c = E_f V_f + E_M V_M$, where E_f and E_M are the respective elastic moduli of the fibers and matrix in a composite in which the volume fractions of these components are V_f and V_M. Modifications to this relationship are necessary for composites reinforced with discontinuous fibers.

Replacing polymeric matrices with metals would improve both the elevated temperature performance and elastic modulus of fiber-reinforced composites, and many attempts have been made to incorporate strong wires and other fibers in aluminium. Examples are hard-drawn stainless steel wires and silica, silicon carbide, boron, or carbon fibers. One exotic application has been the use of an

aluminium alloy reinforced with continuous carbon fibers for the masts of the Hubble space telescope.

Early attempts to produce metal–matrix composites based on aluminium involved interleaving metal foils with silica fibers, fine stainless steel wires, or coated boron fibers which were then hot compacted slowly in a press. In the latter case, composites have shown unidirectional TS as high as 1200 MPa with elastic moduli as high as steel (220 GPa). They could be used at temperatures up to 320°C and at one time were considered as candidates for compressor blades in gas turbine engines, as well as for certain structural components in aircraft. Good elevated temperature performance and high stiffness have been key goals in research and development, although more recent efforts have been directed more at other properties, such as wear resistance, rather than seeking extreme levels of tensile strength.

Special interest is centered on composites in which short fibers or particulates of a high modulus ceramic are incorporated in a metallic matrix (Fig. 8.7). Such materials can be prepared by compacting powders or by the so-called liquid metallurgy route. In this latter case, a porous ceramic preform may be infiltrated by molten aluminium and suitable alloys, or the fibers or particulates may be stirred into the melt before it solidifies. The integrity of such composites depends critically on the ability of the metal to wet the particulate or fiber surfaces, and after considerable research, significant advances have been made. Usually these composites may be remelted, cast, and fabricated by normal processes such as forging and extrusion. The former Alcan Aluminium Ltd successfully marketed a castable metal–matrix composite under the trade name Duralcan and ingots weighing several tonnes were produced in a plant in Quebec, Canada. Billet prices depended on the size of a commercial order and were quoted in the range US$6.5–9 per kg. Billets for subsequent fabrication to wrought products can also be produced by other means. One method is based

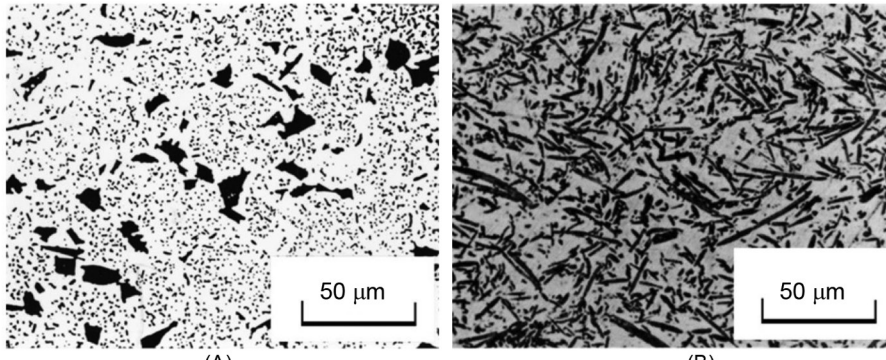


Figure 8.7 Microstructures of metal–matrix composites reinforced with (A) particulates and (B) fibers.

on the Osprey Process (Section 4.6.6) in which ceramic particulates are injected into an atomized stream of molten aluminium in vacuum, or a controlled atmosphere, leading to their co-deposition in solid form on a suitable substrate. Billets weighing several hundred kilograms have been prepared in this way. Other powder metallurgy routes have been pursued in several countries.

Particular attention has been given to composites of aluminium alloys such as 2014 (Al–Cu–Mg–Mn) or 6061 (Al–Mg–Si) with silicon carbide or alumina particles or fibers. These ceramics can be used in various forms: long or short fibers, whiskers, or particles. Reactions at the ceramic/alloy interface are limited so that a coating or diffusion barrier is unnecessary, which also reduces costs. The presence of magnesium as an alloying addition in the matrix improves wetting of the reinforcement. 6061–SiC composites and extrusions containing 20 vol.% SiC as short fibers may have room-temperature tensile strengths as high as 500 MPa combined with an elastic modulus of 120 GPa (cf. 70 GPa for 6061) in the longitudinal direction. However, transverse properties are much lower unless the fibers are randomly orientated. For this composite, values for fracture toughness may be maintained above 30 MPa $m^{1/2}$ until the volume of fibers reaches approximately 15%, after which it falls rapidly to a value of around 10 MPa $m^{1/2}$ at a fiber volume of 25% because of the greater ease of crack propagation (Fig. 8.8). A similar trend has been observed in most other metal–matrix composites. In general, lower values of mechanical properties are obtained when particulates rather than fibers are used but these properties are more isotropic.

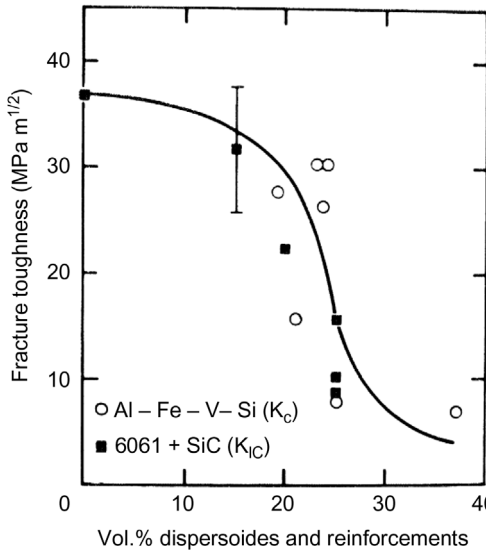


Figure 8.8 Variations in fracture toughness of aluminium alloys with volume % of dispersoids. From Ravichandran, KS and Dwaraksdasa, J: *J. Metals*, 39(5), 28, 1987.

It is also necessary to appreciate that the presence of fibers or particulates may modify the ageing behavior of alloys used for matrices in metal–matrix composites. Such effects arise because of the presence of:

1. higher dislocation densities in the matrix, particularly in the vicinity of the reinforcement, that are generated by thermally induced stresses arising from differences between the coefficients of thermal expansion of matrix and reinforcement. These additional dislocations may modify vacancy contents, facilitate pipe diffusion of solutes, and provide additional sites for the heterogeneous nucleation of precipitating phases;
2. interfaces between matrix and reinforcement which can also serve as sinks for vacancies and facilitate heterogeneous nucleation of precipitates there;
3. chemical reactions between elements in the matrix and reinforcement. Such reactions can result either in the removal of solutes from the surrounding matrix or transfer of solutes to the matrix from the reinforcement.

These modifications to the microstructure of the matrix may, in turn, alter:

1. the level of response to age hardening. As may be expected, the presence of the reinforcement fibers or particles can increase the quench sensitivity of alloy matrices during heat treatment (Section 4.1.5). This effect is demonstrated in Fig. 8.9 in which an experimental metal–matrix composite, Comral 85, achieved higher hardening compared with the matrix alloy 6061 after water quenching, whereas the reverse occurs if materials are air-cooled before ageing at 175°C;
2. ageing kinetics. In most metal–matrix composites, ageing processes at elevated temperatures are accelerated (Fig. 8.9) so that heat treatment schedules need to be changed from those normally used for unreinforced alloys;

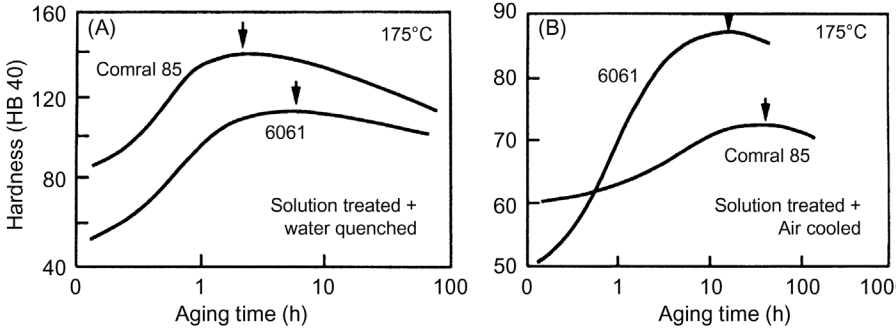


Figure 8.9 Ageing curves at 175°C showing the greater quench sensitivity of the experimental metal–matrix composite Comral 85 (6061 reinforced with 20 vol.% fine mullite/alumina spheres) as compared to the matrix alloy 6061. Courtesy of the former Comalco Aluminium Ltd.

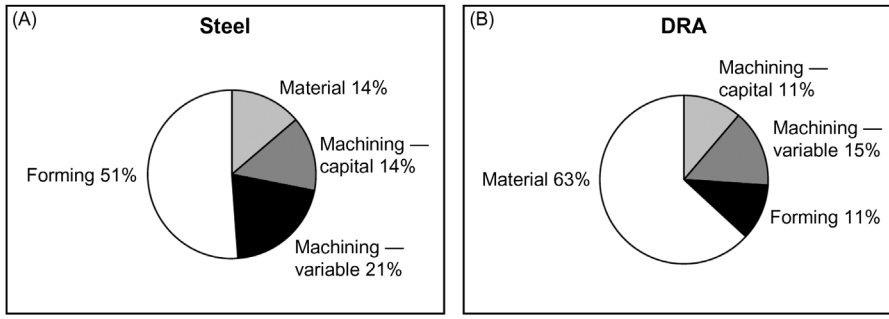


Figure 8.10 Materials and manufacturing costs for a typical automotive component made from (A) steel or (B) DRA. From Allison, JE and Cole, GS: *J. Metals*, 45(1), 19, 1993.

3. ageing processes. As well as accelerating the rate of ageing in matrix alloys, the presence of the reinforcement may also modify the actual mechanism of ageing. GP zone formation tends to be suppressed, presumably because of the loss of quenched-in vacancies, whereas the onset of later stages is accelerated.

Most technological barriers to the introduction of aluminium alloy metal–matrix composites, or the so-called discontinuously reinforced aluminium (DRA), have been overcome and their wider use now depends largely on cost factors. In this regard, Fig. 8.10 compares the earlier total costs (materials plus manufacturing) for a typical automotive component made from steel or DRA. For steel, the material cost is only 14% of the total, whereas this figure is estimated to be as high as 63% for DRA. However, the reverse is true for forming, for which the costs for steel are more than four times that of DRA. Typical properties of some commercially available wrought and cast aluminium alloy metal–matrix composites are compared with some conventional structural alloys in Table 8.1.

Applications for which aluminium alloy metal–matrix composites have been evaluated include high-volume automotive components such as connecting rods, drive shafts, pump housings, brake calipers, and rotors. For connecting rods, the weight saving over steel can be as much as 45% which is critical in reducing undesirable reciprocating forces in the engine. Opportunities for improving wear resistance and elevated temperature properties have been exploited by the Toyota Motor Company which has selectively incorporated short silicon carbide fibers by squeeze casting to reinforce the crown and ring groove of some diesel engine pistons. Examples of products are shown in Fig. 8.11. The high wear resistance of sand and permanent mold cast Duralcan metal–matrix composites reinforced with SiC particles have been utilized for large disk brakes used in rail vehicles operating in Europe. Weight reductions compared with using ferrous alloys can amount to around 200 kg for each axle.

Table 8.1 Typical properties of some commercially available metal–matrix composites and other structural alloys

Alloy	Tensile strength (MPa)	Elastic modulus (GPa)	Specific gravity	Specific modulus
6061	310	69	2.68	25.7
7075–T6(Al–Zn–Mg–Cu)	570	72	2.8	25.7
8090–T6(Al–Cu–Li–Mg)	485	80	2.55	31.4
Common structural steel	500	210	7.8	26.9
Ti–6%Al–4% V	950	106	4.4	24.1
A356–T6(Al–Si–Mg)	280	76	2.67	28.5
6061 + 20% SiC	500	105	2.78	37.5
7075 + 15% SiC	600	95	2.90	31.7
8090 + 17% SiC	540	105	2.65	39.5
A356 + 20% SiC	357	98	2.77	35.4

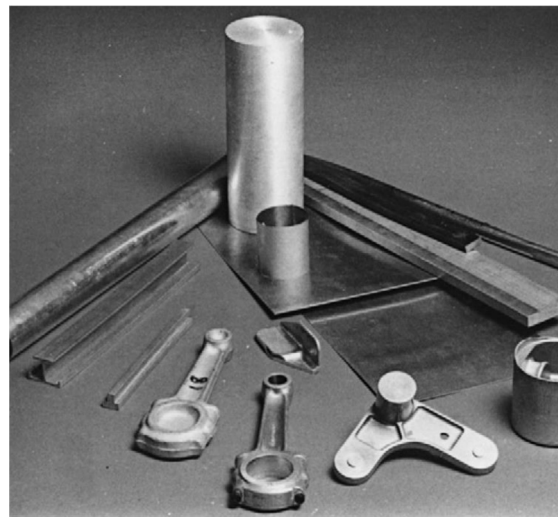


Figure 8.11 Extrusions, forgings, sheet, and a pressure die casting fabricated from DRA. From Willis, TC: *Metals Mater.*, 4, 485, 1988.

The superior thermal conductivity of the aluminium alloy also ensures that thermal stressing of the brake disks never reaches critical levels.

Higher concentrations (20–40 vol.%) of much finer (<1 μm) ceramic particles have been obtained in aluminium and other matrices by a proprietary process known as XD technology which was developed by the former Martin Marietta Corporation in the United States. In this process, powders of the elemental components of high melting point ceramic or intermetallic phases

(X, Y) were heated in the presence of the matrix metal. At some temperature, usually such that the matrix is molten, the component elements X and Y react exothermically forming ultrafine particles of phases such as borides, carbides, nitrides, or mixtures of these compounds (Fig. 8.12). It was claimed that the process is relatively inexpensive and provided the advantage that, after the initial exothermic production step, conventional metallurgical processing (casting, forging, etc.) could be used to produce shapes. As an example, Al–TiB_2 XD-processed alloys have exhibited elastic moduli up to 40% greater than pure aluminium, improved retention of strength at elevated temperatures, as well as useful increases in fatigue and wear resistance. Later research was focused on the production of the so-called designer XD microstructures containing hard phases for strength, relatively soft phases for toughness, and whiskers for creep resistance.

Magnesium alloys Although most studies of metal–matrix composites have been concerned with aluminium alloy matrices, various combinations of magnesium alloys reinforced with ceramic particulates such as SiC, Al_2O_3, and graphite have been investigated. In this regard, magnesium does offer an advantage over aluminium because it has a greater ability to wet most fibers and particulates. Magnesium does not react with graphite or carbides such as SiC or B_4C and Table 8.2 shows the improvements in the properties of extrusions of the medium strength alloy AZ31 (Mg–3Al–1Zn) by incorporating SiC fibers. What is notable is the effective doubling of proof stress and elastic modulus

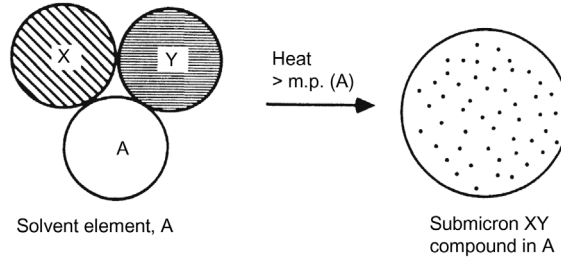


Figure 8.12 Schematic diagram of process for making XD™ dispersion-hardened composite materials. From Westwood, ARC: *Metall. Trans. B*, 19B, 155, 1988.

Table 8.2 Effect of SiC fiber reinforcement of the extruded magnesium alloy AZ31

Alloy	0.2%PS (MPa)	TS (MPa)	Elongation (%)	Elastic modulus (GPa)
AZ31	221	290	15	45
AZ31 + 10% SiC	314	368	1.6	69
AZ31 + 20% SiC	417	447	0.9	100

Courtesy W. Unsworth and J. F. King.

when 20% SiC is added although, as usual, these changes occur at the expense of ductility. As with composites based on aluminium, the presence of the ceramic reinforcement has the added benefit of reducing thermal expansion of the magnesium alloy matrix.

Magnesium does react with oxides such as Al_2O_3 to form the spinel $MgAl_2O_4$ and, if this relatively cheap reinforcement is to be used, it is necessary to process the composite so that liquid metal contact is minimized or avoided. Techniques that have been tried are rapid squeeze casting, spray casting, and hot compaction of mixtures of powders.

Results have been obtained from squeeze castings of the alloy AZ91 (Mg–9Al–1Zn) containing a range of different fibers such as glass, carbon, and Saffil, which is a proprietary preform or woven mat of 14 μm diameter Al_2O_3 fibers. Creep and fatigue test data obtained from a 16 vol.% Saffil-reinforced alloy was compared with standard AZ91 tested under the same conditions. The composite material was found to have a creep life at 180°C which was an order of magnitude better than AZ91 and the fatigue endurance limit at this temperature was double that recorded for this alloy (Fig. 8.13). The presence of fibers does, however, reduce the fracture toughness to a level of 10 MPa $m^{1/2}$ or less as has been observed for fiber-reinforced aluminium alloys (Fig. 8.8).

The prospect of developing ultralight composites based on a matrix of Mg–Li alloys has also been investigated. However, it has been found that severe degradation of the reinforcement occurs during processing due to the reaction of lithium with all but SiC whiskers. Moreover, mechanical properties have been found to be unstable at quite low temperatures as a consequence of the abnormally high

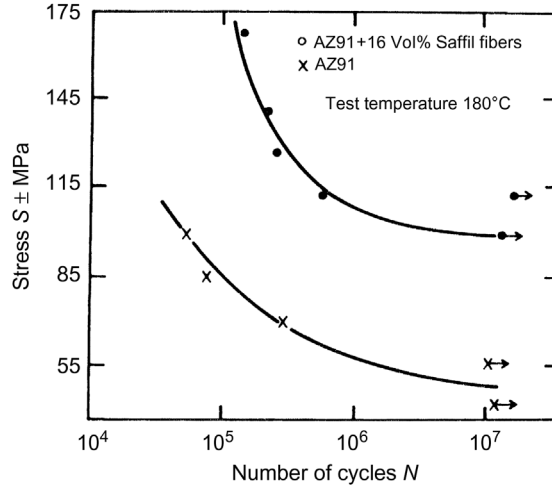


Figure 8.13 High temperature *S/N* fatigue curves for the cast alloy AZ91 and squeeze cast AZ91 containing 16 vol.% of Saffil (Al_2O_3) fibers. From Chadwick, GA: *Magnesium Technology*, Institute of Metals, London, 1986.

mobility of lithium atoms and vacancies in the alloy matrices. This has the effect of relaxing the desirable localized stress gradients that normally develop close to the ends of fibers, even at comparatively high strain rates.

Magnesium composites have found some specialized applications in aerospace engineering, examples being trusses, booms, and other structural members for space platforms and satellites. Elsewhere these composites are largely at an experimental stage and they are also being evaluated for possible use in various automotive components.

Titanium alloys Titanium alloy metal–matrix composites have been considered for certain sophisticated aerospace and defense applications that must withstand severe thermomechanical environments. One example is leading-edge aerofoil structures for proposed hypersonic flight vehicles which may require materials that will maintain adequate stiffness and strength at temperatures of 1100°C and above.

The composites may be prepared by blending and compacting powders in the conventional way. However, special attention has been given to the incorporation of continuous plies or tapes of relatively coarse (e.g., 140 μm) silicon carbide fibers in matrices such as the β-alloy Ti–15V–3Cr–3Al–3Sn (Ti 15–3). Major problems have been control of interfacial reactions between fibers and matrix and thermal fatigue cracking arising because of their different coefficients of thermal expansion. Vapor deposition of the alloy has been employed as a means of precoating the fibers and sections have then been prepared by hot pressing between alloy foils. Such a material system is costly but has the potential to operate at temperatures up to 650°C.

For many years it was known that the addition of boron to titanium and titanium alloys increased strength, stiffness, and microstructural stability due to the formation of TiB particles or whiskers. The most economical way of producing such alloys is by blending, compacting, and sintering powders. In this case, in situ chemical reactions occur during processing which are similar to those described earlier for the XD technology. A commercial application has been the manufacture of two types of titanium alloy composite valves for the engine of a mass-produced Toyota motor car that was mentioned in Section 7.8.2. These composites contain 5% by volume of TiB particles and more than 500,000 valves were manufactured for this purpose which performed well in service. They were, however, double the cost of steel valves. Composites with higher contents of TiB particles, or with mixtures of TiB and TiC particles, show exceptional wear resistance. Such materials can be prepared by using powder blends made from titanium alloys that contain carbon.

8.2 METALLIC FOAMS

Foamed metals and alloys are a novel class of materials that may have extremely low densities combined with high specific stiffness, reduced thermal conductivity, and a high capacity to absorb impact energy and noise. They have

features in common with the natural cellular materials wood and bone. Overall properties depend on the particular metal or alloy and the cell topology, i.e., the size and shape of the pores and whether they are open or closed (Fig. 8.14). Again, much of the developmental work has been carried out on aluminium and

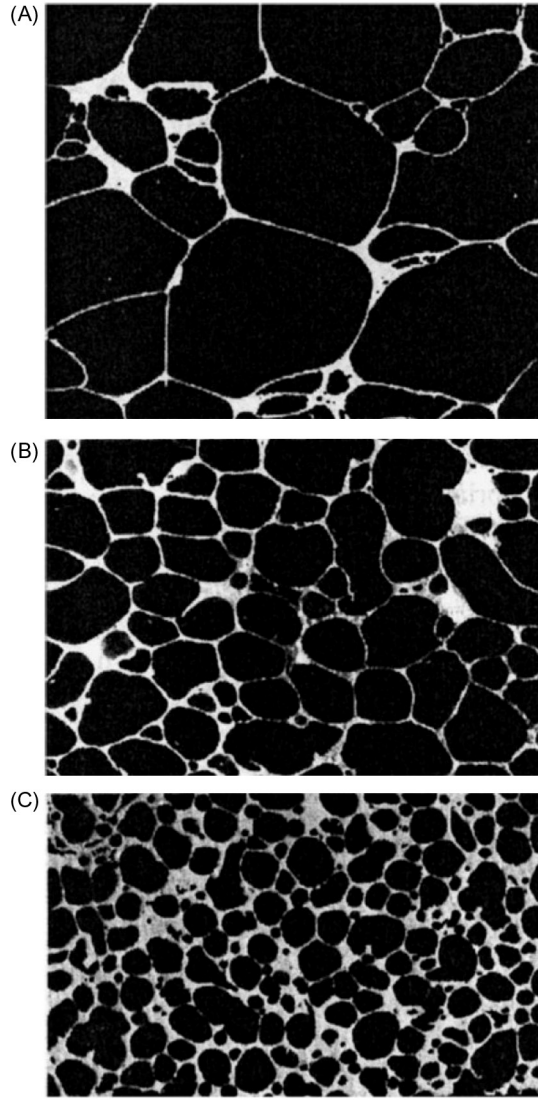


Figure 8.14 Cross sections of aluminium alloy foams. (A) Cymat (Canada) foam formed by gas injection into the melt. Relative density 0.04 ($108\,kg\,m^{-3}$). (B) Alporas (Japan) foam formed from the melt using a TiH_2 blowing agent. Relative density 0.09 ($240\,kg\,m^{-3}$). (C) Alulight (Austria) foam produced from a powder compact. Relative density 0.25 ($435\,kg\,m^{-3}$). Courtesy M. F. Ashby.

its alloys for which foam densities relative to the solid state commonly range from 0.1 to 0.5, although values as low as 0.04 (i.e., $108\,kg\,m^{-3}$) have been recorded. Some foams have also been produced using magnesium or titanium, and a density as low as $50\,kg\,m^{-3}$ has been achieved with the magnesium alloy AZ91 (Mg–9Al–1Zn).

Foams can usually be made from either molten metals or powders, and costs in the case of aluminium have ranged from less than US$10 to several thousand dollars per kg. Stable foams cannot be formed in pure liquid metals simply by blowing in a gas because the bubbles are too buoyant and rise quickly to the surface. It is necessary therefore to increase the viscosity of the melt by stirring in 10–30% of fine particles such as alumina. Alternatively, small amounts (e.g., 1.5%) of calcium may be added to promote the formation of particles of CaO, $CaAl_2O_4$, and Al_4Ca that have been shown to increase melt viscosity by as much as five times. Foaming can then be achieved in three ways: by injecting a gas (air, nitrogen, or argon) into the melt, by causing in situ gas formation through the introduction of a gas releasing agent such as 1–2% TiH_2, or by precipitating a gas that had previously been dissolved in the melt under pressure. It is then possible to solidify the melt while the bubbles remain in suspension. The alternative metal powder route is generally more expensive but offers greater opportunities for near-net shape forming. This method involves mixing the powdered alloy with a gas blowing agent for which TiH_2 is again commonly used. The powder mixture is first compacted and then heated to a mushy condition to release the hydrogen.

Design rules are being developed to facilitate the use of foams in engineering structures. For example, Ashby and colleagues at Cambridge University have shown that strength and elastic modulus are functions of relative density and can be described by:

$$\text{(i)}\quad \frac{\sigma_{pl}}{\sigma_{ys}} = C_1\left(\frac{\rho_f}{\rho_s}\right)^{3/2} \qquad \text{(ii)}\quad \frac{E_f}{E_s} = C_2\left(\frac{\rho_f}{\rho_s}\right)^{2}$$

where σ_{pl} is the plastic collapse of a foam block under compressive load, σ_{ys} is the uniaxial yield strength of foam struts, ρ_f and ρ_s are the densities of the foam block and the solid metal or alloy from which the foam was made, E_f and E_s are the respective elastic moduli, and C_1 and C_2 are constants of about 0.3 and 0.1, respectively. Relationships have also been established for other properties such as toughness.

Some metallic foams are potentially inexpensive, particularly when cost is measured in volumetric terms and commercial products have been produced. One example is for the core of sandwich panels described in the previous section and Karmann GmbH in Germany produced a design for a small, low-weight automobile in which 20% of the structure could be made from foam panels with an estimated weight saving of 60 kg. Foams may be attached to

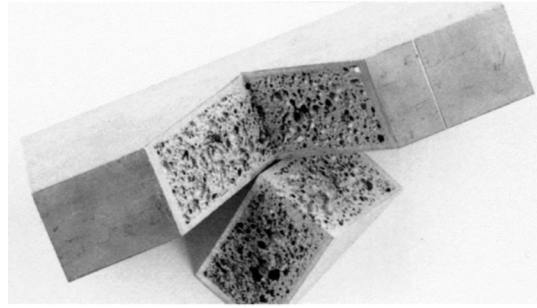


Figure 8.15 Cross-section of an extruded aluminium alloy tube filled aluminium alloy foam. Courtesy of Cymat Corporation.

steel and concrete structures and, in Japan, they have been used experimentally as baffles on the underside of a highway bridge to absorb traffic noise. Other examples of recent applications are structural panels in aircraft and trains, and firewalls, in a range of integrally molded components.

A foam core may be encased by a solid cast skin if spacers are used to position the core within a suitable mold. The molten alloy is then introduced into the mold so that it solidifies around the core creating a mechanical bond with the rough foam surface. Either low-pressure die casting or gravity casting must be used to avoid damage to the relatively fragile core. If metallurgical bonding is required, the foam surface must first be coated with a suitable flux which dissolves the oxide film during casting. Structural members can also be produced by filling extruded aluminium tubes and sections with molten foam as shown in Fig. 8.15. Continuous foam-filled aluminium alloy panels 1.5 m wide and 20–150 mm thick have been produced at a rate of 900 kg per hour by bubbling air through a melt and casting the foam between sheets produced on a belt caster (Fig. 4.5). In the event of a crash, automotive components with foam cores, such as bumper bars, are capable of absorbing large amounts of mechanical force because the energy of impact can be converted into plastic deformation with relative ease. This improves crash resistance and can also help control the deceleration of a vehicle.

Much less attention has been given to the production of magnesium foams. Some success has been achieved using a high-pressure die casting machine if the molten metal is first injected through a separate chamber containing the chemical blowing agent MgH_2 before it enters the die. Hydrogen released in the mold causes a porous structure to form in the center of the cast part whereas a solid skin forms at the walls due to the fast solidification rate.

8.3 RAPID SOLIDIFICATION PROCESSING

During the last three decades, considerable attention has been given to the technique of rapid solidification processing (RSP) as a means of producing entirely

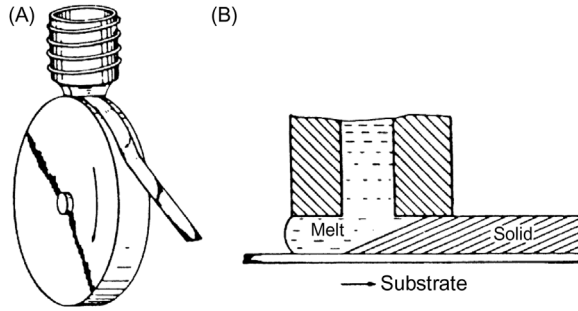


Figure 8.16 RSP by melt spinning: (A) metal is induction melted in a crucible and forced on to a rotating wheel producing RSP ribbon and (B) stable solidification conditions for planar flow casting.

new ranges of alloys having mechanical and corrosion properties superior to those obtainable by conventional ingot metallurgy practices. RSP involves cooling at extreme rates from the melt to produce a powder or splat particulate. Powders are most conveniently prepared by some form of gas atomization in which the molten alloy is sprayed through a nozzle into a stream of a high velocity gas such as nitrogen or argon. Fine particles are formed which are roughly spherical and most have diameters in the range 10–50 μm. Cooling rates are faster the smaller the particles and may be as high as 10^5 °C s^{-1}. The method of splat quenching that appears to have the best practical potential is the so-called melt spinning in which the molten alloy is forced through an orifice on to an internally water cooled, rotating wheel made from a metal such as copper which has a high thermal conductivity. Essential details are shown in Fig. 8.16A and the stable solidification condition that is established has been termed planar flow casting (Fig. 8.16B). Thin (e.g., 20 μm) ribbons are produced at cooling rates of 10^6 °C s^{-1} or higher, which are then pulverized into flakes for subsequent consolidation. The powders or pulverized ribbons are processed by canning, degassing, and hot pressing to produce solid billet for subsequent forming by forging or extrusion. The major obstacle is oxide contamination which may prevent interparticle bonding during processing with consequent deleterious effects on mechanical properties.

Conventional gas atomization of liquid metals is well known, having been used since the 1930s to produce a wide variety of metallic powders for diverse applications. For example, each launching of the former US Space Shuttle consumed 160,000 kg of atomized aluminium powder as part of the solid fuel propellant mixture. Scaling up of other techniques of RSP has occurred in several countries and pilot facilities for continuous melt spinning were developed with capacities for making 50–500 kg of pulverized ribbons. Consolidated billets up to 550 mm diameter, weighing 270 kg, have been processed.

8.3.1 Aluminium alloys

With the extreme rates of cooling, it is possible to extend the solid solubility of elements in aluminium which is particularly useful because, as shown in Table 2.1, relatively few elements have an equilibrium solid solubility exceeding 1 at.%. Moreover, these latter elements, such as magnesium, zinc, and copper, all have high diffusivities in aluminium and result in alloys that have relatively poor thermal stability. Table 8.3 gives examples of the diffusivities of some metals together with the increases in solid solubility that can be achieved by RSP. What is particularly significant are the large amounts of the sparingly soluble elements such as iron and chromium that can be retained in supersaturated solid solutions since each has a very low diffusivity in aluminium. Special interest has been centered on alloys containing one or more of these elements as they have the potential to compete with titanium alloys up to temperatures of 300°C or higher. This compares with a maximum of only around 125°C for most age-hardenable aluminium alloys prepared by ingot metallurgy.

RSP also has several desirable effects on microstructure. A fine, stable grain size can be achieved (e.g., 1 μm or less) which can be retained during subsequent processing due to the presence of second-phase particles in the grain boundaries. Small metastable precipitates may also form within the grains during cooling or processing of the powders or splat particulates. Moreover, if these phases contain elements such as iron (e.g., Al_6Fe and Al_3Fe), they have high thermal stability and are resistant to coarsening (Ostwald ripening) at relatively high temperatures. Finally, the scale of the microstructure is so fine that the alloys are chemically very homogeneous.

The microstructures of aluminium alloys obtained by RSP can be better understood by referring to Fig. 8.17 in which diagram (A) gives a schematic representation of the respective volume fractions of what are called microcellular (or microeutectic), combined cellular and eutectic, and primary intermetallic

Table 8.3 Increased solid solubility in some binary aluminium alloys due to RSP

Solute	Maximum equilibrium solubility		Reported extended solubility		Diffusion coefficient at 425°C
	(wt%)	(at.%)	(wt%)	(at.%)	D_o ($m^2 s^{-1}$)
Cr	0.72	0.44	8–10	5–6	7.7×10^{-21}
Cu	5.65	2.40	40–42	17–18	4.3×10^{-15}
Fe	0.05	0.025	8–12	4–6	2.2×10^{-1}
Mg	17.4	18.5	34–38	36–40	1.5×10^{-14}
Mn	1.82	0.90	12–18	6–9	2.3×10^{-18}
Ni	0.04	0.023	2.4–15.4	1.2–7.7	5.2×10^{-15}

Courtesy H. Jones.

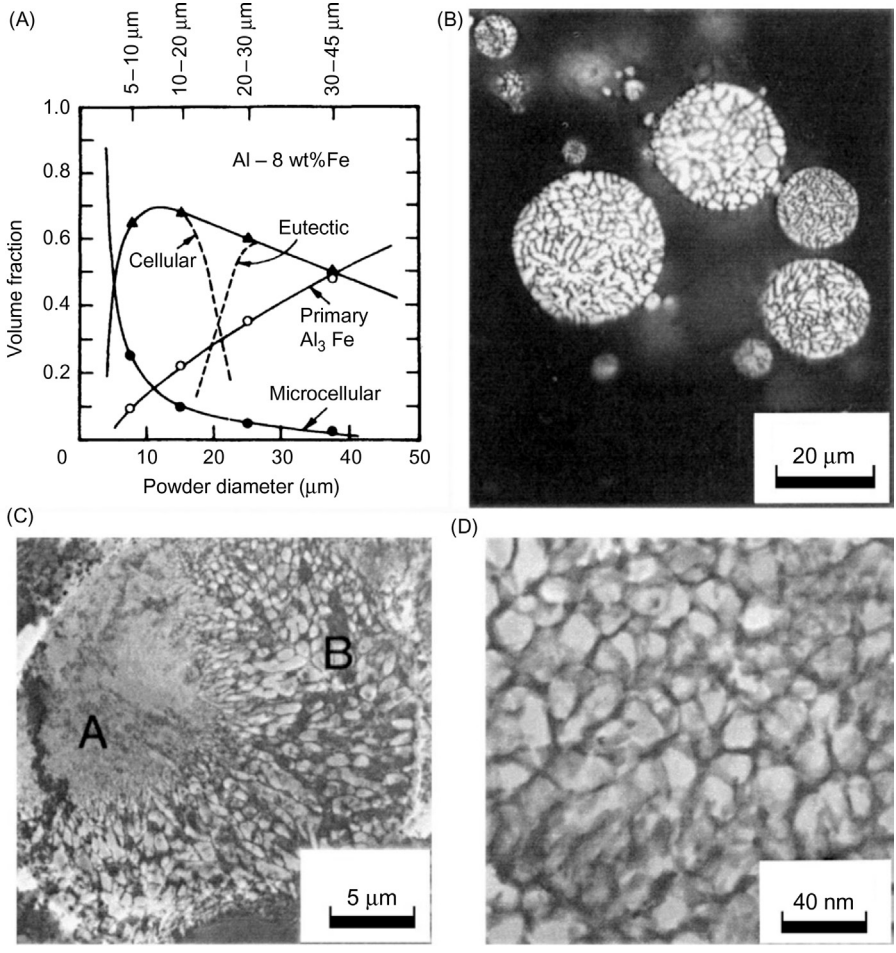


Figure 8.17 (A) Volume fractions of microcellular, combined cellular and eutectic, and primary intermetallic structures as a function of powder diameter in RSP Al–8Fe powders. Possible separate curves for the cellular and eutectic structures are shown dotted. (B) Sections through gas-atomized aluminium alloy powders showing a combined cellular and eutectic (zone B) microstructure having an average grain size of 1 μm. (C) Section of an Al–8Fe powder particle showing the zone B structure and an unresolved zone A region. (D) Zone a microcellular region of an RSP Al–Fe alloy showing an average cell or grain size of 0.02 μm. (A) Courtesy US National Institute of Standards and Technology, formerly National Bureau of Standards. C Courtesy US National Institute of Standards and Technology. (D) Courtesy C. M. Adam.

structures, as a function of powder diameter (i.e., cooling rate) in an RSP Al–8Fe alloy. As expected, the greater the powder diameter (i.e., the slower the cooling rate), the coarser the microstructure becomes. Fig. 8.17B shows a section through some atomized powders which all have cellular (or the so-called "zone B") structures with a grain size of around 1 μm. Another view of this cellular structure is shown at B in Fig. 8.17C which is a transmission electron micrograph containing a central region in which the microstructure has not been resolved ("zone A"). This is the site at which nucleation of the solid powder has occurred and where cooling rate has been highest. This so-called zone A region has the microcellular or microeutectic structure and much higher magnifications are needed to resolve the cells or grains that are revealed as having an exceedingly small average diameter of as little as 20 nm (0.02 μm) (Fig. 8.17D).

Relatively little is known about the zone a microstructures except to say that they may contain metastable phases such as the so-called O-phase that has been identified in some melt spun alloys based on the Al–Fe system cooled at rates of around 10^7 °C s^{-1}. This phase has an icosahedral crystal structure and it decomposes during subsequent thermomechanical processing to produce substantial alloy strengthening.

Comparative studies show the zone A structure to be much harder than zone B. Microstructures of alloys based on the Al–Fe system can contain only large amounts of the zone A structure if they are prepared by a process such as melt spinning rather than gas atomization. In one such case for the alloy Al–12Fe–2V, an elastic modulus at room temperature of 96.5 GPa has been recorded which is some 40% higher than that for conventional aluminium alloys. Moreover, the relatively high values are retained at elevated temperatures (e.g., 78 GPa at 316°C). Tensile strength values for the same alloy can exceed 600 and 350 MPa, respectively, at these two temperatures.

Most of the RSP aluminium alloys that have been studied are based on the Al–Fe system. Examples are Al–8Fe–4Ce (Alcoa), Al–8Fe–2Mo (Pratt & Whitney), and Al–8.5Fe–1.3V–1.7Si (former Allied Signal). The main role of the other elements seems to be to alter the kinetics of precipitation that normally occurs in the binary Al–Fe system. The powders or pulverized ribbons are consolidated and fabricated in the manner as described earlier. Fig. 8.18 gives an example of the elevated temperature properties of several related alloys prepared by RSP in terms of their tensile strength and compares them with the ingot alloys 7075–T6 and 2219–T851. The specific strength needed to equal the widely used titanium alloy Ti–6Al–4V is shown as a dashed line.

RSP powder compacts produced by melt spinning cost some US$100 per kg when they were first produced. These costs have been reduced but apparently remain well above an estimate of US$15 per kg which was predicted using facilities for large-scale production. Early developments were concentrated on aerospace components such as blading and vanes for compressor sections of gas turbines, and forged aircraft landing wheels. In this latter case, it was thought that the potential of the RSP alloys to withstand higher temperatures

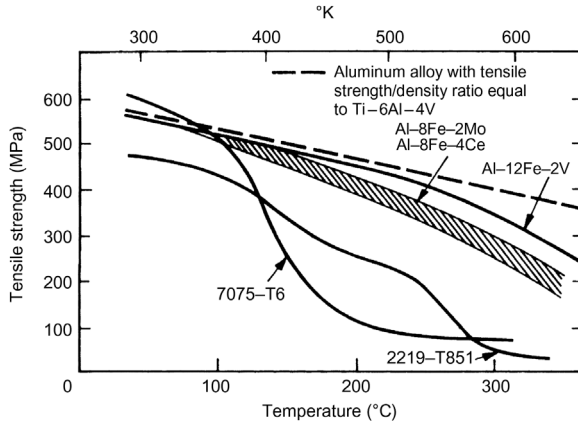


Figure 8.18 Elevated temperature properties of RSP alloys compared with ingot alloys 7075 and 2219. The specific strength needed to equal the titanium alloy Ti–6Al–4V is shown as a dotted line. From Adam, CM and Lewis, RE: *Rapidly Solidified Crystalline Alloys*, Das, SK *et al.* (Eds.), AIME, Warrendale, PA, USA, 157, 1985.

could allow the use of brakes which generate higher frictional forces. However, commercial interest in these RSP alloys has declined because of two major problems. One is their low levels of fracture toughness and the second is that they show progressive decreases in ductility when stressed at slow strain rates at elevated temperatures (e.g., 250°C). These effects are greatest in alloys with fine microstructures and may arise from enhanced diffusion of solute atoms along grain and subgrain boundaries.

The fact that RSP extends the solid solubility of alloying elements in aluminium has also led to a study of experimental compositions containing excess amounts of normally soluble metals such as zinc and magnesium. For example, TS exceeding 800 MPa with elongations of around 4% have been achieved after consolidating atomized powders made from an alloy Al–10Zn–3Mg–2Cu–1.7Mn–0.2Cr. This compares with typical values of 570 MPa and 11%, respectively, for the alloy 7075–T6 (Al–5.6Zn–2.5Mg–1.6Cu–0.2Cr) prepared from ingots. It should be noted, however, that the experimental RSP alloys may have the disadvantage of being more quench sensitive if heat treatment is required (Section 4.1.5). This follows because, during quenching, loss of vacancies and enhanced heterogeneous nucleation of precipitates may occur at the very many sites provided by the finely dispersed compounds and much greater number of grain boundaries in these materials.

Experimental RSP alloys have been produced that are based on the aluminium–lithium system. These alloys incorporated higher lithium contents than ingot alloys and offered further potential for reducing density and increasing stiffness (Section 4.4.6). One example was the composition Al–3.5Li–1Cu–0.5Mg–0.5Zr for which data has been provided by the former Allied-Signal Inc.

in the United States. This alloy had a density of 2.47 g cm^{-3} and an elastic modulus of 80.6 GPa. Typical mechanical properties of extrusions given a T6 heat treatment are as follows:

0.2% Proof stress	455 MPa
Tensile strength	595 MPa
Elongation	8.8%
Fracture toughness	25 MPa m$^{1/2}$

Corrosion rates, measured as weight loss over a period of 70 days in a salt fog test, were only some 15% of that recorded for both the conventional aircraft aluminium alloy 2014–T6 and the powder metallurgy alloys 7090 and 7091. In addition, the rate of growth of fatigue cracks in the RSP alloy was significantly less (Fig. 8.19). However, no significant applications seem to have been reported.

8.3.2 Magnesium alloys

Billets of a number of experimental magnesium alloys have also been produced by RSP as thin ribbons which are then mechanically comminuted into powder, sealed in cans, and extruded to form bars in the manner described earlier. One commercial alloy has been available which is known as EA55RS (Mg–5Al–5Zn–5Nd) and may develop tensile strengths exceeding 500 MPa.

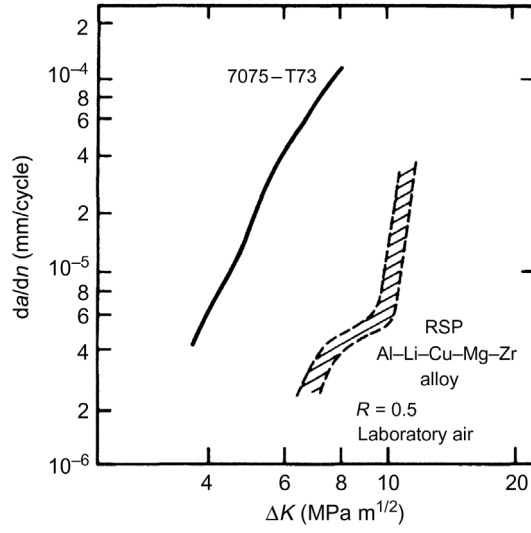


Figure 8.19 Fatigue crack growth rates for the extruded RSP alloy Al–3.5Li–1Cu–0.5Mg–0.5Zr aged to the T6 condition compared with extruded 7075–T73. Courtesy former Allied-Signal Inc.

Some compositions have shown enhanced creep resistance but others in fact undergo accelerated deformation due to enhanced grain boundary sliding in the fine-grained microstructures. However, this behavior can make some RSP magnesium alloys amenable to superplastic forming at temperatures as low as 150°C. Even higher tensile strengths combined with a ductility of 5% have been achieved with small (6 mm diameter) extruded rods prepared from helium gas-atomized (GA) powders of the alloy $Mg_{97}Zn_1Y_2$. The α-magnesium phase of these rods has fine grain sizes of 50–250 nm and is hardened by intermetallic particles of long-period stacking ordered structures (Section 6.3.3).

As with other RSP alloys, the corrosion resistance of magnesium alloys can be notably improved because microstructures are more homogeneous with respect to particulates that can serve as cathodic centers (Section 6.6). Moreover, the extended solubility of various elements may shift the electrode potentials of the alloys to more noble values. Corrosion rates of RSP magnesium alloys compared with conventionally produced compositions are shown in Fig. 8.20.

8.3.3 Titanium alloys

RSP has been successfully applied to a number of titanium alloy systems using techniques similar to those described for aluminium and magnesium alloys. Solubility limits can be extended and microstructures refined. However, the fact that relatively high temperatures are required to consolidate powders or melt spun ribbons presents difficulties because the ultrafine, rapidly solidified structures tend to coarsen leading to reduced mechanical properties.

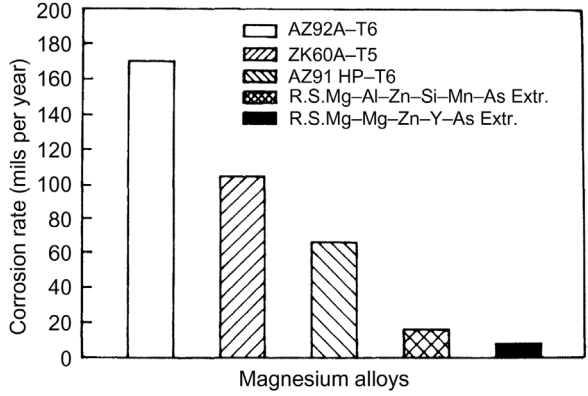


Figure 8.20 Corrosion rates of rapidly solidified magnesium alloys tested in 3% NaCl at 21°C, as compared with some commercial alloys. From Das, SK and Chang, CF: *Rapidly Solidified Alloys*, Das, SK Kear, BH, and Adam, CM (Eds.), AIME, Warrendale, PA, USA, 137, 1985.

The microstructures of rapidly quenched titanium alloys can be significantly more complicated than for aluminium or magnesium alloys because of the β/α allotropic transformation and the occurrence of martensitic and other phase transformations. Special attention has been given to using RSP as a means to improve elevated temperature performance in the following ways:

1. Whereas dispersion-hardened alloys generally display good strength and creep resistance at elevated temperatures, attempts to exploit such microstructures with titanium alloys have generally been hampered by insufficient supersaturation of alloying elements in the as-quenched condition and by rapid coarsening of precipitates. Stable oxides may be formed if rare earth elements are added to titanium and its alloys because they scavenge dissolved oxygen. However, these elements are normally ineffective because of their low solubilities under equilibrium conditions. RSP extends these solubilities and an extensive study has been made of erbium additions for which supersaturations of up to 1 at.% have been achieved. Uniform dispersions of Er_2O_3 particles in the size range 5–25 nm have been obtained by ageing at comparatively high temperatures (e.g., 700°C). Dysprosium, gadolinium, lathanium, and yttrium also form stable oxides and, in α-titanium alloys, all are reported to be resistant to coarsening at 800°C. Coarsening is significant, however, in β-phase alloys apparently due to increased diffusivity.
2. Metalloid phases have also been formed in RSP alloys to improve creep strength. Volume fractions of the precipitate Ti_5Si_3, which is present in some creep-resistant near-α alloys (Section 7.2.3), may be significantly increased. Experimental Ti–B alloys have also been produced containing as much as 10 at.% boron which have the additional advantage of reduced density. Boron additions have also been made to alloys such as Ti–6Al–4V produced by RSP.
3. In Chapter 7, brief reference was made to alloying elements such as iron, chromium, and nickel that form eutectoid systems with titanium. Such reactions are not exploited in conventionally produced alloys because they are sluggish and the microstructures are normally heavily segregated. RSP minimizes segregation and some experimental alloys such as Ti–6Al–3Ni show relatively high tensile strengths at room temperature (e.g., 1000 MPa). However, because most eutectoid reactions occur below 900°C, any potential applications of these alloys will be confined to intermediate temperatures or lower.
4. Titanium combines with aluminium to form several titanium-aluminide intermetallic compounds. These are considered later in Section 8.9 in which reference is made to experimental studies involving RSP techniques.

8.4 QUASICRYSTALS

Solids have generally been classified as being either crystals or glasses. The essential feature of crystals is that they contain a periodic arrangement of

identical unit cells, the centers of which are always equidistant from each other. One consequence of such periodicity is the fact that it is only possible to have two-, three-, four-, and six-fold rotational symmetry. In 1984, Schechman in Israel reported that a metallic solid $Al_{86}Mn_{14}$ exhibited five-fold rotational symmetry that is forbidden with normal crystals, and his work won a Nobel Prize in 2011. Whereas a crystal is said to have periodic translational order, a quasicrystal has quasiperiodic translational order. Such an arrangement allows the spacing between unit cells to be different.

Quasicrystals have since been found in a number of aluminium alloys and Fig. 8.21 shows a single grain formed in an Al–Cu–Fe alloy that was arc melted and annealed for 48 h at 840°C. Such quasicrystals commonly have pentagonal facets because growth is favored along planes of atoms having five-fold rotational symmetry. They have also been found to have the symmetry of a tetrahedron, cube, or prism. Since the transformation of a liquid to a quasicrystal has been shown to proceed by nucleation and growth, the undercooling that occurs during rapid solidification often leads to ultrafine grain sizes.

A series of experimental aluminium alloys with a range of interesting mechanical properties have been developed from extruded compacts of atomized powders in which nanoscale quasicrystalline particles (30–50 nm) solidify first from the melt as the primary phase surrounded by thin films of an α-aluminium matrix. These quasicrystals are present in volume fractions of 60–70%. The alloys contain a range of transition metals and may be divided into three types which are summarized in Table 8.4.

Quasicrystals have also been observed in as-cast magnesium alloys containing rare earth elements and in some rapidly solidified compounds, such as $Mg_{32}(Al,Zn)_{49}$ and Mg_4CuAl_6, that can form as precipitates in aluminium alloys. An as-cast and hot-rolled Mg–Zn–Y alloy with the composition $Mg_{95}Zn_{4.3}Y_{0.7}$ has been found to have a microstructure consisting of an α-Mg matrix hardened

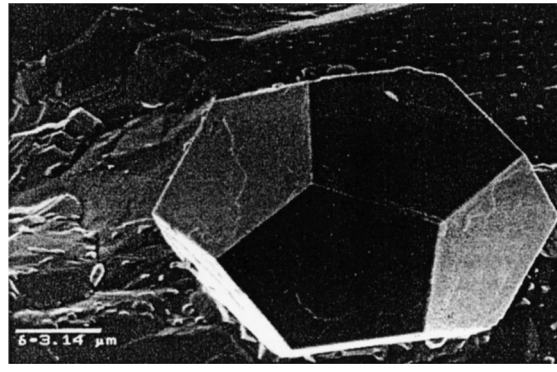


Figure 8.21 Scanning electron microscope image of an icosahedral single-grain quasicrystal of the aluminium alloy $Al_{65}Cu_{20}Fe_{15}$. From Lutz, D: *Mater. Technology*, 11(5), 195, 1996.

Table 8.4 Mechanical properties of powder compacts produced from aluminium alloys hardened by quasicrystalline particles

Type	Alloy system	Mechanical properties
High strength	Al–Cr–Ce–M Al–Mn–Ce	Tensile strength 600–800 MPa Elongation 5–10%
High ductility	Al–Mn–Cu–M Al–Cr–Cu–M	Tensile strength 500–600 MPa Elongation 12–30%
High elevated temperature strength	Al–Fe–Cr–Ti	Tensile strength 350 MPa at 300°C

From Inoue, A and Kimura, HM: *Mater. Sci. Eng., A286, 1, 2000.*
M = elements such as Ti, Co, Ni, Mo.

by a high-volume fraction of fine, stable quasicrystalline particles. The alloy shows good stability at temperatures up to 200°C. A quasicrystalline titanium alloy, $Ti_{45}Zr_{38}Ni_{17}$, has shown promise for the reversible storage of hydrogen gas. Quasicrystals themselves tend to be brittle but have some interesting mechanical, thermal, and chemical properties. Some are very hard (up to 10 GPa) and offer the prospect of being used in wear-resistant coatings. They also have a low coefficient of friction comparable to Teflon and have been proposed for non-stick coatings for cooking utensils where they would have the advantage of being scratch-resistant. They have remarkably low thermal conductivities. As an example, the thermal conductivity of the quasicrystalline form of one alloy that contains as much as 70% aluminium is less than 1% that of aluminium metal at room temperature. Nano-sized quasicrystals of an Al–Pd alloy have been reported to be more efficient than pure palladium when used as a catalyst for cracking methanol.

8.5 AMORPHOUS ALLOYS

It is well known that the mechanical strength of alloys that can be produced with amorphous (or glassy) atomic structures by liquid quenching techniques, such as melt spinning (Fig. 8.16), may be notably greater than those obtained for the normal crystalline state. One prerequisite for this behavior is a large negative enthalpy of mixing of constituent elements which is a feature of certain aluminium and magnesium alloys containing both rare earth and transition metal elements. Moreover, the rare earth elements have a larger atomic size than either aluminium or magnesium, whereas the atoms of transition metals such as copper and nickel are smaller, suggesting that localized strain energy will be reduced if the three types of atoms cluster together. These two factors are presumed to reduce the overall atomic diffusivity during cooling from the molten state, thereby retarding nucleation of crystalline phases. Composition limits for some binary and ternary aluminium and magnesium alloys that are

able to form amorphous structures in the rapidly quenched condition are shown in Fig. 8.22.

The presence of an amorphous phase in aluminium alloys was first observed in rapidly solidified binary systems with metalloid (e.g., silicon) and transition metal (e.g., copper) elements in which there was coexistence with a crystalline phase. The formation of completely amorphous, single-phase, aluminium-based alloys was first achieved in Japan in the Al–Fe–B and Al–Co–B systems. These materials proved to be extremely brittle and, more recently, the Japanese group has obtained good bending ductility combined with TS exceeding 1000 MPa in ternary alloys such as Al–7La–5Ni (at.%). This compares with values of 500–600 MPa for strong, conventionally produced wrought alloys (Table 4.5). Values of hardness (e.g., 300 DPN) and elastic modulus (e.g., 90 GPa) are also significantly higher for the amorphous alloy. Another advantage is that the coefficient of thermal expansion of amorphous alloys is generally lower than values for conventional crystalline alloys.

Bulk specimens of the amorphous alloys can be prepared by extruding pressed, atomized powders and some compositions have now shown some capacity to deform plastically (e.g., elongations of 1–2%). The alloys commonly undergo an amorphous to crystalline transition on heating to temperatures in the range 250–350°C. Even higher mechanical properties have been

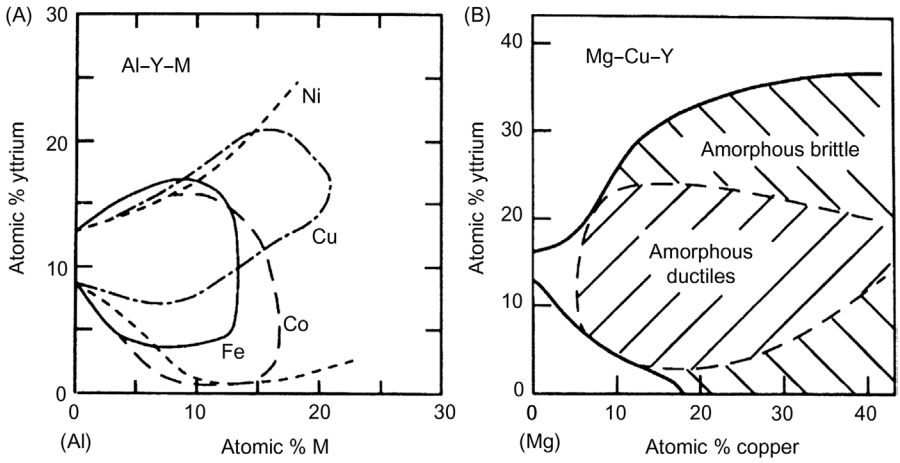


Figure 8.22 (A) Composition loops for binary and ternary aluminium alloys that may form amorphous structures if rapidly quenched from the liquid state. (B) Mg–Cu–Y phase diagram showing compositions of ductile and brittle amorphous alloys. (A) From Inoue, A and Masumoto, T: *Encyclopaedia of Materials Science & Engineering* (Second Supplementary Volume), Cahn, RW (Ed.), Pergamon, Oxford, 1990. (B) From Kim, SG *et al.*: *Mater. Trans. Japan Inst. Met.*, 31, 929, 1990.

obtained from ribbons made from aluminium alloys in which partial crystallization has been encouraged by decreasing cooling rates during melt spinning. Fine crystalline precipitates with sizes as small as 3–4 nm are formed which consist of fcc α-aluminium saturated with solute elements. One such alloy, Al–8Ni–2Y–2Mn (at.%), which contains these particles within an amorphous matrix has recorded a tensile fracture strength as high as 1470 MPa.

Amorphous structures have also been obtained with a range of magnesium alloys, most of which are also ternary compositions containing rare earth and transition metal elements (e.g., Fig. 8.22B). Melt spun ribbons of Mg–Ni–La alloys have shown values of TS, elastic modulus, and hardness in the ranges 610–850 MPa, 40–60 GPa, and 190–230 DPN, respectively, which greatly exceed maximum values of around 300 MPa, 45 GPa, and 85 DPN for the strongest conventionally cast magnesium alloys. Most compositions show good bending ductility, although tensile fracture strains (including elastic strains) lie in the range 0.014–0.018 indicating little or no capacity for plastic deformation. Again, even higher values of TS can be obtained in partially crystallized alloys and some compositions, e.g., Mg–12Zn–3Ce (at.%), show some capacity for plastic deformation.

Amorphous magnesium alloys also show good thermal stability (i.e., crystallization temperatures >300°C) and some compositions can retain amorphous structures at slower cooling rates than those required aluminium alloys. This has opened up the prospect of obtaining these structures in bulk castings, as well as ribbons, and the Japanese group has succeeded in retaining amorphous structures in chill cast cylinders prepared by pressure injecting molten alloys into a copper mold. Amorphous structures have been confirmed in 2 mm diameter cast bars for the alloy Mg–10Cu–10Y (at.%) and in up to 7 mm diameter bars in Mg–25Cu–10Y (at.%) (Fig. 8.23). Mechanical properties have been found to be similar to those obtained for more rapidly cooled, melt spun ribbons even though cooling rates for casting in the copper mold are as low as 10^2 °C s^{-1}. This behavior suggests that amorphous structures may be obtained in industrially produced, thin-walled magnesium alloy castings which would show much higher strength and wear resistance. However, practical applications of these materials have yet to be exploited.

Many experimental titanium alloys have been obtained in the amorphous condition by rapid solidification techniques. They may be classified into metal–metal and metal–metalloid systems; examples are Ti–40Be, Ti–30Co, Ti–25Al–25Ni and Ti–35Be–5Si, Ti–30Co–10B, Ti–40Ni–10P (all at.%), respectively. The metalloid systems, in particular, are characterized by very high values of hardness and strength while retaining significant bend ductility almost up to the crystallization temperature. Some properties are summarized in Table 8.5 and may be compared with values for conventional titanium alloys as given in Table 7.1.

More recently, attention has also been focused on titanium alloys that may retain their amorphous structures in bulk form. Japanese workers have studied alloys based on the eutectic composition $Ti_{50}Cu_{42.5}Ni_{7.5}$ to which were added

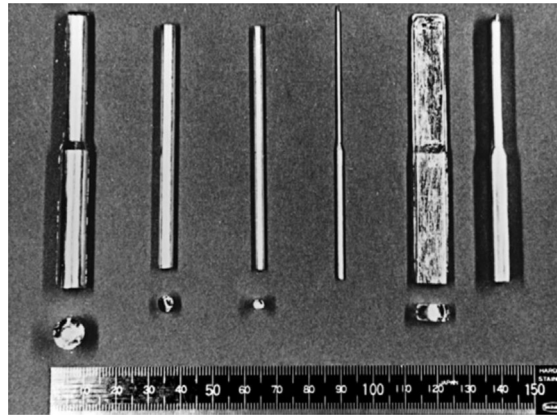


Figure 8.23 Injection chill cast magnesium alloy products showing amorphous structures. Courtesy A. Inoue.

Table 8.5 Mechanical and thermal properties of amorphous titanium metalloid alloys

Metalloid alloy (at.%)	Hardness (DPN)	Yield strength (MPa)	Density ($g\,cm^{-3}$)	Crystallization temperature (°C)
Ti–15Si	510	1960	4.1	429
Ti–20Co–10Si	570	2105	5.0	495
Ti–20Fe–10Si	580	2150	4.8	549
Ti–35Be–5Si	805	2490	3.9	462

From Suryanarayana, C *et al.: Inter. Mater. Rev., 36(3), 85, 1991.*

elements having atomic radii larger or smaller than titanium. The addition of the larger element zirconium was found to promote the formation of a new eutectic, and the critical diameter of a rod capable of retaining its amorphous structure was increased from 200 μm to 1.2 mm. Small amounts of hafnium serve further to enhance the stability of the rapidly solidified liquid and move the modified composition closer to the modified eutectic point. However, the largest effect was recorded when the smaller element silicon was added, and the complex alloy $Ti_{41.5}Cu_{42.4}Zr_{2.5}Hf_5Si_1$ remained amorphous when chill cast in a copper block as a 5 mm diameter rod. The alloy has a tensile strength of 2040 MPa and a compressive strength of 2080 MPa. No plastic deformation was recorded in tension but some slight ductility was evident in compression. The glass transition temperature was found to be 407°C.

One special feature of some amorphous titanium alloys is that they exhibit superconducting behavior if cooled to sufficiently low temperatures (10 K). This applies to both the glassy and crystalline states. Examples are Ti–40Nb–15Si and Ti–40Nb–12Si–3B (at.%).

8.6 MECHANICAL ALLOYING

Mechanical alloying was devised by Benjamin at the International Nickel Company to introduce hard particles, such as oxides and carbides, into a metallic matrix on a scale that is much finer than can be achieved by conventional powder metallurgy practices. The process involves the high-speed attrition of dry, elemental, or simple alloy powders in modified, high-energy ball mills. During milling, ball–powder–ball and ball–powder–container collisions occur which repeatedly deform, cold weld, and fracture the powder particles (Fig. 8.24). The interaction between particle fracture and welding, combined with strain-enhancing diffusion, progressively homogenizes the powders, resulting eventually in alloy formation. Extremely fine grain sizes (<1 μm) can be achieved and solid solubilities may be extended well beyond their equilibrium values.

For aluminium alloys, fine dispersions of Al_2O_3 are introduced from the existing oxide films on the powders whereas the carbide, Al_4C_3, is formed following the breakdown of organic surface reagents, such as stearic acid, that are added to minimize cold welding during processing. The final powder is consolidated by pressing and vacuum degassing and billets weighing as much as several hundred kilograms have been prepared. Sections or components can then be produced by hot extrusion, forging, or isostatic pressing.

A special type of milling, known as cryomilling, has been used to produce very fine nanocrystalline powders. This process involves introducing liquid nitrogen during milling and was first used with aluminium and dilute aluminium alloys strengthened by fine aluminium oxy-nitride particles. The advantages of cryomilling include reduced oxygen contamination from the atmosphere, and faster heat transfer between particles and the cryogenic medium which favors particle fracturing rather than welding when ductile materials are being milled. However, if the methods used for the subsequent consolidation of powders involve elevated temperatures, it is difficult to retain the initial nanocrystalline structure because grain growth may occur.

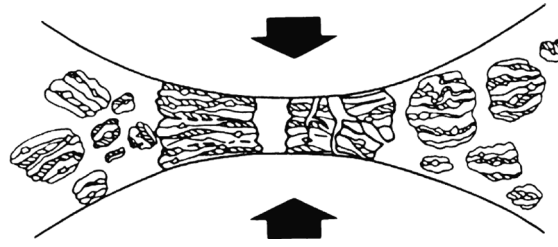


Figure 8.24 Representation of deforming, welding, and fracturing of powders by high-energy ball milling during mechanical alloying. Courtesy F. H. Froes.

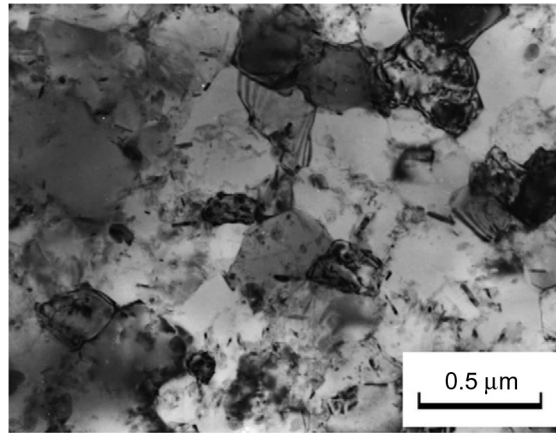


Figure 8.25 Transmission electron micrograph showing fine-grain structure of IN9052 produced by mechanical alloying. Courtesy J. Weber.

Two aluminium alloys developed by Inco Alloys International that are available for use in structural applications are designated IN9052 (Al–4Mg–0.80–1.1C) and IN9021 (Al–4Cu–1.5Mg–0.8O–1.1C). Each may have a fine grain size of 0.5 µm or less that is stabilized by the presence of oxides and carbides commonly in the size range 30–50 nm (Fig. 8.25). The first relies on solid solution and dispersion strengthening (e.g., TS at room temperature 550 MPa, elongation 8%), whereas IN9021 combines precipitation hardening with dispersion strengthening (e.g., TS 600 MPa, elongation 11%). Because of the fine microstructures, mechanical properties in the longitudinal and transverse directions are more isotropic than those found with conventionally fabricated wrought sections (Section 2.5) which is a significant advantage. Both alloys also show exceptional resistance to general corrosion, pitting and exfoliation attack, as well as to stress–corrosion cracking.

Experimental lithium-containing alloys (e.g., Al–4Mg–1.3Li–0.4O–1.1C) have also been prepared by mechanical alloying to take advantage of lower density and higher elastic modulus. One such alloy, designated AL 905XL, has been specified for undercarriage forgings for the European EH101 helicopter (Fig. 4.40). At elevated temperatures, improved performance has been obtained with mechanically alloyed Al–Ti alloys containing 6–12% titanium. Fine particles of stable Al_3Ti are formed which provide dispersion strengthening and values of elastic modulus in the range 85–100 GPa have been recorded which are comparable with those found in metal–matrix composites (Section 8.1.3).

The application of mechanical alloying to the preparation of magnesium and titanium alloys is less well advanced. Magnesium alloys can present problems because they are soft and tend to adhere to the balls and container. Nevertheless the process has been used to produce “supercorroding” magnesium alloys that

operate effectively as short-circuited galvanic cells with the result that they will corrode (react) rapidly with an electrolyte, such as seawater, to produce heat and hydrogen gas. Such an alloy system has been suitable as a heat source for warming deep-sea divers, as well as a gas generator to provide them with buoyancy. It has also been tried as a source of fuel in hydrogen engines or fuel cells. Corrosion rates are maximized because the finely dispersed microstructure formed by mechanical alloying provides very short electrolytic paths, exposes a large surface area, and makes a strong connection (weld) between cathodes and anodes. As one example, extremely fast reaction rates and high-power outputs have been achieved with magnesium alloys containing 12–15%Fe. Several hydrides based on mechanically alloyed magnesium alloys have been evaluated for the safe storage of hydrogen because they have the potential to contain a higher volume density than is present in liquid hydrogen.

Another novel development has been an attempt to prepare titanium and certain alloys, such as Ti–6Al–4V, at ambient temperatures by the direct reduction of $TiCl_4$ with magnesium during grinding. Normally this reduction process is carried out in an inert atmosphere at temperatures around 1000°C (Section 1.4). Some attention has been given to the synthesis of the titanium aluminides Ti_3Al and TiAl by mechanical alloying since attempts to prepare these intermetallics by ingot or powder metallurgy routes have met with limited success (Section 8.9). High-energy grinding has been found to introduce some interesting metastable amorphous phases as well as nanocrystalline regions (Section 8.8) but this work is also at an early stage.

8.7 PHYSICAL VAPOR DEPOSITION

Physical vapor deposition (PVD) involves the high-temperature evaporation of metals and other elements and their redeposition on to a suitable substrate. The technique has been used mainly to produce thin films and coatings, one example being the deposition of titanium nitride to improve the wear resistance of steel tools. Now the development of high-energy-rate processes involving, for example, the use of intense electron beams, is enabling PVD to be applied to produce alloys in bulk. Individual elements can be evaporated and then co-deposited to give new compositions and microstructures having extremely fine grain sizes, extended solubilities and freedom from segregation.

As one example, an experimental aluminium alloy RAE72, containing the normally insoluble elements chromium (7.5%) and iron (1.2%), was produced in England in slab form using PVD. The alloy vapor was deposited on a $500 \times 300\,mm^2$ collector plate at a rate of $6\,mm\,h^{-1}$ to a thickness of 44 mm and then warm rolled to sheet. Elevated temperature tensile results showed that the alloy has a specific strength exceeding that of titanium alloys at temperatures up to 300°C. The high strength of the alloy was attributed to a combination of solid solution strengthening by chromium, precipitation of fine particles of $AlFe_3$, and the very fine grain size of the matrix.

Another use of PVD is to prepare alloy compositions that cannot be produced by ingot metallurgy. One example has been the alloying of titanium with the comparatively volatile metal magnesium which, in fact, boils below the melting point of titanium. Experimental Ti–Mg alloys have been found to respond to age hardening and the precipitates that form appear to be exceptionally stable. Magnesium also has the advantage of reducing the density of titanium by more than 1% for each 1 wt% that is added.

8.8 NANOPHASE ALLOYS

Nanostructured materials are part of a rapidly expanding field referred to as nanotechnology and they have been identified as a key to the development of many new industrial processes and products. In its original context, the name applies to materials with grain sizes of 10 nm or less in which the volume occupied by grain boundary structure can be 30% or more and the density of defects in the material is abnormally high (Fig. 8.26). In effect, a nanophase material can be seen as a composite containing a mixture of crystalline and amorphous regions. As a consequence, the characteristic bulk behavior of a material may be significantly changed leading to modified, and often enhanced, physical or mechanical properties.

Nanophase materials were detected in samples of lunar soils but terrestrial evidence for their existence was lacking until the introduction of the new processing techniques, mechanical alloying, consolidation of amorphous powders and physical vapor deposition. Because grain size is so fine, it is to be expected that nanophase materials may be susceptible to creep at elevated temperature due to the opportunity for grain boundary sliding, and this does appear to be an

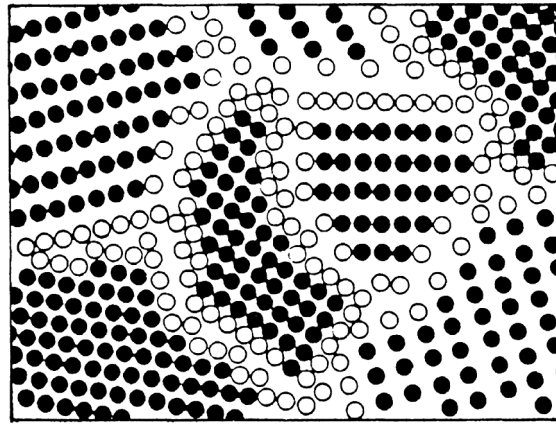


Figure 8.26 Proposed atomic structure of a nanocrystalline material. Black circles represent atoms in normal lattice positions within grains and white circles indicate atoms that are associated with grain boundaries. Courtesy H. Gleiter.

another one of their characteristics. However, a desirable complementary feature should be the ability to undergo superplastic deformation providing their high-energy microstructures remain stable at the appropriate temperatures. Such behavior has been observed in nano- and near-nanoscale aluminium alloys produced by mechanical alloying (e.g., IN9052; Section 8.6) and by consolidating rapidly solidified amorphous powders (Section 8.3). These materials differ from commercial superplastic alloys such as 7475 (Section 4.6.8) in that the abnormal elongations are achieved at much higher strain rates. For example, whereas maximum superplasticity is observed in sheet made from the conventionally produced aluminium alloy 7475 (average grain size 15 μm) deformed at a slow strain rate of approximately $10^{-4}\,s^{-1}$, the equivalent strain rate for mechanically alloyed IN9021 (average grain size 0.5 μm) may be as high as $10–10^{2}\,s^{-1}$. This increase in strain rate of as much as one million times opens up the interesting prospect of achieving superplasticity under impact conditions in nanophase materials.

Much attention is now being directed to obtaining ultrafine grain sizes in bulk materials and one method for achieving this is through processes involving severe plastic deformation such as equal channel angular pressing (ECAP), which is also known as equal channel angular extrusion). This process involves pressing (extruding) a metallic billet through a die-containing two channels of equal cross section that intersect at an angle ϕ (Fig. 8.27A).

To date, ECAP has been carried out at ambient or a moderately elevated temperatures, and at deformation rates substantially faster than most conventional metal working processes. Under these conditions, the billet experiences

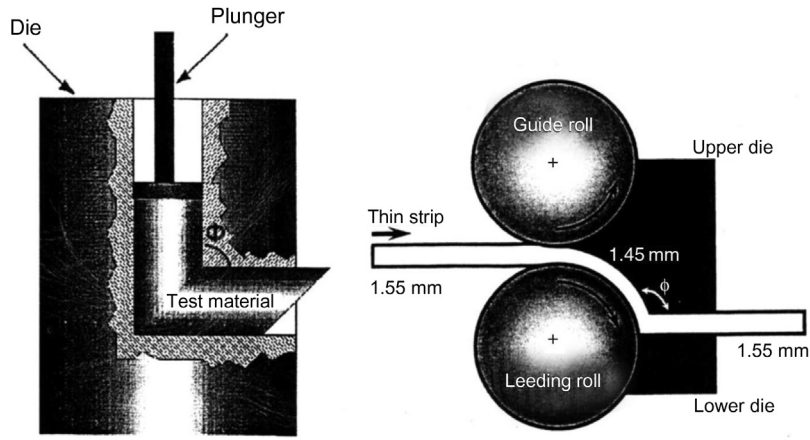


Figure 8.27 Schematic diagrams of ECAP involving (A) extrusion and (B) the concept of continuous confined strip shearing (CCSS) of strip cast sheet. (A) From Lowe, TC and Valiev, RZ: *JOM*, 52(4), 27, 2000. (B) From Lee, J-C *et al.*: *Metall. Mater. Trans. A*, 33A, 665, 2002.

simple shear and, if back pressure is applied, a hydrostatic pressure component is introduced at the intersection of the two channels. Since the dimensions of the pressed material do not change during processing, this process can be repeated several times. Progressively higher levels of strain are accumulated within the material and the total strain ε_N that is achieved in a series if pressings N and a channel intersection angle ϕ is given by:

$$\varepsilon_N = \frac{2N}{\sqrt{3}} \cot\left(\frac{\phi}{2}\right)$$

If the pressed billet is rotated around its longitudinal axis after each pass, the microstructure and texture can be modified to achieve specific engineering purposes. During the early stages of deformation, the relatively coarse grains of the original billet are formed into arrays of subgrains that fragment on further straining to form much finer grains separated by what are potentially high angle boundaries. These ultrafine grains (1 μm or less) contain relatively few dislocations and therefore have the appearance of an annealed structure but with a very much finer grain size (Fig. 8.28).

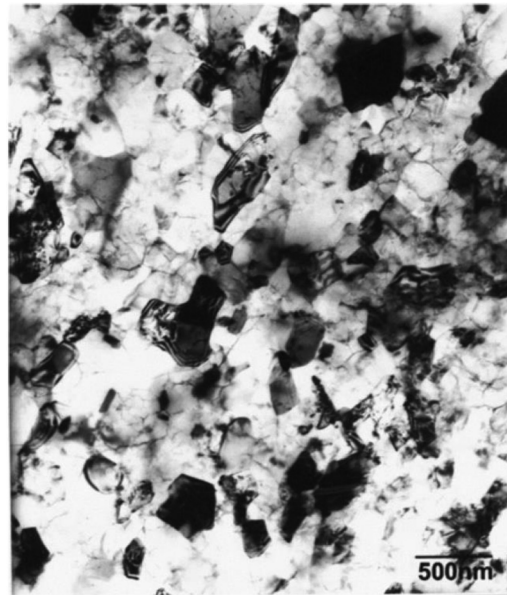


Figure 8.28 Transmission electron micrograph showing an ultrafine grain structure in the Al–Mg–Si alloy 6016 that was solution treated at 560°C for 1 h, furnace cooled, and deformed to an equivalent true strain of about 14 (i.e., 12 passes) by ECAP. The grain size has been reduced from an original average value of about 190 μm and final value of about 0.3 μm. Courtesy P. McKenzie.

ECAP has been applied successfully on a laboratory scale to a number of commercial aluminium alloys including 3004, 5052, 5083, 6061, and 6016. One outcome has been significant increases in strength properties. For example, the solid solution-hardened alloy 5052 (Al–2.5Mg–0.25Cr) typically has a 0.2% proof stress of 255 MPa and a tensile strength of 270 MPa in the H38 strain-hardened condition. After processing by ECAP to an equivalent true stain of 8, these values may be as high as 395 and 420 MPa, respectively, without loss of ductility. Similarly, higher strengths have been achieved in age-hardened alloys such as 6061. These alloys also show promise for superplastic forming at higher rates than are possible with conventionally produced alloys (Section 4.6.8).

The industrial challenge is to convert ECAP from a batch to a more cost-effective continuous process. One promising development has occurred in South Korea which has been termed "continuous confined strip shearing" (CCSS). This process involves passing continuously strip cast sheet between rolls that then force it at high speed through a thinner, curved ECAP channel as shown schematically in Fig. 8.27B. Once the strip experiences shear through this channel, it expands to its original thickness and exits via an outer channel. This process offers the prospect of significantly raising the strength of strip cast alloys for which, normally, the opportunity for doing this by cold rolling is limited.

Magnesium alloys are also good candidates for ECAP because of their limited capacity for forming by conventional methods. Experiments with alloys such as AZ31 and ZK31 have confirmed that ECAP produces a fine and uniform microstructure, as well as textures in which the basal planes of the lattice tend to become aligned parallel to the extrusion direction. Because the critical resolved shear stress is low along these planes, ECAP processing results high ductilities in this direction. Tensile properties increase as the ECAP temperature is reduced. Some prototype components such as automotive knuckle arms, which have been forged from ECAP-processed magnesium alloy feedstock, have shown high resistance to fracture under impact conditions.

Small quantities of some nanophase titanium alloys including Ti–Cu and several titanium aluminides (Section 8.9) have been produced by mechanical alloying. Little information is available concerning mechanical properties although it has been reported that the nano-phase γ-TiAl intermetallic compound may have double the hardness of the equivalent as-cast ingot at room temperature. Softening occurs above 200°C and the hardnesses of the two materials become similar at 300°C.

8.9 TITANIUM ALUMINIDES

As discussed in Section 1.4 and Chapter 7, conventional titanium alloys cannot withstand prolonged exposure to air at temperatures above approximately 600°C, mainly because the surface oxide film keeps dissolving into the titanium

matrix underneath which embrittles the alloys. Moreover, despite their high melting points, the best of these alloys undergoes excessive creep at or above this temperature. There are, however, ordered titanium–aluminium intermetallic compounds that have the potential to be used for components such as turbine blades operating at much higher temperatures. These compounds are now seen as the probable next stage in the development of ingot titanium alloys.

The Ti–Al phase diagram is shown in Fig. 8.29 and the titanium aluminides of interest are Ti_3Al (known as α_2) and TiAl(γ), both of which exist over a range of compositions, together with the stoichiometric compound $TiAl_3$. Physical properties of each of these compounds are summarized in Table 8.6 and their crystal structures are shown in Fig. 8.30.

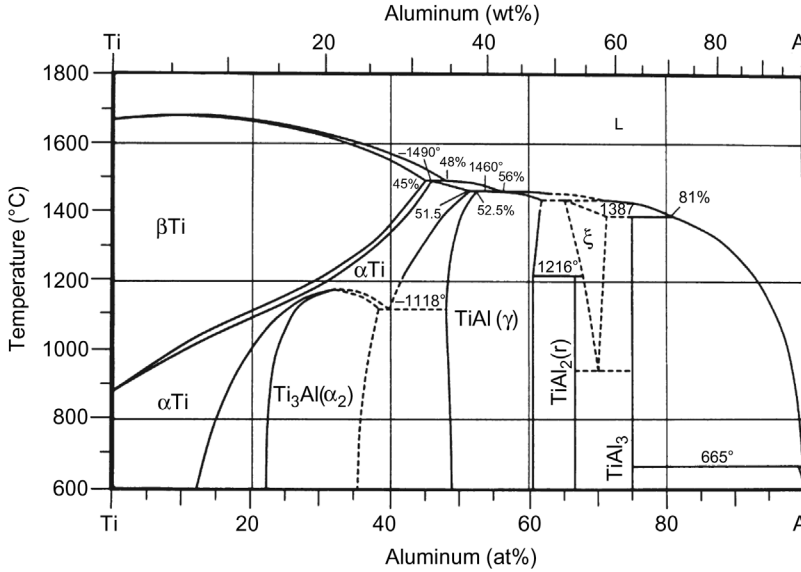


Figure 8.29 Proposed titanium–aluminium phase diagram. From Massalski, TB (Ed.): *Binary Alloy Phase Diagrams*, 2nd Ed., Vol. 1, ASM International, Materials Park, OH, USA, 1990.

Table 8.6 Physical properties of titanium aluminides

Compound	Crystal structure	Lattice parameters (nm)	Melting point (°C)	Density ($g\,cm^{-3}$)	Elastic modulus (GPa)
Ti_3Al	DO_{19} ordered hexagonal	$a = 0.5782$ $c = 0.4629$	1600	4.3	145
TiAl	$L1_o$ ordered face-centered tetragonal	$a = 0.4005$ $c = 0.4070$	1460	3.9	175
$TiAl_3$	DO_{22} ordered tetragonal	$a = 0.3840$ $c = 0.8596$	1340	3.4	200

From Froes, FH *et al.: J. Mater. Sci.*, 27, 5113, 1992.

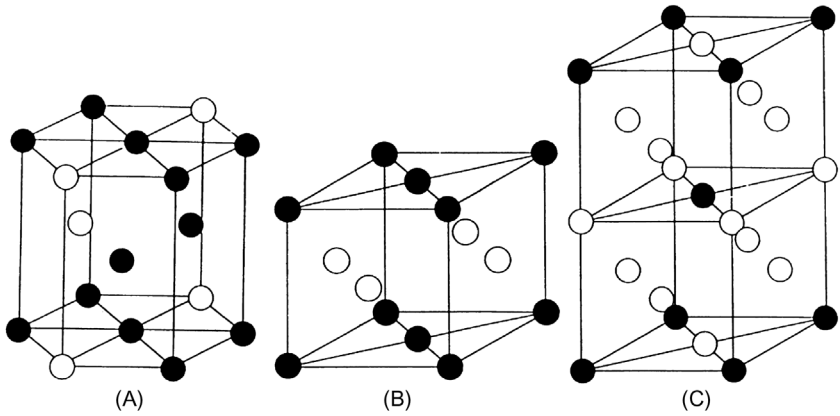


Figure 8.30 Crystal structures of titanium aluminides. (A) Ti_3Al, (B) TiAl, and (C) $TiAl_3$. Black balls are Ti atoms, white balls are Al atoms.

Immediate advantages of these aluminides are improved levels of specific stiffness arising from desirable combinations of lower densities, which are approximately half those of the nickel-based superalloys, and higher values of elastic modulus than normal titanium alloys. Moreover, resistance to oxidation improves progressively as the aluminium content is raised. The ordered crystal structures also promote enhanced creep resistance because the strong bonding between the two different atoms in the superlattices restricts both dislocation motion and atomic diffusion at elevated temperatures. However, these particular features of intermetallic compounds, together with a limited capacity to undergo slip, result in low values of ambient temperature ductility. This situation for titanium aluminides is exacerbated by the presence of interstitial impurity elements such as oxygen and hydrogen.

Titanium aluminides also present formidable problems when preparing castings. Firstly, the molten alloys are difficult to contain because they react chemically with virtually all ceramic refractories. It has therefore been necessary to use cold-wall (internally water cooled) furnaces which limit the ability to superheat to about 60°C and present difficulties with metal flow when pouring into molds. Furthermore, because considerable vaporization of aluminium occurs if melting is carried out in vacuum, it is necessary to introduce an inert gas such as argon which can be entrapped in the castings as they tend to solidify rapidly. The reactive nature of the titanium aluminides also presents difficulties in developing suitable materials for molds when producing cast components. For wrought products, formability at elevated temperatures is restricted and much attention has been directed at improvements through alloying and control of microstructure. Each of the above problems has delayed the wider introduction of the titanium aluminides.

8.9.1 $Ti_3Al(\alpha_2)$

Compositions based on the compound Ti_3Al were the first titanium aluminides to be studied in detail. As shown in Fig. 8.31, they may display outstanding strength:weight ratios when compared with conventional titanium alloys, although improvements in creep strength have been relatively small (Fig. 7.2) and the upper limit for operation in air has been little changed.

Ti_3Al undergoes an order/disorder transition within the composition range 22–39% aluminium to form an ordered DO_{19} hexagonal structure. Low ductility at room temperature is attributed to a coplanar mode of slip (Fig. 2.21A) and the lack of sufficient slip systems parallel, or inclined, to the hexagonal direction of the unit cell. Moreover, in contrast to most other hexagonal metals and alloys, Ti_3Al does not undergo deformation by twinning.

Both the microstructures and mechanical properties of Ti_3Al tend to follow the behavior of more conventional titanium alloys. Thus thermomechanical processing can occur in the β- or α_2–β-phase regions (Fig. 8.29) as was described

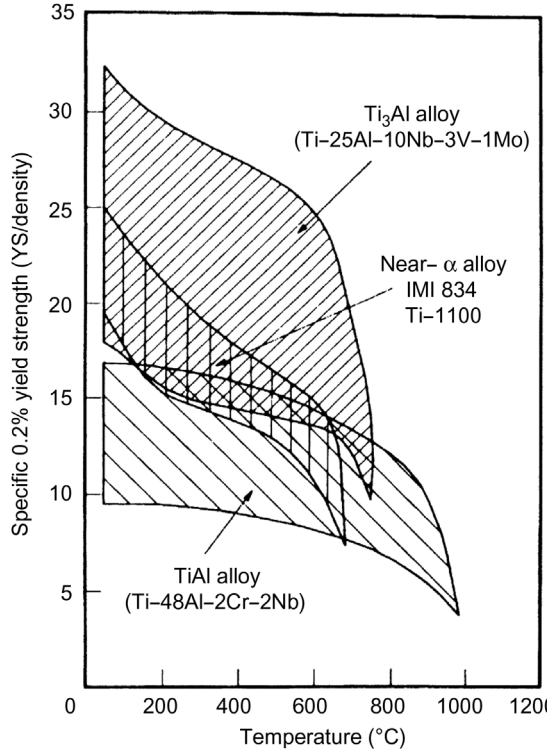


Figure 8.31 Specific yield strength values of titanium aluminides and the conventional near-α alloys IMI 834 and Ti–1100. From Kumpfert, J and Ward, CH: *Advanced Aerospace Materials*, Buhl, H. (Ed.), Springer Verlag, Berlin, 1992.

for the α/β-alloys in Section 7.3. Similarly, Ti_3Al alloys quenched from the β-phase field undergo a variety of martensitic transformations. Additions of β-stabilizing elements such as niobium, molybdenum, and vanadium to Ti_3Al also promote formation of a ductile ordered body-centered cubic phase (B2) in which ω and ω-related phases may form on cooling to room temperature. In summary, transformed β microstructures that produce a basket weave configuration of secondary Widmanstätten plates of α_2 (similar to Fig. 7.4D) together with the phase B2 are considered to provide the best overall combination of mechanical properties.

Niobium has become the most widely used and important addition to Ti_3Al. Niobium atoms substitute for titanium atoms in the crystal lattice which has the effect of improving low-temperature ductility by increasing the number of active slip systems. Molybdenum, in smaller quantities, behaves in the same way and provides the additional advantages of solid solution strengthening and improved creep strength. Vanadium has been used as an alternative to niobium because of its lower density although this element has the disadvantage of reducing oxidation resistance. Examples of alloys that were developed are Ti–24Al–11Nb and Ti–25Al–10Nb–3V–2Mo. Each has a microstructure containing the two phases α_2 and B2.

During the 1990s it was realized that the α_2-Ti_3Al alloys suffered severe environmentally induced embrittlement at temperatures as low as 550°C and development was discontinued in favor of compositions based on the orthorhombic compound Ti_2AlNb (O phase). A balance needed to be obtained between the contents of aluminium, which decreases density and improves oxidation resistance, and niobium which favors the formation of the O phase but increases density and reduces oxidation resistance. Compositions close to Ti–22Al–25Nb appear to provide the best compromise. This alloy is ductile at room temperature, displays good formability, high creep, and fatigue strength, and has moderate oxidation resistance. It also has a coefficient of thermal expansion that is less than that for conventional titanium alloys and γ TiAl.

8.9.2 TiAl(γ)

The development of alloys based on TiAl is of more recent origin because this compound, intrinsically, has even less room temperature ductility than Ti_3Al. Tensile properties are also significantly lower (e.g., Fig. 8.31). Nevertheless γ alloys are now attracting special attention because of their lower densities combined with superior values of elastic modulus (Table 8.6), oxidation resistance, and thermal stability (Fig. 7.2)

TiAl has an $L1_o$ ordered face-centered tetragonal structure in which titanium and aluminium atoms form as successive layers on (002) planes. The composition may extend from 48.5 to 66 at.% aluminium although alloys of possible practical interest lie at the lower end of this range. Tetragonality (*c*/*a* ratio) is close to unity, varying from 1.01 to 1.03 for the two extremes of aluminium content, and the compound remains ordered up to its melting point of 1460°C.

Deformation at low temperatures involves slip although dislocation mobility is again severely restricted. Twinning occurs at higher temperatures and is considered to account for the increased plasticity that is observed. Fracture occurs predominantly by cleavage at both low and high temperatures.

γ alloys of special interest lie in the composition range Ti−(46−52) Al−(1−10)M (at.%) where M represents at least one element from a list that includes the transition metals V, Cr, Mn, Nb, Mn, Mo, and W. Both single-phase γ and two-phase (γ + α_2) alloys are possible for this range of compositions. Generally, two-phase alloys are again favored and these usually have aluminium contents within the range 46–49 at.% together with 1–4% of the individual additional elements. These latter elements can be divided into three groups:

1. Cr, V, Mn, and Si, which improve ductility but reduce oxidation resistance.
2. Nb, Ta, Mo, and W, which enhance oxidation resistance.
3. Si, C, and N which, in relatively smaller amounts, improve creep resistance.

Examples of compositions of two-phase alloys that have been of interest are Ti–48Al–2Nb–2Cr (at.%), Ti–48Al–2V, and Ti–47Al–2.5Nb–2(Cr + V). Densities lie in the range 3.9–4.1 $g\,cm^{-3}$.

TiAl alloys are particularly susceptible to segregation during solidification because of what has been described as the double cascading effect of the two peritectic reactions in this region of the phase diagram (Fig. 8.29). Accordingly special attention must be given to high-temperature homogenization treatments that are usually carried out within a comparatively narrow temperature range in the single-phase α-field prior to subsequent processing.

In addition to alloying, microstructural control is exercised by heat treatment and thermomechanical processing as with other titanium alloys. Lamellar microstructures are common (e.g., Fig. 8.32) but processing can be adjusted so that equiaxed, lamellar, or duplex morphologies are obtained. The equiaxed microstructure consists entirely of γ grains in single-phase alloys, whereas, in two-phase alloys, this structure is predominantly γ grains with small amounts of grain boundary α_2 particles. A fully lamellar microstructure consists of colonies (i.e., grains) of γ plates or, in two-phase alloys, alternating plates of γ + α_2. In this regard, ductility is generally improved up to 10 vol.% α_2. Duplex microstructures contain mixtures of equiaxed grains and lamellar colonies. Different mechanical properties are favored by one of these three types of microstructures, but a two-phase, lamellar morphology is generally considered to provide the best balance so long as the grain (colony) size can be kept fine.

γ-TiAl alloys can show good workability, some tensile plasticity (1–3%) at room temperature, and fracture toughness values of 10–35 $MPa\,m^{-1/2}$. Current creep resistance limits them to an operating temperature of around 700°C. Improvements in strength and creep resistance can be achieved through precipitation hardening from oxides, nitrides, and silicides and carbides. Special attention has been paid to the alloys containing small additions of carbon and holding

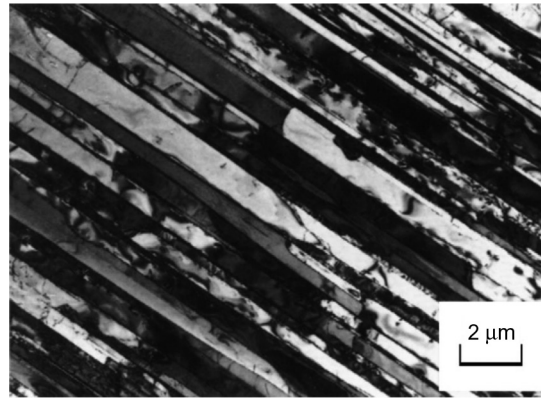


Figure 8.32 Lamellar microstructure in a γ-TiAl alloy. Courtesy C. Suryanarayana.

at 1250°C, quenching and ageing at 750°C leads to precipitation of a high density of particles of the phase Ti_3AlC. The formation of precipitates tends to embrittle the γ-TiAl alloys, although this effect can be reduced by ensuring that the alloys are processed, e.g., by extrusion, to refine the microstructure before the alloys are aged.

8.9.3 $TiAl_3$

This compound, which has an ordered DO_{22} tetragonal crystal structure, has the highest specific stiffness and oxidation resistance of all the titanium aluminides (Table 8.6). It exhibits some compressive ductility above 620°C but is brittle at lower temperatures at which deformation occurs solely by $(111)[11\bar{2}]$ twinning that does not disturb the DO_{22} symmetry.

$TiAl_3$ has received least attention of the titanium aluminides and the main strategy being followed in attempts to improve ductility is to make ternary additions of transition metals that encourage formation of the structurally related, but more symmetric, cubic Ll_2 structure. One example is Ti–65Al–10Ni (at.%) in which the aluminium and nickel atoms occupy the face-centered sites with titanium atoms at the cube corners. Ternary additions of copper, manganese, zinc, iron, and chromium have also been made. However, although these ternary compounds do satisfy the von Mises criterion for plastic deformation by deforming at room temperature by slip on five independent systems of the type $\{111\}\langle\bar{1}10\rangle$ at low temperatures, they are still brittle and exhibit cleavage fracture.

8.9.4 Processing methods

As mentioned earlier, melting and casting of titanium aluminides presents special difficulties. Moreover, the subsequent fabrication of ingots by forging or other methods requires the use of higher temperatures and more stages (smaller

reductions) as compared with the working of conventional titanium alloys. Thus the production of near-net-shape components by casting, or by powder metallurgy techniques, is potentially attractive since the working operations are avoided.

A recent breakthrough has shown that Ti–45Al–8Nb single crystals with controlled lamellar orientations can be fabricated by directional solidification without the use of complex seeding methods. Samples with a lamellar structure archived average room temperature tensile ductility of 6.9% and yield strength of 708 MPa. At 900°C, the yield strength remained high at 637 MPa, with 8.1% ductility and superior creep resistance.

Additive manufacturing (AM) of gamma titanium aluminide (Ti–48Al–2Cr–2Nb) blades by selective electron beam melting (SEBM) has made significant progress since 2010, led by General Electric (GE). After eliminating most porosity by hot isostatic pressing (HIP) and producing a fine-grained duplex microstructure by proper heat treatment, the additively manufactured γ-TiAl blades achieved tensile properties equal to, and high cycle fatigue property better than, GE's reference data. It is expected that serial production of AM γ-TiAl blades by SEBM will be launched by GE at AvioProp in Italy in the near future.

Other innovative practices have also been studied including the production of titanium-aluminide powders by RSP, although the usual cost penalties are imposed on components made in this way (Section 8.3). RSP offers the potential to improve the ductility through disordering of the crystal structures, grain refinement, and deoxidation of the matrix. The opportunity is also available to enhance elevated temperature strength through dispersion strengthening by the introduction of fine, thermodynamically stable, particles that was discussed in Section 8.3. One example of this latter effect is the formation of a rare earth dispersion of Er_2O_3 in Ti_3Al alloys. As compared with cast ingots, improved homogeneity has been achieved in TiAl alloys which, when combined with refined microstructures, does appear to offer significantly higher ductilities than are present in the other material.

Progress has also been made in attempts to incorporate continuous alumina and silicon carbide fibers into hot-pressed foils or powders of the α_2- and γ-titanium aluminides as a means of improving fracture resistance and creep strength. The fibers must be precoated to prevent interfacial reactions at high temperatures and are usually prepared as woven mats. Tensile strengths as high as 1100 MPa have been achieved at 750°C. However, cost has been as high and must be substantially reduced before these materials could find practical applications.

8.9.5 Applications of titanium aluminides

As mentioned earlier, potential applications of these materials reside mainly in the aerospace industry. Substantial weight savings would be possible if monolithic or composite titanium aluminides could be used to replace some nickel-based superalloys for gas turbine engine components such as disks, blades,

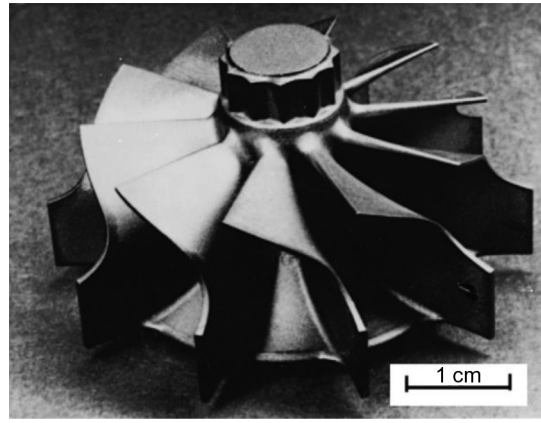


Figure 8.33 Cast γ-TiAl turbocharger rotor. Courtesy Y. Nishiyama.

vanes, and spacer rings. The most significant application today is the γ-TiAl (Ti–48Al–2Cr–2Nb) low-pressure turbine blades (Stages 6 and 7, the last two stages of the seven-stage low-pressure turbine) used on the GEnx engine, which powers the twin-engine Boeing 787 and four-engine Boeing 747-8 aircraft. This is the first large scale use of a TiAl alloy on a commercial jet engine, which reduces the engine weight by approximately 182 kg and contributes significantly to increased fuel efficiency on the GEnx engine over its life span. Potential applications for rolled sheet include exhaust nozzles and internal engine flaps. The titanium aluminides are also seen as contenders for use in the structure of possible hypersonic transatmospheric aircraft of the future which would suffer severe aerodynamic heating during the ascent and descent stages of each flight. In the meantime, applications are likely to be confined to non-critical aerospace applications and to parts for motor car engines such as the cast turbocharger rotor as shown in Fig. 8.33. Providing cost reductions can be achieved, they also have the potential to be used for forged automotive engine valves as their lower density could lead to reductions in fuel consumption of 3–5%.

8.10 ADDITIVE MANUFACTURING OR 3D PRINTING

Metal AM or 3D printing is a technology that builds parts from digital 3D design data, usually layer by layer, from metal powder, wire, or other forms of feedstock materials. The process begins by creating a 3D design of the required component using 3D computer-aided design (CAD) software packages. The 3D design is then converted into a mesh representation such as a STL (STereoLithography) file, which is a triangulated representation of a 3D CAD model and is the de facto file format for most AM systems. The next step is to slice the STL mesh of the model into a stack of 2D horizontal layers, where the

layer thickness can vary over a wide range depending on the AM process to be used. The last step is to determine and generate the scanning patterns or tool paths for the specified AM process. The completed slice data can then be transferred to the AM system for physical buildup.

Many metal AM systems are available today, as shown in Fig. 8.34. They may be classified in terms of the (i) energy source (laser, electron beam, plasma, gas tungsten arc, ultrasonic energy, and kinetic energy), (ii) feedstock form (powder, wire, sheet, and liquid metal), (iii) layer additive means (powder-bed fusion, powder deposition, wire deposition, and binder jetting), or (iv) AM temperature (above the liquidus or melting point, and at room temperature). Among these different metal AM processes, powder-bed fusion and direct metal (powder/wire) deposition are the two mainstream processes. From a production perspective, wire-based deposition processes can achieve a high AM rate (e.g., up to 10 kg h^{-1} for titanium), compared to typically < 1 kg h^{-1} by either powder-based deposition or powder-bed fusion processes.

A wide variety of metallic materials have been additively manufactured, including aluminium, magnesium, titanium, and beryllium alloys, titanium aluminide (TiAl) alloys, and amorphous aluminium alloys (Section 8.5). In principle, all weldable metals can be additively manufactured by a fusion-based approach. Ti–6Al–4V is the single most extensively studied alloy to date in the context of metal AM. In particular, AM Ti–6Al–4V bone implants (e.g., heel, knee, hip, rib, shoulder, neck, and skull) have found increasing applications (Fig. 8.35A). Also, fully qualified Ti–6Al–4V structures for aircraft applications can now be produced by AM processes. In the meantime, AM of aluminium alloys, e.g., Al–(10.5–13.5)Si (AlSi12), Al–(9–11)Si–(0.20–0.45)Mg (AlSi10Mg), and Al–(6.5–7.5)Si–(0.20–0.5)Mg (AlSi7Mg), is receiving increasing attention, and novel aluminium alloys, e.g., those containing scandium and zirconium, are being developed for different AM processes. Fig. 8.35B shows a fully qualified SLM Al–10Si–0.25Mg bracket for Eurostar E3000 telecommunications satellites, which is 35% lighter but 40% stiffer than the previous bracket which comprised four parts and 44 rivets. The rationales for choosing this alloy included its easy availability, technological maturity, and suitability for stiffness-driven designs. As regards titanium-aluminide alloys, Ti–48Al–2Cr–2Nb blades additively manufactured by SEBM for the GEnx engine have passed the tests at GE in the United States.

8.10.1 Metal powder and wire for AM

The majority of metal AM systems installed today use spherical metal powder feedstock. In the powder-bed AM processes, the powder is spread evenly at a layer thickness of typically less than 100 μm, over a platform as large as 800 $\times$ 400 mm^2. The powder characteristics have a significant impact on the flowability, spreading performance, packing ability, and subsequent response to the selective melting process by either laser or electron beam. A dense powder

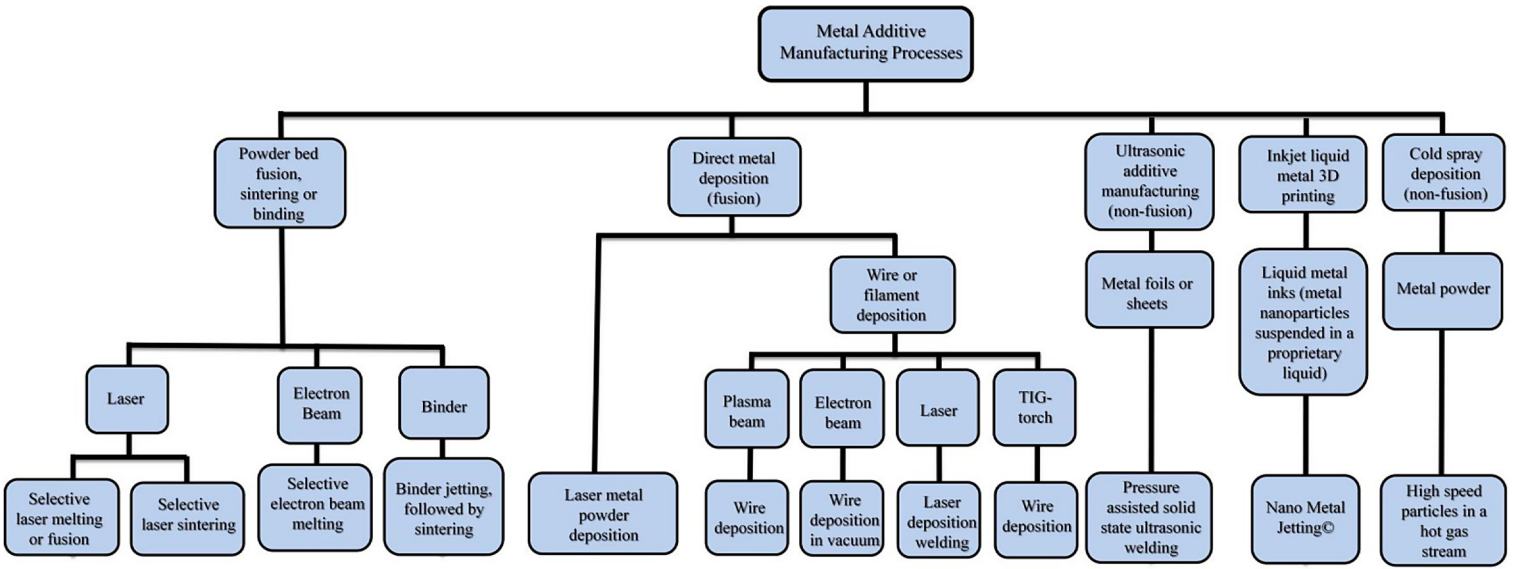


Figure 8.34 Summary of current metal AM processes.

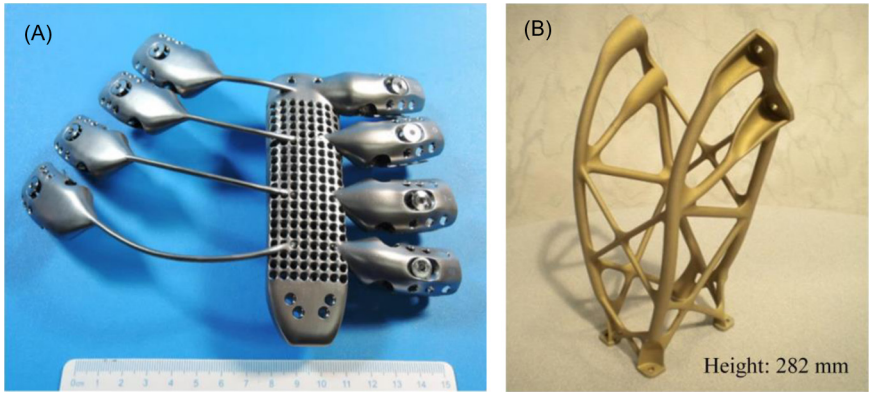


Figure 8.35 (A) Ti–6Al–4V sternum and rib implants by SEBM. Twelve days after the surgery, the 54-year-old patient was discharged from the hospital and has recovered well. (B) A fully qualified SLM Al–10Si–0.25Mg bracket for Eurostar E3000 telecommunications satellites. (A) Courtesy Anatomics Pty Ltd and (B) courtesy Airbus Defence & Space.

layer of even thickness is desired for the production of quality AM parts. This often requires the use of smooth spherical particles (implying small interparticle friction) with a certain particle size distribution as well as noncohesive powder properties. The requirement for particle size varies from system to system. In general, SLM and SEBM use powders in the range of 20–75 and 40–150 μm, respectively. As for laser powder deposition or blown-powder-based AM processes, the maximum particle size allowed depends on the design of the deposition nozzle, which can vary from 70 to 250 μm. Since the powder is delivered to the deposition nozzle by a carrier gas through a long flexible hose (typically 5 mm in diameter and 4.0–6.0 m long), good flowability of the powder is essential in order to ensure smooth and consistent powder flow in the hose. For this reason, most laser powder deposition systems have avoided using powders of less than ~ 40 μm in size.

The metal wire diameter affects the selection of deposition parameters, production rate, microstructure, and mechanical properties of the as-deposited alloy. It varies between 0.4 and 3.5 mm in general. However, since the wire deposition systems can use laser powers up to 10,000 W, it is flexible to choose the wire diameter according to the required production rate and mechanical properties.

8.10.2 Scanning patterns and processing parameters

The scanning patterns (for powder-bed fusion AM systems) and processing parameters can have a decisive influence on the formation of defects, development of residual stresses or distortion, surface finish, microstructure formation and evolution, and mechanical properties. There are a variety of scanning patterns, including the stripe pattern, islands pattern, chessboard pattern, simple

back-and-forth pattern, and their different combinations. The scanning directions can include unidirectional, bidirectional, and spiral. In some cases, the use of a simple back-and-forth scanning strategy has proved to be more effective in producing a homogeneous structure. Other important processing conditions include layer thickness, scanning speed, energy density, hatching spacing, focal offset distance, exposure time of each as-built layer, atmosphere in the chamber, substrate temperature, and whether or not each new layer of powder is preheated. The most appropriate processing conditions need to be determined experimentally and can be time-consuming. However, they can critically affect the microstructure and therefore the mechanical properties. For example, SLM Ti–6Al–4V typically shows a fully martensitic structure. Changing the processing window to enable in situ decomposition of the martensite phase can result in the formation of an ultrafine lamellar α/β structure. Consequently, the resulting SLM Ti–6Al–4V shows superior tensile mechanical properties in the as-fabricated state (e.g., tensile strength >1200 MPa, yield strength >1100 MPa, and elongation >10%).

8.10.3 Surface roughness and defects

The surface conditions of an as-fabricated AM metal part are influenced by the AM system, feedstock material characteristics (e.g., powder or wire size), scanning pattern or build path, processing parameters, and alloy system. SLM Ti–6Al–4V surfaces generally have $R_a \approx$ 10–25 μm (R_a: roughness average) while SEBM Ti–6Al–4V surfaces are rougher with R_a up to 50 μm, similar to sand casting surfaces. Wire-deposited AM parts have the roughest surfaces. Such rough surface conditions adversely affect the tensile and fatigue properties of the as-fabricated part. They can also be detrimental to the corrosion performance. The excellent mechanical properties of additively manufactured alloys reported in the literature were usually obtained from samples with machined ($R_a \approx$ 1 μm) or polished ($R_a \approx$ 0.1–0.4 μm) surfaces. However, intricate AM metal parts often contain internal walls or channels. Their rough surfaces can be a concern if they are designed for load-bearing applications. Acid etching with or without the assistance of pressure and abrasive fluid machining can be used to improve such internal surfaces.

The most common defects in AM metal parts are gas-entrapped pores and lack-of-fusion features as shown in Fig. 8.36. The internal porosity (Fig. 8.36D) in the feedstock powder can contribute to the final porosity. A study has shown that the use of GA Ti–6Al–4V powder containing 0.27 vol.% of internal porosity resulted in 0.19 vol.% of final porosity in the SEBM Ti–6Al–4V parts, while the use of lower-porosity (0.17 vol.%) GA powder led to lower final porosity (0.11 vol.%). Spherical metal powders produced by wire- and rod-based plasma melting processes, e.g., by the *plasma rotating electrode process*, generally contain much less porosity than GA powders. Other reasons for the formation of AM porosity include (i) the volumetric shrinkage from liquid to solid (e.g., about 8% for Ti–6Al–4V), (ii) the dynamic or volatile liquid flow in the

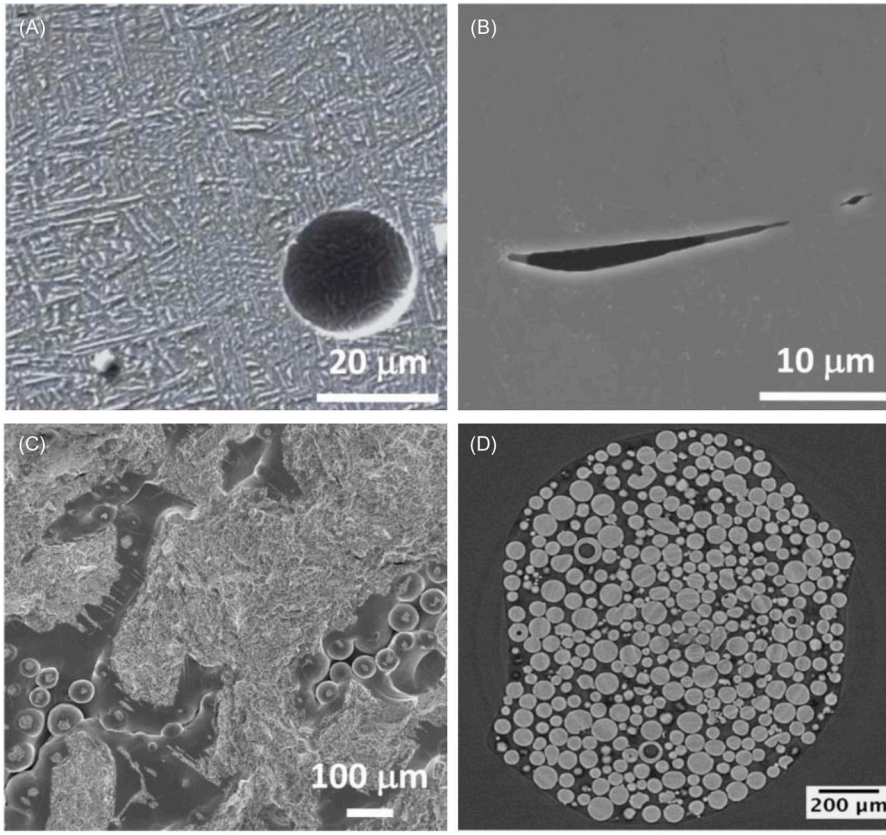


Figure 8.36 Examples of (A) a gas pore and (B) a lack-of-fusion defect in SEBM Ti–6Al–4V. (C) Unmelted Ti–6Al–4V particles observed on a SEBM Ti–6Al–4V tensile fracture surface. (D) Synchrotron X-ray microtomography of internal porosity in GA Ti–6Al–4V particles. Eight out of the 427 particles show internal porosity. (A, B) From Lu, SL *et al.*: *Metall. Mater. Trans. A*, 46, 3824, 2015. (C) From Galarrag, H *et al.*: *Add. Manufacturing*, 10, 47, 2016. (D) From Cunningham, R *et al.*: *JOM*, 68, 765, 2016.

high-temperature melt pool during AM, and (iii) evaporation of low-melting-point alloying elements such as Al in Ti–6Al–4V. The lack-of-fusion defects are more deleterious than gas pores due to their irregular shapes and larger sizes. Their occurrence depends on the AM process as well as the feedstock material used. At present it remains challenging to produce defect-free AM metal parts. Consequently, for fatigue-critical applications, HIP is often used as a remedy to heal or shrink the internal defects. However, research has shown that HIP-shrunk pores in SEBM Ti–6Al–4V can grow and resurface during subsequent

β annealing due to the high internal argon gas pressure. Microcomputed tomography (μCT), synchrotron radiation, and neutron diffraction are advanced technologies for characterization of defects in AM metal parts.

Residual stress is a major concern in the laser AM of large structures. The as-fabricated metal parts can show severe distortion during AM or when unclamped after AM. This remains to be a challenge for the AM of large metal parts. AM by SEBM does not normally have this concern due to the high powder-bed temperature ($\geq 500°C$) that is maintained throughout the SEBM process.

8.10.4 Microstructure and mechanical properties

The melt pool temperature during AM can be well above the liquidus of the alloy. For laser powder deposition of Ti–6Al–4V at the power of 350 W (small power), the peak melt temperature can reach about 2500°C compared to its liquidus of about 1650°C. The maximum cooling rate falls in the range of $(1.0–4.0) \times 10^4\ °C\,s^{-1}$. It is therefore a near rapid solidification process, which leads to fine microstructures and high strengths.

Laser AM metal parts are usually built on a thick metal substrate (the same metal or steel). After fabrication, the part is removed by wire cutting and the substrate is reused until when its thickness is insufficient to counter the distortion or deformation of the next part to be built during the AM process. Since heat transfer occurs primarily via the substrate during AM, columnar grains often develop parallel to the build direction, affected by the alloy chemistry, addition of grain refiners, temperature gradient in the melt pool, and growth rate. AM Ti–6Al–4V typically shows a columnar grain structure, irrespective of the AM process. The solidified metal close to the melt pool is subjected to high cooling rates too (e.g., up to $\sim 6000°C\,s^{-1}$), which result in supersaturated solid solutions (e.g., martensite or massive α phase for Ti–6Al–4V). The successive layers exert a cyclic thermal influence leading to decomposition of the supersaturated solid solution phase or precipitation of second phase particles. The resulting microstructure can vary broadly, depending on both the alloy composition and the AM process. Fig. 8.37 shows several microstructures of AM Ti–6Al–4V obtained from SLM, SEBM, laser powder deposition, and laser wire deposition.

The mechanical properties of AM alloys can exhibit a large degree of scatter and are often anisotropic due to variations in porosity, lack-of-fusion defects, textures, and microstructural inhomogeneity. However, with a proper selection of the AM process and feedstock material, the as-fabricated alloy can achieve tensile properties that are consistently comparable or superior to those of its as-forged state. The same can also happen to the fatigue strength of the alloy in the as-fabricated state (with machined surfaces). Table 8.7 compares the fatigue strengths of AM and non-AM Ti–6Al–4V. The laser wire-deposited Ti–6Al–4V achieved a fatigue strength of 770 MPa ($R = 0.1$), compared to 400–680 MPa for mill-annealed Ti–6Al–4V and 700 MPa for mill-annealed and then solution-treated-and-aged (STA) Ti–6Al–4V.

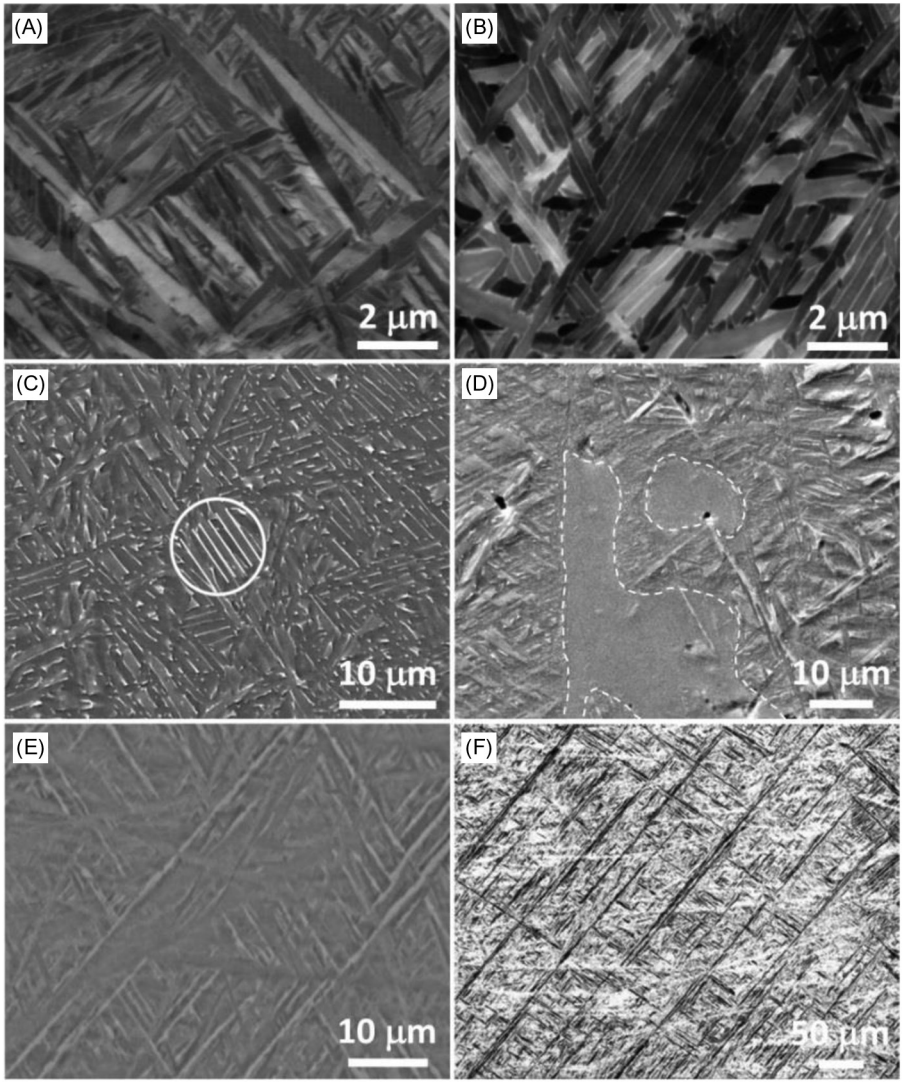


Figure 8.37 Microstructures of AM Ti–6Al–4V. (A) Fully martensitic (α') (SLM) and (B) fully lamellar α/β (SLM). (C) Lamellar α/β, α' and nonlamellar α and β (SEBM). (D) α' + massive α phase (α_m) + lamellar α/β (SEBM). (E) α' + partially decomposed α' (laser powder deposition). (F) α' + partially decomposed α' (laser wire deposition). (A, B) From Xu, W *et al.*: *Acta Mater.*, 85, 74, 2015; (C) from Lu, SL *et al.*: *Metall. Mater. Trans. A*, 46, 3824, 2015; (D) from Lu, SL *et al.*: *Acta Mater.*, 104, 303, 2016; (E) from Qiu, C *et al.*: *J. Alloy Comps.*, 629, 351, 2015; and (F) from Brandl, E *et al.*: *Mater. Des.*, 32, 4665, 2011.

Table 8.7 Fatigue strengths of non-AM and AM Ti–6Al–4V tested at $R = 0.1$

Non-AM Ti–6Al–4V		AM Ti–6Al–4V	
Condition	Fatigue strength at 10^7 cycles (MPa)	AM process	Fatigue strength at 10^7 cycles (MPa)[#]
Cast	200–360	SEBM	Building direction: 390 Horizontal plane: 450
Cast + HIP	520	SLM, stress relieved at 650°C for 4 h	400–510
Mill-annealed	400–680	Laser powder deposition	≥600
Solution treated and aged (STA)	700	Laser wire (1.2 mm diameter, 0.045% O) deposition	770–790

[#]Best fatigue strength data reported in literature. Machined surfaces for all samples.

Post-AM heat treatments can reduce or eliminate the residual stresses, change the microstructure, mitigate the degree of anisotropy, and enhance the mechanical properties. Owing to the high powder-bed temperature (e.g., 500–730°C) that can be used in the SEBM process, SEBM-fabricated metal parts do not normally need post-AM heat treatments, while laser AM parts need to be heat treated in most cases. HIP can heal or shrink internal defects including the gas-entrapped pores and lack-of-fusions defects. The resulting tensile and fatigue properties can satisfy the minimum requirements for forged or extruded products. In the case of Ti–6Al–4V, the columnar grains can also be converted into equiaxed grains by post-AM annealing or HIP above the β-transus temperature.

FURTHER READING

Evans, AG: Lightweight materials and structures, *MRS Bull.*, 26(10), 790, 2001.

Vogelesang, LB, Schijve, J and Fredell, R: Fibre-metal laminates: damage tolerant aerospace materials. In Demaid, A and de Wit, JHW, (Eds.): *Case Studies in Manufacturing with Advanced Materials,* Vol. 2, Elsevier Science B.V., Holland, 1995,

Vlot, A: *Glare: history of the development of a new aircraft material*, Kluwer Academic Publications, Dordrecht, The Netherlands, 2001.

Wu, G and Yang, J-M: The mechanical behaviour of GLARE laminates for aircraft structures, *JOM*, 57(1), 72, 2005.

Allison, JE and Cole, GS: Metal–matrix composites in the automotive industry: opportunities and challenges, *J. Metals*, 45(1), 19, 1993.

Shercliff, HR and Ashby, MF: Design with metal–matrix composites, *Mater. Sci. Tech.*, 10, 443, 1994.

Lloyd, DJ: Particle reinforced aluminium and magnesium metal–matrix composites, *Inter. Mater. Rev.*, 39, 1, 1994.

Ashby, MF, Evans, AG, Fleck, NA, Gibson, LJ, Hutchinson, JW and Wadley, HNG: *Metal Foams: A Design Guide*, Butterworth Heinemann, Oxford, 2000.

Banhart, J: Manufacture, characterization and application of cellular materials and metal foams, *Progr. Mater. Sci.*, 46, 559, 2001.

Lavernia, EJ, Ayers, JD and Srivatsan, TS: Rapid solidification processing with specific application to aluminium alloys, *Inter. Mater. Rev.*, 37(1), 1, 1992.

Inoue, A: Amorphous, nanoquasicrystalline and nanocrystalline alloys in Al-based systems, *Progr. Mater. Sci.*, 43, 365, 1998.

Suryanarayana, C, Froes, FH and Rowe, RG: Rapid solidification processing of titanium alloys, *Inter. Mater, Rev.*, 36(3), 85, 1991.

Lieberman, HH, (Ed.): *Rapidly Solidified Alloys*, Marcel Dekker, New York, NY, USA, 1993.

Suryanarayana, C: Mechanical alloying and milling, *Progr. Mater. Sci.*, 46, 1, 2001.

Inoue, A: High-strength aluminium alloys containing quasicrystalline particles, *Mater. Sci, Eng.*, A286, 1, 2000.

Gleiter, H: Nanocrystalline materials, *Progr. Mater. Sci.*, 33, 223, 1989.

Gleiter, H: Nanostructured materials: basic concepts and microstructure, *Acta Mater.*, 48(1), 2000.

Valiev, RZ, Islamgaliev, RK and Alexandrov, IV: Bulk nanostructured materials from severe plastic deformation, *Progr. Mater. Sci.*, 45(2), 103, 2000.

Froes, FH, Suryananayana, C and Eliezer, D: Review: synthesis, properties and applications of titanium aluminides, *J. Mater. Sci.*, 27, 5113, 1992.

Kim, Y-W Wagner, R, and Yamaguchi, M, (Eds.): *Gamma Titanium Aluminides*, TMS, Warrendale, PA, USA, 1995.

Camm, G and Koçak, M: Progress in joining of advanced materials, *Inter. Mater. Rev.*, 43(1), 1, 1998.

Chen, G, Peng, Y, Zheng, G, Qi, Z, Wang, M, Yu, H, Dong, C and Liu, CT: Polysynthetic twinned TiAl single crystals for high-temperature applications, *Nature Mater.*, 15, 876, 2016.

Qian, M, Xu, W, Brandt, M and Tang, HP: Additive manufacturing and post-processing of Ti–6Al–4V for superior mechanical properties, *MRS Bull.*, 41(10), 775, 2016.

Beese, AM and Caroll, BE: Review of mechanical properties of Ti–6Al–4V made by laser-based additive manufacturing using powder feedstock, *JOM*, 68(3), 724, 2016.

Bian, L, Thompson, SM and Shamsaei, N: Mechanical properties and microstructural features of direct laser-deposited Ti–6Al–4V, *JOM*, 67(3), 629, 2015.

Xu, W, Brandt, M, Sun, S, Elambasseril, J, Liu, Q, Latham, K, Xia, K and Qian, M: Additive manufacturing of strong and ductile Ti–6Al–4V by selective laser melting via in situ martensite decomposition, *Acta Mater.*, 85, 74, 2015.

APPENDIX

Table A.I Unit conversion factors

Property	To convert B to A multiply by	SI units (A)	Non-SI units (B)	To convert A to B multiply by
Mass	0.4536	Kilogram (kg)	Pound (lb)	2.204
	0.4536×10^{-3}	Tonne	lb	2204
	1.0163	Tonne	UK ton	0.9839
Stress	6.894×10^{-3}	Megapascal (MPa) (Meganewtons per square metre)	Pounds force per square inch (psi)	145.04
	15.444	MPa	UK tons force per square inch (tsi)	6.475×10^{-2}
	9.8065	MPa	Kilograms per square millimetre ($kg\ mm^{-2}$)	0.10197
Fracture toughness	1.0989	Megapascal $(metre)^{1/2}$ ($MPa\ m^{1/2}$)	Kilopounds force per square inch $(inch)^{1/2}$ ($ksi\ in^{1/2}$)	0.91004
Thermal conductivity	4.1868×10^{2}	Watts per metre per kelvin	Calories per centimetre per second per degree Celsius	2.3885×10^{-3}
Specific heat capacity	4.1868×10^{3}	Joules per kilogram per kelvin ($J\ kg^{-1}\ K^{-1}$)	Calories per gram per degree Celsius	2.3885×10^{-4}

INDEX

Note: Page numbers followed by "*f*" and "*t*" refer to figures and tables, respectively.

Abundance of elements in earth's crust, 6–7
Additive manufacturing (AM), 395, 404–406, 429–430, 457–459, 505–513
  defects, 509–511
  fatigue strengths, 513*t*
  mechanical properties, 511–513
  metal powder and wire for, 506–508
  microstructure, 511–513
  press-and-sinter process, 434
  surface roughness, 509–511
Adhesive bonding of aluminium, 219–220, 237, 239
Aerospace/aircraft
  aluminium alloys in, 191, 194–195, 197, 202–209, 219, 228–233, 279–282, 284
  composites in, 461, 466
  helicopters, 216, 324–326, 331, 450
  magnesium alloys in, 299*t*, 325*f*, 326, 331, 353, 362–363
  RSP alloys in, 481–482
  titanium alloys in, 384–386, 391–396, 404–405, 419–422, 436, 446–451, 505
Age- (precipitation-) hardening
  of aluminium alloys
    age softening, 183
    ageing processes, 60*t*–62*t*, 68–79, 172–174
    artificial ageing, 48, 77, 79, 103*f*
    cast alloys, 279, 284
    clustering phenomena, 55–56, 60–61, 69–71, 188, 198
    GP zones solvus, 49–52, 198
    GPB zones, 60, 73, 73*f*
    Guinier-Preston (GP) zones, 46–49, 51, 56–57, 60–61, 68–69, 73–74, 76, 78, 102, 172, 198
    hardening mechanisms, 56–67, 71
    intermediate precipitates, 46*f*, 74–76
    interrupted ageing, 47–49, 77–79, 193
    microalloying (trace element) effects in, 49, 51–56, 67, 188–191, 200
    natural ageing, 48, 52, 191, 221
    secondary precipitation and hardening, 76–79, 172–173, 193, 193*t*, 213, 279–280, 323
  decomposition of supersaturated solid solutions, 45–49
  of magnesium alloys, *294–295*, 296*t*, 302*t*, 303–307, 313–318, 321–332, 336, 348–349, 352, 354–355
  precipitate-free zones at grain boundaries, 50–51, 50*f*, 58–59, 101, 198
  of titanium alloys, 376–379, 387–393, 401–424
Alkali metals, 1
  in aluminium –lithium alloys, 211
Allotropic transformation in titanium, 369

Alloy designations
of aluminium alloys
cast alloys, 266–268
wrought alloys, 173–178, 185*t*–186*t*
of magnesium alloys
cast alloys, *295*, 296*t*–297*t*
wrought alloys, *295*, 298*t*–299*t*
of titanium alloys, 370–375
Alpha (α) stabilizers in titanium, 374, 380
Alpha (α) case in titanium, 424
Aluminium-air batteries, 258–261
Aluminium-ion batteries, 261–262
Amorphous alloys, 487–490
Annealing of
α–β titanium alloys, 397–400
aluminium alloys, 43–45, 43*f*
Anodizing
aluminium alloys, 79, 197, 219–220, 452
magnesium alloys, 358
ARALL laminate, 462–463
Architecture, building and construction, 242, 455
Atom probe field ion microscopy, 46–47, 52, 189, 349
Automobiles
brazed heat exchangers, 226–227
cast aluminium alloys in, 148, 279*f*, 282
cast magnesium alloys in,283, 307–309, 312–315, 326, 328–329, 361–364
metal matrix composites in, 470–471, 471*t*
use of aluminium alloys in North America, 1975–2015, 234
wrought aluminium alloys in, 183, 195, 197, 234–240
wrought titanium alloys in, 452–453

Bauxite, 12, 15–16, 19*f*
Bayer process for producing alumina, 16–17
Bearings in aluminium alloys, 184, 251–253
Beryllium
effect on oxidation resistance of cast Al-Mg alloys, 285
Lockalloy (AlBeMet™ 162), 4–6
physical properties, 2, 5*t*
preparation, 6
stiffness, 1–2, 5*t*
uses, 2–4, 6
Beta fleck defects in titanium, 419
Beta (β) stabilizers in titanium, 374, 413–415
Biomaterials
magnesium alloys in, 365
titanium alloys in, 422–424, 455–459
Bismith in
aluminium alloys, 188, 198
magnesium alloys, 288*t*
Blistering in aluminium alloys, 168, 169*f*
Boron in grain refinement of aluminium alloys, 123–125, 160
Bottle caps, 180, 184
Brazing in
aluminium alloys, 173–174, 180, 226–227, 286
titanium alloys, 433
Brucite as magnesium source, 22

Cadmium
in aluminium alloys, 52, 188
solid solubility in
aluminium, 32*t*
magnesium, 288*t*
Calcium
in magnesium alloys, 288, 291*f*, 292*t*, 295, 296*t*, 300*t*, 312, 314*t*, 316*f*, 338*f*, 339, 346–347, 349
in superplastic aluminium alloy, 254
Canstock in wrought aluminium alloys, 12, 88, 161, 182, 243–245
Carbon in titanium alloys, 389–390, 406, 419
Carnallite as magnesium source, 22
Casting processes, 109, 131–132, 134–135, 139–149, 154–155, 159–163
Ablation, 149
Alusuisse, 162
application of external fields, 150–155
castability, 127–131
compocasting, 142
Cosworth, 146–147, 146*f*, 147*f*
direct-chill (DC), 154, 159–161, 255
graphite mould casting of titanium alloys, 436–437
gravity and low-pressure casting processes, 144–145

Hazelett, 162–163
high pressure die casting, 134–139, 307–315
Hunter, 161*f*
ILP (improved low pressure), 148
investment casting of titanium alloys, 436–437, 455
melt conditioning, 132–134
permanent mould (gravity die) casting, 144, 268, 271*t*–272*t*, 276, 282, 284–285, 296*t*–297*t*
pressure die, 129, 134–139, 268, 285, 296*t*–297*t*, 361–365
Properzi, 161*f*, 256
rheocasting, 139
sand casting, 145–148, 266, 268, 276, 283*f*, 285, 296*t*–297*t*
semi-solid, 139–142, 154
squeeze casting, 141–143
strip casting of magnesium alloys, 154–155
thixomolding, 139–140, 141*f*, 142
T-Mag process, 148–149, 149*f*
ultrasound and magnetic fields, 151–153
Cathodic protection by
aluminium alloys, 83, 359
magnesium alloys, 359
Chill crystals, 112
Clinching, 239
Coarse intermetallic (constituent) particles
in wrought aluminium alloys, 35–36, 44, 88–90, 89*f*, 91–93, 91*f*, 214
Cobalt
in powder metallurgy aluminium alloys, 186*t*, 248*t*
solid solubility in aluminium, 32*t*
Cold working of titanium alloys, 426–427
Cold-chamber machines, 135, 138–139
Commercially pure titanium, 27, 370–374, 381–384, 425–430, 442–455
Commonwealth Scientific and Industrial Research Organisation in Australia (CSIRO), 148–149
Composites, 461–474
laminated composites, 461–464
metal matrix composites, 466–474
sandwich panels, 464–466
Constitutional supercooling. *See* Constitutional undercooling
Constitutional undercooling, 111–114, 114*f*, 122
Consumable-electrode arc furnace, 27, 27*f*
Consumption of light metals, 8–11, 10*f*, 363
Continuous casting of aluminium alloys, 161–163
Corrosion
in cast aluminium alloys, 271*t*, 272*t*, 285
cavitation, 85–86
cladding of sheet, 83–84, 166–167, 167*f*, 169, 177, 191, 252, 252*f*
conversion coatings, 79–80
crevice, 85, 443
dissimilar metals, contact with, 80–82
electrode potentials, 81, 81*t*, 82, 82*t*
exfoliation (layer) corrosion, 83, 84*f*, 203–204
filiform, 85
in magnesium alloys, 291, 292*t*–293*t, 294*, 307, 314*t*, 322, 322*t*, 356–359, 484
pitting, 80, 82–83, 83*t*, 444
in rapidly solidified alloys, 484*f*
in titanium alloys, 369, 441–443, 451–455
waterline corrosion, 86
in wrought aluminium alloys, 79–87
Corrosion fatigue in
aluminium alloys, 104, 191
clad alloys, 191
titanium alloys, 445–446, 452
Cosworth process, 146–147, 146*f*, 147*f*
Creep age forming (CAF) of aluminium alloys, 231
Creep forming of titanium, 425–426
Creep in
aluminium alloys, 104–106, 105*f*, 188, 190*f*, 191, 194–195, 214, 247
magnesium alloys, 291, 304–314, 308*f, 318–321*, 324, 326, 328–332, 473
titanium alloys, 375*f*, 379–391, 389*f*, 399–400, 425–426, 437
Crystal bar process for production of titanium, 25

Deformation (transition) bands in rolled aluminium alloys, 34–35, 35*f*
Degassing of molten
  aluminium alloys, 157–159, 477
  magnesium alloys, 133–134
Die soldering during die casting, 135–136, 139
Diffusion bonding of titanium alloys, 426, 432–433, 446–447, 450–451
Diffusion coefficients of elements in aluminium, 163
Direct chill cast (DC cast), 124, 159–161, 160*f*
Directionality of grain structure in
  cast aluminium alloys, 143, 148
  wrought aluminium alloys, 86–87, 87*f*, 90, 101–102
Discontinuous (cellular) precipitation in
  magnesium–aluminium alloys, 304–306
  titanium alloys, 408–410
Dispersoids in wrought aluminium alloys, 88, 92–93, 95–96, 164, 164*f*, 170–171
Dolomite as magnesium source, 22
Duralcan metal matrix composites, 467–468
Duralumin, 191, 202

Earing of aluminium alloy sheet, 41–42, 42*f*, 244
Electric storage batteries, 258–262, 259*f*
Electrical conductor aluminium alloys, 181*t*, 182, 184, 256–258, 257*f*
Electron backscattered diffraction (EBSD), 41, 338*f*
Elfinal process, 125–126
Equal angular extrusion (ECAE), 495
Equal channel angular pressing (ECAP), 495
Erbium in titanium alloys, 485
Eutectic solidification, 120–121
Eutectoid-type β-stabilizers in titanium, 374–375, 391–393, 409, 413–445, 485
Extrudability
  magnesium alloys, 344–346
Extrusion
  of aluminium alloys, 87, 98, 165–166, 166*f*, 181*t*, 187*t*, 195, 197, 230, 247
  of magnesium alloys, 333, 343–356
  of powder alloys, 247, 251, 477–478, 483
  recrystallized grains at surface of, 86–87, 165–166, 166*f*

Fatigue
  aluminium alloys, 94–99, 94*f*, 96*f*, 98*f*, 143, 173, 193, 194*f*, 280–282, 281*f*
  clad aluminium alloy sheet, 191
  effects of thermomechanical processing, 96, 97*f*, 173
  fretting damage, 440
  magnesium alloys, 349–350
  metal matrix composites, 473, 473*f*
  rapidly solidified alloys, 483*f*
  squeeze cast alloys, 143, 473
  steel, 94*f*
  titanium alloys, 383, 388–390, 394–395, 394*t*, 399–401, 417–418, 429*t*, 436*f*, 438–440
  welded aluminium alloys, 222, 223
Fluidity in cast aluminium alloys, 128–129
Fluxes
  brazing aluminium alloys, 226
  melting of aluminium alloys, 159
  melting of magnesium alloys, 132–134, 321–322
Foams metallic, 474–477
Foil, wrought aluminium alloys in, 157, 181*t*, 182, 245–246
Forgings of
  aluminium alloys, 87, 143, 168, 170, 187*t*, 188, 203
  magnesium alloys, 356
  titanium alloys, 384–391, 394–395, 394*f*, 400, 413, 424, 425*t*
Formability
  magnesium alloys, 333–343
Forming limit curves for
  aluminium alloy sheet, 39–40, 40*f*
  magnesium alloy sheet, 341–343

Gadolinium in magnesium alloys, 288*t*, *321f*, 323–324, 329–330, 340*t*, 341, 353–355
Galling in titanium alloys, 425–426, 430, 440

Gallium in
aluminium alloys, 201–202, 260
titanium alloys, 370–374, 381
Gas solubility
hydrogen in
aluminium, 157, 168
magnesium, 133–134
titanium, 374–375, 379–381, 386, 406, 419, 426, 434–435
GLARE laminate, 462–464
Global warming potential (GWP), 133
Grain formation
grain growth and morphology, 117–120, 117*f*, 118*f*
nucleation of primary phase, 115–117
Grain refinement of
aluminium alloys, 84
influencing factors, 121–123
magnesium alloys, 291–294
by refinement methods and inoculation with master alloys, 123–127
Gravity and low-pressure casting processes, 144–145
Guinier-Preston zones (GP zones), 46
in age hardening, 46, 54–56, 68, 70–71
in aluminium alloys, 33*f*, 46–49, 54, 57, 69
in magnesium alloys, 300*t*–302*t*, 306–307, 322–323, 332

Hall–Héroult process of aluminium production, 17–21
Hall–Petch effect in α-titanium alloys, 382
Hardenability effects in titanium alloys, 396, 415–419
Hazelett process for thin slab casting of aluminium alloys, 162–163
Heat exchangers
brazed aluminium alloys in automobiles, 227
titanium alloys in, 384, 451–452
Heat treatment, 136–138
High-pressure die castings (HPDC), 119–120, 134–139
aluminium alloys, 134–135, 143*t*
die soldering, 135–136
heat treatment, 136–138
magnesium alloys, 138–139, 138*f*
Homogenization of aluminium alloys, 163–165, 243
Hot cracking during extrusion, 345–346
Hot isostatic pressing (HIP), 433–437, 504
Hot shortness. *See* Hot cracking during extrusion; Hot tearing
Hot tearing, 130–131, 130*f*
during solidification, 265, 312
Hot working of titanium alloys, 424–426
Hunter process
production of titanium, 25
strip casting of aluminium alloys, 161*f*
Hydride formation in
magnesium alloys, 326–327
titanium alloys, 381, 439, 445
Hydrogen, embrittlement of
aluminium alloys, 102, 211
titanium alloys, 381, 426, 434–435, 439, 445

Ilmenite as titanium source, 26
ILP (improved low pressure) casting process, 146, 148, 148*f*
Indium in aluminium alloys, 52, 201–202, 260
Intercrystalline cracking of aluminium alloys, 83–84, 83*f*, 84*f*, 201–202, 202*f*
Interfacial segregation of solutes, 75, 75*f*, 139, 190*f*, 217, 217*f*
Ion plating of titanium alloys, 431, 442
Isomorphous β-stabilizers in titanium, 374–376, 409–415, 443

Kroll process for production of titanium, 25

Lead in aluminium alloys, 188, 198, 248, 253
Liquation (overheating), of aluminium alloys, 167–168, 168*f*, 201
Lithium-containing
aluminium alloys, 209–219
magnesium alloys, 291*f*, 298*t*, 336–337, 337*f*, 341*f*
Lüders bands (stretcher strain markings)
in aluminium alloy sheet, 42–43, 183, 235–236

Machining of
aluminium alloys, 188, 198, 283, 286
magnesium alloys, 360
titanium alloys, 429–431
Magnesite as magnesium source, 22
Magnesium alloys, 110
deformation modes, 288–290
extrudate, 343–356, 347*f*
grain refinement in, 125–127, 126*f*, 127*f*
HPDC, 138–139, 138*f*
melting, 132–134
sheet, 334–343
Martensite
in magnesium alloys, 365–366
in titanium alloys
hexagonal α′-phase, 380, 387, 401–405, 404*f*, 411*f*, 428*f*, 500
lath martensite, 401–403, 404*f*
orthorhombic (α″) martensite, 404–405, 404*f*, 409, 411–412, 423
tempering (ageing), 408–409
twinned martensite, 404*f*, 408–409
Massive transformations in titanium alloys, 377, 382, 396–406, 511–512
Mechanical alloying, 491–493
Melt conditioning, 150–151
Melt injection temperature, 136
Melt spinning, 477–478, 484–485, 487
Melting and casting of
aluminium alloys, 132, 157–161
magnesium alloys, 132–134
titanium alloys, 27, 436–437
Metal hydride reduction process for producing titanium powder, 434–435
Metal matrix composites, 466–474
aluminium alloys, 466–472
magnesium alloys, 472–474
titanium alloys, 474
Military equipment, 184, 199, 455
Modification of aluminium–silicon alloys, 274–278

Nanophase alloys, 494–497
Niobium in titanium, 379, 389, 410, 419, 422–424, 443
Nitinol, 423
Nucleation-free zone (NFZ), 116–117

O phase in rapidly solidified aluminium alloys, 481
Omega (Ω) phase in aged aluminium alloys, 55, 188–191, 189*f*, 190*f*, 284–285
Omega (ω) phase in titanium alloys, 409–412, 415–420, 422–423
Orange peeling of aluminium alloy sheet, 42, 45
Ordering in α-titanium alloys, 380, 386, 388, 390–391

Packaging, wrought aluminium alloys in, 9–10, 10*f*, 13, 182, 243–246
Paint bake cycle for aluminium alloy automotive sheet, 236
Palladium in titanium, 374, 381–384, 442–443
Partitioning of elements in titanium alloys, 380, 411–412
Peening of aluminium alloy welds, 223
Phosphorus in aluminium–silicon alloys, 274–275, 283, 284*f*
Physical properties of metals, 5*t*
Physical vapor deposition (PVD), 431, 493–494
π-phase in cast Al–Si–Mg alloys, 280
Pidgeon process for magnesium production, 22, 24
Plasma nitriding of titanium alloys, 431
Plate. *See* Sheet and plate
Porosity in cast aluminium alloys, 129–130
Portevin Le Chatelier effect, 42–43
Positron annihilation spectroscopy, 76, 77*f*
Powder metallurgy
aluminium alloys, 246–251, 248*t*, 249*f*
atomization of powders, 246, 250–251, 250*f*, 434, 478, 480*f*, 488–489
titanium alloys, 433–434
Precipitate shearing by dislocations, 57–60, 210–211, 216–218
Precipitation processes in
aluminium alloys. *See* Age-(precipitation-) hardening
magnesium alloys, 294–295, 300*t*–302*t*, 304–307, 316–319, 321–332
Production of
aluminium, 7*f*, 9, 15–21, 18*f*, 19*f*, 20*f*

magnesium, 21–24
titanium, 10–11, 25–28
Properzi process, 161*f*, 256

Q-phase in Al–Mg–Si–Cu alloys, 198
Quasicrystals, 485–487
Quench sensitivity, 170–172, 171*f*, 197, 200–203, 207, 230, 469
Quenching of
titanium alloys, 391, 401–408, 413–419
wrought aluminium alloys, 169–172, 197, 203

Rapid solidification processing (RSP), 477–485
Recycling of light alloys, 8, 11–15, 12*f*, 13*t*, 14*f*, 235, 243
Retrogression and reageing (RRA), 205–206, 206*f*
Rheocasting, 139
Rivets and riveting, 175, 191, 219, 237, 450–451
Rolling of magnesium alloys, 334–335
Ruthenium in titanium, 442
Rutile as titanium source, 25
R-values in sheet, 39, 41, 342–343, 429

Sand and precision sand casting processes, 145–148
Cosworth process, 146–147, 146*f*, 147*f*
ILP process, 148, 148*f*
low-pressure die casting machine, 144*f*
sand casting, 145–146
Scandium in
aluminium alloys, 56, 219
magnesium alloys, 288*t*, 291*t*, 324, 365–366
Sea water as magnesium source, 22
Segregation in titanium alloys, 419–420, 485
Semi-solid casting of
aluminium alloys, 139–142
magnesium alloys, 142
Shape memory
in magnesium alloys, 365–366, 365*f*
in titanium alloys, 423, 456–457
Shear bands in rolled aluminium alloys, 34–35
Sheet and plate
aluminium alloys, 92–93, 169, 175–184, 181*t*, 187*t*, 191, 195, 228, 230, 232, 234–242
canstock, 243–245
magnesium alloys, 298*t*–299*t*, 334–343
roll cladding of aluminium alloys, 166–167
strip casting of sheet, 154–155, 162–163, 162*f*
superplastic alloys, 253–256, 426
titanium alloys, 424–427, 432, 455
welding of thin sheet, 220–221
Shipping, 240–242
Short transverse direction in wrought
aluminium alloys, 86–87, 87*f*, 90–91, 100–101, 192*t*, 195*f*, 208*f*
titanium alloys, 427–428
Silver
in magnesium alloys, 330–331
microalloying effects in aged aluminium alloys, 52, 54, 188–191, 204–205, 248, 284
Sodium
in aluminium–lithium alloys, 211, 212*f*
modification of cast aluminium–silicon alloys, 274–275
Soldering of aluminium alloys, 227
Solid solubility of elements in
aluminium, 60
magnesium, 288*t*
rapidly solidified alloys, 479*t*
titanium, 370–374
Solid solution strengthening in
aluminium alloys, 31, 34*f*, 36, 180
magnesium alloys, 295, 304*f*
titanium alloys, 380, 386, 395*t*, 434–435
Solidification of light alloys, 109–121
Solute clustering in
aluminium alloys, 69–71
magnesium alloys, , 294–295, 303, 300*t*–301*t*
Solution treatment of
aluminium alloys, 45, 51, 69, 167–169, 174, 197
magnesium alloys, 316, 326, 327*t*, 330, 352, 354
titanium alloys, 371*t*–372*t*, 387, 391, 406, 415

Spray forming (Ospray process) of aluminium alloys, 250–251
Squeeze casting of
  aluminium alloys, 142–143
  direct squeeze casting, 142
  magnesium alloys, 473
Stiffness of materials
  composites, 461–474
  metals and alloys, 1–2, 2*f*, 4*f*, 209–210
Strength/density relationships for engineering materials, 3*f*
Stress-corrosion cracking
  cast Al–Mg alloys, 285
  effects of aging in aluminium alloys, 172, 198–207
  magnesium alloys, 335, 358
  mechanism in aluminium alloys, 83*f*, 99–103
  powder metallurgy aluminium alloys, 248
  relationship to grain direction, 86–87, 87*f*
  titanium alloys, 443–445
  welded Al–Zn–Mg alloys, 198–202, 201*f*, 202*f*
  wrought aluminium alloys, 193, 195, 195*f*, 202–209, 203*f*, 208*f*, 218
Strontium in
  cast Al–Si alloys, 273*f*, 276
  magnesium alloys, 288*t*, 296*t*, 312, 314*t*
Superconductivity in
  amorphous alloys, 490
  magnesium-boron alloy, 365
  titanium alloys, 410, 422–423
Superplasticity
  in aluminium alloys, 253–256, 255*f*, 256*f*
  in nanophase alloys, 495
  in titanium alloys, 423–424, 426
Surface treatment
  of aluminium alloys, 80, 223
  of magnesium alloys, 358–359
  of titanium alloys, 431

T1 precipitate in Al–Cu–Li alloys, 214, 215*f*
Temper designations
  cast aluminium alloys, 266–268
  magnesium alloys, 295–303, 296*t*–297*t*
  wrought aluminium alloys, 173–178
Tempering (ageing) of titanium martensites, 408–409
Textures in
  aluminium alloys, 40–42, 42*f*, 244, 244*f*
  magnesium alloys, 333, 337–341, 353–354
  titanium alloys, 427–428, 439
Thermomechanical treatment of wrought
  aluminium alloys, 206, 255
  magnesium alloys, 179*t*
Thixmolding
  of aluminium alloys, 139
  of magnesium alloys, 140, 142
Titanium alloys, 369
  in aerospace, 419–422, 446–451
  aluminium equivalent, 380–381
  in dental and medical applications, 395, 422–424, 455–458
  diffusion of alloying elements, 377–379
  in general applications, 451–455
  heat treatment, 376–379, 386–392, 396–413, 415–419
  molybdenum equivalent, 385, 415
  self-diffusion, 377–379
Titanium aluminides, 437, 485, 497–505
Titanium in grain refining aluminium alloys, 124–125
Toughness and fracture toughness in
  aluminium alloys, 90–94, 191–193, 192*f*, 192*t, 193t*, 207–208, 211, 274
  composites, 463, 468, 473
  magnesium alloys*, 348*, 349*t*
  rapidly solidified alloys, 482–483
  titanium alloys, 383, 413, 428, 440–441, 453, 502–503
Turbine blades
  gas turbines, 384, 446–448
  steam turbines, 446, 452
Twinning in magnesium alloys, 289*f*, 290, 295, 333–334, 343, 347, 355
Twin-roll casting of magnesium, 154–155, 155*f*

Ultrasonic treatment, 116, 151–152
Ultrasound fields, 151–153
US Space Shuttle fuel tank, 218, 218*f*

Volumetric shrinkage in cast aluminium alloys, 129

Wall crystals, 112, 116
Welding of
  aluminium alloys, 153, 155–156, 198–202, 220–226
    friction stir welding, 224–225, 224*f*
    laser welding, 225
    metal inert gas (MIG) arc welding, 220–223, 221*f*
    TIG dressing of welds, 223
    tungsten inert gas (TIG) arc welding, 220–223, 221*f*
    'white zones' adjacent to welds, 201, 202*f*
  magnesium alloys, 360–361
  titanium alloys, 431–432
Widmanstätten microstructure in titanium alloys, 382, 383*f*, 387, 400, 412
Work (strain) hardening of wrought aluminium alloys
  non-heat-treatable alloys, 178–184
  secondary effects, 42–43
  strain-hardening characteristics, 36–39, 37*f*, 39*f*
  substructure hardening, 38–39
  textures, 41–42, 244
  work-hardening exponent, 37

Z phase in aged Al–Cu–Mg–(Ag) alloys, 55–56
Zirconium
  in aluminium alloys, 123*t*, 125, 171*f*, 185*t*, 186*t*
  in magnesium alloys, 123*t*, 126–127, 126*f*, 127*f*, 288*t*, 291–294, 293*t*, 297*t*–299*t*, 319–332, 340*t*, 345, 345*t*, 348–349, 353–355
  in titanium, 374–389, 409, 418–422, 490, 506